AIT Series

Trends in earth observation

Volume 3

Earth Observation: current challenges and opportunities for environmental monitoring

Edited by

Associazione Italiana di Telerilevamento (AIT)

Earth Observation: current challenges and opportunities for environmental monitoring

---

Edited by

Associazione Italiana di Telerilevamento (AIT)

AIT Series: Trends in earth observation

Volume 3 - Published in November 2024
Edited by Associazione Italiana di Telerilevamento (AIT)
Published on behalf of the Associazione Italiana di Telerilevamento (AIT)
Via Lucca 50
50142 Firenze, Italy

ISSN 2612-7148
ISBN 978-88-944687-2-4
DOI: 10.978.88944687/24
AIT Series “Trends in earth Observation” is indexed in Scopus and Web of Science

All contributions published in the Volume “Earth Observation: current challenges and opportunities for environmental monitoring” were subject to blind peer review from independent reviewers.
Publication Ethics and Publication Malpractice Statement
Editors, Reviewers and Authors agreed with Publication Ethics and Publication Malpractice Statement

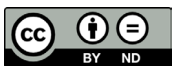

Preface

Since its foundation 1986, the Italian Society of Remote Sensing (Associazione Italiana di Telerilevamento – AIT) has been engaged in the dissemination of knowledge of remote sensing and Earth Observation (EO), with a particular effort in fostering scientific and operational consciousness about their exploitation.

AIT is specifically committed to:

(i) create a network connecting people from Research, Academia, hi-tech Companies, Administrative Institutions and Professionals involved in territory management and involved, or interested, in the development of Earth Observation methods, techniques and applications;

(ii) promote and coordinate initiatives to foster the exploitation and the technology transfer of remote sensing technologies, like the organization of congresses, conferences, workshops and thematic Summer/Winter schools;

(iii) promote the exchange of knowledge and cooperation among its members to "shorten" the technology transfer chain;

(iv) serve as the Italian national representative and reference player on matters pertaining to remote sensing and Earth observation-related issues for institutions, agencies, and companies, at the national and international levels;

(v) maintain an ongoing observation of technological and scientific advances, with particular attention to datasets, products and services from open, or commercial archives, to ensure a conscious and proper exploitation by users;

(vi) draft guidelines for the definition of possible standards about data quality, data processing, validation methods and accuracy metrics related to EO.

As AIT President for 2023-26, I specifically encouraged the Executive Board to focus on points (iv-vi), whose inner meaning have to be better specified.

Concerning point (iv), the 2023 AIT Congress, from which the contributions of this volume were derived, made evident the high expectations that Institutional players have in respect of the EO scientific community, especially related to the ongoing post-pandemic Italian National Plan for Recovery and Resilience (PNRR). The newly programmed Italian IRIDE Program for EO, supported by ASI and ESA, and the various territorial needs discussed along the congress sessions, definitely highlighted the strategic role of EO in this framework.

Discussions at the 2023 AIT Congress also highlighted we are experiencing a too-fast technology advancement, paradoxically slowing down the technology transfer. In fact, low-cost and user-friendly tools are continuously made available, providing users with the illusion of operational autonomy despite their domain knowledge is low or non-existent. This situation makes it extremely difficult to recognize applications based on a solid and proved EO-, or more generally, Geomatics-related knowledge, thus introducing a high degree of unreliability of results and deductions, especially when quantitative measures are required.

The EO and Geomatics scientific communities may have reacted too slowly and disjointedly to this phenomenon and now need to regain a new role in supporting a proper (reliable) technology transfer. I retain that the main reason about this failure relays on the new and reverted relationship linking the Applied Sciences with the technological market. Today, more than ever, technology often anticipates applied sciences requirements, proposing solutions to problems that have yet to be solved. The feeling is that scientists and scholars are currently being asked to go back along the supply chains to obtain proper technical specifications needed to consciously experience new devices (or products and services) and test them under the right conditions. In most of the cases, they are also called to find a suitable and valuable application that the newly proposed low-cost technology can be useful for.

A further, recent new challenge is coming from the unstoppable introduction of Artificial Intelligence in our life, including EO and Geomatic processes. The 2023 AIT Congress proved that the EO context is one of the mostly involved sectors from this point of view. But, is this really healthy for Science? Is this safe for a sustainable development? AIT opinion is that scientific societies and Academia are called to slow down this trend where an immediate exploitation of new continued technological advances has to come. A new paradigm has to be introduced where the ongoing "continuous" technology transfer has to move to a "discrete" one. This means that, at the application level, the technological (and algorithmic) level have to be fixed at a certain point and reconsidered/updated after a time step consistent with the time of: (i) engineering of processes; (ii) definition of controlled (by reference subjects) procedures for both data processing and validation of results; (iii) validation of global data/services at the local level. This would permit a proper ingestion and exploitation of the technological advances that we are ordinarily stimulated about, and a proper development of users' consciousness needed to prepare a more effective advance in the next evolution step. AIT, under my leadership, supports a SLOW, but conscious, SCIENCE.

In this framework, AIT supports open and wide-ranging actions involving multiple players and scientific associations at national and international levels. Among these actions, one deals with the education/formation in EO with a special focus on the importance of consciousness of data and methods. In 2020, AIT has strongly supported the launch of the Italian National PhD Course in Earth Observation specifically designed with the main goal of training professional figures with transversal and integrated skills of Earth Observation and Geomatics, and specific application, administrative and legal skills, able to effectively support the wider exploitation and use of the EO programs and related services.

AIT, together with Stati Generali dell'Innovazione - SGI and AM/FM GIS, is supporting the Italian National Copernicus User Forum in collecting Geomatics-related needs from users and providing proper guidelines for conscious exploitation of the available technology and data. The goal is to build a unique solid entity having the scientific strength and the political weight of acting like the accredited interlocutor when a Geomatics-related need arises from institutions (but not only). it is AIT conviction that this would permit an immediate and unambiguous recognition from users of their reference speaker, when a geospatial information-related problem has to be faced. Additionally, this would trigger a virtuous process for even defining standards for data acquisition and processing able to recover a leading role for the Geomatics and EO community in the framework of a conscious and sustainable technology transfer process.

To achieve the above-mentioned goals, AIT operates through the following actions:

(i) it is presently a partner of the Italian National Copernicus User Forum;

(i) it is the reference scientific society of the European Journal of Remote Sensing, an open-access scholarly journal published by Taylor & Francis;

(ii) it is the reference scientific society of the European Journal of Remote Sensing, an open-access scholarly journal published by Taylor & Francis;

(iii) it is one of the 4 confederated scientific societies of ASITA, the Italian Confederation of the Scientific Associations for Territorial and Environmental Information, where EO integrates with the other branches of Geomatics at Italian national level;

(iv) since 2016 AIT started to propose and give its International thematic summer/winter schools mainly addressed to support the conscious exploitation of the Copernicus and ASI (Italian Space Agency) data, products and services;

(v) AIT organizes its Congress every two years. Selected and blinded reviewed contributions from the Congress are gathered and published in a Scopus and WoS indexed book Series named “Trends in Earth Observations (TEO)”. These volumes are intended to present a snapshot of the state-of-the-art in several application fields and advice about potentialities and limits from the ongoing trends of EO technology transfer.

AIT President (2023-2026)
Enrico Borgogno Mondino

Contents

Introduction

Earth Observation: current challenges and opportunities for environmental monitoring

It is precisely to achieve the AIT goals highlighted in the President's "Preface" that this volume was edited by AIT, collecting contributions from AIT last Congress held in Bari (Italy) in June 2023. The AIT 2023 event was the 11th AIT Congress, and it has inaugurated a new trend of cooperation and integration among different scientific societies. A whole week was programmed as a unique event, named **GEOdaysIT 2023**, including two congresses from three scientific societies: **AIT 2023** from AIT, and **FOSS4G** from GFOSS.it and Wikimedia.

Given the above-mentioned important and open discussion, the editors believe this volume can proficiently support the sharing of mutual knowledge within the community of EO data users.

This volume collects 34 selected articles presented at the GEOdaysIT 2023 event by authors from universities, research centers, public institutions and private companies. The variety of contributing profiles demonstrates the significant impact that EO shows at whatever level of civil society.

The Volume is the 3rd one of the new AIT publication series, inaugurated in 2018 to collect peer-reviewed contributions selected from the ones presented at the bi-annual AIT Conference.

The articles, published as extended abstracts, have been grouped into 4 chapters internally organized in thematic clusters. All of them refer to the impacts of human activity on the environment, highlighting the state-of-the-art potentialities of Earth Observation in the context of environmental analysis, monitoring and protection, with particular concerns about climate change-related effects, natural resources and human health.

The first chapter, "Urban & cultural heritage", includes 7 contributions presenting different perspectives of analysis of urban areas and cultural heritage. It focuses on contributions given by EO in the framework of environmental risks, urban planning, cultural heritage monitoring and documentation, and energetic efficiency.

The second chapter, "Environment" includes 13 works representing a wide range of studies at the territorial scale about different environmental components (air, water, ice, soil) in relationship with the ongoing threads that climate change has introduced (e.g. extension and evolution of glaciers). Additionally, contributions from this chapter highlight i) the EO contribution to planning; ii) possible roles for the Copernicus Emergency Management Service; iii) the added value coming from a multi-sensor and multi-platform approach to environmental monitoring.

The third chapter, "Agriculture and Forestry", includes 8 works showing the increasing role of EO In the agricultural and forest fields, especially related to the multiple roles they are assuming that move from the direct economic values of crop/forest production to the environmental sustainability of management, to the carbon stocks balances. Most of the works rely on the integration of spatial analysis tools (GIS) with EO data (multi-e hyper-spectral, radar, satellite, aerial and drone-based). Applications range from crop classification, waste management, circular economy, vegetation monitoring (plant life cycle analysis) and others.

The fourth chapter, "Algorithm & sensors", includes 7 works presenting and comparing new approaches (including some Machine Learning and AI-based ones) and algorithms to support sensitive needs from civil society, like photovoltaic plants monitoring and location, oil spills, infrastructures monitoring.

Urban & cultural heritage

POINT CLOUD CLASSIFICATION USING MACHINE LEARNING ALGORITHMS: APPLICATIONS IN CULTURAL HERITAGE ENVIRONMENT

D. Costantino [1]*, V.S. Alfio [1], M. Pepe [2], D. Scaringi [1]

[1] Department of Civil, Environmental, Land, Construction and Chemistry - DICATECh, Polytechnic University of Bari, Italy - (domenica.costantino, vincenzosaverio.alfio, daniele.scaringi)@poliba.it
[2] Department of Engineering and Geology (InGeo), "G. D'Annunzio" University of Chieti-Pescara, Italy massimiliano.pepe@unich.it

KEY WORDS: Random Forest, Machine Learning, Point Cloud Classification, Cultural Heritage, Overall Accuracy, F1-score

ABSTRACT:

3D point clouds are a source for generating 3D models of individual objects or cities due to the simplicity of acquiring and managing geospatial data. For this reason, 3D point cloud classification represents an interesting area of research due to its many advantages in different fields of application. Therefore, the aim of the paper is to identify a suitable methodology for semantic segmentation of the point cloud based on a multi-scale approach and machine learning algorithms. This methodology was applied on the following datasets belonging to the cultural heritage: Temple of Hera (Italy) and Sacro Monte di Ghiffa (Italy). The validation of the results obtained was carried out using appropriate performance indices (Precision, Overall Accuracy, Recall and F1-score) whose values showed the quality of the proposed method that is applicable to complex morphologies both at the scale of the individual artefact and at the urban scale. In addition, a comparison with approaches in the literature shows encouraging results in terms of both accuracy and speed of point cloud classification.

1. INTRODUCTION

Today the use of sensors, active or passive, for the acquisition of 3D point clouds destined for the restitution of Cultural Heritage (CH) of buildings and urban scenes (urban scenes US), including three-dimensional ones (3D city model), is increasingly widespread. The purposes are multiple: in the field of CH, the construction of semantic 3D models of heritage allows morphological analysis, mapping of degradation, digitisation of information and the restitution of assets, through a process called Heritage Building Information Modelling, (HBIM). This process can be realized in several ways and using suitable software, such as Autodesk Revit that allows multi-temporal and multilayer information management (Croce et al., 2021). Point cloud classification can apply to both the individual building and urban scale. In the field of US, 3D city modelling is fundamental for urban management and planning, for cadastral uses and for the restitution of information models such as OpenStreetMap (Ozdemir et al., 2018). Already according to (Axelsson, 1998) automatic procedures for the interpretation and classification of laser data could be successfully used in numerous applications through statistical classification methods; the same author suggested more general classification approaches based on the radiometric characteristics of the laser scanner used. Today, given the now widespread use and numerous fields of application involving these point clouds, research is pushing towards new methodologies for their automatic semantic classification and segmentation, in order to better understand the different spatial, geometric, multi-spectral and radiometric information that can be extracted from the point cloud (Grilli et al., 2017). Generally, semantic classification or segmentation refers to the process of grouping similar data into subsets (called segments); the latter show one or more characteristics (geometric, radiometric, etc.), through which it is possible to distinguish and identify different parts that make up an image, a point cloud or a polygonal model (Grilli, 2019). Machine and Deep learning (ML/DL) are fields of application of artificial intelligence (AI), based on the development of algorithms that allow computers to make decisions based on initial input data, called training data. Specifically, DL is considered a branch of ML that is based on the use of artificial neural networks (ANNs) with two or more layers (hidden layers) to process information in a non-linear manner (Grilli, 2019). These learning methodologies are mainly distinguished into two approaches (Teruggi et al., 2020): Supervised Approach and Unsupervised Approaches. In the supervised approach, typical of ML, such as Random Forest, the algorithms take as input some manually annotated parts of the point cloud together with so-called "features", attributes of a geometric and/or radiometric nature specially selected by the operator to facilitate the learning and distinction of the classes sought, In the unsupervised approaches, typical of DL algorithms, they involve the algorithm automatically generating the features it learns during the training phase on a large amount of input data. In Grilli et al., 2020, an automatic classification method is proposed, based on a multi-level, multi-resolution (MLMR) approach combined with an ML algorithm; this latter ML method hierarchically classifies 3D data at different geometric resolutions to facilitate the learning process and optimise classification results. In this latter paper, the test was performed on both the Duomo di Milano and the "Abbazia di Pomposa"; in this latter case study, the authors once again validate and demonstrate how ML approaches are faster in classification than an operator, define general rules that can be replicated for other cultural heritage assets and emphasise how hierarchical segmentation (down to single instances) of 3D data is a fundamental tool for H-BIM. Also, in Croce et al., 2021 a semi-automatic approach for the transition from unstructured 3D point cloud to H-BIM model was proposed; the authors first propose an automatic segmentation using the RF classifier, then a scan-to-BIM reconstruction in Autodesk Revit software; the proposed methodology was applied to the "Certosa di Pisa" and

* Corresponding author

allowed the reconstruction of an H-BIM model starting from the unstructured 3D point cloud; in this way, it was possible to obtain not only the semantic information coming from the classification was preserved but also a rich model was built in a BIM environment that is fundamental for the preservation and archiving of numerous useful information for restoration and conservation purposes.
In Pierdicca et al., 2020 an innovative DL framework is proposed for the semantic segmentation of 3D point clouds, which starting from an existing convolutional network, known as DGCNN-Dynamic Graph Convolutional Neural Network, optimises the segmentation process by introducing significant features such as normals and radiometric component. To test the approach, some point clouds belonging to the dataset provided by PoliTO were used: ArCH (Architectural Cultural Heritage).
In Matrone et al., 2020, different ML and DL approaches are compared with the aim not only to compare the algorithms but also to understand which is the best for automatic CH classification; it is emerges is that RF is certainly the best ML classifier in terms of OA (overall accuracy) when compared to all other methodologies, however comparable results are also obtained with a modified DGCNN that includes the use of both geometric and radiometric features called DGCNN-Mod by the authors. Tests were conducted on two scenes; in both studies, it can be seen that Random Forest performs better (as measured by OA) than all other ML approaches, and in general is often even more accurate than DL approaches.

2. DATA

The point clouds used in the experimentation are: Temple of Hera (Italy) and Sacro Monte Ghiffa (Italy).
The temple of Hera, also known as the "Tavole Palatine", was built in the 6th century B.C. next to the Bradano, located in the archaeological area of Metapontum (Italy). The dense point cloud of the Tavole Palatine was obtained through a UAV photogrammetric survey (Pepe et al, 2022) and consists of 973.125 points (Appendix A).
The Sacro Monte of Ghiffa stands under Monte Carciago in a magnificent position overlooking Lago Maggiore. It is an unfinished Baroque complex based on the Borromean conception and architectural models of the Sacred Mounts of Orta and Varese. It consists of the sanctuary church, three chapels and the portico of the Vie Crucis. The dense point cloud of the Sacro Monte of Ghiffa was obtained by a UAV photogrammetric survey combined with a terrestrial laser scanner (TLS) for a total of 17,798,012 points (Appendix B). This latter dataset was obtained from a benchmark made available by the Politecnico di Torino called "Architectural Cultural Heritage" (Matrone et al., 2020).

3. METHOD

3.1 Methodological approach

Automatic classification using Random Forest requires several preliminary steps. This is mainly related to the type of algorithm that requires a prior supervised learning phase. The steps followed for classification purposes are as follows and were all performed in the open-source software CloudCompare (CC) and via Anaconda, the world's most widely used data science platform with Python: i) Cloud pre-processing; ii) Manual partitioning and annotation; iii) Calculation of geometric features; iv) Preparation of input threads for RF; v) Execution of the RF model. In order to characterise each point, both radiometric features (R, G, B) and geometric features were combined. The geometric feature is known as "covariance features" because they allow a deep knowledge of the point cloud geometry, highlighting the architectural discontinuities present. These features are derived from the eigenvalues $\lambda_1, \lambda_2, \lambda_3$ of the covariance matrix, computed in a spherical surround of known radius of the point considered. The formula of the several geometric features computed and used in the experimentation are reported below (Weinmann et al., 2015; Mohamed et al., 2021).

$$\text{Linearity} \quad L_\lambda = \frac{\lambda_1 - \lambda_2}{\lambda_1} \tag{1}$$

$$\text{Planarity} \quad P_\lambda = \frac{\lambda_2 - \lambda_3}{\lambda_1} \tag{2}$$

$$\text{Sphericity} \quad S_\lambda = \frac{\lambda_3}{\lambda_1} \tag{3}$$

$$\text{Surface Variation} \quad C_\lambda = \frac{\lambda_3}{\sum \lambda} \tag{4}$$

$$\text{Anisotropy} \quad A_\lambda = \frac{\lambda_1 - \lambda_3}{\lambda_1} \tag{5}$$

$$\text{Verticality} \quad V = 1 - v_z \tag{6}$$

In addition to these latter features, the RGB radiometric components, the Z-coordinate of the points and the verticality V (Equation 6), where v_z represents the vertical component of the normal vector $v \in \mathbb{R}^3$, can be taken into account. The computation of all features to be provided as input to the classifier was performed on CC using the "compute geometric features" tool. The choice of the above-mentioned features is linked to the identification of the various architectural elements by the classifier. In fact, linearity, planarity and sphericity allow RF to distinguish linear, planar elements (such as the floor or roof) and volumetric elements such as columns. The feature verticality and Z-coordinate of the points, on the other hand, are essential to allow the classifier to distinguish the elevation variations and elevation of the points; in particular, these latter features are useful to identify wall and floor, pavement, or ground classes.
For each test, several performance indicator were considered; the performance indicators were generated taking into account the True Positive (TP), i.e. the number of features that belong to a particular class, the True Negative (TN) is the number of features that do not belong to a class but were wrongly assigned to a class other than theirs, False Positive (FP) occur when the feature do not belong to a class but were predicted positively to the class and False Negative (FN) are the features that belong to a class but were not predicted as any class in the image. In particular, the Precision is a very common performer index that represents the ratio of the correctly segmented classes that are positive for each class which can be measured with TP and FP (Davis et al., 2006; Yekeen et al., 2020):

$$Precision = \frac{TP}{TP + FP} \tag{6}$$

The Overall Accuracy (OA) parameter can be calculated using the following formula (Congalton et al., 1991, Pepe et al., 2018):

$$\text{OA} = \frac{\text{Number of correct predictions}}{\text{Total number of predictions}} \tag{7}$$

The Recall is the ratio of the correctly classified positive classes (Powers, 2020; Xu et al., 2021; Foody 2023):

$$Recall = \frac{TP}{TP + FN} \tag{8}$$

F1-score is the harmonic mean of the precision and recall (Raghavan et al., 1989; Pepe et al., 2021):

$$\mathrm{F}_1 - \mathrm{score} = 2\frac{Precision \cdot Recall}{Precision + Recall} \quad (9)$$

3.2 Test on datasets

The first fundamental step involves the cleaning of the point cloud and then removing the elements that one did not want to classify. For this operation, we made use of the command in the CC plugins known as "Cloth Simulation Filter". This latter tool, based on Zhang et al., 2016, makes it possible to automatically remove the soil by initially setting a general parameter on the type of soil (steep terrain, hilly terrain, flat terrain) and then 3 detailed parameters, in this case left equal to those predefined by the software. In this way it is possible to subdivide the points subject to classification, i.e. the colonnade, from those in the terrain that will not be used.

The same operation was carried out manually using the "cross section" command available in CC. This terrain removal operation was only necessary for the "Tavole Palatine" dataset. The only operation performed on this point cloud concerned the extraction of only the portico, the subject of the classification. Using the "cross section" tool, it was possible to divide the entrance to the sanctuary from the portico.

This operation reduced the number of points to be processed to 11,303,645. However, for the purposes of visualisation and subsequent processing, the point cloud was still extremely dense; for these reasons, through the "Cloud sub sampling" command, the point cloud was resampled with a minimum distance between points of 0.05 m. The operations of terrain removal and resampling of the point cloud were useful to reduce the computational time and improve the management of the point cloud.

Once this phase has been completed, it is necessary to annotate, and thus manually divide the point cloud into homogeneous classes. This operation is fundamental since as input to the classifier we will have to supply two portions of the point cloud already annotated: one portion for the supervised learning phase (training) and one portion for evaluating the goodness of the model (evaluation); the latter allows us to evaluate the performance of the model through the confusion matrix and thus the calculation of the precision, recall and F1-score parameters.

Manual semantic segmentation was conducted on CC. Initially, both datasets were divided to distinguish the part of the point cloud intended for classifier training and the part to be classified. The latter portion of the point cloud always has a much higher number of points than its counterpart. As mentioned, the part intended for training was further divided and annotated.

For the Tavole Palatine dataset, two columns were annotated for the training phase and the remaining 3 for the evaluation. In total, 5 classes were identified: architrave, capital, column, stylobate, stereobate; the remaining 9 columns were classified by RF (Appendix A).

In the case of the Sacro Monte portico, no manual annotation was necessary; in this latter case, 10 classes are identified by the same authors (Appendix B).

In the case of the two CH datasets (Temple of Hera and Porticato) the search radii were as follows: 0.2m, 0.4m (equal to the average radius of the columns), 0.8m (equal to the average diameter of the columns), 1m, 1.2m and 1.4m.

Once these operations were completed, it was necessary to organise the data according to a specific format; this task was carried out in MS Excel software.

X1	Y1	Z1	R1	G1	B1	F11	…	F1n	class
X2	Y2	Z2	R2	G2	B2	F21	…	F2n	class
.	.	.	.	.	.	.	.	.	.
.	.	.	.	.	.	.	.	.	.
Xn	Yn	Zn	Rn	Gn	Bn	Fm1	…	Fmn	class
(a)			(b)			(c)			(d)

Table 1. Data organisation for classification: (a) geometric coordinates, (b) radiometric features, (c) geometric features and (d) class.

Indeed, the point cloud in "txt" format was imported into the programme and the data was organised in a structure characterised by the following matrix structure (Table 1).

The geometric characteristics, from smallest to largest radius, are: linearity, flatness, sphericity, surface variation, verticality and anisotropy. The resulting datasets are ready to be used as input in the predictive model (the cloud fractions for classification do not have the last column for "class"). The classifier used in this work is the RF algorithm and available on the web platform for developers "GitHub" (https://github.com/3DOM-FBK/RF4PCC). We need to prepare a folder in which, in addition to the Python codes for training ("train.py") and for classification ("classify.py"), there are the text files containing the parts of the point cloud intended for training, evaluation and classification. In addition, it is necessary to have a text file containing on the first line the indices of the features that the model will use (indices start at 0) for training and on the second line the index of the column defined as "class". The result of executing the code is the generation of a .pkl file (relating to the number of random trees generated by the classification) and a .txt file containing the dataset for the evaluation with a new column for the classes provided. It will also be possible to observe a vector called "feature importance" to evaluate the most significant features in the training phase and the confusion matrix.

4. RESULTS

The approach used involves selecting the 8 most significant features from the initial 40 (36 geometric features, 3 radiometric features and the Z-coordinate).

A different search and reiterative selection analysis of the input features was therefore conducted on the dataset. The selection of features to be discarded took place in all tests based on a threshold value that was not exceeded. The choice of this value depended on the non-linear reduction of the features; in fact, the tests were conducted starting with 40 features, then moving on to 30, 15 and finally 8 significant features. At the end of each test, repeated feature selection was performed, and the confusion matrix associated with the accuracy, recall and F1-score metric parameters, calculated for each class and in average terms, was determined.

Finally, summary graphs were produced on the overall performance of the classifier as the number of input features varied.

A total of 7 tests were conducted on this point cloud of Tavole Palatine. The first four were conducted on the raw point cloud, the further 3 with 30, 15 and 8 features respectively on the resampled 0.05 m to lighten the point cloud and reduce the computational stress to which the computer was subjected. In this way, it is possible to assess the differences in terms of OA. In addition, based on the average F1-score values obtained from the various confusion matrices, it was possible to diagram both the trend of the F1-score parameter and the trend of the computation time according to the number of features input to the classifier (Appendix A).

In the case study of Sacro Monte di Ghiffa, four tests were performed on this dataset in a similar manner to the previous case study, calculating 36 geometric features to which the RGB radiometric components and the Z-coordinate of the points and the verticality V were added.
Once the tests were completed, the parameters considered for an analysis of the RF performance are shown in the Table 2.

TEST	NUMBER OF FEATURES	O.A. (%)	F_1.SCORE (%)	TRAINING TIME (s)	CLASSIFCATION TIME (s)
T1	40	72.16	62.89114	89.09	19.08
T2	30	71.91	63.57512	73.2	13.52
T3	15	80.31	67.98156	44.99	10.56
T4	8	82.22	64.91441	35.55	8.49

Table 2. Performance analysis obtained in Sacro Monte di Ghiffa

As in the previous case, the OA parameter was calculated for each test. In addition, based on the average F1-score values obtained from the various confusion matrices, it was possible to diagram both the trend of the F1-score parameter and the trend of the computational times according to the number of features input to the classifier (Appendix B).

5. DISCUSSION AND CONCLUSIONS

The paper showed a deep learning-based point cloud classification method applied in cultural heritage context. To validate the method, two datasets of the point cloud were taken into consideration.
The results achieved from the various tests carried out on the Temple of Hera dataset underscore how the multiscale reiterative approach of searching and selecting input features made it possible to select, with 4 repetitions, the best 8 features for classification purposes. The choice of removing an increasing number of irrelevant features at each iteration made it possible to speed up computational times considerably.
The results obtained in terms of OA of 97.5% and F1-score of 96.2% show how efficiently the classifier worked, achieving excellent results in a very short time. Analyses on the same resampled cloud showed how a greater discretisation of the points mainly reduces the computational time. However, differences emerge in terms of OA and F1-score. It is observed that in order to have comparable results in terms of OA and F1-score between the non-resampled and resampled dataset, it is necessary to provide a higher number of features as input: from 8 to 13. Concerning the dataset related to the case study of the Porticato del Sacro Monte di Ghiffa, the results demonstrate the quality of the proposed method.
The proposed method based on a multiscale reiterative search and selection of features to an RF classifier proposed in the paper was shown to be efficient in reconciling the best results in terms of metrics, evaluated by OA and F1-score, computational time and manual operations to be performed by the operator. It was also possible to note how the density of the resampled cloud positively affects the computational time, while negatively affecting, albeit by a few percentage fractions, the overall accuracy and F1-score parameter. Therefore, by virtue of the number of points in the dataset and the classes identified, the effectiveness of the approach is demonstrated, and it is deduced that the 6 geometric features, calculated in spherical contours of dimensions correlated to the architectural dimensions of the elements to be classified, the radiometric components and the Z-coordinate of the points alone are sufficient to obtain a robust classification of the dataset. The overall accuracy achieved was of 80% which is comparable with the existing literature.
For future work, more investigations can be made in relation to the density of the point cloud and using multi sensors in order to obtain multispectral data that further facilitate classification processes.

REFERENCES

Axelsson, P. (1999). Processing of laser scanner data—algorithms and applications. ISPRS Journal of Photogrammetry and Remote Sensing, 54(2-3), 138-147.

Congalton, R. G. (1991). A review of assessing the accuracy of classifications of remotely sensed data. Remote sensing of environment, 37(1), 35-46.

Croce, V., Caroti, G., De Luca, L., Jacquot, K., Piemonte, A., & Véron, P. (2021). From the Semantic Point Cloud to Heritage-Building Information Modeling: A Semiautomatic Approach Exploiting Machine Learning. Remote Sensing, 13(3), 461.

Davis, J., & Goadrich, M. (2006, June). The relationship between Precision-Recall and ROC curves. In Proceedings of the 23rd international conference on Machine learning (pp. 233-240).

Foody, G. M. (2023). Challenges in the real world use of classification accuracy metrics: From recall and precision to the Matthews correlation coefficient. Plos one, 18(10), e0291908.

Grilli, E., Menna, F., & Remondino, F. (2017). A review of point clouds segmentation and classification algorithms. The International Archives of the Photogrammetry, Remote Sensing and Spatial Information Sciences, 42, 339-344.

Grilli, E., Farella, E. M., Torresani, A., & Remondino, F. (2019). Geometric features analysis for the classification of cultural heritage point clouds. The International Archives of the Photogrammetry, Remote Sensing and Spatial Information Sciences, 42, 541-548.

Grilli, E., Özdemir, E., & Remondino, F. (2019). Application of Machine and Deep Learning strategies for the classification of heritage point clouds. International Archives of the Photogrammetry, Remote Sensing & Spatial Information Sciences.

Matrone, F., Lingua, A., Pierdicca, R., Malinverni, E. S., Paolanti, M., Grilli, E., Remondino, F., Murtiyoso, A., & Landes, T. (2020). A benchmark for large-scale heritage point cloud semantic segmentation. The International Archives of the Photogrammetry, Remote Sensing and Spatial Information Sciences, 43, 1419-1426.

Mohamed, M., Morsy, S., & El-Shazly, A. (2021). Machine learning for mobile LIDAR data classification of 3D road environment. The International Archives of the Photogrammetry, Remote Sensing and Spatial Information Sciences, 44, 113-117.

Özdemir, E., & Remondino, F. (2018). Segmentation of 3D photogrammetric point cloud for 3D building modeling. The International Archives of the Photogrammetry, Remote Sensing and Spatial Information Sciences, 42, 135-142.

Pepe, M., & Parente, C. (2018). Burned area recognition by change detection analysis using images derived from Sentinel-2 satellite: The case study of Sorrento Peninsula, Italy. Journal of Applied Engineering Science, 16(2), 225-232.

Pepe, M., Costantino, D., Alfio, V. S., Vozza, G., & Cartellino, E. (2021). A novel method based on deep learning, GIS and geomatics software for building a 3D city model from VHR satellite stereo imagery. ISPRS International Journal of Geo-Information, 10(10), 697.

Pepe, M., Alfio, V. S., Costantino, D., & Scaringi, D. (2022). Data for 3D reconstruction and point cloud classification using machine learning in cultural heritage environment. Data in Brief, 42, 108250.

Pierdicca, R., Paolanti, M., Matrone, F., Martini, M., Morbidoni, C., Malinverni, E. S., ... & Lingua, A. M. (2020). Point cloud semantic segmentation using a deep learning framework for cultural heritage. Remote Sensing, 12(6), 1005.

Powers DM. (2020). Evaluation: from precision, recall and F-measure to ROC, informedness, markedness and correlation. arXiv preprint arXiv:2010.16061. 2020 Oct 11.

Raghavan, V., Bollmann, P., & Jung, G. S. (1989). A critical investigation of recall and precision as measures of retrieval system performance. ACM Transactions on Information Systems (TOIS), 7(3), 205-229.

Teruggi, S., Grilli, E., Russo, M., Fassi, F., & Remondino, F. (2020). A hierarchical machine learning approach for multi-level and multi-resolution 3D point cloud classification. Remote Sensing, 12(16), 2598.

Xu, X., Chen, Y., Zhang, J., Chen, Y., Anandhan, P., & Manickam, A. (2021). A novel approach for scene classification from remote sensing images using deep learning methods. European Journal of Remote Sensing, 54(sup2), 383-395.

Yekeen, S. T., Balogun, A. L., & Yusof, K. B. W. (2020). A novel deep learning instance segmentation model for automated marine oil spill detection. ISPRS Journal of Photogrammetry and Remote Sensing, 167, 190-200.

Weinmann, M., Jutzi, B., Hinz, S., & Mallet, C. (2015). Semantic point cloud interpretation based on optimal neighborhoods, relevant features and efficient classifiers. ISPRS Journal of Photogrammetry and Remote Sensing, 105, 286-304.

Zhang, W., Qi, J., Wan, P., Wang, H., Xie, D., Wang, X., & Yan, G. (2016). An easy-to-use airborne LiDAR data filtering method based on cloth simulation. Remote sensing, 8(6), 501.

APPENDIX A

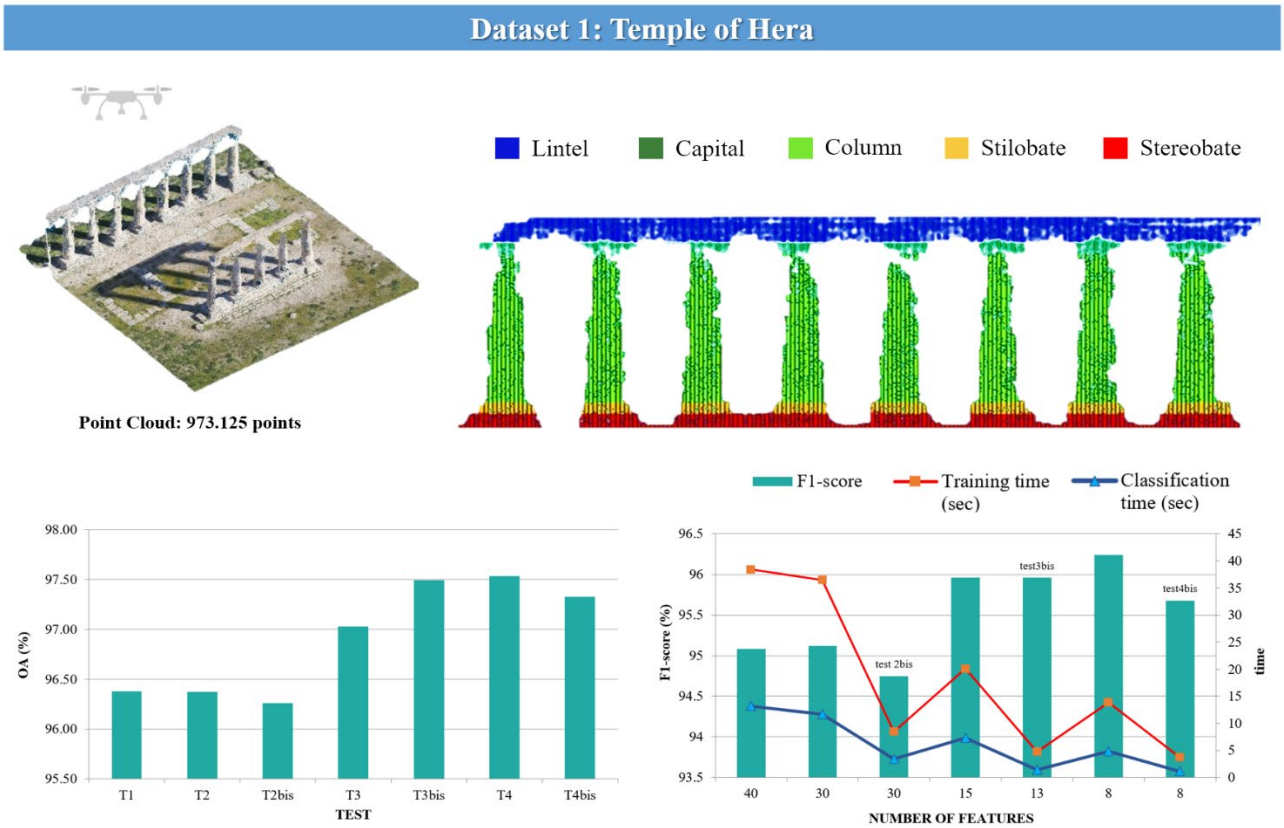

APPENDIX B

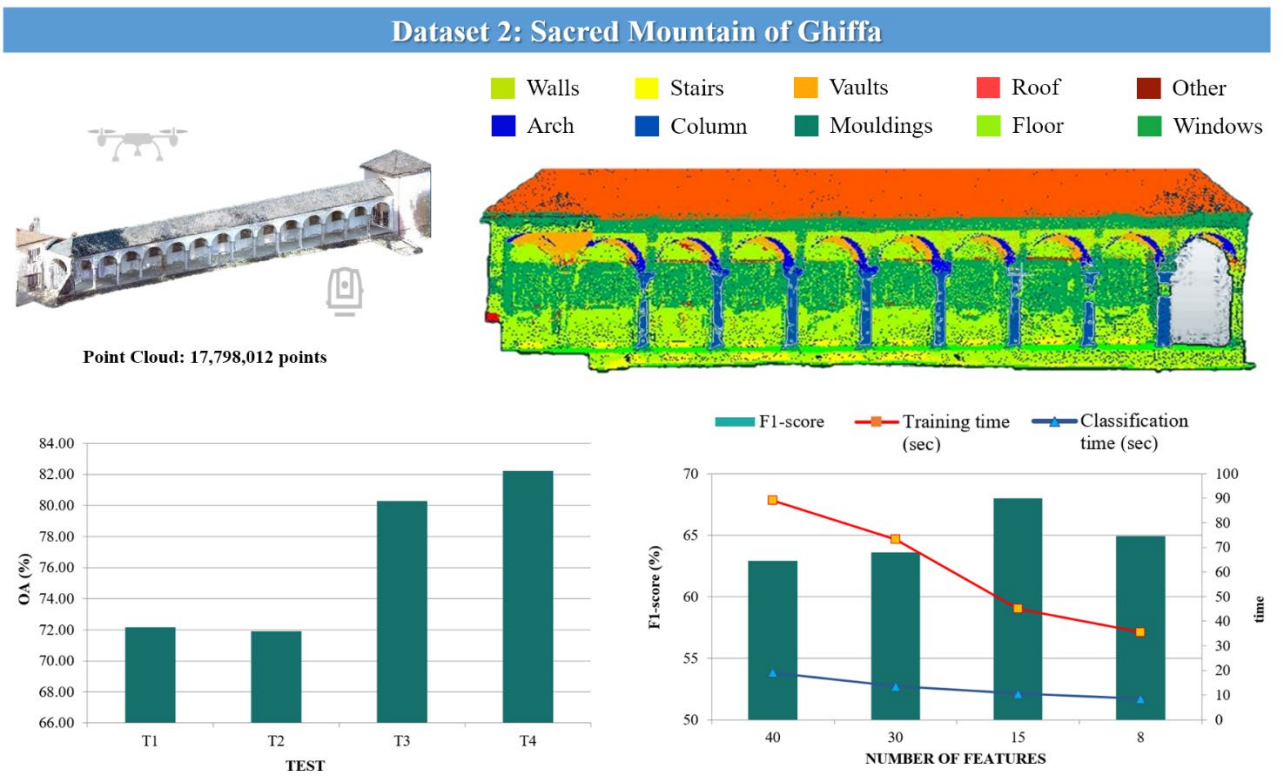

STRUCTURAL MONITORING OF CULTURAL HERITAGE ASSETS AT URBAN AND LOCAL SCALE THROUGH MT-INSAR

A. Caprino *, F. Lorenzoni , F. da Porto

Department of Geosciences, University of Padova, Italy
amedeo.caprino@phd.unipd.it, (filippo.lorenzoni, francesca.daporto)@unipd.it

KEY WORDS: MT-InSAR, Cultural Heritage, Structural Health Monitoring, Remote Sensing, Multi-scale

ABSTRACT:

The preservation and monitoring of cultural heritage are topics of constant interest, leading to the ongoing exploration of new methods and techniques, especially in countries rich of assets with high historical and artistic value, such as Italy. Multi-Temporal Interferometric Synthetic Aperture Radar (MT-InSAR) has gained popularity for Structural Health Monitoring (SHM), offering precise ground deformation measurements via Synthetic Aperture Radar (SAR) imagery from multiple timeframes. Urban applications, benefiting from SAR's high reflectivity, have seen the development of tailored interferometric algorithms. The advent of high-resolution SAR satellite constellations, such as COSMO-SkyMed, has further enhanced MT-InSAR's capabilities, enabling dense Measurement Points (MPs) and detailed structural data collection. MT-InSAR proves valuable for SHM at both urban and local scales, identifying critical areas and individual structures. Despite certain limitations, it remains a cost-effective tool for monitoring structures, offering insights into their stability and health. In this study, MT-InSAR is applied in Verona, Italy, renowned for its Cultural Heritage assets. COSMO-SkyMed imagery from 2011-2022 is analyzed for urban and local deformations. Initial interpolation reveals Verona's overall stability, with critical areas in the northern town beltway. Cultural assets like the Roman Arena, Lamberti Tower, and Roman Theater are also assessed with multiple MPs, offering insights into their stability and deformation trends. Despite relatively low magnitudes of displacements, this research underscores MT-InSAR's potential in monitoring Cultural Heritage structures, serving as a powerful, cost-efficient tool for SHM, with anticipated expanded usage owing to the increasing availability of high-quality SAR imagery.

1. INTRODUCTION

Multi-Temporal Interferometric Synthetic Aperture Radar (MT-InSAR) has gained popularity as a Structural Health Monitoring (SHM) tool in recent years. By utilizing Synthetic Aperture Radar (SAR) data from different time periods, the method enables the assessment of ground deformation with high precision and spatial resolution. Due to the high reflectivity offered by structures, making them visible in SAR imaging, MT-InSAR has proven particularly useful in urban scenarios (Tapete and Cigna, 2012; Cigna et al., 2014). It is now possible to extract comprehensive information on structures and infrastructure thanks to a number of interferometric techniques developed specifically for the urban environment. Moreover, the expanding usage of MT-InSAR for SHM applications has been facilitated by the growing accessibility of high-resolution SAR satellite constellations, such as the Italian COSMO-SkyMed (Cuca et al., 2023). These constellations provide high-quality SAR imagery in which a high density of Measurement Points (MP) can be detected, allowing for the recording of detailed information on individual structures. With MT-InSAR, it is feasible to gather data on deformations at the global and local scales, identifying the most vulnerable regions within the urban environment or concentrating on specific structures (Bonaldo et al., 2023).). Despite its many benefits, MT-InSAR has various disadvantages that must be taken into account (Caprino et al., 2023). Technical issues, including geocoding errors and noise in the time series, can arise throughout the analysis. The technique demands expert interpretation of results to prevent data misreading. Additionally, the method is sensitive to environmental changes, such as alterations in vegetation cover or weather, which may impact the accuracy of SAR imaging.

In this study, the MT-InSAR technique is used in the urban area of Verona, a city with numerous cultural heritage assets in northern Italy. To identify deformations at both the global and local scales, the study analyzed images collected by the COSMO-SkyMed constellation in Stripmap mode for both ascending and descending orbits during the years 2011–2022. In the initial phase, spatial interpolation methods were used to assess overall urban deformations and define the most significant areas. Subsequently, focus shifted to some of the city's most important historical sites, notably the Roman Arena, Lamberti Tower, and Roman Theatre. Thanks to the data on each MP's displacement velocity and displacement time series, several MPs emerged for each asset, spread along the height of the structures. It is possible to investigate the structural stability and the progression of deformations over the monitoring period.

2. MATERIALS AND METHODS

2.1 Case-studies

Verona is a city in the Veneto region, north Italy. Its historic center, situated on a bend in the Adige River, dates back to medieval times, but significant traces of the Roman era still exist, solidifying the city's status as an important historical and artistic center of the nation (see Figure 1). Among the city's prominent cultural assets, three were selected as reference sites for this study:

- Roman Arena: This amphitheater stands as one of the best preserved and most renowned Roman structures globally. Constructed around the first century AD, it continues to serve as a venue for major events to this

* Corresponding author

day. The amphitheater's load-bearing structure consists of three elliptical rings, with the outer ring measuring 150x120m and the inner ring measuring 77x40m. These rings are interconnected by a series of radial walls and vaults, forming the galleries used for access. Originally, a fourth outer ring existed but collapsed during the 1117 earthquake event, leaving only the remaining portion known as the Wing, which has become a symbol of the amphitheater and the city itself.

- Roman Theatre: This open-air theater, constructed in the 1st century B.C. on San Pietro Hill along the left bank of the Adige River within Verona's Roman walls, serves as another significant cultural site. After falling into disuse during the Middle Ages, the structure gradually deteriorated, and an entire neighborhood was eventually built upon its remains. It wasn't until the nineteenth and early twentieth centuries that archaeological excavations and restoration efforts began to reveal the remaining structure. Today, the monument comprises several free septa, the main staircase, remnants of the scene structure, and the church of saints Siro and Libera, a Catholic church built around the tenth century.
- Lamberti Tower: Standing at 84 meters, this medieval tower is the tallest structure in the city. Located just steps away from the main square, the tower is partially integrated into the "Palazzo della Ragione", which serves as the headquarters of the municipality. The floor plan measures about 9x9m, making it an extremely slender structure.

Figure 1. Verona urban center and location of case studies: Roman Arena in red, Roman Theatre in blue, Lamberti tower in green

2.2 Dataset and processing

In this study, a dataset comprising 303 COSMO-SkyMed (CSK) images from 2011 to 2022 for both ascending and descending orbit was processed (Table 1 and Figure 2), with a pixel dimension of 3x3m. The PS-InSAR technique (Ferretti et al., 2001, 2007) was employed using SARscape software to process the COSMO-SkyMed images. This multi-temporal SAR technique mitigates atmospheric influences while enhancing displacement accuracy by identifying Permanent Scatterers (PS), which are coherent radar signal reflectors such as buildings, monuments, infrastructures, antennae, rocky outcrops, etc.

Orbit	Average revisiting time	Monitoring period	Number of images
Ascending	25dd	06/2012 – 09/2022	156
Descending	26dd	05/2011 – 12/2021	157

Table 1. Characteristics of the processed dataset

The interferometric process involved several steps as outlined below. The first phase entailed creating a connection graph wherein the reference picture is linked to all secondary images to form pairs. Subsequently, the secondary images were co-registered with the reference image to generate interferograms. During this stage, the topographic component of each interferogram was removed using the Japanese Aerospace Exploration Agency's (JAXA) 30m ALOS-DEM. In the first inversion step, PSs were identified by considering the Amplitude Dispersion Index (ADI), calculated as the ratio between the standard deviation and the mean of a pixel's amplitude values. Additionally, a linear velocity model was utilized to estimate residual height and displacement velocity during the first inversion. The atmospheric phase component was then estimated and filtered using both high-pass and low-pass filters in the second inversion. Finally, geocoding was performed, involving discarding PSs with coherence less than 0.70 and geocoding the interferometric products in the WGS 84 coordinate system.

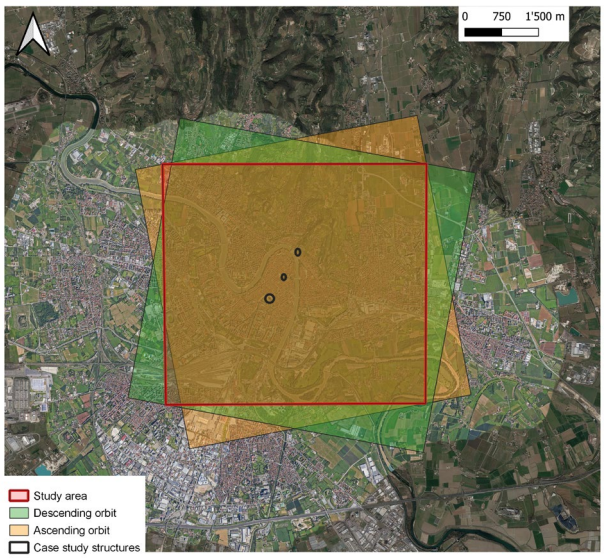

Figure 2. Extension of the case study area (red), ascending orbit path (orange) and descending orbit path (green)

3. RESULTS

Figure 3 depicts the displacement velocity detected for both ascending and descending orbits. A very low displacement rate is observed, with the majority of values falling within the considered stable range (1.5 mm/year) (Floris et al., 2019). Higher velocity values are evident in some suburban locations, particularly on infrastructures like the northern section of the beltway. It is plausible to state that the city is not affected by any particular large-scale deformation phenomena (such as subsidence). However, it's important to note that the analysis of deformation velocities alone cannot be the sole tool for data interpretation, especially in cases of prolonged monitoring like this study, as very slow phenomena could be hidden and

difficult to detect. Therefore, a more detailed time series analysis would also be beneficial.

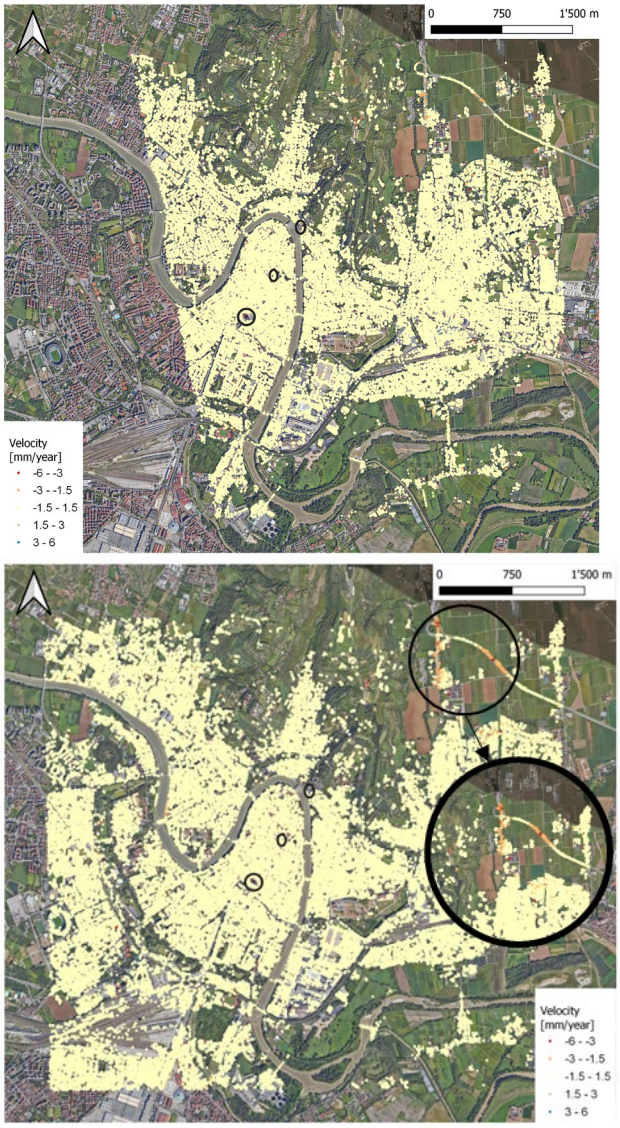

Figure 3. Velocity displacement for ascending orbit (above) and descending orbit (below)

Transitioning to the local-scale analysis, the results for the structures of interest are presented below. The following images display the MPs identified for both the descending orbit (triangles) and ascending orbit (squares), distributed in both plan and elevation using a geometric model.

Regarding the Arena (Figure 4), a total of 330 MPs were identified, with some placed in correspondence of the wing, likely the most vulnerable element of the structure. As observed from the presented time series, the wing demonstrates a substantially stable behavior. However, it is crucial to highlight a limitation linked to satellite data monitoring. Considering the element's conformation, it is conceivable that the most vulnerable direction is the one out of plan coinciding with the south-north direction. However, due to satellite acquisition geometry, movements along this direction are difficult to identify, potentially resulting in any out-of-plane movement of the wing being improperly recorded by the system.

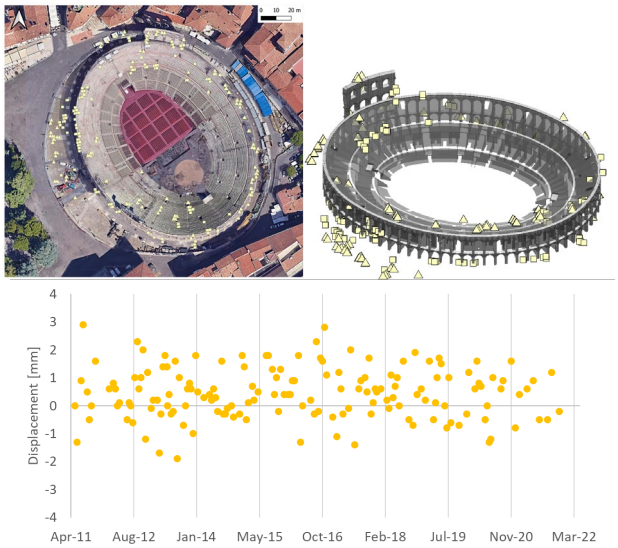

Figure 4. MPs detected on the Roman Arena (above) and time series of a MP detected on the wing (below)

In the case of the Roman Theatre (Figure 5), it is possible to notice that very few MPs are detected (about 50), all presenting displacement velocity values within the stability range. The low number of identified points poses a significant drawback to InSAR application for structure monitoring, potentially compromising result quality. Additionally, peculiar aspects of this case study should be considered. Firstly, the in-plane dimensions of the walls are smaller than the pixel dimensions in Stripmap mode acquisition (3x3m), making it challenging to identify the walls as coherent reflective objects. This issue could be addressed by using higher resolution images, such as spotlights, although their availability is limited. Moreover, as the structure is still used for several events, it undergoes numerous operations to be prepared for the purpose (stage assembly, seating, escape routes, etc...). Thus, the appearance of the structure is constantly changing, being covered for a good part. Consequently, the technique may not properly identify coherent MPs since they are compromised by preparation operations, especially during long monitoring periods like in this case. This aspect is crucial for the analysis of cultural heritage structures, given their frequent modification through events and restoration works. The impact of this issue on the analysis could be mitigated by shortening the period of interest or dividing the entire monitoring period into multiple analyses.

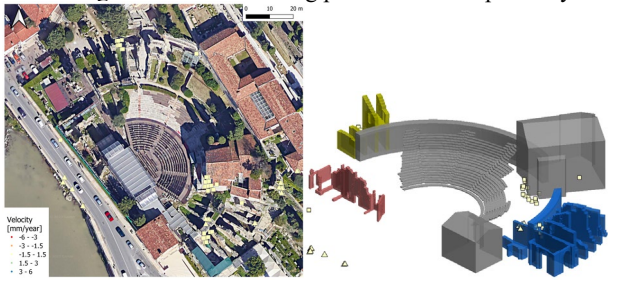

Figure 5. MPs detected on the Roman Theatre visualized in GIS (left) and in a more accurate geometrical model (right)

Finally, in the case of the Lamberti Tower, the 346 detected MPs are presented in Figure 6. Here, all points demonstrate a stable displacement trend, with no critical areas observed in either the tower or the palace. However, an important consideration arises in this application. To properly study the behavior of a structure, understanding the precise location of the MPs and the structural component to which they relate. Thus,

geo-visualization tools are necessary in the post-processing phase, often implemented using GIS instruments. However, in the case of complex structures, relying solely on GIS visualization can make it difficult to understand the actual distribution of points. For instance, in the tower's case (Figure 6 left), assessing whether a point belongs to the tower or the palace with sufficient certainty is challenging. Therefore, for proper analysis of complex cultural heritage assets, a more detailed geometrical model is needed, as presented in Figure 6 right. Additionally, positioning errors along the three spatial coordinates (east–west, south–north, and vertical height) must be considered, as they could affect result interpretation. For example, in PSI processing with CSK acquisitions, the positioning error is approximately 1–3 meters (Wasowski and Bovenga, 2014).

Figure 6. MPs detected on the Lamberti Tower visualized in GIS (left) and in a more accurate geometrical model (right)

4. CONCLUSIONS

The analysis of satellite images through Multi-Temporal InSAR methods has become an essential tool for structural monitoring. This technique enables the extraction of valuable information regarding displacement velocity and time series, both at large and local scales. Moreover, it provides insights into past deformations of structures, as data have been available since the launch of the constellation. These advantages, coupled with the fact that physical sensors are not required, make this technique particularly suitable for Cultural Heritage applications. However, certain drawbacks still exist, primarily concerning the intensive post-processing phase required to obtain reliable results. Additionally, limitations related to the geometry of measurements may render this technique ineffective in some cases.

ACKNOWLEDGEMENTS

Project carried out using COSMO-SkyMed Products, © of the Italian Space Agency (ASI), delivered under a license to use by ASI. This research was conducted in the framework of the research project DPC-RELUIS 2022–2024 WP6 “Structural Health Monitoring and Satellite Data”.

REFERENCES

Bonaldo, G., Caprino, A., Lorenzoni, F., da Porto, F., 2023. Monitoring Displacements and Damage Detection through Satellite MT-InSAR Techniques: A New Methodology and Application to a Case Study in Rome (Italy). Remote Sensing 15. https://doi.org/10.3390/rs15051177

Caprino, A., Puliero, S., Lorenzoni, F., Floris, M., da Porto, F., 2023. Satellite SAR Interferometry and On-Site Traditional SHM to Monitor the Post-Earthquake Behavior of the Civic Tower in L’Aquila (Abruzzo Region, Italy). Remote Sensing 15. https://doi.org/10.3390/rs15061587

Cigna, F., Lasaponara, R., Masini, N., Milillo, P., Tapete, D., 2014. Persistent Scatterer Interferometry Processing of COSMO-SkyMed StripMap HIMAGE Time Series to Depict Deformation of the Historic Centre of Rome, Italy. Remote Sensing 6, 12593–12618. https://doi.org/10.3390/rs61212593

Cuca, B., Zaina, F., Tapete, D., 2023. Monitoring of Damages to Cultural Heritage across Europe Using Remote Sensing and Earth Observation: Assessment of Scientific and Grey Literature. Remote Sensing 15. https://doi.org/10.3390/rs15153748

Ferretti, A., Prati, C., Rocca, F., 2001. Permanent scatterers in SAR interferometry. IEEE Trans. Geosci. Remote Sensing 39, 8–20. https://doi.org/10.1109/36.898661

Ferretti, A., Savio, G., Barzaghi, R., Borghi, A., Musazzi, S., Novali, F., Prati, C., Rocca, F., 2007. Submillimeter Accuracy of InSAR Time Series: Experimental Validation. IEEE Transactions on Geoscience and Remote Sensing 45, 1142–1153. https://doi.org/10.1109/TGRS.2007.894440

Floris, M., Fontana, A., Tessari, G., Mulè, M., 2019. Subsidence Zonation Through Satellite Interferometry in Coastal Plain Environments of NE Italy: A Possible Tool for Geological and Geomorphological Mapping in Urban Areas. Remote Sensing 11, 165. https://doi.org/10.3390/rs11020165

Tapete, D., Cigna, F., 2012. Rapid Mapping and Deformation Analysis over Cultural Heritage and Rural Sites Based on Persistent Scatterer Interferometry. International Journal of Geophysics 2012, 618609. https://doi.org/10.1155/2012/618609

Wasowski, J., Bovenga, F., 2014. Investigating landslides and unstable slopes with satellite Multi Temporal Interferometry: Current issues and future perspectives. Engineering Geology 174, 103–138. https://doi.org/10.1016/j.enggeo.2014.03.003

STUDY OF INTERACTION OF SLOW SLOPE GRAVITATIONAL DEFORMATIOS WITH INFRASTRUCTURES BASED ON REMOTE SENSING TECHNIQUE

G. D'Ambrosio[1]*, D. O. Nitti[2], R. Nutricato[2], A. Doglioni[1]

[1] Department of Civil, Environmental and Structural Engineering and Chemistry (DICATECh), Politecnico di Bari, Italy – (giovanna.dambrosio, angelo.doglioni)@poliba.it
[2] Geophysical Applications Processing - G.A.P. SrL, c/o Dipartimento Interateneo di Fisica "Michelangelo Merlin", Via Amendola 173, 70126 Bari, Italy – (davide.nitti, raffaele.nutricato)@gapsrl.eu

KEY WORDS: Slow slope gravitational deformation, multi-temporal synthetic aperture radar interferometry, damaged bridge, infrastructure damages

ABSTRACT:

Slope gravitational deformations and landslides are a natural hazard quite commons in young geological countries as Italy, that can cause significant damages to infrastructure, including bridges, tunnels, railways and buildings. In particular, slow slope gravitational deformations may have a long-term impact on bridges and viaducts as they often occur over extended periods, and the resulting deformation can be difficult to detect. Remote sensing technologies have emerged as an effective tool for detecting slow landslides and monitoring their impact on bridges.
This work provides some examples of the interaction between slow and very slow slope gravitative deformations and bridges and their analysis using remote sensing techniques. First, the causes and types of slow slope gravitative deformations are discussed, with a focus on their impact on bridges. Several factors contribute to slow movements that have been examined by the use of remote sensing for analysing the impact of slow movements on bridges.
The main findings of this study are presented, by highlighting the potential for remote sensing technologies to improve our understanding of the interaction between slow slope gravitational deformations and bridges.

1. MODERN TOOLS TO INVESTIGATE SLOW GRAVITATIONAL DEFORMATIONS

1.1 Slow Gravitational Deformations and Infrastructure

Italy is a geologically young territory still undergoing significant and continuous geomorphological evolution. This evolution manifests through landslides and slow slope deformation phenomena, which are sometimes imperceptible but have the potential to cause long-term damage to infrastructure, particularly roads and railways, including bridges, viaducts, and tunnels (Forlati et al., 2001; Barla, 2018; D'Ambrosio et al., 2023). The progressive accumulation of millimetric deformations can exert long-term stress on infrastructure, leading to its damage or, in severe cases, collapse. Therefore, it becomes crucial to study methods for coexistence between the presence of infrastructure networks and instability phenomena.
In regions with recent tectonics, slow gravitational movements of slopes are relatively more common than you might think. These movements are challenging to recognize and investigate due to their nature, and they began to be studied only in the late 1970s (Guerricchio and Melidoro, 1981; Guerricchio, 2000b, Agliardi et al., 2001). Gravitational phenomena are not easily distinguishable from tectonic movements caused by the regional plate movement, combined with the movement of geological units with rigid mechanical behaviour situated above other, more deformable units at shallow depths (Guerricchio, 2022; Galeandro et al., 2013).
Although these phenomena develop in large areas, inside them it could be identified smaller items, which could evolve differently and require specific monitoring (Guerricchio, 2000).
A famous case of a complete collapse of a bridge due the interaction between slow landslide and infrastructures is the Albiano-Magra bridge, which was indagated with the InSAR technique; the investigations show that the landslide has a continuous displacement, that compressed the south abutment (Simeone, personal communication).
Southern Italy presents several examples of these phenomena, with the most famous being the Serra railway bridge, close to Lagonegro, constructed between 1915 and 1929. It was closed in 1953 due to the excess of deformations of one of its five arches, which were caused by deep-seated gravitational slope movement. The case studies analysed in this paper are in the area where was recognised a deep-seated gravitational slope deformation in the Lucanian - Ionian coastal arch; the movement of this landslide is a deep rotational, mainly directed from east to west. Deformations have originated by a strike-slip fault, that bring the disarticulation of the clay masses (Guerricchio and Melidoro, 1986).

1.2 MTInSAR technique applications

Modern technologies have enabled monitoring through satellite images of very small deformations that occur on a large scale, thanks, for example, to spaceborne radar interferometry techniques (Wasowski et al., 2019; Vinielles et al., 2021). However, the use of these techniques requires specific and professional processing of data.
In this study, the SPINUA algorithm (Stable Point Interferometry even in Unurbanized Areas) (Bovenga et al., 2004) was used. It is a Multi-temporal Interferometric SAR algorithm (MTInSAR) developed by the spinoff company of the Polytechnic University of Bari, GAP (Geophysical Applications Processing - http://www.gapsrl.eu). SPINUA was chosen because it has been tested on both persistent and distributed scatterers (PS and DS) acquired by SAR. It can detect millimetric displacements, even

* Corresponding author

in rural areas with limited PS availability. SPINUA has been tested for slope instability phenomena as well as for monitoring structures and infrastructure such as bridges, railways, dams, etc.. This technique offers several advantages, including the ability to obtain measurements over large areas without the need for on-site equipment installation, daily data acquisition in all weather conditions, the ability to analyse mass movements in periods preceding the start of investigations, and adaptability to slow movements. However, there are limitations, such as the lack of information on north-south horizontal displacements, a scarcity of measurement points in sparsely urbanized areas, snow cover at high altitudes, and the possibility of geometric distortions in the presence of slopes and the inability to find measurement points once investigations have begun (Wasowski et al., 2014).

2. CASE STUDIES

The investigation sites are located in Bradanic foredeep, in a vast area of outcropping of sub-Apennine clays, with veins of regressive terraced marine deposits, and traces of alluvial deposits on the bottom. The structure of the area is complex, in fact the clays of the middle-upper Pliocene rest on a thin layer of sands and then of clays of the Quaternary and then on alternating layers of clays and sands of the middle-upper Pleistocene. There are several deep narrow valleys which origin is due not only to erosive factors but also to the tectonic uplift (Doglioni et al., 2019). The flanks of the valley are affected by deformations and landslides that tend to close these incision valleys.

2.1 Bridge on SP 154

The first case study is the bridge on the provincial street 154 in Basilicata, between Bernalda (MT) and Ginosa (TA), near the border with Puglia.

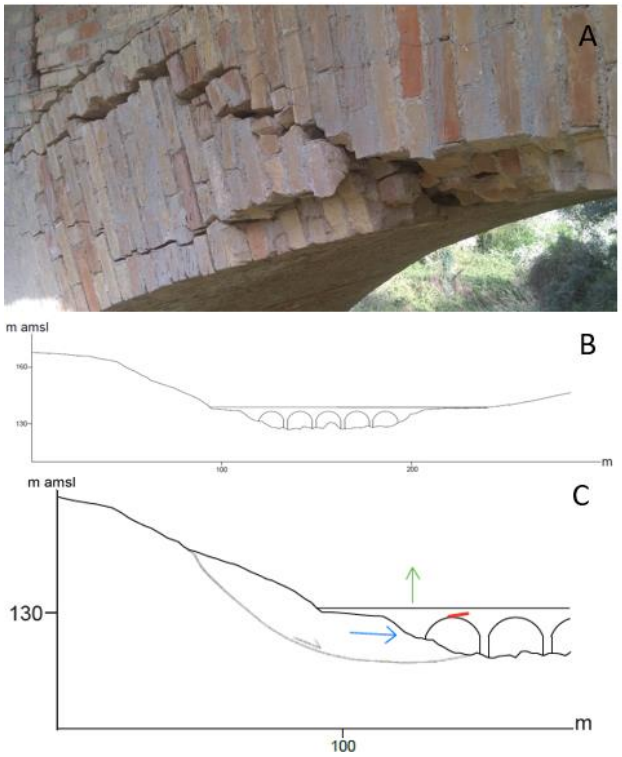

Figure 1. Bridge on SP 154: (A) Fissure over the arch, cross the keystone. (B) Reconstruction of the bridge in the valley terrain profile. (C) Reconstruction of the movement affecting the right flank.

It is a masonry bridge, 115m long and 8m large, crossing a deep narrow valley. It is damaged on right part of the first arch (Figure 1-A), where is evident a deep crack, probably caused, in the authors interpretations, by the movement of a very slow deformations of the slope and it is possible to see on the road pavement cracks and deformation.
On the right slope the inclination change, with a sort of bulging of the ground, where is the curve right before the abutment of the bridge; it is assumed that there is a slow gravitational deformation movement as shown in the Figure 1-C, and that has slowly put the bridge in compression, leading to the cracks.

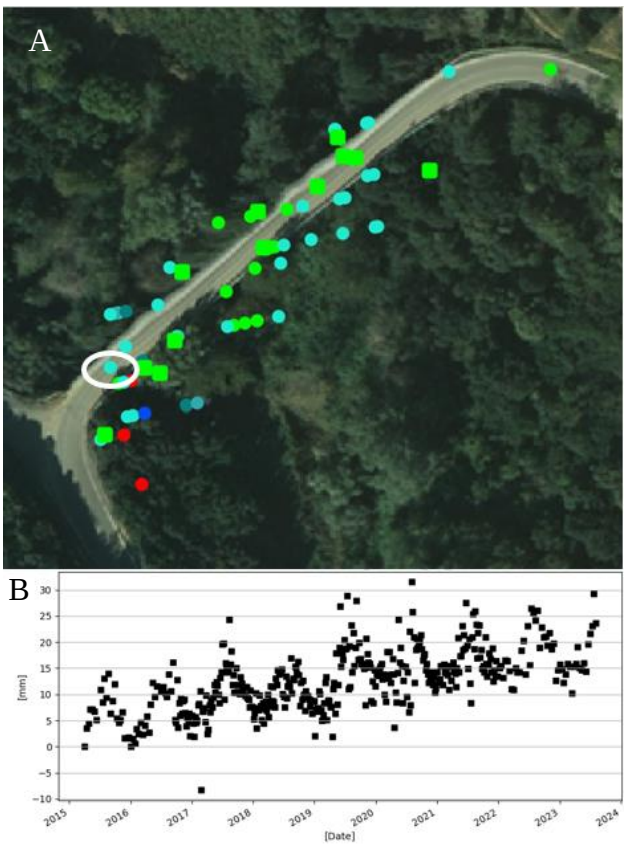

Figure 2. Bridge on SP 154: (A) 51 PS in ascending geometry (circular dots) and 12 in descending (square dots), with evidence of the selected PS. (B) Displacement time series for the selected PS.

The period of Sentinel-1 data acquisition starts on 01/04/2015, and end in 05/08/2023, with a total of 409 data, with a range of revisitation period between 12 and 6 days.
In the area of the bridge have been recognized the presence of: 51 PS in ascending geometry (circular dots) and 12 in descending (square dots) (Figure 2-A) The area of interest is delimitated at the contact zone between the instability phenomena and the abutment of the bridge. So, among the several available PS a point in ascending geometry on the bridge has been chosen, close to the flank is considered reliable because non affected by local surficial deformations. The displacement of this point, even if is affected by seasonal effects, shows a trend moving towards the satellite. The velocity individuated by the satellite is about 2 mm/year on the point.
Satellite finds out a movement that could be directed in uplifting or E-W, or a combination of both: in absence of descending points, in low number in this case, it is impossible to be sure about the real displacement of the bridge, in addiction of the limit of the technique about N-S displacement.

However, if PS are not available on both the ascending/descending geometries, it is possible to infer the movement of the area just from one; but this scenario requires other signals of the target movement and an expert opinion, that could use the InSAR technique to interpret the case studies.
In this case it is hypothesized that the movement of landslide put in compression the abutment that causes an uplifting of the bridge, which evidence are cracks on the arch.

2.2 Partially collapsed bridge on SP 103

On night of the 23th February 2013 half of a bridge on the SP103 in Pisticci (MT) collapsed (see Figure 3).

Figure 3. Bridge on SP 103: picture taken a few day after the collapse.

A few days before the collapse, vehicular traffic was closed due the failure and then it has been built up a new bridge in a different position.

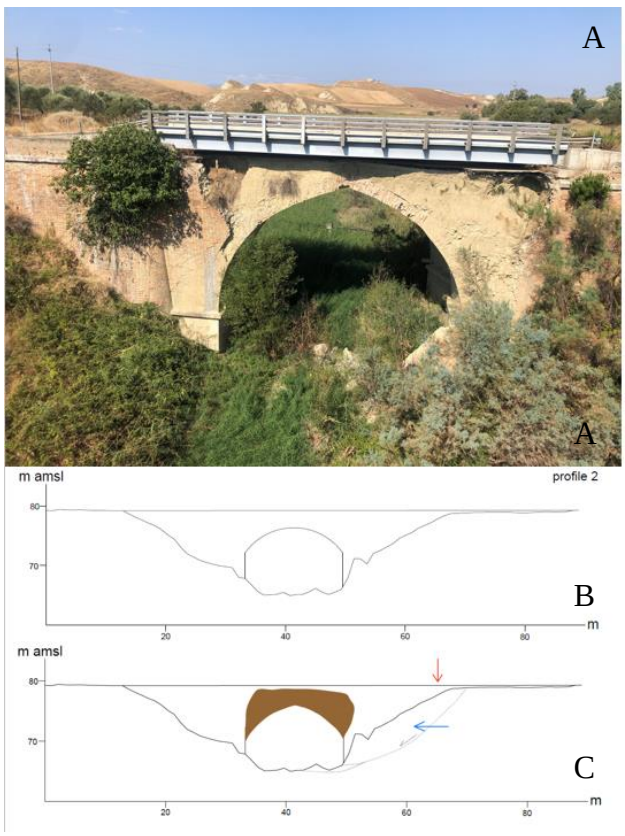

Figure 4. Bridge on SP 103: (A) Deformed arch. (B) Reconstruction of the bridge on the terrain profile. (C) Ogival deformation of the arch and main deformation direction.

The damage caused an important inconvenience to road traffic, because the SP 103 is the only direct connection between Craco and Pisticci; indeed after a few years the bridge was replaced by a new one, built near the older.
The bridge is constituted by a single arch in masonry, parallel to a railway line in disuse, and long 25m and large 6 m.
After the analysis of the altimetric profiles, it is supposed that the instability phenomena affect the left abutment, as shown in Figure 4; so, there were considered a few PSs in this area, on the abutment and on the arch, before the collapsed part of the lane.
The abundance of PS in descending geometry is justified by the parallelism between the bridge and the satellite trajectory, indeed there are only 6 points in ascending geometry and 66 in descending. The period of Sentinel-1 acquisitions begins on 12/04/2015 and ends on 04/08/2023, with a collection of 398 images. Unfortunately, the period of acquisition started after the collapse, and there are no PS found with the ENVISAT and ERS for their lower resolution. Anyway, among the several available PSs, it was chosen a group of points on the bridge, near the abutment of the bridge involved by the gravitational deformation, considered reliable because non affected by local surficial deformations.
It is possible to identify two separate movement:

- The first one, between the abutment and the terrain (Figure 5-B), show only moving away from the satellite, with a well definite displacement trend, so it is supposed that part of the bridge subsides, following the movement of the landslide;
- The second one, on the arch, shows a moving towards the satellite, so this fits the hypothesis of an uplifting of this area that brought at the collapse of the bridge in 2013.

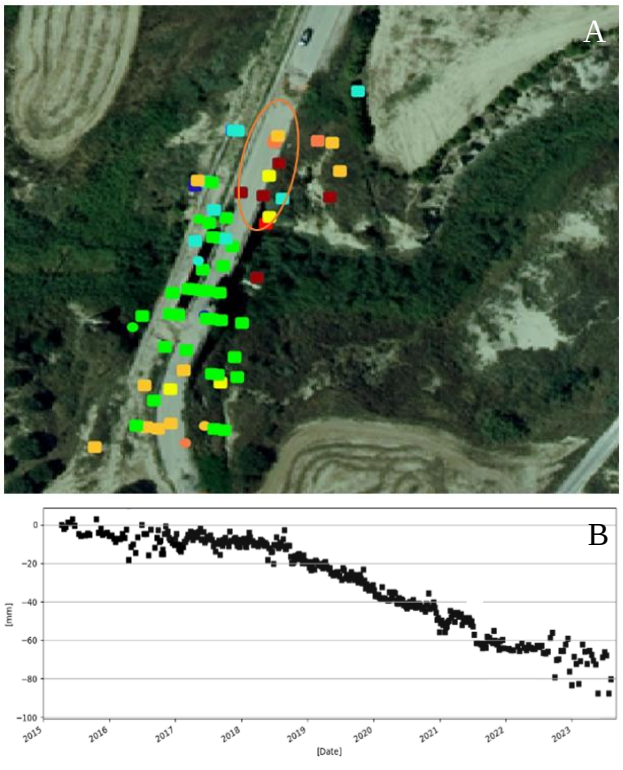

Figure 5. Bridge on SP103: (A) Circular and square dots refer to PS in ascending and descending geometries, respectively. In the area circled in orange, PSs have negative velocity. (B) Displacement time series of the selected PS which shows a well-defined trend, an elevated velocity and a moderate coherence.

3. CONCLUSION

The cases illustrated show how very slow landslide movements can cause significant damage to infrastructure and bring to the loss of functionality to, with all the direct and indirect consequences, and potentially loss of human lives.
A common mistake is to consider the cracks as a sign of infrastructures ageing, considering them detached from the geological context. These two cases are representative of huge number of similar cases in Italy, poorly investigated, but still dangerous.
Satellite interferometry technique represent an important monitoring tool that can help to clarify the ongoing dynamics of landslide-infrastructure interaction; but the technique alone can't explain the complexity of the interaction terrain-infrastructure, so it is required an expert opinion. In addiction it is needed a deep knowledge of the area, in fact, in the bridge on SP 154, some of the points near the chosen two, could deceive an inexperienced observer, because these points are in an area not affected by the landslide.

ACKNOWLEDGEMENTS

This work is part of the project: "Analysis of the impacts on slow landslides based on remote sensing techniques", granted by Apulian Regional Government, RIPARTI, project number 39786e0f.
The authors are sincerely grateful to prof. Vincenzo Simeone, for his critical review of the paper and for the constructive discussion on this subject.

REFERENCES

Agliardi, F., Crosta, G.B., Zanchi, A., 2001. Structural constraints on deep-seated slope deformation kinematics. *Engineering Geology*,- 59, pp. 83–102.

Barla, G., 2018. Numerical modeling of deep-seated landslides interacting with man-made structures. *J. Rock Mech. Geotech. Eng*. 10, pp. 1020–1036.

Bovenga, F., Refice, A., Nutricato, R., Guerriero, L., Chiaradia, M.T., 2004. SPINUA: a flexible processing chain for ERS / ENVISAT long term interferometry, Proceedings of ESA-ENVISAT Symposium 2004, 6-10 September, 2004, Saltzburg, Austria.

D'Ambrosio, G., Doglioni, A., Nitti, D. O., 2023. The impact of very slow moving gravitative slope deformations on infrastructures: the case study of the Bridge of Ginosa. *Italian Journal of Engineering Geology and Environment*, pp. 33–38, https://doi.org/10.4408/IJEGE.2023-01.S-05

Doglioni, A., Simeone, V., 2019. Gravine: peculiar morphological elements of the landscape in south-east Italy It. *Jour. Eng. Geol. and Env.*, Special Issue n. 1 2019, pp. 29-32, Sapienza Univ. Roma Ed., dio.org/10.4408/IJEGE.2019-01.S-05.

Forlati, F., Gioda, G., Scavia, C., 2001. Finite element analysis of a deep seated slope deformation. *Rock Mech. Rock Eng*. 34(2), pp. 135-159.

Galeandro, A., Doglioni, A., Guerricchio, A, Simeone, V., 2013. Hydraulic stream network conditioning by a tectonically induced giant deep-seated landslide along the front of the Apennine chain (South Italy), *Nat. Hazards and Earth Syst. Sci.*, 13, pp. 1269–1283.

Guerricchio, A., Melidoro, G., 1981. Movimenti di massa pseudo-tettonici nell'Appennino dell'Italia meridionale. *Geol. Appl. e Idrogeol.*, 16, pp. 251– 294.

Guerricchio, A. e Melidoro, G., 1986. Problematiche di geologia applicata lungo la fascia costiera ionica del Golfo di Taranto. *Atti del Convegno: "Evoluzione dei litorali, problematiche relativa al golfo di Taranto". Enea: Centro Ricerche Energia della Trisaia (Rotondella), Policoro (MT)*, pp. 263-294.

Guerricchio, A. 2000. La fragilità del territorio dell'Italia centro-meridionale desumibile dalle immagini da satellite. *X Congresso Nazionale dei Geologi: Il "Territorio fragile" – Ricerca e Appl. Diss. Idrog.* – I, pp. 443-482, Roma.

Guerricchio, A., 2022. Convivere con i grandi movimenti di massa. *Rivista Italiana di Geotecnica*, anno LVI N. 3-4, 3-186.

López-Vinielles, J., Fernández-Merodo, J.A., Ezquerro, P., García-Davalillo, J.C., Sarro, R.; Reyes-Carmona, C., Barra, A., Navarro, J.A., Krishnakumar, V., Alvioli, M., et al. 2021, Combining Satellite InSAR, Slope Units and Finite Element Modeling for Stability Analysis in MiningWaste Disposal Areas. *Remote Sensing*, 13(10), 2008, doi.org/10.3390/rs1310 2008

Wasowski, J.; Pisano, L.; 2019, Long-term InSAR, borehole inclinometer, and rainfall records provide insight into the mechanism and activity patterns of an extremely slow urbanized landslide. Landslides, 17(3), doi.org/10.1007/s10346-019-01276-7

TURIN DIGITAL TWINS: INITIATIVES AND CHALLENGES

L. la Riccia, V. Scolamiero, Y. Yadav, Allegra Eusebio

Inter-university Department of Regional & Urban Studies and Planning (DIST), Politecnico di Torino, Italy

KEY WORDS: Digital Twins, LiDAR, Photogrammetry, Smart Cities, Data Integration, 3D modeling.

ABSTRACT

The ability of the Digital Twins (DT) to provide value-added information simplistically has paved a completely new and broader path of opportunities in the field of Remote Sensing (RS) and digital 3D modeling. The presence of state-of-the-art RS techniques like LiDAR, SLAM, close-range photogrammetry, aerial photogrammetry, and their possible integration have even broadened the horizons and scopes for the creation and update of DT. In addition to 3D modelling, DT features the fourth dimension, time, which itself alters the data and the associated semantic information. DT enables the end users with a simplistic browsable and interactive web environment to analyze the past, present, and future of urban dynamics. Urban DT represents the virtual picture of a complex and dynamic physical world with a variety of applications in mobility, planning, energy, and many others. In this contribution, we focus on the ongoing progress and initiative in the project of creating the DT for the city of Turin Italy and deriving products from it. The DT project is aimed at the extraction of the built environment features, land use data, road network, and signs along with the update of the model with time.

1. INTRODUCTION

The concept of Digital Twin (DT) has been developed in the last years as part of the more general discourse on smart cities, with the aim of providing a physical infrastructure, data, information and procedures for the management of complex anthropogenic systems. The traditional association between DT and smart city derives from the ability of the former to analyze big data, provide services and applications and guarantee continuous monitoring, But Digital Twins are way more than just smart cities built in 3D, as they incorporate time as a variable that modify data and semantic information.

There are several applications of urban DT. Representing the virtual simulation of a complex dynamic reality, it can be used efficiently in various fields, for instance: energy, environment, mobility, spatial planning, emergency management and security. A DT can be understood as a bridge between physical reality and the virtual world i.e., a digital replica of physical objects and systems in the virtual world with the inclusion of sensors, smart Internet of Things (IoT) technology, Artificial Intelligence (AI) and dynamic simulations (Lehtola et al., 2022; Lu et al., 2020). In the field of Urban Planning, 3D models for DT are employed at multiple scales ranging from a single building to a regional scale.

The necessity to analyze urban dynamics and evaluate them beforehand in order to maximize the effectiveness and influence of new projects is what drives the urbanistic application of this instrument. Furthermore, DT can become an incredibly useful tools for public administration. In the framework of the SDG 11 - Make cities inclusive, safe, resilient and sustainable, in fact, developing a city-DT means not only adopting the principles of security, sustainability, and equity that future urban policies should pursue, but also becoming aware of the climate-altering impacts due to the increasing anthropic pressure on the city–landscape–inhabitant system (Shahat et al., 2021). The data sources for a DT can be satellite images, RGB images, point clouds, and hybrid 3D modelling methods. (Ying et al., 2023). For the image-based DT creation, most applications use the stereo-images based 3D reconstruction providing the detailed geoinformation with a larger coverage (Rothermel et al., 2020). As for point cloud dataset, they can accurately collect high-resolution 3D information of the ground features both in small and large scale urban scenes. Moreover, point cloud provides abundant 3D data and represents the vertical dimension straightforwardly i.e., building heights and surface occlusions from trees and buildings are represented well. The point cloud-based DT are focused on the building reconstruction in boundary classification and feature extraction as point data is enriched with semantic labels (roof, door, window, openings, etc.) (Albano, 2019; dos Santos et al., 2020; Erener et al., 2018) They provide height information and depict the building outline accurately. This adds significant value to DT visualization and semantic information input (Gevaert et al., 2017).

Another possibility for the creation of a DT involves hybrid data sources like 3D city models, 3D GIS, BIM-GIS and a few others. A 3D city DT includes information about the geometry, structure and covering data of numerous morphological aspects, infrastructure, vegetation, and buildings (Julin et al., 2018). The applications of the 3D city DT encompass anything from energy applications to urban spatio-temporal change detection and noise mapping (Zhao et al., 2017; Zięba-Kulawik et al., 2020; Zirak et al., 2020). For instance, low level of Details (LoD) concentrates on extracting large-scale building information (such as volume, height, and density), but high LoD examines nuanced 3D influence, which may be overlooked due to poor data resolution (for example, trees may cast shadows on houses on low-store levels). In addition, the 3D visualization breaks the 2D barrier, which is advantageous for various real estate stakeholders (Biljecki et al., 2016) Figure 1 illustrates the different applications and use-cases of a Digital Twin of a smart city.

Taking into consideration what stated above, the present paper intends to present some first results of the on-going project of creation of the Turin Digital Twin by the SDG11Lab in the DIST Department of the Politecnico di Torino. In the next lines it will be explained in detail the process of acquisition and

* Corresponding author

processing of the city-level data used to create the 3D model for the DT. The objective of this contribution is to propose a method for data acquisition which enrich the quality of the final 3D model, thanks to the combined use of Lidar and image data. The proposed outcomes of the Turin DT project are an easily accessible and browsable digital ecosystem that describes the behavior of the real world and its evolution over time as well as the effects of future urban developments.

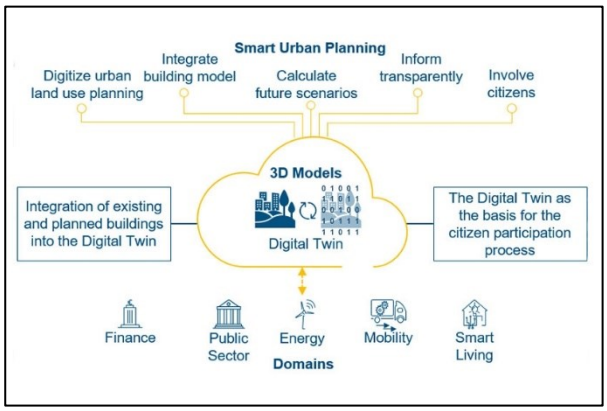

Figure 1: Urban Digital Twins for a smart city (Biljecki et al., 2016)

One of the main objectives of this work is to equip the public administration with a privileged tool to plan the future of the city and to manage past, present and future information at the same time.
First step to achieve these objectives is the construction of a digital model, integrating different sources, and the realization of a virtual environment where it is possible to visualize and to analyze different kind of data. Another goal is represented by the extraction of the built environment features, like land use data, road network, public infrastructure, buildings and green areas. Compared to a static 3D model, this application allows to reduce time for simulation and testing and opens the way to real time experience. Another end goal of the Turin DT project is the update of the model over time, , with a planned acquisition plan with different kind of sensors. This is necessary for the digital environment to maintain consistency over time and, at the same time, to bring the attention to a multitemporal and multiscale approach.

2. PRODUCTION OF DT

To build up this digital environment we analyzed a 3d web platforms that reflect an ever greater interest to Open Source (OS) software, interoperability and collaboration standard, in order to work in openness ecosystem. The next paragraph will explain the methodology of acquisition and processing of the city-level data that were used to create the 3D model for the Turin Digital Twin.

2.1 Data collection and study site

Turin is the third-largest city of Italy located in the North of Italy and is home to numerous UNESCO heritage structures. The location of the city of Turin is shown below in Figure 2. The dataset used to model the Turin DT is acquired on January 28-29, 2022, using the new Leica City Mapper-2 (Figure 3), a hybrid digital sensor onboard an aircraft and is composed by optical images as well as LiDAR point cloud. Figure 4 below shows one of the captures from the data acquisition phase in Turin.

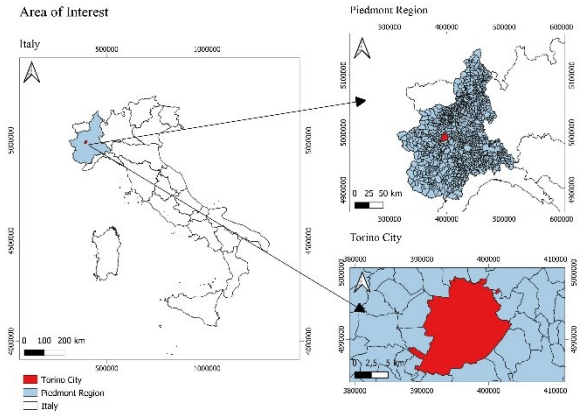

Figure 2: Location of the city of Turin

Figure 3: Data acquisition for Turin DT project with Leica CityMapper-2

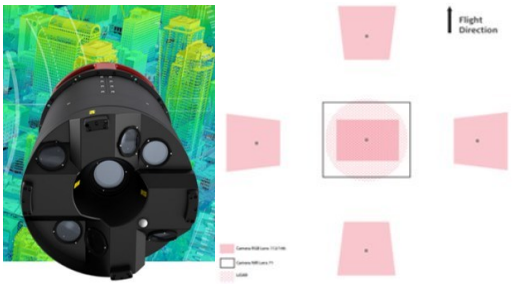

Figure 4: Dataset acquisition systems and acquisition schema

For the optical imagery data 20.291 images were acquired over the city of Turin at a flying altitude of around 1 km. For every capture location, one Nadir and four oblique images were acquired, as it is shown in the data acquisition schema in Figure 3. The photogrammetric takens was characterized by a GSD of 5 cm, 60% of lateral images overlapping and 80% of longitudinal images overlapping. Moreover, the sensor is equipped with two different cameras: the Camera NIR Lens 71 for nadir and multispectral acquisition and the Camera RGB Lens 112/145 for oblique acquisition. The scheme of acquisition was based on a traditional grid with nadir and oblique taken. The LiDAR data was collected simultaneously to the images, with a point density of 30-40 m^2. with an acquisition angle of 20°. This system is characterized by a conical scan pattern that allows vertical surfaces in the resulting point cloud in all direction.

2.2 Data management and data processing

The optical imagery and LiDAR data with initial orientations and trajectories were processed with Agisoft Metashape and nFrames SURE to derive classified dense point clouds, 3D mesh, precise and detailed orthophoto, DTM and DSM for the city of Turin. The use of combined dataset aims to improve the quality of the final model, as for instance the use of oblique images and LiDAR system represent an advantage for the modelling of vertical surface or provide additional information like the intensity, useful for point classification (Figure 5). In fact, while with the image data the classification regards only the land-use and land-cover visible on the images, with the LiDAR data we can classify the ground, the vegetation and the buildings. Furthermore, a complementary benefit of using the LiDAR – which is an active sensor – in combination with image data is the possibility to compensate the necessity of the sunlight with the ability to acquire in the shadows and under the vegetation.

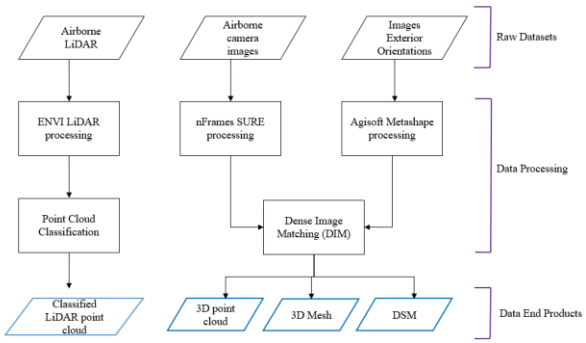

Figure 5: General Data Processing Methodology

Moreover, for 3D mesh the combining of LiDAR and image it's essential because one is used during the geometrical modelling end the other to texturing the 3D model.
The processing phase on nFrames Sure (Figure 6) combine LiDAR data and image data, this software offers the possibility to use LiDAR data to improve the 2.5D and 3D product. The LiDAR point clouds is useful where the geometry of the surface is difficult to reconstruct only from the images, in particular where the density of the city is very high or where the images is affected by shadow areas or occlusion. The following scheme shows the nFrames workflow.

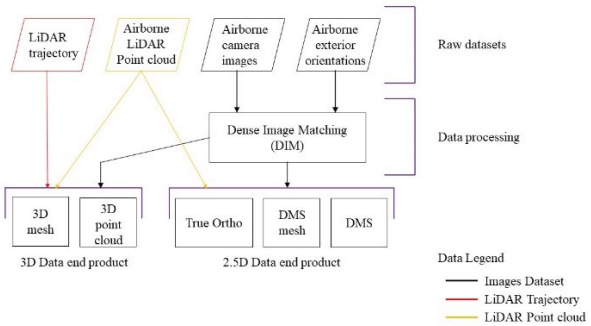

Figure 6: nFrames Sure workflow

The integration of the photogrammetric data with a LiDAR data, as shown in the figure 4, took place during the processing phase, so it is important that the initial data already match. The first step is called Dense Image Matching (DIM), and regard only the images. In this phase the images and the relative orientations were processed in order to obtain a 2.5D output.

After the DIM, LiDAR data are used only to reach a 3D output, like 3D mesh and 3D point cloud, and to enrichment the True Ortho.
Adopting LiDAR point cloud as a complement to the image data, the final 3D model result more complete and geometrically improved, as it allows to correct typical photogrammetric errors, during surface reconstruction phase. The following images show the difference between an image-based model and an integrated model in a zone afflicted by a shadow due to trees foliage.

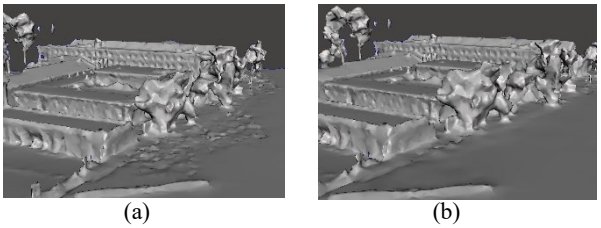

(a) (b)

Figure 7: Difference between (a) image-based model and (b) integrated model

The data were georeferred using the initial trajectory of the flight. The Leica City Mapper-2 is equipped with a multi-frequency and multi-constellation GNSS (Global Navigation Satellite System) receiver and IMU (Inertial Measurement Unit) gyro and accelerometer measurements. The absolutely accuracy of GNSS positioning with the stability of IMU generate a 3D navigation solution, used to georeferencing the data.

2.3 The 3D mesh model

The 3D model developed in the first phase of this work represents the base for future application of the Digital Twin. Thanks to the synergy and integration of different technologies, the previous stages allow to obtain a metrically correct model of the city, which will be useful to analyze and describe all the different feature of the urban environment. For instance, with the 2.5D DSM is possible to establish the high of the building and to extract the topography features, while the 3D Point cloud is used to classify the points in different class, like building and roof shapes, high and low vegetation, ground and road infrastructures. Moreover, the 3D model can be used for visualization and dissemination application on the web. All these applications can be translated into virtual layers that describe the city of Turin and that can be enriched by semantic content.

(a)

(b)

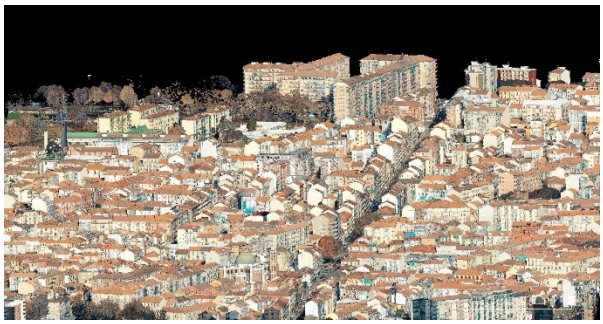

(c)

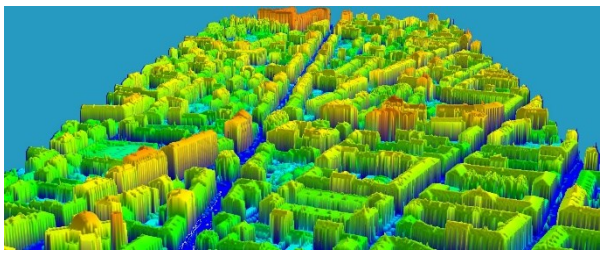

(d)

Figure 8: Processed Data Products (a) LiDAR point cloud (b) 3D point cloud from Photogrammetry (c) 3D mesh (d) DSM for the locality Corso Palermo in Turin

3. CHALLENGES AND OPPORTUNITIES

There are several challenges associated with this research project, related both to technical and semantic aspects. As for the technical aspect, the challenge consists in the processing of larger datasets or their cost-efficiency factor. Relating to the semantic aspects, there are issues concerning the rapid rate of growth and development of the city and the complexity of the solutions, which support the need for further research in the area of multitemporal updating of the model. Many are the solution that exist for the integration of 3D models from different sources for DT, but the key problem is still to have an operational and simplistic product that can be understood and implemented by the direct stakeholders. In this way the 3D model represents a key product which is at the base, in general, of DT.

Regarding the technical aspects, one of the challenges with 3D LiDAR and photogrammetry datasets is the requirement of stronger computational hardware for the processing. A workstation with moderately high computational strength is required for processing and visualization of 3D point cloud datasets from LiDAR and Photogrammetry. Also, when using airborne data along with ground based Close Range Photogrammetry (CRP), Terrestrial Laser Scanning (TLS) and SLAM, wide attention must be made to georeferencing errors that come from the integration of different data sources.

Another key challenge with a city level DT is the solution for sharing with the stakeholders. An open-source solutions would be optimal but it provides a limited storage capacity.

Not only challenges but also great opportunity come with this project. The development of an urban 3D model in an Open-Source system in fact could represent the chance for public administrations to have access to interactive analysis and simulation on the urban environment. Furthermore, particular attention can be paid to model update with collaborative and crowdsourcing solutions, with the perspective to develop a community able to use and update the 3D model.

Further experimentations will regard data integration for improvement of the model: not only ground-based Terrestrial Laser Scanning (TLS) data with aerial photogrammetry point cloud, but also crowdsourced data.

4. CONCLUSION AND FUTURE PERSPECTIVE

The proposed outcomes of the Turin DT project are an easily accessible and browsable digital ecosystem that describes the behavior of the real world and its evolution over time and an environment simulating the effects of future urban developments on the digital copy of reality.

REFERENCES

Lei, Binyu, et al. "Challenges of urban digital twins: A systematic review and a Delphi expert survey." *Automation in Construction* 147 (2023): 104716.

Deng, Tianhu, Keren Zhang, and Zuo-Jun Max Shen. "A systematic review of a digital twin city: A new pattern of urban governance toward smart cities." Journal of Management Science and Engineering 6.2 (2021): 125-134.

Biljecki, Filip, et al. "Applications of 3D city models: State of the art review." ISPRS International Journal of Geo-Information 4.4 (2015): 2842-2889.

Caprari, Giorgio, et al. "Digital twin for urban planning in the green deal era: A state of the art and future perspectives." Sustainability 14.10 (2022): 6263.

Tao, Fei, et al. "Digital twin modeling." Journal of Manufacturing Systems 64 (2022): 372-389.

Lehtola, Ville V., et al. "Digital twin of a city: Review of technology serving city needs." International Journal of Applied Earth Observation and Geoinformation (2022): 102915.

Hämäläinen, Mervi. "Urban development with dynamic digital twins in Helsinki city." IET Smart Cities 3.4 (2021): 201-210.

Bacher, Uwe. "Hybrid Aerial Sensor Data as Basis for a Geospatial Digital Twin." The International Archives of the Photogrammetry, Remote Sensing and Spatial Information Sciences 43 (2022): 653-659.

Xia, Haishan, et al. "Study on city digital twin technologies for sustainable smart city design: A review and bibliometric analysis of geographic information system and building information modeling integration." Sustainable Cities and Society 84 (2022): 104009.

Schrotter, Gerhard, and Christian Hürzeler. "The digital twin of the city of Zurich for urban planning." PFG–Journal of

Photogrammetry, Remote Sensing and Geoinformation Science 88.1 (2020): 99-112.

Dembski, Fbian, et al. "Urban digital twins for smart cities and citizens: The case study of Herrenberg, Germany." Sustainability 12.6 (2020): 2307.

Eriksson, Helen, and Lars Harrie. "Versioning of 3D city models for municipality applications: Needs, obstacles and recommendations." ISPRS International Journal of Geo-Information 10.2 (2021): 55.

Griffiths, David, and Jan Boehm. "A review on deep learning techniques for 3D sensed data classification." Remote Sensing 11.12 (2019): 149.

Albano, R. (2019). Investigation on roof segmentation for 3D building reconstruction from aerial LIDAR point clouds. Applied Sciences (Switzerland), 9(21). https://doi.org/10.3390/app9214674

Biljecki, F., Ledoux, H., Stoter, J., & Vosselman, G. (2016). The variants of an LOD of a 3D building model and their influence on spatial analyses. ISPRS Journal of Photogrammetry and Remote Sensing, 116, 42–54. https://doi.org/https://doi.org/10.1016/j.isprsjprs.2016.03.003

dos Santos, R. C., Galo, M., & Habib, A. F. (2020). Regularization of building roof boundaries from airborne LiDAR data using an iterative CD-spline. Remote Sensing, 12(12). https://doi.org/10.3390/rs12121904

Erener, A., Sarp, G., Muhammet, &, & Karaca, I. (2018). An approach to urban building height and floor estimation by using LiDAR data. https://doi.org/10.1007/s12517-020-06006-1/Published

Gevaert, C. M., Persello, C., Sliuzas, R., & Vosselman, G. (2017). Informal settlement classification using point-cloud and image-based features from UAV data. ISPRS Journal of Photogrammetry and Remote Sensing, 125, 225–236. https://doi.org/https://doi.org/10.1016/j.isprsjprs.2017.01.017

Julin, A., Jaalama, K., Virtanen, J. P., Pouke, M., Ylipulli, J., Vaaja, M., Hyyppä, J., & Hyyppä, H. (2018). Characterizing 3d city modeling projects: Towards a harmonized interoperable system. ISPRS International Journal of Geo-Information, 7(2). https://doi.org/10.3390/ijgi7020055

Rothermel, M., Gong, K., Fritsch, D., Schindler, K., & Haala, N. (2020). Photometric multi-view mesh refinement for high-resolution satellite images. ISPRS Journal of Photogrammetry and Remote Sensing, 166, 52–62. https://doi.org/https://doi.org/10.1016/j.isprsjprs.2020.05.001

Shahat, E., Hyun, C. T., & Yeom, C. (2021). City digital twin potentials: A review and research agenda. In Sustainability (Switzerland) (Vol. 13, Issue 6). MDPI AG. https://doi.org/10.3390/su13063386

Ying, Y., Koeva, M., Kuffer, M., & Zevenbergen, J. (2023). Toward 3D Property Valuation—A Review of Urban 3D Modelling Methods for Digital Twin Creation. In ISPRS International Journal of Geo-Information (Vol. 12, Issue 1). MDPI. https://doi.org/10.3390/ijgi12010002

Zhao, W.-J., Liu, E.-X., Poh, H. J., Wang, B., Gao, S.-P., Png, C. E., Li, K. W., & Chong, S. H. (2017). 3D traffic noise mapping using unstructured surface mesh representation of buildings and roads. Applied Acoustics, 127, 297–304. https://doi.org/https://doi.org/10.1016/j.apacoust.2017.06.025

Zięba-Kulawik, K., Skoczylas, K., Mustafa, A., Wężyk, P., Gerber, P., Teller, J., & Omrani, H. (2020). Spatiotemporal changes in 3d building density with lidar and geobia: A city-level analysis. Remote Sensing, 12(21), 1–23. https://doi.org/10.3390/rs12213668

Zirak, M., Weiler, V., Hein, M., & Eicker, U. (2020). Urban models enrichment for energy applications: Challenges in energy simulation using different data sources for building age information. Energy, 190, 116292. https://doi.org/https://doi.org/10.1016/j.energy.2019.116292.

AERIAL LIDAR AND INFRARED THERMOGRAPHY FOR URBAN-SCALE ENERGY ASSESSMENT AND PLANNING

S. Anselmo [1]*, M. Ferrara [2], Y. Yadav [1], P. Boccardo [1]

[1] Interuniversity Department of Regional and Urban Studies and Planning, Politecnico di Torino, Italy
(sebastiano.anselmo, yogender.yadav, piero.boccardo)@polito.it
[2] Department of Energy, Politecnico di Torino, Italy
maria.ferrara@polito.it

KEY WORDS: Aerial Thermography, LiDAR, energy planning, urban simulation, 3D data

ABSTRACT:

Recent policies at the national and international levels showed the need for effective tools supporting policymaking. This study – primarily based on energy classification – uses thermographic pictures and GIS technology to define the energy needs of a district in Turin, Italy. Potential savings – in terms of primary energy consumption and carbon dioxide emissions – are assessed based on two retrofit scenarios and alternative energy supply options. A further element, i.e. the photovoltaic potential, is introduced to assess – starting from classified LiDAR data – the possibility to introduce self-production forms for reducing even more the impacts of the energy sector. The results show the potential for further studies based on 3D modelling, oriented towards the implementation of a thematic layer for the Urban Digital Twin.

1. INTRODUCTION

1.1 Framing of the study

With the ongoing urbanization trend, there is a pressing need for policies to reduce energy demand and deriving environmental problems. In this context, the fit for 55 package – including the revision of the Renewable Energy Directive, Energy Efficiency Directive and Energy Performance of Buildings Directive – targets an 80-95% reduction of GHG emissions (compared to 1990 levels) by 2050.
Policymakers require effective tools for supporting their decisions, e.g. mapping the current status of energy performance according to the EPBD. Geographic Information System is a powerful tool to integrate and synthesize multiple datasets – be they tables, vectors or imagery. In the energy sector, GIS can be used to draft Urban Building Energy Models with a low appeal to archetypes thanks to the continuity granted by geographic data. Aerial thermography can be used to define a consumption model based on the thermal dispersion of buildings. While this method is widely validated on a building scale (Martin et al., 2022), its potential on district and city scales still has to be unlocked. Moreover, it is possible to georeference the information contained in Energy Performance Certificates – required since 2002 before any intervention – to improve the calculation model by adding further parameters.

1.2 Workflow

The work is structured in two main components: a consumption and photovoltaic productivity analyses are carried out contextually, thus exploring the possibility to create a Renewable Energy Community in the area of interest.
The demand estimation is conducted by estimating the thermal performance of the envelope from thermographic pictures and correlating the energy performance class observed in a set of Energy Performance Certificates issued for the area of analysis. Potential productivity from photovoltaic panels – intended to understand the share of renewable energy to meet the total demand – is estimated with a GIS-based viewshed algorithm from the Digital Surface Model, realised starting from a LiDAR point cloud.
Two renovation scenarios are then explored, considering the potential benefits from renovating the building stock and partially electrifying the energy systems for heating and cooling.

1.3 Study area

The study area is located in the Northern part of Turin, in the *Barriera di Milano* district. It is bounded by relevant mobility infrastructures – a former railway in the North and high-capacity avenues on the other three sides – with further two principal roads crossing it and characterised by problems affecting both its physical and social structures. Two main clusters were highlighted for this research, with a former industrial plant in the North and a functionally mixed area in the South.
The study area is heterogeneous, with an inner dense residential fabric and industrial buildings – partially reconverted for commercial purposes – on the borders. Indeed, the district grew after the post-war economic boom, with industries along the commercial axes and residential buildings to meet the deriving housing demand. The quick and serial realisation led to poor-quality constructions, resulting now in problems such as inadequate energy performance. From this it arose the need for a wide-scale energy classification, supporting future policies for extensive energy renovations and assessing the results of refurbishments which already happened. Further details are provided in (Anselmo et al., 2023).

2. CONSUMPTION ANALYSIS

2.1 Thermographic acquisition

The evaluation of the thermal energy demand started from thermographic images acquired on 9/1/2022 with a FLIR A8581 MWIR HD camera – registering wavelengths of 3-5 µm with

* Corresponding author

±1°C accuracy. They were orthorectified to remove distortions, producing thermal orthoimages. Despite the possibility to see the roofs only due to the nadiral perspective, the 1.3 MP resolution ensures the recognition of disturbing elements – like chimneys and dormers – affecting the results. However, the diurnal acquisition – around midday – led to shading problems, with sunny pitches returning considerably higher values compared to the shadowed ones. Due to the exploratory nature of this research, it was not possible to have a dedicated acquisition, resorting instead to existing datasets with limited availability.
The thermographic pictures – provided orthorectified but not geolocalised – were first georeferenced with ArcGIS Pro. After a first adaptation through scaling and rotation, the georeferencing tool requires the user to input Ground Control Points by comparing the image to be georeferenced with a georeferenced one, requiring a higher resolution not to reduce the accuracy. In this case, a precision orthophoto – 5 cm accurate – realised in the TerraItaly™ Metro HD project for the SDG11 Lab was used. On average, the resulting forward error was 0.941, while the inverse was 1.412. The five images – one stand-alone and the others grouped in couples – cover an area of approximately 0.35 km^2.

2.2 Definition of consumptions

Thermographic pictures return the outer temperature of buildings. Assuming the internal temperature as constant – considering that the flight was carried out during the heating season, with the temperature set by Presidential Decree 16 April 2013 n. 74 to be 20°C – and the roofs to be homogeneous – realised with the same material, thus resulting in similar thermal storage and emissivity – the outer surface temperature can be used to quantify the thermal dispersion and therefore the energy class. For this step, Energy Performance Certificates – regulated in Italy by the Legislative Decree 192/2005 – were gathered, defining the distribution of buildings in the classes and the reference Global Energy Performance Index (as the median of the values registered in the EPCs for that class). Results are summarised in Table 1, with differences emerging in the intervals between the values. They are minimum for central classes, increasing towards lower classes: class G requires approximately 100 kWh/m^2 more than class F, while only 15 kWh/m^2 divide classes C and E. As for the count, class F is the one with the most units, with less performing classes outnumbering the upper ones.

Energy class	Count [-]	Share [%]	Reference GEPI [kWh/m^2]
B	3	4.65	98.06
C	3	4.65	118.95
D	11	16.74	123.15
E	17	25.58	130.49
F	20	30.23	176.24
G	12	18.14	276.22
Average	11	16.61	153.85

Table 1 – Energy classes and reference GEPI

The reference GEPI was multiplied by the gross floor surface – defined as the footprint multiplied by the number of floors – and divided by the conversion factor of the natural gas to compute the thermal energy demand. On the other hand, the electricity demand was esteemed as 1113 kWh/inhabitant, based on ISTAT data. The total energy demand is shown in Figure 1.

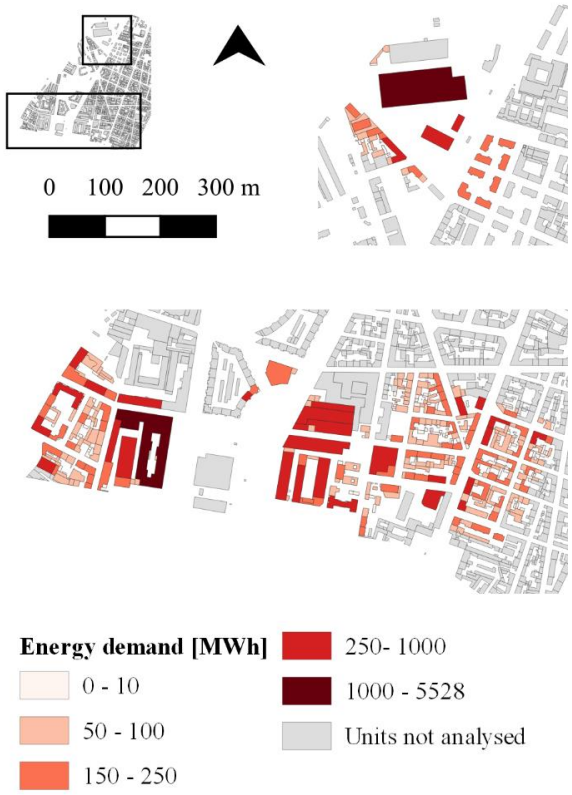

Figure 1. Total energy demand

The former industrial plant in the North is composed of the most energy-intensive units, due to low performance and big surfaces to be heated. The westernmost area – partially renovated – has some of the most performing buildings, while there is high heterogeneity in the Eastern cluster. As for class characteristics, the gross floor surface increases constantly from B to F, while class G buildings are smaller compared to the previous class. This partially mitigates their impact, resulting from high consumption. The total thermal energy demand amount to 42 GWh/year, equal to 155 kWh/m^2, which makes the average building classifiable in class E. As for electricity demand, 37% of the buildings have residential units, with a total need of 3 GWh/year (9% of the total energy demand), corresponding to 19460 kWh/year per building.

3. LIDAR POINT CLOUDS

In this work, a DSM produced by Compagnia Generale Ripreseaeree was used, but it is relevant to mention how LiDAR point clouds are processed to produce a DSM.

3.1 LiDAR classification

Light Detection and Ranging (LiDAR) is one of the principal technologies for large-scale 3D modelling. It generates a brief laser pulse and registers the reflection (Croneborg et al., 2020), thus creating a cloud of points with known positions.
There are two main methods for LiDAR data classification: feature extraction and machine learning. The former segments the dataset based on spatial and radiometric information, while the latter has seen recent evolutions in the field of computer vision and deep learning. PointNet is a deep neural network processing the 3D point cloud without conversion, unordered. It uses transformation matrices and the max pooling method to classify the point cloud elements, abstracting the features of the original point cloud through subsequent iterations (Zhongyang et

al., 2018). The segmented point cloud can be used to return different products, according to the required application.

3.2 DEMs production

Classified point clouds can be used to produce a 2.5D Digital Surface Model (DSM), which describes on a bi-dimensional raster map the surface of objects from the real world. For the rasterisation, two types of processes can be carried out. Among the semi-automated solutions, CloudCompare requires the user to input the cell size of the regular grid to be returned, the vertical direction (Z) and the interpolation method to be used to fill up the spaces with no information. On the other hand, the module DSM in OPALS (Orientation and Processing of Airborne Laser Scanning data) – developed by TU Wien – is fully automated. It is based on the iteration of sub-sampling grids until either the neighbour count or the maximum search radius is reached, followed by a moving planes interpolation.
While the DSM takes into account the whole point cloud, pre-processing is required to derive other Digital Elevation Models (DEMs), such as the Digital Terrain Model. In particular, in this case, a filtering phase is required to select only the ground points. The appropriate DEM is to be selected according to the application and the required accuracy, so as to minimise elaboration times.

4. PHOTOVOLTAIC POTENTIAL

Solar energy is the most suitable Renewable Energy Source (RES) for being installed in the built environment, due to the possibility to integrate solar panels on the roofs. This reduces both the investment costs – not requiring the construction of further structures – and the visual impact of this technology. The photovoltaic potential was calculated based on the solar radiation striking the roofs, according to the Suri equation (1):

$$PV_{potential} = \text{Solar energy} * PI * \eta * \text{surface [kWh/year]} \quad (1)$$

Where Performance Index PI – quantifying the efficiency of the system – was assumed to be 75%, the conversion efficiency η depends on the technology to be installed and the surface is assumed to be 40% of the unit footprint – a value which includes correction factors for inclination and presence of obstacles.

4.1 Solar radiation evaluation

Starting from the DSM elaborated from LiDAR data, it was possible to evaluate the solar energy using the "Area solar radiation" tool of ArcGIS Pro (ESRI). Parameters were set according to the need to minimise the elaboration time while keeping the calculation accurate. The default sky size – 200 – was kept, while the hour interval was increased to 1 hour, analysing the radiation with a "whole year" time configuration. Thus, by default, the day interval is set to 14 days, using 2022 as the reference year. The "slope and aspect input type" was shifted to the option which uses the input DSM for calculating the exposition, calculation directions were reduced from 32 to 16.
The crucial aspects were the radiation parameters. As "diffuse model type" it was chosen the "standard overcast sky", with which the diffuse radiation flux varies based on the zenith angle. Diffuse proportion and transmissivity values – summarised in Table 2– make the study site-specific by including weather data differentiated depending on the season. Diffuse proportion is returned by PVGIS – an online tool by the European Commission – while for the latter further calculations are required, crossing data from the same source with fixed parameters as the LINKE turbidity factor and the solar constant.

Season	Diffuse proportion	Transmissivity
Winter	0.38	0.56
Summer	0.38	0.76
Spring/autumn	0.42	0.67

Table 2. Diffuse proportion and transmissivity parameters

The tool processes on average around 0.7 km^2/h, thus requiring nearly two hours to process the area of interest for each iteration. For this reason, seasonal averages were used, aggregating four months for each.
The "Area solar radiation" tool returns monthly values, making therefore possible the comparison of different months. By checking the two months for which the radiation is minimal – December – and maximal – August – it is possible to observe a relevant difference apart from the one in the energy values, that is the solar height. In summer the sun rays strike not only the roofs but also the roads and open areas. On the contrary, in winter months the roofs are the only surfaces with relevant production values, thus justifying their selection for the installation of photovoltaic modules. Values were then aggregated yearly, as shown in Figure 2.

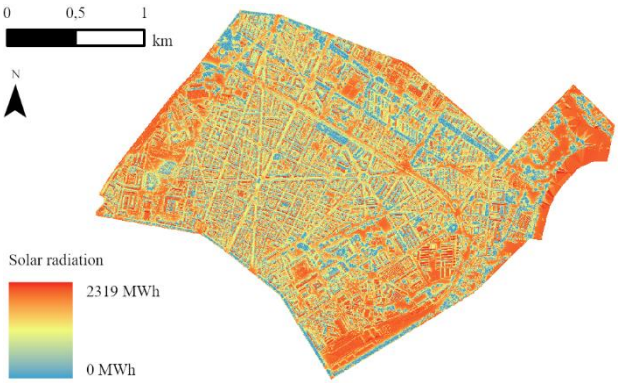

Figure 2. Yearly solar radiation

4.2 Producibility of photovoltaic panels

Once having calculated the solar radiation, it is necessary to refer production values to the volumetric units. This can be done in a few steps, converting each cell of the raster output to points and joining the values of the closest point to the centre of the volumetric unit. By choosing this procedure instead of calculating zonal statistics based on the volumetric units, the portion with the highest radiation is taken, not considering the potential errors on the roof edges.
After that each volumetric unit is assigned a reference radiation value, it is possible to compute the potential production. Conversion efficiency, according to (Green et al., 2022), was esteemed to be 24.2% for crystalline cells, 18.4% for polycrystalline and 11% for thin film. When installing the second, approximately 8.8 GWh can be produced yearly, with a great variability for each volumetric unity, mostly based on the exploitable surface. Indeed, all buildings producing more than 120 MWh/year have 1200 m^2 of available roof surface or more. Compared to polycrystalline, monocrystalline modules have higher productivity, thus being able to produce the same amount of energy with a lower surface or produce more with the same surface. On the other hand, thin-film modules produce less but are also cheaper.
Comparing the potential polycrystalline production to the esteemed consumptions – assumed to be 1000 kWh/person/year, it emerges that around half of the volumetric units could produce by itself the electricity needs. Moreover, 15% of the units can

produce twice their demand, with the ratio between total production and consumption being 83.2%. Therefore, collaboration forms can be foreseen, dividing benefits and burdens within the community.

5. RENOVATION SCENARIOS

The previous results were integrated to elaborate two alternative retrofit scenarios. The first is the optimum, foreseeing a reclassification of all buildings in class B, and the second targets an improvement by two classes for every unit. They were compared by assessing four alternative energy supply options, that are District Heating (DH), natural gas (G), a mix of district eating and natural gas (M) and heating pumps – partially covering the demand through photovoltaic production – (HP+PV). In the first three scenarios, electricity is taken from the grid.

5.1 Energy saving

The first assessment concerned the savings in terms of primary energy. Figure 3 shows the current state – with all buildings heated through natural gas boilers – and the comparison of the two scenarios with different energy supply options.

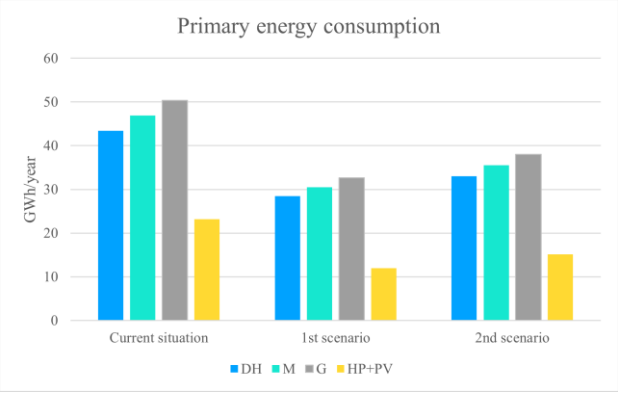

Figure 3. Primary energy Consumption

The least savings are achieved by renovating the buildings without changing the systems servicing them, while the installation of photovoltaic panels and heating pumps would lead to a doubling of the savings. District heating – likely to be introduced in the district in the medium term according to the project North East – is the most effective energy supply option which does not foresee electrification for maximising the savings, reducing consumption 15% more than with natural gas boilers.
The optimum scenario would grant savings of at least 35%, with additional 4 GWh of primary energy saved yearly in the case of district heating implementation. Self-production and the use of heating pumps would cut the consumption by ¾, that are 48 GWh.
In the second scenario – the most likely thanks to lower investments needed – 26% of the volumetric units would fall into class B, decreasing primary energy consumption by 25% to 70%, depending on the energy supply. This makes it suitable to use the second scenario as an intermediate step towards a full renovation. Moving from this scenario to the optimum without changing the energy supply would result in savings from 14% to 21%. However, an even wider difference – 25% equal to 9.6 GWh/year – can be observed between the second configuration with natural gas boilers and the first with district heating.

5.2 Decarbonisation potential

An energy retrofit would also help the Municipality to achieve climate neutrality, considering that in Turin the residential sector causes 37.2% of the total carbon dioxide emissions.
Figure 4 quantifies the savings in terms of tonnes of equivalent CO_2 in the two scenarios, with the general outcomes being similar to the takeaways of the primary energy analysis. The HP+PV solution in the two scenarios would grant – respectively – savings equal to 59.53% and 56.59%.

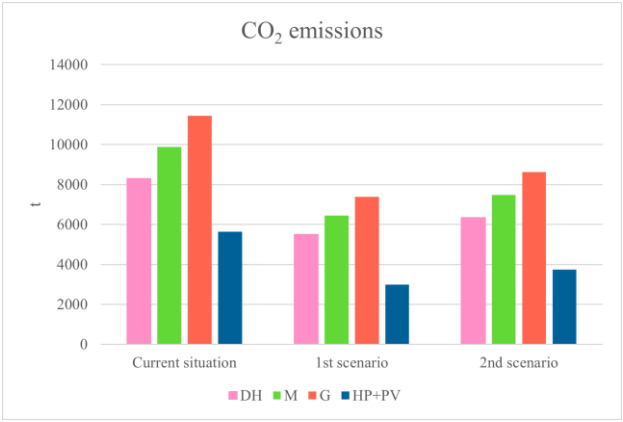

Figure 4. CO_2 emissions

At least 2829 tonnes of CO_2 could be saved – improving the building stock by two classes and keeping natural gas boilers –, with savings reaching 8460 t_{CO_2} in the best option.
Compared to the previous analysis, with this parameter the upgrade from the second to the first scenario is more convenient. A transition towards district heating would result in savings 10% higher, 6% in case of a mixed scenario. On the other hand, savings are 3% lower considering heating pumps.

6. CONCLUSIONS AND FURTHER DEVELOPMENTS

This article focused on a method to perform an energy assessment – for both production and consumption – through the tools of remote sensing. Two retrofitting scenarios were compared in terms of primary energy saving and prevented emissions, taking into account alternative energy vectors. The first scenario grants the most benefits, but the second requires a lower investment, being therefore a better trade-off between costs and benefits. Investments would be needed also for the electrification scenario, thus requiring additional calculations on the payback period, based on the relevant savings which would derive.
This method proved to be simple and easy to use so that it can be attractive for policymakers. On the other hand, there were problems with data availability and simplification. A first improvement would derive from the acquisition of a better thermographic dataset – granting oblique pictures for full 3D reconstruction and the absence of solar radiation flawing the results – which can push the automation of the processing. Another key aspect is the definition of the necessary technologies for increasing energy efficiency, quantifying the necessary investments too. Moreover, also the costs relative to the installation phase should be taken into account.
Finally, this could be a first supporting tool towards the identification of areas suitable for the creation of Renewable Energy Communities, based on their potential and limitations – in terms of dimensioning and potential production. To do so, the principal aspect to take into account is correlation, defined as the time shift between the peaks of energy production and consumption, both during the day and the seasons. The two

scenarios can be used for the definition of a roadmap towards the creation of energy communities, reducing the energy needs for taking a step forward in the direction of self-production.

ACKNOWLEDGEMENTS

This report is part of the project NODES which has received funding from the MUR - M4C2 1.5 of PNRR with grant agreement no. ECS00000036; it was developed according to the framework agreement between the City of Turin and the Polytechnic of Turin, signed on 9th February 2023, for the realisation of pilot projects towards the implementation of a Digital Twin. Moreover, our gratitude to DigiSky S.r.l. for providing the thermographic pictures.

REFERENCES

Anselmo, S., Ferrara, M., Corgnati, S.P., & Boccardo, P. (2023). Aerial urban observation to enhance energy assessment and planning towards climate-neutrality: A pilot application to the city of Turin. In *Sustainable Cities and Society*, 99, 104938. https://doi.org/10.1016/j.scs.2023.104938

Croneborg, L., Saito, K., Matera, M., McKeown, D., & van Aardt, J. (2020). *Digital Elevation Models*. World Bank, Washington, DC. https://doi.org/10.1596/34445

Green, M. A., Dunlop, E. D., Hohl-Ebinger, J., Yoshita, M., Kopidakis, N., & Hao, X., 2022. Solar cell efficiency tables (version 59). In *Progress in Photovoltaics: Research and Applications*, 30(1), 3–12. https://doi.org/10.1002/pip.3506

Martin, M., Chong, A., Biljecki, F., & Miller, C., 2022). Infrared thermography in the built environment: A multi-scale review. In *Renewable and Sustainable Energy Reviews*, 165, 112540. https://doi.org/10.1016/j.rser.2022.112540

Zhongyang, Z., Yinglei, C., Xiaosong, S., Xianxiang, Q., & Li, S. (2018). Classification of LiDAR Point Cloud based on Multiscale Features and PointNet. In *2018 Eighth International Conference on Image Processing Theory, Tools and Applications (IPTA)*, 1–7. https://doi.org/10.1109/IPTA.2018.8608120

SATELLITE TECHNOLOGIES FOR CULTURAL HERITAGE: STATE OF THE ART, PERSPECTIVES AND ITALIAN SPACE AGENCY'S CONTRIBUTION

D. Tapete [1] *, M. Virelli [1], F. Cigna [2]

[1] Italian Space Agency (ASI), Italy
(deodato.tapete, maria.virelli)@asi.it

[2] Institute of Atmospheric Sciences and Climate, National Research Council (CNR-ISAC), Italy
f.cigna@isac.cnr.it

KEY WORDS: Cultural heritage, Built heritage, Archaeological sites, COSMO-SkyMed, Synthetic Aperture Radar, Satellite, Monitoring

ABSTRACT:

In the last 20 years, satellite technologies have been increasingly used for study, monitoring, conservation and promotion of cultural heritage, with a growing trend at both national and international levels. While satellite images collected from optical sensors have already become common data exploited by (geo-)archaeologists, researchers and heritage experts, Synthetic Aperture Radar (SAR) technologies are increasingly being tested and exploited, also beyond the specialist image analyst community. At European level, the Italian ecosystem undoubtedly represents an excellence. First of all, there is long tradition in exploitation of innovative technologies for cultural heritage across many countries in Europe. Moreover, several investments were made into not only Earth Observation (EO) missions with characteristics of image acquisition that well suit the user needs and requirements for this application domain, but also initiatives promoting downstream applications and services development engaging small, medium and large enterprises. The present paper therefore illustrates ASI's contribution for cultural heritage, alongside the current perspectives, in light of the COSMO-SkyMed programme (upstream) and "Multi-mission and Multi-Frequency SAR" and "Innovation for Downstream Preparation" (I4DP) programmes (downstream), the latter with particular focus on the initiative dedicated to scientific users (I4DP_SCIENCE).

1. INTRODUCTION

There is a substantial body of literature and developed case studies demonstrating how satellite technologies have become one of the technological means to address more than one of the main phases of cultural heritage management, i.e. discovery, study, monitoring, conservation and promotion. This growing trend is witnessed at both national and international levels. Recent publications critically reviewing the specialist scientific literature highlight a significant level of maturity of satellite applications in this domain (Luo et al., 2019; Tapete and Cigna, 2019a), so as satellite images collected from optical sensors have already become common data exploited by (geo-)archaeologists, researchers and heritage experts.

At the same time, Synthetic Aperture Radar (SAR) technologies are increasingly being tested and exploited, also beyond the specialist image analyst community, thanks to multidisciplinary collaboration between different professionals (Tapete and Cigna, 2017) and facilitated SAR data access given the increasing provision by e.g. space agencies, data centres and commercial providers, also in "ready to use" formats (Tapete and Cigna, 2019b).

The Italian ecosystem – composed by scientific and academia community developing solutions, small, medium and large enterprises able to engineer innovative scientific algorithms and prototyping novel services, and heritage bodies that play a pivotal role to test such developments based on EO data on real-world cases, and thus assess whether they can become solutions – undoubtedly represents an excellence, at least at European level. Therefore, it is true to state that in Italy there is the full chain leading from upstream satellite assets to downstream exploitation of EO data.

The Italian Space Agency (ASI) is at the core of this national ecosystem, thanks to its continuous investment in EO data exploitation and applications development, as new satellite missions are designed and launched.

The present paper has manifold objectives: to provide an overview of current achievements in the application domain of satellite technologies for cultural heritage; to outline existing trends and future perspectives; in light of the above, to illustrate ASI's contribution to the growth of this field; and to describe ongoing initiatives at national level to continue nurture this downstream sector.

2. ACHIEVEMENTS AND TRENDS

Nowadays, the use of satellite technologies for cultural heritage is not novel per se, given that it is long time that satellite technologies are used for heritage prospection, monitoring and conservation. Cuca and Hadjimitsis (2017) already provided an overview of the operational period of satellites (both ongoing and no longer active) carrying sensors of interest for archaeological prospection. That census clearly highlighted that, at different levels, several members of the archaeological and cultural heritage communities had already identified what existing satellites could offer to complement the available means and data sources to address cultural heritage applications.

Such inventory would definitely require to be updated to account for not only the most recent launches of satellites of potential interest for cultural heritage – e.g. hyperspectral missions like PRISMA (Loizzo et al., 2019; Giacomo et al., 2020) and EnMap (Storch et al., 2023) or sensors such as DESIS (Alonso et al., 2019) –, but also the new technologies in sensors and platforms. In this respect, mini- and nano-satellite constellations are increasingly being launched and enhance the range of (very) high

* Corresponding author

spatial resolution products accessible from the user community. These space assets are expected to not only widen the observation solutions available to users, but also boost the temporal resolution. While first papers on the use of PRISMA (Alicandro et al., 2022) and DESIS (Cerra et al., 2021) in archaeology are gradually appearing in the literature, the assessment of the impact of mini and nano-satellites on cultural heritage applications is yet to be unfold, and thus remains an area of further investigation.

Moreover, although satellite technologies are yet to be embedded in operational workflows by various strands of the community, review exercises of the specialist literature undertaken separately and independently by different research groups on different topics show an increasing trend of experimentations and use of satellite technologies for cultural heritage (Tapete and Cigna, 2017, 2019a; Luo et al., 2019; Cuca et al., 2023; Zingaro et al., 2023).

During the European Space Agency (ESA) Living Planet Symposium (LPS) held in Milan, Italy, in 2019 (LPS 19), ASI organised and chaired the session "Sentinels and Copernicus Contributing Missions for Cultural & Natural Heritage", in collaboration with Politecnico di Milano and Romanian Space Agency (ROSA) (Tapete et al., 2021). After the open call for abstracts and a peer-review process involving experts in the field, 12 presentations and 19 posters were included in the final programme. An assorted cross-section of the user community was brought together, with a good representation of the remote sensing science core regarding EO applications on cultural heritage, experts from academia and research institutes, companies working with public authorities as well as space archaeologists engaging with stakeholders in Middle East, North Africa and Asia.

The following elements were common to all the presentations:

- Clear identification of user category
- Type of question(s) to address (e.g. archaeological research, condition assessment, operational service)
- Satellite data type and methods used
- Lessons learnt, including things that did not work well or could have been improved
- Engagement of further users and stakeholders, and their degree of involvement
- Suggestions for improvements or specific requirements

Sentinel-1 and Sentinel-2 of the Copernicus fleet were the main satellite constellations used. A direct relationship was found between satellite data type, application and user expertise. Sentinel-1 SAR data were mostly exploited for ground stability and condition assessment studies based on interferometric methods, by very expert users capable to process these data themselves. Thanks to project partnerships, end-users (e.g. public authorities and conservators) were directly involved to define user requirements and set up the portals and workflows to exchange the extracted information, so to inform the decision making process. Sentinel-2 multispectral data were, instead, most preferred by archaeologists for desk-based studies aiming to gather evidence base to verify later in the field.

It was also evident that processing platforms (e.g. Google Earth Engine) were already increasingly exploited by the space archaeology community to process Sentinel time series or other EO datasets (e.g. Agapiou, 2021; Brandolini et al., 2021), thus making the data handling task more sustainable, without the need to host and manage in-house expensive hardware and software infrastructure. Such exploitation has reached a level of maturity across the archaeological community that a debate on proven benefits and still open avenues had been already started (Alcover Firpi, 2016).

While no specific needs were expressed to access more or new satellite data, or for new science/operational satellites – and this was a surprising outcome of the session compared to other scientific communities participating in ESA LPS 19 –, a growing use of "virtual constellation" data for archaeology & cultural heritage was recorded (e.g. Agapiou et al., 2019; Tapete and Cigna, 2020). Archaeologists and archaeological remote sensing analysts combine multi-sensor data as they were collected according to a coordinated observation plan by a virtual constellation (see the concept "Virtual constellation" promoted by CEOS, 2023). However, such exploitation is typically made by expert users who are aware of the various opportunities offered by satellite missions. Therefore, one of the key conclusions was that more could be done to make the user community aware of the value of Copernicus Contributing Missions, either optical and SAR, to complement the Sentinel data.

Same comment can be made with regard to the existing downstream services tailored to the specific needs of Copernicus users, such as the Climate Change service that was not yet considered to investigate the spatial and temporal changes of meteorological conditions and vegetation cover contributing to environmental threats at archaeological sites. Corine and higher resolution land cover products released at European scale by the Copernicus Land Monitoring Service, are definitely more used. However, some issues were found for the implementation at local scale in certain geographic contexts, due to the characteristics of the crops (e.g. in Poland).

3. ASI'S CONTRIBUTIONS TO THE FIELD

Cultural heritage is among the R&D topics that ASI has supported with a certain continuity over years. Several initiatives were put in place, in particular along the following directions:

- Undertaking scientific research and development, also through real-world user-driven use cases, e.g. demonstrating the performance achievable using national assets such as COSMO-SkyMed data (Tapete and Cigna, 2019b, 2020, 2021, 2022);
- Supporting COSMO-SkyMed data exploitation in projects with Italian institutions (e.g. Ministry of Culture, Archaeological Park of Colosseum), and activities devoted to downstream applications and services development (e.g. in Pompeii, Capo Colonna) (Virelli et al., 2020);
- Promoting downstream by scientific, commercial and institutional users through the new programme "Innovation for Downstream Preparation" (I4DP), wherein safeguard of environment, cultural heritage and national landscape is among the key application domains.

The most recent account of the above activities can be found in Virelli et al. (2023).

From the technical and scientific research point of view, experimentations done in the framework of ASI's internal research demonstrated that, despite the common knowledge that X-band SAR sensors cannot penetrate soils to detect buried features, backscattering anomalies in bare ground with limited vegetation coverage can be detected in COSMO-SkyMed images, especially at 1 m spatial resolution in Enhanced Spotlight mode (Figure 1). Such evidence further corroborates capabilities for archaeological prospection that had been proved by earlier research studies (Chen et al., 2015; Monterroso Checa and Martínez Reche, 2018) and has stimulated more recent applications in vegetated temperate environments (Cigna et al., 2023).

Even more developed is the contribution that COSMO-SkyMed currently brings to condition assessment and conservation of cultural heritage. Data from COSMO-SkyMed constellation are well consolidated in R&D activities aiming to monitor structural

stability of historical buildings and archaeological ruins and the ground beneath them by means of Interferometric SAR (InSAR) techniques. Higher spatial and temporal resolutions of input imagery result in much denser datasets of deformation estimates over the monitored monument or site. There is also an improvement in geometric accuracy along the elevation of buildings. These technical advantages make monitoring activities based on COSMO-SkyMed long time series definitely a substantial upgrade compared to an initial wider area screening based on Sentinel-1 collections, and a more appropriate means to achieve structural health assessment at single building level.

This type of application represents an Italian success story with respect to the development of the so-called satellite-based "scientific downstream", i.e. applications that can serve institutional and real-world purposes based on mature and validated algorithms that were originally developed to answer scientific questions and/or retrieve geophysical parameters, and were brought to the stage that they can generate products addressing specific user needs beyond scientific and academic purposes only (Tapete and Coletta, 2022).

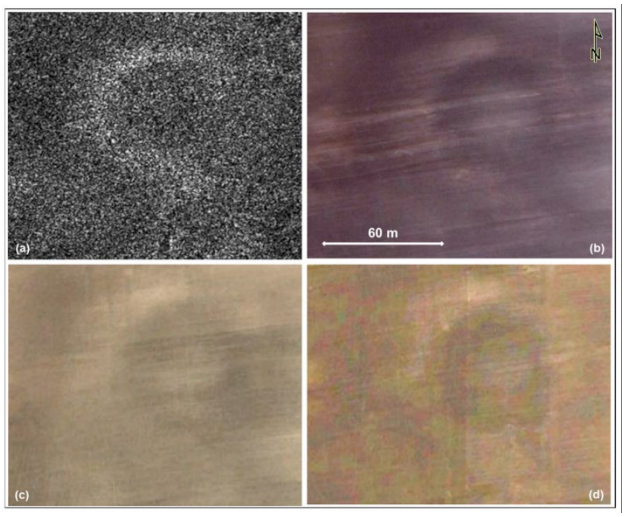

Figure 1. (**a**) Backscattering anomaly related to buried archaeological remains in bare ground within an archaeological site (precise location undisclosed for security concerns) observed in a COSMO-SkyMed Enhanced Spotlight image at 1-m ground resolution acquired in the summer with an incidence angle of 39°. The soil/damp mark is also visible in very high resolution optical satellite imagery (Google Earth © DigitalGlobe) acquired in (**b**) summer, (**c**) autumn and (**d**) winter. COSMO-SkyMed® Product ©ASI—Italian Space Agency—2018. All Rights Reserved (reproduced from Tapete and Cigna, 2019b).

In the time span of less than a decade, the COSMO-SkyMed technology and the InSAR algorithms to process their long time series of imagery moved from earlier scientific studies demonstrating the feasibility of multi-temporal monitoring of cultural heritage (e.g. Cigna et al., 2014) to more operational exploitation (e.g. Raspini et al., 2023) and structural engineering and architectural studies (e.g. Caprino et al., 2023). In parallel to this scientific consolidation process, COSMO-SkyMed data were also part of pilot demonstrations undertaken by the national commercial community through projects funded by either ASI or ESA or carried out in the framework of institutional collaborations promoted by ASI, that engaged final end-users to test InSAR technology in support of heritage bodies and site managers for their duty tasks of heritage monitoring and protection.

Among the many projects, it is worth mentioning POMERIUM (Ferri and Francioni, 2022) and AMOR (Dore et al., 2021) that were funded in the framework of ESA "5G for l'ART (L'Aquila, Roma, Torino)", co-funded by ASI, and aimed to demonstrate downstream services for the conservation and promotion of cultural heritage. Both projects focused on monuments in Rome that was a test-bed for many InSAR studies to investigate cultural heritage (see Cigna et al., 2014 and references therein).

With the collaboration of reference users encompassing the Capitoline Superintendence of Cultural Heritage of Rome, the Colosseum Archaeological Park and the Special Superintendence for Archaeology, Arts and Landscapes of Rome of Italian Ministry of Culture (MiC), POMERIUM project exploited Persistent Scatterers retrieved from InSAR processing of COSMO-SkyMed 2010-2020 to address the risk scenario related to deformation of the Colosseum, Pyramid of Cestius and Aurelian Walls. The 2D/3D AWARE web platform designed and implemented by e-GEOS S.p.A. acted as the unique entry point to data and analysis services for final users interested in understanding and monitoring the threats to the conservation of the monuments the users themselves are in charge of.

With a similar approach, the AMOR project (Advanced Multimedia and Observation services for the Rome cultural heritage ecosystem) led by NAIS S.r.l. has investigated the structural issues and ground motions affecting the Baths of Caracalla, the southern portion of the Aurelia Walls using InSAR data, alongside weed vegetation analysis and change detection techniques, by combining SAR and optical data. In this case the St'ART® platform was exploited to let final users access the information and help them in planning interventions.

A common feature of these experiences was therefore the need of making information extracted from satellite data accessible to users in a way that they can use such information within the daily workflow.

A step forward in user uptake of satellite technologies is achieved when the process is entirely managed and driven by the user. An exemplar experience in this respect is represented by the collaboration with the Colosseum Archaeological Park. A few years ago, the Park initiated a dedicated monitoring project covering the whole extent of the park. This project was inspired by the desire to build a sustainable system of protection and conservation, then allowing a proper tourism valorisation. The Colosseum Archaeological Park developed a static and dynamic monitoring project wherein satellite monitoring (historical analysis of the satellite data) were directly embedded into the system and analysed in order to monitor possible ground deformation, alongside in situ monitoring data from traditional geotechnical instruments. Satellite data therefore contribute to a multi-parameter system of permanent control of the entire archaeological area, with associated indicators of the level of risk. More specifically, the interferometric outputs were included in the WebAPP system (namely SyPEAH; Della Giovampaola, 2021) developed by the Archaeological Park itself as the heritage body's tool for an effective activity of programmed conservation of cultural heritage with particular regard to archaeological structures. COSMO-SkyMed data were ingested into the institutional user workflow, instead of remaining a dataset interpreted externally to the decision-making process, as unfortunately frequently happens in research-focused studies or consultancies. Figure 2 shows the implementation of historical deformation analysis over the Flavian Amphitheatre.

Currently, in the framework of the ASI-MiC agreement signed in February 2023, ASI is involved in the implementation of the work phases of the "Extraordinary Plan of Monitoring and Conservation of Immovable Cultural Heritage" (*Piano Straordinario di Monitoraggio e Conservazione dei Beni Culturali Immobili*). The Plan defines the criteria to identify the

properties that are to be monitored and where conservation measures need to be made, alongside the required priority order of the inspections and controls, also based on specific indices of territorial hazard and the individual vulnerability of each property. The Plan also aims to define the systems for instrumental control to exploit and the implementation modalities of safety, conservation and safeguard measures (MiC, 2023).

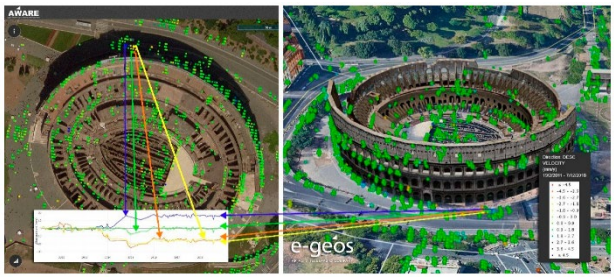

Figure 2. Implementation of historical deformation analysis over the Flavian Amphitheatre, Colosseum Archaeological Park, Italy, whose geometric and material characteristics made it particularly suitable for structural monitoring with interferometric processing and analysis (COSMO-SkyMed data processed by e-GEOS) (reproduced from Della Giovampaola, 2021).

As a further proof that satellite technologies are nowadays well embedded in the heritage management practice at Italian institutional levels, the Plan (MiC, 2023):

1. matches the requirements expressed by the national users in charge of monitoring and conservation of cultural heritage in the framework of consultancy activities of users of the National Copernicus User Forum (ISPRA, 2024);
2. contributes to the definition of the technical requirements for the national operational services of territorial monitoring that will be provided through the implementation of the Space Economy – Mirror Copernicus Program (see e.g. Taramelli, 2021);
3. foresees the harmonisation of existing laws concerning satellite monitoring, in the framework of the activities of the "Earth Observation" Working Group of the Italian Government Presidency of the Council of Ministers (PCM).

The first of the five levels through which the Plan is developed focuses on the identification of the data needed for monitoring and acquisition/return model. The Plan therefore promotes the integration of EO and remote sensing data collected from different observation platforms (satellites, airborne, terrestrial) with territorial surveys and in situ measurements. Satellite products are conceived as the first element of an "observation chain", allowing preliminary identification of critical areas (anomalies) where detail investigations are further undertaken.

In this context, over 2022, ASI provided MiC and its partners with access to long time series of COSMO-SkyMed first and second generation satellite data that were mostly collected over several monumental and archaeological areas in Italy via the Map Italy project (ASI, 2023) since 2011 and 2021, respectively. The wide portfolio of sites span from Venice, Padua, Verona in the north to Pienza, Volterra, Aurelian Walls in Rome in the centre to Phlegraean Fields Archaeological Park, Paestum and Velia in the south of Italy. COSMO-SkyMed data were then processed using Persistent Scatterer Interferometry (PSI) and change detection techniques, also in synergy and continuation with existing projects and recent initiatives (see for example Caprino et al., 2023; Raspini et al., 2023). The results are currently analysed by the various research teams involved in the Plan, and the perspective is that ASI will support MiC not only with the further provision of COSMO-SkyMed data, but also with the definition of guidelines and protocols for integration of the different monitoring technologies and calibration of satellite monitoring techniques, alongside an integrated satellite and in situ instrumental monitoring.

4. KEY REMARKS AND PERSPECTIVES

In the current national and international context by which satellite technologies are increasingly exploited in cultural heritage applications and the launch of new satellites will continue trigger R&D activities to improve existing algorithms and develop novel analytical methods and prototype new products, the crucial achievement for satellite data to effectively play a role in the management cycle of cultural heritage is that users perceive that these data are relevant to their activities and thus useful, and are part of the information layers to substantiate and address the decision making process.

The continuous investment made by ASI in this field of application definitely contributed to generate opportunities for an effective downstream that, initially, was purely scientific and then encompassed both the commercial and institutional perspectives. In order to strengthen this pathway towards downstream, protection of cultural heritage is explicitly mentioned among the key application domains supported by the current ASI programme called "Innovation for Downstream Preparation" (I4DP). The programme supports the demonstrative development of new technologies, products and services, using not only EO data but also Navigation and Telecommunications and promoting the integration with other edge technologies (e.g. Artificial Intelligence, Data analytics, IoT). I4DP is structured around the three main categories of final users (i.e. Commercial, Scientific and Public Administrations).

The initiative dedicated to the Scientific User Community, i.e. Italian Universities and Public Research Bodies, is named I4DP_SCIENCE and was launched by ASI in early 2022. I4DP_SCIENCE is composed of joint demonstration projects aiming to "Development of applications based on novel methods and algorithms for satellite data analysis and training of medium-high professional qualification personnel, in different application fields and scientific downstream". The projects are selected by means of thematic "calls for ideas" issued on a regular basis on selected topics of national relevance, e.g. defined by the National Copernicus User Forum, and/or falling within international agendas, e.g. the United Nations' Sustainable Development Goals (SDGs). I4DP_SCIENCE allows for algorithms and methods at Scientific and/or Technological Readiness Level at least equal or higher to 4 i.e. "Proof of concept" to be demonstrated in real-world scenarios, thus it offers an open arena for innovation in cultural heritage applications.

ACKNOWLEDGEMENTS

Activities presented in this paper were undertaken in the framework of (in order): internal ASI research based on COSMO-SkyMed® Products, ©Italian Space Agency (ASI), delivered under a license to use by ASI (Projects "Multi-SAR" and "LARICI", led by Deodato Tapete, and "BigSAR" led by Francesca Cigna); the Project of Colosseum Archaeological Park and the Italian Network of Archaeological Parks; the Extraordinary Plan of Monitoring and Conservation of Immovable Cultural Heritage funded by the Ministry of Culture (MiC) and the ASI – MiC cooperation agreement n. 2023-2-Q.0; ASI's programme "Innovation for Downstream Preparation (I4DP)" under the Italian Government Presidency of the Council of Ministers (PCM)'s funding ex art. 1, c. 254, Law 160/2019, ASI – PCM agreement 27 December 2021.

REFERENCES

Agapiou, A., 2021. Multi-Temporal Change Detection Analysis of Vertical Sprawl over Limassol City Centre and Amathus Archaeological Site in Cyprus during 2015–2020 Using the Sentinel-1 Sensor and the Google Earth Engine Platform. *Sensors*, 21, 1884, doi: 10.3390/s21051884

Agapiou, A., Alexakis, D.D., Hadjimitsis, D.G., 2019. Potential of Virtual Earth Observation Constellations in Archaeological Research. *Sensors*, 19, 4066, doi: 10.3390/s19194066

Alcover Firpi, O.A., 2016. Satellite Data for All? Review of Google Earth Engine for Archaeological Remote Sensing, *Internet Archaeology*, 42, doi: 10.11141/ia.42.10

Alicandro, M., Candigliota, E., Dominici, D., Immordino, F., Masin, F., Pascucci, N., Quaresima, R., Zollini, S., 2022. Hyperspectral PRISMA and Sentinel-2 Preliminary Assessment Comparison in Alba Fucens and Sinuessa Archaeological Sites (Italy). *Land*, 11, 2070, doi: 10.3390/land11112070

Alonso, K., Bachmann, M., Burch, K., Carmona, E., Cerra, D., de los Reyes, R., Dietrich, D., Heiden, U., Hölderlin, A., Ickes, J., et al., 2019. Data Products, Quality and Validation of the DLR Earth Sensing Imaging Spectrometer (DESIS). *Sensors*, *19*, 4471, doi: 10.3390/s19204471

ASI, 2023. ASI – Italian Space Agency upgrades access to MapItaly data. https://www.asi.it/en/2023/12/asi-italian-space-agency-upgrades-access-to-mapitaly-data/

Brandolini, F. et al., 2021. A Google Earth Engine-enabled Python approach for the identification of anthropogenic palaeo-landscape features. *Open Research Europe*, 1(22), doi: 10.12688/openreseurope.13135.2

Caporusso, G., Lopinto, E., Lorusso, R., Loizzo, R., Rocchina, G., Daraio, M.G., Sacco, P., 2020. The Hyperspectral Prisma Mission in Operations. In: "IGARSS 2020 - 2020 IEEE International Geoscience and Remote Sensing Symposium", Waikoloa, HI, USA, 2020, pp. 3282-3285, doi: 10.1109/IGARSS39084.2020.9323301.

Caprino A. et al., 2023. Application of Multi-Temporal InSAR (MT-InSAR) for structural monitoring: the case study of Scrovegni Chapel in Padova. *Procedia Structural Integrity*, 44, pp. 1578-1585. doi: 10.1016/j.prostr.2023.01.202

CEOS, 2023. Virtual constellations https://ceos.org/ourwork/virtual-constellations/ (29 October 2023)

Cerra, D., Gege, P., Evagorou, E., Agapiou, A., de los Reyes, R., 2021. Monitoring Submerged Cultural Heritage Sites with DESIS. 1st DESIS User Workshop 2021, 28. Sep. - 1. Oct. 2021, online, https://elib.dlr.de/145687/.

Chen, F., et al., 2015. A space view of radar archaeological marks: First applications of COSMO-SkyMed X-band data. *Remote Sensing*, 7, pp. 24–50. doi: 10.3390/rs70100024

Cigna F. et al., 2014. Persistent Scatterer Interferometry Processing of COSMO-SkyMed StripMap HIMAGE Time Series to Depict Deformation of the Historic Centre of Rome, Italy. *Remote Sensing*, 6, pp. 12593-12618. doi: 10.3390/rs61212593

Cigna F. et al., 2023. Exploiting satellite SAR for archaeological prospection and heritage site protection. *Geo-spatial Information Science*. doi: 10.1080/10095020.2023.2223603

Cuca, B., Hadjimitsis, D.G., 2017. Space technology meets policy: An overview of Earth Observation sensors for monitoring of cultural landscapes within policy framework for Cultural Heritage. *Journal of Archaeological Science Reports* 14, 727-733, doi: 10.1016/j.jasrep.2017.05.001

Cuca, B., Zaina, F., Tapete, D., 2023. Monitoring of Damages to Cultural Heritage across Europe Using Remote Sensing and Earth Observation: Assessment of Scientific and Grey Literature. *Remote Sensing*, 15, 3748. doi: 10.3390/rs15153748

Della Giovampaola, I., 2021. SyPEAH: The WebAPP System for Protection and Education to Archaeological Heritage in the Parco Archeologico del Colosseo. *Geosciences*, 11, 246. doi: 10.3390/geosciences11060246

Dore N. et al., 2021. Progetto AMOR: quando la tecnologia incontra i Beni Culturali. *Archeomatica*, 4(12), pp. 14-17.

Ferri M., Francioni, E., 2022. POMERIUM, un Sistema multi-tecnologico per il Monitoraggio Avanzato dei Beni Culturali. In: 13° Workshop Tematico di Telerilevamento "Telerilevamento Applicato Ai Processi di Conoscenza e Gestione del Territorio", Oratorio San Filippo Neri, Via Manzoni 5 – Bologna, 22-23 settembre 2022, pp. 22-24.

ISPRA, 2024. Programma Copernicus. https://www.isprambiente.gov.it/it/programma-copernicus

Loizzo, R., Daraio, M., Guarini, R., Longo, F., Lorusso, R., Dini, L., Lopinto, E., 2019. PRISMA Mission Status and Perspective. In: "IGARSS 2019 - 2019 IEEE International Geoscience and Remote Sensing Symposium", Yokohama, Japan, July 2019, pp. 4503-4506, doi: 10.1109/IGARSS.2019.8899272.

Luo, L. et al., 2019. Airborne and spaceborne remote sensing for archaeological and cultural heritage applications: A review of the century (1907–2017). *Remote Sensing of Environment*, 232, 111280, doi: 10.1016/j.rse.2019.111280

Ministero della Cultura (MiC), 2023. Piano straordinario di monitoraggio e conservazione dei beni culturali immobili https://dgspatrimonioculturale.beniculturali.it/attivita-direzione-generale-sicurezza-del-patrimonio-culturale/bozza-automaticapiano-straordinario-di-monitoraggio-e-conservazione-dei-beni-culturali-immobili/

Monterroso Checa, A., Martínez Reche, T., 2018. COSMO SkyMed X-Band SAR application—Combined with thermal and RGB images—In the archaeological landscape of Roman Mellaria (Fuente Obejuna-Córdoba, Spain). *Archaeological Prospection*, 25, pp. 301–314. doi: 10.1002/arp.1709

Raspini F. et al., 2023. The Potential of Satellite Interferometry for Geohazard Assessment in Cultural Heritage Sites. In: G.M. El-Qady, C. Margottini (eds.), Sustainable Conservation of UNESCO and Other Heritage Sites Through Proactive Geosciences Springer Geology, Springer, Cham, pp. 587-595.

Storch, T. et al., 2023. The EnMAP imaging spectroscopy mission towards operations. *Remote Sensing of Environment*, 294, 113632, doi: 10.1016/j.rse.2023.113632.

Tapete, D. et al. 2021. Listening to archaeologists and practitioners: analysis of the user feedback on the use of Copernicus data. In: Computer Applications and Quantitative Methods in Archaeology (CAA) 2021 "Digital Crossroads", 15 June 2021, Limassol, Cyprus, pp. 163-165.

Tapete, D., Cigna, F., 2017. Trends and perspectives of space-borne SAR remote sensing for archaeological landscape and cultural heritage applications. *Journal of Archaeological Science Reports*, 14, pp. 716–726. doi: 10.1016/j.jasrep.2016.07.017

Tapete, D., Cigna, F., 2019a. Detection of Archaeological Looting from Space: Methods, Achievements and Challenges. *Remote Sensing*, 11, 2389. doi: 10.3390/rs11202389

Tapete, D., Cigna, F., 2019b. COSMO-SkyMed SAR for detection and monitoring of archaeological and cultural heritage sites. *Remote Sensing*, 11, 1326. doi: 10.3390/rs11111326

Tapete, D., Cigna, F., 2020. Poorly known 2018 floods in Bosra UNESCO site and Sergiopolis in Syria unveiled from space using

Sentinel-1/2 and COSMO-SkyMed. *Scientific Reports*, 10, 12307, doi: 10.1038/s41598-020-69181-x

Tapete, D., Coletta, A., 2022. ASI's roadmap towards scientific downstream applications of satellite data, EGU General Assembly 2022, Vienna, Austria, 23–27 May 2022, EGU22-5643. doi: 10.5194/egusphere-egu22-5643, 2022.

Taramelli, A., 2021. Mirror Copernicus per lo sviluppo e la competitività della Space Economy italiana. In: Ricerca e Innovazione per la sfida spaziale, ENEA Magazine, 3, September - December 2021 doi: 10.12910/EAI2021-078

Virelli M. et al., 2020. COSMO-SkyMed: uno strumento satellitare per il monitoraggio dei beni culturali. In: Monitoraggio e Manutenzione delle Aree Archeologiche. Cambiamenti climatici, dissesto idrogeologico, degrado chimico-ambientale / Atti del Convegno Internazionale di Studi, Roma, Curia Iulia, 20-21 marzo 2019, «L'ERMA» di BRETSCHNEIDER, pp. 103-112.

Virelli M. et al., 2023. COSMO-SkyMed: a satellite tool for monitoring cultural heritage. In: *International Archives of the Photogrammetry, Remote Sensing and Spatial Information Sciences*, XLVIII-M-2-2023, pp. 1621–1627, doi: 10.5194/isprs-archives-XLVIII-M-2-2023-1621-2023.

Zingaro, M., Scicchitano, G., Capolongo, D., 2023. The Innovative Growth of Space Archaeology: A Brief Overview of Concepts and Approaches in Detection, Monitoring, and Promotion of the Archaeological Heritage. *Remote Sensing*, 15, 3049. doi: 10.3390/rs15123049

Enviroment

EXPLOITATION OF MULTI-TEMPORAL INSAR DATA FOR ENVIRONMENTAL RISK ASSESSMENT SERVICES

N. Ricciardi [1], R. Nutricato [1], K. Tijani [1], A. Morea [1], D.O. Nitti [1]*, F.Bovenga [2]

[1] Geophysical Applications Processing s.r.l., c/o Dipartimento di Fisica interateneo di Bari, Bari, Italy,
(nicolo.ricciardi, raffaele.nutricato, khalid.tijani, alberto.morea, davide.nitti)@gapsrl.eu

[2] Consiglio Nazionale delle Ricerche CNR IREA, Bari, Italy - bovenga.f@irea.cnr.it

KEY WORDS: Landslide Risk assessment, Multi-temporal SAR interferometry

ABSTRACT:

Multi-temporal SAR Interferometry allows detecting and monitoring millimetric ground displacements occurring on selected point targets that exhibit coherent radar backscattering properties over time. The technological maturity of these techniques, as well as the wide availability of SAR data, fostered the development of continuous ground motion services that can be used to support systems devoted to environmental monitoring and risk management. This paper outlines the main outcomes of SeVaRA ("Environmental Risk Assessment Service"), a project aimed at implementing an innovative system for calculating an aggregate environmental risk index, derived from several parameters related to hydrogeological instability phenomena and/or weather-related extreme events. In particular, the present work is focused on the analysis of the "SeVaRA Deformation Sub-System", that has been designed for the computation of risk indices related to structural and ground instabilities (landslides).

1. INTRODUCTION

Multi-temporal Synthetic Aperture Radar Interferometry (MTInSAR) techniques enable the identification and continuous tracking of sub-millimeter-scale displacements occurring in specific point targets that maintain consistent radar backscattering characteristics over time. Successful applications to different geophysical phenomena such as the monitoring of landslides (Bovenga et al., 2006; Wasowski et al., 2014) or subsidence/uplifts due to groundwater withdrawal/entry or from the excavation of mines and tunnels (Wasowski et al., 2009) have been already demonstrated in literature. During the last several years, new application opportunities have emerged thanks to the greater data availability offered by recent launches of radar satellites, and the improved capabilities of the new space radar sensors in terms of both resolution and revisit time.
Currently, many space-borne Synthetic Aperture Radar (SAR) data are operational for InSAR applications, such as the Italian COSMO-SkyMed (CSK) constellation and the Copernicus Sentinel-1 (S1) mission.
Each CSK satellite is equipped with an X-band SAR sensor that acquires data with spatial resolution reaching metric values, thus leading to a very high spatial density of the measurable targets and allowing the monitoring of very local scale events. Thanks to the nationwide acquisition plan named MapItaly, devised by the Italian Space Agency (ASI) and fully operational since 2010 (Milillo et al., 2014), CSK constellation can provide X-band images covering the Italian territory with a best effort revisit time of 16 days, while the follow-on constellation, namely COSMO-SkyMed Second Generation (CSG), allows to ensure the full operational continuity of the entire CSK mission.
The MapItaly project was developed by ASI and the Department of Civil Protection, with eGEOS support. The project goal is to provide a mapping of the entire Italian territory with the CSK interferometric mode StripMap HIMAGE (HH polarization), in either right Ascending or right Descending orbit. For an HIMAGE coverage at Italian latitude, four overlapped different beams are needed.
Sentinel-1 mission is instead operational since 2014 and acquires in C-band at medium resolution (5x20 m^2) with a minimum revisit time of 12 days (only 6 days between 2016 and 2021, when the full S1 constellation was operational), thus allowing to perform ground instability monitoring back in time almost all over the Earth. Moreover, all data acquired by the S1 mission are provided on an open and free basis by the European Space Agency (ESA) and the European Commission (EC), for promoting full utilization of S1 data, with the aim of increasing the scientific research, growing the EO markets and developing continuous monitoring services, such as:

- European Ground Motion Service (EGMS)
- Rheticus® Displacement Geo-information Service.

The European Ground Motion Service is based on the multi-temporal interferometric analysis of S1 radar images at full resolution, updated annually. EGMS provides consistent and reliable information regarding natural and anthropogenic ground motion over the Copernicus Participating States and across national borders, with millimeter accuracy (Costantini et al., 2021).
Rheticus® is a cloud-based platform developed by Planetek Italia srl and provides continuous monitoring services of the Earth's surface (Samarelli et al., 2018). One of the services provided by Rheticus® is the Displacement Geo-information Service (Figure *1*), which offers even *monthly updates* of the millimetric displacements of the ground surface.

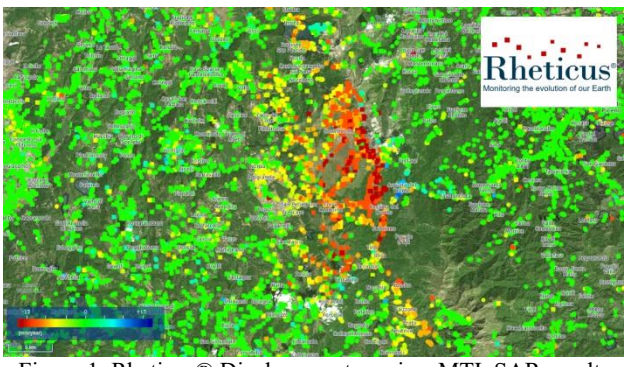

Figure 1. Rheticus® Displacement service: MTInSAR results over Arquata del Tronto and surrounding areas (Central Italy).

* Corresponding author

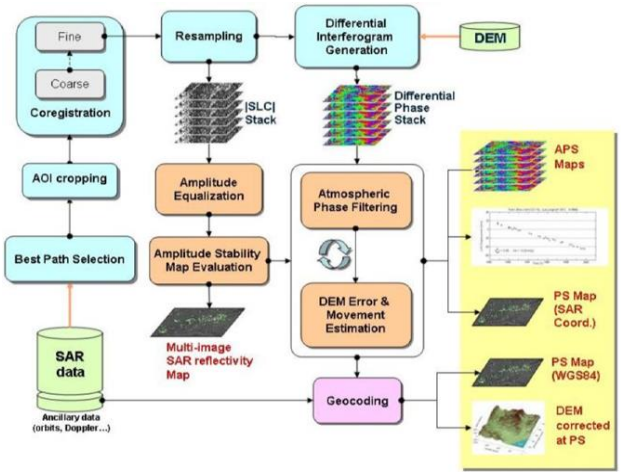

Figure 2. Flowchart of the SPINUA processing chain

To provide this information, the Rheticus® platform processes a large amount of Geospatial Big Data through the MTInSAR processing chain based on the SPINUA© algorithm ("Stable Point Interferometry even in Un-urbanized Areas"), maintained by GAP srl and sketched in Figure 2 (Bovenga et al., 2004). SPINUA is capable of processing SAR images acquired by space-borne or airborne SAR missions in C, L and X- band, including CSK and S1.

MTInSAR is one of the remote sensing techniques used for collecting measurements and information necessary for geohazards and landslide risk assessment. Furthermore, according to (Van Westen et al., 2008), the exploitation of MTInSAR techniques is always significant, regardless of the spatial scale of the phenomenon considered (e.g., Regional, Medium, Large or Detailed Scale). Thanks to the actual technological maturity of MTInSAR techniques as well as to the wide availability of SAR data, these ground motion services can be used to support systems devoted to environmental monitoring and risk management.

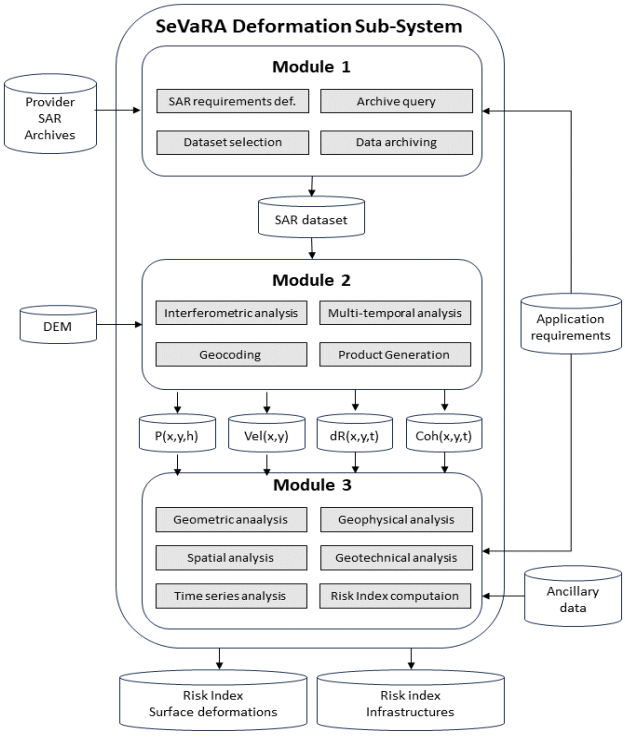

Figure 3. Architecture of the SeVaRA Deformation Sub-System

This work outlines the main outcomes achieved within the SeVaRA project, which stands for "Environmental Risk Assessment Service". The goal of SeVaRA is to develop an innovative system for the calculation of a comprehensive environmental risk index. This index is derived from numerous parameters associated with hydrogeological instability phenomena and extreme weather events. More specifically, this research focuses on the "SeVaRA Deformation Sub-System", which has been specifically designed computing risk indices pertaining to structural and ground instabilities, notably landslide events, by exploiting MTInSAR techniques.

Central Italy has been chosen as applicative example in this work, because of the simultaneous presence of weather- and earthquake-induces landslides. In particular, the 2016-2017 seismic swarm that struck the wide epicentral area triggered many landslides in the surrounding zones.

2. OVERVIEW OF THE SEVARA DEFORMATION SUB-SYSTEM

The flowchart of the "SeVaRA Deformation Sub-System" is outlined in Figure *3*. It consists of three main blocks. In the **first module**, SAR data archives are browsed online in order to select the interferometric SAR stacks available on the Region Of Interest (ROI).

Then, the selected InSAR dataset is provided in input to the **second module** in Figure *3*, with the aim to detect Persistent/Distributed Scatterers (PS/DS) and monitor their displacements over time. The SeVaRA "Deformation Sub-System" has been primarily designed to be interfaced with the SPINUA algorithm implemented in the Rheticus® Displacement Service (because of its high refresh rate in the generation of PS/DS maps), but it also supports products generated by the EGMS service, as well as by other MTInSAR services available on the EO markets.

Finally, the **third module** in the workflow of Figure *3* exploits the outcomes of the MTInSAR service with the aim to calculate landslide risk indices and other risk indices related to single infrastructures. The landslide risk index is computed by multiplying the hazard with the expected losses for all different types of elements at risk (Varnes, 1984, Lee and Jones, 2004):

$$Risk = \sum(H \sum(VA)) \quad (1)$$

where H is the hazard expressed as probability of occurrence within a reference period, V is the physical vulnerability of a particular type of element at risk (from 0 to 1) for a specific type of hazard and for a specific element at risk, A is the amount (or cost or exposure) of the elements at risk (e.g., number of buildings, cost of buildings, number of people, etc.).

The procedure for calculating risk indices can be very complex (Van Westen et al., 2005, 2008). In general, to determine the hazard of a landslide event, it is necessary to estimate the spatio-temporal probability of triggering a landslide. In the calculation of susceptibility, i.e. the spatial probability of landslide triggering, a series of environmental parameters are involved (land use, geology, lithology, geomorphology, ...), and it is necessary to have an inventory of landslides from which to derive information on the type of landslide, as well as on the magnitude and state of quiescence/activity of the landslide over time. The calculation of the temporal probability of triggering a landslide is instead strongly conditioned by the trigger factors of a landslide which are typically intense rainfalls (weather-induced landslides) or seismic events (earthquake-induced landslides), and in any case are related to the detection of accelerations in the ground movement trends.

In order to implement a fully automatic and configurable processing chain for the Landslide Hazard Map (LHM) computation, an algorithmic solution has been proposed and implemented in SeVaRA, based on and improved from the main achievements of a previous FPV EC Project called LEWIS (Landslide Early-Warning Integrated System), coordinated by the Remote Sensing Group of the Department of Physics of Bari (Guerriero et al., 2005). The proposed approach for the LHM computation in SeVaRA requires several EO and geo-spatial data as input, as sketched in the flowchart shown in Figure 4. The National mosaic of landslide hazard zones provided by ISPRA (Luti et al., 2020) is used as reference Landslide Hazard Map (Figure 5). This map is updated by considering several factors and source data, as follows.
The first step consists in the import of the susceptibility map, i.e. the spatial probability of triggering a landslide.

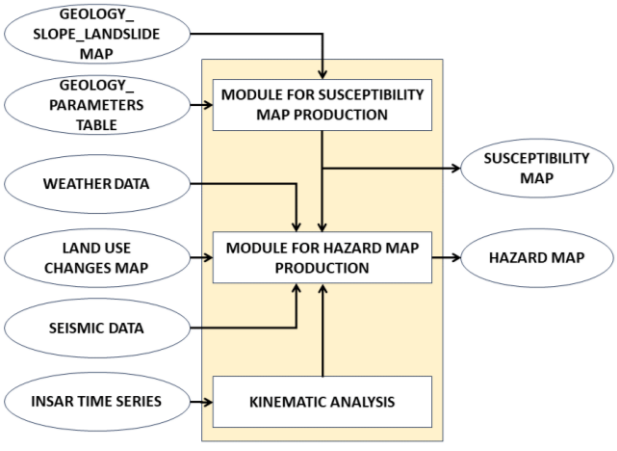

Figure 4. Schematic approach for the computation of the Landslide Hazard Map in the SEVARA project.

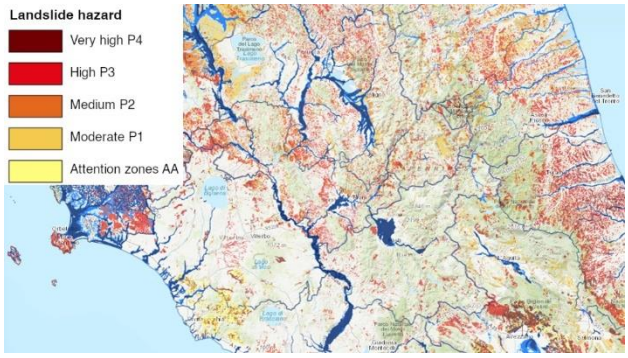

Figure 5. LHM provided by ISPRA (Central Italy)

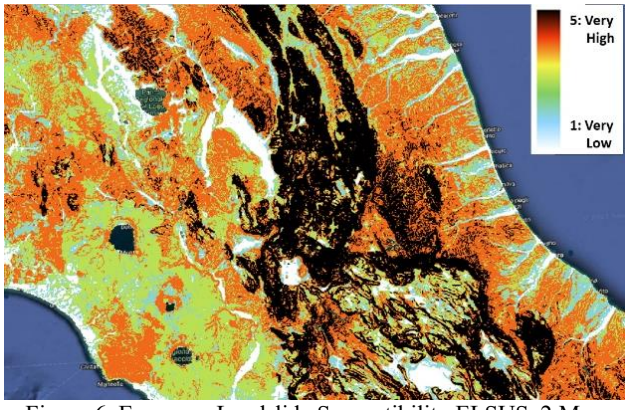

Figure 6. European Landslide Susceptibility ELSUSv2 Map provided by the ESDAC over Central Italy

We selected the European Landslide Susceptibility Map (ELSUSv2), provided by the European Soil Data Centre (Wilde et al., 2018), which covers almost all the European Countries (in Figure 6 the ELSUSv2 map over Central Italy).
In case the region of interest is not covered by the ELSUSv2 map, the SeVaRA processing chain is capable to independently estimate the Susceptibility Map from Lithology, Digital Elevation Models and other geological layers, in agreement with the algorithmic solutions validated in the framework of the previous LEWIS FPV project.

The second step consists in the calculation of the temporal probability of triggering a landslide.
The first trigger factor is related to intense rainfalls. Precipitations can be cumulated in a configurable range time in SeVaRA (24H, 72H, or even more), in order to assess and monitor the risk of rainfall-induced landslides. These data are derived by cumulating ground measurement data collected by weather stations, if available in proximity of the region of interest, or derived by interpolating hourly rainfall data provided by other services, such OpenWeatherMap or the Global Satellite Mapping of Precipitation service (Hou et al., 2014, Kubota et al., 2020), offered by the JAXA Global Rainfall Watch (Figure *7*).

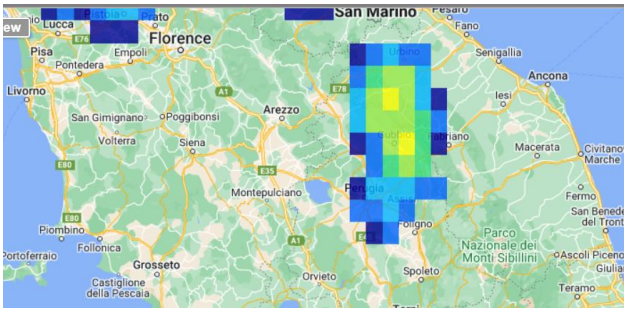

Figure 7. Rainfall data provided by the JAXA Global Rainfall Watch (URL: https://sharaku.eorc.jaxa.jp/GSMaP/index.htm)

Another input layer is represented by the Land Cover Map and the Land Cover Change Map (Buttner et al., 2004), such as those available in the CORINE inventory (Figure *8*). As a matter of fact, a land cover change can represent an important landslide triggering factor, as it is in case of deforestation.

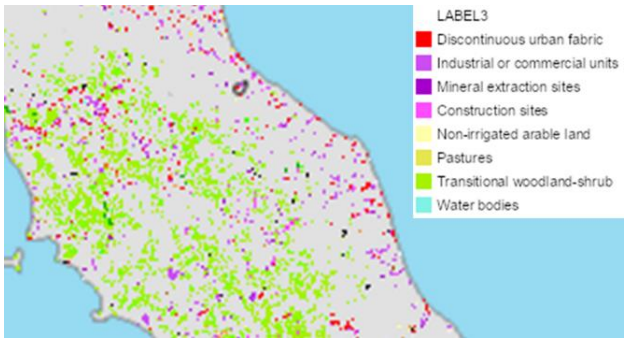

Figure 8. CORINE Land Cover Change Map 2012-2018.

The database of seismic events, provided by INGV (Luzi et al., 2020), is also essential to account for earthquake-induced landslides (an example is reported in Figure *9* over Central Italy). MTInSAR ground displacement time series are the last (but not least) source data for the identification of hazards, as mentioned in the introductory section. The post-seismic PS/DS map in the Central Italy, covering the areas struck by the 2016-2017 seismic swarm, is shown in Figure *1*.

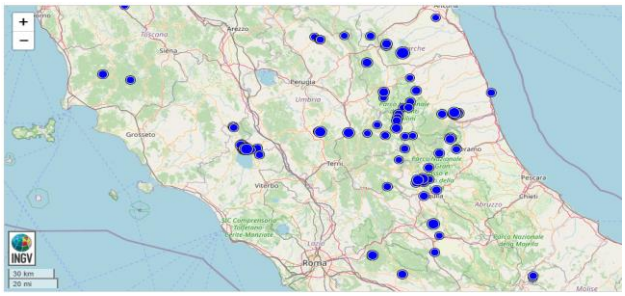

Figure 9. Epicentre positions of earthquakes of magnitude greater than 2, occurred in central Italy during September 2023, as reported in the database of seismic events provided by INGV (URL: https://terremoti.ingv.it/).

The temporal analysis of the displacement trends is essential to detect unstable targets. In the past, the revisit frequency of historical SAR sensors was unsatisfactory, and the average velocity was the only kinematic parameter to be estimated to detect unstable targets. Currently, thanks to the short revisit time of the Sentinel-1 constellation, it is at last possible to estimate much more kinematic parameters than in the past, like last-year velocities, abrupt accelerations, and seasonal trends: some examples of linear and non-linear displacement time-series are shown in Figure *11* (the examples refer to test sites in Northern, Central and Southern Italy). Both linear and non-linear kinematic parameters are fruitfully exploited in the SeVARA system to provide early warnings and to detect and monitor landslide triggering factors.

According to the schematic approach depicted in Figure 4, all the aforementioned source data are combined in the SeVaRA Deformation Sub-System in order to produce the LHM product: an example of LHM generated by the SeVaRA system is finally shown in Figure *10* over Central Italy and for a specific reference date.

We remark that the input data layers have different update rates, that ranges from years (i.e., the susceptibility map and land cover), to weeks/months (i.e., interferometric time series) up to few hours/days, in case of precipitation data. Currently, the SeVaRA system has been designed to provide a landslide hazard map over the area of interest with a daily frequency.

The SeVaRA Deformation Sub-System is highly configurable. The parametric configuration can be tuned according to the indications of a pool of geologists involved in the development team of the SeVaRA project. The validation of the implemented algorithmic solution is beyond the scope of the present work and it is not discussed here.

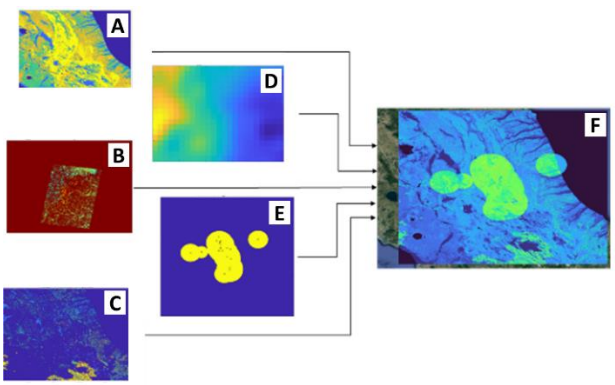

Figure 10. Example of LHM computation over Central Italy (F), obtained by combining susceptibility map (A), MTInSAR data (B), land use change map (C), rainfall map (D) and seismic data (E), according to the approach sketched in Figure 4.

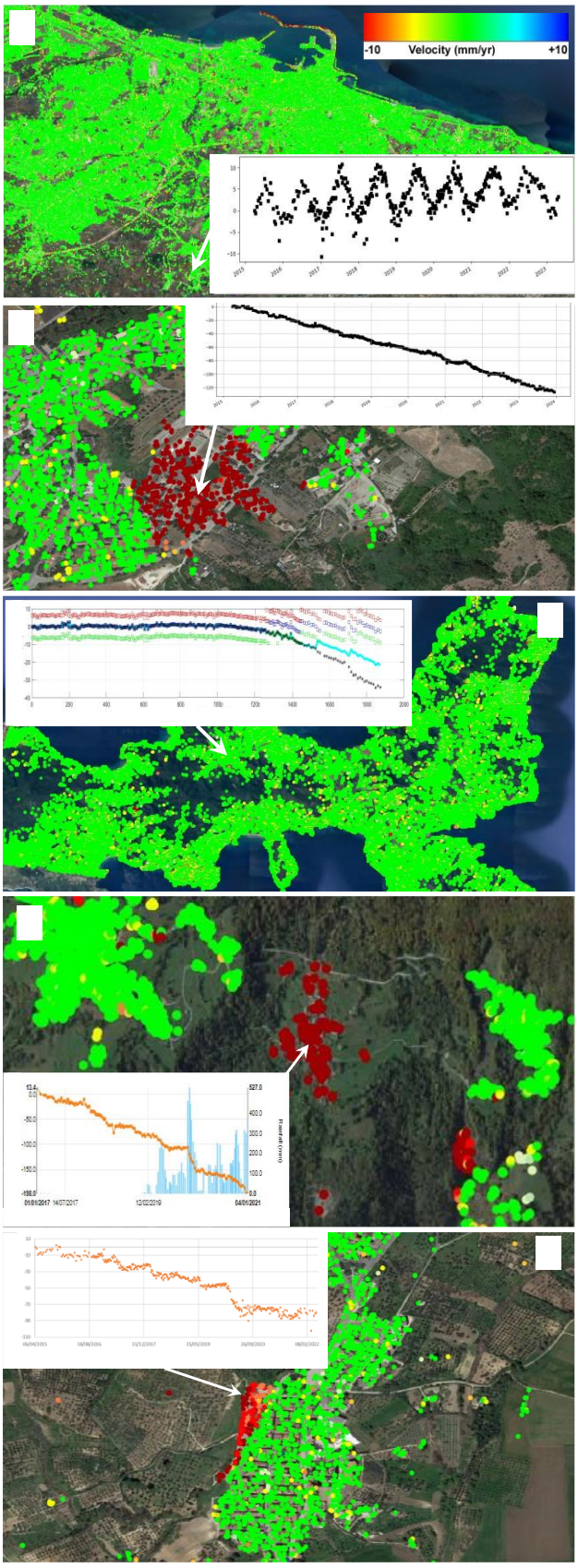

Figure 11. Examples of PS displacement trends identified by processing S1 data through the SPINUA algorithm (Rheticus® Displacement service) in Northern, Central and Southern Italy: (A) seasonal trend, (B) linear trend, (C) accelerating trend, (D,E) complex trends with abrupt acceleration/deceleration cycles

3. CONCLUSIONS

The technological maturity of the multi-temporal interferometric techniques, as well as the wide availability of SAR data, fostered the development of continuous ground motion services that can be used to support systems devoted to environmental monitoring and risk management, like SeVaRA.
In the present work we briefly outlined the main components of the SeVaRA Deformation Sub-System, designed for the computation of risk indices related to structural and ground instabilities.
It should be remarked that, thanks to the low revisit time of the Sentinel-1 constellation, it is currently possible to analyse the displacement trends for estimating much more kinematic parameters than in the past (like acceleration, discontinuities, seasonal trends, ...). These parameters can be fruitfully exploited for improving the computation of Landslide Hazard Maps, to provide early warnings and to detect and monitor landslide triggering factors.

ACKNOWLEDGEMENTS

This work was carried out in the framework of the SeVaRA project ("Environmental Risk Assessment Service"), funded by Apulia Region (PO FESR 2014/2020) and coordinated by Omnitech srl. Rheticus® is a registered trademark of Planetek Italia srl. Sentinel-1 data are provided by the European Space Agency. COSMO-SkyMed® Products, © of the Italian Space Agency (ASI), are delivered under a license to use by ASI.

REFERENCES

Bovenga, F., Refice, A., Nutricato, R., Guerriero, L., Chiaradia, M.T., 2004. SPINUA: a flexible processing chain for ERS / ENVISAT long term interferometry. *Proceedings of ESA-ENVISAT Symposium 2004, Saltzburg, Austria.*

Bovenga, F., Nutricato, R., Refice, A., Wasowski, J., 2006. Application of Multi-temporal Differential Interferometry to Slope Instability Detection in Urban/Peri-urban Areas. *Engineering Geology*, 88 (3-4), pp. 218-239, doi.org/10.1016/j.enggeo.2006.09.015.

Buttner, G., Feranec, J., Jaffrain, G., Mari, L., Maucha, G., Soukup, T., 2004. The CORINE land cover 2000 project. *EARSeL eProceedings*. 3. 331-346.

Costantini, M., Minati, F., Trillo, F., Ferretti, A., Novali, F., Passera, E., Dehls, J., et al., 2021. European Ground Motion Service (EGMS). *2021 IEEE International Geoscience and Remote Sensing Symposium IGARSS, Brussels, Belgium,* pp. 3293–3296, doi:10.1109/IGARSS47720.2021.9553562

Guerriero, L., Bovenga, F., Nutricato, R., Refice, A., Wasowski, J., 2005. The role of PS Interferometry in the Landslide Early Warning Integrated System (LEWIS) Project. *Proceedings of Workshop di Telerilevamento e dissesto idrogeologico*, 7-8 July 2005, Cagliari, Italy.

Hou, A. Y., Kakar, R. K., Neeck, S., Azarbarzin, A. A. Kummerow, C. D., Kojima, M., Oki, R., Nakamura, K., Iguchi, T., 2014. The Global Precipitation Measurement Mission. *Bulletin of the American Meteorological Society*, 95(5), pp. 701-722, doi.org/10.1175/BAMS-D-13-00164.1.

Kubota, T., Aonashi, K., Ushio, T., Shige, S., Takayabu, Y. N., Kachi, M., Arai, Y., Tashima, T., Masaki, T., Kawamoto, N., Mega, T., Yamamoto, M. K., Hamada, A., Yamaji, M., Liu, G., Oki, R., 2020. Global Satellite Mapping of Precipitation (GSMaP) Products in the GPM Era. *In: Levizzani, V., et al. (eds) Satellite Precipitation Measurement. Advances in Global Change Research*, (67). Springer, Cham. doi.org/10.1007/978-3-030-24568-9_20.

Lee, E. M., Jones, D.K.C., 2004. Landslide risk assessment. *Thomas Telford, London*, pp 454.

Luzi, L., Lanzano, G., Felicetta, C., D'Amico, M. C., Russo, E., Sgobba, S., ORFEUS Working Group 5, 2020. Engineering Strong Motion Database (ESM), version 2.0, *Istituto Nazionale di Geofisica e Vulcanologia (INGV),* doi.org/10.13127/ESM.2

Luti, T., Segoni, S., Catani, F., Munafò, M., Casagli, N., 2020. Integration of remotely sensed soil sealing data in landslide susceptibility mapping. *Remote Sensing*, 12(9), 1486, doi.org/10.3390/rs12091486.

Milillo, P., Shanker, A., Pascale, S., Serio, C., Sdao, F., 2014. Persistent scatterer interferometry based on COSMO- SkyMed imagery. *Proceedings of 33rd EARSeL Symposium: Towards Horizon 2020: Earth Observation and Social Perspectives,* June 2013, doi.org/10.13140/2.1.3980.8009.

Samarelli S., Agrimano L., Epicoco I., Cafaro, M., Nutricato, R., Nitti, D. O., Bovenga, F., 2018. Rheticus®: a Cloud-Based Geo-Information Service for Ground Instabilities Detection and Monitoring. *In: 2018 IEEE International Geoscience and Remote Sensing Symposium*. IEEE, pp. 2238–2240, doi.org/10.1109/IGARSS.2018. 8518226

Van Westen, C.J., Van Asch, T.W.J., Soeters, R., 2005. Landslide hazard and risk zonation; why is it still so difficult? *Bulletin of Engineering geology and the Environment*, 65(2), pp. 167–184, doi.org/10.1007/s10064-005-0023-0

Van Westen, C. J., Castellanos, E., Kuriakose, S. L., 2008. Spatial data for landslide susceptibility, hazard, and vulnerability assessment: An overview. *Engineering Geology*, 102(3–4), pp 112-131, doi.org/10.1016/j.enggeo.2008.03.010.

Varnes, D. J., 1984. Landslide hazard zonation: a review of principles and practice. *United Nations International, Paris.*

Wasowski, J., Bovenga, F., Nutricato, R., Conte, D., Refice, A., Graniczny, M., Kowalski, Z., 2009. Spatial distribution of subsidence in the Wieliczka Salt Mine area as detected through satellite interferometry. *In Przeglad Geologiczny*, 57(2), pp. 164-172.

Wasowski, J., Bovenga, F, 2014. Investigating landslides and unstable slopes with satellite Multi-Temporal Interferometry: Current issues and future perspectives. *Engineering Geology*, 174, pp. 103-138.

Wilde, M., Günther, A., Reichenbach, P., Malet J., Hervás J. 2018. Pan-European landslide susceptibility mapping: ELSUS Version 2. *Journal of Maps*, 14(2), pp. 97-104, doi.org/10.1080/17445647.2018.1432511

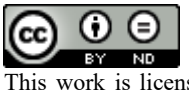

EXTREME THINNING OF THE BRENVA GLACIER TONGUE FROM REPEAT UAV DEMs

D. Fugazza[1]*, F.Troilo [2]

[1] Department of Environmental Science and Policy, Università degli studi di Milano, Italy
davide.fugazza@unimi.it

[2] Fondazione Montagna Sicura, Courmayeur (AO), Italy - ftroilo@fms.it

KEY WORDS: Glacier, UAV, thickness changes, debris cover, Mont Blanc

ABSTRACT:

Brenva glacier is one of the largest (5.95 km^2) glaciers on the southern side of Mont Blanc, in Italy. The glacier is notable as its tongue is entirely covered by debris and it is located at the lowest elevation of all glaciers in the Italian Alps (1415 m a.s.l.). Since 2004, the glacier tongue is separated from the upper glacier body and is therefore subject to intense ice thinning, which we evaluated in this study from a comparison of digital elevation models (DEMs) obtained from two UAV surveys carried out in 2019 and 2020 using commercial unmanned aircraft. The DEMs were generated using a structure from motion pipeline. From the comparison, extreme ice losses are evident, with an average of 13.22 m over the common survey area of 2019 and 2020 (an area of 0.14 km^2), with peaks of over 45 m. This exceeds even the high losses of other Alpine glaciers and we postulate it is the result of the high summer temperatures found at the low elevation of the tongue and the lack of mass transfer from the upper glacier body.

1. INTRODUCTION

1.1 The importance of debris covered glaciers

Debris covered glaciers are a common sight in many mid-latitude mountain ranges of the world, particularly in the Himalayas (Ojha et al., 2017), dry Andes (Janke et al., 2015), and New Zealand Alps (Baumann et al., 2020), and increasingly found in the Caucasus (Tielidze and Wheate, 2018) and European Alps (Azzoni et al., 2018; Fleischer et al., 2021; Fugazza et al., 2023). Runoff from debris covered glaciers is an important freshwater source in many areas of the world (Zhang et al., 2019). The input of debris to the glaciers often comes from large discrete events such as rockfall and avalanches (Kirkbride, 2011). However, there is also evidence that supraglacial debris cover is increasing as glaciers retreat through an increased input from the valley walls, led by rock disaggregation through freeze-thaw cycles, the emergence of englacial debris and transport from the lateral moraines (Azzoni et al., 2018; Ojha et al., 2017; Xie et al., 2020). A large debris mantle causes the decoupling of the glacier area from the climate signal, as once a critical debris thickness is reached (generally 1-5 cm, Foster et al., 2012), it shields the underlying ice, reducing ablation (Foster et al., 2012; Mihalcea et al., 2006). Retreat rates of debris covered glaciers are thus much lower than those of debris-free glaciers (Xiang et al., 2018), and for some, the area can persist almost unchanged for decades; however, they continue reducing in volume, with some studies suggesting that the thinning rates can be as fast as those of debris-free glaciers. Thinning is known to occur in the clean ice sections and through back wasting of ice cliffs, especially in association with supraglacial lakes (Steiner et al., 2019).

In addition, on some glaciers the debris covered tongue can detach from the main glacier trunk. With no transfer of ice available to nourish it, the glacier tongue is therefore left stagnating and its melt out can accelerate. These detachments have become increasingly frequent in the Alps: on the southern, Italian side, Lys is a remarkable example (Fugazza et al., 2020). The short-term evolution of these detached glacier tongues however is poorly documented.

In this study, we examine the recent (2019-2020) evolution of the tongue of Brenva glacier (Mont Blanc range, Italy), through a comparison of DEMs obtained from UAV photogrammetry from two different epochs. In doing so, we extend the previous study of D'Agata et al. (2005) and D'Agata and Zanutta (2007), since the separation of the glacier tongue from the upper trunk.

1.2 1.2 Study Area

Brenva glacier (45.83° N, 6.90° E) is one of the largest glaciers on the southern side of the Mont Blanc massif (see Fig. 1). The glacier flows down from the summit of Mont Blanc itself and its tongue reaches 1415 m a.s.l., the lowest terminus elevation on the Italian side of the Alps (Cerutti, 2005; D'Agata and Zanutta, 2007), one kilometre away from the village of Entrèves. The supply of supraglacial debris has mainly originated from several discrete rock avalanche events: the most recent ones occurred in 1920 and 1997, but several others are known to have occurred throughout the Holocene. The glacier tongue has been debris covered since at least the end of the Little Ice Age (LIA) and thus Brenva has sustained very low retreat rates compared to neighbouring glaciers, never retreating by more than 900 m from its LIA maximum for most of the 20th century (Deline et al., 2015).

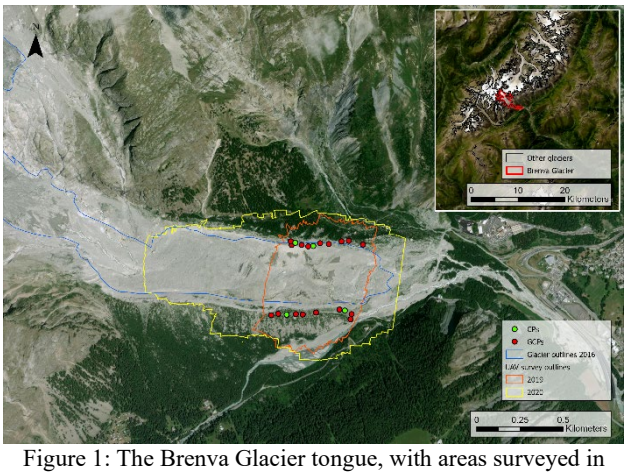

Figure 1: The Brenva Glacier tongue, with areas surveyed in 2019 and 2020. The sub panel shows the location of Brenva Glacier within the Mont Blanc Massif. Background images from ESRI basemap.

* Corresponding author

The valley tongue was once nourished by a large ice fall which descended from the accumulation basin along the steep walls of a large rocky crag. Since the end of the 1980s, the ice fall started to gradually thin through a period of prolonged high summer temperatures; a rockfall in 1997 further accelerated the process by causing a number of ice avalanches which deplenished the ice cover; in September 2004, ice flow from the seracs to the glacier tongue was interrupted, leaving the tongue to stagnate (Cerutti, 2005). Brenva glacier and its tongue can now be considered two separate glacial entities: data from the last Alpine glacier inventory report an area of 5.95 km^2 (Paul et al., 2020), combining the upper part of the glacier and the tongue (5.18 and 0.77 km^2, respectively). In spite of its position close to inhabited villages, the glacier has received comparatively little attention: D'Agata and Zanutta (2007) estimated thickness changes from 1959 to 2003 using DEMs derived from maps and aerial photogrammetric surveys. Malekian et al. (2023) and Scaioni et al. (2023) further explored the potential of historical aerial imagery to reconstruct the glacier thickness changes since the 1960s. Other studies have included Brenva glacier as part of a regional investigation of the Mont Blanc area, e.g. Berthier et al. (2016, 2014), who also investigated thickness and mass changes in the past decade using SPOT, Pleiades and ASTER derived DEMs.

2. DATASETS AND METHODS

2.1 UAV Surveys

2.1.1 2019: The survey was conducted on 30 April 2019. The UAV used for this survey was a DJI Mavic Pro, equipped with a 20 Mp Hasselblad digital camera, using a CMOS 1" sensor, f/2.8-f/11 aperture, 10-bit D-Log M color profile with 10-bit HDR 4K. Individual flights were performed manually as lateral rock faces can be very close to the aircraft; further still, both touristic and rescue air traffic is very intense in the Mont Blanc area and needs immediate reaction from the pilot in case other aircraft is approaching. Photographs were acquired with the camera tilted nadir. The flight path was maintained at around 110 m above ground, with a grid spacing of 30 metres, giving a forward overlap exceeding 60% with shooting intervals of 3 seconds and a flight speed of 3 m/s. The resulting average ground sampling distance (GSD) was 3.7 cm. Additionally, a Geomax RTK GNSS, with a Zenith 25 PRO antenna was used to measure absolute positions of 21 targets (see Figure 1) which were marked on the lateral moraines, by spraying stable rocks with acrylic paint. The GNSS rover was connected to a virtual reference station streaming RTK corrections through a 4G data network. XY errors of the targets are in the range 2-3 cm while the average elevation error is in the 4 cm range. Base station corrections were obtained from the SPIN GNSS regional correction network (http://www.spingnss.it/spiderweb/frmIndex.aspx).

2.1.2 2020: On 9 September 2020, a survey of the glacier tongue was conducted using two UAVs, namely a DJI Phantom 4 RTK and a DJI Mavic, to increase coverage compared to the previous survey of 2019. The DJI Mavic was the same drone used in the previous survey; the DJI Phantom 4 RTK is a commercial drone equipped with a 20 Mp digital camera and a gimbal, allowing pictures to be acquired in nadir as well as oblique mode (Taddia et al., 2020). It features a multi-GNSS antenna and RTK module to receive differential corrections from a base station through a proprietary protocol or from a network through the NTRIP protocol. We operated the DJI Mavic in manual mode, while the DJI Phantom 4 RTK was flown in automatic mode, conducting 3 flights with a duration of approximately 15 minutes at an altitude of 80 m above take-off and 160 m above ground. The flight settings allowed for an image overlap of 80% along track and 70% across track. The resulting average GSD was 3.6 cm. The Phantom 4 was connected to a cellular network with a SIM card and received GNSS corrections in real time from the SPIN GNSS positional service through a virtual reference station. To further improve georeferencing of the DJI Mavic survey, which did not have a RTK module, the same targets used in the previous surveys (see Figure 1) were used, with the positions measured in 2019. Images acquired by the two UAVs had a small overlap in the central portion; the DJI Phantom 4 mainly covered the upper part of the tongue, while the DJI Mavic survey covered the lower part. Images were acquired with clear sky conditions during the late morning hours of the day (approximately 10-12 AM), to ensure optimal illumination conditions.

2.2 DEM generation

The images acquired during the UAV surveys from 2019 and 2020 were processed separately using Agisoft Metashape version 1.2.5 following its structure from motion pipeline, including tie point extraction and matching, image orientation and generation of a sparse point cloud, bundle-adjustment, point cloud densification, generation and export of DEMs. Tie point extraction was carried out using the "high" quality setting in the software, which uses the images without down- or up-sampling; the same setting was used for point cloud densification, which results in a 2x downsampling of the images, and was chosen as a trade-off between accuracy and computation speed. Bundle adjustment was carried out by the introduction of the targets in the Metashape project and their manual collimation in the UAV images. Self-calibration of the cameras was also performed in this step. Out of the 21 targets, 17 were used as ground control points (GCPs) and 4 as checkpoints (CPs). We thus produced DEMs with a final resolution of 0.14 m for the 2019 and 2020 surveys. Both DEMs were exported in the UTM32N WGS84 coordinate system. The area of the 2019 DEM is 0.39 km^2, compared to 0.95 km^2 in 2020, which includes all of the area surveyed in 2019 (see Figure 1).

3. RESULTS

3.1 Accuracy of UAV DEMs

The precision and accuracy of the resulting datasets were estimated by first considering the residuals of the photogrammetric reconstruction on the GCPs and CPs, which are reported in Table 1.

2019	XY error (m)	Z error (m)	Error (m)
GCPs	0.04	0.02	0.04
CPs	0.03	0.05	0.06
2020	**XY error (m)**	**Z error (m)**	**Error (m)**
GCPs	0.04	0.04	0.05
CPs	0.02	0.03	0.04

Table 1. Root mean square error (RMSE) statistics of the residuals on images, ground control points (GCPs) and check points (CPs) on the 2019 and 2020 surveys

Additionally, we compared the two UAV DEMs on off-glacier areas, including the northernmost and southernmost parts of the surveys. These areas (0.11 km^2 in total) consist in the slopes of the surrounding LIA moraines on the hydrographic left and right of the glacier, and are affected by the presence of sparse vegetation at different phenological stages in the two surveys. Once vegetation areas were manually removed, we found a mean difference in elevation of 0.03 m between the two surveys, with a standard deviation and root mean square error (RMSE) of 0.33 m and a normalized median absolute deviation of 0.21 m.

3.2 Glacier thickness changes

The map of ice thickness changes between 2019 and 2020 is shown in Figure 2. Ice thinning averages 13.22 m on the common part of the glacier tongue surveyed in 2019 and 2020 (0.14 km^2), with a maximum of 45.73 m. The resulting loss in ice volume was 1.82×10^6 m^3. The thinning is particularly evident in two areas (green to blue in Figure 2) where the ice loss is > 15 m, an almost complete melt over the period of investigation.

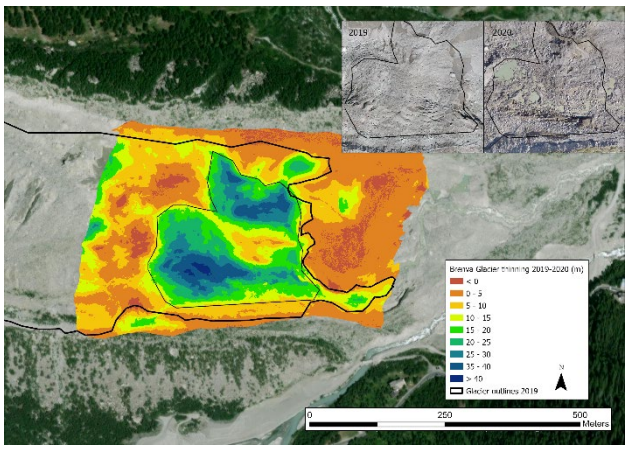

Figure 2: thickness changes of Brenva glacier from 2019 to 2020 from the UAV surveys. The insets show the UAV orthomosaics in 2019 and 2020

While the area of comparison considered in this study is small, the changes reported here greatly surpass those of other Alpine glaciers, even much less debris-covered such as Forni glacier, whose ice tongue underwent an average ice loss of 5.20 m between 2014 and 2016 (Scaioni et al., 2017). This is likely the result of the combination of two factors: the loss of mass transfer from the upper part of the glacier and the low elevation of the glacier tongue, which is therefore subject to high temperatures in summer. The average daily air temperature at Courmayeur Dolonne (1200 m a.s.l., 2.90 km away from the glacier terminus) was 17.30 °C in summer 2019 and 17.54°C in summer 2020. The thick debris cover of the glacier is thus unable to shield the underlying ice. The mechanism of glacier thinning is likely a combination of ice cliff back wasting and the development of supraglacial lakes, as evident in the comparison of orthomosaics in Figure 2.

4. CONCLUSIONS

In this study, we generated DEMs from two UAV surveys of the tongue of Brenva glacier, a debris covered glacier on the southern side of Mt. Blanc, Italy, with a tongue lying at low elevation, detached from the main glacier body. The comparison between the DEMs on areas outside the glacier showed a mean difference in elevation of 0.03 m and a normalized median absolute deviation of 0.21 m; this residual difference could be caused by the presence of vegetation in these areas. Thickness changes on the glacier surface showed an average elevation difference of 13.22 m with maximum change of -45.73 m from 2019 to 2020. These values are higher than those reported for other Alpine glaciers and testify the down-wasting of the glacier tongue, subsequent to the tongue severing from the upper part of the glacier and high summer temperatures. Future surveys with UAVs using other payload, e.g. thermal cameras or ground penetrating radars could be used to infer the thickness of the debris layer and the remaining ice.

ACKNOWLEDGEMENTS

The authors would like to thank the Fondazione Montagna sicura staff for their support for the present research, as well as the Regione Autonoma Valle d'Aosta regional government.

REFERENCES

Azzoni, R.S., Fugazza, D., Zerboni, A., Senese, A., D'Agata, C., Maragno, D., Carzaniga, A., Cernuschi, M., Diolaiuti, G.A., 2018. Evaluating high-resolution remote sensing data for reconstructing the recent evolution of supra glacial debris: A study in the Central Alps (Stelvio Park, Italy). Progress in Physical Geography: Earth and Environment 42, 3–23. https://doi.org/10.1177/0309133317749434

Baumann, S., Anderson, B., Chinn, T., Mackintosh, A., Collier, C., Lorrey, A.M., Rack, W., Purdie, H., Eaves, S., 2020. Updated inventory of glacier ice in New Zealand based on 2016 satellite imagery. Journal of Glaciology 1–14. https://doi.org/10.1017/jog.2020.78

Berthier, E., Cabot, V., Vincent, C., Six, D., 2016. Decadal Region-Wide and Glacier-Wide Mass Balances Derived from Multi-Temporal ASTER Satellite Digital Elevation Models. Validation over the Mont-Blanc Area. Front. Earth Sci. 4. https://doi.org/10.3389/feart.2016.00063

Berthier, E., Vincent, C., Magnússon, E., Gunnlaugsson, Á.Þ., Pitte, P., Le Meur, E., Masiokas, M., Ruiz, L., Pálsson, F., Belart, J.M.C., Wagnon, P., 2014. Glacier topography and elevation changes derived from Pléiades sub-meter stereo images. The Cryosphere 8, 2275–2291. https://doi.org/10.5194/tc-8-2275-2014

Cerutti, A.V., 2005. The Brenva glacier (Mt. Blanc, Alps) has lost its great valley tongue. Geografia Fisica e Dinamica Quaternaria 28, 229–231.

D'Agata, C., Smiraglia, C., Zanutta, A., Mancini, F., 2005.

Recent variations of a debris-covered glacier (Brenva glacier) in the Italian Alps monitored by comparison of maps and digital orthophotos. Journal of Glaciology 51, 183–185. https://doi.org/10.3189/S0022143000215232

D'Agata, C., Zanutta, A., 2007. Reconstruction of the recent changes of a debris-covered glacier (Brenva Glacier, Mont Blanc Massif, Italy) using indirect sources: Methods, results and validation. Global and Planetary Change, Climate Change Impacts on Mountain Glaciers and Permafrost 56, 57–68. https://doi.org/10.1016/j.gloplacha.2006.07.021

Deline, P., Akçar, N., Ivy-Ochs, S., Kubik, P.W., 2015. Repeated Holocene rock avalanches onto the Brenva Glacier, Mont Blanc massif, Italy: A chronology. Quaternary Science Reviews 126, 186–200. https://doi.org/10.1016/j.quascirev.2015.09.004

Fleischer, F., Otto, J.-C., Junker, R.R., Hölbling, D., 2021. Evolution of debris cover on glaciers of the Eastern Alps, Austria, between 1996 and 2015. Earth Surface Processes and Landforms 46, 1673–1691. https://doi.org/10.1002/esp.5065

Foster, L.A., Brock, B.W., Cutler, M.E.J., Diotri, F., 2012. A physically based method for estimating supraglacial debris thickness from thermal band remote-sensing data. Journal of Glaciology 58, 677–691. https://doi.org/10.3189/2012JoG11J194

Fugazza, D., Senese, A., Azzoni, R.S., D'Agata, C., Cat Berro, D., Mercalli, L., Ventura, F., Smiraglia, C., Diolaiuti, G.A., 2020. Variations of Lys Glacier (Monte Rosa Massif, Italy) from the Little Ice Age to the Present from Historical and Remote Sensing Datasets, in: Kanao, M., Godone, D., De Matteis, N. (Eds.), Antarctica - a Window To Remote Knowledge. Intech Open, p. 23. https://doi.org/10.5772/intechopen.91202

Fugazza, D., Valle, B., Caccianiga, M.S., Gobbi, M., Traversa, G., Tognetti, M., Diolaiuti, G.A., Senese, A., 2023. Glaciological and meteorological investigations of an Alpine debris-covered glacier: the case study of Amola Glacier (Italy). Cold Regions Science and Technology 216, 104008. https://doi.org/10.1016/j.coldregions.2023.104008

Janke, J.R., Bellisario, A.C., Ferrando, F.A., 2015. Classification of debris-covered glaciers and rock glaciers in the Andes of central Chile. Geomorphology 241, 98–121. https://doi.org/10.1016/j.geomorph.2015.03.034

Kirkbride, M.P., 2011. Debris-covered glaciers, in: Singh, V.P., Singh, P., Haritashya, U.K. (Eds.), Encyclopedia of Snow, Ice and Glaciers, Encyclopedia of Earth Sciences. Springer, pp. 190–192. https://doi.org/10.1007/978-90-481-2642-2

Malekian, A., Fugazza, D., Scaioni, M., 2023. Photogrammetric reconstruction and multi-temporal comparison of Brenva glacier (Italy) from archive photos. ISPRS Annals of the Photogrammetry, Remote Sensing and Spatial Information Sciences X-4-W1-2022, 459–466. https://doi.org/10.5194/isprs-annals-X-4-W1-2022-459-2023

Mihalcea, C., Mayer, C., Diolaiuti, G., Lambrecht, A., Smiraglia, C., Tartari, G., 2006. Ice ablation and meteorological conditions on the debris-covered area of Baltoro glacier, Karakoram, Pakistan. Annals of Glaciology 43, 292–300. https://doi.org/10.3189/172756406781812104

Ojha, S., Fujita, K., Sakai, A., Nagai, H., Lamsal, D., 2017. Topographic controls on the debris-cover extent of glaciers in the Eastern Himalayas: Regional analysis using a novel high-resolution glacier inventory. Quaternary International, Japanese Quaternary Studies 2 (Part I) 455, 82–92. https://doi.org/10.1016/j.quaint.2017.08.007

Paul, F., Rastner, P., Azzoni, R.S., Diolaiuti, G., Fugazza, D., Le Bris, R., Nemec, J., Rabatel, A., Ramusovic, M., Schwaizer, G., Smiraglia, C., 2020. Glacier shrinkage in the Alps continues unabated as revealed by a new glacier inventory from Sentinel-2. Earth System Science Data 12, 1805–1821. https://doi.org/10.5194/essd-12-1805-2020

Scaioni, M., Corti, M., Diolaiuti, G., Fugazza, D., Cernuschi, M., 2017. Local and general monitoring of Forni glacier (Italian Alps) using multi-platform Structure-From-Motion photogrammetry, in: The International Archives of the Photogrammetry, Remote Sensing and Spatial Information Sciences. Presented at the ISPRS Geospatial Week 2017 (Volume XLII-2/W7) - 18-22 September, Wuhan, China, Copernicus GmbH, pp. 1547–1554. https://doi.org/10.5194/isprs-archives-XLII-2-W7-1547-2017

Scaioni, M., Malekian, A., Fugazza, D., 2023. Techniques for comparing multi-temporal archive aerial imagery for glacier monitoring with poor ground control. The International Archives of the Photogrammetry, Remote Sensing and Spatial Information Sciences XLVIII-M-1–2023, 293–300. https://doi.org/10.5194/isprs-archives-XLVIII-M-1-2023-293-2023

Steiner, J.F., Buri, P., Miles, E.S., Ragettli, S., Pellicciotti, F., 2019. Supraglacial ice cliffs and ponds on debris-covered glaciers: spatio-temporal distribution and characteristics. Journal of Glaciology 65, 617–632. https://doi.org/10.1017/jog.2019.40

Taddia, Y., González-García, L., Zambello, E., Pellegrinelli, A., 2020. Quality Assessment of Photogrammetric Models for Façade and Building Reconstruction Using DJI Phantom 4 RTK. Remote Sensing 12, 3144. https://doi.org/10.3390/rs12193144

Tielidze, L.G., Wheate, R.D., 2018. The Greater Caucasus Glacier Inventory (Russia, Georgia and Azerbaijan). The Cryosphere 12, 81–94. https://doi.org/10.5194/tc-12-81-2018

Xiang, Y., Yao, T., Gao, Y., Zhang, G., Wang, W., Tian, L., 2018. Retreat rates of debris-covered and debris-free glaciers in the Koshi River Basin, central Himalayas, from 1975 to 2010. Environ Earth Sci 77, 285. https://doi.org/10.1007/s12665-018-7457-8

Xie, F., Liu, S., Wu, K., Zhu, Y., Gao, Y., Qi, M., Duan, S., Saifullah, M., Tahir, A.A., 2020. Upward Expansion of Supra-Glacial Debris Cover in the Hunza Valley, Karakoram, During 1990 ~ 2019. Front. Earth Sci. 8. https://doi.org/10.3389/feart.2020.00308

Zhang, Y., Liu, S., Liu, Q., Wang, X., Jiang, Z., Wei, J., 2019. The Role of Debris Cover in Catchment Runoff: A Case Study of the Hailuogou Catchment, South-Eastern Tibetan Plateau. Water 11, 2601. https://doi.org/10.3390/w11122601

INVESTIGATING THE DEPENDENCY BETWEEN SENTINEL-2 MULTISPECTRAL IMAGES AND GROUND-BASED FIELD MEASUREMENTS OF SOIL MOISTURE IN MENDATICA, LIGURIA, ITALY

A. Iacopino [1], S. Gachpaz [1,2], G. Boni [1], R. Bovolenta [1], G. Moser [3], B.Federici [1] *

[1] Department of Civil, Chemical and Environmental Engineering (DICCA), University of Genoa, Italy
(alessandro.iacopino, rossella.bovolenta, giorgio.boni, bianca.federici)@unige.it, saba.gachpaz@edu.unige.it

[2] Dipartimento di Ingegneria Civile, Edile E Ambientale (DICEA), Sapienza University, Italy – saba.gachpaz@uniroma1.it

[3] Department of Electrical, Electronics and Telecommunication Engineering and Naval Architecture (DITEN), University of Genoa, Italy
gabriele.moser@unige.it

KEY WORDS: Dependency analysis, Machine learning, Multispectral images, Sentinel-2, Surface Soil Moisture

ABSTRACT:
In the present study, the potential of Sentinel-2 (S-2) multispectral satellite images for Surface Soil Moisture (SSM) estimate is investigated. For this purpose, dependency is looked for between S-2 images and an 18-months (from 1st of January 2020 to 30th of June 2021) dataset of hourly SSM measurements, acquired at four different depths (-10cm, -35cm, -55cm, -85cm) from each of the nodes of a monitoring network in Mendatica (Liguria, Italy). Data acquired by the sensors were previously calibrated, considering the soil-specific characteristics of the areas, and the reliability of the dataset was verified. After performing the required preprocessing on satellite images, the performance of three nonlinear regression methods, when applied to four different types of inputs (12 spectral channels, NDVI, NDWI and NDMI), was quantitatively assessed.

1. INTRODUCTION

Surface Soil Moisture (SSM) is an Essential Climate Variable (ECV) that crucially influences rainfall-triggered landslides, where slope stability can be markedly affected by the propagation of the saturation front within the unsaturated zone (Viaggio et al., 2022). SSM can be monitored using traditional methods such as ground-based measurements through contact sensors; they provide accurate but single-point measurements, require manual placement and intensive maintenance and are therefore particularly onerous over wide areas (Nguyen et al., 2022). Since SSM is a heterogeneous variable in terms of space and time, data acquisition with traditional single-point measurement methods is limited to the local scale. Remote Sensing (RS) offers the possibility to continuously observe the land surface and characterize the spatio-temporal variation of the SSM (Adab et al., 2020), because it is one of the influential factors that control the radiation emitted from the Earth's surface (Gao et al., 2013). All parts of the electromagnetic (EM) spectrum normally used for Earth Observation (EO) can be analyzed for quantitative SSM estimate. RS-based methods for SSM retrieval can be classified into three categories, as a function of the type of input data: thermal, microwave, and optical. Most globally available SSM products are derived from microwave RS, due to the ability of microwave radiation to penetrate cloud cover, and their potential to provide all-weather all-time sensing (Yuana et al., 2020). However, soil moisture products obtained from input space-borne passive microwave data are sensitive to surface roughness and have coarse spatial resolution (in the range of km), making them inefficient for studies over small areas (Fang et al., 2019). Active microwave data can be used for retrieving soil moisture at higher spatial resolution (e.g., 20m), although their potential for this retrieval task often decreases in the case of vegetation covered areas (Cui et al, 2023, Graldi and Vitti, 2022). Thermal RS usually exploits the differences between Land Surface Temperature (LST) and air temperature to estimate evaporative fraction as a proxy of the SM (Sini et al, 2008). Separating LST from canopy temperature is anyway a difficult task (Gao et al., 2013). Optical RS, in the visible, near-infrared (NIR), and shortwave infrared (SWIR) ranges, measures the reflected radiation from the earth surface, which can be correlated with soil moisture to provide very high spatial resolution data (Adab et al., 2020). Numerous researches focused on multi-sensor data fusion, satellite-derived vegetation, water and soil indices, and different Machine Learning (ML) techniques (Nguyen et al., 2022). Multispectral indices, like Normalized Difference Vegetation Index (NDVI) and Normalized Difference Water Index (NDWI), have demonstrated strong associations with SSM (Ramat et al, 2022, Hachani et al., 2023, Serrano et al., 2019). Several ML techniques, such as Gradient Boosting Regression (GBR), Support Vector Regression (SVR), Elastic Net Regression (ENR), and Random Forest (RF), showed great potential (Adab et al., 2020). In the present study, the potential of multispectral satellite images acquired by Sentinel-2 (S-2) for SSM extraction at the spatial resolution of 10 meters is investigated. For this purpose, an 18-months dataset of hourly SSM measurements, acquired by sensors placed at four different depths in four nodes of a monitoring network in Mendatica (Liguria, Italy), from 1st of January 2020 to 30th of June 2021, is used to look for dependency with S-2 images. For this purpose, the ML algorithms RF, SVR, and GBR, have been trained for each measurement node and at the various depth, and the resulting regression performance have been evaluated and compared.

2. SOIL MOISTURE MONITORING NETWORK: CHARACTERISTICS, CALIBRATION AND RELIABILITY ANALYSIS

Capacitive sensors are the most versatile and economically sustainable soil moisture sensors. They are relatively easy to install and replace and can be installed in the soil at different depths and locations in the study area, thus creating a monitoring network (Bovolenta et al., 2020). Such monitoring network was installed in Mendatica (Liguria, Italy), using the WaterScout SM100 (Spectrum Tec.). The network consists of five measurement nodes (M1, M2, M3, M4, M5) and a retriever node, that collects and sends data. Each node is connected with four sensors placed at different depths (-10cm, -35cm, -55cm, -85cm), providing information on soil water content along a vertical measuring line (Viaggio et al., 2022). However, the M2 node was not considered in the further analysis, because unrepresentative of the study area. The adopted soil moisture sensors need to be site-specifically calibrated considering the characteristics of the soil samples taken from the study area at the measuring points. The results of the soil-specific calibration are shown in Table 1, in which θ defines the volumetric water content of the soil while the ratio between output and input voltage (V_{out}/V_{in}) represents the raw data from the soil moisture sensors.

* Corresponding author

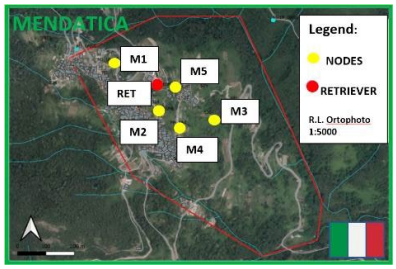

Figure 1. Mendatica soil moisture monitoring network (Regione Liguria orthophoto on the background)

Equation	Number of data samples	a	b	R^2	RMSE [%]
$\theta = \alpha \frac{V_{OUT}}{V_{IN}} + b$	64	286.8	-89.3	0.95	3.1

Table 1. Calibration function for SM100 in Mendatica. R^2: coefficient of determination; RMSE: root mean square error.

The reliability verification of the acquisitions obtained through the SM monitoring network was conducted through the analysis of the correlation between rainfall and volumetric water content θ variations recorded by the four sensors along the vertical of each measurement node. As expected, a higher correlation between rainfall and SM is evident in the shallower sensors, with maximum values positioned at short lags. A decrease in correlation is evident for the deepest sensors, with a progressive delay of the peaks (Figure 2). In Figure 3 an example of SM acquisition performed by M1 node is presented.

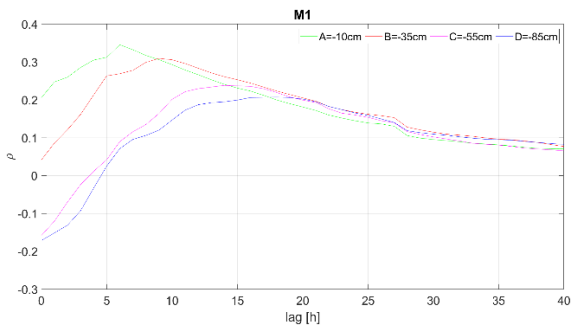

Figure 2. Rainfall-θ cross-covariance referred to May 2021.

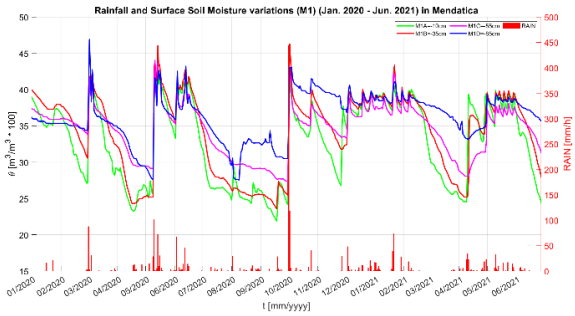

Figure 3. SM data measured by M1 measurement node at different depth, and rainfall data during the study period.

3. SATELLITE REMOTE SENSING DATA

S-2 provides systematic global acquisition of high-resolution multispectral images (MSI) with 12 spectral bands at spatial resolutions of 10m, 20m and 60m. The availability of cloud-based platforms for acquiring and processing satellite images has significantly simplified the implementation of large-scale RS applications like time series analysis (Duan et al., 2020). In this study, we used the Harmonized S-2 MSI Level 2A ("COPERNICUS/S2-SR-HARMONIZED") image collection in Google Earth Engine over the considered study period. This image collection contains Surface Reflectance (SR) values of 12 spectral bands. SR values for all bands of S-2 were used in this study to train regression models. SR was exported for all bands from the image collection with 10 meter spatial resolution on each measurement node in the monitoring network through the study period. Accordingly, a dataset containing values of SR of each band based on the specific geometry for the whole study period was generated.

3.1. Machine Learning for Supervised Regression

In order to train the model, all bands of S-2 were set as input observations and the field-measured SSM at each node (M1, M3, M4 and M5) was considered as the target variable. Separate regression models were trained with measurement data at distinct depths. In the following, working SM sensors (11 in total) connected to measurement nodes are identified with a notation that defines their measurement depth XX in cm (SSMXX). Optical reflectance can serve as an indirect measure of root-zone SM. Most vegetation indices, related to biomass and leaf area index like Normalized Different Vegetation Index (NDVI), or canopy water-based indices like Normalized Different Water Index (NDWI) and Normalized Difference Moisture Index (NDMI), are associated with root-zone SM (Liu et al, 2018). Subsequently, each regression method was trained using three indices in input: the NDVI, the NDWI, and the NDMI. Each site was considered independent because of the different land-use types at the various locations. Hence, soil moisture content has been estimated at four sites and the available depths, by developing eleven individual models for each regression algorithm used, i.e. RF, SVR, and GBR. The following model selection settings were chosen: for RF, the maximum number of features to be used in each split was set using the well-known rule of thumb of the square root, while the number of trees in the ensemble was fixed to 10.000. For SVR, four different kernels, i.e., linear, sigmoidal, polynomial, and Gaussian radial basis function (RBF) were used. The regularization parameters *C* and ε were set to 1 and 0.1, respectively. For GBR, the number of estimators, the learning rate (shrinkage), the minimum number of observations at each node and the maximum depth were 100, 0.1, 10 and 3, respectively. In this study, the dataset was split as 80% for training the models and 20% for testing their performances. The total number of acquisitions for sites M1 (land use: agriculture), M3 (land use: woods and brambles), M4 (land use: agriculture close to houses) and M5 (land use: agriculture close to woods) were 106, 113, 108, and 108, respectively. Discrepancies in acquisition numbers arose due to the cloud cover or shadow obscuring the desired pixels. External tests help to ensure the robustness of the model. Accuracy assessment was done using the root mean squared error (RMSE) to evaluate the difference between the observed values of SSM and the retrieved values computed by the different regression algorithms on the test samples.

4. RESULTS AND CONCLUSIONS

The main goal of this study was to explore the relationship between S-2 MSI data and ground-based SSM measurements. Initially, 12 different spectral channels (B1 to B12) were

considered as potential variables for model training. Subsequently, common vegetation indices were examined, due to the significant impact of vegetation cover on the received surface reflectance from earth surface. Table 2 shows that the accuracy of the results is considerably dependent on the training dataset, hence the land-use types at each location and the analysed depth. The highest dependency between the measured soil moisture and the inputs of the regression models was observed at the deepest measurement depth across all monitoring nodes (M1, M3, M4, and M5). Except for the M4 sensor, which operates in areas characterized by high heterogeneity in land use, both NDVI and NDMI exhibited a more pronounced dependency on soil moisture for the remaining measurement nodes. This highlights the substantial impact of vegetation dynamics on soil moisture assessment, particularly as measurement depth increases. Previous studies (Liu et al, 2018) have emphasized the effectiveness of vegetation indices such as NDVI in elucidating the relationship between SSM, root-zone SM, and crop water content. Root-zone SM significantly influences vegetation cover and alters the surface energy balance.

			M1 Node				M3 Node		M4 Node			M5 Node	
	Method	kernel	SSM10	SSM30	SSM50	SSM80	SSM10	SSM85	SSM10	SSM35	SSM55	SSM10	SSM50
12 Channels	RF		4.21	5.12	3.42	**2.62**	3.64	2.13	**6.43**	6.43	2.55	**2.89**	1.87
	SVR	Linear	**3.39**	**3.67**	3.11	3.26	**2.69**	**1.76**	6.71	5.31	5.80	4.90	2.62
		Sigmoid	4.18	4.46	**3.08**	3.11	2.99	2.43	8.40	4.82	4.71	4.97	2.84
		RBF	4.34	4.72	3.16	**2.62**	3.33	2.27	8.54	4.51	5.00	4.77	1.78
		Polynomial	4.58	5.05	3.46	3.36	2.87	2.05	13.82	21.99	16.1	6.00	2.89
	GBR		5.47	5.35	4.04	3.29	3.35	2.39	6.74	**3.02**	**2.25**	3.16	**1.68**
NDVI	RF		**2.93**	**3.64**	**1.81**	**1.76**	**2.15**	**1.38**	7.63	6.12	6.59	**2.15**	**1.42**
	SVR	Linear	5.71	6.76	3.64	3.43	3.94	2.79	7.61	7.61	7.66	4.60	3.15
		Sigmoid	5.71	6.85	5.47	5.69	5.47	4.72	7.86	8.06	8.20	6.12	5.82
		RBF	5.66	6.68	3.54	3.37	3.85	2.75	**7.32**	7.56	7.60	4.52	2.91
		Polynomial	5.72	6.78	3.61	3.46	3.95	2.78	8.03	8.12	8.05	4.68	3.20
	GBR		4.63	6.03	3.96	5.09	3.27	2.27	8.65	**5.02**	**5.22**	3.70	2.41
NDWI	RF		**2.50**	**3.09**	**1.82**	**1.93**	**2.15**	**1.29**	**4.52**	**3.05**	**3.12**	**2.17**	**1.45**
	SVR	Linear	4.91	6.09	3.21	3.49	3.99	2.85	8.12	5.54	5.82	4.58	2.99
		Sigmoid	4.93	6.14	3.23	3.51	5.92	5.86	8.58	7.19	7.40	4.68	4.65
		RBF	4.97	6.15	3.21	3.46	3.85	2.66	8.17	5.33	5.63	4.48	2.87
		Polynomial	4.89	6.07	3.26	3.49	3.96	2.79	8.26	5.77	6.22	4.61	3.09
	GBR		3.69	4.64	2.47	2.73	3.28	2.15	6.51	4.34	4.38	3.64	2.29
NDMI	RF		**2.78**	**3.29**	**1.74**	**1.86**	**1.88**	**1.27**	**4.52**	**3.05**	**3.12**	**2.31**	**1.61**
	SVR	Linear	5.59	6.53	3.51	3.51	3.81	2.82	8.79	6.19	6.62	4.60	3.24
		Sigmoid	5.62	6.49	3.74	5.51	5.18	4.00	8.85	6.15	7.18	5.00	3.41
		RBF	5.51	6.33	3.35	3.26	3.68	2.71	8.39	5.92	6.02	4.46	2.96
		Polynomial	5.64	6.77	3.65	3.47	3.88	2.89	8.92	6.12	6.59	4.53	3.35
	GBR		4.46	5.13	2.73	2.77	3.03	2.07	7.14	4.77	4.75	3.57	4.72

Table 2. RMSE of Volumetric Water Content data (expressed as percentage) using different ML algorithms. The lowest values for each sensor and each training are highlighted in bold.

The findings of this study indicate that the greenness-based vegetation index (NDVI) is more reliant on variations in soil moisture in the root-zone area in agricultural land use cases (M1 and M5), compared to canopy water content indices like NDWI and NDMI, particularly evident in M3 with denser vegetation cover. Among the three algorithms used to estimate soil moisture, the RF method demonstrated the highest proficiency in soil moisture retrieval, particularly when combined with NDVI, consistent with findings from other studies (Wang and Fu, 2023). For future works, it is suggested to consider the homogeneity of land use within each pixel and verify that the selected pixel accurately represents the area surrounding the sensor.

ACKNOWLEDGEMENTS

The authors acknowledge the support given by AD-VITAM Partners. A particular acknowledgement goes to the Unione dei Comuni della Valle Argentina e Armea and to the lab technicians of the Department of Civil, Chemical and Environmental Engineering of the University of Genoa.

REFERENCES

Adab, H., Morbidelli, R., Saltalippi, C., Moradian, M., and Fallah Ghalhari, G.A., 2020. "Machine Learning to Estimate Surface Soil Moisture from Remote Sensing Data". Water, 12(11). https://doi.org/10.3390/w12113223.

Bovolenta, R.; Iacopino, A.; Passalacqua, R.; Federici, B., 2020. "Field Measurements of Soil Water Content at Shallow Depths for Landslide Monitoring". Geosciences 2020, 10, 409. https://doi.org/10.3390/geosciences10100409.

Cui, H., Jiang, L., Paloscia, S., Santi, E., Pettinato, S., Wang, J., Fang, X., Liao, W., 2021. "The potential of ALOS-2 and Sentinel-1 radar data for soil moisture retrieval with high spatial resolution over agroforestry areas, China". IEEE transactions on geoscience and remote sensing.

Duan, Y., Li, X., Zhang, L., Chen, D., Liu, S., and Ji, H., 2020. "Mapping national-scale aquaculture ponds based on the Google Earth Engine in the Chinese coastal zone". Aquaculture, 520. https://doi.org/10.1016/j.aquaculture.2019.734666

Fang, B., Lakshmi, V., Jackson, T, J., Bindlish, R., Coliander, A., 2019. "Passive/ active microwave soil moisture change disaggregation using SMAPVEX12 data". Journal of Hydrology, 574, 1085-1098.

Gao, Z., Xu, X., Wang, J., Yang, H., Huang, W., Feng, H., 2013. "A method of estimating soil moisture based on the linear decomposition of mixture pixels". Mathematical and computer modelling, 58(3-4), 606-613. https://doi.org/10.1016/j.mcm.2011.10.054.

Graldi, G., Vitti, V., 2022. "Identifying time patterns at the field scale for retrieving superficial soil moisture on an agricultural area with a change detection method: a preliminary analysis". The international archives of photogrammetry, remote sensing and spatial information science, volum XLIII-B3-2022. XXIV ISPRS congress, 6-11 June 2022, Nice, France. https://doi.org/10.5194/isprs-archives-XLIII-B3-2022-879-2022.

Hachani, A., Ramat, G., Paloscia, S., Santi, E., Baroni, F., Fontanelli, G., Lapini, A., Pettinato, A., Pilia, S., Santurri, L., 2023. "Remote sensing techniques for soil humidity monitoring in drought areas: case study of the Wadi Hallouf/Oum Zessar watershed (Tunesia)". International workshop on meteorology for agriculture and forestry.

Liu, L., Yang, X., Liu, S., Zhou, L., Li, X., Yang, J., Wu, J., 2018. "Relationship of root zone soil moisture with solar-induced chlorophyll fluorescence and vegetation indices in winter wheat: a comparative study based on continuous ground-measurements". Ecological indicators, 90, 9-17. https://doi.org/10.1016/j.ecolind.2018.02.048

Nguyen, T., Ngo, H, H., Guo, W., Chang, S, W., Nguyen, D, D., Nguyen, C, T., Zhang, J., Liang, S., Bui, X, T., Hoang, N, B., 2022. "A low-cost approach for soil moisture prediction using multi-sensor data and machine learning algorithm". Science of The Total Environment, 833.

Ramat, G., Santi, E., Paloscia, S., Fontanelli, G., Pettinato, S., Santurri, L., Souissi, N., Da Ponte, E., Abdel Wahab, M., Khalil, A., H.Essa, Y., Ouessar, M., Dhaou, H., Sghaier, A., Hachani, A., Kassouk, K., Chabaane, Z., 2022. "Remote sensing techniques for water management and climate change monitoring in drought areas: case studies in Egypt and Tunisia". European Journal of Remote Sensing, 56(1). https://doi.org/10.1080/22797254.2022.2157335

Serrano, J., Shahidian, S., Da Silva, J., 2019. "Evaluation of normalized difference water index as a tool for monitoring pasture seasonal and inter annual variability in a mediterranean agro-silvo-pastoral system". Water, 11(1). https://doi.org/10.3390/w11010062

Sini, F., Boni, G., Entekhabi, D. , 2009. "Measurements of Hydrological Variables from Satellite: Application to Mediterranean Regions". In: Sorooshian, S., Hsu, KL., Coppola, E., Tomassetti, B., Verdecchia, M., Visconti, G. (eds) Hydrological Modelling and the Water Cycle. Water Science and Technology Library, vol 63. Springer, Berlin, Heidelberg. https://doi.org/10.1007/978-3-540-77843-1_5

Viaggio, S.; Iacopino, A.; Bovolenta, R.; Federici, B., 2022. "Landslide Susceptibility Assessment: Soil Moisture Monitoring Data Processed by an Automatic Procedure in GIS for 3D Description of the Soil Shear Strength". The international archives of photogrammetry, remote sensing and spatial information sciences. XLVIII-4/W1-2022: 517–523. https://doi.org/10.5194/isprs-archives-XLVIII-4-W1-2022-517-2022.

Wang, S., and Fu, G., 2023. "Modelling soil moisture using climate data and normalized difference vegetation index based on nine algorithms in alpine grasslands". Front.Environ.Sci. 11:1130448.doi: 10.3389/fenvs.2023.1130448

Yuana, Q., Xua, B., H., Lic, T., Shenb, C., D., H., and Zhang, L., 2020. "Estimating surface soil moisture from satellite observations using a generalized regression neural network trained on sparse ground-based measurements in the continental U.S". Hydrology, 580

NEW REMOTE SENSING METHODOLOGY TO MAP THE GLACIER EXTENT: THE NEW INVENTORY OF GLACIERS IN PAKISTAN

M.T. Melis [1]*, D. Fugazza [2], L. Naitza [1], M. Gallo [3], F. Dessì [1], M. Casu [1], A. Ahmad [2], B. Barbagallo[2], G. Diolaiuti [2], A. Senese[2], R. Ul Hassan [4], M. Aurang Zaib [4], S. Munir [4], A. Hussain [4], D. Simonetti [5]

[1] Department of Chemical and Geological Sciences, University of Cagliari, Monserrato, Italy - titimelis@unica.it
[2] Department of Environmental Science and Policy, Università degli Studi di Milano Statale, Via Celoria 2, 20133 Milano davide.fugazza, guglielmina.diolaiuti@unimi.it
[3] Associazione Riconosciuta EvK2-CNR, Bergamo, Via San Bernardino 145, CAP 24126, Italy - maurigallo00@gmail.com
[4] EvK2CNR Pakistan, Skardu – Gilgit Baltistan, Pakistan Italian K2 Museum (PTDC Motels) Hamid Ghar Chowk, Reg. N 4(5)EA/NGO/2009 - riaz.hassan@evk2cnr.org
[5] Joint Research Centre, via Enrico Fermi 2749, TP250, 21027 Ispra (VA), Italy - gis.dario.simonetti@gmail.com

KEY WORDS: Sentinel-2, Segmentation, Object-based classification, Hindu-Kush, Karakorum, Himalaya

ABSTRACT:

Satellite imagery from the Sentinel-2 MSI platforms provides systematic global acquisitions of high-resolution imagery of the Earth's surface with a 5-day revisit time at the equator, having a great potential for monitoring and mapping regions where the land cover is particularly sensitive to the dynamics of climate change, such as the glaciers environments.
Although several attempts at automatic procedures have been tested by the scientific community in recent years, very often the remote sensing mapping of the glaciers requires the use of personnel with expertise in the photo-interpretation of the glacial morphology, for the detection of the landform features. The strategy of this project can be divided in two main goals: i) Developing a new methodology to map the glaciers in the region of Hindu-Kush Karakorum ranges in Pakistan, where a number of more than 10,000, with a large number of them debris-covered, has been reported; ii) Involving the Pakistani and Italian students into the process of recognition of the glacier's boundaries and their mapping. In order to reduce the subjectivity of the human interpretation, a new proposal of a semi-automated process for the classification of glacial landform features from Sentinel-2 data was implemented.

1. INTRODUCTION

Optical satellite data has been widely used for the glacier mapping, starting from the first Landsat imagery in the '70s years. The revisit time and the availability of these data can be considered the most important characteristics the researchers employed to create the first existing glaciers inventories based on the satellite imagery interpretation. Multispectral data allowed to propose algorithms, like the spectral indexes, for the masking of the cloud cover and the recognition of snow and ice and then map the glacier extent (Paul et al., 2005). The resulting new images can support the mapping, but two main concerns can be measured: i) a unique threshold of the adopted spectral index is inclined to give a good result only locally with homogeneous geomorphological, slope and aspect conditions; ii) multispectral indexes based on optical data cannot clearly identify the debris-covered or partially covered glaciers confused with the surroundings moraines or rock outcrops. This last is one of the primary and well-known challenge, especially when it comes to identifying glacier terminus points (snouts). Researchers propose different methods based on thermal data or the integration of high spatial resolution optical and topographic data, to compare the landform due to the presence of debris (Kraaijenbrink et al., 2016; Mölg et al., 2020).
Moreover, the application of automatic classification of spectral data, supported by high performance of digital processing systems has been applied in limited glacier areas (Paul et al., 2016), suggesting that when analysing a very large area, a systematic step-by-step approach must be implemented, with a thorough examination of the results. For this reason, in this project the automatic extraction of the glacier's boundaries using a pattern recognition technique has been controlled by human interpretation.
This study is designed to describe and discuss a new methodology to map the glaciers from satellite data. The research has been developed in the framework of the UNDP (United Nations Development Programme) and EvK2CNR-Italy Project "Glaciers and Students - A scientific based approach to monitor climate and glaciers in Pakistan Mountain Regions to support hydrogeological risk prevention". The main expected result of this project will be the updated glaciers inventory of Pakistan. The region of Hindu-Kush Karakorum ranges in Pakistan hosts a number of more than 10,000 glaciers, and a large number of them are debris-covered.
Starting from these expected outputs, and considering the new technical performance that can be activated in the using by satellite data, the strategy of this project can be divided in two main goals:

- Developing a new methodological approach to map the glaciers;
- Involving the Pakistani and Italian students into the process of recognition of the glacier's boundaries.

Based on these objectives, the results presented in this research primarily centre around detailing the newly discussed glacier inventory methodology.

2. DATA AND METHODS

2.1 Satellite data and software environment

The new inventory of Pakistan's glaciers has been developed using optical data obtained from the European Space Agency's Sentinel-2 twin satellites. This choice is dictated by the need to

* Corresponding author

respond to the requirement to have homogeneous coverage of the entire territory under examination in terms of image acquisition dates, cloud cover and good spatial resolution, that allow the recognition of glaciers and their mapping.
Furthermore, particular attention in the selection of the data processing and mapping methods was given for the expected prospect activity of updating the glaciers perimeters and monitoring changes in the future.
Sentinel-2 twin satellites acquire data through an optical multispectral sensor with 10 meters of spatial resolution in the visible and Near-Infrared and 20 meters in the Short-Wave Infrared, allows to apply the useful algorithms for the spectral recognition of the glaciers (Kääb et al., 2016; Paul et al., 2016).
Several software can be used for image processing and editing in GIS environment, either free or commercial.
Moreover, the available DEM has been used to divide the Gilgit-Baltistan region in hydrographic basins allowing the recognition of glaciers in each of them separately, and to let each user to concentrate the analysis and the glaciers classification in a bordered area.
IMPACT Toolbox has been chosen for the pre-processing and the semi-automatic classification of the satellite data (http://forobs.jrc.ec.europa.eu/products/software). GIS

2.2 Methodology

The applied methods can be divided in two main sections, as in Figure 1:

- Satellite data arrangement
- Glaciers recognition (classification) and mapping

The first section was dedicated to the preparation of the base data used by the researchers and students for the classification: recognition and mapping of the glacier's boundaries. The second part of the methodology includes the activities of mapping, recognizing the polygons of the segmentation belonging to the glacier surface.
The applied classification of satellite data is based on the Segmentation function of the composite image. In the next paragraph, the specific steps to create the composite image used to spectrally discriminate the glacial bodies and extract their limits is described. The output of these functions is a file in polygonal vector format (shapefile), where each feature can belong to a glacier.

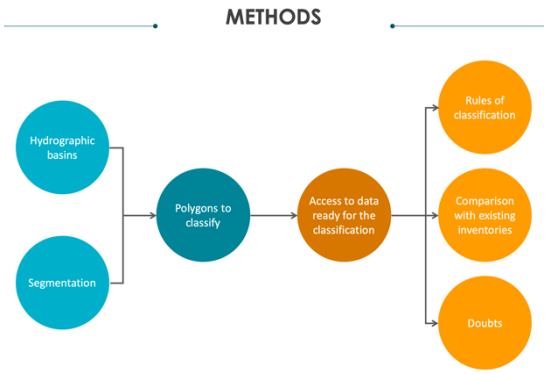

Figure 1. Schema of the approach with the steps of the adopted methodology

From the synthetic image of Sentinel 2, spectral indexes referred to snow and ice-cover, and the image segmentation to partitioning of the composite into relatively homogeneous regions were applied. The resulting regions (polygons) can belong or not to a glacier, and the interpretation by the users is supported by their boundaries.

2.3 Image Segmentation

The workflow in the applied procedure is constituted of three main steps:

- Satellite data acquisition and composite;
- Spectral Index extraction;
- Data classification and segmentation.

Satellite data acquisition and composite
The first step aims at the production of a single/mosaic multi-spectral dataset reproducing the mountain range in northern Pakistan free of clouds, cloud-shadows and haze. A large number of Sentinel-2 data are needed to cover this area and to guarantee the cloud-free observations. Considering the swath of each image and the temporal resolution of these data, the possibility to use the cloud platform Google Earth Engine has been adopted for the creation of a unique multispectral data for the whole region. It is generally known, finding all cloud-free images covering the whole is highly challenging. So, the approach in this project has been based on the creation of a single multi-band composite cloud-free image, starting from the selection of acquisitions during the summer season.
The cloud-cleaning technique applied in this project is based on the PINO cloud mask image processing procedure, applied in JavaScript code through the Google Earth Engine platform to create multi-temporal data composites (Simonetti et al., 2021). The PINO function returns the same Sentinel-2 image received as input after replacing every pixel, classified as clouds or shadows, with no-data. Filtering the annual image collection before extracting the median value of each pixel, increases the probability of obtaining a cloud-free composite in cloud-prone areas or whenever the atmospheric contaminations affect more than 50% of the acquisitions. For each pixel of the resulting image, and for each band, the most frequent pixel value (median) at the correspondent position in the given time series is assigned. For the computation of median digital numbers, pixel values recognized as belonging to clouds, cloud-shadows or haze by the PINO cloud mask algorithm, are automatically skipped, resulting in a data composite clean from atmospheric contaminants. The time series of Sentinel-2 L1C data in the acquisition period from "2022-07-31" to "2022-10-01" was processed. The resulting image composite is a cloud free Sentinel-2 multiband dataset, time-centred at the end of August (Figure 2)

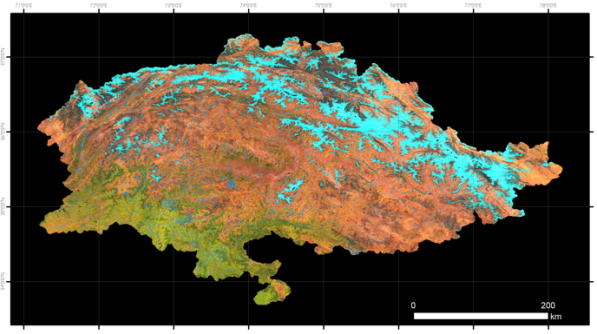

Figure 2. Sentinel-2 RGB composite image of the Pakistan region used in this inventory. This image is the synthesis of all the images acquired by the Sentinel-2 satellites in the period "2022-07-31" -"2022-10-01. In the Red, Green and Blue channels the SWIR, NIR and Red bands are represented. The main land cover types can be identified: in bright blue the snow, in dark blue the ice, in bright and dark tones of red the bare soils and rocks, and in green the vegetated areas.

Spectral Index extraction
The second step of the approach is focused on the enhancement of the spectral differences among objects composing the scene,

and the spectral investigation was concentrated on the distinction of glaciers ice/snow, glaciers debris and rocky slopes. The normalized-difference snow index (NDSI) was adopted (Dozier, 1989):

$$NDSI = (B3(green) - B11(SWIR1)) / (B3(green) + B11(SWIR1))$$

In order to distinguish the glaciers debris (not covered by ice or snow) from rocky slopes, it is hypothesized that the vegetation has a discriminating role, being present in the second (especially during the summer, such as the acquisition period chosen for the synthetic composite), even if sparse and low, and is almost absent in the first, because of the slow but constant friction, movement and tilling of sediments in the dynamism of the glaciers. According to this hypothesis, the normalized-difference vegetation index (NDVI) was calculated:

$$NDVI = (B8(NIR) - B4(Red)) / (B8(NIR) + B4(Red))$$

Since, the best contrast strategy to distinguishing the landforms of interest is based on the spectral indices mentioned above, a new dataset was prepared using NDSI, NDVI and Band4 (red), creating a new multiband image stack. Then, the segmentation classification algorithm was applied to this new multiband dataset, in order to aggregate pixels on the base of the proximity and of the similarity in the response in the NDSI, NDVI and Red reflectance.

Data classification and segmentation

The third step in the workflow regards the data classification. In this project we adopted image segmentation technique, aimed at the partitioning of the dataset into multiple polygons (segments) based on spectral, geometric or texture properties, calculated in conjunction with user-defined parameters describing size, shape and similarity to adjacent segments.

The following parameters have to be considered in the classification process:

• bands and weights: raster bands and associated weight values to use;

• scale factor: factor that controls the spectral heterogeneity of the objects in the image and is therefore related to their average size, the low value of which allows obtaining a high number of objects and vice versa;

• colour: spectral component of the Baatz algorithm [0,0; 1.0] (Baatz et al., 2000);

• compactness: morphological component of the Baatz algorithm [0,0; 1.0];

• Euclidean distance: minimum distance (expressed in DN values) to set for the process union of the segments that cross two adjacent links; high values will allow the aggregation of heterogeneous objects between the meshes, while low values will preserve the sharp boundaries of the meshes;

• MMU: minimum map unit, i.e. the spatial resolution in meters per pixel of the segmentation layer; for the images collected by Sentinel-2, 1 MMU corresponds to an area of 100 m^2, i.e. a surface of 10 x 10 m on each side, the spatial resolution of Sentinel-2 being 10 m (Simonetti et al., 2015).

In this project, the segmentation process was applied through the functionality available in the JRC IMPACT free software, which is based on the Baatz-Schape open source segmenter libraries (Inpe's TerraAIDA Operators). The NDSI-NDVI-B4 multiband dataset was processed adopting the setting, as proposed by the application as optimal ("majority" as aggregation rule, 0.8 as compactness, 0.9 as similarity in a scale 0-1, 0.9 as colour). The minimum map unit (MMU) parameter was empirically tested by setting two different values: 250 and 100. Applying the first value, the segmentation process produces a reduced number of aggregations, distinguishing landforms quite correctly. However, in some cases (e.g. where the slope shadow affects the scene) the detail of the output is not enough accurate to precisely perimeter the landforms as efficiently as the MMU parameter 100 does. On the other end, the output of the segmentation achieved setting 100 as MMU parameter, returns a number of aggregations blocks considerably higher, less easy to analyse for a photo-interpreter (Figure 3).

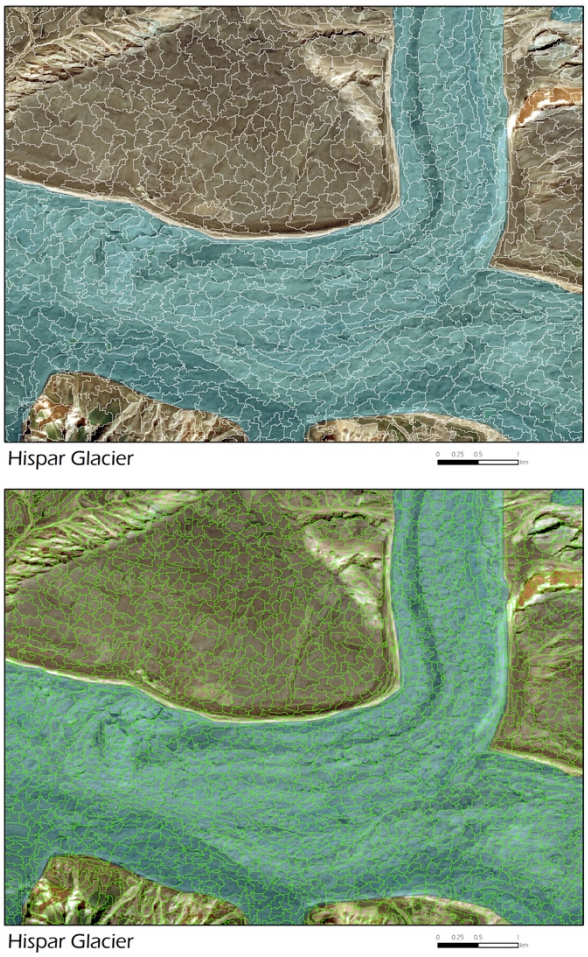

Figure 3. Comparison of the subsets of the image in true colour representing a central region of Hispar glacier. The area covered by the glacier is in blue, and is delineated merging the segmented polygons belonging to the glacier. In the upper image, the polygons with MMU of 250 are represented in white, and in the lower image, the polygons with MMU 100 are in green.

3. RESULTS AND DISCUSSION

3.1 Glaciers recognition (classification) and mapping

The methodology has been implemented in a Geographic Information System (GIS) environment. Subsets of the composite have been created for each basin. In a dedicated cloud server all the data has been uploaded, allowing each researcher and student to access to an assigned basin in a folder. For each basin, four thematic data were available, as shown in Figure 4:

- The composite multiband image with the bands
- The spectral indexes
- The shapefile with the polygons of the segmentation with the MMU of 250
- The shapefile with the polygons of the segmentation with the MMU of 100.

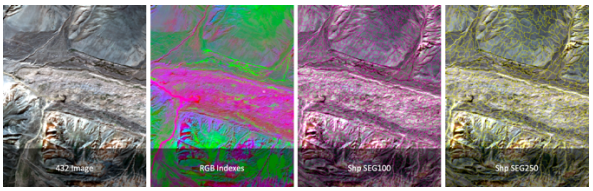

Figure 4. Contents of the working folders for each basin.

As in Figure 1, starting from these data, the steps of mapping were driven by an initial training activity and periodic online meetings which allowed the working group to discuss and share the procedures for assigning each polygon to a glacier or not. The first results of this activity can be seen in the Figure 3: the polygons created with the segmentation follow the limit of the glacial tongues with a good accuracy, allowing them to be identified very precisely. The process of identification of the polygons has been supported by accessible datasets, like the existing glaciers inventories, the very high-resolution satellite data of Google Earth and Google maps, and the base map available in the GIS software. However, the final decision and the final limit was drawn based on the Sentinel image, thus ensuring a homogeneity of the detection date.
A specific activity of comparison of each glacier with the available high-resolution imagery has been done in the final phase of validation, considering their acquisition date.

4. CONCLUSIONS

The improvement of knowledge of the cryosphere processes and the impacts of the climate changes can generate a new awareness in the local communities in formulating long term strategies for disaster risk reduction and for the environment sustainability. As resulting effects, better decisions and actions in these sectors will have positive impacts on the management of water and land resources, ultimately enabling to establish better responses to climate change and contribute in poverty reduction (Sustainable Development Goals No. 1, 6, 13 and 15). The use of remote sensing confirms their potential as monitoring system in the areas data particularly sensitive to climate change and capable of rapid geomorphic responses to perturbation (Melis et al., 2023).
The final product of the research project described in this study is a map in vector format (shapefile), where each glacier results from the merging of the polygons inside its boundary. The proposed method, and the software infrastructure planned for this study, has been considered suited to familiarize with the mapping process using satellite images by the students from the Italian and Pakistan universities involved in the project with a basic knowledge of remote sensing, GIS, and glacier's mapping. For these topics, training activities have been organized and guidance materials in form of videos have been shared.
Although in the proposed method the assignment of a "Glacier label" is based on visual recognition, each interpreter is guided by a vector basis automatically extracted from the Sentinel-2 spectral products.
The outcomes of this study allow to plan the updating of the inventory annually, according to a procedure that guarantees the replicability and comparability of the results. Furthermore, in this way, the method can be adopted to guarantee the necessary monitoring action of these immense water reservoirs which constitute the primary resource for the life of millions of people living in the Asian region.

ACKNOWLEDGEMENTS

This study is part of the Project "Glaciers and Students: - A scientific based approach to monitor climate and glaciers in Pakistan Mountain Regions to support hydrogeological risk prevention", in the framework of the "Project cooperation agreement between the United Nations Development Programme and Ev-K2-CNR Italy, funded by the Agenzia Italiana della Cooperazione e Sviluppo (AICS). Special greetings are given to the President coordinator of Ev-K2-CNR activities Agostino Da Polenza and the colleagues of Ev-K2-CNR-Pakistan.

REFERENCES

Baatz, M. and Schape, A. (2000) Multiresolution Segmentation: An Optimization Approach for High Quality Multi-Scale Image Segmentation. In: *Strobl, J., Blaschke, T. and Griesbner, G., Eds., Angewandte Geographische Informations-Verarbeitung*, XII, Wichmann Verlag, Karlsruhe, Germany, 12-23.

Dozier, J. Spectral Signature of Alpine Snow Cover from the Landsat Thematic Mapper. *Remote Sensing of Environment* 1989, 28, 9–22, doi:https://doi.org/10.1016/0034-4257(89)90101-6.

Kääb, A.; Winsvold, S.H.; Altena, B.; Nuth, C.; Nagler, T.; Wuite, J. Glacier Remote Sensing Using Sentinel-2. Part I: Radiometric and Geometric Performance, and Application to Ice Velocity. *Remote Sensing* 2016, 8, doi:10.3390/rs8070598.

Kraaijenbrink, P.D.A.; Shea, J.M.; Pellicciotti, F.; Jong, S.M. de; Immerzeel, W.W. Object-Based Analysis of Unmanned Aerial Vehicle Imagery to Map and Characterise Surface Features on a Debris-Covered Glacier. *Remote Sensing of Environment* 2016, 186, 581–595, doi:https://doi.org/10.1016/j.rse.2016.09.013.

Melis, M.T.; Dessì, F.G.; Casu, M. New Remote Sensing Data on the Potential Presence of Permafrost in the Deosai Plateau in the Himalayan Portion of Pakistan. Remote Sens. 2023, 15, 1800. https://doi.org/10.3390/rs15071800

Mölg, N.; Ferguson, J.; Bolch, T.; Vieli, A. On the Influence of Debris Cover on Glacier Morphology: How High-Relief Structures Evolve from Smooth Surfaces. *Geomorphology* 2020, 357, 107092, doi:10.1016/j.geomorph.2020.107092.

Paul, F.; Kääb, A. Perspectives on the Production of a Glacier Inventory from Multispectral Satellite Data in Arctic Canada: Cumberland Peninsula, Baffin Island. Annals of Glaciology 2005, 42, 59–66, doi:10.3189/172756405781813087.

Paul, F.; Winsvold, S.H.; Kääb, A.; Nagler, T.; Schwaizer, G. Glacier Remote Sensing Using Sentinel-2. Part II: Mapping Glacier Extents and Surface Facies, and Comparison to Landsat 8. *Remote Sensing* 2016, 8, doi:10.3390/rs8070575.

Simonetti D., Marelli A., Eva H., IMPACToolbox, Portable GIS Toolbox for Image Processing and Land Cover Mapping. Joint Research Centre – Institute for Environment and Sustainability, Luxembourg: Publications Office of the European Union 2015, http://doi.org/10.2788/143497.

Simonetti D., Pimple U., Langner A., Marelli A., Pan-tropical Sentinel-2 cloud-free annual composite datasets, Volume 39, 2021, 107488, ISSN 2352-3409, https://doi.org/10.1016/j.dib.2021.107488.

BARTONELLA SPP. DISTRIBUTION ASSESSMENT IN FOXES COUPLING GEOSPATIALLY-BASED TECHNIQUES

A. Viani[1*], T. Orusa[2, 3, 4], S. Divari[5], S. Lovisolo[5], S. Zanet[5], E. Borgogno-Mondino[2],

R. Orusa[1], E. Bollo[5]

[1] Istituto Zooprofilattico Sperimentale del Piemonte, Liguria e Valle d'Aosta (IZS PLV) SC Aosta-CeRMAS (National Reference Center for Wildlife Diseases), Località Amerique 7/C, 11020 Quart (AO), Italy – annalisa.viani@izsto.it

[2] Department of Agricultural, Forest and Food Sciences (DISAFA), GEO4Agri DISAFA Lab, Università degli Studi di Torino, Largo Paolo Braccini 2, 10095 Grugliasco, Italy – enrico.borgogno@unito.it

[3] Earth Observation Valle d'Aosta - eoVdA, Località L'Île-Blonde, 5, 11020 Brissogne, Italy – torusa@invallee.it

[4] IN.VA spa, GIS Unit, Località L'Île-Blonde5, 11020 Brissogne, Italy – torusa@invallee.it

[5]Department of Veterinary Sciences (DSV), Università degli Studi di Torino, Largo Paolo Braccini 2, 10095 Grugliasco, Italy – enrico.bollo@unito.it

KEY WORDS: *Bartonella* spp; Wildlife; Foxes; Remote Sensing; TCW; Landsat

ABSTRACT:

In this study, the presence of *Bartonella* spp. in 114 red foxes (*Vulpes vulpes* L.) of Piedmont (province of Cuneo and Biella) and Aosta Valley (Italy) was investigated. Spleen samples of hunted foxes were collected for *Bartonella* spp. DNA detection, and qPCR assay of *ssrA* locus detection was used as initial screening. The samples positive for *Bartonella* spp. DNA were subjected to end-point PCR to detect *ssrA*, *gltA* and *rpoB* loci. Based on qPCR results, the prevalence of infection with *Bartonella* spp. was 7.9% (9/114). After sequencing, *Bartonella schoenbuchensis* R1 was found to be the most isolated Bartonella species (5/8, 62,5%). *Candidatus* "Bartonella gerbillinarum" was found in two samples (2/8, 25%). In conclusion, this work can contribute to the study of Bartonella infection in fox populations in Italy, allowing for a more comprehensive epidemiological picture on a national scale. Concerning remote sensing contribution, data from NASA USGS Landsat 4-9 missions (TOA collection), ranging from 2011 to 2022, were processed in Google Earth Engine. Assuming that pathogens, especially in rangelands, can be influenced by humidity, the Tasseled Cap Wetness index (TCW) was computed for each date temporal profile consisting of composite images for each meteorological season. Seasonal TCW was positively associated to Bartonella spp. infection in foxes as infection was always associated to TCW >0.7. Moreover, Canonical Cor-responding Analysis between pathogen prevalence and municipal-based TCW show a strong link between positivity and TCW, demonstrating the possible use of TCW as a parameter to facilitate disease management and control.

1. INTRODUCTION

The recent exponential development of science and technologies applied to GIS has contributed to the enhancement of epidemiological data analysis capabilities and has provided new and powerful tools for animal disease surveillance. GIS, spatial analysis techniques and the use of satellites provide useful methods for collecting and managing the information necessary for epidemiological studies. Still little explored in the veterinary field is the use and development of applications and methodologies based on "Earth Observation Data"(Orusa, Viani, e Borgogno-Mondino 2024). In this regard, within the European space program "Copernicus" and other historical programs such as the NASA Landsat missions, geospatial data with medium-high geometric and temporal resolution would make it possible to exploit and expand ordinary risk analysis techniques, translating them into a transfer technology for the veterinary sector. To date, in fact, only a few application ns have been explored with the use of medium-low resolution data in the context of the NASA MODIS Terra and Aqua missions (Carella et al. 2022; Viani, Orusa, Borgogno-Mondino, et al. 2023; Orusa et al. 2020). Bartonella infection in foxes has been described worldwide (Álvarez-Fernández, Breitschwerdt, e Solano-Gallego 2018; Bai et al. 2016; Birtles et al. 2002; Breitschwerdt e Kordick 2000; Henn et al. 2009; Kosoy e Goodrich 2019), while it has been rarely reported in wolves in Spain (Gerrikagoitia et al. 2012). Since both the wolf and the red fox can have contact with domesticated animals, especially dogs, they may play a crucial role in the ecology and spread of Bartonella (Alsarraf et al. 2017; Brenner et al. 1993; Chomel et al. 2012; de Paiva Diniz et al. 2009; Foil et al. 1998; Maggi et al. 2011; Gutiérrez et al. 2015; Minnick e Anderson 2015). In Italy,

* Corresponding author

B. bovis and *B. chomelii* are the only species reported in wildlife, starting from deer tick (Millán et al. 2016). In particular, there is a lack of data on infection in wild canids, although *B. vinsonii* subsp. *berkhoffii* and *Candidatus B. merieuxii* have been reported in hunting dogs in southern Italy. It is worth to note that *B. vinsonii* subsp. *berkhofii* genotype III can be highly pathogenic to dogs (Greco et al. 2021). In scientific literature there are not many reports about *Bartonella* spp. in Italy, especially in wild canids. In this study, the prevalence of *Bartonella* spp. was investigated with reference to fox populations (*Vulpes Vulpes* L.) living in the provinces of Cuneo and Biella (Piedmont) and Aosta Valley (NW Italy).

The study represent a collaboration between scientific institutions (Reference Center for Wild Animal Diseases of Aosta (CeRMAS), Department of Veterinary Sciences of the University of Turin, Department of Agricultural and Forestry Sciences of the University of Turin), and among these and the pool of research collaborators, such as hunters and public agencies responsible for wildlife management (Forestry Corps and Agriculture Department, Natural Resources of the Autonomous Region of Valle d'Aosta). The analysis was achieved at municipality level by coupling molecular diagnostic techniques and satellite remote sensing with the aim of testing possible relationships between pathogen presence and environmental conditions. The DNA extracted from the spleen of 114 sampled animals was initially subjected to the qPCR for the *ssrA* locus and then to the end-point PCR for the *ssrA*, *gltA* and *rpoB* loci.

2. MATERIALS AND METHODS

Foxes examined belong to *Vulpes vulpes* L. species. The study involved the collection of a spleen sample from each fox hunted during the hunting seasons in the Piedmont districts of the province of Cuneo (CACN) and from each fox found dead in the province of Biella (BI), from 2011 to 2022, for a total of 101 samples. The samples were stored and kept in a freezer (-20°C) at the Parasitic Diseases laboratories of the Department of Veterinary Sciences, University of Turin. Regarding samples from Valle d'Aosta, CeRMAS has made directly available to the Pathological Anatomy laboratory of the Department of Veterinary Sciences spleens from 13 foxes found dead in the Valle d'Aosta area and stored at -20 °C. Spleen samples (about 30 mg) were thawed and subjected to DNA extraction using "E.Z.N.A. Tissue DNA kit" (Omega Bio-Tek, Norcross, USA). qPCR (quantitative PCR) allows the observation of amplification products during the progression of the PCR reaction and the quantification of the DNA present in the sample. Briefly, the amplification product can be detected using fluorescent dyes that emit light by intercalating themselves in the DNA double strand (for example, Sybr Green I) or using fluorescent probes. In the present work was used a Dual-Labeled probe also known by the name "TaqMan". The CFX Connect Real-Time System (BioRad, Hercules, USA) was used for qPCR and the locus taken into consideration is transfer-messenger RNA (*ssrA*) (Sigma-Aldrich 2014). The protocol includes an initial denaturation at 95°C for 3 minutes, followed by 45 cycles of denaturation (at 95°C for 15 seconds), hybridization and extension (at 60°C for 1 minute). The genomic DNA of *Bartonella* spp. FG4-1 was used as a positive control (Divari et al. 2021). Samples with a Cq value lower than 32 were considered positive and were subjected to subsequent analyses.

The citrate synthase gene (*gltA*), RNA polymerase gene (*rpoB*), and *ssrA* loci were amplified using end-point PCR. For the *gltA* locus, two PCR end-point assays were applied, generating 700 bp (Birtles et al. 2002) and 380 bp (Norman et al. 1995) amplicons. Amplification was performed using a T100 Thermal Cycler (BioRad, Hercules, USA). The protocols applied in the end-point PCR were the following:

- *gltA* (380 bp): an initial denaturation at 95°C for 15 minutes followed by 35 cycles at 95°C for 20 seconds, at 51°C for 30 seconds and at 72°C for 2 minutes;
- *gltA* (700 bp): an initial denaturation at 95°C for 15 minutes followed by 40 cycles at 95°C for 30 seconds, at 48°C for 1 minute, at 72°C for 1 minute; finally, an extension at 72°C for 7 minutes;
- *rpoB*: an initial denaturation at 95°C for 15 minutes followed by 35 cycles at 95°C for 30 seconds, at 53°C 78 for 30 seconds, at 72°C for 1 minute; finally, an extension at 72°C for 2 minutes;
- *ssrA*: an initial denaturation at 95°C for 30 seconds followed by 40 cycles at 95°C for 15 seconds, at 60°C for 1 minute, at 72°C for 30 seconds; finally, an extension at 72°C for 3 minutes.

End-point PCR products were separated on 1.5% agarose gel in Tris-Acetate-EDTA (TAE) buffer. For DNA visualization, MIDORI Green Advance DNA stain (Nippon Genetics, Düren, Germany) was spiked into the gel. The MWD100 FastGene DNA Ladder (Nippon Genetics, Düren, Germany) was used as a reference marker for band length. The electrophoretic run was set at 100V for the duration of 35 or 60 minutes. The results were visualized and photographed with FastGene® UV Transilluminator (Nippon Genetics, Düren, Germany), considering positive the samples having bands that presented a length like the positive control. The amplicons obtained for *ssrA* and *gltA* were purified with MinElute PCR Purification Kit (Qiagen, Hilden, Germany). Briefly, 5 volumes of Buffer PB were added to one volume of amplification product and transferred to a MinElute column. 750 µl of Buffer PE, containing ethanol (96-100%) were then added. After centrifugation, the DNA was eluted from the column with 10 µl of nuclease-free water. The purified amplification products were sent for bidirectional sequencing (DNA Sanger sequencing) (BMR Genomics, Padua, Italy). According to the company's indications, before shipment, the samples were prepared in a concentration between 12 and 24 ng. Each purified amplification product was dispensed into two 0.2 ml microtubes to which 6.4 pmol of forward and reverse primers relating to the *gltA* loci (380 and 700 bp) and *ssrA* were added separately. The solutions were dehydrated at 65°C. Once the sequencing was done, the obtained chromatograms were corrected manually using the Geneious Prime 2020.1 program. The corrected sequences were aligned with the sequences deposited in GenBank, by BLAST. For each sequence aligned with the sequences deposited in the database, the following were considered: (a) ID% identity percentage (the percentage of identity of the sequences aligned with the deposited sequences); (b) expected (E) value (the probability that the alignment of the correct sequence with the deposited sequences is random); (c) percentage of Query Coverage (the percentage of

the sequence that has been considered in alignment with the deposited sequences). The results obtained were analysed using the GraphPad Prism 8.4.2 software (GraphPad Software, California, USA). Fisher's test was used to evaluate the association between the presence of *Bartonella* spp. and gender, age, season, and period of catching foxes. The Chi square test was used to evaluate the association between the presence of *Bartonella* spp. and the place of capture of animals. A 95% confidence interval was set and results with p-value<0.05 were considered statistically significant.

The GIS analyses were carried out using the software QGIS vers 3.16.4 Hannover. For the geospatial analyses, we used multispectral optical remote sensing data from the NASA USGS Landsat missions with 16-day time resolution starting from 1972 for the whole globe and spatial resolution as a function of the considered spectral band of 30 m for the most part of the spectral bands used. For this work, data from the USGS Landsat 5 and USGS Landsat 8 missions were used, respectively from the Multispectral Scanner (MSS) and Operational Land Imager (OLI) sensors. In particular, the cloud-based platform Google Earth Engine (hereinafter called as GEE) was adopted for the processing of remote sensing data (Orusa e Borgogno Mondino 2021; Orusa e Mondino 2019; Orusa, Viani, Cammareri, et al. 2023; Orusa, Cammareri, e Borgogno Mondino 2022b), which allows large-scale processing of satellite images to detect changes, map trends and quantify differences on the Earth's surface (Orusa, Cammareri, e Borgogno Mondino 2022a; Orusa, Viani, Moyo, et al. 2023; Viani, Orusa, Mandola, et al. 2023; Latini, Bagliani, e Orusa 2021; Bagliani et al. 2019; Caimotto et al. 2020; Tartaglino e Orusa 2020) by accessing petabytes of various satellite missions from different global space agencies.

In particular, the following GEE collections were used: (a) LANDSAT/LT05/C02/T1_TOA: Landsat 5 MSS TM with reflectance calibrated at the level of the upper part of the atmosphere (TOA). Calibration coefficients are extracted from each scene's metadata for TOA calculation based on (DeVries et al. 2016); (b) LANDSAT/LC08/C02/T1_TOA: Landsat 8 OLI TIRS with reflectance calibrated at the level of the upper part of the atmosphere (TOA). Calibration coefficients are extracted from each scene's metadata for TOA calculation based on (DeVries et al. 2016). Below are the characteristics of the sensors of the missions with the adopted bands and relative masks. Starting from the sample collection data of the entire population of foxes considered aggregated by meteorological season and related year using a GEO4Agri DISAFA Lab script, average composite images were created for each meteorological season starting from the year 2011 until summer 2022. From the empirical evidence reported in the literature (Jameson et al., 1995; Rothenburger et al., 2018) in which the pathogen appears to be influenced by humidity, we computed for each scene from which the composites were obtained the multispectral Tasseled Cap Wetness (TCW) index. The Tasseled Cap was generated based on spectral information from the Landsat satellite. The Tasseled Cap coefficients used in the linear equation of the Tasseled Cap transformation are sensor specific and therefore have been derived for each sensor system. The index is related to principal component analysis and vegetation indices. In this casereference was made only to the TCW, a multispectral index of humidity. A measured value for soil and canopy moisture interactions(Sarvia et al. 2021; De Marinis et al. 2021; Samuele et al. 2021; Farbo et al. 2022; Borgogno-Mondino et al. 2022).

$$TCW = (p_{blue} * \alpha_1) + (p_{green} * \alpha_2) + (p_{red} * \alpha_3) + (p_{NIR} * \alpha_4) + (p_{SWIR1} * \alpha_5) + (p_{SWIR2} * \alpha_6)$$

where: ρ = TOA reflectance corresponding to the regions of the electromagnetic spectrum of interest; α = coefficient for the specific TCW transformation for each Landsat band 5 and 8 respectively.

3. RESULTS AND DISCUSSIONS

All 114 selected animals were analyzed by qPCR for the presence of the *ssrA* locus. Nine out of one hundred fourteen (7.9 %) samples were positive by qPCR analysis and in particular 7/102 (6.9%) and 2/13 (15.4%) in red foxes collected in Piedmont and Aosta Valley respectively. The positive samples further analyzed with end-point PCR yielded 7/9 samples positive for the ssrA locus, of which 3/9 positive for the *gltA* locus (380 bp and 700 bp) and none for the *rpoB* locus. Two sequences were not evaluable due to low quality. Based on the sequencing of the amplicons related to the *ssrA* locus, the most represented Bartonella species was *B. schoenbuchensis* R1 (5/9, 55.6%); *Candidatus* "Bartonella gerbillinarum" was identified in two animals (2/9, 22.2%). *B. schoenbuchensis* R1 was also confirmed by sequencing the *gltA* locus in 3/9 animals. No statistically significant associations were observed between the presence of *Bartonella* spp. and the sex, age of the foxes, season, time and place of capture of the foxes. In order to analyse a possible relationship between TCW and the presence of *Bartonella* spp. for the composite timeseries on a seasonal basis for the years of interest, zonal statics were created: in this case Spatial Join on a municipal basis for the provinces of Aosta, Biella and Cuneo respectively. The municipal-based and non-punctual analysis was dictated by the fact that the samples were not punctually georeferenced and starting from the assumption that the place where the animal was found (the municipality and neighbouring area) is its vital habitat (moreover since we are dealing with foxes, the assumption finds correspondence in the ecology and ethology of this species) [41]. From the geostatistical analyses it emerges that in the years in which positive animals are found there is an average value of TCW>0.7. That observation is repeated spatially and temporally throughout areas of thoughtful study. This threshold seems to be an important parameter for analysing the risk and potential transmissibility of the pathogen. To this end, to demonstrate a possible relationship between the environ-mental components TCW mappable by remote sensing and municipal-based positivity, Moran's index I was calculated to test the existence of a spatial problem, which in all cases was higher than Moran I>0.90, consequently significant:

$$I = \frac{N}{\Sigma i \Sigma j Wij} \frac{\Sigma y \Sigma j Wij(xi - \mu)}{\Sigma i(xi - \mu)}$$

where: N = is the number of geographical units; x_i= is the variable that describes the phenomenon under study in region i;μ = represents the sample mean and therefore (x_i-μ) is the deviation from the mean of the variable of interest; Wij = is the weight matrix (where "i" is different from "j"); I = varies between -1.0 and +1.0 and its numerator is interpreted as the covariance between contiguous units. Correspondence analyses on positive samples appear to show a strong link be-tween positivity and

TCW; therefore, in order to map the risk of diffusion based on the geo-statistics obtained, LISA maps (Local Spatial Autocorrelation Indicators) were created on a municipal scale for the periods of interest. It can be observed that in the years of identification of the positives, the maps report on average a high average value of TCW for each municipality. In Figure 1 is reported an example of LISA map of the province of Cuneo in the winter season 2020 (Figure 1).

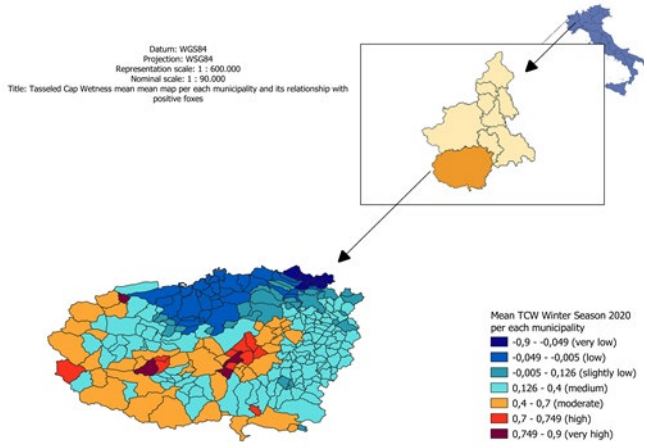

Fig.1 LISA maps of *Bartonella* spp. on foxes and TCW in the winter season 2020 in the province of Cuneo (Piedmont).

4. CONCLUSIONS

This study provided a better understanding of the prevalence and genetic diversity of Bartonella species in the fox populations of Piedmont and Valle d'Aosta. Two species of Bartonella have been detected in foxes, including *B. schoenbuchensis* R1, capable of causing infection in humans. The results found raise the potential threats to public health from the *Bartonella* species: for these reasons, its surveillance in animals and investigations into suspected clinical cases in humans must be strengthened not only in the provinces of the Regions studied, but also to the rest of the Italian territory, as already demonstrated by the recent study by (Greco et al. 2021). Moreover, the present study highlights the added value of satellite data and geospatial analysis in scientific field (Orusa, et al. 2023) and the potentiality offered not only in term of data archiving but also for understand the possible relationship between environmental conditions and disease spreading (Floris et al. 2024; Viani, Orusa, Mandola, et al. 2023; Viani, Divari, Lovisolo, et al. 2023).

REFERENCES

Alsarraf, Mohammed, Eman ME Mohallal, Ewa J Mierzejewska, Jolanta Behnke-Borowczyk, et al. 2017. «Description of Candidatus Bartonella fadhilae n. sp. and Candidatus Bartonella sanaae n. sp.(Bartonellaceae) from Dipodillus dasyurus and Sekeetamys calurus (Gerbillinae) from the Sinai Massif (Egypt)». *Vector-Borne and Zoonotic Diseases* 17 (7): 483–94.

Álvarez-Fernández, Alejandra, Edward B Breitschwerdt, e Laia Solano-Gallego. 2018. «Bartonella infections in cats and dogs including zoonotic aspects». *Parasites & vectors* 11 (1): 1–21.

Bagliani, Marco Maria, Maria Cristina Caimotto, Gianni Latini, e Tommaso Orusa. 2019. «Lessico e Nuvole: le parole del cambiamento climatico».

Bai, Ying, Amy Gilbert, Karen Fox, Lynn Osikowicz, e Michael Kosoy. 2016. «Bartonella rochalimae and B. vinsonii subsp. berkhoffii in wild carnivores from Colorado, USA». *Journal of Wildlife Diseases* 52 (4): 844–49.

Birtles, RJ, G Laycock, MJ Day, MJ Kenny, e SE Shaw. 2002. «Prevalence of Bartonella species causing bacteraemia in domesticated and companion animals in the United Kingdom». *Veterinary Record* 151 (8): 225–29.

Borgogno-Mondino, Enrico, Alessandro Farbo, Vittorino Novello, e Laura de Palma. 2022. «A Fast Regression-Based Approach to Map Water Status of Pomegranate Orchards with Sentinel 2 Data». *Horticulturae* 8 (9): 759.

Breitschwerdt, Edward B, e Dorsey L Kordick. 2000. «Bartonella infection in animals: carriership, reservoir potential, pathogenicity, and zoonotic potential for human infection». *Clinical microbiology reviews* 13 (3): 428–38.

Brenner, Don J, STEVEN P O'CONNOR, Herbert H Winkler, e Arnold G Steigerwalt. 1993. «Proposals to unify the genera Bartonella and Rochalimaea, with descriptions of Bartonella quintana comb. nov., Bartonella vinsonii comb. nov., Bartonella henselae comb. nov., and Bartonella elizabethae comb. nov., and to remove the family Bartonellaceae from the order Rickettsiales». *International Journal of Systematic and Evolutionary Microbiology* 43 (4): 777–86.

Caimotto, Maria Cristina, Daniela Fargione, Cristiano Gino Furiassi, Tommaso Orusa, Piovan Alex, e others. 2020. «Parlare è pensare». In *Lessico e nuvole: le parole del cambiamento climatico (seconda edizione)*, 281–84. Università degli Studi di Torino.

Carella, Emanuele, Tommaso Orusa, Annalisa Viani, Daniela Meloni, Enrico Borgogno-Mondino, e Riccardo Orusa. 2022. «An Integrated, Tentative Remote-Sensing Approach Based on NDVI Entropy to Model Canine Distemper Virus in Wildlife and to Prompt Science-Based Management Policies». *Animals* 12 (8): 1049.

Chomel, Bruno B, Audrey C McMillan-Cole, Rickie W Kasten, Matthew J Stuckey, Shingo Sato, Soichi Maruyama, Pedro PVP Diniz, e Edward B Breitschwerdt. 2012. «Candidatus Bartonella merieuxii, a potential new zoonotic Bartonella species in canids from Iraq».

De Marinis, Pietro, Samuele De Petris, Filippo Sarvia, Giacinto Manfron, Evelyn Joan Momo, Tommaso Orusa, Gianmarco Corvino, Guido Sali, e Enrico Mondino Borgogno. 2021. «Supporting Pro-Poor Reforms of Agricultural Systems in Eastern DRC (Africa) with Remotely Sensed Data: A Possible Contribution of Spatial Entropy to interpret Land Management Practices». *Land* 10 (12): 1368.

DeVries, Ben, Arun Kumar Pratihast, Jan Verbesselt, Lammert Kooistra, e Martin Herold. 2016. «Characterizing forest change

using community-based monitoring data and Landsat time series». *PloS one* 11 (3): e0147121.

Divari, Sara, Marta Danelli, Paola Pregel, Giovanni Ghielmetti, Nicole Borel, e Enrico Bollo. 2021. «Biomolecular investigation of Bartonella spp. in wild rodents of two Swiss regions». *Pathogens* 10 (10): 1331.

Farbo, A, F Sarvia, S De Petris, e E Borgogno-Mondino. 2022. «PRELIMINARY CONCERNS ABOUT AGRONOMIC INTERPRETATION OF NDVI TIME SERIES FROM SENTINEL-2 DATA: PHENOLOGY AND THERMAL EFFICIENCY OF WINTER WHEAT IN PIEMONTE (NW ITALY)». *The International Archives of Photogrammetry, Remote Sensing and Spatial Information Sciences* 43: 863–70.

Floris, Irene, Andrea Vannuccini, Carmela Ligotti, Noemi Musolino, Angelo Romano, Annalisa Viani, Daniela Manila Bianchi, Serena Robetto, e Lucia Decastelli. 2024. «Detection and Characterization of Zoonotic Pathogens in Game Meat Hunted in Northwestern Italy». *Animals* 14 (4): 562.

Foil, Lane, Earl Andress, Rebecca L Freeland, Alma F Roy, Roxanne Rutledge, Patricia C Triche, e Kathy L O'Reilly. 1998. «Experimental infection of domestic cats with Bartonella henselae by inoculation of Ctenocephalides felis (Siphonaptera: Pulicidae) feces.» *Journal of medical entomology* 35 (5): 625–28.

Gerrikagoitia, Xeider, Horacio Gil, Coral García-Esteban, Pedro Anda, RA Juste, e Marta Barral. 2012. «Presence of Bartonella species in wild carnivores of northern Spain». *Applied and environmental microbiology* 78 (3): 885–88.

Greco, Grazia, Aya Attia Koraney Zarea, Giovanni Sgroi, Maria Tempesta, Nicola D'Alessio, Gianvito Lanave, Marcos Antônio Bezerra-Santos, et al. 2021. «Zoonotic Bartonella species in Eurasian wolves and other free-ranging wild mammals from Italy». *Zoonoses and Public Health* 68 (4): 316–26.

Gutiérrez, Ricardo, Boris Krasnov, Danny Morick, Yuval Gottlieb, Irina S Khokhlova, e Shimon Harrus. 2015. «Bartonella infection in rodents and their flea ectoparasites: an overview». *Vector-Borne and Zoonotic Diseases* 15 (1): 27–39.

Henn, Jennifer B, Bruno B Chomel, Henri-Jean Boulouis, Rickie W Kasten, William J Murray, Gila K Bar-Gal, Roni King, Jean-François Courreau, e Gad Baneth. 2009. «Bartonella rochalimae in raccoons, coyotes, and red foxes». *Emerging infectious diseases* 15 (12): 1984.

Kosoy, Michael, e Irina Goodrich. 2019. «Comparative ecology of Bartonella and Brucella infections in wild carnivores». *Frontiers in veterinary science* 5: 322.

Latini, Gianni, Marco Bagliani, e Tommaso Orusa. 2021. *Lessico e nuvole: le parole del cambiamento climatico*. Youcanprint.

Maggi, Ricardo G, Patricia E Mascarelli, Elizabeth L Pultorak, Barbara C Hegarty, Julie M Bradley, B Robert Mozayeni, e Edward B Breitschwerdt. 2011. «Bartonella spp. bacteremia in high-risk immunocompetent patients». *Diagnostic microbiology and infectious disease* 71 (4): 430–37.

Millán, Javier, Tatiana Proboste, Isabel G Fernández de Mera, Andrea D Chirife, José de la Fuente, e Laura Altet. 2016. «Molecular detection of vector-borne pathogens in wild and domestic carnivores and their ticks at the human–wildlife interface». *Ticks and tick-borne Diseases* 7 (2): 284–90.

Minnick, Michael F, e Burt E Anderson. 2015. «Bartonella». In *Molecular medical microbiology*, 1911–39. Elsevier.

Norman, AF, R Regnery, P Jameson, C Greene, e DC228273 Krause. 1995. «Differentiation of Bartonella-like isolates at the species level by PCR-restriction fragment length polymorphism in the citrate synthase gene». *Journal of clinical microbiology* 33 (7): 1797–1803.

Orusa, Tommaso, e Enrico Borgogno Mondino. 2021. «Exploring Short-Term Climate Change Effects on Rangelands and Broad-Leaved Forests by Free Satellite Data in Aosta Valley (Northwest Italy)». *Climate* 9 (3): 47.

Orusa, Tommaso, Duke Cammareri, e Enrico Borgogno Mondino. 2022a. «A Possible Land Cover EAGLE Approach to Overcome Remote Sensing Limitations in the Alps Based on Sentinel-1 and Sentinel-2: The Case of Aosta Valley (NW Italy)». *Remote Sensing* 15 (1): 178.

———. 2022b. «A Scalable Earth Observation Service to Map Land Cover in Geomorphological Complex Areas beyond the Dynamic World: An Application in Aosta Valley (NW Italy)». *Applied Sciences* 13 (1): 390.

Orusa, Tommaso, e E. Borgogno Mondino. 2019. «Landsat 8 thermal data to support urban management and planning in the climate change era: A case study in Torino area, NW Italy». In *Remote Sensing Technologies and Applications in UrbanEnvironments IV*, 11157:111570O. International Society for Optics and Photonics.

Orusa, Tommaso, Riccardo Orusa, Annalisa Viani, Emanuele Carella, e Enrico Borgogno Mondino. 2020. «Geomatics and EO data to support wildlife diseases assessment at landscape level: A pilot experience to map infectious keratoconjunctivitis in chamois and phenological trends in Aosta Valley (NW Italy)». *Remote Sensing* 12 (21): 3542.

Orusa, Tommaso, Annalisa Viani, e Enrico Borgogno-Mondino. 2023. «IRIDE the Euro-Italian Earth Observation Program: Overview, Current Progress, Global Expectations and Recommendations». *perspective* 2: 10.

———. 2024. «Earth Observation Data and Geospatial Deep Learning AI to Assign Contributions to European Municipalities Sen4MUN: An Empirical Application in Aosta Valley (NW Italy)». *Land* 13 (1): 80.

Orusa, Tommaso, Annalisa Viani, Duke Cammareri, e Enrico Borgogno Mondino. 2023. «A Google Earth Engine Algorithm to Map Phenological Metrics in Mountain Areas Worldwide with Landsat Collection and Sentinel-2». *Geomatics* 3 (1): 221–38.

Orusa, Tommaso, Annalisa Viani, Boineelo Moyo, Duke Cammareri, e Enrico Borgogno-Mondino. 2023. «Risk Assessment of Rising Temperatures Using Landsat 4–9 LST

Time Series and Meta® Population Dataset: An Application in Aosta Valley, NW Italy». *Remote Sensing* 15 (9): 2348.

Paiva Diniz, Pedro Paulo Vissotto de, Michael Wood, Ricardo G Maggi, Sushama Sontakke, Matt Stepnik, e Edward B Breitschwerdt. 2009. «Co-isolation of Bartonella henselae and Bartonella vinsonii subsp. berkhoffii from blood, joint and subcutaneous seroma fluids from two naturally infected dogs». *Veterinary microbiology* 138 (3–4): 368–72.

Samuele, De Petris, Sarvia Filippo, Tommaso Orusa, e Borgogno-Mondino Enrico. 2021. «Mapping SAR geometric distortions and their stability along time: a new tool in Google Earth Engine based on Sentinel-1 image time series». *International Journal of Remote Sensing* 42 (23): 9135–54.

Sarvia, Filippo, Samuele De Petris, Tommaso Orusa, e Enrico Borgogno-Mondino. 2021. «MAIA S2 Versus Sentinel 2: Spectral Issues and Their Effects in the Precision Farming Context». In *International Conference on Computational Science and Its Applications*, 63–77. Springer.

Sigma-Aldrich. 2014. *Technical Guide to PCR Technologies*.

Tartaglino, Andrea, e Tommaso Orusa. 2020. «Bilancio energetico/Energy Balance in Lessico e nuvole: le parole del cambiamento climatico II ed. Università degli studi Torino». In *Bilancio Energetico*, 61–63. Università degli studi di Torino.

Viani, Annalisa, Sara Divari, Stella Lovisolo, Stefania Zanet, Enrico Borgogno-Mondino, Riccardo Orusa, Enrico Bollo, e others. 2023. «Bartonella spp. distribution assessment in red foxes (Vulpes vulpes) coupling geospatially-based techniques». In *Atti SISVet*, 69–69. SISVet.

Viani, Annalisa, Tommaso Orusa, Enrico Borgogno-Mondino, e Riccardo Orusa. 2023. «Snow Metrics as Proxy to Assess Sarcoptic Mange in Wild Boar: Preliminary Results in Aosta Valley (Italy)». *Life* 13 (4): 987.

Viani, Annalisa, Tommaso Orusa, Maria Lucia Mandola, Serena Robetto, Manuela Belvedere, Giovanna Renna, Sonia Scala, Enrico Borgogno-Mondino, e Riccardo Orusa. 2023. «R07. 5 Tick's suitability habitat maps and tick-host relationships in wildlife. A One Health approach based on multitemporal remote sensed data, entropy and Meta® population dataset in Aosta Valley, NW Italy.» In *GeoVet 2023 International Conference*.

INTEGRATING GEOGRAPHICAL DATA WITH SURVEYS CONDUCTED WITH UAVS FOR PLANNING AREAS OF HIGH ENVIRONMENTAL VALUE

P. Picuno*, M. Minchilli, D. Statuto

School of Agricultural, Forestry, Food and Environmental Sciences (SAFE),
University of Basilicata, 85100, Potenza, Italy
pietro.picuno@unibas.it

KEY WORDS: Free geodata; UAV surveys; Photogrammetric analyses; Geo-referenced database; Natural habitats; Floristic-vegetational planning

ABSTRACT:

The setting up of a general framework for the environmental and landscape planning of a protected area requires a basic detailed survey of this area and its vegetation, accompanied by a constant monitoring of the latter, so that a specific maintenance plan can be implemented accordingly. With reference to an area of high environmental, landscape and archaeological value, such as the '*Pulo di Molfetta'* (Municipality of Molfetta – Southern Italy), some georeferenced floristic surveys have been carried out, with relative mapping and monitoring of vegetation growth. In this way, it has been possible to draw up some specific management measures for the vegetation, as well as to plan suitable interventions of ecological engineering, aimed at determining the most appropriate conditions for the recovery, use and sustainable management of this area, even for tourism purposes. These activities have been conducted through the construction of a basic model implemented in a Geographical Information System (GIS), structured on the basis of some Free and Open-Source geographic data, integrated with a geo-localized 3D survey of the geomorphology, architectural structures and the flora-vegetation habitat. The metric analyses have been conducted with commercial instruments, such as UAVs systems, GNSS and photogrammetric processing software. The obtained results have allowed the inclusion of the geo-localized 3D model in a GIS base for the knowledge of the flora-vegetation habitat, thanks to which it would be possible to provide support for the decision-making from local politicians and landscape planners.

1. INTRODUCTION

Planning technical interventions in areas of high landscape and environmental importance requires the convergence of multiple skills, which must be mutually integrated, in order to identify the most appropriate option for their management. Particularly when these areas, as it increasingly happens, find significant opportunities for tourist valorization (Statuto & Picuno, 2017), this planning activity is extremely important and requires an appropriate technical approach, which must be based on surveys - geomatic, geological, floristic, physiognomic-structural, *etc.* - of the whole area (Picuno P., 2022; Statuto et al., 2013).

The management of smart cities or particular zones, need to start from an accurate geometric survey, generating highly detailed 3D models (Adami et al., 2023). The topic of the photogrammetric survey of urban or natural areas is of great interest, both for the selected most suitable technical solutions and for the purposes and uses of the generated point cloud. The size of the surveyed area and the goals of the survey, drive the choice of the most appropriate technical tools for the survey, like the type of drone, the camera and its resolution, the quality and mode of image acquisition, the photogrammetric processing parameters, and the georeferencing approach. Although several advanced technologies have been used by surveyors and engineers for generating the structural 3D models, Unmanned Aerial Vehicle (UAV)-based photogrammetry and Terrestrial Laser Scanning (TLS) are among the most common methods used in this regard (Mohammadi et al., 2021). The resulting Unmanned Aerial System (UAS) photogrammetry point cloud can have a higher or lower density of points, according to the flight altitude and the resolution of the camera used. The recent developments in automated image processing for 3D reconstruction purposes have led to the diffusion of low-cost and open-source solutions, which can be used by everyone to produce 3D models. The level of automation is so high that many solutions are black-boxes, with poor repeatability and low reliability (Remondino et al., 2012).

In the present paper, the realization of a geolocalized3D model is described. This tool has been realized, in order to address and initiate its insertion into a Geographical Information System (GIS) base, constructed for checking the formal consistency of the cartographic and photogrammetric layers and for knowledge, and preliminary decision aid, of the floristic-vegetational habitat in an area of particular environmental, landscape and archaeological importance, the "*Pulo di Molfetta*". In this area, located in the Municipality of Molfetta (Apulia Region – Southern Italy - 41°12′N 16°36′E), the GIS that has been implemented, has been aimed to constantly enable, plan and schedule the best decisions for the management of this particular site. The construction of a georeferenced, explorable, editable and queryable database was carried out in a GIS O.S. (Open Source, QGIS) software, to facilitate rapid data interchange, into a widely used development environment.

2. MAIN BODY

2.1 Instrument selection: survey methodology

The photogrammetric analysis was carried out with low-altitude aerial photography taken by UAV with Max Take Off Weight (MTOW) < 5 Kg. The EASA (European Aviation Safety Agency) requires to fly over an area free of people overhead and, in our case, it was necessary to solve the problems regarding both the visibility, covered by tall vegetation, and the side walls of the cliffs, rich in karst phenomena of both archaeological and geological interest. The digital photo sensor used has a mechanical shutter to eliminate, during the flight path, deformation caused by electronic shutters ("rolling shutter", present on most of the cheaper sensors). The georeferenced network, preliminary to the execution of flights, was materialized on the ground, to distribute vertices on the entire area affected by the 3D model. Both photographic points (such as edges of artifacts, horizontal markings on asphalt, *etc.*) and high-contrast

* Corresponding author

targets, of appropriate size for both flight altitude and pixel size on the ground (GSD - Ground Sampling Distance), were used.

2.2 Case study description

The "*Pulo di Molfetta*" is a doline extending over an area of about 3 Ha and about 35 m deep, characterized by peculiar archaeological and naturalistic features (Figure 1). This type of surface karst formations originated as a result of the collapse of the vault of underground cavities, excavated by the erosive and corrosive action of water infiltrating the limestone substrata.

Figure 1. Localization of the City of Molfetta (Apulia Region – Italy) and the "Pulo di Molfetta" area (encapsulated photo).

In the flat bottom of this doline there are vestiges of an old saltpeter factory, used in the 19th century by the Bourbons for the production of gunpowder.
This area has an extraordinary natural, archaeological and anthropological value. From a naturalistic point of view, it constitutes a treasure trove of biological diversity, due to the millennial interaction between man and a unique natural environment in terms of both microclimate and vegetation.
A geo-localized 3D survey of the geomorphology, architectural structures and floro-vegetational habitat has been performed. The surveying, georeferencing and formation of a 3D model, has referred to a planimetric extension of approximately 30,000 m^2 with an altimetric difference in height of 30-34 m.
Moreover, also mapping and monitoring of vegetation and georeferenced floristic surveys have been performed, with the aim to implement an ordinary and extraordinary maintenance plan, enabling the calculation of forest biomass as well.
The implemented methodology has also enabled a context analysis and planning of some integrated interventions, based on the investigation of the naturalistic/environmental conditions (biodiversity, ecosystems, *etc.*) of the site, also supported by the implementation of a GIS. These interventions would also include the forecast of appropriate naturalistic/ecological engineering works (Cillis et al., 2021/a), like the construction of retaining/consolidation structures (*e.g.*: dry-stone retaining walls; gabion walls; cliffs; *etc.*), and/or rockfall protection works, as well as works with a fencing/perimeter function, *e.g.*: dry-stone walls; wooden fences; *etc.* Indeed, this kind of works, may contribute to a mitigation of wetland loss, thanks to the designing and executing specific targeted technical interventions, *i.e.*, building or restoring existing constructions, able to create local micro-environment favourable for some amphibian and reptile species, restoring existing wetlands or constructing new artificial ones, *etc.* Several studies have anyway demonstrated the difficulty of replicating natural habitats when attempting to create the suitable environment for these species (Picuno P., 2017).

2.3 Data acquisition and implementation of a GIS

For the image acquisition phases related to the photogrammetric survey, two surveys were carried out, during which the areas covered by the aerial coverage were chosen.
The geo-localized 3D model has been included in a GIS for knowledge and decision support of the flora-vegetation habitat. Indeed, a GIS-based approach may enable – mostly when including both historical cartographies and remotely-sensed data, freely available online (Cillis et al., 2021/b) - the evaluation of spatial and statistical variations of the forest landscape, assessing how much, where and how the forest landscape has changed, in order to provide a methodology to support more detailed and targeted studies. Given the characteristics of the geodata and the fact that the tools are fully open-source, the techniques can be replicated and even partly improved in relation to specific needs. This GIS, would therefore also include future trans-disciplinary contributions from experts in other disciplines, *e.g.*: geologists; hydrogeologists; speleologists; geo-technicians; archaeologists; *etc.*
The survey, georeferencing and 3D model formation operations have been conducted by means of:
1) photogrammetric aerial images at low and ultra-low relative flight height, according to the orography, to obtain a 3D digital modelling with a ground resolution of at least 2 cm/pixel;
2) image coverages with nadiral and sub-horizontal shooting axes orientation for optimize the analysis of both the geomorphology and the existing vegetation;
3) creation of a framing and support network, materialized with high-contrast photographic targets, measured with RTK (Real Time Kinematics) methodologies of GNSS (Global Navigation Satellite System) satellite positioning and accuracy $\leq$ 3 cm, georeferenced in the RDN2008 Reference Coordinate System - as per the Italian regulations;
4) construction of a 3D digital model, obtained with digital photogrammetric restitution, formed by point clouds and then triangular mesh and photographic texture;
5) formation of a very-high resolution ortho-photomosaic, with GSD (Ground Sampling Distance) $\leq$ 15 mm, and of an adequate number of radial sections, with two views, each one orthogonal to the section plane;
6) georeferenced identification of the individual floristic-vegetational elements and help for the construction of a database containing the agreed attributes defined and aimed at planning the vegetation layers present;
7) provision of digital bases, of the indicated products, in the most popular formats and of hardcopy prints, having a layout as for the Municipality needs.
Following the selection and materialization of the points, a topographic campaign of absolute coordinate acquisition was carried out with a GNSS employed in RTK technology.
The differential correction of coordinates (included in RTK technology) was carried out inside the Network of Permanent GNSS stations managed by the Apulia Region. The acquisition of the points, reprojected in the Absolute Coordinate System RDN2008 UTM - Fuse 33 N, was possible for all the targets on the boundary of the imaged area, but not for others identified on the bottom of the sinkhole. In fact, in such areas there is unfortunately both poor reception of the signal from the Satellites (GPS and GLONASS series), as well as the correction signals transmitted through telephone operators (shadow of the cell phone signal). However, even with this limitation, the distribution of points was optimal and allowed for all acquisitions to contain the plano-altimetric tolerance within $\pm$ 2 cm, thus largely within the design limits and for the purposes of the survey.

2.4 Photogrammetric process

The photogrammetric restitution stages were performed in the Metashape environment (Agisoft ver.2.0.1 and later) with modern SfM techniques, in which the simultaneous orientation of the frames, along with the associated self-calibration, are performed *en-bloc* with Bundle Block Aero-triangulation (aero-triangulation by projective stars) methodologies (Pepe et al., 2019).
The results were very good and exceeded the design target data at the end of compensation (Figure 2). The final plano-altimetric deviations of the GSDs used were less than ±7 mm as shown in the following table.

Markers	Easting (m)	Northing (m)	Altitude (m)	Accuracy (m)	Error (m)	Projection	Error (pix)
TGT_010	632172.850000	4561473.874000	41.589000	0.010000	0.001844	55	0.046
TGT_009	632144.207000	4561468.478000	41.754000	0.010000	0.002732	43	0.029
TGT_008	632110.807000	4561471.548000	41.771000	0.010000	0.006195	50	0.035
TGT_007	632079.225000	4561509.871000	38.201000	0.010000	0.010118	43	0.094
TGT_006	632230.618000	4561629.442000	35.236000	0.010000	0.006226	48	0.070
TGT_005	632230.770000	4561593.900000	35.645000	0.010000	0.008857	46	0.055
FOT_008	632075.877000	4561532.368000	37.238000	0.010000	0.025402	41	0.747
FOT_007	632073.734000	4561537.127000	37.305000	0.010000	0.026002	67	0.571
FOT_004	632204.613000	4561649.391000	35.860000	0.010000	0.007669	43	0.091
FOT_003	632154.438000	4561650.078000	36.357000	0.010000	0.002280	41	0.138
FOT_002	632085.957000	4561622.779000	38.966000	0.010000	0.006649	44	0.048
FOT_001	632068.015000	4561595.145000	37.763000	0.010000	0.009806	20	0.053
Total Error							
Control points					0.006879		0.072

Figure 2. Final plano-altimetric deviations of the GSDs used were less than ±7 mm.

Subsequent to the refinement of the guidelines, the same development environment was used to produce:
1) a dense point cloud (about 50,000,000 points) that represents a product of wide interoperability for subsequent processing also in the O.S. (Open Source) environment (Figure 3);

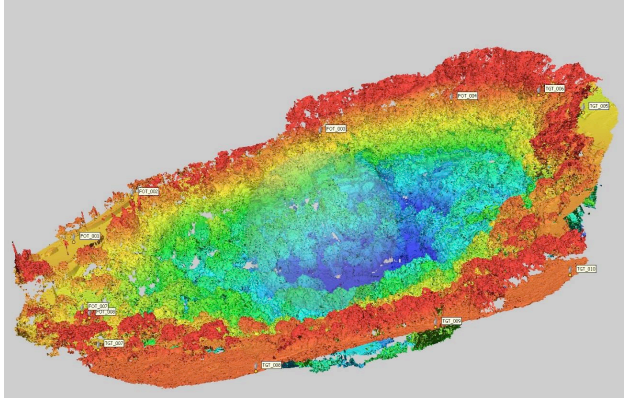

Figure 3. Representation of a dense point cloud

2) a triangular mesh formed by about 4,200,000 triangles for materializing the elementary surfaces constituting the 3D model;
3) a photo texture obtained by projecting image pixels onto the faces of triangles produced in the mesh (Figure 4);
4) an ortho-photo-plane obtained by digital projection, on a reference plane of elementary portions of the orthorectified images, with a resolution equal to 1x1 cm GSD, georeferenced in consistent way with all previous orientations, in the Reference System RDN2008. In this way, the product – *i.e.*, a georeferenced image at very high resolution - can be easily used as a base map in a GIS, where there are numerous other map layers in the respective Reference System (Figure 5 and 6).
5) the realization of 4 sections, in the vertical plane, obtained on radial orientations most significant for reading the sinkhole.

Figure 4. Image of the obtained photo texture.

Figure 5. Orthophoto (GSD = 1 cm) produced as an overlay to Apulia orthophoto (GSD (50x50 cm) year 2006.

Figure 6. Overlay of Orthophoto (GSD = 1 cm) produced on the Apulia orthophoto (GSD (50x50 cm) year 2006 - detail.

2.5 Results and Discussions

In order to address and initiate the insertion of the geolocated 3D model, an initial GIS base was constructed for checking the formal consistency of the cartographic and photogrammetric layers and for knowledge, and preliminary decision aid, of the floristic-vegetational habitat. The construction of a georeferenced, explorable, editable database, that can be queried by its user, was carried out in a O.S. (Open Source, QGIS) GIS, to facilitate rapid data interchange, within a widely used development environment.
The first frame acquisition campaign consisted of a (high) cross-swipe flight and nadiral axes (for photographic shadow

optimization) consisting of about 1050 images. In addition, a series of flights were performed at lower absolute altitudes, aimed at very-high resolution coverage of the lower area and some stripes with pseudo-horizontal camera axes, for multiple coverage of cliff faces. The total number of frames was thus 1050 (nadiral) and about 400 with variously tilted axes, for a grand total of 1447 calibrated digital images.

Based on the geolocated 3D model, some Immersive Virtual Tours (IVR) of the geomorphology, the structures architecture and floristic-vegetational habitat (Figure 7), were performed as well:

1. No. 12 terrestrial shots: (19/04/2023) with 360° camera RICOH THETA Z1 for spherical images 6720x3360 pix used on dedicated stand, positioning of station points with GNSS Leica G14 connected in RTK to the Permanent Stations Network of the Apulia Region;
2. No. 180 aerial shots: (17/5/2023) flights with non-photogrammetric purposes but aimed at producing 360° "spherical" photos taken from no.7 points aerial shots taken by the same technique with a scheduled specific.

In this way, the aircraft maintains, at the chosen altitude, its coordinates acquired by the GPS/GLONASS System, by taking n.25 shots distributed over a solid angle of 360°. Figure 7 is the initial page of a Digital Virtual Route (DVR) that allows, with on-line and/or Wlan network interrogation, an access to the visibility of about 20 spherical images, both terrestrial and aerial, useful in the observation of vegetation details, not visible from the ortho-photo-projection.

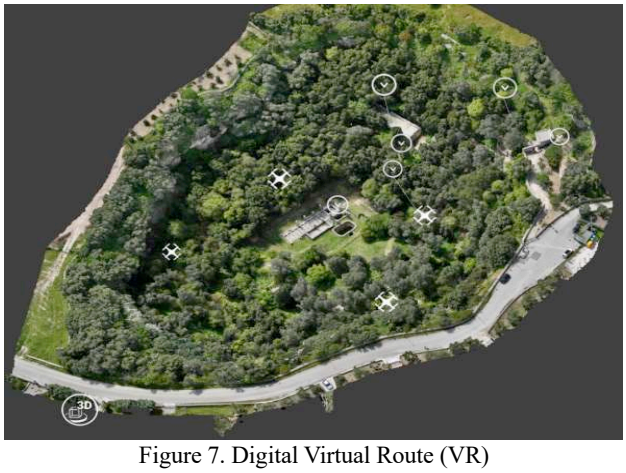

Figure 7. Digital Virtual Route (VR)

CONCLUSIONS

The photogrammetric survey of the area of high environmental, landscape and archaeological value "*Pulo di Molfetta*" has enabled the construction of a basic model implemented in a Geographical Information System, which has revealed very useful to study this particular area. The photos taken on-site were exploited through a photogrammetric process, to generate an orthophoto of the area with a pixel size of 1 cm.

The presented approach is suitable for the generation of high resolution orthophoto and highly detailed point cloud, to be used for further environmental studies, which will enable policy makers to implement the right and proper planning and management strategies for this area. It would contribute to plan also appropriate actions mitigating anthropic interventions, so incorporating into the rural landscape suitable elements able to protect natural components, enabling the development of a more sustainable tourism as well.

FUNDING INFORMATION

This work has been financed by the Municipality of Molfetta, in the framework of the agreement it has signed with the SAFE School of the University of Basilicata.

REFERENCES

Adami, A., Treccani, D., Fregonese, L. 2023. Lesson learnt from the high resolution UAS Photogrammetric survey of a historic urban area: UNESCO site of Sabbioneta. In: *The International Archives of the Photogrammetry, Remote Sensing and Spatial Information Sciences, Volume XLVIII-M-2-2023,* 29th CIPA Symposium "Documenting, Understanding, Preserving Cultural Heritage: Humanities and Digital Technologies for Shaping the Future", 25–30 June 2023, Florence, Italy

Cillis G., Statuto D., Picuno P. (2021)/a. Integrating remote-sensed and historical geodata to assess interactions between rural buildings and agroforestry land. Journal of Environmental Engineering and Landscape Management, 29 (3), 229-243.

Cillis G., Statuto D., Picuno P. (2021)/b. Historical GIS as a Tool for Monitoring, Preserving and Planning Forest Landscape: A Case Study in a Mediterranean Region. Land, 10, 851, 1-20.

Mohammadi, M., Rashidi, M., Mousavi, V., Karami, A., Yu, Y., Samali, B. 2021.Case study on accuracy comparison of digital twins developed for a heritage bridge via UAV photogrammetry and terrestrial laser scanning. In: *Proceedings of the 10th International Conference on Structural Health Monitoring of Intelligent Infrastructure, SHMII 10 Porto, Portugal, 30 June - 2 July 2021*.

Pepe, M., Costantino, D., Crocetto, N., Restuccia Garofalo, A. 2019. 3D modeling of roman bridge by the integration of terrestrial and UAV photogrammetric survey for structural analysis purpose. In: *International Archives of the Photogrammetry, Remote Sensing and Spatial Information Sciences - ISPRS Archives*, 2019, vol. 42, pp.249-255.

Picuno P. (2017). Biosystems engineering techniques for habitat restoration in protected areas. IN: Proceedings of the 45th Symposium on: "*Actual Tasks on Agricultural Engineering* – ATAE 2017, Opatija (Croatia), 21-24 February 2017. UDC 551.58:631.23, pp. 613-622.

Picuno P. (2022). Farm Buildings as Drivers of the Rural Environment. Frontiers in Built Environment, Vol. 8, Article 693876.

Remondino, F., Del Pizzo, S., Kersten, T. P., Troisi, S. 2012. Low-Cost and Open-Source Solutions for Automated Image Orientation – A Critical Overview. Conference Paper in *Lecture Notes in Computer Science, October 2012*. doi: 10.1007/978-3-642-34234-9_5.

Statuto D., Tortora A., Picuno P. (2013). A GIS approach for the quantification of forest and agricultural biomass in the Basilicata region. Journal of Agricultural Engineering, XLIV(sI):e125: 627-631.

Statuto D., Picuno P. (2017). Valorisation of vernacular farm buildings for the sustainable development of rural tourism in mountain areas of the Adriatic-Ionian macro-region. Journal of Agricultural Engineering, XLVIII (S1):643, pp. 21-26.

A QUANTITATIVE ANALYSIS OF THE DROUGHT EFFECTS ON THE PO RIVER: THE EVOLUTION OF SURFACE WATERS IN 2020-2021-2022

N. Tolio[1], B. Gori[2], C. Masetto[3]*, U. Trivelloni[4]

[1] Engineering Ingegneria Informatica S.p.A., Padova, Italy - niccolo.tolio@eng.it
[2] Directorate for Spatial Planning, Veneto Region, Venice, Italy - benedetta.gori@studenti.unipd.it
[3] Directorate for Spatial Planning, Veneto Region, Venice, Italy - carlo.masetto@regione.veneto.it
[4] Directorate for Spatial Planning, Veneto Region, Venice, Italy - umberto.trivelloni@regione.veneto.it

KEY WORDS: Land, climate-change, drought, waterbodies, remote sensing, machine learning

ABSTRACT:

In recent years, the global effects of climate change are also affecting Europe, leading to a greater frequency of extreme events, in terms of heat waves, droughts and high-intensity precipitations. In 2022, the Veneto Region -as well as most of Italy- was affected by a severe and prolonged drought, caused by low cumulative rainfall and extraordinarily high temperatures. As a consequence, a significant decrease in the flow of the main hydrographic networks was recorded during the summer period. These effects were particularly evident for the Italian main river, the Po River, where numerous sandy islands emerged due to the low flow. This work aimed to define an operational methodology to perform a quantitative analysis of the areas occupied by water surfaces and sandy islands in an area of the Po River basin, using satellite data through a supervised classification algorithm (Random Forest). The supervised classification was therefore performed on Sentinel-2 images acquired for three consecutive years 2020-2021-2022 in the month of July, in order to monitor the evolution of the river surface in dry conditions. The results of the supervised classification showed a high accuracy (90%), suggesting this methodology can offer trustful results in drought monitoring, with a relatively simple procedure.

1. INTRODUCTION

In 2022, Northern Italy and Veneto Region had to face the consequences of dry climatic conditions, which led to heavy impacts on agriculture and water reservoirs management for electricity production. The estimated economic damage on agricultural production at a national scale amounted to approximately 6 billion €, equal to 10% of the value of national agricultural food production (Coldiretti, 2022). Drought resulted from a combination of positive thermal anomalies, lack of rainfall and a decrease in snow precipitation affected the water resources availability.

According to "Climate in Italy in 2022" report (SNPA, 2023), the average temperature in Italy recorded an anomaly of +1.23°C compared to average 1991-2020 period, resulting in the warmest year since 1961.

Autumn, but even more so summer, were the hottest seasons: during the latter the difference compared to the thirty-year average was almost everywhere in Veneto Region above 2°C (ARPAV, 2023).

On the other hand, during the year 2022 an average of 774 mm of precipitation fell on the Veneto Region; the average annual precipitation, referring to the period 1993-2021, is 1,128 mm: this indicates that precipitation was 31% lower than the average (ARPAV, 2023). Comparing the trend of monthly rainfall in 2022 with that of the period 1993-2021, the precipitations were well below average during most of the summer period, leading to dry conditions: June (-44%), July (- 40%).

An anomaly on the snow precipitation during the winter affected natural water reservoirs for Italian catchments and hydrological conditions. In fact, relevant deficits of snow-covered area in the Alps district were recorded (Koehler at al., 2022): up to 83% in the Western Alps (catchment of Sesia, March 2022) and up to 61% in the Eastern Alps (catchment of Brenta, March 2022).

This period of hydrological drought caused negative effects on the environment. Some rivers, canals and waterbodies showed significant reduction in water-flows or hydrometric height. This effect was particularly visible for the largest Italian river, the Po, heavily affected by drought in its basin, especially during the summer months. The Permanent Observatory on water uses in the Po River hydrographic district highlighted a scenario of severe water deficit (Ranzi et al., 2022). In July, the various flow measurement stations along the river (from Piacenza to Pontelagoscuro) recorded significant reductions in flow and hydrometric level, below the monthly minimum (ADBPO, 2022). This followed the dry conditions occurred during the month of March, where a discharge deficit of 66% (264 m^3/s instead of the expected 819 m^3/s) has been reported at the station in Piacenza, and even higher deficits of around 75% have been observed in the Po's Alpine tributaries Dora Baltea, Adda, and Ticino (Koehler et al., 2022).

The low flows of the river have also determined the rise of the salt wedge intrusion for several kilometres (36) from the river mouth (CNR Drought Observatory, 2022).

All these combined factors resulted in an evident change in the river morphology; sand islands were observed emerging from the Po riverbed and increasing their area, while the water surface decreased. The aim of this study is to quantify, through remote sensing techniques and the use of machine learning algorithms, the extent of these sand islands and analyse their evolution through the years 2020-2022, in order to assess with a simplified procedure, the impact of drought on the morphology and ecosystem of the Po river.

* Corresponding author

2. STUDY AREA

The study site is a 118 km^2 area located between the municipalities of Occhiobello (RO), Canaro (RO) and Ferrara (FE), where the Po River flows on the borders between Veneto and Emilia Romagna Regions (Figure 1). It is an agricultural area, with some urban settlements along the river. Being the most important river in Italy, Po is strategic to satisfy the water needs of the agricultural sector. Furthermore, it is also valuable from an environmental point of view, hosting habitats for different species of plants and animals.

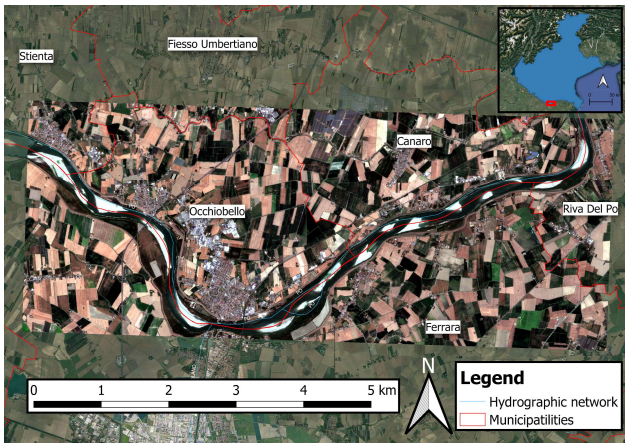

Figure 1. Study area area in Veneto and Emilia Romagna regions. Reference frame: Sentinel L2A in true colour visualization. Acquisition date: 22-07-2022

In July 2022 - the month selected for the analysis - this area was affected by a severe drought with high temperatures. The mean monthly Land Surface Temperature (LST) retrieved by Terra MODIS satellite data (Wan et al., 2021) is reported in figure 2.

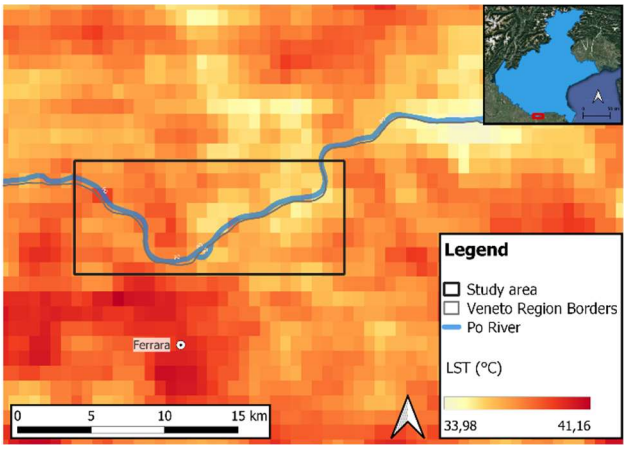

Figure 2. Processed values of the mean monthly LST for the study area (July 2022).

Heat stress on the local agricultural ecosystems (Gori, 2023) was assessed by combining the "severely dry" conditions - of the SPI-3 (Standardized Precipitation Index) drought index which measures precipitation anomalies compared to a long-term series of rainfall data (McKee Doesken, Kleist,1993; WMO, 2012) - and the mean monthly LST. The heat stress on agricultural ecosystems is shown in figure 3; all the study area suffered from LST > 35°C and severe drought condition.

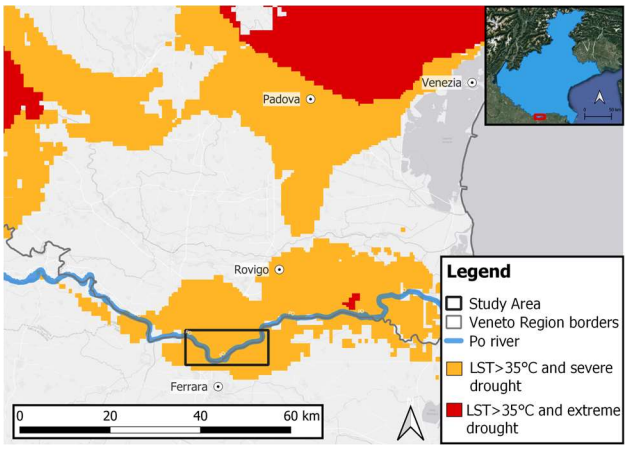

Figure 3. Heat stress on agricultural ecosystems in the study area.

3. MATERIALS AND METHODS

Materials

For the purpose of this work, Sentinel-2 multispectral images acquired in July 2020, 2021 and 2022 were analysed. Data were downloaded from the cloud service Sentinel-hub EO Browser (https://apps.sentinel-hub.com/eo-browser/, Sinergise Ltd.). Images have the same spatial resolution (10 m x 10 m), are co-registered (i.e., pixels' arrays coincide, therefore they perfectly overlap) and clipped to identify the same amount of surface.
To estimate the LST in the study area, data from the Land Surface product Terra MODIS Temperature/Emissivity 8-Day (MOD11A2) Version 6.1 were used, which offers LST data averaged over 8 days (average of averages), with a spatial resolution of 1km (Gori, 2023). The SPI index was calculated based on the monthly precipitation data provided by ARPAV[1] meteorological stations for the years 1994-2022.

Methods

Given the aim to distinguish the water and sand classes, the analysis focused on Sentinel-2 bands: B02 (blue), B03 (green) and B04 (red), corresponding to the wavelengths of the visible, and B08 (NIR - Near Infra-Red). The band B08 was included in the analysis since the different reflectance values for soil/sand class and water; in fact, waterbodies have very poor reflection in this wavelength interval.
This predictive model applied to remote sensing classifies image pixels based on different user-specified classes. To perform the classification, the model is provided of selected groups of pixels which have specific values, named 'ground truth' or ROI (Region of Interest). This process has been performed selecting regions of interest both for water and sand classes and observing the clear, regular pattern in the original image. The model classifies the images by randomly selecting some of these training polygons, while the rest are used to evaluate the accuracy of the result. . All the tasks and operations described in this section were performed using the software QGIS, version 3.22 – Bialowieza. Instead, only the Semi-Automatic Classification Plugin (SCP) was performed using the version 7.10.8.

[1] *Agenzia Regionale per la Prevenzione e Protezione Ambientale del Veneto*

The classes identified for this study area the following, each one representing a different land cover type:

4. Class 1: Sand;
5. Class 2: Water;
6. Class 3: Bare Soil;
7. Class 4: Vegetation;
8. Class 5: Urban.

Such a number of classes aimed to distinguish sand and water as effectively as possible (Classes 1 and 2, respectively). Being them the target of the analysis, they are highlighted with a specific colour in Figures 4, 5 and 6, while the other classes are in grey scale.
Accuracy of the classification was assessed considering the error matrix. The evaluation of accuracy was also made using Semi-Automatic Classification Plugin (SCP). The error matrix is the result of a comparison between pixels from ROIs selected as reference (that can be considered "ground truth") and the result of supervised classification (Congedo, 2014).

4. RESULTS & DISCUSSION

Images' observation provides a rather clear idea of the gravity of the situation for year 2022 (Figure 3, 4, 5), confirming the consequences of the severity of the drought. The number of sand islands has clearly increased compared to the previous two years, and the greater extension of those already present is evident. These preliminary conclusions are confirmed by data analysis, whose results are summarized in the following tables.

	2020	
Class	**Area (m^2)**	**Percentage**
1 - Sand	532.300	0,45%
2 - Water	8.127.100	6,88%
3 - Bare Soil	15.149.500	12,83%
4 - Vegetation	50.260.700	42,57%
5 - Urban	43.984.600	37,26%

Table 1. Surface (in m^2 and %) of each class of the Supervised Classification performed on Sentinel-2 images of July 2020.

	2021	
Class	**Area (m^2)**	**Percentage**
1 - Sand	908.600	0,77%
2 - Water	6.919.300	5,86%
3 - Bare Soil	25.592.700	21,68%
4 - Vegetation	45.307.100	38,38%
5 - Urban	39.326.500	33,31%

Table 2. Surface (in m^2 and %) of each class of the Supervised Classification performed on Sentinel-2 images of July 2021.

	2022	
Class	**Area (m^2)**	**Percentage**
1 - Sand	2.027.800	1,72%
2 - Water	5.361.500	4,54%
3 - Bare Soil	31.613.000	26,78%
4 - Vegetation	36.133.100	30,61%
5 - Urban	42.918.800	36,36%

Table 3. Surface (in m^2 and %) of each class of the Supervised Classification performed on Sentinel-2 images of July 2022.

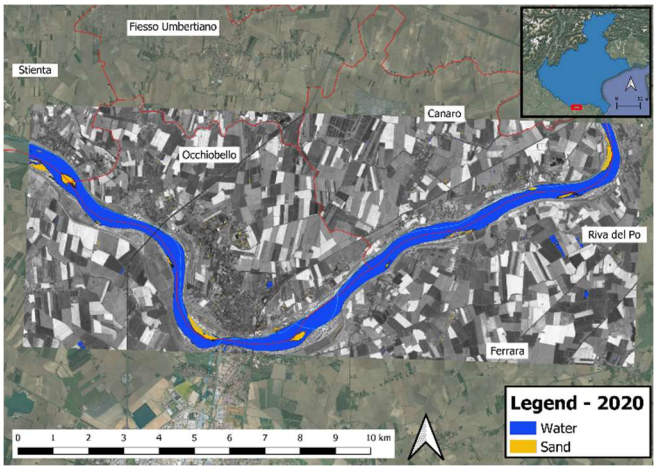

Figure 4. Supervised classification (Random Forest model) of the study area. Reference frame: Sentinel L2A in true colour visualization. Acquisition date: 22-07-2020.

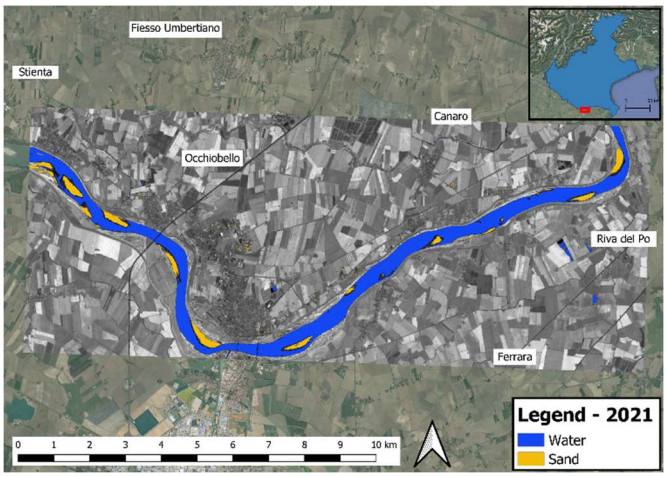

Figure 5. Supervised classification (Random Forest model) of the study area. Reference frame: Sentinel L2A in true colour visualization. Acquisition date: 12-07-2021.

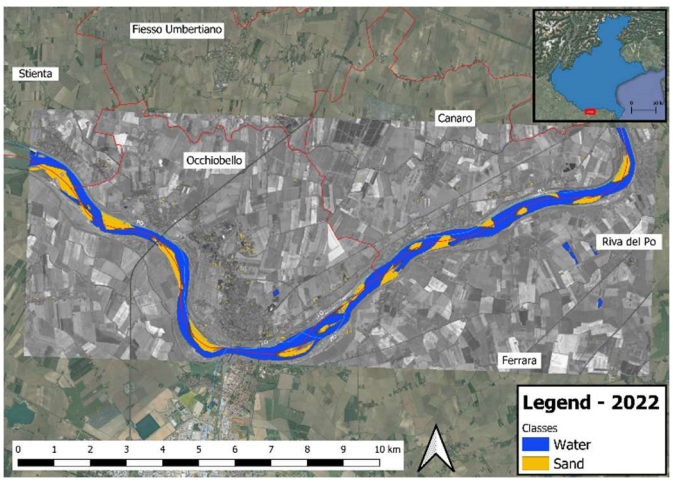

Figure 6. Supervised classification (Random Forest model) of the study area. Reference frame: Sentinel L2A in true colour visualization. Acquisition date: 22-07-2022.

Class 1 (Sand) constantly increased in the years being analysed, while Class 2 (Water) decreased both in 2021 and in 2022. Similar considerations can be applied to Classes 3 and 4: Bare Soil increased in 2020-2022, while Vegetation decreased. Class 5 (Urban) is lower in 2021 and 2022 than in 2020, due to the different training polygons used for each image. The urban

territory, in fact, has extremely various pixel values. The use of different polygons for every image provided dissimilar data to the classifiers, which therefore could recognize some portions of land as Class 5 in an image, while belonging to Classes 3 or 4 in the others, or vice versa. However, this does not invalidate the analysis focused on Classes 1 and 2, which are both correctly distinguished.

The resulting classifications show high accuracy, equal to approx. 98% for 2020, 96% for 2021 and 98% for 2022.

The percentage of the study area covered by sand islands increased from 0.45% to 0.77% between 2020 and 2021, reaching 1.72% in 2022. Apparently small variations in terms of % values actually corresponded to alarming data if considered in terms of surface (m^2): sand surface increased from 532.300 m^2 to 908.600 m^2 between 2020 and 2021 (approx. + 70%); the further increase to 2.027.800 m^2 in 2022 was equal to + 123% of the area if compared to the previous year, and + 280% approx. if compared to 2020 (Plot 1).

The same analysis was done for the water surface of the Po River. Other water bodies – Laghi Al Chiaro di Luna (RO) and Laghi Dorati (FE) - were also present in the study area's images, therefore their surfaces (around 20.000 m^2) were subtracted from the overall values shown in the tables.

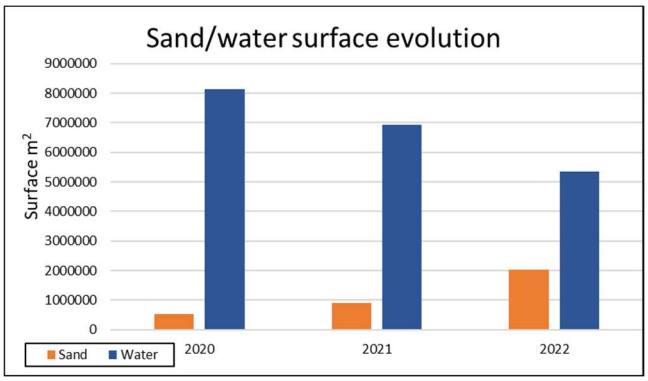

Plot 1. Sand and Water development in the last three years.

According to the results from the classification, Po River covered an area of 8.020.600 m^2 in 2020 (6.80% of the study area), which dropped to 6.813.000 m^2 in 2021 (5.78% of the study area), meaning its water surface decreased by approximately -17%. This value dropped further to 5.262.200 m^2 in 2022 (4.46% of the study area), meaning the river surface area decreased by -23% (2021) and -35% (2020) (Plot 1).

5. CONCLUSIONS

The results of the supervised classification and its high accuracy remarked the importance of remote sensing and classification tools application in measuring, monitoring and understanding the effects of extra-ordinary natural events, such as the severe drought of 2022, which affected the Po River basin.

It was here shown and quantified the extent of the constant decrease of its water surface due to the low water levels in 2020-2021-2022, and the parallel growth of sand island surfaces. The analysis of the areas classified as Bare Soil and Vegetation showed how green areas steadily shrank as well, leaving space to bare soil - another very likely consequence of drought conditions. This study allowed us to better understand the severity of the situation in 2022 and some of the heavy consequences that drought had on the environment. The high accuracy of the performed analysis proves relevant and reliable for monitoring the negative effects of drought, with a relatively simple quantitative procedure, based just on remote-sensing data.

It is important to underline that this analysis, however, cannot be used for a quantitative assessment of the impact of drought on water resources in terms of volumes and flow rates, if it is not integrated with data relating to hydrometric heights, flow rates and with an adequate hydraulic system model, which however was not the aim of this work.

Furthermore, the study only covered a three-year period and therefore no trend could be clearly identified, as the data was not statistically significant. It would be desirable to replicate the analysis with longer time series on a multi-year scale, in order to verify any trends.

Therefore, a possible development of such work is to combine multi-year scale data of the areal extent of Sand, Water, Bare Soil and Vegetation classes. This could in fact provide valuable indications on the desirable adaptation of the agricultural cultures as an answer to climate change.

6. REFERENCES

A.D.B.PO, 2022, "Monthly report of the Permanent observatory on water uses in the Po river hydrographic district, 2022". Available online: https://www.adbpo.it/wp-content/uploads/2022/07/12_Bollettino_22luglio22_Osservatorio.pdf (accessed on 24 May 2023).

A.R.P.A.V., 2023, "Climate regional data monitoring", 2023, https://www.arpa.veneto.it/arpavinforma/indicatori-ambientali/indicatori_ambientali/clima-e-rischi-naturali/clima/temperatura/2022 (accessed on 10 June 2023).

Belgiu M., Drăguţ L., 2016. Random forest in remote sensing: A review of applications and future directions. *ISPRS Journal of Photogrammetry and Remote Sensing,* 114, pp. 24-31, https://doi.org/10.1016/j.isprsjprs.2016.01.011.

Breiman, L., 2001. Random Forests. *Machine Learning,* 45, 5–32, https://doi.org/10.1023/A:1010933404324.

Coldiretti, 2022, "Clima: 6mld. di danni dalla peggiore siccità da 500 anni", available online: https://www.coldiretti.it/meteo_clima/clima-6-mld-di-danni-dalla-peggiore-siccita-da-500-anni (accessed on 24 October 2022).

CNR IBE Climate Services, 2022 "Osservatorio Siccità, Bollettino Luglio 2022", available online: https://drought.climateservices.it/bollettino-italia/bollettino-luglio-2022/ (accessed on 10 June 2023).

Congedo L., 2014, "Accuracy Assessment Using Random Points and the Semi-Automatic Classification Plugin for QGIS", available online: https://fromgistors.blogspot.com/2014/09/accuracy-assessment-using-random-points.html_ (accessed on 25 May 2023)

Gori, B., 2023, "Identificazione dei sistemi agricoli della Regione del Veneto maggiormente colpiti dalla siccità nel 2022", final project for the "Advanced Master in GIScience e Sistemi a Pilotaggio Remoto per la gestione integrata del territorio e delle risorse naturali", University of Padua, Department of Civil, Environmental and Architectural Engineering.

Koehler J., Dietz A.J, Zellner P., Baumhoer C.A., Dirscherl M., Cattani L., Vlahovic Z., Alasawedah M. H., Mayer K., Haslinger K., Bertoldi G., Jacob A., Kuenzer C., 2022, "Drought in Northern Italy: Long Earth Observation Time Series Reveal Snow Line Elevation to Be Several Hundred Meters Above Long-Term Average in 2022", *Remote Sensing*, 14, no. 23: 6091. https://doi.org/10.3390/rs14236091.

Ranzi, R.; Rigon, R.; Toth, E., 2022, "Alcune considerazioni della società idrologica italiana sulla grave siccità dell'estate

2022", available online: http://www.sii-ihs.it/files/allegatiFile/Riflessioni%20della%20SII%20sulla%20Siccita%CC%80%20del%202022_28sett_Finale.pdf (accessed on 15 May 2023).

Rodriguez-Galiano, V.F.; Ghimire, B.; Rogan, J.; Chica-Olmo, M.; Rigol-Sanchez, J.P., 2012, "An assessment of the effectiveness of a random forest classifier for land-cover classification", ISPRS J. Photogramm. Remote Sens. 2012, 67, 93–104.

Staffellini E., Tarolli P., 2023, "Climate change induced aridity is affecting agriculture in Northeast Italy", *Agricultural Systems*, 208, https://doi.org/10.1016/j.agsy.2023.103647.

S.N.P.A (Sistema nazionale per la protezione dell'Ambiente), 2023, "Il clima in Italia nel 2022, Report SNPA 36", available online: https://www.snpambiente.it/2023/07/20/il-clima-in-italia-nel-2022/ (accessed on 25 September 2023)

McKee T.B., Doesken N.J., Kleist J.,1993. The relationship of drought frequency and duration to time Scale. In: *Proceedings of the Eighth Conference on Applied Climatology*, Anaheim, California.

Svoboda, J.; Štych, P.; Laštovička, J.; Paluba, D.; Kobliuk, N., 2022, "Random Forest Classification of Land Use, Land-Use Change and Forestry (LULUCF) Using Sentinel-2 Data—A Case Study of Czechia". *Remote Sens.* 2022, *14*, 1189. https://doi.org/10.3390/rs14051189.

Wan, Z., Hook, S., Hulley, G., 2021, "MODIS/Terra Land Surface Temperature/Emissivity Daily L3 Global 1km SIN Grid V061", NASA EOSDIS Land Processes Distributed Active Archive Center. https://doi.org/10.5067/MODIS/MOD11A1.061

World Meteorological Organization, 2012, "Precipitation Index User Guide", World Meteorological Organization, No. 1090. Geneva, Switzerland. ISBN 978-92-63-11091-6

MONITORING DISPERSAL PATTERNS SEA FOAM INJECTED BY REGASIFICATION PLANTS USING SATELLITE OPTICAL MULTISPECTRAL IMAGERY

M. Tedeschi[1], F. Filipponi [2] *, M. Picone [1], A. Grillo [1], M. Gabellini [1], G. Trinchera [1]

[1] ISPRA – Istituto Superiore per la Protezione e la Ricerca Ambientale, Italy (marilena.tedeschi, marco.picone, alessandro.grillo, massimo.gabellini, giuseppe.trinchera@isprambiente.it)
[2] CNR - Italian National Research Council, Institute of Environmental Geology and Geoengineering (IGAG), Italy (formerly: ISPRA) (federico.filipponi@cnr.it)

KEY WORDS: Sea foam, Regasification plants, Spatial patterns, Sentinel-2 MSI, Spatial filtering, Dispersal patterns

ABSTRACT:

Liquefied natural gas regasification plants can use seawater as a fluid in the process of converting gas from liquid to gas. In some cases, in correspondence with the discharge into the sea of the water used in the regasification process, "foams" may develop. In order to assist the overall evaluation of the phenomenon, an initiative was launched aimed at identifying foams with the use of satellite Earth observation data. Satellite optical multispectral imagery acquired by MSI sensor aboard Copernicus Sentinel-2 satellite constellation have been used to map areal distribution of sea foam generated from offshore platform and dispersed over sea. A sea foam detection procedure has been developed, including the following processing steps: i) cloud masking; ii) cloud mask refinement; iii) sea foam detection; iv) spatial filtering.
Sea foam spatial patterns, identified from Sentinel-2 MSI satellite acquisitions in the period 2015-2022, have been complemented with information related to dispersal direction and maximum distance from platform discharge point, and related to sea state and weather conditions, specifically, wind, waves, currents, and rainfall data. Results showed that the proposed procedure is effective in sea foam dispersal patterns identification and can be extended to other high-resolution remote sensing imagery.

1. INTRODUCTION

The phenomenon of foam formation at the regasification plant, in some cases, appears to be related to the breakdown of microorganisms naturally present in the sea water, subjected to mechanical stress and thermal shock along the water flow circuit in the vaporization systems and in relation to local weather and climatic conditions.
An example of this phenomenon can be seen in northern Adriatic Sea, where the Adriatic LNG offshore regasification terminal (Figure 1) is located 15 nautical miles from the coast of Porto Viro (RO), a platform 375 meters long and 115 meters wide, resting on the seabed at 29 meters deep approximately.
For this installation, the formation of foams was observed from the early stages of operation of the plant, also in consideration of the trophic state of these marine systems and the configuration of the discharge, which releases water in free fall inside a basin during regasification plant activities, trapping air and contributing to the amplification of the phenomenon.
To control and mitigate foams dispersal, initiatives have been launched aimed at the mechanical abatement of foams by nebulized sea water, for which the Italian Institute for the Environmental Protection and Research (ISPRA) and the regional environmental agency (ARPAV), monitors its operation. To assist the overall evaluation of the phenomenon, the Institute has launched a study phase aimed at identifying foams with the use of satellite Earth observation data. Experimental radiometric samplings demonstrated that sea foam reflectance decreases substantially with wavelength in the near-infrared, with values in the visible (0.44 µm) reduced by typically 40% at 0.85 µm, 50% at 1.02 µm, and 85% at 1.65 µm (Frouin and Deschamps, 1996). The spectral effect can be explained by the nature of the foam, which is composed of large bubbles of air separated by a thin layer of water and of bubbles of air injected in the underlayer. The presence of bubbles in the underlayer enhances water absorption and thus reduces reflectance in the near-infrared (Frouin and Deschamps, 1996).
Use of multispectral satellite observations to investigate marine debris characteristics, highlighted that spectral discrimination from other sea surface features (e.g., ships, foam) is not straightforward (Acuña-Ruz et al., 2018). Indeed, differentiating floating plastic debris from bright features, such as sea foam, sun-glint, clouds, is currently considered very challenging (Martínez-Vicente et al., 2019). Sea foam recorded at river fronts or coastal wave breaking area resulted in lower evaluation scores than other spectral targets when using classification models trained with the machine learning algorithms (Kikaki et al., 2022). Shoreline detection methods using very-high spatial resolution satellite images can be hampered by sea foam spectral target and require sea foam to be taken into account when discriminating between land and ocean pixels in coastal waters (Minghelli et al., 2020).

Figure 1. Adriatic LNG

This research study aims at proposing an approach to identify sea foam injected by regasification plants using satellite optical multispectral imagery, in order to provide an operational system to monitor spatial distribution over time, to support practitioners environmental control and to verify the effectiveness of mitigation strategies. Statistical analysis on detected sea foam allowed to identify typical dispersal patterns and to further analyse physical forcings role for selected cases resulting in broader distribution.

* Corresponding author

2. MATERIALS AND METHODS

Satellite optical multispectral imagery acquired by MSI sensor aboard Copernicus Sentinel-2 satellite constellation have been used to map areal distribution of sea foam generated from offshore platform and dispersed over sea. The high spatial resolution (10 m, 20 m and 60 m), the high revisit time (5 days with two satellites), and the 13 spectral bands (from the visible to shortwave infrared) are the characteristics of the S2 Multi-Spectral Instrument (MSI) sensor. All Sentinel-2 MSI acquisitions (top of atmosphere reflectance – L1C) acquired in the period 2015-2021, with cloud cover lower than 90%, were collected for the area of interest (about 700 images).

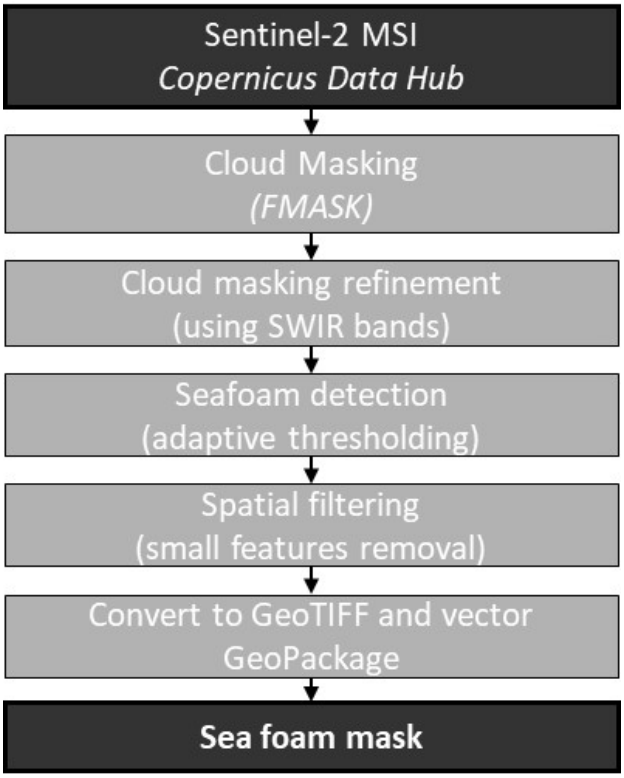

Figure 2. Detection procedure flowchart.

A sea foam detection procedure (Figure 2) has been developed, including the following processing steps: i) cloud masking; ii) cloud mask refinement; iii) sea foam detection; iv) spatial filtering.

In situ spectral measurements, acquired using a portable spectroradiometer, allowed to identify sea foam spectral signatures (Figure 3) in radiometric interval 400-900 nm. Measured sea foam reflectance showed significantly higher values than background seawater reflectance.

Taking under consideration sea foam spectral characteristics, and its similarity with cloud spectral signature in the visible and near-infrared radiometric interval, MSI SWIR spectral bands have been used to refine detected cloud pixels identified using 'fmask' cloud masking algorithm (Frantz et al., 2018), while all available spectral bands at 10 m spatial resolution have been used to locate pixels corresponding to floating sea foam.

The detection processing step consists of an adaptive thresholding method, to find brighter pixels than the background ones within a 0.5 km spatial buffer. Sum of reflectance value of all the available spectral bands at 10 m spatial resolution in the visible and near infrared radiometric interval has been used for the analysis. Threshold value has been set to value 0.25, which has been selected from the inspection by expert operators of sum of reflectance values over seafoam pixels, performed on 5% of the acquisitions. Spatial filtering of detected bright pixels is finally applied, in order to remove small patches corresponding to false positives (i.e. whitecaps, sun-glint, ship-generated sea foam, etc.). As a result, sea foam raster binary mask is generated from each satellite acquisition date.

Validation exercise, through supervision of the produced binary masks superimposed on true-color RGB images in GIS software run expert technicians, allowed to evaluate detection performances, providing information related to false negative pixels, typically in areas with thin clouds removed during cloud masking step, and false positive pixels, remaining after spatial filtering.

Sea foam spatial patterns identified from Sentinel-2 MSI satellite acquisition in the period 2015-2022, have been complemented with information related to dispersal direction and maximum distance from platform discharge point, and related to sea state and weather conditions. Specifically, wind, waves, currents and rainfall data, collected on the offshore platform or by a nearby buoy, have been compared with sea foam spatial distribution, in order to find typical dispersal patterns and identify physical forcings that could contribute broader distribution.

All the analysis was done using software SNAP, QGIS and R-cran.

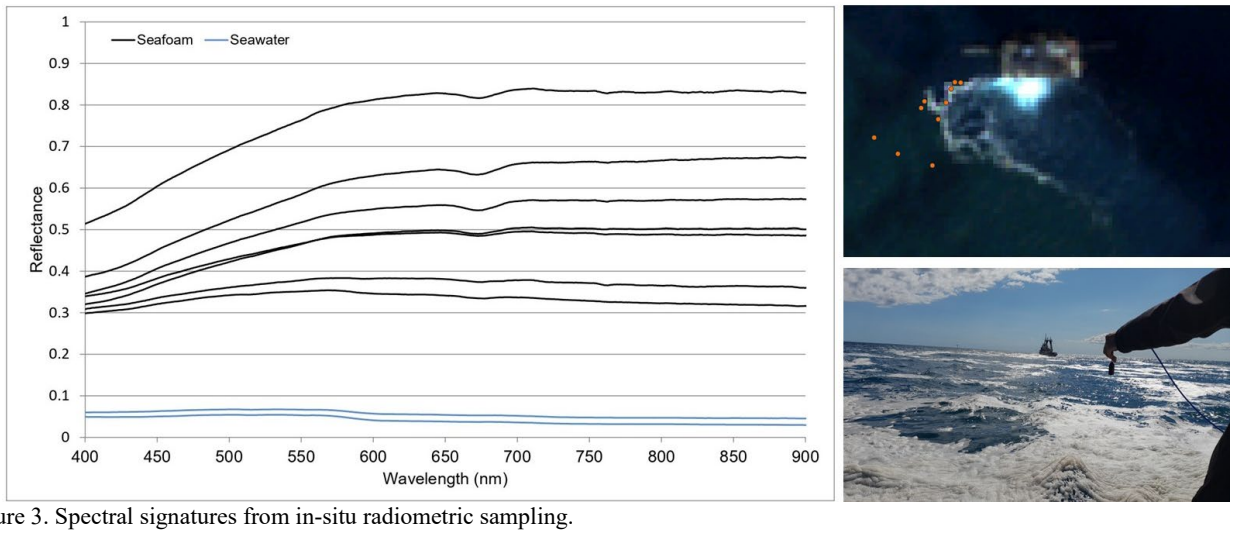

Figure 3. Spectral signatures from in-situ radiometric sampling.

3. RESULTS AND DISCUSSION

Detection approach allowed to reach a classification accuracy of 0.774. A total of 204 acquisitions (29.19 %) do not show any sea foam generated from regasification plant.
Most cases examined show a dispersion that typically concentrates within the distance of 1.5 nautical miles from the point of discharge the regasification water on sea. Maximum detected distance is 4.71 nautical miles. Typically, the direction and position of the dispersion area is in a southerly direction with respect to the terminal, due to the location of the emission point (Figure 4).

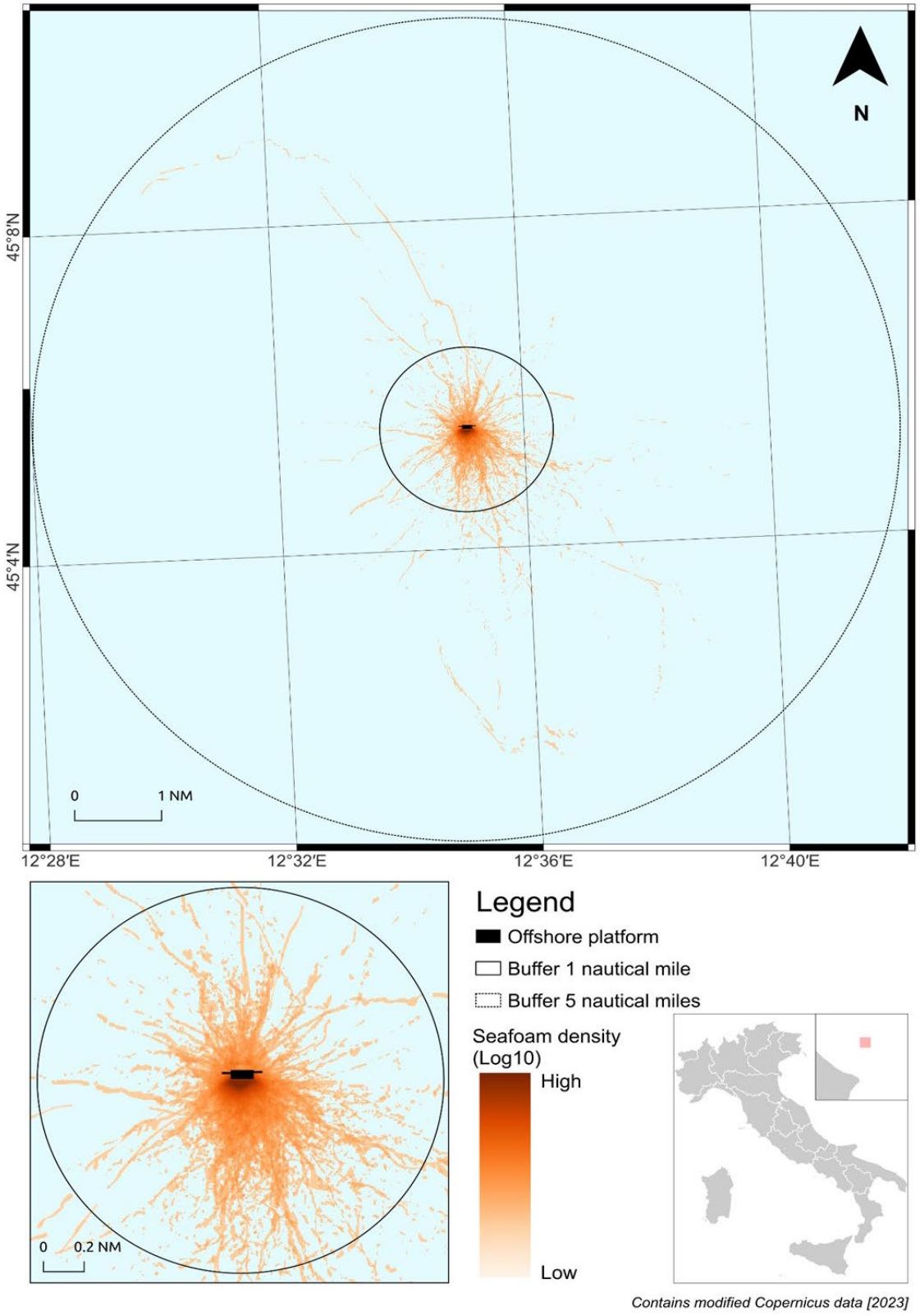

Figure 4. Sea foam dispersal patterns
for the period July 2015 – November 2022.

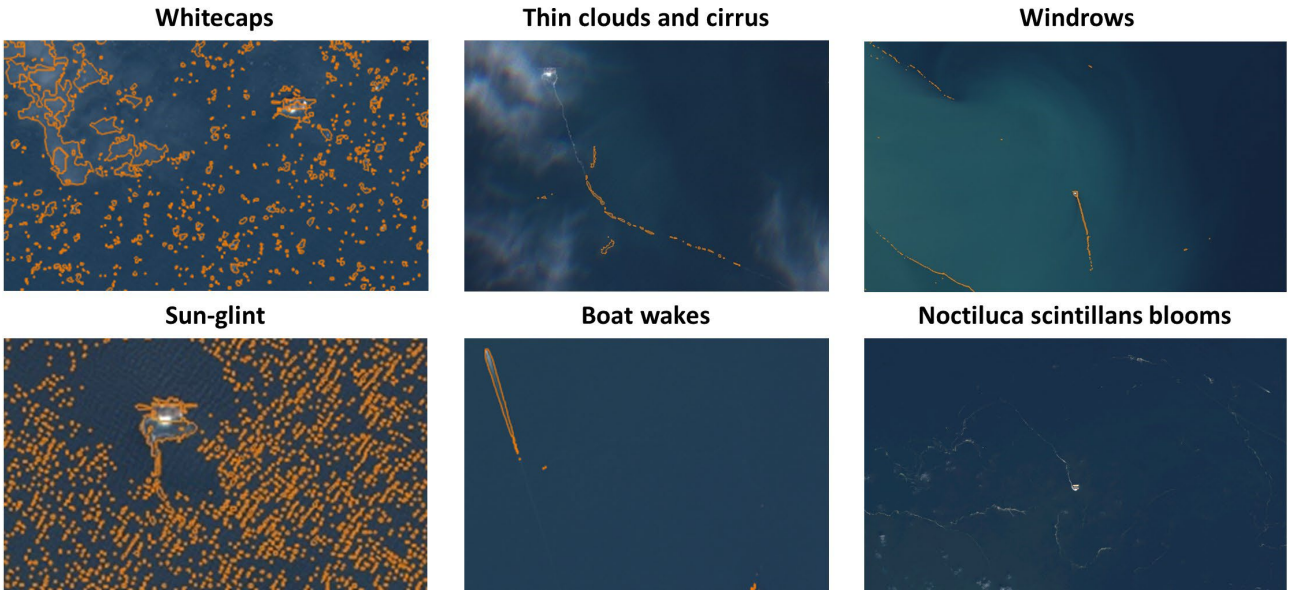

Figure 5. Sea foam false negatives and false positives cases. Detected sea foam is shown in orange color.

The selection of top of atmosphere reflectance in place of bottom of atmosphere reflectance for sea foam identification it is due to two reasons: i) in situ radiometric sampling show a significant difference between seafoam and seawater spectral signatures; ii) atmospheric correction algorithms can alter reflectance values so as to reduce detection capability.

Atmospheric correction algorithm used to process Sentinel-2 MSI data distributed to the users, namely Sen2Cor, performs relatively poorly in the coastal waters due to the land-based methodology, which generates scene parameters requiring a distribution of pixels containing land (Warren et al. 2019). On the other side, atmospheric correction algorithms specifically designed for water applications, used to retrieve bottom of atmosphere water-leaving reflectance, may use a correction for whitecaps, dampening seafoam reflectance. Considering that the objective of the research study is not concerning robust retrieval of optically active water constituents, that requires accurate atmospheric correction over seawater, top of atmosphere reflectance has been used to identify sea foams.

Only spectral bands at 10 m spatial resolution have been used for the sea foam detection, considering the scale of the investigated phenomenon. Same spectral bands set is available on many other very-high spatial resolution sensor onboard satellites and Unmanned Aircraft Systems (UAS), opening the way for extending the proposed detection approach to other optical multispectral acquisitions.

False negatives generated by the proposed detection procedure, corresponding to 22.5%, are mainly related to pixels with sea foam still observable under thin clouds (Figure 5), that are masked out by cloud masking processing step. False positives, partly deleted by spatial filtering for small features removal, are represented by bright pixels whose high reflectance values can be related to the presence of: whitecaps, especially during windy conditions; boat wakes; sun-glint, especially during summer months; algal blooms, like Noctiluca scintillans blooms; and windrows. Windrow is a long-established term for the aggregations of sea foam, seaweeds, plankton and natural debris that appear on the ocean surface, it usually forms stripes from tens up to thousands of meters long (Cózar et al, 2021).

The analysis was deepened on a set of cases selected on the basis of relevant events (significant distance of the foams from the terminal) and clear identification of the foams via algorithm (i.e. in the absence of those phenomena that disturb the identification of the area occupied by the foams). A selection of satellite acquisitions for which the identified seafoam dispersal exceeded 1.66 nautical miles from the emission point allowed to identify 30 cases.

Spatially explicit database of detected sea foam was complemented with the meteorological conditions (waves, currents, winds) observed by measuring instruments positioned near the terminal.

Assuming that the area occupied by the foams develops due to the meteorological conditions occurring in the last few hours, each parameter analysed is evaluated in average terms considering the average of the six hours preceding each satellite acquisition time. Two cases among the identified ones are showed, being marine physical forcings perfectly describing the development of foam in the area. The analysis of the first selected case (Table 1) highlighted that the applied algorithm, given the good visibility conditions at satellite acquisition time, was able to clearly identify the imprint taken by the formation of the foams (Figure 6). From the analysis of the foam dispersion during the case, it was possible to verify how much the marine physical forcings active on that day correspond to the direction of propagation that the foams assumed.

Figure 6. Sea foam dispersal pattern (in yellow) as seen by Sentinel-2 MSI acquired on 30/01/2022.

The platform position is often decisive in influencing the prevailing direction towards a south-south-east direction. meteorological conditions may correspond to a prevailing direction of distribution of the foams.

Sea foam dispersion: South (first branch), south-east (second branch), 138° (from North, clockwise)	
Satellite acquisition date	30/01/2022
Maximum distance	4543 m
Total area of the sea foam	54100 m^2
Current speed (last 3 hours)	0.25 m/s
Current direction (last 3 hours)	132°
Current speed (last 6 hours)	0.25 m/s
Current direction (last 6 hours)	123°
Wave height (last 3 hours)	0.21 m
Wave direction (last 3 hours)	133°
Wave height (last 6 hours)	0.18 m
Wave direction (last 6 hours)	118°
Wind speed (last 3 hours)	3.1 m/s
Wind direction (last 3 hours)	144°
Wind speed (last 6 hours)	2.5 m/s
Wind direction (last 6 hours)	133°

Table 1. Information related to selected case identified from Sentinel-2 MSI acquired on 30/01/2022.

In the other case shown, relating to the satellite acquisition of 24/05/2019 (Figure 7), it can be clearly highlighted how the direction taken by the foams was conditioned by the current and wind forcing (Table 2), which on that specific day showed a prevalent component towards the west. The height of the waves and their direction, given the mild intensity, do not affect the direction of propagation of the foams originating from the terminal.

Figure 7. Sea foam dispersal pattern (in yellow) as seen by Sentinel-2 MSI acquired on 24/05/2019.

Sea foam dispersion: West -87° (from North, anti-clockwise)	
Satellite acquisition date	24/05/2019
Maximum distance	3522 m
Total area of the sea foam	49800 m^2
Current speed (last 3 hours)	0.33 m/s
Current direction (last 3 hours)	-135°
Current speed (last 6 hours)	0.37 m/s
Current direction (last 6 hours)	-119°
Wave height (last 3 hours)	0.12 m
Wave direction (last 3 hours)	104°
Wave height (last 6 hours)	0.13 m
Wave direction (last 6 hours)	108°
Wind speed (last 3 hours)	2.0 m/s
Wind direction (last 3 hours)	-108°
Wind speed (last 6 hours)	2.3 m/s
Wind direction (last 6 hours)	-100°

Table 2. Information related to selected case identified from Sentinel-2 MSI acquired on 24/05/2019.

4. CONCLUSION

The proposed approach showed a good capacity in identifying sea foam injected by regasification plants from satellite optical multispectral acquisitions, as well as monitoring the dispersal patterns. It was possible to verify, for selected cases examined, that certain marine weather conditions affect the development and the areal propagation of foams. The analysis also tried to explain what are the physical forcings that determine the broader dispersal, representing cases that need special attention. Further development should test the proposed approach for the analysis very-high spatial resolution optical multispectral data and identify strategies to reduce the detection of false positives.

ACKNOWLEDGEMENTS

This work contains modified Copernicus Sentinel data (2023). Sentinel-2 MSI data used were available at no cost from Copernicus Open Access Hub.

REFERENCES

Acuña-Ruz, T., Uribe, D., Taylor, R., Amézquita, L., Guzmán, M. C., Merrill, J., Martínez, P., Voisin, L., & Mattar, C. (2018). Anthropogenic marine debris over beaches: Spectral characterization for remote sensing applications. *Remote Sensing of Environment*, 217, 309-322. https://doi.org/10.1016/j.rse.2018.08.008

Cózar, A., Aliani, S., Basurko, O. C., Arias, M., Isobe, A., Topouzelis, K., Rubio, A., & Morales-Caselles, C. (2021). Marine litter windrows: a strategic target to understand and manage the ocean plastic pollution. *Frontiers in Marine Science*, 8, 571796. https://doi.org/10.3389/fmars.2021.571796

Frantz, D., Hass, E., Uhl, A., Stoffels, J., & Hill, J. (2018). Improvement of the Fmask algorithm for Sentinel-2 images: Separating clouds from bright surfaces based on parallax effects. *Remote Sensing of Environment*, 215, 471-481. https://doi.org/10.1016/j.rse.2018.04.046

Frouin, R., Schwindling, M., & Deschamps, P. Y. (1996). Spectral reflectance of sea foam in the visible and near-infrared: In situ measurements and remote sensing implications. *Journal of Geophysical Research: Oceans*, 101(C6), 14361-14371. https://doi.org/10.1029/96JC00629

Kikaki, K., Kakogeorgiou, I., Mikeli, P., Raitsos, D. E., & Karantzalos, K. (2022). MARIDA: A benchmark for Marine Debris detection from Sentinel-2 remote sensing data. *PloS one*, 17(1), e0262247. https://doi.org/10.1371/journal.pone.0262247

Martínez-Vicente, V., Clark, J. R., Corradi, P., Aliani, S., Arias, M., Bochow, M., ... & Vethaak, A. D. (2019). Measuring marine plastic debris from space: Initial assessment of observation requirements. *Remote Sensing*, 11(20), 2443. https://doi.org/10.3390/rs11202443

Minghelli, A., Spagnoli, J., Lei, M., Chami, M., & Charmasson, S. (2020). Shoreline extraction from WorldView2 satellite data in the presence of foam pixels using multispectral classification method. *Remote Sensing*, 12(16), 2664. https://doi.org/10.3390/rs12162664

Warren, M. A., Simis, S. G., Martinez-Vicente, V., Poser, K., Bresciani, M., Alikas, K., Spyrakos, E., Giardino, C., & Ansper, A. (2019). Assessment of atmospheric correction algorithms for the Sentinel-2A MultiSpectral Imager over coastal and inland waters. *Remote sensing of environment*, 225, 267-289. https://doi.org/10.1016/j.rse.2019.03.018

OPEN SOURCE TECHNOLOGIES FOR MAPPING: IMPACT TOOLBOX AND THE LAND COVER MAP OF SARDINIA

C. Collu [1, 2], D. Simonetti [3], F. Dessì [1], L. Naitza [1], P. Lasio [4], P. Botti [4], M.T. Melis [1 1]*

[1] Department of Chemical and Geological Sciences, University of Cagliari, Monserrato, Italy
(claudia.collu, fdessi, titimelis)@unica.it; lnaitza@gmail.com
[2] Department of Civil, Constructional and Environmental Engineering, Sapienza University of Rome, Rome, Italy - claudia.collu@uniroma1.it
[3] European Commission - Joint Research Centre, Ispra, Italy - dario.simonetti@ext.ec.europa.eu
[4] Directorate General of the Regional Agency of the Hydrographic District of Sardinia, Cagliari, Italy
(plasio, pbotti)@regione.sardegna.it

KEY WORDS: Land Cover, IMPACT Toolbox, Earth Observation, GEE, Sentinel, classification

ABSTRACT:

In recent years, EO data has played a key role in land cover mapping and land cover change monitoring. This study describes the methodology adopted for the land cover mapping of the Sardinian island (IT) using the IMPACT Toolbox, a free and open source framework for EO image processing, analysis and classification. Moreover, IMPACT provides a user-friendly interface to facilitate the visual inspection, interpretation and accuracy assessment of land cover maps.The first release of Sardinia Land Cover Map has been produced through three subsequent steps, including i) pixel-based multi-temporal classification of Sentinel-1 and 2 and ancillary data performed in GEE, ii) image segmentation of a Sentinel-1 and 2 annual synthesis and objects pre-labeling using the Baatz algorithm available in IMPACT, iii) visual inspection and refinement of the preliminary object-based land cover map. Despite the $5x10^6$ polygons over an area of $2{,}4x10^4$ km^2, the use of object-based map reduces the amount of isolated pixels and the 'salt&pepper' effect, facilitating the visual inspection and relabelling of individual objects or entire categories. In addition, to enhance user collaboration and speed up the assessment process, IMPACT operates as a one-stop-shop on a server platform, enabling multi-user verification and validation. The obtained results give the input to propose a system of semi-automatic update of the land cover map using new data acquisition, with the creation of new spectral indices for change analysis and sub-segmentation of entire classes, in order to subsequently improve or update the map over time.

1. INTRODUCTION

Over the past decade, Land Use and Land Cover (LULC) mapping has witnessed remarkable progress driven by technological advancements and the increasing availability of Earth Observation data. One of the most significant developments has been the proliferation of multispectral high-resolution satellite imagery, such as Landsat 9 and Sentinel-2, allowing more accurate land cover classification using time series analysis in combination with machine learning algorithms, with both pixel-based and object-based approaches. Further, satellite data represent a valuable resource for monitoring of land cover changes through change detection techniques (Chughtai A. H. et al., 2021).

However, the main challenges in land cover mapping at regional scale are related to the difficulty of extracting LULC information entirely from multispectral imagery, thus several remotely sensed datasets and ancillary data are requested (Zhang C. et al, 2022). Therefore, LULC classification requires processing a significant number of orbital images for multitemporal analysis and several datasets that involve complex computational infrastructure for data storage, management and processing capacity.

In addition, visual inspection and validation of resulting land cover maps, especially in large and heterogeneous landscapes, involve adequate ground-truthing to assess misclassifications and the accuracy of the map. Thus, land cover mapping requires various processing tools and platforms, considerable resources and often licensing costs.

This study aims to introduce the IMPACT Toolbox, a free and open source tool to access, storing, organising and processing Earth Observation data for land cover mapping production Originally developed by the European Commission (Simonetti D. et al, 2015a) as a portable GIS desktop application , it has been further improved to support multi-user and server execution to produce the 2020 Land Cover Map of Sardinia (Collu C. et al, 2022), Italy (Figure 1).

Figure 1. Location of the island of Sardinia (Italy).

2. IMPACT TOOLBOX

Originally designed as a stand-alone and portable Windows application for EO image processing and LULC mapping,

[1]* Corresponding author

IMPACT Toolbox has been further developed to match the project requirements such as the possibility of storing, processing, and rendering large volume of raster and vector data in a centralised infrastructure accessible online by the different actors involved in the mapping and validation activities (Figure 2). The server version of IMPACT has been developed and deployed using a Docker image containing Ubuntu OS, NGINx and Tornado as load balancer and web server as well as Python and ExtJs for the backend and frontend respectively.
Image processing modules (Python) and the rendering engine (Mapserver) are mainly relying on the Geospatial Data Abstraction Library (GDAL).

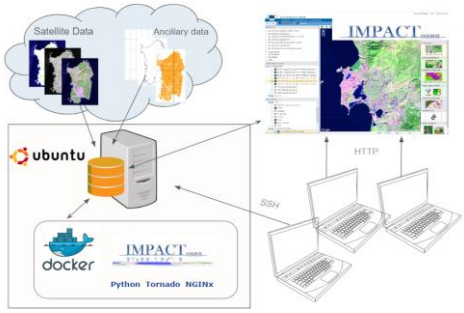

Figure 2. IMPACT Toolbox architecture

Through a user-friendly web interface, it is possible to carry out EO data processing such as image conversion, clipping, classification, segmentation as well as visual interpretation of LCLU map, ground-truthing and accuracy assessment by multiple operators simultaneously. Moreover, any modification done on the LCLU map during the visual inspection is immediately saved on the server, ensuring the rendering of the latest version on the web pages of connected operators.

3. MATERIALS AND METHODS

The Land Cover Map of Sardinia for the 2020 reference year, was produced using multi-source data: Sentinel-2 multispectral and Sentinel-1 radar data from 2019 to 2020, and a series of ancillary data and existing thematic maps from Sardinian Geoportal, Open Street Map and Joint Research Centre (JRC), including:

a) Land Use map of Sardinia (2008), the latest LULC map of Sardinia at a scale of 1:25 000;
b) Geo-Topographic Database (DBGT-2020) at a scale of 1: 10 000, from which viability, construction, hydrography and vegetation information were extracted;
c) Open Street Map features available in January 2021, i.e., water feature, roads, infrastructures and build up;
b) Phenological Based Synthesis, a multi-temporal land cover classification of Sentinel-2 images spanning from 2019 to 2020 developed at JRC (Simonetti D. et al., 2015b)

Furthermore, 2016 and 2020 orthophotos of the Sardinia Island, with a spatial resolution of 0.20m/pixel in R, G, B, NIR bands, have been integrated in IMPACT Toolbox via WMS services as provided by the AGEA (https://www.agea.gov.it/) (Collu C. et al, 2022).
The methodology adopted for the LCLU map generation involves three subsequent steps: 1) preliminary pixel-based classification, performed in Google Earth Engine platform, 2) image segmentation and pre-labeling of the obtained segments, 3) visual inspection and refinement of the resulting map; both step 2 and 3 are performed in IMPACT (Figure 3).

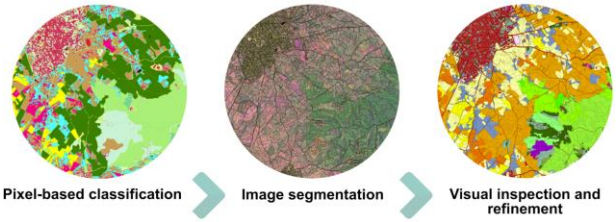

Figure 3. Key image processing step

3.1 Pixel-based classification

Pixel-based classification following CORINE schema (third or fourth level) was based on ancillary data and satellite data products, obtained from processing of Sentinel-1 (VV and VH polarizations, Level-1 GRD) and Sentinel-2 level-2A imagery (for further comprehensive details, consult the work of Collu C. et al., 2022).

3.2 Image segmentation and object pre-labeling

Image segmentation is an object-oriented analysis that involves image partitioning into a set of objects or segments, containing groups of pixels with similar spectral characteristics and mutual relations (Rejaur Rahman M. et al., 2008). In particular, Baatz multiresolution segmentation algorithm is widely used in land cover mapping and object-based image analysis, and operates with a multi-resolution approach, with bottom-up region merging strategy. Initially, individual pixels are treated as distinct objects, and then pairs of image objects are combined to create larger segments (Baatz M. and Schape A., 2000). The merging decision is based on a local homogeneity criterion, represented by user-defined thresholds, i.e. a) scale, that determines the average size of the image objects produced during segmentation, as it serves as a threshold that controls the permitted change in homogeneity throughout the segmentation process, thus a higher scale parameter results in larger merged objects, as it allows more merging of image segments., b) colour, that refers to the spectral homogeneity criterion used in the segmentation process, measures the similarity in spectral values between adjacent image objects, adjusting the colour parameter, users can control the relative influence of colour (spectral homogeneity) versus shape properties (shape homogeneity) on the generation of image objects, c) compactness, a component of the shape homogeneity criterion, it affects the shape properties of the generated image objects, thus users can use it to determine whether the segmented objects should be more compact (i.e., closely packed or fringed) or more smooth (with less irregularities). The IMPACT Toolbox segmentation algorithm (Simonetti et al., 2015a) is based on Baatz strategy and has been developed by Brazil's National Institute for Space Research (INPE), and involves similarity parameter in addition to Baatz components, that is related to the minimum grade of homogeneity within objects during segments merging.
This segmentation algorithm implemented in IMPACT was performed on an image composed by three bands: a) GREEN and NIR bands from an annual composite of Sentinel-2 images collected in 2020, produced by computing the median value of each band, 2) and a band derived from the computed mean value of VV and VH polarisation bands of a Sentinel-1 annual composite of 2020's acquisitions, created by calculating the mean value of VV and VH bands. A scale factor of 4 pixels

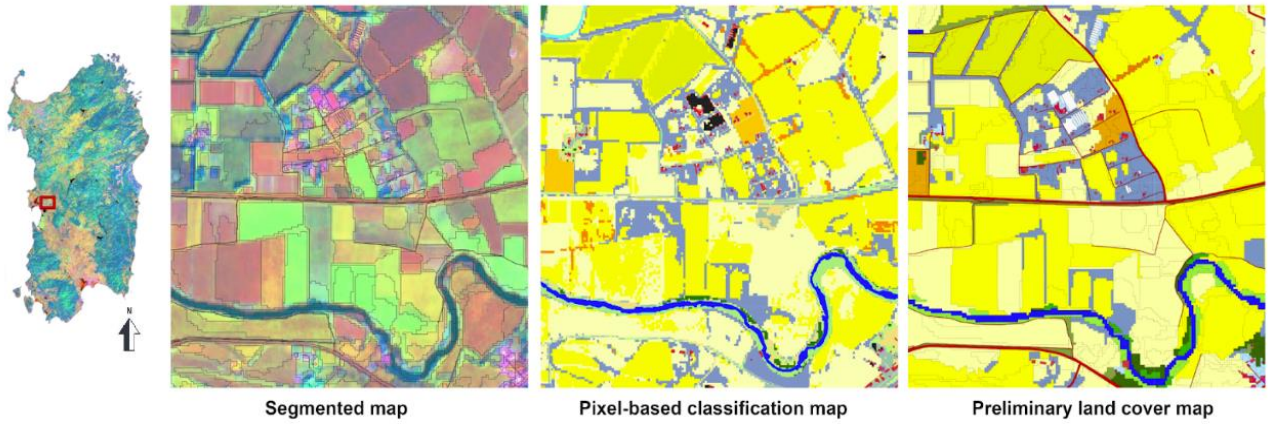

Figure 4. An example of segmented map (basemap: Red: GREEN Sentinel-2 annual composite, Green: NIR Sentinel-2 annual composite, Blue: average VV-VH of Sentinel-1 annual composite) on the left, pixel-based classification map (centre), and preliminary land cover map (right) of an agricultural area near Oristano city. The preliminary land cover map shows the reduction of salt&pepper noise, resulting in higher visual clarity.

(400m2), a color of 0.9, a compactness of 0.7 and a similarity of 0.82 were used.

Finally, land cover classes derived from pixel-based classification map have been assigned to the objects resulting from the segmentation process, based on the majority occurrence rule, thus the class assigned to each object was the one that was most frequently observed within it.

The resulting preliminary map has been overlaid with a) the build-up information from DBGT-2020, b) the 1m-buffered road and railway network shapefile derived from OSM downloaded in December 2022, and labelled with relative CORINE code (class 122), to enhance the detail of the map.

3.3 Visual inspection and refinement

The visual inspection of the preliminary map is a semi-manual process that evaluates the classifier's performance, confirming or reassigning legend codes. Despite time and resource demanding, this is a crucial phase in the map production workflow and allows the recoding of objects or entire CORINE classes that couldn't be automatically extracted due to their spectral similarity or lack appropriate information.

IMPACT Toolbox comes with an optimized and user friendly map editor environment that speeds up the editing of the map by multiple operators in a non-conventional way by facilitating the selection of objects on the base of i) ancillary information stored in the attribute table, ii) the assigned LCLU classes or iii) punctual selection, giving the possibility of recoding them by clicking on the most appropriate class from a popup menu (instead of the traditional manual editing of the DBF file). Moreover, the possibility of enabling or disabling classes, both in rendering and selection mode, eases the identification and reclassification of omission and commission errors respectively. The customised rendering engine and libraries as well as the file optimizations (pyramids, spatial indexing) guarantee a smooth editing experience even when dealing with millions of polygons and vector data of several Gb.

3.1 3.4 Ground reference data collection for accuracy assessment

In order to assess the accuracy of the land cover map, the ongoing validation process involves the collection of about 10000 ground reference points, using a stratified random approach over the Sardinian territory and in the various land cover classes. Ground truthing is carried out in IMPACT Toolbox by a detailed photo-interpretation of data coming from Google Earth imagery, AGEA orthophotos, ancillary datasets and time series analysis through Landsat and Sentinel-2 time series visualizer powered by GEE and implemented in IMPACT, a valuable tool especially concerning seasonality analysis for crop identification.

ADD 1 line about field data and the fact that this is an ongoing activity.

4. RESULTS

The preliminary map, resulting from segmentation and pre-labelling processes, consists of 12 million segments covering the entire Sardinian territory, an area of 24,000 square kilometres, with more fragmented areas corresponding to urban environments and larger polygons in natural territories, confirming the robustness of the Baatz segmenter available in IMPACT. Furthermore, thanks to the appropriate selection of the input image and bads as well as the segmentation parameters (scale factor, colour, compactness and similarity), we do not observe under or over-segmentation in spectral homogeneous or heterogeneous areas (Figure 4). In addition, segmentation and pre-labelling of segments have improved the quality and the visual clarity of the pixel-based classification map, reducing isolated pixels and the well-known “salt&pepper” effect (Blaschke et al., 2000), a noise typically caused by random variations in pixel-values, as it is shown in Figure 4.

The visual inspection of the preliminary map has highlighted advantages and disadvantages of both pixel-based classification and segmentation, and has permitted the refinement of the preliminary map, by re-coding i) macro classification errors derived from incorrect pixel-based classification, ii) small isolated polygons (Figure 5) making use of automatic object selection based on spatial extent, thematic filter as well as a more accurate manual selection (Figure 6).

Figure 5. LCLU map before (left) and after (right) the recoding of small polygon along the road network

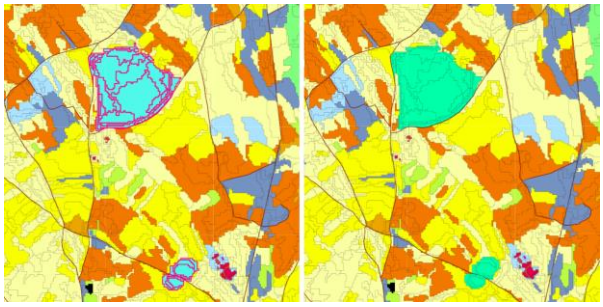

Figure 6. Example of multiple selection in one click and recoding in IMPACT environment of two salted water bodies, uncorrectly classified as inland waters.

To date, visual inspection has resulted in manual and automatic adjustment of 1 million segments. Most segments have been recoded to natural classes (65%), mainly from artificial surfaces and agricultural areas (trees among crop fields), and from other natural categories (39%), less vegetated areas were recoded to pastures, forests, and sclerophyllous vegetation. Approximately 27% of the altered segments were reclassified to agricultural land, especially from sclerophyllous vegetation and artificial land.

5. CONCLUSIONS

Precise land cover mapping represents a crucial point in environmental monitoring and land management. However, the necessity of multi-source data and the use of several processing tools and software solutions can be time-consuming and often can lead to licensing costs. These challenges are being addressed in a remarkable way by IMPACT Toolbox, offering a free and portable solution with centralised data management on a unified infrastructure, simplifying data organisation and accessibility for multiple users.

The results of land cover mapping in the Sardinia region obtained from segmentation, visual inspection, and validation processes, all conducted within the IMPACT Toolbox, have enhanced the potential of this application for land cover map production. In particular, the IMPACT segmentation algorithm has shown the efficiency of object-based classification, overcoming the salt&pepper effect, and thus improving the visual clarity of the map, making it easier to distinguish larger, meaningful and more coherent regions, simplifying also the subsequent visual inspection. This procedure is further facilitated by specific analysis and editing tools implemented in IMPACT, e.g. automatic selection of objects with the possibility to adopt statistical approach to detect and recode class outliers.

Moreover, IMPACT allows for continuous updates of the land cover map directly on the server, eliminating the need for local operations and ensuring that the most current information is readily available.

A new module has been developed for semi-automatic update of land cover maps over time using up-to-date remote sensing imagery. Existing vector map objects are dissolved by class, and sub-segmented on the basis of the spectral properties of the new image as well as new processing parameters. The resulting map maintains existing outmost class boundaries while allowing for the selection of changed areas based on spectral information or visual methods. This procedure enables the reconstruction of the change trajectory for each object (polygon) over time without the need for traditional GIS attribute table operations like intersections or spatial joins.

In conclusion, the IMPACT toolbox introduces a new era of land cover mapping. It addresses long standing challenges, making land cover and land cover change mapping more accessible and efficient.

ACKNOWLEDGEMENTS

This study has been supported by the Directorate General of the Regional Agency of the Hydrographic District of Sardinia in the framework of the “Activities of realisation of the cartography of the Sardinian soil cover and of the monitoring system of the irrigated areas of Sardinia from remote sensing data”.

REFERENCES

Baatz M. and Schape A. (2000). Multiresolution Segmentation - An Optimization Approach for High Quality Multi-Scale Image Segmentation. Strobl, J., Blaschke, T. and Griesebner, G., Eds., Angewandte geographische informations verarbeitung, Heidelberg, 12-23.

Blaschke T., S. Lang E. Lorup, J. Strobl, and P. Zeil (2000). Object-Oriented Image Processing in an Integrated GIS/Remote Sensing Environment and Perspectives for Environmental Applications. Environmental Information for Planning, Politics and the Public 2: 555–570.

Chughtai A.H., Abbasi H., Karas I. R (2021). A review on change detection method and accuracy assessment for land use land cover, Remote Sensing Applications: Society and Environment, Volume 22. https://doi.org/10.1016/j.rsase.2021.100482.

Collu C., Dessì F., Simonetti D., Lasio P., Botti P., Melis M. T. (2022). Titolo del lavoro: On the Application of Remote Sensing Time Series Analysis For Land Cover Mapping: Spectral indices For Crops Classification. Int. Arch. Photogramm. Remote Sens. Spatial Inf. Sci., XLIII-B3-2022, 61–68. https://doi.org/10.5194/isprs-archives-XLIII-B3-2022-61-2022.

Rejaur Rahman M., Saha S.K. (2008). Multi-resolution segmentation for object-based classification and accuracy assessment of land use/land cover classification using remotely sensed data. J Indian Soc Remote Sens 36, 189–201 . https://doi.org/10.1007/s12524-008-0020-4.

Simonetti D., Marelli A., Eva H.D. (2015a). IMPACT: Portable GIS toolbox image processing and land cover mapping. Luxembourg: EUR 27358. Luxembourg (Luxembourg): Publications Office of the European Union, JRC96789 https://dx.doi.org/10.2788/143497.

Simonetti D., Simonetti E., Szantoi Z., Lupi A., Eva H. D. (2015b). First Results From the Phenology-Based Synthesis Classifier Using Landsat 8 Imagery, IEEE Geoscience and Remote Sensing Letters, vol. 12, no. 7, Art. no. 7, https://10.1109/lgrs.2015.2409982.

Zhang, C.; Li, X (2022). Land Use and Land Cover Mapping in the Era of Big Data. Land, 11(10), 1692. https://doi.org/10.3390/land11101692.

OVERWATCH - INTEGRATED HOLOGRAPHIC CRISIS MANAGEMENT MAP: POTENTIAL IMPACT IN THE COPERNICUS EMERGENCY MANAGEMENT RAPID MAPPING MAPS PRODUCTION WORKFLOW

V. Fissore[1]*, C. Monaco[1], D. Lisi[1], S. Bassetti[1], C. Rossi[2], E.Arnaudo[2], L.Barco[2], P. Boccardo[3]

[1] Ithaca S.r.l., Via PierCarlo Boggio 61, 10128, Torino (TO) , Italy

(vanina.fissore, cristina.monaco, davide.lisi, stefano.bassetti)@ithacaweb.org

[2] Fondazione LINKS, Via PierCarlo Boggio 61, 10128, Torino (TO), Italy

(claudio.rossi, edoardo.arnaudo, luca.barco)@linksfoundation.com

[3]DIST - Interuniversity Department of Regional and Urban Studies and Planning, Politecnico of Turin, Torino (TO), Italy; piero.boccardo@polito.it

KEY WORDS: OVERWATCH, CEMS RM, wildfire delineation, AI model, Sentinel-2.

ABSTRACT:

Climate change heightens the frequency of natural disasters, including forest fires and floods, causing severe problems such as fatalities and economic losses. The OVERWATCH project, leveraging the latest technologies of AI, drones, and Earth observation data, aims at developing an integrated system to manage disaster events. Among its objectives, the projects proposes to improve some data processing steps within the workflow of the CEMS Rapid Mapping service, by using machine learning for automatic burned and flooded area delineation. This work outlines current progresses in Earth Observation and AI components of the OVERWATCH system, focusing on automated burned area assessment. In this context, we exploit several data sources, including Copernicus EMS and EFFIS, to train a delineation model on historical wildfires, validating the results on recent large-scale CEMS RM activations.

1. INTRODUCTION

Climate change is expected to lead to an increase in frequency of significant natural hazards, which in turn will contribute to fatalities, displacement, devastation, and strong economic repercussions. Forest fires and floods prominently stand out among the risks faced by countries worldwide. The European Union (EU) boasts extensive forested areas, covering nearly 160 million hectares or 37.7% of the EU's territory (Milicevic, 2023). Just in in 2022 alone, wildfires have scorched over 1.6 million hectares of land, leading to significant economic losses (Joint Research Center, 2023). While wildfires have historically been a concern in the Mediterranean region, they now pose a significant risk in other parts of the EU, including northern Europe and the Arctic. Similarly, floods can cause significant loss of life and property damage, both in direct losses and in the context of impacting the economy by disrupting transportation, damaging businesses, and causing losses in agriculture and other industries. European countries have been implementing flood management strategies to mitigate these risks, such as early warning systems, floodplain mapping, and infrastructure improvements such as dams and levees, as floods cause the largest share of disaster losses in Europe (World Bank, 2021). However, despite these efforts, floods remain a significant hazard. Consequently, effective disaster management and control will be imperative to mitigate the impacts of these events.

In this context, the Copernicus EU program aims at developing information services at European level based on satellite Earth Observation and in situ (non-space) data**.** Among the provided services, the Copernicus Emergency Management Service (CEMS) of mapping uses satellite imagery and other geospatial data to provide free of charge mapping service in cases of natural disasters, human-made emergency situations and humanitarian crises throughout the world (Copernicus Emergency Management Service, 2023a). Notably, the Rapid Mapping (RM) service delivers standardized mapping products to authorized users within hours or days of service activation, providing immediate support in the aftermath of a disaster. As an example of RM products, the Delineation (DEL) products must be finalized within 7 hours from the activation's initiation.

The OVERWATCH project here introduced, funded in the Horizon Europe Program (CALL:HORIZON-EUSPA-2021-SPACE under Grant Agreement 101082320) (https://overwatchproject.eu/en/) fits into this context. OVERWATCH aims, in fact, to develop an integrated holographic crisis management system, boosted by the European Global Navigation Satellite System (EGNSS) and Copernicus Emergency Management Service (CEMS). The main goal is to address the complexity of disaster management and control and enhance communication, information collection, and coordination among disaster response teams and, in general, stakeholders. The system will make use of innovative digital technologies and components, including an artificial intelligence-based backend management system (AIMS), a fallback communication system (FCS), VTOL (Vertical Take Off and Landing) and quadcopter drones (DR), augmented reality (AR) and earth observation data (EO), to deliver precise information and to enhance operational efficiency. The project will also develop a reliable and efficient communication infrastructure to gather and disseminate information for improved situational awareness.

Among its objectives, the OVERWATCH project looks forward to improve and speed up the EO data processing workflow that is ordinarily addressed by the PS (Production Sites) within the Rapid Mapping service to deliver the requested mapping products related to wildfires and floods delineation.

The expected improvements involve expediting labor-intensive manual tasks and data processing methods, through the application of machine learning algorithms, particularly in the context of delineating and grading flooded and burned areas. Moreover, the outputs produced are anticipated to require minimal post-processing, thereby reducing the time operators spend on output verification and refinement.

In this paper, authors presents some preliminary results about the progress made in the EO and AI components of the

* Corresponding author

OVERWATCH system, with specific reference to the wildfire event type, i.e. delineation of the burned area.

2. MATERIALS AND METHODS

The task at hand involves creating a machine learning model for burned area segmentation, robust to different geographical areas and conditions. The objective is to train the model exploiting manually delineated affected areas with reference to some CEMS RM activations from past wildfire events. To this end, we employ a multitask framework (Arnaudo et al., 2023), where the architecture consists of a standard segmentation network, but the decoder representations are simultaneously shared among two tasks, namely burn scar and land cover segmentation.
The adopted methodology consists of different subsequent and necessary steps: 1) creation of the annotated dataset necessary for the machine learning process, 2) training of the algorithm, 3) validation of the outputs.

2.1 Data Preparation: creation of the annotated dataset for the machine learning process

The two ground truths adopted for the joint training, and displayed in Figure 1, are derived from CEMS and ESA World Cover dataset. The input consists of Sentinel-2 satellite images (Copernicus Sentinel-2, 2021) based on coordinates and times of each event, capturing data across 12 spectral bands at resolutions ranging from 10 to 60 meters. Our focus is on the L2A product, which corrects reflectance to Bottom-of-Atmosphere (BoA) values. In addition to satellite imagery and burned area delineation maps, we retrieve the land cover data from the ESA World Cover on the same area to exploit it as auxiliary output and improve the generalization capabilities of the model. The resulting CEMS dataset comprises a total of 433 samples, spanning from 2017 to Q1 2023, thus providing a substantial amount of data for a full training.

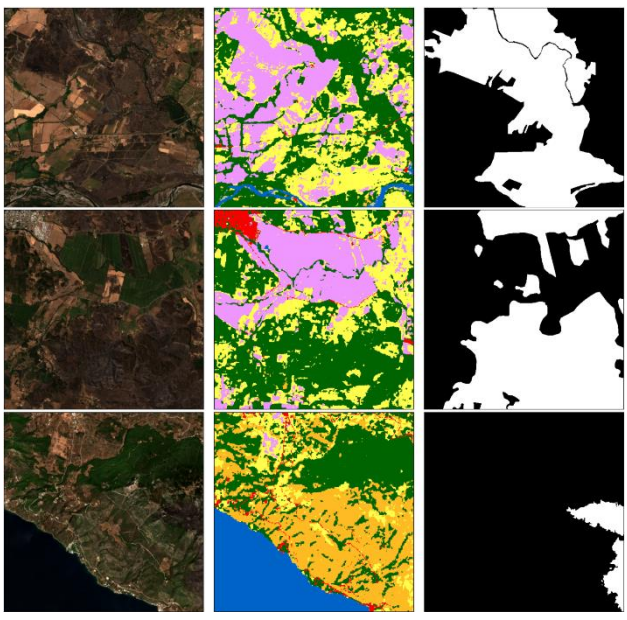

Figure 1. Some samples extracted from the multitask training dataset. From left to right: Sentinel-2 image, land cover map (ESA WorldCover), delineation map.

After this first phase, the delineation algorithm undergoes an additional finetuning using a dataset generated from pre- and post-event images derived from EFFIS fire activations. All the following steps and relative computations were run using Phyton programming language.
The post and pre -event images were employed to automatically generate initial approximations of the burned area delineation, utilizing a procedure based on the computation of the difference Normalized Burn Ratio (dNBR) index.
The dNBR is dependent on the previous Normalized Burned Ratio (NBR) indexes computation, for both the pre and post event situations, accordingly to the following ratio:

$$NBR = \frac{NIR - SWIR}{NIR + SWIR} \quad (1)$$

where NIR and SWIR are the Near Infrared and Shortwave Infrared bands of the Sentinel-2 images (B8 and B12, respectively).
As above mentioned, the availability of NBR for pre-event and of NBR for post-event situations, permit to retrieve the dNBR, calculated as:

$$dNBR = NBR_{pre} - NBR_{post} \quad (2)$$

The output is a raster file that is then subjected to a thresholding analysis based on pixel values, in order to assess the fire severity and thus identify burned areas. The pixel dNBR value considered for thresholding was +0.3, which, accordingly to current researches, generally corresponds to moderate-low severity burned areas (Keeley, 2009) (Key, 2006). By applying such thresholding value, all pixels presenting dNBR values $\geq$ +0.3 were selected and considered in the analysis. The obtained grid files were then converted into shapefiles.
Finally, the shapefiles underwent manual verification and refinement by operators in QGIS v.3.28.11 LTR environment (QGIS.org, 2023), resulting in an annotated dataset that includes ground truth data along with the corresponding post-event images. Although the dNBR procedure often yielded accurate results, several challenges were encountered during the dataset preparation. In particular, areas that were already burned in the pre-event images were often missed and had to be manually included (false negatives). Additionally, in some instances, water bodies and terrains undergoing substantial changes between the pre and post-event phases, were erroneously categorized as burned areas (false positives).
The final training dataset for the machine learning process was constituted by 236 shapefiles representing burned areas.

2.2 Training of the algorithm: Multitask learning framework

The training of the adopted model comprises two subsequent steps: first, a full multitask training using the CEMS dataset to learn robust features, followed by a finetuning based on the previously created dataset of 236 shapefiles representing burned areas, that were subsequently rasterized to get a binary classification of reference for the model: pixel value 1, burned area; pixel value 0, non-burned area.
With regard to the learning model type, we adopted a standard multitask learning framework, as illustrated in Figure 2.
We train the complete model, denoted as f_θ, by simultaneously performing burned area delineation and land cover segmentation. This is accomplished using shared representations from the decoder stage, denoted as φ_θ. By sharing the features, the model can capture and leverage common patterns between these two tasks, potentially leading to improved segmentation results. During the training process, we utilize standard Cross Entropy loss, both in its binary and multi-class variants. The gradients

from both tasks are jointly propagated back to update the model's parameters.

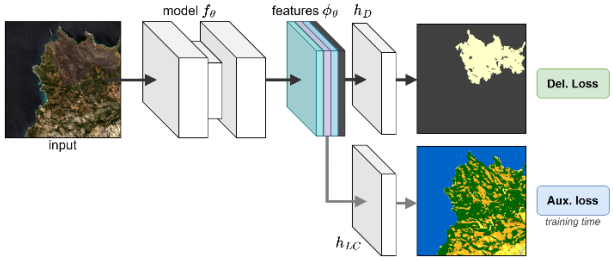

Figure 2. Training framework adopted in this work. The model is jointly trained on both burned area delineation, and land cover segmentation as auxiliary output.

At finetuning and testing phase, we focus solely on burned area delineation performance, omitting the auxiliary head and performing standard binary segmentation. Following previous works, we adopt a Unified Perceptual Parsing network (UPerNet) (Xiao et al., 2018) paired with a ResNet50 encoder as our architecture. We train the complete framework for 30 epochs, using AdamW with a learning rate of 1×10^{-4} as optimizer.

2.3 Validation of the model outputs

The resulting model was then validated using two recent CEMS RM wildfire activations, namely EMSR675 and EMSR674, which were not included in the machine learning process. EMSR674 pertains a fire which broke out near Kallithea village on the afternoon of July 17, 2023. The fire, classified as Extreme Danger according to the Fire Danger Forecast (EFFIS), caused significant damage to residences in nearby villages. Around 1,200 ha of land burned, and 500 people were potentially affected. (Copernicus Emergency Management Service, 2023b). Similarly, EMSR675 concerns a wildfire that started on the afternoon of July 18, 2023, in a forested area on the island of Rhodes. The fire also classified as Extreme Danger, spiraled out of control, resulting in the destruction of dense pine tree and cypress forests, along with wildlife habitats. Around 17,774 ha of land burned, and 750 people were potentially affected. (Copernicus Emergency Management Service, 2023c).
To carry out our validation tests, we retrieved the Sentinel-2 images of the selected RM activations using the SentinelHub service (SentinelHub, 2023). We exploited the ground truth polygon bounds as spatial delimiter, extracting the satellite acquisition with the least amount of cloud coverage in the weeks following the event. We then generate a full-size prediction by tiling with fixed overlap in smaller crops with size 512x512 pixels and recomposing the original shape via interpolation across tiles.
We tested the algorithm on the selected areas using macro-averaged F1 score and Intersection over Union (IoU), also known as Jaccard index, computed as:

$$F1 = 2 * \frac{precision * recall}{precision + recall} \qquad IoU = \frac{|A \cap B|}{|A \cup B|}$$

where, A and B represent the predicted mask and the ground truth delineation respectively. Intuitively, a good degree of overlap between them will produce a high IoU score. Given the focus on rapid and effective delineation, we also evaluate the total amount of time required to provide the complete delineation. This includes the preparation of the inputs, subdividing the input image in overlapping tiles, the inference time itself, and the reconstruction time to recompose the full inference from the tile prediction, as detailed in the following section.

3. RESULTS AND DISCUSSIONS

Table **1** displays the results of the validation tests: F1 and IoU scores, computed over the final predictions with respect to the original EMS activation, as well as the total number of seconds required to generate the complete inference.
Considering the EMSR674 activation, we achieve a F1 score of 94.50 and 89.57 of IoU, showing a high degree of agreement between human annotation and automated output. Additionally, the inference time for this activation was relatively low at 13.92 seconds.
In the case of EMSR675, the results were even higher in terms of accuracy, with an F1 score of 96.57. This reflects the model's precision in identifying burned areas, as well as its robustness to different geographical conditions. The inference time was relatively higher, at 221.04 seconds, probably due to the larger area that was interested by the fire, i.e. around 20,000 ha. While the algorithm demonstrates good performance, providing high-quality delineations in different settings, it's important to note that it may not yet match the precision of a human annotator. Nevertheless, the notable advantage of the machine learning approach lies in its automated processing and significantly faster processing capabilities. This trade-off between precision and speed makes it a valuable tool, especially in scenarios where timely responses are critical.

Activation	F1	IoU	Inference Time (s)
EMSR674	94.50	89.57	13.92
EMSR675	96.57	93.37	221.04

Table 1. Results obtained on the selected activations in terms of F1 and IoU scores, and the required inference time in seconds.

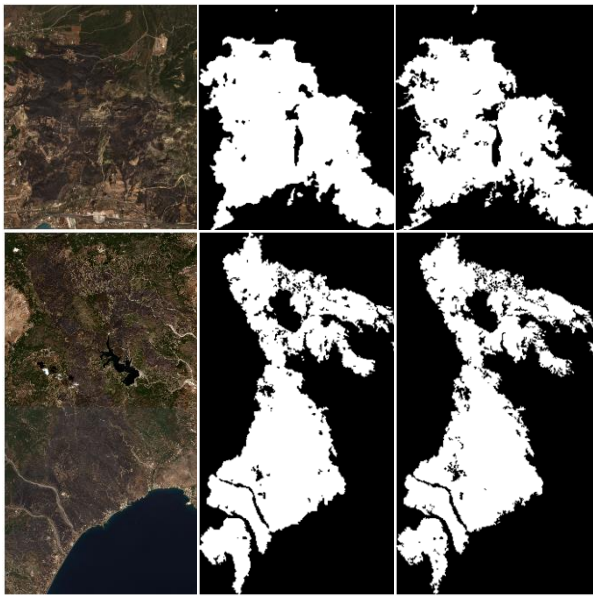

Figure 3. Qualitative results obtained from the model validation on the selected areas. From left to right: Sentinel-2 RGB composite, model prediction, CEMS RM reference data.

4. CONCLUSIONS

This work presents current progresses in Earth Observation and AI components of the OVERWATCH system, focusing on automated burned area assessment. By exploiting several data sources such as Copernicus EMS and EFFIS, we generated a training dataset from Sentinel-2 images to train a delineation model on historical wildfire events and validating the results with respect to two recent CEMS RM wildfires activations. The performed validation tests were run to assess 1) the model' precision in identifying burned areas, i.e. the degree of agreement between human-made annotation and automated model, and 2) the time required to provide the complete delineation of the two events.

Preliminary obtained results showed high values of both F1 and IoU scores, representative for model' precision in burned area delineation, as well as for the inference time (13.92 seconds for EMSR674 and 221.04 for EMSR675) that the model spent to generate the automated outputs. With reference to the specific context of CEMS RM data processing, where timing is a pivotal element, these first results are very promising.

Next steps of the work will be to provide the same AI-based approach also for flood events assessment, as foreseen by the OVERWATCH project proposition. Moreover, different kind of EO optical data (e.g. VHR data) will be used to train the machine learning model, accordingly adapted depending on the type of data to be used as input data for the training process.

REFERENCES

Arnaudo et al., 2023. Robust Burned Area Delineation through Multitask Learning. Conference on Machine Learning and Principles and Practice of Knowledge Discovery in Databases 2023. Preprint: https://arxiv.org/abs/2309.08368v1

Copernicus Emergency Management Service, 2023a. What is Copernicus. https://emergency.copernicus.eu/mapping/ems/what-copernicus (3 October 2023)

Copernicus Emergency Management Service, 2023b. Wildfire in Eastern Peloponnese Region, Greece – EMSR674 – Situational reporting, August 4, 2023. https://rapidmapping.emergency.copernicus.eu/EMSR674/reporting

Copernicus Emergency Management Service, 2023c. Fire in Rhodes, Greece – EMSR675 – Situational reporting, August 4, 2023. https://rapidmapping.emergency.copernicus.eu/EMSR675/reporting

Copernicus Sentinel-2 (processed by ESA), 2021. MSI Level-2A BOA Reflectance Product, collection 1. European Space Agency. https://doi.org/10.5270/S2_-6eb6imz

Joint Research Center, 2023. The EU 2022 wildfire season was the second worst on record. JRC portfolios, Crisis management. https://joint-research-centre.ec.europa.eu/jrc-news-and-updates/eu-2022-wildfire-season-was-second-worst-record-2023-05-02_en

Keeley, J. E., 2009. Fire intensity, fire severity and burn severity: a brief review and suggested usage. *International Journal of Wildland Fire*, 18(1), pp. 116-126. https://doi.org/10.1071/WF07049

Key, C.H., Benson, N.C., 2006. Landscape Assessment (LA) sampling and analysis methods. USDA Forest Service - General Technical Report RMRS-GTR, 164 RMRS-GTR.

Milicevic, V., 2023. European Parliament, Fact Sheets on the European Union: The Common Agricultural Policy in figures. https://www.europarl.europa.eu/factsheets/en/sheet/104/the-common-agricultural-policy-in-figures

QGIS.org, 2023. QGIS Geographic Information System. Open Source Geospatial Foundation Project. http://qgis.org

SentinelHub, 2023. Cloud API for Satellite Imagery. https://www.sentinel-hub.com/ (29 October 2023)

World Bank, 2021. Investment in Disaster Risk Management in Europe Makes Economic Sense: Background Report. https://doi.org/10.1596/35686

Xiao, Tete, et al. "Unified perceptual parsing for scene understanding." Proceedings of the European conference on computer vision (ECCV). 2018. ECCV 2018 Open Access Repository (thecvf.com)

ASSESSING GLACIER EXTENT CHANGES THROUGH MACHINE LEARNING ALGORITHMS AND REMOTE SENSING DATA

D. Lisi[1], L. Ranaldi[2], A. La Rocca[1], M. Frigerio[1], D. Sanmartino[1], P. Boccardo[2]

[1] Ithaca S.r.l Via Pier Carlo Boggio 61, 10128, Torino (TO) , Italy
davide.lisi@ithacaweb.org
[2] Geodesy and Geomatic area, La Sapienza University, Roma (RO), Italy
lorenza.ranaldi@uniroma1.it
[3] DIST - Interuniversity Department of Regional and Urban Studies and Planning, Politecnico of Turin, Torino (TO), Italy;
piero.boccardo@polito.it

KEY WORDS: Glaciers, Machine Learning, OS HR satellite data, segmentation models, changes prediction

ABSTRACT:

Glaciers are critical elements in the Earth's climate system. Understanding and monitoring glacier extent changes is critical to informing climate policies, assessing natural hazards, and safeguarding global water resources. Remote sensing technologies are proven and widely adopted sources of information in this sense. The proposed study aims to develop a forecasting model able to predict future changes in glacier and snow extent, using supervised machine learning algorithms applied to open access data, including HR satellite data of the EU Copernicus program. Two machine learning models are developed. The first model is a segmentation model that employs a U-Net architecture to digitalize glacier features from satellite images. The purpose of the segmentation model is to expand the dataset required by the forecasting model, in terms of glacier surface values. This dataset is generated using the segmentation model previously trained, applied to multiple glaciers, spanning a 30-year period and a consistent seasonal interval. The second model is a multivariate forecasting model that seeks to identify the relationships between Land Surface Temperature (LST) and glacier/snow extent. Both models are validated on testing data to assess their generalization capabilities and their performance on real-world cases. A subset of the segmentation dataset is kept aside to extrapolate metrics such as the Intersection-Over-Union (IoU). For the forecasting model, error metrics such as the Root-Mean Squared Error (RMSE) are considered to assess the model performance.

1. INTRODUCTION

Glaciers are a crucial component of the Earth's cryosphere, covering approximately 11% of the planet's land surface and holding around 69% of its total freshwater (Gleick, 1996).
They are sensitive indicators of climate change, and the significant increase in global temperatures resulting from human-induced climate change has profoundly affected glaciers worldwide (Li et al., 2023). Melting glaciers, a result of human-induced climate change, have far-reaching consequences. They disrupt water availability, affecting downstream ecosystems and communities dependent on glacial meltwater for drinking water, agriculture, and hydropower (Kaser et al. 2010). Changes in water flow patterns and nutrient availability lead to biodiversity loss, resource conflicts, community displacement, and ecological disturbances (Losapio et al. 2021). The European Alps stands out as one of the regions experiencing the most significant glacier shrinkage. Seasonal observations conducted by Glacier Monitoring Switzerland (GLAMOS) reveal that Alpine glaciers began the year 2018 with a snow cover up to 50% thicker compared to the period from 1961 to 1990. However, the exceptionally long, warm, and sunny summer transformed the year into yet another one characterized by extreme loss of glacier mass in this region (Copernicus Climate Change Service, 2018). Accurately monitoring changes in glacier extent is of utmost importance for informing climate policies, assessing natural hazards, and safeguarding global water resources. Remote sensing technologies have emerged as a proven and widely embraced source of information. Satellite imagery and other techniques offer scientists the means to acquire detailed data on glacier extents. With the ability to gather data over vast and inaccessible regions, remote sensing enables a more comprehensive understanding of glacial processes. It provides a continuous and long-term monitoring capability, facilitating the detection of subtle changes and trends in glacier behaviour. Moreover, the integration of artificial intelligence methodologies has immense potential to enhance and automate knowledge extraction from large datasets, allowing for the extraction of valuable insights from Earth Observation data. Within this context, the objective of this study is to formulate and apply a preliminary methodology employing two machine learning models: an image segmentation model and a multivariate block recurrent neural network model (RNN). The aim is to predict changes in glacier extents and snow coverage in the coming years by leveraging publicly available data, specifically optical satellite imagery and land surface temperature (LST) measurements. By harnessing these readily accessible data sources, this research seeks to establish a preliminary framework that can contribute to improving our understanding of the impacts of climate change on glaciers.

2. MATERIALS AND METHODS

2.1 Study area and data collection

The European Alps were chosen as the study area due to the significant shrinkage observed in the recent decades. The study focused on 13 alpine glaciers: Dei Forni, Adamello, Morteratsch, Tschierva, Del Forno, Ventina, Aletsch, Gorner, Findel, Geant, Corbassiere, and Trient glaciers, as shown in Figure 1. These regions were defined using the Global Land Ice Measurements from Space (GLIMS) database, which provides georeferenced extents of glaciers worldwide across different measurement dates (Raup et al., 2007). These extents served as references for collecting publicly available satellite data. To

* Corresponding author

Figure 1. Localization in the Alpine region of the glaciers considered in this study.

cover a time span of at least 30 years, from 1990 to 2022, data from Landsat-5 (TM), Landsat-7 (ETM+), Landsat-8 (OLI) Level 2 collections, and Sentinel-2 collection 1 were gathered. This data was collected using the open-access Copernicus HUB portal for Sentinel-2 and the USGS EarthExplorer portal for Landsat (European Space Agency, 2023)(United States Geological Survey, 2023). Glacier images were acquired during the summer period, primarily in August and September to minimize snow coverage. In cases of limited image availability due to excessive cloud cover, July and June were also considered. Additionally, data on Land Surface Temperature (LST) spanning from 1995 to 2022 was collected, with the primary source being the ESA Land Surface Temperature Climate Change Initiative (LST_CCI) (Ghent et al., 2022). To train the segmentation model, the Hindu Kush Himalayas glacier mapping dataset was employed, which includes imagery and glacier location polygons for the Hindu Kush Himalayas region, serving as ground truth (Baraka et al., 2020).

2.2 Automatic classification of glaciers

In the field of digital image processing, image segmentation refers to the task of dividing a digital image into distinct regions, comprising sets of pixels (Shih, 2009). The primary objective of segmentation is to assign a label to each pixel based on shared characteristics among pixels with the same label. In this study, we focus on automating the digitization of a specific class of interest: glaciers and areas covered by snow and ice as well. This enables swift computation of the extents, facilitating the creation of multiple time series, which serve as input for the forecasting multivariate block RNN model. To achieve this objective, the adopted approach was to use a U-Net architecture (Ronneberger et al., 2015). The U-Net was trained on the Hindu Kush Himalayas dataset, which is based on Landsat 7 images, employing a composite of bands consisting of Shortwave Infrared (1.55-1.75 µm), Near-Infrared (0.77-0.90 µm), and Red (0.63-0.69 µm). This combination of bands facilitates more accurate segmentation of icy and snowy features. Additionally, we also developed an automatic procedure based on two spectral indices, defined as follows:

$$\left(\frac{SWIR-NIR}{SWIR+NIR} < t_1 + \frac{RED-NIR}{RED+NIR} > t_2\right) > 0 \quad (1)$$

Empirical thresholds, denoted as t_1 and t_2, were established individually for each satellite. Specifically, for Landsat, the values selected were 0.021 for t_1 and -0.24 for t_2, while for Sentinel-2, the chosen thresholds were 0.065 for t_1 and -0.35 for t_2. The selection process for these thresholds was suboptimal, relying on empirical methods. Therefore, it would be advantageous in future research to devise an automated procedure for optimizing threshold definitions. The AI-based and the spectral indices solutions were implemented together, to improve the overall effectiveness of the classification. The procedure was implemented into a QGis plugin, which was extensively used to compute the extent of glaciers and snowy areas on the satellite images which were previously collected for the study area. The same composition of bands, namely SWIR-NIR-RED, was considered, to ensure consistency throughout the analysis process. An example of a classification output, for the Aletsch glacier, is displayed in figure 2. The model seems to be able to accurately detect regions heavily covered by snow as well as regions covered by mixtures of debris and ices.

2.3 Multivariate Block Recurrent Neural Network Model

In addition to generating the time series of ice and snow extents through the automatic classification tool, time series for the LST of each region were also computed. These LST values were calculated as averages over the four summer months (June, July, August, September) of each year, as well as the spatial average within each respective region. To streamline this process, another dedicated QGIS plugin was developed specifically for this task. As there was no available data prior to 1995, values up to 1990 were linearly extrapolated. The resulting time series of LST served as the past covariate in the forecasting model. Both the extents of glaciers/snow and LST time series were normalized with respect to the 1990 values, for each considered region.

The forecasting model employed is based on a Block Recurrent

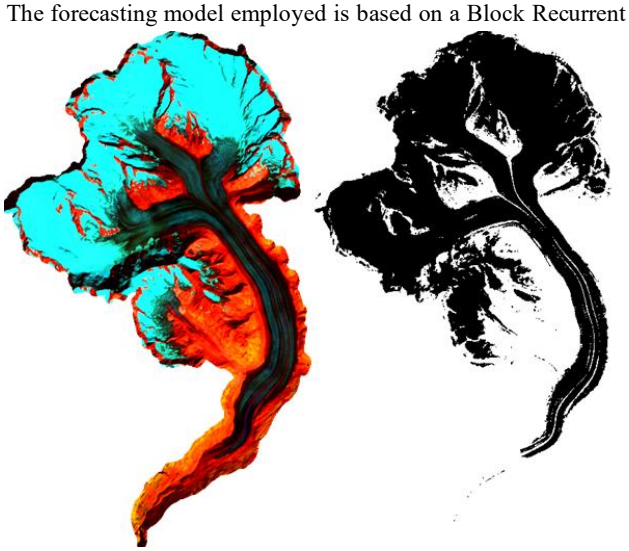

Figure 2. Output example of the classification model, for the Aletsch glacier (image acquired the 30/08/2015)

Neural Network architecture. This neural network model utilizes an RNN encoder to encode fixed-length input chunks and a fully connected network to generate fixed-length outputs, while also incorporating past covariates. Considering the relatively limited time considered (approximately 30 years), the model was designed with an input chunk length of 20 and an output chunk length of 10. Two recurrent layers were utilized, and the model was trained for 550 epochs using a stochastic approach. A key distinction between probabilistic models and their deterministic counterparts lies in their approach to future predictions. Instead of directly predicting future values, probabilistic models estimate parameters of a given distribution that describe the likelihood of observing future values. In this study, a normal distribution was considered. Consequently, our model's predictions include a confidence interval defined by the 0.05 and 0.95 quantiles of the sampled time series in addition to the median, which represents the most likely observed time series.

3. RESULTS

3.1 Classification model validation

The U-net model was defined with a resnet101 backbone and trained for 300 epochs, minimizing a Binary Cross Entropy (BCE) loss function and a Dice loss function. The resulting mean value of Intersection-over-Union (IoU) on the training test was around 83.9%, which is an reasonable result considering the state of the art (Minaee et al., 2022). The IoU metric evaluates the overlap of the Ground Truth and Prediction regions, as defined as follows:

$$IoU = \frac{TP}{TP+FP+FN} \quad (2)$$

Where TP, FP and FN stand for true positive, false positive and false negative respectively. To improve the results, different and more modern architectures with different backbones are expected to be employed in future studies.

3.2 Forecasting model validation

The forecasting model was trained using 70% of the generated dataset, while the remaining portion was reserved as the validation dataset. To assess the model's performance, backtests were conducted on both the training and testing samples, and the root-mean-squared error (RMSE) metric was computed. RMSE is a measure of the differences between the model's predicted values and the observed values. It is always positive and dependent on the scale of the data, but it provides valuable insights into the accuracy of trained models. The RMSE is defined as follows:

$$RMSE = \sqrt{\frac{\sum_{i=1}^{N}(\hat{y}_i - y_i)^2}{N}} \quad (3)$$

Region	RMSE (no LST)	RMSE (with LST)
Training sample		
Dei Forni	0.090	0.089
Morteratsch	0.057	0.047
Tschierva	0.029	0.071
Del Forno	0.083	0.134
Ventina	0.088	0.066
Aletsch	0.087	0.058
Gorner	0.052	0.043
Findel	0.061	0.039
Corbassière	0.078	0.045
Trient	0.158	0.143
Average	0.078	0.073
Validation sample		
Adamello	0.035	0.041
Argentiere	0.144	0.090
Geant	0.137	0.081
Average	0.105	0.071

Table 1. Root-mean-squared error (RMSE) computed for each region, with and without using the LST time series as past covariate.

The RMSE was computed for each region with and without implementing the LST time series as past covariate. The results are collected in Table 1.
While the inclusion of the LST time series as a past covariate resulted in a slight improvement in the RMSE values for most regions, this improvement was relatively modest. It may be worth exploring, in the future, the potential effectiveness of other covariates, such as precipitations and elevation, which may yield more significant improvements in forecasting accuracy. Furthermore, it is important to note that the RMSE values obtained are only approximately one order of magnitude smaller than the actual relative changes in glacier and snow extent. This suggests that further improvements are needed to enhance the accuracy of the model. These improvements could

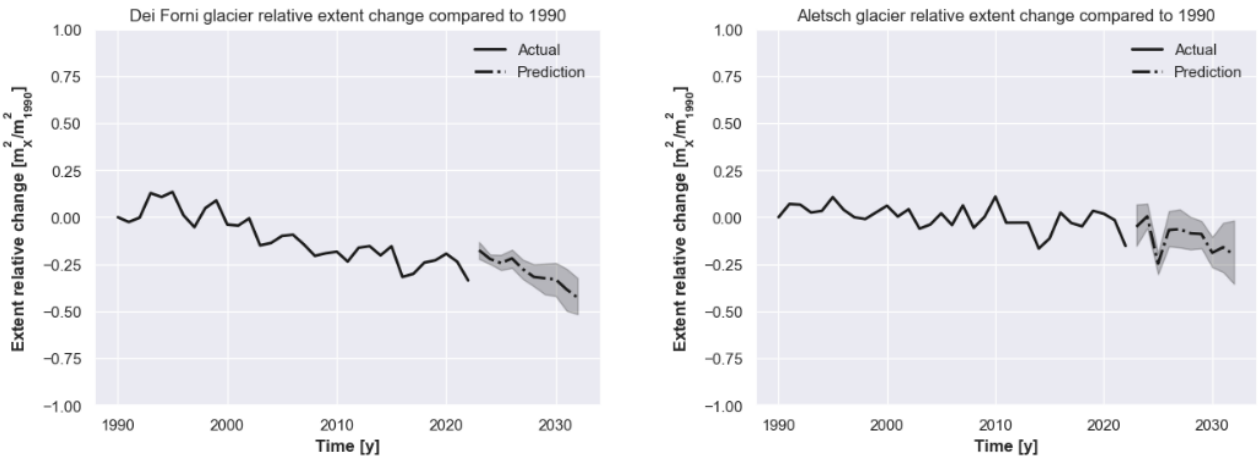

Figure 3. Comparative changes in glacier and snow extent relative to 1990, along with a 10-year projection for the Dei Forni glacier (left) and the Aletsch glacier (right).

be achieved by incorporating additional and more effective covariates, as well as expanding the dataset to include a broader range of regions and longer time periods.

3.3 Forecasts

Finally, the trained block RNN model was used to predict the evolution of the relative extent changes compared to 1990 for the next 10 years. Most glaciers follow, with some oscillations, an overall decreasing trend, which is in line with the expectations. Some significant examples are reported in this document. Figure 3 shows the forecast obtained for both the Dei Forni glacier and the Aletsch glacier. The Dei Forni glacier has seen significant and continuous shrinkage in the last decades, and the model predicts that the trend will steadily continue in the next 10 years. On the other hand, the Aletsch glacier is the region, among the studied ones, displaying the least amount of retreat in the last 30 years. Also in this case, the prediction obtained appears consistent with the observed past trend.

4. CONCLUSIONS

This study aimed to develop a preliminary methodology for predicting glacier extent changes using remote sensing and machine learning techniques. The methodology was applied to glaciers in the European Alps. The study involved the development of an image segmentation U-Net model, enhanced by the analysis of two spectral indices, for classifying glaciers and snow-covered areas. The classifier performed well, but in the future, exploring more modern and improved architectures could result in even better segmentation results. Additionally, a multivariate block recurrent neural network (RNN) model was developed to forecast glacier extent changes, with land surface temperature as a covariate. The RNN model's performance was evaluated using the root-mean-squared error (RMSE) metric, while the U-Net model was evaluated using the Intersection-over-Union (IoU) metric. The results indicated that including land surface temperature as a covariate very slightly improved the RNN model's performance, but further enhancements are necessary for higher accuracy. Exploring other covariates, such as precipitations for each year, and elevation, may lead to better forecasts. The trained RNN model predicted the relative extent changes of glaciers compared to 1990 for the next 10 years, revealing a decreasing trend consistent with historical observations. However, more research is needed to enhance the models by incorporating additional covariates and expanding the dataset both spatially and temporally Thankfully, expanding the dataset spatially will be straightforward, as the biggest strength of this methodology resides in the capability of expanding the forecasting dataset very rapidly, thanks to the automatic classifier. On the other hand, obtaining data for earlier years presents more challenges, but temporal expansion can still be achieved by broadening the dataset to include data points beyond the summer period.

REFERENCES

Baraka, S., Akera, B., Aryal, B., Sherpa, T., Shresta, F., Ortiz, A., Sankaran, K., Ferres, J.L., Matin, M., Bengio, Y., 2020. Machine Learning for Glacier Monitoring in the Hindu Kush Himalaya. NeurIPS 2020 Workshop on Tackling Climate Change with Machine Learning
https://www.climatechange.ai/papers/neurips2020/57

Copernicus Climate Change Service, 2018. European State of the Climate 2018, Alpine glaciers
https://climate.copernicus.eu/alpine-glaciers (11 September 2023).

European Space Agency – ESA, 2023. Copernicus Open Access Hub.
https://scihub.copernicus.eu/

Ghent, D., Veal, K., Perry, M., 2022. ESA Land Surface Temperature Climate Change Initiative (LST_cci): Monthly Multisensor Infra-Red (IR) Low Earth Orbit (LEO) land surface temperature (LST) time series level 3 supercollated (L3S) global product (1995-2020), version 2.00. NERC EDS Centre for Environmental Data Analysis, 2022.
https://dx.doi.org/10.5285/785ef9d3965442669bff899540747e28

Gleick, P.H., 1996. Water Resources. In: *Encyclopedia of Climate and Weather*, Schneider, S.H., Ed., Oxford University Press, New York, Vol. 2, pp. 817-823.

Kaser, G., Großhauser, M., Marzeion, B., 2010. Contribution potential of glaciers to water availability in different climate regimes. *Proceedings of the National Academy of Sciences of the United States of America*, 107(47), pp. 20223–20227.
https://doi.org/10.1073/pnas.100816210

Li, J., Xu, X., 2023. Glacier Change and Its Response to Climate Change in Western China. *Land*, 12(3), pp. 623.
https://doi.org/10.3390/land12030623

Losapio, G., Cerabolini, B. E. L., Maffioletti, C., Tampucci, D., Gobbi, M., Caccianiga, M., 2021. The Consequences of Glacier Retreat Are Uneven Between Plant Species. *Frontiers in Ecology and Evolution*, Vol. 8.
https://doi.org/10.3389/fevo.2020.616562

Minaee, S., Boykov, Y., Porikli, F., Plaza, A., Kehtarnavaz, N., Terzopoulos, D., 2022. Image Segmentation Using Deep Learning: A Survey. *IEEE Transactions on Pattern Analysis & Machine Intelligence*, 44(7), pp. 3523-3542.
https://doi.org/10.1109/TPAMI.2021.3059968

Raup, B.H., Racoviteanu, A., Khalsa, S.J.S., Helm, C., Armstrong, R., Arnaud, Y., 2007. The GLIMS Geospatial Glacier Database: a New Tool for Studying Glacier Change. *Global and Planetary Change*, 56(1-2), pp. 101-110.
https://doi.org/10.1016/j.gloplacha.2006.07.018

Ronneberger, O., Fischer, P., Brox, T., 2015. U-Net: Convolutional Networks for Biomedical Image Segmentation. In: Navab, N., Hornegger, J., Wells, W., Frangi, A. (eds) Medical Image Computing and Computer-Assisted Intervention – MICCAI 2015. MICCAI 2015. Lecture Notes in Computer Science(), vol. 9351. Springer, Cham.
https://doi.org/10.1007/978-3-319-24574-4_28

Shih, F.Y., 2009. Image Segmentation. In: *Encyclopedia of Database Systems*. Springer, Boston, MA, pp. 1389-1395.
https://doi.org/10.1007/978-0-387-39940-9_1011

United States Geological Survey – USGS, 2023. EarthExplorer.
https://earthexplorer.usgs.gov/

DIGITAL TWIN PROTOTYPE OF THE ALPS: PRELIMINARY CONSIDERATIONS AND 3D MODEL GENERATION USING OPEN-SOURCE SATELLITE HR DATA

L. Ranaldi[1], D. Lisi[2], V. Fissore[2], L. Bovio[2], P. Boccardo[3]

[1] Geodesy and Geomatic area, La Sapienza University, Roma (RO), Italy
lorenza.ranaldi@uniroma1.it
[2] Ithaca S.r.l., Via PierCarlo Boggio 61, 10128, Torino , Italy
(davide.lisi, vanina.fissore, lorenza.bovio)@ithacaweb.org
[2] LINKS Foundation, Turin, Italy
[3] DIST - Interuniversity Department of Regional and Urban Studies and Planning, Politecnico of Turin, Torino (TO), Italy;
piero.boccardo@polito.it

KEY WORDS: Digital Twin, Alps, 3D Models, OS HR satellite data, DEM

ABSTRACT:

The Alpine Region, spanning across several European countries, holds great significance due to its diverse natural, historical, and cultural aspects. Recognizing the Alpine Region's importance, it's crucial to manage and preserve its heritage. Digital Twin (DT) technology is utilized for monitoring and managing complex systems, which encompass aspects such as biodiversity, climate, and land use. DTs create high-precision digital replicas of Earth's systems, which can be continuously updated with Earth Observation (EO) data and in-situ measurements. This work aims to present some preliminary considerations about a DT prototype of Italian Alps, and to create one of the basic element for such a DT: the 3D model of the Italian Alps, only relying on open-access high-resolution satellite data and freely available DEMs. With specific reference to 3D model generation, the goal was to create two 3D models for different seasons (one for autumn/winter and one for spring/summer seasons) while minimizing seasonality effects and cloud cover issues, incorporating multi-spectral Sentinel-2 optical images and 10m spatial resolution DEMs from INGV (Istituto Nazionale di Geofisica e Vulcanologia). Multi-spectral images allow for thematic 3D models characterizing of vegetation, water bodies, lithotypes, etc. The data were processed by using open source software (e.g. QGIS for raster handling and CloudCompare for the generation of the point clouds). Some considerations about the limits and potentialities of the adopted open source data, and about the enabled applications coming from the seasonal models, are also presented. Despite some identified limitations, these 3D models offer interesting approaches for the monitoring of natural ecosystems and for potential innovative analysis.

1. INTRODUCTION

The Alpine Region holds significant importance in the European context because of its distinctive and diverse natural, historical, and cultural attributes. Spanning several countries, including France, Italy, Switzerland, Liechtenstein, Austria, Germany, and Slovenia, its central location has fostered cultural diversity and richness. In fact, human-nature coexistence in the Alps traces its origins back to around 7800 BC (Kutschera et al., 2014). This region also features natural attractions like glaciers, lakes, waterfalls, and mountain peaks. Recognizing the significance of the Alpine Region, it becomes imperative to effectively manage and safeguard its natural and cultural heritage. To accomplish this objective, harnessing innovative technologies becomes essential. Specifically, leveraging Digital Twin (DT) technology can facilitate the monitoring and management of natural processes, encompassing biodiversity, climate, and land use. In the digital space, a DT is a virtual representation of a complex physical asset, created with the aim of closely characterizing the operations of the original physical process or system (Grieves, 2014). The advantages of DT technology, which enables the execution of what-if analyses in the digital realm, are already manifesting in various applications, encompassing high-value manufacturing industries, personalized medicine, oil refinery management, as well as risk identification and urban planning (Thelen et al., 2022).

Within the realm of earth science, DT represents an approach to constructing a precise digital replica of the Earth's systems and processes. A further definition considers the DT as a combination of three different parts: the physical entities, the digital representation, and the connection between the physical and digital entities (El Saddik, 2018). Thus, the DT is not just a mathematical 3D model of a complex environment, but it is strictly connected to it by specific relationships. To support the realization of these innovative models, the European Commission introduced the Destination Earth (DestinE) initiative to create, by year 2030, a very high precision digital model of the whole Earth, to interactively explore the various natural processes and human activities that ordinarily take place on our planet (European Commission, 2020). The initiative should contribute to achieving the objectives of the twin transition, as part of the European Commission's Green Deal and Digital Strategy. On the wave of DestinE, the scientific community started to delineate theoretical frameworks of reference for digital replicas (DTs) related to different earth science applications. This is a necessary starting point because, depending on the selected application/earth science domain, the information provided by the relative DT changes. A DT, in fact, is use case driven (EC, 2020) and consequently it is fed by diverse input data. These theoretical frameworks, which refer to potential prototypes of DTs, provide the identification and definition of the needed elements that a DT must contain to provide a reliable digital representation of the selected physical entity to be replicated. Specifically, such framework delineations were proposed for a forest digital twin (Buonocore L. et al. 2022), and for a DT prototype for Alpine glaciers monitoring (Fissore V. et al. 2023).

Given the considerable focus on these themes, this work aims to establish initial considerations as a step toward accomplishing the wider goal of developing a model at Italian Alpine level. This model will aim to pave the way for new opportunities in supporting continuous monitoring of Alpine natural ecosystems and generating innovative analyses and assessments. Since DestinE should be built upon already existing data and

* Corresponding author

capabilities provided by the EU and national and international institutions (*e.g.,* European in-situ data coordination by EEA), and upon European excellence programmes (*e.g.,* Copernicus services and data) (ESA, 2022), the here proposed model is based on open-source HR satellite data, open-source elevation data and open-source software for data processing. Moreover, the adoption of open-source data as input data to feed the proposed Italian Alpine DT, guarantees that the data can be easily reviewed and implemented by any user.
Finally, this approach permitted to focus on and to underline the limits and potentialities deriving from the adoption of current available open source data.

2. MATERIALS AND METHODS

2.1 Data collection

The study area for the current research pertains to the Italian Alpine Region, encompassing the entire mountainous northern region of Italy. To define the borders of the interested area, the SOUISA (Suddivisione Orografica Internazionale Unificata del Sistema Alpino - International Standardized Mountain Subdivision of the Alps) was consulted. The classification was formulated by Italian researcher Sergio Marazzi with the aim of standardizing and normalizing the original classification of the Alpine Region, which was established in the early 19th century (Marazzi, 2005). By consulting the SOUISA, it became feasible to delineate the portion of the Alpine Region classified under Italian administration. However, it's important to note that this entails considering only a segment of the mountainous terrain that extends across various territorial boundaries.
The study focused on employing two distinct products, namely the Digital Elevation Models (DEM) and HR optical satellite imagery.
Regarding the DEMs, the study utilized the most recent and updated dataset released in January 2023 by the INGV (Istituto Nazionale di Geofisica e Vulcanologia) (Tarquini et al., 2023). This dataset comprises a mosaic of DEMs with a spatial resolution of 10 meters, encompassing the entirety of Italy. The model was generated through the integration of different data, i.e. Technical Cartography, GPS, and Airborne laser-scanner altimetry data available on the Italian territory. This data was collected by the Italian Ministry of the Environment, the Italian Regions and Provinces, the River Basin Authorities and IGM (Tarquini et al., 2007). For the analysis, the DEMs specific to the Italian Alpine Region were chosen, adhering to the borders delineated by the SOUISA. These altimetric data were employed directly, as they had already undergone pre-processing procedures, including filtering, classification, and regularization.
Concerning the optical satellite images, multi-spectral Sentinel-2 (S2) (L2A products) optical images sourced from the open-access Copernicus HUB were employed (ESA, 2023). These images were chosen to cover distinct time periods, considering that, as an initial prototype, the primary objective was to construct 3D models for both the winter and summer seasons of 2022. Consequently, the selected images corresponded to the following timeframes: December 31, 2021, to February 28, 2022, for the winter season, and June 1, 2022, to September 16, 2022, for the summer season.
Furthermore, the choice of S2 images prioritized those with minimal cloud cover, aiming for less than 5%. Despite these efforts, variations in weather and lighting conditions introduced some discrepancies among the images, impacting the uniform resolution of the final model.

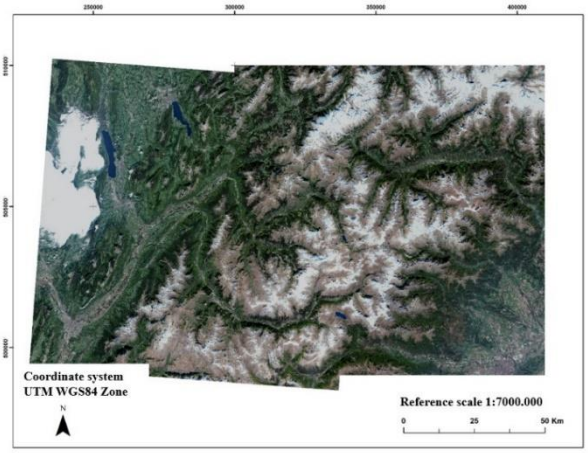

Figure 1. Example of adopted S-2 image (10m GSD) over the Alpine Region, RGB composite bands.

2.2 3D models generation

The entire 3D models creation process can be divided into three main steps.
First, an essential dataset organization phase was undertaken. Given that the model covered the entire Italian Alpine Region, a huge amount of S2 images needed to be selected. To effectively manage this data, it became necessary to sort the images into various folders. This approach was adopted to facilitate the creation of both real-color and false-color models, capitalizing on the extensive band options offered by the Sentinel-2 images.
The dataset was structured to first incorporate the bands associated with the natural color combination: red (B4), green (B3), and blue (B2). Subsequently, it was organized to utilize another combination comprising Short Wave Infrared - SWIR (B11), Visible and Near Infrared - VNIR (B8A), and red (B4). This strategic arrangement allowed for detailed recognition of natural systems such as glaciers and various types of vegetation.
It's worth noting that when downloading images from the Copernicus HUB, it is often required to request the selected products since they were frequently offline from the catalogue. This introduced variable delays in accessing the images. As for the altimetric data, the INGV DEMs were obtained as individual small raster files, each covering a specific area of interest. To create a unified model, these raster files were merged together.
The second phase of the work involved processing the previously organized data using the open-source software QGIS (QGIS, 2023). To simplify the analysis and reduce numerical computational costs, the study area was divided into five larger regions. For each of these regions, the corresponding optical images were carefully selected and merged to create a single image mosaic specific to that area. The chosen bands combination was also taken into account.
Subsequently, both the DEM and the mosaic images were clipped using a polygon mask of identical size to the region under examination. This process yielded two products with matching extents but offering distinct information about the surveyed territory. To streamline this procedure across all five regions and adapt it to the varying areas of interest, a QGIS plugin was developed for automation, facilitating efficient data processing.
Subsequently, in the third step of the process, digital models were generated using the open-source software CloudCompare (CloudCompare, 2023). This software was chosen because of its capability to manage various data sources and integrate the information derived from them. It offers a range of fundamental tools for manually editing and rendering 3D point clouds and triangular meshes.

In this context, the two products resulting from the processing in QGIS were extracted as raster files and imported into CloudCompare as point clouds. Since both entities had identical extents, it became possible to merge color texture and altimetric data to create the 3D model. The software features a specific tool for this purpose called "Interpolate from another entities," which, for each point in the selected cloud, identifies the nearest point in the other entity and extracts its color. This straightforward operation yields a point cloud containing both altimetric and georeferenced data. Moreover, it allows for territorial analysis by leveraging the texture derived from the satellite images.
After completing the entire model production steps, specific analyses related to texture' interpretation were then conducted over the 3D models to fully leverage the potential information derived from each of them. For this particular case, the administrative area of the municipality of Courmayeur, including the Italian part of Monte Bianco, was chosen.

3. RESULTS AND DISCUSSION

Two 3D models for the Italian Alpine Region were at the end created, one representing the summer season and one for the winter season, with reference to year 2022, as illustrated in Figure 2.

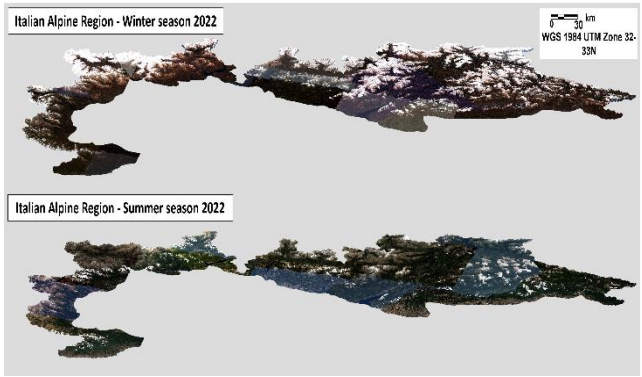

Figure 2. 3D models for the Italian Alpine Region, in winter (top), and summer (bottom).

As previously mentioned, a specific area corresponding to the municipality of Courmayeur, was chosen to perform some further interpretation analysis. Three different composite bands of the same area were obtained to test possible varying insights of the terrain (see Figure 3): RGB color (left), false color (B11-B8A-B4) (middle), slope terrain (right).

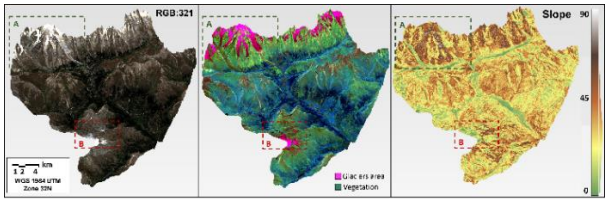

Figure 3. 3D models of Courmayeur area with different representations: true color (left), false color as B11-B8A-B4 (middle), terrain slope (right).

Notably, the slope terrain representation (right side) specifically addresses variations in the terrain, also underlying different slope conditions, as solely derived from elevation data. However, if only this model is examined, limited observations can be made: it is possible to differentiate between mountains and flat areas, but identifying glacier formations, for instance, is not as straightforward. Conversely, when incorporating the information of the true-color representation (left), along with the particular combination of color bands, the terrain morphology becomes easily discernible. For an easier interpretation, two areas have been identified: A area in the upper left corner, in grey color, and B area, in the bottom centre, in red color. For instance, in A area, numerous glacial tongues alternate with debris and moraine-covered regions. These distinctions are challenging to be noted solely relying on the slope model, and the supporting information coming from the texture models helps with an enhanced readability of such morphological features.
Moreover, considering B area, one might mistakenly interpret it as hilly or lowland terrain. Yet, when examining the first two models, the presence of the Rutor glacial complex, one of the largest in the Aosta Valley, becomes evident.
In order to test some other potential applications, the two seasonal models (winter vs. summer models) were compared for the same area. The performed tests allowed for the estimation of the change rate in snow and ice coverage along season variation. To this end, Figure 4 depicts the same area during winter (top) and summer (bottom).

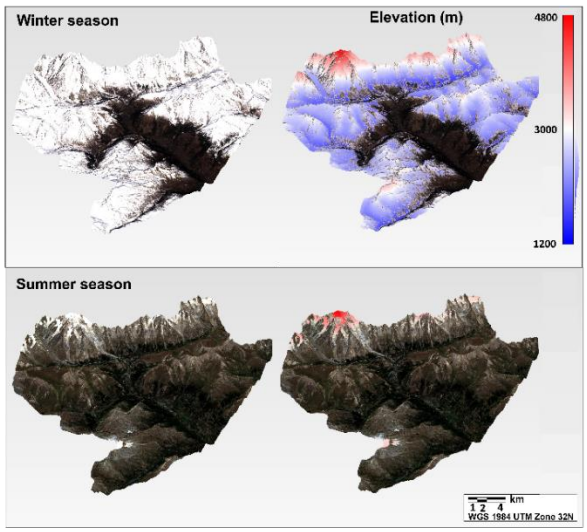

Figure 4. 3D models of the Courmayeur area in winter (top) and summer (bottom) with highlighted elevation ranges (from blue – low/middle values – to red - high elevations).

On the right part of the image, the colored texture shows in a very intuitive manner the elevation values of the area, allowing for the rapid identification of the permanent and temporary snow accumulation points. By comparing the winter model (top image) to the summer one (bottom image), the following considerations can be done: in red color, the elevation areas for which the ice/snow accumulation persists also during the summer season (permanent areas) are showed; while, in blue color, the temporary areas that are interested by snow melting during the summer are evidenced.
The link between glacier/snow permanent areas with specific elevation ranges is one of the potential applications enabled by the adoption of a 3D model that considers seasonal variations as additional information further to the elevation ones.
While exploring various examples, the potential of these models become apparent. However, it is crucial to recognize that the analyses rely on static information, which may not exhibit perfect correlation over time, due to the differing temporal acquisition intervals in Sentinel-2 images and the native data used to generate the TINITALY DEMs. This discrepancy could result, for example, in a morphology depicted by the DEM different from

what is observed in the images, thereby failing to achieve a perfect correlation between the two datasets. Consequently, there is an need to refine these models to establish temporal correspondences and spatial relationships among elements within a specific region. One approach could involve analysing dynamic DEMs generated over a narrow temporal window, aligned with both optical satellite and field data acquisitions. This refinement is crucial for enabling proactive and responsive disaster management strategies that must adapt to the dynamic nature of such events. Furthermore, it is closely linked to the fundamental concept of the Digital Twin, which integrates dynamic systems to monitor various aspects of the Earth's ecosystem.

4. CONCLUSIONS

In this work we presented some preliminary considerations about the DT prototype of Italian Alps, with specific focus on the generation of the reference data for such a DT, i.e. the 3D model of the Italian Alpine Region. The goal was to create two 3D models of reference for year 2022 for different seasons (one for autumn/winter and one for spring/summer seasons), that allow for different applications, only relying on HR multispectral Sentinel-2 imagery and 10m spatial resolution DEMs freely provided by INGV. The processing of the data was also performed only using open-access software.

The results obtained are an advancement in the utilization of digital surface models. Typically, these models provide elevation information about the terrain but lack texture or symbolism. However, by combining them with corresponding satellite images depicting the studied area, it becomes possible to integrate three-dimensional terrain information with spectral information, thus contributing in describing its features and status. The work provided an example of how 3D models with textures beyond RGB composite bands, enable the interpretation of the different morphological features, gathering a complete overview of the analysed area. In fact, the possibility of exploiting the spectral content of the satellite data, beyond the VIS part of the electromagnetic spectrum and, thus, the NIR, MIR and TIR windows, and consequently also of related spectral indexes, would permit the generation of specific thematic 3D models for the characterization of the different features over the surface: vegetation, water bodies, outcropping lithotypes, etc.. These will allow for an extensive use of the derivable information, shaping it as a powerful tool for territory management, by the in charge authorities.

Moreover, the two seasonal 3D models, i.e. winter vs. summer, allow for different potential applications, placing it as base layer data for further and in depth analysis. While the summer model offers important insights for land cover and LC change analysis, identification and monitoring of landslides and wildfires, etc…, the winter model, instead, permits the development of analysis related to glaciers monitoring, snow and avalanches dynamics, shaping both also as useful tools in the emergency prevention and monitoring phases. Also the comparison between the seasonal models allows for further analysis such as the identification of the link between glacier/snow permanent areas and specific elevation ranges, improving the monitoring of climate-change related effects.

Some limitations were encountered, mainly related to the vast size of the dataset used for analysing the entire Italian Alpine Region that posed computational and technological challenges

Another limitation is related to the static nature of the DEMs used, compared to the optical satellite data which is updated more frequently. These limitations can be for sure exceeded with more automation by developing ML approaches, from data gathering to processing. Moreover, the model updating with real-time satellite acquisition, that of course requires cloud computing capacities, it is a necessary step to permit also multitemporal analysis with data cube techniques. Finally, the integration with other data sources such as aerial acquisitions data, in-situ surveys, crowdsourcing, etc.. will provide a solid foundation for the subsequent development of the digital twin.

REFERENCES

Buonocore, L.; Yates, J.; Valentini, R. A Proposal for a Forest Digital Twin Framework and Its Perspectives. Forests 2022, 13, 498. https://doi.org/10.3390/f13040498

CloudCompare, 2023. 3D point cloud and mesh processing software, Open Source Project, Version 2.13. https://www.cloudcompare.org/

El Saddik, A., 2018. Digital Twins: The Convergence of Multimedia Technologies. IEEE MultiMedia, 25(2), pp. 87-92. https://doi.org/10.1109/MMUL.2018.023121167

European Commission, Joint Research Centre, Nativi, S., Craglia, M., Delipetrev, B., *Destination Earth – Survey on "Digital Twins" technologies and activities, in the Green Deal area*, Publications Office, 2020, https://data.europa.eu/doi/10.2760/430025.

European Commission, Directorate-General for Communications Networks, Content and Technology, 2022. Destination Earth https://data.europa.eu/doi/10.2759/847043

ESA-star Publication. Available online: https://esastar-publication-ext.sso.esa.int/ESATenderActions/details/21940 (accessed on 25/03/2022).

European Space Agency – ESA, 2023. Copernicus Open Access Hub. https://scihub.copernicus.eu/

Fissore, V.; Bovio, L.; Perotti, L.; Boccardo, P.; Borgogno-Mondino, E. Towards a Digital Twin Prototype of Alpine Glaciers: Proposal for a Possible Theoretical Framework. Remote Sens. 2023, 15, 2844. https://doi.org/10.3390/rs15112844

Grieves, M., 2014. Digital twin: manufacturing excellence through virtual factory replication. White Paper.

Kutschera, W., Patzelt, G., M. Wild, E., Haas-Jettmar, B., Kofler, W., Lippert, A., Oeggl, K., Pak, E., Priller, A., Steier, P., Wahlmüller-Oeggl, N., Zanesco, A., 2014. Evidence for Early Human Presence at High Altitude in the Ötztal Alps (Austria/Italy). *Radiocarbon,* 56(3), pp. 923-947. https://doi.org/10.2458/56.17919

Marazzi, S., 2005. Atlante orografico delle Alpi - SOIUSA: suddivisione orografica internazionale unificata del sistema alpino. Ed. Priuli & Verlucca, ISBN: 9788880682738

QGIS.org, 2023. QGIS Geographic Information System. Open Source Geospatial Foundation Project. http://qgis.org

Tarquini, S., Isola, I., Favalli, M., Battistini, A., Dotta, G., 2023. TINITALY, a digital elevation model of Italy with a 10 meters cell size (Version 1.1). Istituto Nazionale di Geofisica e Vulcanologia (INGV). https://doi.org/10.13127/tinitaly/1.1

Tarquini, S., Isola, I., Favalli, M., Mazzarini F., Bisson, M., Pareschi, MT, Boschi, E., 2007. TINITALY/01: a new Triangular Irregular Network of Italy. Ann. Geophys. https://doi.org/10.4401/ag-4424

Thelen, A., Zhang, X., Fink, O., Lu, Y., Ghosh, S., Youn, B.D., Todd, M.D., Mahadevan, S., Hu, C., Hu, Z., 2022. A comprehensive review of digital twin — part 1: modeling and twinning enabling technologies. *Structural and Multidisciplinary Optimizatio*n, 65, no. 354. https://doi.org/10.1007/s00158-022-03425-4

SATELLITE IMAGES AND BATHYMETRIC LiDAR FOR MAPPING SEAGRASS MEADOWS: AN OVERVIEW

V. Baiocchi [1], F. Cianfanelli [1], E. Nocerino[2]

[1] DICEA, SAPIENZA – University of Rome, Italy - valerio.baiocchi@uniroma1.it, flavia.cianfanelli@uniroma1.it

[2] Department of Humanities and Social Sciences, University of Sassari, Italy – enocerino@uniss.it

KEY WORDS: Posidonia oceanica, monitoring, habitat mapping, Remote Sensing, LiDAR, satellite images, multibeam echosounder, bathymetry

ABSTRACT:

The main goal of this study is to analyze the potentialities and weaknesses of remote sensing techniques to map and monitor Posidonia oceanica (Linnaeus) Delile meadows in the Mediterranean Sea which represent a highly significant marine plant that provides a series of environmental functions such as coastal protection and carbon restoration. We present an overview of state-of-the-art methods that enable the possibility of carrying out surveys in brief periods and with low environmental impact, based on the use of high-resolution satellites, images, and bathymetric LiDAR. Those data can be collected and elaborated to create a time series to trace trends of growth and decline of seagrass meadow. That information can also be used as indicators to guide environmental monitoring, management, and development of the territory as well as the setup of restoration sites. With this contribution, we aim to illustrate the criticalities and insights of these methods.

1. THE IMPORTANCE OF COASTAL AND MARINE HABITAT MONITORING

The Mediterranean Sea Basin, located at the crossroads of Europe, Asia, and Africa, is a biome characterized by strong resilience to different stress factors. The features of this area and the lucky combination of exogenous factors, such as average temperature, limited rainfall, and a continuous supply of sunlight, allow the growth of numerous plant species and a variety of habitats.

At present, owing to the expansion of anthropological activities on the coastline, such as dredging, implementation of bathing establishments, and anchoring (Marre et al., 2020), coastal and marine habitats are weakened by those actions that mine their fragile ecosystem (Abadie et al. 2020). The coastal environment is a vulnerable area, regularly stressed by different disturbing factors and cyclical events as, to give an example, tides which can influence coastal erosion and deposition. Consequently, this environment and its constituting habitats must be regularly monitored and preserved.

Habitat mapping is the term indicating methods which allow identifying, delineating, and documenting the spatial distribution of habitats in a specific geographical area. Throughout Geographic Information Systems (GIS), remote sensing, and field surveys, we can collect data on vegetation types, their location, and their evolution in the specific geographical area.

Marine and coastal areas are continuously subjected to a wide range of cyclic variations (e.g. tides), erosive actions (e.g. swirls) and less frequent violent phenomena such as sea storms. Nowadays, climate change has increased the frequency of extreme phenomena that undermine coastal areas. Stressors include increased water turbidity, which causes less sunlight penetrating thus negatively impacting the underwater vegetation (Silva et al., 2009; Telesca et al., 2015), and removal of biomass caused by natural as well as human-induced events (Borfecchia et al., 2021). These vulnerable habitats must be preserved implementing monitoring and protection actions.

In this contribution, the habitat of interest is Posidonia oceanica (from now on, P. oceanica) meadows, whose environmental functions will be widely discussed in the next paragraph.

In this study, we focus on remote sensing techniques to monitor the distribution and evolution of P. oceanica meadows. Within the range of available approaches, we will deepen on the use of satellite images which allow a broad and systemic coverage of the area of interest, with known revisit times and the possibility of highly automated data analysis.

1.1 Focus on the P. oceanica (L.) Delile specie

The Mediterranean Sea hosts the P. oceanica (L.) Delile, a native and endemic species widely distributed along the coasts of countries bordering the Mediterranean: from Spain to Turkey, from France to the Nord of Africa, including Italy, Balkan coast, and Greece (figure 1).

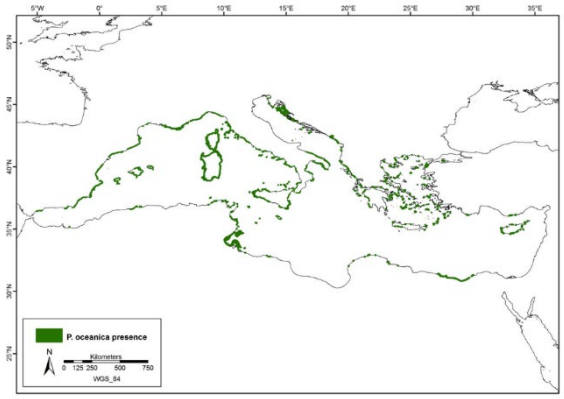

Figure 1. Representation of P. oceanica distribution is highlighted by green areas on the Mediterranean coastline (Telesca et al., 2015).

P. oceanica is characterized by its ability to perform chlorophyll photosynthesis even though it is located below sea level; therefore, it develops within a maximum depth of 50 meters under the water level (Yücel-Gier et al., 2020) where, considering the water transparency and clarity, it can be reached by sunlight. P. oceanica develops constituting meadows, whose extent would depend by several factors, including environmental stressor. Mostly it develops constituting large and thick agglomerations –

* Corresponding author

which take the proper name of meadows – but, in particularly turbulent or shaded areas, it distributes in small, disconnected clusters (Matta et al., 2014).
P. oceanica carries out several important environmental functions: firstly, it moderates the coastal erosion by creating a thick roots net that compact the sand terrain; it plays the same function also when it is not alive anymore by distributing on the coastline forming the "banquette" agglomerations composed by the death leaves that protect the coastline form the wave motion (Iacofano e Lo Brutto, 2016; Panagou et al., 2020). Secondly P. oceanica meadows represent one of the three habitats in the world constituting the blue carbon stocking areas (Silva et al., 2009). Mangrove forests, salt marshes and P. oceanica meadows can hold carbon dioxide and collect it, creating stock areas, in that way those habitats mitigate the emission of CO_2 in the atmosphere, and, for that reason, the CO_2 stocked in the vegetation is called "blue carbon" (Dat Pham et al., 2019).
To detect and monitor the distribution of P. oceanica is crucial, not only for the important functions that it plays on preserving the coastal and marine habitat, but also because the meadows' health state has been considered from different authors (Borfecchia et al., 2013; Thorhaug et al., 2007) a valid information to evaluate the health state and resilience of the entire sea basin to environmental stressors (Blasi et al., 2011; Marre et al., 2020).

2. MONITORING P. OCEANICA USING LIDAR AND SATELLITE IMAGES

The literature presents a broad spectrum of studies applying different methods for habitat mapping - which main goal is to analyze the territory on different scales considering the habitat size and the peculiar elements that constitute it - focusing on the presence of P. oceanica meadows in the Mediterranean.
In fact, to evaluate the presence of P. oceanica meadows it is necessary to own a bathymetry model that we can link to the vegetation positioning info. It often happens that P. oceanica meadows appear very dark in satellite images, showing very low reflectance values, sometimes even lower than those recorded on the seafloor (Traganos et al., 2018). This phenomenon can lead to the error of registering areas with P. oceanica meadows as depressions compared to the seafloor, resulting in an inaccurate description of reality. For this reason, it is necessary to complement the study and the correction of reflectance values in satellite images with a bathymetric map of the area in question (Matarrese et al. 2008). Bathymetry designates the depth of water bodies' floor and, for extension, represents topographic maps or surface models of oceans', lakes' and rivers' bed. Bathymetric models can be built using different methods specifically for this type of surveys in literature authors have been developed techniques based on acoustic sensing. Nowadays, optic remote sensing is also used for the construction of bathymetric models: in the next paragraph we will illustrate the different characteristics in the seabed detection by using soundwaves (then illustrated by the usage of multibeam echosounder) and electromagnetic waves (Bathymetric LiDAR) to delineate the weakness and strengths in the usage of those two methods.

2.1 Sensors used to detect seafloor: a focus on soundwaves and electromagnetic waves through water

To detect the seafloor and build seabed models two types of sensors are commonly employed: ones that use soundwaves and other ones that work with electromagnetic waves. Both types of waves are impacted by the refraction effect which is a deterministic phenomenon that implies the deviation of the impulse in its path to the seabed.
The transmission of sound and light in water involves distinct characteristics and behaviors due to the differences in these two forms of energy:
on one hand, acoustic sensing is affected by variations in temperature and density between water layers, which are known as 'thermoclines'. Sound waves in water are reflected and refracted among these variations. Sensors using sound waves are usually positioned in water because sound waves cannot pass through the air-water interface. This happens because sound waves are subject to total internal reflection, meaning the sound wave remains in one of the two layers (either air or water) and does not pass through the interface considering the different densities of the two media.
On the other hand, electromagnetic waves can cross the air-water interface: sensors that use those kinds of waves are placed on remote sensing platforms, from above and pass through the density transition between the two layers. Refraction effect occurs both when the signal passes through the air-water interface and within the water column: inside the water columns the electromagnetic wave is bent due to changes in water temperature or salinity (Quan, Fry, 1995).
Moreover, some of the energy of the electromagnetic wave is absorbed and scattered by water molecules, particles, or suspended materials (Hossain et al., 2015). This is why optical rays can reach only the shallow layers of the water column.
Considering this, most instruments used for underwater surveys employ sound waves because the acoustic signal propagates very quickly (given the higher density of water). Unlike electromagnetic waves that are scattered in water, sound waves are much less affected by scattering compared to electromagnetic waves and can measure depths of up to kilometers.
In the specific case of our research, when conducting habitat mapping surveys, especially for P. oceanica, optical sensors can still be utilized because the object of interest is typically found within the shallow meters of depth. However, when using optical sensors for habitat reconnaissance, it is necessary to correct for the ray deviation caused by refraction during the processing phase as we will illustrate in the paragraph concerning the usage of satellite images (2.3).

2.2 Bathymetric LiDAR for P. oceanica observation

One of the most classic methods aimed at building bathymetries is multibeam echosounder (MBES) employed to produce bathymetric models of large portions of territory. This method detects points on the seabed using a sensor positioned on the bottom of a boat that send acoustic impulses to the seabed which return to the sensor: the sensor estimates the distance between the sea floor and the sea level (depth) by measuring the travelling time between the transmission and the reception of the acoustic signal. MBES provide depth measurements up to 6000 meters from the sea level (Codevintec, 2023), with a potential accuracy complying with the performance standards defined by the Special Publication 44 of the International Hydrographic Organization's performance standards for precision mapping (Iho, 2022).
The limitations of this technique is that it requires long surveying times and cannot be used in areas where the boat cannot enter (such as canals or the shoreline), for that reason, an alternative to overcome this limitation can be found by using Bathymetric LiDAR (Light Detection and Ranging) which can build bathymetric Digital Elevation Model (DEM) up to 50 meters depth from the water level (Collin et al., 2008). This range of

measurement is sufficient for monitoring P. oceanica meadows, as they develop in the first 50 meters from the sea level.
In literature, bathymetries are often built using laser scanner techniques in the coastline areas where depth is lower and MBES can't access and detect points. Specifically, bathymetric LiDAR can be placed on different kinds of aircrafts such as drones or airplanes and usually works by using two different ray lights: infrared and green light. The infrared wave allows to measure accurately the distance between the sensor and the interface atmosphere-water, while the green wave can see through the water column and reach the seabed (Zhang et al. 2011, Webster, 2017).As explained in previous paragraphs, the refraction effect must be taken into account when dealing with bathymetric LiDAR. Different approaches have been proposed to correct or mitigate the measurement error introduced by refraction, using, for example, rigorous ray tracing methods following the Snell's law (Mandlburger et al., 2013, Mulsow et al, 2020) and estimating the ray's deviation in its transition from atmosphere to water. Some others have developed specific algorithms that mitigate the distortion: for example, Saylam et al. (2018) computed the water column, claiming that the refraction effect is a variable closely linked to the proper location characteristic, especially considering the water temperature and salinity levels.
Webster et al. (2017) utilized a multi-echo LiDAR sensor to detect P. oceanica meadows. Analyzing the LiDAR full waveform with multiple echoes, they distinguished bathymetry, vegetation, and suspended material trough the water column.
In the last years, it has been widely demonstrated that the integration of remote sensing with machine learning can lead to higher accuracy levels in detecting the elements on a habitat. Along with these methods, machine learning techniques, such as leaf area index (LAI), Random Forest (RF) or k-nearest neighbor are exploited classify data (Traganos et al., 2018; Papakonstantinou et al., 2020) and analyze specific biophysical parameters (Borfecchia et al., 2013), to which are functional for reading acquired data.

2.3 Satellite images for P. oceanica monitoring

When it comes to work on satellite images for habitat mapping purposes, the most frequently used are multispectral images: Landsat_8 and Landsat_9 (Topouzelis et al., 2018; Panayotidis et al. 2022; Traganos et al., 2018), Sentinel_2 (Güzel Yücel-Gier et al., 2020; Traganos et al., 2018; Borfecchia et al., 2021; Traganos et al. 2022; Traganos et al., 2018; Dat Pham et al. 2019); PRISMA (Borfecchia et al. 2021), MIVIS, Kompsat_2, RapidEye (Matta et al. 2014), ASTER, IKONOS (Matarrese et al. 2008) and Pléiades (Rende et al. 2020). These studies typically took place in Italy, Grece and Spain, where P. oceanica meadows is an endemic specie.
To perimeter the distribution of P. oceanica on satellite images, in literature, usually authors work with RGB images (Papakonstantinou et al., 2020) and "pixel based" methods by associating a spectral signature (Lyons et al. 2011) to the vegetation species, thus detecting its presence or absence. This approach may sometimes seem more suitable for delineating meadows compared to the object-based technique considering, therefore, that sometimes, meadow geometries could appear continuous and of large dimensions, while some other times, they might appear as small, discontinuous clusters of P. oceanica due to the specific environmental conditions of the observed location (Matta et al., 2014). However, considering the environmental characteristics of the observed territory, reference can be made to object-based techniques, to the extent that some authors have used the object-based classification algorithms, which classify image pixels exploiting by the combination of the bands and the geometry of their distribution (Parrish et al., 2016).
These kind of analysis on satellite images can only be carried out after a structured and systematic work of correction of the images themselves. During the postprocessing stages of the images, indeed, we consider to be essential the extremely meticulous step of geometric correction of the images (orthorectification) without which the investigations carried out on the satellite images would not acquire spatial meaning. Only once the orthorectification of the images has been carried out, the elements represented can be identified by assigning the chosen coordinates to each of them, such as in this case P. oceanica meadows presence.
To extract information about the meadows distribution from satellite images also reflectance values can be exploited: by measuring the reflectance and the chlorophyll levels not only it is possible to determine the distribution of the meadow but also its health state (Thorhaug et al., 2007, Qiu et al., 2019).
Generally, it is claimed that in most cases the single use of satellite images is not sufficient to conduct an accurate evaluation of underwater meadows presence and distribution (Matarrese et al., 2008; Tien Dat Pham et al., 2019; Papakonstantinou et al., 2020; Rende et al., 2020; Borfecchia et al., 2022) due to environmental disturb factors such as water turbidity, low water transparency or deep seabed (Panayotidis et al., 2022).
Instead, the combination of data extracted from satellite images analysis with bathymetric DEM built using the multibeam echosounder or bathymetric LiDAR for shallower areas, could lead to better results that the ones gained by the single use of one of the two instruments alone (Matarrese et al., 2008, Rende et al., 2020).

3. DISCUSSION

In the first part of Chapter 2 we illustrated the importance of updated bathymetry DEM to evaluate the underwater vegetation presence. Bathymetries are obtained using soundwaves or electromagnetic waves.
Depending on the specific guidelines of the research project, authors will choose the most suitable method for their own research purposes.
For P. oceanica monitoring, LiDAR bathymetry has proved to be an effective method. With full-waveform LiDAR, the presence of underwater vegetation can be detected, hypothesis that can be validated by the observation from satellite images and/or by checking surveys *in situ*.
By using bathymetric LiDAR, we can detect coastal and shallow water areas, in a range of observation from 1 to 60 meters in depth (Guenther et al., 2000). Those areas, as well known in literature, are difficult areas to monitor with "classical" bathymetric techniques, such as multibeam echosounder. This technique, on the other hand, is the best choice when it comes to detect deeper areas considering the limitation of bathymetric LiDAR: refraction effect, turbidity and suspended materials that absorb electromagnetic waves (Webster, T., 2017; Marre et al., 2020).
We consider as the biggest potentiality of bathymetric LiDAR is the rapidity with which data can be acquired comparing to classical methods (Irish & White, 1998) , as illustrated in par. 2.2, MBES takes a bigger amount of time to survey an entire area (Collin et al., 2008), while bathymetric LiDAR placed on an aerial vehicle of different type (airplane, helicopter, or drone) detects the seabed more quickly, keeping in mind that the detected study field is limited and depends on the vehicle where the sensor is positioned (with drones we can observe smaller areas, with airplanes we observe bigger areas).
The further application that can be achieved using bathymetric LiDAR also aimed at recording underwater vegetation is the combination of machine learning methods to LiDAR bathymetry data: by joining these applications we can detect different

territorial elements and distinguish vegetational species (Parrish et al., 2016; Amami et al., 2022).
By using satellite imagery, methodologies have been developed to map the areas where P. oceanica is located. By combining satellite images with bathymetric models, we can conduct rapid territorial surveys, offering a wide range of available material and, furthermore, having no environmental impact. Through photo interpretation of RGB satellite images or the use of machine learning techniques, several studies have demonstrated the feasibility of recognizing P. oceanica meadows using satellite images.
The usage of satellite images implemented to detect P. oceanica in the Mediterranean Sea offers a vast scale of opportunities, but we also must keep in mind the limitations of this technique: following we present a Table 1 illustrates pros and cons in the use of satellite images for P. oceanica mapping.

PROS	*CONS*
Depending on the satellite constellation, data are available for any area of interest	Images must have a very high spatial and spectral resolution, and this leads to a reduced swath
The acquisition has low environmental impact on the study field	The acquisition is limited by water turbidity and swirl
We can carry out surveys on large areas simultaneously comparing to other bathymetric survey techniques	Images must be postprocessed keeping a special regard to the geometric correction linked to the refraction effect to which electromagnetic waves are subjected

Tab. 1. Pros and Cons in the usage of satellite images declined to detect P. oceanica meadows.

Plus, considering the opportunity provided using satellite images, which are becoming more and more common, we can observe the same area at defined time intervals, leading to the generation of time series which can provide evidence of progression, regression, variation on the distribution of P. oceanica meadows (Lyons et al., 2013; Traganos et al., 2018).
However, remote sensing alone presents a series of challenges, primarily including image distortions caused by acquisition and difficulties with techniques using optical sensors to observe areas below sea level. Refraction certainly poses one of the major obstacles to the use of this methodology, as methods to mitigate those distortions are still being developed and do not find complete consensus in the scientific community.
Considering these issues, in the literature authors associates to the analysis on satellite images other data obtained through in-situ remote sensing techniques (such as images acquired through scuba diving) as a parameter for assessing the accuracy of P. oceanica detections from satellite images (Panayotidis et al., 2022). Several studies show that the combination of different remote sensing instruments is the optimal method to gather the necessary information for an effective monitoring activity. Different authors verify the accuracy of the data derived from remote sensing techniques with multibeam echosounder data collected for the same area (Papakonstantinou et al., 2020; Panayodis et al., 2022) or on field measurements as underwater photographs (Zavalas et al., 2014). Moreover, different instruments are applied to detect different zones of the study field: for example, shallow waters are registered by LiDAR, while the deepest waters are detected by using multibeam echosounder. By combining LiDAR and high-resolution multispectral images data, it has been proven that the accuracy in the habitat mapping increases (Chust et al., 2008; Collings et al., 2019, Amani et al., 2022).
Through a complementary analysis of the outcomes provided by different techniques employed in the same area, a more comprehensive study can be achieved, also allowing a better understanding of changes in the area (Dat Pham et al., 2019).
The integration of different geomatic techniques, allowing seamlessly the observation of vast (e.g. with satellite data) and limited (e.g. with aerial and underwater drones) areas, can enable the implementation of a multiscale approach where elements and phenomena can be analyzed at on different territorial extensions and with different levels of details. This approach can properly describe complex systems, permits a comprehensive understanding of the territory dynamics, and considers the elements interactions across various scales (Tomasello et al., 2022).

4. CONCLUSIONS

We briefly illustrated different techniques that can be exploited to build bathymetric models and detect underwater habitats; the major differences between the usage of acoustic and electromagnet waves, considering their pros and cons in this context, have been highlighted.
These methods can be considered when the surveys must be conducted in strict deadlines or, for example, when surveys are desired to be carried out on a seasonal or annual basis to compare variations in habitat distribution. If cyclic survey campaigns are to be conducted, remote sensing techniques can prove to be the only practical means to analyse medium to large-sized test sites. As shown in this review, many authors support the possibility to conduct habitat mapping surveys through remote sensing techniques. The integration of data coming from different techniques can encourage a better understanding of the territory offering the opportunity to analyze it in a multiscale perspective.

ACKNOWLEDGEMENTS

This work has been partially developed within the framework of the project e.INS- Ecosystem of Innovation for Next Generation Sardinia (cod. ECS 00000038) funded by the Italian Ministry for Research and Education (MUR) under the National Recovery and Resilience Plan (NRRP) – MISSION 4 COMPONENT 2, “From research to business” INVESTMENT 1.5, “Creation and strengthening of Ecosystems of innovation” and construction of “Territorial R&D Leaders”.
The authors acknowledge–the support of NBFC to University of Sassari, funded by the Italian Ministry of University and Research, PNRR, Missione 4 Componente 2, “Dalla 20iocon20r all’impresa”, Investimento 1.4, Project CN00000033.

REFERENCES

Abadie, A., Boissery, P., Viala, C. (2020). Study of the Posidonia Oceanica meadows’ upper limit with georeferenced underwater photogrammetry. Life and Environment 70 (3-4), 297-301. https://doi.org/10.1063/1.57377

Amani, M., Macdonald, C., Salehi, A., Mahdavi, S., & Gullage, M. (2022). Marine Habitat Mapping Using Bathymetric LiDAR Data: A Case Study from Bonne Bay, Newfoundland. Water, 14(23), 3809.

Blasi, C., Marignani, M., Copiz, R., Fipaldini, M., Bonacquisti, S., Del Vico, E., et al. (2011). Important plant areas in Italy: From

data to mapping. Biological Conservation, 144(1), 220–226. http://dx.doi.org/10.1016/j.biocon.2010.08.019

Borfecchia, F., de Cecco, L., Martini, S., Ceriola, G., Bollanos, S., Vlachopoulos, G., Valiante, L. M., Belmonte, A., & Micheli, C. (2013). Posidonia oceanica genetic and biometry mapping through high-resolution satellite spectral vegetation indices and sea-truth calibration. International Journal of Remote Sensing, 34(13), 4680–4701. https://doi.org/10.1080/01431161.2013.781701

Borfecchia, F., Micheli, C., De Cecco, L., Sannino, G., Struglia, M. V., Di Sarra, A. G., Gomez, C., & Mattiazzo, G. (2021). Satellite multi/hyper spectral HR sensors for mapping the Posidonia oceanica in south mediterranean islands. Sustainability (Switzerland), 13(24). https://doi.org/10.3390/su132413715

Chust, G., Galparsoro, I., Borja, Á., Franco, J., & Uriarte, A. (2008). Coastal and estuarine habitat mapping, using LIDAR height and intensity and multi-spectral imagery. Estuarine, Coastal and Shelf Science, 78(4), 633–643. https://doi.org/10.1016/j.ecss.2008.02.003

Codevintec (2023) https://www.codevintec.it/multibeam/ (30 October 2023)

Collin, A., Archambault, P., & Long, B. (2008). Mapping the shallow water seabed habitat with the SHOALS. IEEE Transactions on Geoscience and Remote Sensing, 46(10), 2947–2955. https://doi.org/10.1109/TGRS.2008.920020

Collings, S., Campbell, N. A., & Keesing, J. K. (2019). Quantifying the discriminatory power of remote sensing technologies for benthic habitat mapping. International Journal of Remote Sensing, 40(7), 2717–2738. https://doi.org/10.1080/01431161.2018.1531316

Dat Pham, T., Xia, J., Thang Ha, N., Tien Bui, D., Nhu Le, N., & Tekeuchi, W. (2019). A review of remote sensing approaches for monitoring blue carbon ecosystems: Mangroves, sea grasses and salt marshes during 2010–2018. Sensors (Switzerland), 19(8). https://doi.org/10.3390/s19081933

Hossain, M. S., Bujang, J. S., Zakaria, M. H., & Hashim, M. (2015). Application of Landsat images to seagrass areal cover change analysis for Lawas, Terengganu and Kelantan of Malaysia. Continental Shelf Research, 110, 124–148. https://doi.org/10.1016/j.csr.2015.10.009

Guenther, G. C., Cunningham, A. G., LaRocque, P. E., & Reid, D. J. (2000). Meeting the Accuracy Challenge in Airborne Bathymetry. Proceedings of EARSeL-SIG Workshiop, 1, 1.
Iacofano D. e Lo Brutto, S. (2016). Re-description of Orchestia stephenseni Cecchini, 1928: designation of neotype and senior synonym to Orchestia constricta A. Costa, 1853 (Crustacea: Amphipoda: Talitridae) by Reversal of Precedence, Zootaxa 4150 (1): 040–060, http://doi.org/10.11646/zootaxa.4150.1.2

Iho (2022) https://iho.int/uploads/user/pubs/standards/s-44/S-44_Edition_6.1.0.pdf (30 October 2023)

Irish, J. L., & White, T. E. (1998). Coastal engineering applications of high-resolution lidar bathymetry. Coastal Engineering, 35(1–2), 47–71. https://doi.org/10.1016/S0378-3839(98)00022-2

Lyons, M., Phinn, S., & Roelfsema, C. (2011). Integrating Quickbird multi-spectral satellite and field data: Mapping bathymetry, seagrass cover, seagrass species and change in Moreton Bay, Australia in 2004 and 2007. Remote Sensing, 3(1), 42–64. https://doi.org/10.3390/rs3010042

Lyons, M.B., Roelfsema, C.M., and Pinn, S.R. (2013) Towards Understanding Temporal and Spatial Dynamics of Seagrass Landscapes Using Time-Series Remote Sensing. Estuarine, Coastal and Shelf Science 120:42–53.

Mandlburger, G. (2022). A Review of Active and Passive Optical Methods in Hydrography. The international hydrographic review, https://doi.org/10.58440/ihr-28-a15

Matarrese, R., Acquaro, M., Morea, A., Tijani, K., & Chiaradia, M. T. (2008). Applications of remote sensing techniques for mapping posidonia oceanica meadows. International Geoscience and Remote Sensing Symposium (IGARSS), 4(1), 906–909. https://doi.org/10.1109/IGARSS.2008.4779870

Matta, E., Aiello, M., Bresciani, M., Gianinetto, M., Musanti, M., & Giardino, C. (2014). Mapping Posidonia meadow from high spatial resolution images in the Gulf of Oristano (Italy). International Geoscience and Remote Sensing Symposium (IGARSS), 5152–5155. https://doi.org/10.1109/IGARSS.2014.6947658

Marre, G., Deter, J., Holon, F., Boissery, P., & Luque, S. (2020). Fine-scale automatic mapping of living posidonia oceanica seagrass beds with underwater photogrammetry. Marine Ecology Progress Series, 643, 63–74. https://doi.org/10.3354/meps13338

Mulsow, C., Mandlburger, G., & Maas, H. G. (2020). Comparison of Subaquatic Digital Elevation Models from Airborne Laser Scanning and Imagery. ISPRS Annals of the Photogrammetry, Remote Sensing and Spatial Information Sciences, 5(2), 671–677. https://doi.org/10.5194/isprs-annals-V-2-2020-671-2020

Panagou, T., Oikonomou, E., Hasiotis, T., & Velegrakis, A. F., (2020) Shallow Water Bathymetry Derived from Green Wavelength Terrestrial Laser Scanner, Marine Geodesy, 43:5, 472-492, DOI: 10.1080/01490419.2020.1737602

Panayotidis, P., Papathanasiou, V., Gerakaris, V., Fakiris, E., Orfanidis, S., Papatheodorou, G., Kosmidou, M., Georgiou, N., Drakopoulou, V., & Loukaidi, V. (2022). Seagrass meadows in the Greek Seas: Presence, abundance and spatial distribution. Botanica Marina, 65(4), 289–299. https://doi.org/10.1515/bot-2022-0011

Papakonstantinou, A., Stamati, C., & Topouzelis, K. (2020). Comparison of true-color and multispectral unmanned aerial systems imagery for marine habitat mapping using object-based image analysis. Remote Sensing, 12(3). https://doi.org/10.3390/rs12030554

Parrish, C. E., Dijkstra, J. A., O'Neil-Dunne, J. P., McKenna, L., & Pe'eri, S. (2016). Post-Sandy benthic habitat mapping using new topobathymetric lidar technology and object-based image classification. Journal of Coastal Research, (76 (10076)), 200-208.
Quan, X., and E. S. Fry. 1995. "Empirical Equation for the Index of Refraction of Seawater." Applied Optics 34: 3477–3480. Doi:10.1364/AO.34.003477.

Qiu, Feng, Jing M. Chen, Holly Croft, Jing Li, Qian Zhang, Yongqin Zhang, and Weimin Ju. 2019. "Retrieving Leaf Chlorophyll Content by Incorporating Variable Leaf Surface Reflectance in the PROSPECT Model." Remote Sensing 11(13).

Rende, Sante Francesco, Bosman, A., Mento, R. Di, Bruno, F., Lagudi, A., Irving, A. D., Dattola, L., Giambattista, L. Di, Lanera, P., Proietti, R., Parlagreco, L., Stroobant, M., & Cellini, E. (2020). Ultra high-resolution mapping of Posidonia oceanica (L.) delile meadows through acoustic, optical data and object-based image classification. Journal of Marine Science and Engineering, 8(9). https://doi.org/10.3390/JMSE8090647

Saylam, K., Hupp, J. R., Averett, A. R., Gutelius, W. F., & Gelhar, B. W. (2018). Airborne lidar bathymetry: assessing quality assurance and quality control methods with Leica Chiroptera examples. International Journal of Remote Sensing, 39(8), 2518–2542. https://doi.org/10.1080/01431161.2018.1430916

Silva, J., Sharon, Y., Santos, R., Beer, S., (2009). Measuring seagrass photosynthesis: methods and applications. Aquatic Biol. 7, 127–141. https://doi.org/10.3354/ab00173

Telesca, L., Belluscio, A., Criscoli, A., Ardizzone, G., Apostolaki, E. T., Fraschetti, S., Gristina, M., Knittweis, L., S. Martin, C., Pergent, G., Alagna, A.,Badalamenti, F., Garofalo, G., Gerakaris, V., Pace, M. L., Pergent-Martini, C., and Salomidi, M. 2015. "Seagrass Meadows (Posidonia Oceanica) Distribution and Trajectories of Change." Scientific Reports 5:1–14.

Thorhaug, A., Richardson, A. D. & Berlyn, G. P. (2007) Spectral reflectance of the seagrasses: Thalassia testudinum, Halodule wrightii, Syringodium filiforme and five marine algae, International Journal of Remote Sensing, 28:7, 1487-1501, DOI: 10.1080/01431160600954662

Tomasello A., Bosman A., Signa G., Rende S.F., Andolina C., Cilluffo G., Cassetti F.P., Mazzola A., Calvo S., Randazzo G., Scarpato A., Vizzini S. (2022) 3D-Reconstruction of a Giant Posidonia oceanica Beach Wrack (Banquette): sizing biomass, carbon and nutrient stocks by combining field data with high-resolution UAV photogrammetry. Frontiers in Marine Science, 9, art. No. 903138. DOI: 10.3389/fmars.2022.903138

Topouzelis, K., Makri, D., Stoupas, N., Papakonstantinou, A., & Katsanevakis, S. (2018). Seagrass mapping in Greek territorial waters using Landsat-8 satellite images. International Journal of Applied Earth Observation and Geoinformation, 67(December 2017), 98–113. https://doi.org/10.1016/j.jag.2017.12.013

Traganos, D., Aggarwal, B., Poursanidis, D., Topouzelis, K., Chrysoulakis, N., & Reinartz, P. (2018). Towards global-scale seagrass mapping and monitoring using Sentinel-2 on Google Earth Engine: The case study of the Aegean and Ionian Seas. Remote Sensing, 10(8), 1–14. https://doi.org/10.3390/rs10081227

Traganos, D., Lee, C. B., Blume, A., Poursanidis, D., Čižmek, H., Deter, J., Mačić, V., Montefalcone, M., Pergent, G., Pergent-Martini, C., Ricart, A. M., & Reinartz, P. (2022). Spatially Explicit Seagrass Extent Mapping Across the Entire Mediterranean. Frontiers in Marine Science, 9(July), 1–13. https://doi.org/10.3389/fmars.2022.871799

Webster, T. (2017). Results from 3 seasons of surveys in maritime Canada using the Leica Chiroptera II shallow water topo-bathymetric lidar sensor. OCEANS 2017 - Aberdeen, 2017-Octob, 1–4. https://doi.org/10.1109/OCEANSE.2017.8084681

Yücel-Gier, G., Koçak, G., Akçalı, B., İlhan, T., & Duman, M. (2020). Evaluation of posidonia oceanica map generated by sentinel-2 image: Gülbahçe bay test site. Turkish Journal of Fisheries and Aquatic Sciences, 20(7), 571–581. https://doi.org/10.4194/1303-2712-v20_7_07

Zhang, Yi Fei, Xiao Tong Wang, and Hui Yang (2011). "Design of Seabed Terrain Aided Navigation System Based on the Technology of Laser Bathymetry." 2011 Symposium on Photonics and Optoelectronics, SOPO 2011.

Zavalas, R., Ierodiaconou Daniel, D., Ryan, D., Rattray, A., & Monk, J. (2014). Habitat classification of temperate marine macroalgal communities using bathymetric LiDAR. Remote Sensing, 6(3), 2154–2175. https://doi.org/10.3390/rs6032154

Wilson, M. F. J., O'Connell, B., Brown, C., Guinan, J. C., & Grehan, A. J. (2007). Multiscale terrain analysis of multibeam bathymetry data for habitat mapping on the continental slope. In Marine Geodesy (Vol. 30, Issues 1–2). https://doi.org/10.1080/01490410701295962

Agriculture & forestry

A GIS-BASED SPATIAL ANALYSIS FOR AGRICULTURAL PRUNING WASTE MANAGEMENT IN THE CIRCULAR ECONOMY PERSPECTIVE

F. Convertino *, A.C. Dell'Acqua , E. Schettini

Department of Soil, Plant and Food Sciences, University of Bari, Italy
(fabiana.convertino, annachiara.dellacqua, evelia.schettini)@uniba.it

KEY WORDS: Orthophoto, Remote sensing imagery, Sustainability, Agricultural waste, Biomass, Land use map, Energy recovery

ABSTRACT:

Agricultural activities produce huge amounts of agro-residues usable as resources in the optic of the circular economy. Among these, those from pruning olive groves, vineyards and fruit plantations can be particularly relevant. Biomass residues from agricultural pruning represent a typical case of agro-residues yearly produced and hardly ever used. Mismanagement practices are very common and cause serious human and environmental health issues. It is necessary to overcome technical and logistic problems that farmers experience by developing a proper management system. This study aims to contribute to the design of an effective collection system for agricultural pruning biomass. Data from earth observations are precious to achieve this objective. In this study, the GIS tools were used to work on earth observation products and perform a territorial analysis. The attention was focused on an area particularly suited to agriculture in the Apulia Region (Italy). Land use maps derived from orthophotos were used to identify areas of pruning waste production. By defining and applying pruning indices for each crop, pruning residues were quantified and localized. Based on this, the suitable position of the collection centres was defined. The obtained maps can be easily used and continuously updated with remote sensing imagery. The study highlights the power of the methodology implying land use maps based on orthophotos and in turn on earth observations and GIS tools for this purpose. The results represent a first step towards the improvement of the agro-residues management system and can help policymakers and stakeholders to promote more sustainable actions.

1. INTRODUCTION

Over the last 20 years, the most spread economic model was the linear based on "take-make-use-dispose". This model unsustainably exploited huge quantities of readily available raw materials and non-renewable energy sources. As consequences, the linear model has led to rapid depletion of natural resources, progressive loss of biodiversity with dramatic impacts to the environmental system and pressures from climate change (European Commission, 2012).

After the energy sector (68.1%), agriculture is the second largest production sector with the highest environmental impacts in terms of greenhouse gases emissions (19.9%) (Lamb et al., 2021), and the first sector for environmental impacts due to land use (90%) (Kusumastuti et al., 2016). Furthermore, the world agricultural production system is responsible for a huge amount of solid waste (Kamusoko et al., 2021). Agricultural waste can be divided into two categories: inorganic and organic waste. The former includes plastic, chemical containers, and other materials used in farming activities. Agricultural organic waste is represented by biomass; it is estimated that 60% of the world's agricultural biomass comes from plant production (Sommer et al., 2015).

Biomass is the biodegradable fraction of product, industrial and municipal waste, and any residues of biological origin from agriculture (including plant and animal substances), forestry and related industries, such as fisheries and aquaculture (European Parliament and Council, 2009)

These agro-residues represent a resource as they are a stored source of solar energy and fixed in the form of organic carbon (McKendry, 2002). This intrinsic value can be used prospectively in the circular economy and bioeconomy policy. The circular economy aims at making production processes sustainable by reducing the influx of resources and the production of waste, minimizing environmental impact.

In optics based on "reuse, recycle or biodegradation", biomass can be efficiently used as renewable energy source and as secondary raw material in other production processes (FAO, 1997). Today, energy obtained from biomass, through various physical and chemical processes, is considerable; in the world biomass is the fourth natural source of energy, after coal, oil, and natural gas (Tong, 2019).

Biomass is not only used as a source of energy to produce biofuel. Recent research is increasingly investigating possibilities to convert biomass waste in value-added products for diverse applications, such as construction materials, medicine, and food packaging (Zhou and Wang, 2020). Through different treatments and production methods, biomass waste is used to produce construction materials with good mechanical and thermo-hygrometric properties (Barbieri et al., 2019; Liuzzi et al., 2020; Ryłko-Polak et al., 2022), good performing materials to be used in agriculture (Babu et al., 2022; Vox et al., 2005), biosorbents (Anastopoulos et al., 2019; Nampeera et al., 2022), and many other products used for electronic components, coatings for packaging, in paper industry and in other industrial applications (Babu et al., 2022; Tripathi et al., 2019; Zhou and Wang, 2020).

In the Mediterranean basin, most of the agro-residues are represented by pruning waste from permanent crops typical of the local agrosystem, such as vineyards, olive groves, and almond trees (García-Galindo et al., 2016).

Over 13 million tons of pruning waste are produced in Europe but represent an unexploited resource. In fact, a large fraction of these agro-residues is left in the field to decompose naturally, or disposed of in dump, or in the worst cases burned. It is estimated that 25% of the produced agricultural waste is burned in the open field (Venkatramanan et al., 2021). Wrong management of agro-waste causes damage to human and environmental health, threatening food and energy security. The poor management of waste is due to a series of factors such as low awareness of the

* Corresponding author

intrinsic value of the product, high costs for collection, logistical barriers due to the geographical dispersion of waste, seasonality, inhomogeneity of production between crops and production realities, and lack of localized collection centres on the territory (Velázquez-Martí et al., 2011).
Knowing the amount of residual biomass for each type of crop and its location in the territory allows the design and planning of a pruning residues management system. The matter is complex and data from earth observations are the key to start addressing it. Earth observation products and their application, involving the use of geographic information systems (GISs) tools are crucial to the study purpose and can lead to the development of a georeferenced database. GISs allow managing large amount of data, georeferencing, storing, analysing, and visualizing it (Hachem et al., 2023). Therefore, a GIS, implemented with earth observation data, can be very precious to perform territorial analyses, identify biomass production sites and design a management system. The resulting database can be continuously updated through the updating of land use base maps and remote sensing imagery (Lanorte et al., 2017).
The aim of this study is to apply the methodology based on earth observation products, GIS, and specific residues indices to quantify and localize biomass production from pruning activity in an agricultural area, as a first step towards the design of an appropriate management system. Moreover, suitable positions for biomass collection centres are identified. The study could be further developed by including other parameters relevant to the objective and with the support of remote imagery. The obtained georeferenced database can be a useful tool to improve the agricultural waste management system. The produced maps, easily updatable and manageable, can be used by planners and policymakers to promote sustainable approaches for the development of rural territory and landscape.

2. MATERIALS AND METHODS

The study focuses on an area particularly suited to agriculture in the Apulia Region (Southern Italy). The area has mean coordinates of latitude 40.962834° and longitude 17.207541° and the elevation ranges from 0 m asl to 408 m asl. It measures about 400 km^2 and consists of four municipalities. The four municipalities, Monopoli, Polignano a Mare, Conversano and Mola di Bari, are grouped since they represent a single optimal administrative collection area in the Province of Bari. Given the strong vocation for agriculture, the production of agro-residues in this area is abundant.
The attention was focused on the biomass waste coming from pruning activities. A GIS database was obtained and pruning residues were georeferenced on the territory.
The methodology implied the use of land use map files freely available thanks to the territorial information system of the Apulia Region (http://www.sit.puglia.it). Apulian land use map, available at scale 1:5000, derives from colour orthophotos with 0.50 m spatial resolution. These are digital true colour aerial data recorded by a digital mapping camera. Land use map was useful to identify the cultivated area and the crops distribution in the study area.
The free software QGIS (https://www.qgis.org) was used to perform the territorial analysis, starting from the land use map. By observing the crops distribution on the land use map and by calculating the area per feature through the specific QGIS geometry tool, three main crops emerged: olive groves (35%), orchards (20%) and vineyards (11%). Olive groves are mainly cultivated in the southern part of the study area, orchards essentially in the centre and vineyards mostly in the northern part (Figure 1).

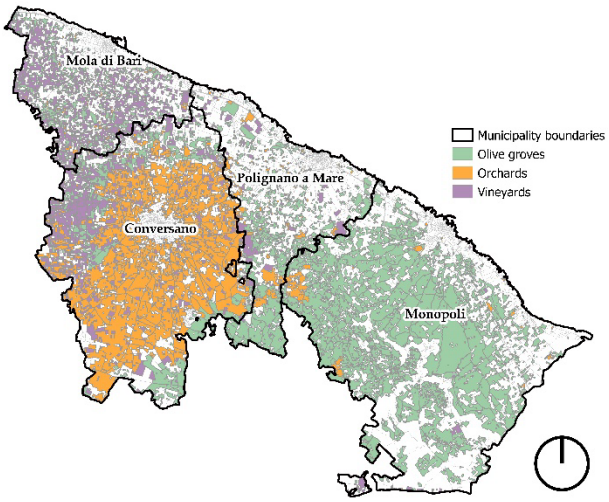

Figure 1. Land use map of the study area identifying the three most widespread crops: olive groves, orchards, and vineyards.

The attention was then focused on the identified predominant crops. To quantify and localize the pruning residues from these cultivations, pruning indices were defined and calculated per crop. Indices were derived based on data available in the literature concerning: the crops distribution on the cultivated area and the related quantity of pruning residues per crop, which strongly depends on the specific pruning methods in the area (ISPRA, 2010). Specifically, data in Table 1, deriving from a report of the Italian Institute for Environmental Protection and Research (ISPRA, 2010) were used for indices calculation. This data, resulting from a detailed estimation approach, was considered reliable for the purpose of the present study. The estimates are mainly based on three parameters: statistical data on the total production per each crop (retrieved from the Italian National Institute of Statistics, ISTAT, database); ratio of main by-product to product; fraction or percentage of the waste or by-product already recycled or reused. The combination of these three parameters led to the provincial estimates of the agro-residues.

Crop type	Surface [ha]	Residues [kt/yr of dry matter]
Olive groves	129450	115.4
Vineyards	37595	116.62
Almond trees	20850	27.08
Cherry trees	16700	1.71
Peach trees	830	2.35
Apple trees	100	0.14
Apricot trees	40	0.04
Kiwi trees	20	0.03
Citrus	14	0.05
Pear trees	12	0.01
Plum trees	8	0.01

Table 1. Distribution of the agricultural surface per crop type in the province of Bari and related pruning residues (ISPRA, 2010).

The pruning residues indices (*PRIs*) to be applied in the study area were calculated based on Table 1 as:

$$PRI_{crop} = R_{crop}/S_{crop} \quad (1)$$

where PRI_{crop} = pruning residues index per crop [t ha^{-1} yr^{-1}]
R_{crop} = amount of pruning residues per crop [t yr^{-1} of dry matter]
S_{crop} = cultivated surface per crop [ha]

PRIs were obtained for each of the three crops. Concerning orchards, the weighted mean was considered in order to proper take into account all the species cultivated in the area as well as their spread.
The land use map with the selected crops was then integrated by adding the new field of the PRIs in the attribute table, reporting the specific index per crop. The amount of pruning residues per crop (PR_{crop}, t yr^{-1}) was obtained based on PRI_{crop} and on the area of each feature (S_i, ha) as:

$$PR_{crop} = PRI_{crop} \cdot S_i \quad (2)$$

The pruning waste was quantified and localized on the map of the area.
Suitable positions of collection centres were then assessed, also considering different management approaches. To this end, the coordinates of the features centroids weighted by the specific PRI_{crop} were evaluated as well as the mean coordinates of the centroids distinguished per crop, per municipality and for the whole area. This was made possible by using the "mean coordinates" vector analysis tool available in QGIS. This tool calculates a point layer (collection centres location) with the centre of mass of the geometries contained in an input layer (centroids of features polygons obtained through the "centroids" geometry tool). Moreover, an attribute of the layer attribute table can be specified as a weight to be applied to each element when calculating the centre of mass. In this case, the weighting factor was the amount of pruning residues calculated per each feature.

3. RESULTS AND DISCUSSION

The application of the PRIs on the land use map resulted in the spatial distribution of pruning waste, which is actually a by-product, in the study area (Figure 2). The highest production of biomass from pruning is localized in the municipality of Conversano (13115.6 t yr^{-1}) followed by Monopoli (7709.6 t yr^{-1}), Mola di Bari (5628.3 t yr^{-1}) and Polignano a Mare (3330.7 t yr^{-1}).

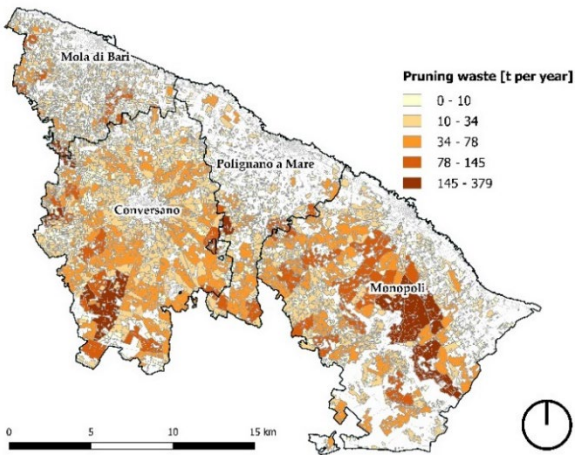

Figure 2. Distribution of the pruning waste from olive groves, orchards, and vineyards in the study area.

Concerning the management system for these pruning residues, it is important to identify the most suitable position of collection centres. In this regard, different approaches were investigated. It is possible to define different collection centres, distinguished per crop type and per municipality. This would lead to three collection centres for each municipality (Figure 3). According to the most widespread cultivations in each of the municipalities, the dimensions of the three collection centres could be set. As shown in Figure 3, the biggest collection centre should be the one for olive groves residues in Monopoli, where this crop is widely cultivated. This centre should be almost barycentrically located. The biggest centres for orchards and vineyards residues should be in Conversano, coherently with the land use map. The one for vineyards in a decentralised position towards the border with Mola di Bari, while the one for orchards more central.

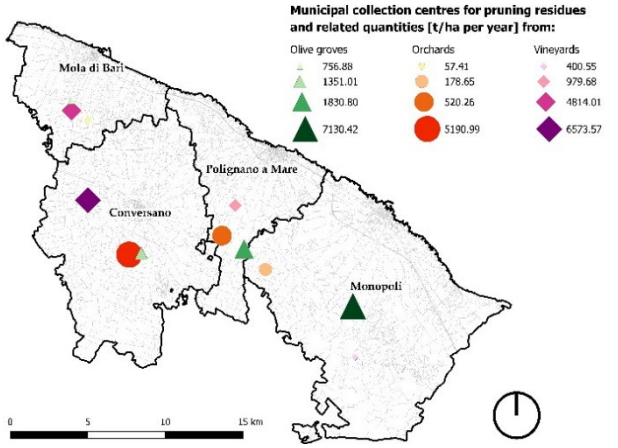

Figure 3. Suitable locations of municipal collection centres and related quantities of pruning waste per crop type in the study area.

This system based on different municipal centres could be optimized by considering the possibility to have three intermunicipal collection centres in total, one for each crop residues (Figure 4). As expected, the collection centres should be placed in Monopoli and Conversano. The intermunicipal centre for olive groves pruning residues should be in Monopoli, but moved towards the border with Polignano a Mare, to serve the whole area. The ones for orchards and vineyards should be placed in Conversano in barycentric positions considering the localization of these crops in the area. The biggest collection centre should be for vineyards pruning residues, followed by the ones for olive groves and orchards (Figure 5).

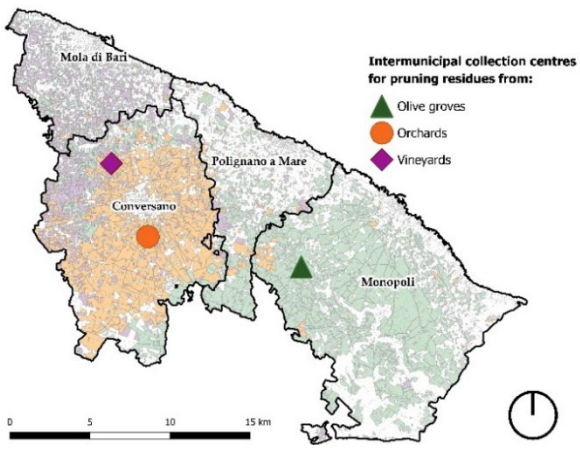

Figure 4. Suitable locations of intermunicipal collection centres for pruning waste per crop type in the study area.

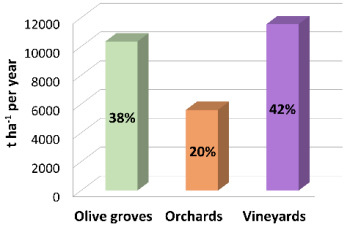

Figure 5. Amount of pruning waste per crop type and percentage distribution in the study area.

A further optimization could be to set a unique intermunicipal collection centre for all the crops (Figure 6). This should be in Monopoli but very close to the border with Polignano a Mare and here would converge the whole amount of biomass from pruning produced in the area.

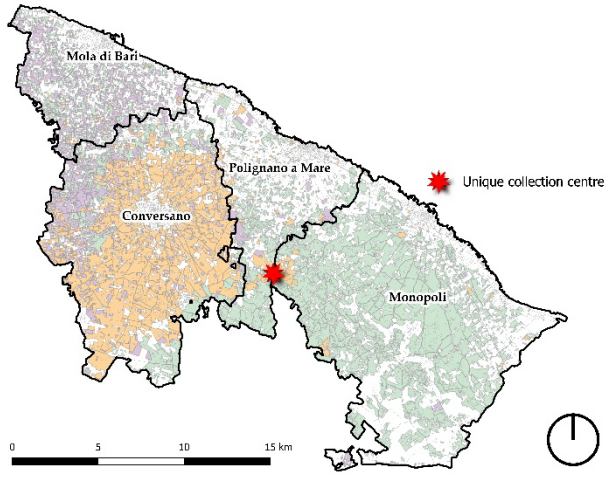

Figure 6. Suitable location of an intermunicipal collection centre for pruning waste in the study area.

Suitable locations of collection centres in the different analysed scenarios were mathematically obtained as weighted mean coordinates. In this very first study other parameters were not taken into account. The methodology proposed and in turn the results could be enhanced by considering other relevant aspects, specific of this issue, in the optic of designing an efficient biomass management system. It should be considered that pruning residues production is seasonally based and occurs in very limited time spans. The production of such by-product is very spotted on the territory, consequently there are relevant mechanization and transportation needs to be addressed. Finally, the management system should aim not only to the environmental sustainability, but it should also be technically and economically sustainable. Thus, it is crucial to have detailed and updated information on the pruning residues density and distribution on the territory. To include all these other aspects, the process of defining the most suitable location of collection centres and designing the whole management system should include the implementation of other data. It could be useful to implement data on environmental constraints, context favourable or unfavourable variables, the altimetry of the territory and the availability of infrastructures and transport facilities. Updated remote sensing data is fundamental to perform analyses and guide the whole process, from the actual quantification and distribution of the biomass production to the design of the management system, and for a continuous monitoring.

4. CONCLUSIONS

Agricultural activities are characterized by the production of considerable quantities of solid waste, some of which are actually by-products as in the case of the agro-residues deriving from pruning. These biomass residues are particularly precious and could become an important resource if considered and managed as such and not as a useless waste. To support the sustainable management of this biomass, a proper management system is mandatory. In this regard, earth observation products and their implementation in GIS environment can provide a fundamental support.

The study focuses on the production of agro-residues from pruning of olive groves, orchards and vineyards in four municipalities of Apulia Region. Thanks to land use map, derived from orthophotos and in turn from aerial photogrammetry, and by using GIS tools, the territorial analysis was performed. This allowed the quantification and localization of the biomass from pruning and the investigation of suitable positions of collection centres. The land use map was updated including information on pruning residues, resulting in a georeferenced database. Such database can be easily recreated and updated by using remote sensing imagery as well.

This study suggests that the proposed methodology, based on the use of earth observation data, and the obtained results could be precious tools for planners and policymakers for setting up a proper management system of this resource. Further studies aiming at designing the biomass management system should overcome the limitations of this first stage research by including other relevant parameters such as the presence of environmental constraints and infrastructures availability and accessibility. The use of remote sensing imagery can also be useful in the improvement phase of the study and for the monitoring stage.

ACKNOWLEDGEMENTS

The contribution to programming and conducting this research was equally shared between the Authors.

This research has been developed in the framework of the activities of the “Centro Interdipartimentale di Ricerca per la Cooperazione allo Sviluppo” (CPS) of the University of Bari, Italy.

REFERENCES

Anastopoulos, I., Pashalidis, I., Hosseini-Bandegharaei, A., Giannakoudakis, D.A., Robalds, A., Usman, M., Escudero, L.B., Zhou, Y., Colmenares, J.C., Núñez-Delgado, A., and Lima, É.C., 2019. Agricultural biomass/waste as adsorbents for toxic metal decontamination of aqueous solutions. *Journal of Molecular Liquids*, 295, 111684. https://doi.org/10.1016/j.molliq.2019.111684.

Babu, S., Singh Rathore, S., Singh, R., Kumar, S., Singh, V.K., Yadav, S.K., Yadav, V., Raj, R., Yadav, D., Shekhawat, K., and Ali Wani, O., 2022. Exploring agricultural waste biomass for energy, food and feed production and pollution mitigation: A review. *Bioresource Technology*, 360, 127566. https://doi.org/10.1016/j.biortech.2022.127566.

Barbieri, L., Andreola, F., Lancellotti, I., and Taurino, R., 2013. Management of agricultural biomass wastes: Preliminary study on characterization and valorisation in clay matrix bricks. *Waste Management*, 33, pp. 2307-2315. http://dx.doi.org/10.1016/j.wasman.2013.03.014.

European Commission, Directorate-General for Research and Innovation, 2012. Innovating for sustainable growth: a bioeconomy for Europe. https://data.europa.eu/doi/10.2777/6462.

European Parliament and Council Directive 2009/28/CE on the promotion of the use of energy from renewable sources and amending and subsequently repealing Directives 2001/77/EC and 2003/30/EC, L 140/16.

FAO, 1997. The role of wood energy in Europe and OECD: (WETT) Wood energy Today for Tomorrow.

García-Galindo, D., López, E., Gomez, M., Sebastián, F., Gebresenbet, G., Jirjis, R., Kern, J., Germer, S., Pari, L., Suardi, A., Dyjakon, A., den Boer, J., Bukowski, P., Hunkin, S., Bundgaard-Jørgensen, U., Sagarna, J., Lapeña, A., Frackowiak, P., Adamczyk, F., Naldoni, D., Bischoff, W-A., Olsson, S., Kleinert, L., Abadías, J., Deval, X., and Poutrin, C, 2016. Europruning Project: summary of final results. https://doi.org/10.5071/24thEUBCE2016-1BO.9.1.

Hachem, A., Vox, G., Convertino, F., 2023. Prospective Scenarios for Addressing the Agricultural Plastic Waste Issue: Results of a Territorial Analysis. *Applied Sciences*, 13, 612. https://doi.org/10.3390/ app13010612.

ISPRA, 2010. Studio sull'utilizzo di biomasse combustibili e biomasse rifiuto per la produzione di energia. Rapporti 111/2010.

Kamusoko, R., Jingura, R.M., Parawira, W., and Chikwambi, Z., 2021. Strategies for the valorization of crop residues into biofuels and other value-added products. *Biofuels, Bioproducts and Biorefining*, 15, pp. 1950-1964. https://doi.org/10.1002/bbb.2282.

Kusumastuti, R.D., Van Donk, D.P., and Teunter, R., 2016. Crop-related harvesting and processing planning: a review. *International Journal of Production Economics*, 174, pp. 76-92. https://doi.org/10.1016/j.ijpe.2016.01.010.

Lamb, W.F., Wiedmann, T., Pongratz, J., Andrew, R., Crippa, M., Olivier, J.G.J., Wiedenhofer, D., Mattioli, G., Khourdajie, A. A., House, J., Pachauri, S., Figueroa, M., Saheb, Y., Slade, R., Hubacek, K., Sun, L., Ribeiro, S.K., Khennas, S., De La Rue Du Can, S., and Minx, J., 2021. A review of trends and drivers of greenhouse gas emissions by sector from 1990 to 2018. *Environmental Research Letters*, 16(7), 073005. https://doi.org/10.1088/1748-9326/abee4e.

Lanorte, A., De Santis, F., Nolè, G., Blanco, I., Loisi, R.V., Schettini, E., Vox, G., 2017. Agricultural plastic waste spatial estimation by Landsat 8 satellite images. *Computers and Electronics in Agriculture*, 141, pp. 35-45. http://dx.doi.org/10.1016/j.compag.2017.07.003

Liuzzi, S., Rubino, C., Martellotta, F., Stefanizzi, P., Casavola, C., and Pappalettera, G., 2020. Characterization of biomass-based materials for building applications: The case of straw and olive tree waste. *Industrial Crops & Products*, 147, 112229. https://doi.org/10.1016/j.indcrop.2020.112229.

McKendry, P., 2002. Energy production from biomass (part 1): overview of biomass. *Bioresource Technology*, 83(1), pp. 37-46. https://doi.org/10.1016/S0960-8524(01)00118-3.

Nampeera, J., Recepoğlu, Y.K., and Yuksel, A., 2022. Valorization of olive tree pruning waste for potential utilization in lithium recovery from aqueous solutions. *Biomass Conversion and Biorefinery*, 1, pp. 1-13. https://doi.org/10.1007/s13399-022-02647-2.

QGIS. https://www.qgis.org.

Ryłko-Polak, I., Komala, W., and Białowiec, A., 2022. The Reuse of Biomass and Industrial Waste in Biocomposite Construction Materials for Decreasing Natural Resource Use and Mitigating the Environmental Impact of the Construction Industry: A Review. *Materials*, 15, 4078. https://doi.org/10.3390/ma15124078.

Sommer, S.G., Hamelin, L., Olesen, J.E., Montes, F., Jia, W., Chen, Q., and Triolo, J.M., 2015. Agricultural waste biomass. In: *Supply Chain Management for Sustainable Food Networks*, pp. 67-106. https://doi.org/10.1002/9781118937495.CH3.

Tong, C., 2019. Introduction to materials for advanced energy systems. Cham (Switzerland): Springer.

Tripathi, N., Hills, C.D., Singh, R.S., and Atkinson, C.J., 2019. Biomass waste utilisation in low-carbon products: harnessing a major potential resource. *Climate and Atmospheric Science*, 2, 35. https://doi.org/10.1038/s41612-019-0093-5.

Velázquez-Martí, B., Fernández-González, E., López-Cortés, I., and Salazar-Hernández, D.M., 2011. Quantification of the residual biomass obtained from pruning of trees in Mediterranean olive groves. *Biomass and Bioenergy*, 35(7), pp. 3208-3217. https://doi.org/10.1016/j.biombioe.2011.04.042.

Venkatramanan, V., Shah, S., Rai, A.K., and Prasad, R., 2021. Nexus Between Crop Residue Burning, Bioeconomy and Sustainable Development Goals Over North-Western India. *Frontiers in Energy Research*, 8, 614212 https://doi.org/10.3389/fenrg.2020.614212.

Vox, G., Schettini, E., and Scarascia-Mugnozza, G., 2005. Radiometric properties of biodegradable films for horticultural protected cultivation. *Acta Horticulturae*, 691 (2), pp. 575-582. https://doi.org/10.17660/ActaHortic.2005.691.69.

Zhou, C., and Wang, Y., 2020. Recent progress in the conversion of biomass wastes into functional materials for value-added applications. *Science and Technology of Advanced Materials*, 21(1), pp. 787-804. https://doi.org/10.1080/14686996.2020.1848213.

A GIS-BASED MODEL TO MAP GRAVITY CENTERS OF AGRICULTURAL END-OF-LIFE PLASTICS FOR A SUSTAINABLE WASTE MANAGEMENT

A. Hachem [1], I. Blanco [2], G. Scarascia Mugnozza [3], G. Vox [1] *

[1] Department of Soil, Plant and Food Sciences (DiSSPA), University of Bari, Italy
[2] Department of Biological and Environmental Sciences and Technologies (DiSTeBA), University of Salento, Italy
[3] Department of Civil, Environmental, Land, Building Engineering and Chemistry (DICATECh), Polytechnic University of Bari, Italy

KEY WORDS: Plastic waste indices, Collection center, Land use maps, Earth observation products

ABSTRACT:

Agricultural plastics applications are essential for quality and production enhancement of agricultural systems. However, they generate significant amounts of waste that pose a serious threat to the environment. Effective waste management strategies are required to address this issue such as the development of a comprehensive map of agricultural plastic waste (APW). This paper presents a GIS-based model for mapping APWs and identify their gravity centers in the provinces of Bari and Brindisi in Southern Italy.

Land use maps and APW indices were used to identify location and amount of APWs. Suitable areas for the first collection of end-of-life plastics were determined as buffer area around the gravity centers location. Land use maps based on orthophotos made available on the Apulia region website, in Italy, were used. The use of earth observation products, easily updatable, makes it possible to manage the spatial and temporal dispersion of waste related to the seasonality of agricultural production.

The results of the research show that the model is effective in identifying areas with APW generation. The location of the APW gravity centers was found in areas with intensive agriculture.

Overall, this research demonstrated the potential of GIS-based models for siting APW first collection centers. The GIS database relies on land use maps obtained from orthophotos as earth observation product, but land use maps can be easily created and updated with remote sensing imagery. By implementing this model decision makers, managers and land planners can take proactive measures to promote sustainable waste management chains.

1. INTRODUCTION

1.1 Plastics in agriculture

In modern agriculture, plastic serves a diverse range of purposes contributing to overall higher productivity (King et al. 2023). These include plastic films for greenhouses and mulching which contribute to an improved growing environment allowing crops to thrive even under harsh environmental conditions as well as in periods where these crops would not normally live (Cillis et al. 2022).

Plastic use is also important especially in irrigation systems such as drip or trickle irrigation which involves the precise delivery of water directly to the root zones of plants through a network of tubes and emitters. Plastic components are integral to this system, as they provide the necessary durability, flexibility, and resistance to moisture, ensuring that water reaches the plants efficiently. Furthermore, plastic is instrumental in other aspects of agriculture, including the packaging of fertilizers and pesticides. Plastic containers and bags provide an effective barrier for human safety and against moisture and contaminants, ensuring the quality and potency of these agricultural inputs. This is essential for farmers to achieve optimal results relative to their production systems.

In crop protection, plastic nets play a vital role. They serve as shields against pests, birds, and other environmental factors that can harm crops. On the other hand, in livestock farming, plastic silage bags have become indispensable for collecting and storing animal feed. These bags offer an airtight and moisture-resistant environment, preventing spoilage and ensuring that the feed retains its nutritional value over an extended period (King et al. 2023).

1.2 Agricultural plastic waste

The widespread use of plastic in agriculture has undoubtedly improved production efficiency, but agricultural plastics have a short useful life (Schettini and Vox, 2012; Blanco et al., 2022). This results in the production of a huge quantity of plastic waste materials, which needs a correct collection, disposal and recycling process (Vox et al., 2005). The quantity of worldwide agricultural plastic waste is not well known, but it ranges in the literature from 2 to 6.5 million tons per year (Meng et al. 2016). Farmers often resort to burning or improperly disposing of plastic waste, compounding the environmental challenges associated with plastic pollution (Briassoulis et al. 2010). These improper disposal practices result in a significant cost to the environment and soil health.

Making matters worse is that agricultural plastic waste (APW) has often been overlooked in recycling efforts, despite the pressing need to address this issue. The volume of APW is substantial and continues to grow exponentially, largely driven by global population growth and the increasing demand for agricultural products. When this waste is improperly managed, it not only contributes to environmental degradation but also poses a threat to human health and biodiversity (Hachem et al. 2023).

Recognizing these challenges, recycling agricultural plastics has become a paramount concern. Recycling not only helps mitigate the negative environmental impacts of improper disposal but also offers several other important benefits. First and foremost, it conserves valuable resources by extending the lifecycle of plastic materials, reducing the need for virgin plastic production. Additionally, recycling agricultural plastics contributes to energy conservation by reducing the energy-intensive process of manufacturing new plastic products from raw materials.

Perhaps most significantly, recycling agricultural plastics aligns with the principles of a circular economy, where resources are

* Corresponding author

used efficiently, waste is minimized, and materials are reused and recycled whenever possible (Scarascia-Mugnozza et al. 2008).
The first problem in the chain of recovery, storage and subsequent recycling of agricultural plastics is their dispersion in space and time due to the seasonality of agricultural production. Key tools for mapping and defining the routes of agricultural waste are GIS (Geographical Information System) technologies. These are based on earth observation products such as orthophotos, satellite or drone imagery. This research proposes a GIS methodology based on maps made from orthophotos to map agricultural plastic waste and to locate first collection centers.

1.3 APW collection centers siting using land analysis tools

Mapping plastics used in agricultural land (Picuno et al. 2011; Tarantino and Figorito, 2012; Novelli and Tarantino, 2015; Novelli et al. 2016), plastic waste quantification (Blanco et al. 2018) and set-up of collection strategies are necessary steps in a sustainable agricultural production (Briassoulis et al. 2013). Earth observation products and their application in land analysis tools are of fundamental support for this purpose. Plastic waste mapping, analysis and management can be realized by using a GIS. This is a powerful tool for land analysis and management (Díaz-Palacios-Sisternes et al., 2014; Borgogno Mondino et al., 2015). Data can be organized in GIS database that can be easily updated and managed, increasing the knowledge about land use, productive activities, and environmental threats. Updates of regional land-use databases or other earth observation products could be used to detect changes in land use and thus to update the GIS database (Lanorte et al., 2017).
This approach assists the planning of actions oriented toward increasing the environmental sustainability of a specific territory. GIS can support decision makers, managers and land planners in defining the best waste management facilities and action plans.
A sustainable waste management needs comprehensive solutions, including the strategic placement of collection centers tailored to specific types of plastic applications (Blanco et al. 2018). These collection centers serve as critical hubs where waste generated from various agricultural plastic uses can be systematically gathered, sorted, and processed. By customizing these centers to suit the distinct characteristics of different plastic applications, we can streamline the recycling and disposal processes, making them more efficient and environmentally friendly (Blanco et al. 2018).
This approach not only helps mitigate the adverse environmental impact of plastic waste but also aligns with the broader goal of sustainable resource management. It acknowledges the inevitability of plastic use in agriculture and seeks to find responsible ways to manage the resulting waste, contributing to a more sustainable and environmentally conscious agricultural industry. The methodology proposed in our research was based on the use of orthophoto-based GIS tools to locate the gravity centers of different kinds of APW. Suitable areas for the placement of centers of waste first collection were defined around the gravity centers.

2. MATERIALS AND METHODS

APW first collection centers location was defined based on APW gravity centers identification. Center of gravity theory was applied to analyze the spatial distribution of APW generation (Zhang et al., 2012; Cobos-Mora et al., 2023). To this end, Plastic Waste Indices (PWIs) were defined for the quantification of plastic waste generated from the different agricultural practices. PWIs were applied to the land features, each describing the crop type, as obtained by the land use map.

2.1 Indices for APW quantification

The PWI serves as a valuable tool for assessing the annual average waste quantity (kg ha^{-1} yr^{-1}) produced per cultivated area, considering various plastic applications in different crop types. It is crucial to acknowledge that each plastic type has its distinct lifespan.
PWIs were calculated based on several factors mainly crop type, plastic application used in the cultivation process and plastic properties (Blanco et al., 2018). Experience with agricultural plastic applications, questionnaires and interactions with farmers and their associations as well as field surveys were essential for the validation process of the different PWI indices. Plastic properties include the density of the plastics, their thickness, their life duration as well as a correction factor that considers the increase of the plastic material surface due to the coverage slope with respect to the soil surface, in case of greenhouse, low tunnel or vineyard covering materials. For irrigation systems, diameter of small and large pipelines is also considered. PWIs assigned to bags of fertilizers and containers of pesticides were acquired by interaction with farmers, data from the literature (Briassoulis et al. 2013) and databases in the University of Bari.
As an example of a plastic waste index and to better know the methodology of its calculation, the following equation applies when quantifying waste generated from plastic films of greenhouses, low tunnels and vineyards covering materials:

$$PWI_{Films} = \frac{\rho \cdot T}{years} \cdot F_{correction} \qquad (1)$$

where ρ = density of plastic material [kg m^{-3}]
T = thickness of plastic material [m]
$F_{correction}$= correction factor
Years = useful life [year]

PWI is expressed in kg ha^{-1}year^{-1}. $F_{correction}$ takes into account the slope of the coverage relative to the area of ground covered.

Table 1. Plastic waste indices for crop type and plastic application

Plastic waste index (kg ha^{-1}yr^{-1})			
Covering films		**Agrochemical containers**	
Vineyards	613.8	Wine grapes	6.0
Orchards	764.2	Table grapes	10.0
Greenhouses	565.0	Olive groves	0.6
Low tunnel films		Orchards	1.8
Vegetables in open field	936.0	Vegetables	1.7
Nets		Greenhouses	3.4
Vineyards (anti-hail nets)	159.0	**Fertilizers bags**	
Olive groves (nets for olive collection)	43.2	Vineyards	1.6
Orchards (nets for crop protection)	192.2	Olive groves	0.5
Greenhouses (shading nets)	133.3	Orchards	2.2
Irrigation pipes		Vegetables	2.5
Vineyards	60.0	Greenhouses	2.0
Olive groves	36.0		
Orchards	45.0		
Vegetables	50.0		
Greenhouses	75.0		

More indices for different crop types and plastic applications are presented in Table 1.

2.2 Land use maps in provinces of interest

Using the open source QGIS geographic information system software (QGIS, 2023), provinces of Bari and Brindisi in Apulia Region, Southern Italy were delimited.
Single featured land use maps of these two provinces were acquired by the official regional website (Regione Puglia, 2023). The land use map of the Apulia Region, scale 1:5000, derives from orthophotos, featuring 50 cm pixels, created using a photogrammetric camera. The legend of the map is compliant with the European CORINE Land Cover Changes Database with an expansion to the fourth level.
Area calculations were performed for individual features using the field calculator in QGIS. Then, the selection was refined to retain only the features of interest, each feature being characterized by one land use only. Next, PWIs were assigned to each feature. Finally, geo-referenced maps of APW were obtained.
Figure 1 shows the delimitation of the provinces with respect to Italy, as well as the distinction between different land uses inside the study area. Land uses we considered in the study were orchards, olives, vineyards, irrigated covered crops and non-irrigated covered crops. Everything other than agricultural activities were excluded from the study.

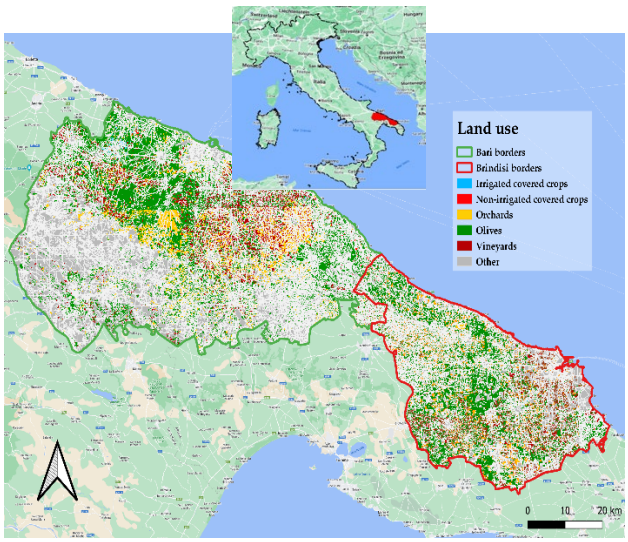

Figure 1. Land use in Bari and Brindisi provinces

2.3 Creation of features centroids

The centroid for each polygon (feature) corresponding to the crops under study (irrigated cover crops, non-irrigated covered crops, orchards, olives and vineyards), in the land use map was created by using the centroids geometry tool for further facilitation in localizing the waste collection centers. All the other polygons, associated to others land uses, were neglected to detect the optimal siting of collection centers dedicated only to waste generated from the crop systems previously mentioned. Figure 2 shows the centroids acquired for each polygon.

2.4 Collection centers localization in each province

QGIS offers an analysis tool that is the “mean coordinates” tool. It allows to return the mean coordinates of a set of points, in this case, the features centroids. This tool takes into account a weight field, which, in our case, is the APW amount of the feature, associated with the centroid. This was realized for each plastic application in this study (nets, films, irrigation, bags and containers).
To this extent, APW gravity centers were identified at the mean coordinates as a single point that is relevant to each of the plastic application mentioned. Then, a buffer zone of 3 km was assigned to each APW gravity center to allow freedom of localization of the collection center inside of this area in case of presence of any kind of obstruction.
After acquiring potential area for collection centers siting for each province separately, the same procedure was followed to obtain the potential site of waste collection centers for both provinces merged.

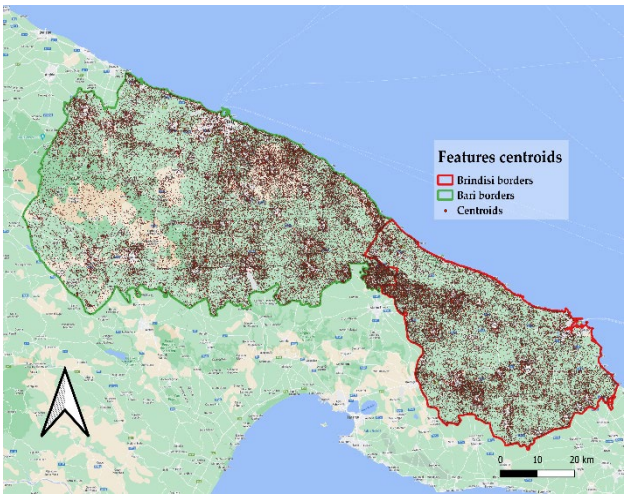

Figure 2. Features centroids in Bari and Brindisi provinces

3. RESULTS

For each province, five candidate areas for collection centers were obtained depending on the APW considered during the quantification process. The collection centers location mainly depended on the type of usage of plastic material in the production system. They included collection centers for irrigation systems, pesticidal containers, fertilizers bags, nets for crop protection and olive collection, and films for greenhouses.

3.1 Bari province collection centers

The most cultivated crops in Bari province were olives and grapes which explains the localization of the collection centers close to these types of production. The locations of the collection centers of Bari province are shown in Figure 3 along with their 3 km buffer zones, allowing for a freedom of localization for further environmental analysis in case needed.

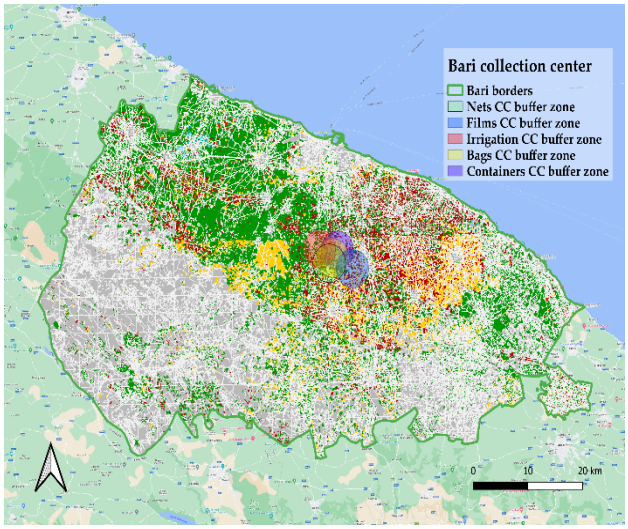

Figure 3. Bari province waste collection centers location

3.2 Brindisi province collection centers

Brindisi province had the same results as Bari regarding the place of localization of collection centers, since the dominant crops inside this area were also olives and grapes. Figure 4 shows the collection centers locations inside Brindisi province as well as the 3 km buffer zones.

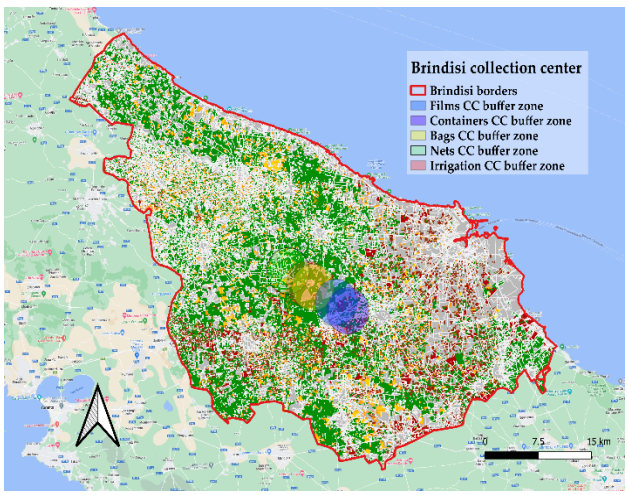

Figure 4. Brindisi province waste collection centers location

3.3 Merged provinces waste collection centers

The same previous procedure of each province was also performed by merging the coordinates of Bari and Brindisi provinces together and by executing the mean based on the APW of both. Figure 5 shows the collection centers location after merging all the features of the provinces.
Since Bari province is bigger and agricultural activities inside it are much more intense than Brindisi, collection centers were mainly located inside Bari but in the vicinity of the borders of Brindisi province, which was expected.

4. CONCLUSIONS

Managing agricultural waste effectively is imperative, primarily because it's unrealistic to curtail plastic usage in the face of a growing population's demands.

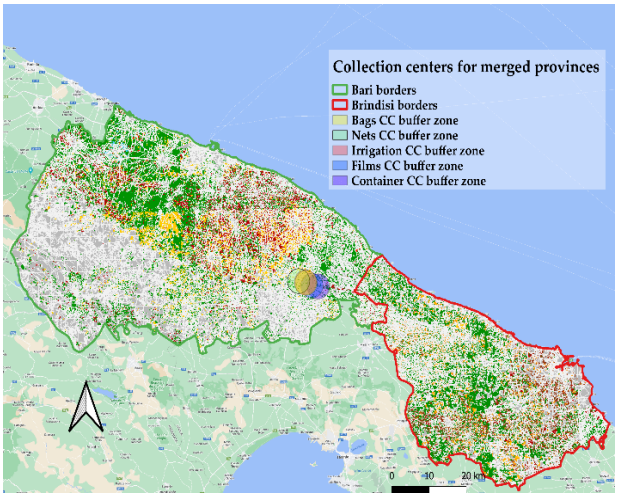

Figure 5. Merged provinces collection centers

The use of GIS with earth observation products in APW management has become an indispensable tool. This offers a comprehensive approach to addressing the challenges associated with plastic waste by harnessing the power of spatial data analysis and visualization. Despite the usage of GIS in this study on a small scale, it can be further extended to a larger scale, on the country level or even globally. This can create a database of waste quantities that can trigger policymakers to have awareness along with the producers on the damage caused by APW mismanagement.

ACKNOWLEDGEMENTS

The contribution to programming and conducting this research was equally shared between the Authors.
This research has been developed in the framework of the activities of the “Centro Interdipartimentale di Ricerca per la Cooperazione allo Sviluppo” (CPS) of the University of Bari, Italy.

REFERENCES

Blanco, I., Loisi, R.V., Sica, C., Schettini E., and Vox, G., 2018. Agricultural plastic waste mapping using GIS. A case study in Italy. *Resources, Conservation and Recycling*, 137, pp. 229-242. https://doi.org/10.1016/j.resconrec.2018.06.008

Blanco, I., Luvisi, A., De Bellis, L., Schettini, E., Vox, G., and Scarascia Mugnozza, G., 2022. Research Trends on Greenhouse Engineering Using a Science Mapping Approach. *Horticulturae* 2022, 8, 833. https://doi.org/10.3390/horticulturae8090833

Borgogno Mondino, E., Fabrizio, E., and Chiabrando, R., 2015. Site Selection of Large Ground-Mounted Photovoltaic Plants: A GIS Decision Support System and an Application to Italy, International Journal of Green Energy, 12:5, pp. 515-525. https://doi.org/10.1080/15435075.2013.858047

Briassoulis, D., Hiskakis, M., Scarascia-Mugnozza, G., Picuno, P., Delgado, C., and Dejean, C., 2010. Labeling scheme for agricultural plastic wastes in Europe. *Quality Assurance and Safety of Crops and Foods*, 2(2), pp. 93-104. https://doi.org/10.1111/j.1757-837X.2010.00061.x

Briassoulis, D., Babou, E., Hiskakis, M., Scarascia-Mugnozza, G., Picuno, P., Guarde, D., Dejean, C., 2013. Review, mapping

and analysis of the agricultural plastic waste generation and consolidation in Europe. *Waste Manage. Res*., 31 (12), pp. 1262–1278. http://dx.doi.org/10.1177/0734242X13507968

Cillis, G., Statuto, D., Schettini, E., Vox, G., and Picuno, P., 2022. Implementing a GIS-based digital atlas of agricultural plastics to reduce their environmental footprint; Part I: a deductive approach. *Applied Sciences*, 12(3), 1330. https://doi.org/10.3390/app12031330

Cobos-Mora, S.L., Guamán-Aucapiña, J., and Zúñiga-Ruiz, J., 2023. Suitable site selection for transfer stations in a solid waste management system using analytical hierarchy process as a multi-criteria decision analysis: a case study in Azuay-Ecuador. *Environ Dev Sustain*, 25, pp. 1944–1977. https://doi.org/10.1007/s10668-022-02134-8

Díaz-Palacios-Sisternes, S., Ayuga, F., García, A.I., 2014. A method for detecting and describing land use transformations: An examination of Madrid's southern urban-rural gradient between 1990 and 2006. *Cities*, 40, pp. 99-110. https://doi.org/10.1016/j.cities.2014.03.010

Hachem, A., Vox, G., and Convertino F., 2023. Prospective scenarios for addressing the agricultural plastic waste issue: results of a territorial analysis. *Applied Sciences*, 13(1), 612. https://doi.org/10.3390/app13010612

King, C.D., Stephens, C.G., Lynch, J.P., and Jordan, S.N., 2023. Farmers' attitudes towards agricultural plastics – Management and disposal, awareness and perceptions of the environmental impacts. *Science of the Total Environment*, 864, 160955. https://doi.org/10.1016/j.scitotenv.2022.160955

Meng, T., Klepacka, A.M., Florkowski, W.J., Braman, K., 2016. Determinants of recycling common types of plastic product waste in environmental horticulture industry: the case of Georgia. *Waste Manag*., 48, 81e88. https://doi.org/10.1016/j.wasman.2012.01.018

Lanorte, A., De Santis, F., Nolè, G., Blanco, I., Loisi, R.V., Schettini, E., Vox, G., 2017. Agricultural plastic waste spatial estimation by Landsat 8 satellite images. *Computers and Electronics in Agriculture*. 141, 35–45. http://dx.doi.org/10.1016/j.compag.2017.07.003.

Novelli, A., Tarantino, E., 2015. Combining ad hoc spectral indices based on LANDSAT-8 OLI/TIRS sensor data for the detection of plastic cover vineyard. *Remote Sens. Lett.*, 6 (12), pp. 933–941. http://doi.org/10.1080/2150704X.2015.1093186

Novelli, A., Aguilar, M.A., Nemmaoui, A., Aguilar, F.J., Tarantino, E., 2016. Performance evaluation of object based greenhouse detection from Sentinel-2 MSI and Landsat 8 OLI data: A case study from Almería (Spain). *Int. J. Appl. Earth Obs.*, 52, pp. 403–411. http://doi.org/10.1016/j.jag.2016.07.011

Picuno, P., Tortora, A., Capobianco, R.L., 2011. Analysis of plasticulture landscapes in Southern Italy through remote sensing and solid modelling techniques. *Landscape Urban Plan*, 100 (1–2), pp. 45–56. http://doi.org/10.1016/j.landurbplan.2010.11.008

QGIS, 2023. A Free and Open Source Geographic Information System. https://www.qgis.org/en/site/ (accessed on 15 April 2023).

Scarascia-Mugnozza, G., Sica, C., and Picuno, P., 2008. The optimisation of the management of agricultural plastic waste in Italy using a geographical information system. *Acta Horticulturae*, 801, pp. 219-226. https://doi.org/10.17660/ActaHortic.2008.801.20

Schettini, E., Vox, G., 2012. Effects of agrochemicals on the radiometric properties of different anti-UV stabilized EVA plastic films, *Acta Horticulturae*, 956, pp. 515 – 522. http://dx.doi.org/10.17660/ActaHortic.2012.956.61

Regione Puglia, 2023. SIT Puglia, Maps website. http://www.sit.puglia.it/ (accessed on 27 April 2023).

Tarantino, E., Figorito, B., 2012. Mapping rural areas with widespread plastic covered vineyards using true color aerial data. *Rem. Sens.*, 4 (7), 1913e1928. https://doi.org/10.3390/rs4071913

Vox, G., Schettini, E., Scarascia-Mugnozza, G., 2005. Radiometric properties of biodegradable films for horticultural protected cultivation, *Acta Horticulturae*, 691, pp. 575 – 582. http://dx.doi.org/10.17660/ActaHortic.2005.691.69

Zhang, Y., Zhang, J., Yang, Z., & Li, J. (2012). Analysis of the distribution and evolution of energy supply and demand centers of gravity in China. *Energy Policy*, 49, pp. 695–706. https://doi.org/10.1016/j.enpol.2012.07.012

AN AUTOMATIC AND EFFECTIVE PIPELINE FOR INDIVIDUAL TREE DETECTION USING LOW-DENSITY AIRBORNE LASER SCANNING DATA IN LARGE AREAS OF MEDITERRANEAN FOREST

A. Nemmaoui *, F.J. Aguilar, M.A. Aguilar

Department of Engineering and Research Centre CIAIMBITAL, University of Almería, Carretera de Sacramento s/n, La Cañada de San Urbano, 04120 Almería, Spain; an932@ual.es (A.N.); faguilar@ual.es (F.J.A.); maguilar@ual.es (M.A.A.).

KEY WORDS: Forest inventory, Tree detection, Above ground biomass (AGB), Low-Density Airborne Laser Scanning (LD-ALS).

ABSTRACT:

State-of-the-art approaches use different algorithms for individual tree detection. For each algorithm, a specific methodology to create the input Canopy Height Model and/or many parameters should be tuned to adapt the segmentation algorithm to each particular forest stand. The main goal of this work aims at developing a pipeline that requires minimal user interaction when working with Low-Density Airborne Laser Scanner data in large areas of Mediterranean forest. Therefore, in this paper three open source raster-based algorithms and one point-cloud-based algorithm were tested to automatically extract tree location, total tree height and tree crown diameter. Through intensive experiments, from tuning the input Canopy Height Models and the sets of parameters, it could be concluded that the point-cloud-based algorithm performed better results. However, by applying this same methodology over large areas and using the same set of parameters in all reference plots, it was shown that the raster-based algorithms obtained better and more robust results. In this sense, these results confirm the usefulness of Low-Density Airborne Laser Scanner data to segment trees (F1-score > 70%) and estimate their height and crown diameter in large areas of Mediterranean forest, also highlighting some key aspects related to the choice of the correct method and tuning parameters.

1. INTRODUCTION

Forests act as important carbon sinks and are therefore key components of the global carbon cycle. The carbon dioxide emissions account is essential for climate regulation policies and the evaluation of the effects of these policies, as well as for understanding the services they provide to societies (Ameray et al., 2021).

Traditionally, forest inventories are completed by ground-based expert crews. These field surveys are uneconomical, time consuming and exhausting (especially when applied over large and remote areas), not being adequate for studies dealing with periodic data collection (Tang and Shao, 2015). Consequently, one of the key topics in forest applications is to find an effective method to produce efficient and accurate inventories.

In recent years, Remote Sensing (RS) has proven to be capable of providing independent, timely and reliable forest information. RS data are used to estimate several forest variables of silvicultural interest such as crown diameter (CD), height (H), diameter at breast height (DBH) and aboveground biomass (AGB) (Aguilar et al., 2022, 2021, 2019). In this sense, and due to its ability to estimate attributes at tree level, point cloud data (e.g., LiDAR, ALS, UAV-imagery based data, etc.) has become a valuable data source in the field of efficient and accurate detection and segmentation of individual trees.

State-of-the-art approaches use different algorithms for Individual Tree Detection (ITD), which consists of labelling point cloud data at the scale of individual trees. For each algorithm, a specific methodology to create the input Canopy Height Model (CHM) and/or many parameters should be tuned to somehow adapt the segmentation algorithm to each particular forest stand. This approach makes the results highly dependent on the applied local fitting parameters, which implies difficulties when applied for large-scale mapping. In addition, the parameter setting process is quite time consuming and requires learning and understanding the meaning and role of each parameter.

The main goal of this work aims at developing a pipeline that requires minimal user interaction when working on large areas of Mediterranean forest. The expected results should facilitate the production of broad-extend individual tree maps and extract the corresponding dendrometric parameters from Low-Density Airborne Laser Scanner (LD-ALS) data without wasting time adjusting the algorithm parameters.

2. MATERIAL AND METHODS

2.1 Study area

The study area was located at "Sierra de María-Los Vélez Natural Park" (Fig. 1). With an area of 22562 hectares, it is located in the southeastern area of the Iberian Peninsula, in the northern-most sector of the province of Almeria. Thirty-eight representative square plots of 25 m side were selected in the study area (Fig. 1d), mainly harbouring almost exclusively Aleppo pine (*Pinus halepensis* Mill.) as the dominant species (between 76% and 98%) with different percentages of vegetation cover ranging from 20% to 87%.

Figure 1. Location of the study area. a) Province of Almeria (Spain) in white. b) Region of "Los Vélez" (in green). c) Sierra de María-Los Vélez Natural Park (in blue). d) Reference field plots are represented as white dots.

* Corresponding author

2.2 Low-Density Aerial Laser Scanner data (LD-ALS)

The LD-ALS data used in this study was provided by the National Plan of Aerial Orthophotography of Spain (PNOA). The acquisition of this data was carried out between October 12 and 13, 2020. The geodetic reference system for X and Y coordinates was ETRS 1989 UTM Zone 30N, while heights were referred to the official Spanish geoid EGM08-REDNAP. The average point density was 1.5 points/m^2 (all returns), presenting a nominal (at nadir) horizontal and vertical accuracy lower than 0.3 m and 0.15 m, respectively.

Thirty-eight subsets (square shape of 31 m×31 m, including an extended buffer area of 3 m) of LD-ALS point clouds corresponding to the previously defined reference plots were extracted. The choice of this expanded area was made to avoid the "edge effects" that would have produced the loss of data points belonging to trees just on the boundary of the reference plots of 25 m side. The final point cloud density took an average value of 3.5 point/m^2, ranging from 2.12 to 10.00 point/m^2. The mathematical framework based on a Gaussian Markov Random Field (GMRF) ((freely available code at https://github.com/3DLAB- UAL/dem-gmrf) was used to extract DTMs with a grid spacing of 0.5 m and free of outliers using the workflow proposed in Nemmaoui et al. (2023). This GMRF-DTMs was used for the normalization of the canopy surface models.

2.3 Reference Data – Ground Truth

The field survey was carried out from 31 May to 11 June 2021. Any tree with DBH ≥ 7.5 cm and H ≥ 2 m was recorded. The ERTS89 coordinates of each tree were collected using the Emlid Reach GPS RTK RS2 (rover and base). Tree height was also measured using a Nikon® Forestry Pro II rangefinder/hypsometer, while CD was estimated from a 3 cm/pixel RGB orthoimages obtained by using Agisoft Metashape software and stereo-images taken by an Unmanned Aerial Vehicles (UAV). In this sense, different missions were programmed between March 4 and 8, 2021, using a DJI Phantom 4 Advance© with a flying height of 75 m above ground.

Table 1 depicts the most important dasometric characteristics of the thirty-eight reference field plots. It includes the vegetation cover, the tree density per hectare, the tree heights, the basal area and Lorey´s mean height (Lh).

	VC (%)	Density (Trees/ha)	Height (m)	G (m^2/ha)	Lh (m)
Max	86.79	1504	18.66	36.03	16.21
Min	19.99	96	2.03	1.52	3.48
Average	45.29	371.37	8.85	18.36	9.79

Table 1. Characteristics, (max, min and average) of the 38 references plots: Vegetation cover (CV), Density, Height, Basal area (G) and Lorey´s height (Lh).

The vegetation cover took an average value of 45.29% (ranging from 19.99% to 86.79%), while the values of basal area ranged from 1.52 to 36.03 m^2/ha (average of 18.36 m^2/ha). Lorey´s mean height presented an average of 9.79 m, ranging from 3.48 m to 16.21 m. The mean height took an average value of 8.85 m, ranging between 2.03 m and 18.66 m. The thirty-eight selected references plots presented an average tree density of 371.37 trees/ha (ranging from 96 trees/ha to 1504 trees/ha).

2.4 Processing and workflow

Figure 2 provides an overview of the methodology and workflow adopted in this study. This workflow consisted of four steps: i) point cloud data normalization and input data generation, ii) ITD, iii) accuracy assessment and iv) selection of the best sets of tuning parameters.

The normalization process is performed by subtracting the corresponding terrain elevation of the corresponding GMRF-DTM, obtained from the method described in Nemmaoui et al. (2023), from each point cloud Z value. In this way, the resulting normalized point cloud stores the elevation of each point as its vertical height above the ground.

Two different interpolation algorithms, such as Point-to-raster (P2R) and Pit-free (PF), were tested to build a raster product called normalized digital surface model, better known as CHM. This CHM was used as input for the raster-based (RB) tree segmentation methods of Silva2016 (Silva et al., 2016) and Dalponte2016 (Dalponte and Coomes, 2016) (see workflow depicted in Figure 2).

P2R method consists of establishing a regular grid at a defined resolution and attributing the elevation of the highest point to each pixel. A fixed smoothing 3×3 pixels mean filter was performed to the resulting CHM. In this way, a smoothed CHM with a spatial resolution of 0.5 m was built for each reference plot.

PF method is based on horizontally segmenting the normalized point cloud at different heights (usually 0.2, 5, 10, and 15 m). For each segmented layer, multiple-level CHM are generated according to the highest point. Finally, the pit-free CHM is generated by taking the maximum value of these multiple-level CHM in the corresponding pixels (Khosravipour et al., 2014). A fixed smoothing 3×3 pixels mean filter was also applied to the resulting CHM. All these functions have been implemented in R software, Version 1.4.1103 (R Core Team, 2022).

The third pre-processing algorithm used was the method implemented in the Digital Forestry Toolbox (DFT) (Parkan, 2018) to build the corresponding CHM from the normalized point cloud. In this case, the Inverse Distance Weighted (IDW) interpolation method (Bartier and Keller, 1996) was applied to obtain the raster CHM, also using a smoothing 3×3 pixels Gaussian low pass filter to the IDW-based CHM. Note that DFT can only be executed in Matlab (MathWorks, Inc., Natick, MA, USA).

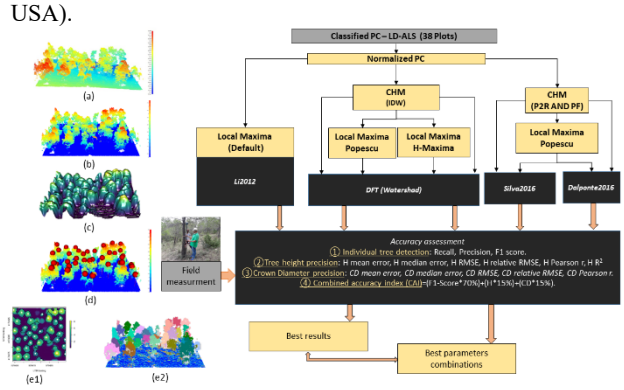

Figure 2. Workflow of the LD-ALS data processing, individual tree detection, accuracy assessment and best parameters extraction. (a) Classified point cloud (b) Normalized point cloud (c) CHM (d) Normalized point cloud with Seeds in red (e1) and (e2) Extracted parameters (position, H, CD) presented in 2D and 3D, respectively.

Once obtained the CHM for each reference plot, three RB ITD methods were tested to segment trees: Dalponte2016 (Dalponte and Coomes, 2016), Silva2016 (Silva et al., 2016), and DFT approaches (Parkan, 2018) (we invite the reader to check the references for more details of each method).

Dalponte2016 uses local maxima identification with a region growing strategy headed up to group unlabelled pixels to an adjacent region if the difference of intensities between the pixel

and the local maxima (LM) is less than a user-defined parameter. The LM searching has been implemented in the LM function available in the LidR package (Roussel et al., 2020). It is based on a variable Tree Window Size (TWS) adopting the linear regression with a quadratic model using only height as the predictor variable (Popescu and Wynne, 2004) in pines forests (see equation 1). Crossing all input CHM and the three parameters of the Dalponte2016 function (see reference), the number of output segmentations was 1296 in total for each reference plot.

$$\text{Crown width} = 3.75105 - 0.17919H + 0.01241H^2 \quad (1)$$

Silva2016 is focused on the way to better approximating the intersecting canopy of multiple trees after locating treetops by LM. A centroidal Voronoi tessellation is computed based on the location of the treetops. Then, the crown of each tree is computed by region growing inside each Voronoi cell. The region growing approach starts from the LM, including those closer pixels that satisfy the user-fixed threshold. Again, crossing the input CHM and the two parameters of Silva2016 function (see reference), the number of output segmentations was 162 for each reference plot.
The last RB algorithm tested in this study is included in the library DFT. In this case, two methods identify the treetops based on LM were checked. The first one is based on the method reported in Popescu and Wyne (2004) (DFT-P hereinafter). The second one relies on the methodology proposed by Kwak et al. (2007) (DFT-HM hereinafter). In this case, LM treetops are detected using the extended maxima transformation and distance transformation of the morphological image-analysis methods. In this study, the optimal H value was estimated for the range between 0.1 to 0.7 in steps of 0.05 (14 output (13 of DFT-HM + 1 of DFT-P) segmentations for each reference plot). In both cases, the final RB tree segmentation was faced by applying the algorithm marker controlled watershed (Kwak et al., 2007).
The only point-cloud-based (PCB) algorithm tested in this work was the method proposed by Li et al. (2012) (Li2012 hereinafter). It is a growing region approach working at 3D point cloud level. Crossing the four parameters of Li2012 function parameters (see reference), the number of output segmentations was 864 in total for each reference plot.
Following the workflow shown in Figure 2, and once the tree segmentations were extracted, the next step involved the accuracy assessment of the following three variables: i) ITD accuracy, ii) tree height estimation accuracy, and iii) tree crown diameter estimation accuracy.

a) ITD accuracy: tree detection ratio was evaluated in terms of recall (r), precision (p) and F1-score (Equations 2, 3 and 4).

$$r = \frac{TP}{(TP+FN)} \quad (2); \quad p = \frac{TP}{(TP+FP)} \quad (3);$$

$$\text{F1-score} = \frac{2*r*p}{r+p} \quad (4)$$

[TP: True positive (correct detection); FN: False Negative (omission error); FP: false positive (commission error)]

The value of r, p and F1-score were calculated as percentage (0-100%). The higher the value, the better the tree segmentation accuracy. These metrics have been used in several studies (Goutte and Gaussier, 2005; Li et al., 2012; Silva et al., 2016; Sokolova et al., 2006).
b) Tree height estimation accuracy: it was evaluated by applying some error metrics to each pair of estimated and observed H values for each correctly segmented tree. The selected robust metrics includes H mean error and H median error to estimate the systematic error. Due to its wide use, the H root mean square error (H RMSE) was also calculated to estimate random error. In addition, the H relative values of RMSE divided by the observed H mean value were computed to intuitively scale the magnitude of the random error. The Pearson's coefficient of linear correlation and r^2 coefficient between H estimated and observed were also computed. Note that the residuals (difference in heights) were calculated by subtracting the observed tree height from the tree height extracted with the algorithm.
c) Tree crown diameter estimation accuracy: the CD has been extracted from the concave area extracted by each algorithm used in this study. As for the height accuracy assessment, the calculated statistical parameters were the following: CD mean error, CD median error, CD RMSE, CD relative RMSE and CD Pearson r.
In this study, it has been considered that each algorithm must comply with the following goals: i) identifying the maximum number of trees existing in each reference plot, ii) extracting the height and crown diameter of each tree with the highest possible accuracy. For this reason, a combined accuracy index (CAI) (Equation 5) ranging from 0 to 100% was introduced to weight the importance of each goal. The first step, tree detection, is the most critical and should have the most importance (i.e., 70% of the weight). Once the trees have been correctly detected, the objective is to determine the dendrometric parameters (H and CD) of each tree.

$$CAI = (F1 - \text{score} * 70\%) + (Hp * 15\%) + (CDp * 15\%) \quad (5)$$

[F1-score (see equation 4) ranging from 0 to 1. H_p and CD_p: Pearson's coefficient of linear correlation for H and CD]

CAI was used to select the best performing ITD parameters set for each algorithm tested in this study. Next, the sets of parameters that most frequently gave the best results were applied to all plots with the aim of estimating the robustness of each of the tested methods. In this way, we attempted to approximate the potential accuracy of each method if it were applied to a large area.

3. RESULTS AND DISCUSSION

3.1 Tree detection

Table 2 depicts the tree detection accuracy in terms of recall, precision and F1-score for each algorithm tested in this study. The F1-score obtained was greater than 72% in all cases. The best accuracy was provided by the PCB algorithm, reaching a value of 89.51%. Working with a similar set of data in a mixed multi-layered forest in the French Alps and adopting a point-based approach, Vega et al. (2014) reported an overall performance of 75% (F1-score) including all trees (dominant, codominant and dominated trees).

Algorithm	CHM	Recall	Precision	F1-score
SILVA2016	Best of P2R and PF	74.76	**97.95**	83.54
	P2R	74.18	97.94	83.13
	PF	72.64	97.87	81.92
DALPONTE 2016	Best of P2R and PF	72.72	96.26	81.60
	P2R	72.12	95.77	80.96
	PF	70.78	95.56	79.84
DFT-HM	IDW-GS	79.76	69.61	72.14
DFT-P	IDW-GS	78.67	76.41	75.66
Li 2012	-	**86.08**	94.32	**89.51**

Table 2. Tree detection accuracy for the tested algorithms in terms of Recall, Precision and F1-score. GS: Gaussian smoothing.

Regarding the tested RB algorithms, Silva2016 was the best (F1-score = 83.54%), followed by Dalponte2016 (F1-score =

81.60%), DFT-P (F1-score = 75.66 %) and DFT-HM (F1-score = 72.14%).
In the case of Silva2016 and Dalponte2016 algorithms, and when comparing the two algorithms tested to build the input CHMs, it was observed that the P2R algorithm performed better.

3.2 Tree height estimation accuracy

Table 3 shows the statistical parameters computed to assess the accuracy of the estimated tree heights.

	CHM	H mean error	H median error	H RMSE	H relative RMSE	H Pearson r	H R^2
SILVA2016	Best of P2R and PF	-0.19	-0.22	0.47	5.44	0.94	0.82
	P2R	-0.19	-0.22	0.47	5.44	0.94	0.82
	PF	-0.2	-0.23	0.48	5.54	0.93	0.79
DALP-ONTE2016	Best of P2R and PF	-0.2	-0.23	0.48	5.45	0.94	0.81
	P2R	-0.2	-0.23	0.46	5.26	0.95	0.82
	PF	-0.22	-0.23	0.43	5.12	0.94	0.82
DFT-HM	IDW-GS	-0.24	-0.27	0.56	6.5	0.92	0.71
DFT-P	IDW-GS	-0.24	-0.27	0.54	6.09	0.93	0.70
Li2012	-	-0.26	-0.23	0.49	6.01	0.94	0.81

Table 3. Tree height estimation accuracy for the tested algorithms in terms of H mean error (m), H median error (m), H RMSE (m), H relative RMSE (%), H Pearson´s r and r^2 coefficient. GS: Gaussian smoothing.

Regarding systematic error, the bias for all the tested algorithms showed average values better than -26 cm and -27 cm for the mean and median high error, respectively, which pointed to a slight underestimation of the "true" elevation of the trees represented by LD-ALS data. This underestimation was also reported in other studies (e.g., Véga and Durrieu, 2011) and it is explained by the relation between the point density and the proportion of sampled tree apices. This effect is due to the low density of ALS data producing few laser impacts on the tops of the trees, a circumstance that makes it difficult to record just the apex of the tree. Focusing on the random error, RMSE presents values lower than 56 cm, which implies a relative RMSE lower than 6.5%. All algorithms showed a very good fit between the estimated and observed tree heights, reaching high values of the Pearson's coefficient with values greater than 0.92.

3.3 Crown diameter estimation accuracy

Table 4 depicts the statistical parameters computed to assess the accuracy of the estimated crown diameters. Almost all RB algorithms showed a negative systematic error, so pointing to an underestimation of the observed CD. Regarding the random error, it presented values ranging from 0.64 m to 2.47 m, with the Li2012 algorithm being the one that obtained the worst results. The highest values of the Pearson linear correlation coefficient were achieved using the Silva2016 algorithm.

	CHM	CD mean error	CD median error	CD RMSE	CD relative RMSE	CD Pearson r
SILVA-2016	Best of P2R and PF	-0.04	-0.05	0.64	15.24	0.75
	P2R	-0.10	-0.09	0.68	15.92	0.75
	PF	-0.08	-0.03	0.75	17.91	0.69
DALP-ONTE 2016	Best of P2R and PF	-0.01	-0.02	0.84	19.98	0.65
	P2R	0.04	0.04	0.8	18.89	0.66
	PF	-0.33	-0.33	0.88	21.18	0.62
DFT-HM	IDW-GS	-0.51	-0.54	1.36	30.86	0.61
DFT-P	IDW-GS	-0.28	-0.27	1.27	28.81	0.61
Li2012	-	1.86	1.89	2.47	56.9	0.57

Table 4. Tree crown diameter estimation accuracy for the tested algorithms in terms of CD mean error (m), CD median error (m), CD RMSE (m), CD relative RMSE (%) and CD Pearson's r. GS: Gaussian smoothing.

3.4 Combined accuracy index and large-scale mapping

All tested algorithms were grouped into three categories (gold, silver and bronze medals) based on the CAI awarded (Table 5).

	CHM	CAI (%)	Category
SILVA2016	Best of P2R and PF	**83.83**	**Silver**
	P2R	83.53	Silver
	PF	81.73	Silver
DALPONTE2016	Best of P2R and PF	**81.02**	**Bronze**
	P2R	80.81	Bronze
	PF	79.32	Bronze
DFT-HM	IDW-GS	73.48	
DFT-P	IDW-GS	**76.08**	
Li2012	-	**85.27**	**Gold**

Table 5. Combined accuracy index (CAI). The tree best algorithms have been ranked and the optimal value of each position is shown in bold. GS: Gaussian smoothing.

In view of the results obtained, it can be highlighted that the gold medal clearly went to the Li2012 algorithm, reaching a CAI value of 85.27%. In fact, this PBC algorithm obtained very good results in the ITD and H extraction phases, although it was the worst at extracting CDs. The silver medal was achieved by the Silva2016 algorithm, reaching CAI values of 83.83% when both the input CHMs and the Silva2016 parameters were tuned. Similar results (i.e. CAI = 83.53%) were obtained using the CHM generated with the P2R algorithm. The Dalponte2016 algorithm, with CAI values greater than 79%, achieved the bronze medal, with the DFT algorithm placing fourth place with CAI values slightly greater than 73%.
A second "round" of individual tree segmentation was carried out by applying the sets of parameters that ensured the best results in terms of CAI to all references plots (a proxy of large-scale mapping accuracy). The results obtained in this second round are depicted in Table 6, while the final selected sets of parameters are shown in Table 7.

	CHM	F1-Score	H Pearson´r	CD Pearson´r	CAI (%)
SILVA-2016	P2R	0.83	0.94	0.68	**82.12**
	PF	0.81	0.94	0.69	81.23
DALPO-NTE2016	P2R	0.80	0.94	0.25	74.18
	PF	0.79	0.94	0.20	72.70
DFT-HM	IDW-GS	0.70	0.93	0.61	72.03
DFT-P	IDW-GS	0.76	0.93	0.61	**76.08**
Li2012	-	0.83	0.94	0.55	**80.14**

Table 6. Tree detection accuracy and H and CD estimation accuracy computed for the tested algorithms applying the same sets of parameters to the 38 references plots (large-scale mapping). The algorithms are ranked from best to worst with gold, silver and bronze medals. GS: Gaussian smoothing.

In the case of large-scale mapping, the Li2012 algorithm obtained also very good results both in ITD and H extraction phases, showing a F1-score of 0.83 and a H Pearson´s r of 0.94. These results were similar to those obtained by the Silva2016 algorithm, which awarded the gold medal in this second round. However,

Li2012 failed when estimating CD, yielding a low Pearson´s r of 0.55. On the contrary, Silva2016 managed to obtain better results in terms of CD estimation, which allowed it to be placed in the first position of the ranking.

	CHM	Parameters	LD-ALS
SILVA2016	P2R	max_cr_factor	0.3
		exclusion	0.4
	PF	max_cr_factor	0.4
		exclusion	0.5
DALPONTE 2016	P2R	th_tree	2
		th_seed	0.2
		th_cr	0.1
	PF	max_cr	4
		th_tree	2
		th_seed	0.1
		th_cr	0.1
DFT-HM	IDW	max_cr	4
		Optimal H value	0.7
DFT-P	IDW	-	-
Li2012	-	dt1	2
		dt2	2.2
		R	2
		Zu	15
		hmin	2
		Speed-up	5

Table 7. Sets of parameters corresponding to the best results (CAI) applied to the 38 references plots (large-scale mapping).

With CAI values of 82.12% and 81.23% for P2R and PF, respectively, Silva2016 is undoubtedly the best option to cope with large-scale mapping (i.e., the same tuning parameters in all reference plots) when using LD-ALS data in Mediterranean forests. The algorithms implemented in DFT achieved the bronze medal, reaching a CAI value of 76.08% in the case of the DFT-P version. Finally, the Dalponte2016 method was left off the podium. It is worth noting that applying the same set of parameters to all the reference plots decreased the accuracy in CD estimation. This fact is reflected in lower values of the Pearson r coefficient of determination, which means a poorer fit between the estimated and observed CD.

4. CONCLUSIONS

This paper assessed the performance of several ITD algorithms applied to LD-ALS data. Thus, four different algorithms (three RB and one PCB) were tested. The results obtained demonstrate that the pipeline proposed in this work can be used to accurately extract individual trees and their corresponding dendrometric parameters.

Through intensive experiments, consisting in testing different algorithms to build the inputs CHMs, localizing treetops and setting the ITD parameters, it was concluded that the PCB Li2012 algorithm achieved better results. The local calibration of the ITD parameters provided an optimum tree detection and accurate dendrometric variables extraction. These results proved that LD-ALS data are a good option to accurately extract individual trees (F1-score > 89%) and the corresponding H and CD. By emulating large-scale mapping by applying the same set of parameters to all plots, Silva2016 proved to be the best option. In this case, the recommended set of parameters to detect Aleppo pine was 0.3 and 0.4 as thresholds for the maximum crown factor and the exclusion parameters, respectively. It is also recommended to build the input CHM with the P2R algorithm and detect treetops using a LM based on a variable Tree Window Size (TWS). This combination allowed to reach a CAI of 82.40% (F1-score = 83%; H Pearson's r = 0.94 and CD Pearson's r = 0.68).

ACKNOWLEDGEMENTS

This study was funded by the following research projects: 1) "*Enabling interdisciplinary collaboration to foster Mediterranean forest sustainable management and socio-economic valuation (ECO2-FOREST)"* (Proyecto Retos Junta de Andalucía, Spain. Grant number P18-RT-2327). 2) "*Intervention strategies for an integrated and sustainable management of the Mediterranean forest based on an interdisciplinary analysis and its economic assessment*" (Programa Operativo FEDER Andalucía 2014-2020, Spain. Grant number UAL2020-SEJ-D1931). Finally, this work takes part of the general research lines promoted by the Agrifood Campus of International Excellence ceiA3, Spain (http://www.ceia3.es/). Finally, we appreciate the kind comments made by the editors and reviewers which have undoubtedly improved the paper.

REFERENCES

Aguilar, F.J., Nemmaoui, A., Aguilar, M.A., Jiménez-Lao, R., 2022. Aleppe Pine Allometric Modeling Through Integrating UAV Image-Based Clouds and Ground Based Data, in: ISPRS Annals of the Photogrammetry, Remote Sensing and Spatial Information Sciences. pp. 353–360. https://doi.org/10.5194/isprs-annals-V-3-2022-353-2022

Aguilar, F.J., Nemmaoui, A., Aguilar, M.A., Peñalver, A., 2021. Building Tree Allometry Relationships Based on TLS Point Clouds and Machine Learning Regression. Appl. Sci. 11, 10139. https://doi.org/10.3390/APP112110139

Aguilar, F.J., Nemmaoui, A., Peñalver, A., Rivas, J.R., Aguilar, M.A., 2019. Developing Allometric Equations for Teak Plantations Located in the Coastal Region of Ecuador from Terrestrial Laser Scanning Data. Forests 10, 1050. https://doi.org/10.3390/F10121050

Ameray, A., Bergeron, Y., Valeria, O., Montoro Girona, M., Cavard, X., 2021. Forest Carbon Management: a Review of Silvicultural Practices and Management Strategies Across Boreal, Temperate and Tropical Forests. Curr. For. Reports 7, 245–266. https://doi.org/10.1007/S40725-021-00151-W/TABLES/2

Bartier, P.M., Keller, C.P., 1996. Multivariate interpolation to incorporate thematic surface data using inverse distance weighting (IDW). Comput. Geosci. 22, 795–799. https://doi.org/10.1016/0098-3004(96)00021-0

Dalponte, M., Coomes, D.A., 2016. Tree-centric mapping of forest carbon density from airborne laser scanning and hyperspectral data. Methods Ecol. Evol. 7, 1236–1245. https://doi.org/10.1111/2041-210X.12575

Goutte, C., Gaussier, E., 2005. A Probabilistic Interpretation of Precision, Recall and F-Score, with Implication for Evaluation. Lect. Notes Comput. Sci. 3408, 345–359. https://doi.org/10.1007/978-3-540-31865-1_25/COVER

Khosravipour, A., Skidmore, A.K., Isenburg, M., Wang, T., Hussin, Y.A., 2014. Generating pit - free canopy height models from airborne lidar. Photogramm. Eng. Remote Sens. PE&RS 80, 863–872. https://doi.org/10.14358/PERS.80.9.863

Kwak, D.A., Lee, W.K., Lee, J.H., Biging, G.S., Gong, P., 2007. Detection of individual trees and estimation of tree height using LiDAR data. J. For. Res. 12, 425–434. https://doi.org/10.1007/S10310-007-0041-9/TABLES/4

Li, W., Guo, Q., Jakubowski, M.K., Kelly, M., 2012. A New Method for Segmenting Individual Trees from the Lidar Point

Cloud. Photogramm. Eng. Remote Sens. 78, 75–84.

Nemmaoui, A., Aguilar, F.J., Aguilar, M.A., 2023. UAV-Based Digital Terrain Model Generation to Support Accurate Inventories in Mediterranean Forests, in: Cavas-Martínez, F., Marín Granados, M.D., Mirálbes Buil, R., De-Cózar-Macías, O.D. (Eds.), Advances in Design Engineering III. INGEGRAF 2022. Lecture Notes in Mechanical Engineering. Springer International Publishing, Cham, pp. 565–581. https://doi.org/10.1007/978-3-031-20325-1_45

Parkan, M., 2018. Digital Forestry Toolbox for Matlab/Octave [WWW Document]. https://doi.org/10.5281/zenodo.1213013

Popescu, S.C., Wynne, R.H., 2004. Seeing the trees in the forest: Using lidar and multispectral data fusion with local filtering and variable window size for estimating tree height. Photogramm. Eng. Remote Sensing 70, 589–604. https://doi.org/10.14358/PERS.70.5.589

R Core Team, 2022. R: The R Project for Statistical Computing [WWW Document]. R Found. Stat. Comput. Vienna,. URL https://www.r-project.org/

Roussel, J.R., Auty, D., Coops, N.C., Tompalski, P., Goodbody, T.R.H., Meador, A.S., Bourdon, J.F., de Boissieu, F., Achim, A., 2020. lidR: An R package for analysis of Airborne Laser Scanning (ALS) data. Remote Sens. Environ. 251, 112061. https://doi.org/10.1016/J.RSE.2020.112061

Silva, C.A., Hudak, A.T., Vierling, L.A., Loudermilk, E.L., O'Brien, J.J., Hiers, J.K., Jack, S.B., Gonzalez-Benecke, C., Lee, H., Falkowski, M.J., Khosravipour, A., 2016. Imputation of individual longleaf pine (Pinus palustris Mill.) tree attributes from field and LiDAR data. Can. J. Remote Sens. 42, 554–573. https://doi.org/10.1080/07038992.2016.1196582

Sokolova, M., Japkowicz, N., Szpakowicz, S., 2006. Beyond accuracy, F-score and ROC: A family of discriminant measures for performance evaluation. AAAI Work. - Tech. Rep. WS-06-06, 24–29. https://doi.org/10.1007/11941439_114/COVER

Tang, L., Shao, G., 2015. Drone remote sensing for forestry research and practices. J. For. Res. 26, 791–797. https://doi.org/10.1007/S11676-015-0088-Y/FIGURES/2

Véga, C., Durrieu, S., 2011. Multi-level filtering segmentation to measure individual tree parameters based on Lidar data: Application to a mountainous forest with heterogeneous stands. Int. J. Appl. Earth Obs. Geoinf. 13, 646–656. https://doi.org/10.1016/J.JAG.2011.04.002

Vega, C., Hamrouni, A., El Mokhtari, A., Morel, M., Bock, J., Renaud, J.P., Bouvier, M., Durrieue, S., 2014. PTrees: A point-based approach to forest tree extraction from lidar data. Int. J. Appl. Earth Obs. Geoinf. 33, 98–108. https://doi.org/10.1016/J.JAG.2014.05.001

CHARACTERIZATION OF ALPINE PASTURES USING MULTITEMPORAL EARTH OBSERVATION DATA WITHIN THE CLIMATE CHANGE FRAMEWORK

T. Orusa[1,2,3*], A. Farbo[1], S. De Petris[1], F. Sarvia[1], D. Cammareri[2,3], E. Borgogno-Mondino[1]

[1] Department of Agricultural, Forest and Food Sciences (DISAFA), GEO4Agri DISAFA Lab, Università degli Studi di Torino, Largo Paolo Braccini 2, 10095 Grugliasco, Italy
(tommaso.orusa, alessandro.farbo, samuele.depetris, filippo.sarvia, enrico.borgogno)@unito.it
[2] Earth Observation Valle d'Aosta - eoVdA, Località L'Île-Blonde, 5, 11020 Brissogne, Italy – torusa@invallee.it
[3] IN.VA spa, GIS Unit, Località L'Île-Blonde, 5, 11020 Brissogne, Italy – dcammareri@invallee.it

KEY WORDS: Landsat missions, LST, NDVI, Trends modelling, pastures, climate change, Aosta Valley, Italy

ABSTRACT:

Climate change is profoundly affecting alpine ecosystems. Therefore, pastures monitoring represents a key point. Long time-series of Earth Observation (EO) data can be used to explore spectral and thermal behaviour of these surfaces in the climate change framework. In this work, almost 40 years of data were considered, with more than 900 acquisitions covering the period 1984-2022, from the Landsat 5-9 missions were obtained through Google Earth Engine (GEE) and the correspondent maps of Land Surface Temperature (LST) and Normalized Difference Vegetation Index (NDVI) were analysed. Pasture areas were mapped with reference to the available cadastral maps from the Aosta Valley (Italy). LST and NDVI were initially pre-processed by filtering out, at pixel level, defective observations and regularize the remaining ones. The yearly LST/NDVI yearly maxima were then computed to synthetise the phenological season with yearly granularity. A 1st order polynomial was used to fit 39 yearly values of LST and NDVI at pixel level on pastures pixels solely. The correspondent gain and offset values were mapped and used to investigate pastures reaction to climate changes looking for relationship between local behaviour and topographic features. LST trends was adopted to explored the pastures capability of limiting/improving thermal fluxes. NDVI trends was used to read the biomass temporal behaviour and support heat fluxes interpretation. EO data allow to understand and preliminary quantify how alpine pastures respond to climate change and detect the main drivers of such changes.

1. INTRODUCTION

Climate change is profoundly affecting alpine ecosystems (Peringer, Frank, e Snell 2022; Herzog e Seidl 2018). Specifically, global warming poses a significant threat to mountain pastures (Godde et al. 2020), which are already among the most vulnerable habitat due to weak management and their location at high altitudes where the effects are amplified (Bellini et al. 2022). Monitoring these areas is crucial for understanding their response to changing conditions and informing management strategies in various fields, including ecosystem and climate studies (De Marinis et al. 2021). Beyond their ecological importance, pastures play a vital role in the rural economy of alpine regions, supporting agricultural-forestry and pastoral production that often forms a substantial portion of local Gross Domestic Product (GDP), as seen in Aosta Valley with over 20% contribution (Floris et al. 2024). Given this critical role, long-term monitoring is essential to track how pastures are adapting to the shifting climate. In this scenario, long time-series (about 40 years) of Earth Observation (EO) data, with special concerns about the United States Geological Survey (USGS) NASA Landsat missions, can be effectively used to explore spectral and thermal behaviour of these areas in the climate change framework (Viani et al. 2023; Carella et al. 2022). Nowadays, remote sensed data may help in monitoring and modelling biophysical trends and detect changes that occurs on the Earth surfaces worldwide (Vincenzi et al. 2021; Bagliani et al. 2019; Latini et al. 2021; Tartaglino et al. 2020; Caimotto et al. 2020). Unfortunately, there are few missions with decadal data despite the fact that in the last decade Earth observation programs by both public and private agencies have grown exponentially thanks to massive investments in the space economy (Ippoliti et al. 2019; Samuele et al. 2021). While newer programs like ESA's Copernicus and Google's Planet offer data with impressive spectral and temporal resolution, they lack the decadal time series (spanning at least 30 years) crucial for climate studies (Viani al. 2023; Floris et al. 2024; Mandola, et al. 2023), promising endeavours like Italy's IRIDE project are still under development (Orusa et al. 2023). Currently, the Landsat missions stand as the lone provider of free, long-term, medium-high resolution data suitable for climate-related research on mountain pastures. Several studies have used the Landsat legacy data to monitor and model the greening trend in the Alpine arc (B. Z. Carlson et al. 2017; Bolton et al. 2020) or using LandTrender algorithm (Kennedy et al. 2018) to model land cover changes (Parracciani et al. 2024) and assess vegetation and water response to climate change (Fu et al. 2022). Other studies have focused on monitoring forestry and carbon dynamics (Banskota et al. 2014).

Currently, climate and land interactions and related modelling based on EO data can only be conducted thanks to Landsat Legacy with global data from 1984 to today and in some cases from 1972 and almost half a century of observations.

In this work, more than 900 acquisitions covering the period 1984-2022, from the Landsat 5-9 missions were obtained through Google Earth Engine (GEE) (Gorelick et al. 2017) and the correspondent maps of Land Surface Temperature (LST) and Normalized Difference Vegetation Index (NDVI) analysed and related trends modelled involving pastures areas. The aims of the present work were: (i) developing a remote-sensed based continuous monitoring approach to map alpine pastures reaction to climate change scalable to the whole alpine realities; (ii) modelling and mapping alpine pasture reaction to rising temperature in Aosta Valley; (iii) preliminary quantifying the role of other environmental features such as terrain altitude, aspect in thermal/ biomass trends within the study area. All these analysis and related deductions can support local/national institutions policy to understand and mitigate climate change effects.

1.1 Study Area

This study was performed over Aosta Valley Autonomous Region (AV) in the NW Italy (fig.1). Despite it is the smallest region in Italy, hosts the highest mountains in Europe and almost 1/3 of its overall surface is covered by grassland (Orusa, Cammareri, e Borgogno Mondino 2022b; 2022a)

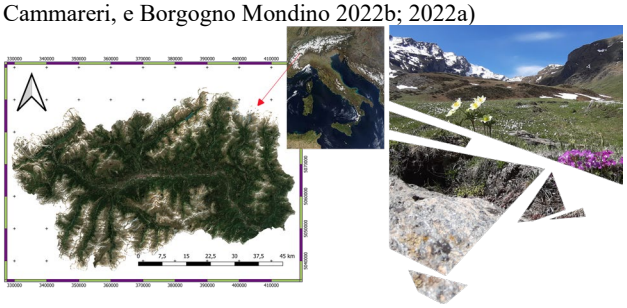

Figure 1. Aosta Valley Autonomous Region, NW Italy. (Reference system UTM/ED50 zone 32 N, EPSG: 23032)

2. MATERIALS AND METHODS

LST trends was adopted to explored the pastures capability of limiting/improving thermal fluxes. NDVI trends was used to read the biomass temporal behaviour and support heat fluxes interpretation. More than 900 acquisitions covering the period 1984-2022 mapping TOA brightness temperature (T_b) available in collection 1 of Landsat TOA products from Landsat 5; 7; 8-9 missions, were selected and processed in GEE.

It is worth to note that NDVI was computed from Landsat Level 2 product which is already calibrated at surface reflectance. Clouds, shadows and defective pixels were filtered out from each selected image using Radiometric saturation QA and Pixel QA Pixel Bitmask (quality attributes generated from the CFMASK algorithm by NASA) associated to each imagery and available per each Landsat collection within GEE (further information available at https://www.usgs.gov/landsat-missions/landsat-collection-2-level-1-data last accessed on 2024 February). A regularization involving all the observation at a monthly step was performed according to (Ermida et al. 2020) approach. Gain and offset values were mapped and used to investigate pastures reaction to climate changes looking for eventual relationship between local behaviour (in terms of both LST and NDVI) and topographic features (altitude and aspect) as derivable from the AV Regional DTM. A binning onto terrain components, NDVI and LST gain and offset was conducted in order to explore and test eventual relationships. 20 bins were done per each variable involving: aspect (with step each 0.1 rad); slope (with step each 0.1 rad); altitude (with step each 150 m); NDVI mean gain (with step each 0.003) and NDVI mean offset (step each 0.1). It is worth to note that these variables were binned against LST. Landsat data pre-processing were directly performed in GEE and bands missions shifting and sensors comparability adjusted using the (Ermida et al. 2020) approach. Surface emissivity maps, needed for LST computation from T_b images (Orusa e Mondino 2019), were obtained according to the Fractional Vegetation Cover (FVC) approach of eq.1 (Rubio, Caselles, e Badenas 1997):

$$\varepsilon = FVC_{\varepsilon v} + (1 - FVC)_{\varepsilon s} \qquad (1)$$

where $FVC_{\varepsilon v}$ and $FVC_{\varepsilon s}$ are the FVC values computed for a completely vegetated and a pure bare soil pixel, respectively. FVC can be computed with reference to eq.2 (T. N. Carlson e Ripley 1997)

$$FVC = \left(\frac{NDVI - NDVI_s}{NDVI_v - NDVI_s}\right)^2 \qquad (2)$$

where $NDVI_s$ and $NDVI_v$ are the NDVI values corresponding to completely bare soil and vegetated pixels, respectively. According to previous studies (Jiménez-Muñoz et al. 2009), $NDVI_s$ and $NDVI_v$ were set to 0.2 and 0.86, respectively. Once emissivity maps were obtained for all the acquisitions, correspondent LST images were finally computed by the Statistical Mono-Window (SMW) algorithm (Orusa, Viani, Moyo, et al. 2023) from the Climate Monitoring Satellite Application Facility (CM-SAF). This technique uses an empirical relationship between T_b and LST (Ermida et al. 2018), based on a linearization of the radiative transfer equation showing an explicit dependence from emissivity eq.3.

$$LST = A_i\left(\frac{T_b}{\varepsilon}\right) + \frac{B_i}{\varepsilon} + C_i \qquad (3)$$

where T_b is the TOA brightness temperature, and ε is the surface emissivity. A_i, B_i, and C_i are coefficients modelling the Total Column Water Vapor (TCWV) effect on LST. These coefficients are made available by NCEP/NCAR re-analysis project and can be accessed and used through GEE depending on the considered Landsat collection. Subsequently, for each year the maximum value within the range June-August was computed and mapped for NDVI and LST. This composite strategy allows to better consider only NDVI and LST values during phenological active period. It is worth noting that the choice of June-August is based on the timing of vegetation maxima. This timeframe was selected after verifying that the maxima of both LST NDVI and associated phenological metrics MAXVI consistently occur within this period across all years studied adopting (Orusa et al. 2023) algorithm. While acknowledging the potential influence of climate change on vegetation and phenology, a comprehensive pre-check encompassing the entire year for each pixel within the study area confirmed that June-August indeed captures the maxima of LST NDVI for all years involved. This ensures that the analysis focuses on the period of peak activity. Finally, 39 maps of NDVI and LST were separately stacked along time series and clipped on pasture parcels extracted from AV cadastre retrieved from AV SCT Geoportal. From the same geoportal the Digital Terrain Model (DTM) was also download for in this work (https://geoportale.regione.vda.it/ last accessed 2024 February). This masking procedure made possible to focus the analysis on the pastures pixels solely form the LST/NDVI time-series. The LST/NDVI stacks were finally exported from GEE and analysed in SAGA GIS v.8.5.0 and R Studio (Conrad et al. 2015; Racine 2012). Pettitt's test (James, James, e Siegmund 1987; Sarvia et al. 2021) was locally applied to NDVI stack in R Studio in order to select only pixels that possibly did not change their meaning (remains pastures for all the considered period). This test detects the moment when a NDVI multitemporal profile shows an abrupt change (breakpoint), possibly related to pasture removal, along the time series. Pixels having a significant breakpoint were masked out also in LST stack since represent surfaces where land cover/land use is changed thus affecting local emissivity. For unchanged pixels the local trend was approximated by a 1st order polynomial (eq. 4):

$$\vartheta = \alpha \times t + \beta \qquad (4)$$

Where: θ: is the parameter to model in this case LST and NDVI; α: is the gain; t: is the time integer index; β: is the offset.

3. RESULTS AND DISCUSSIONS

The trends modelled involving LST and NDVI by a 1st order polynomial after a de-trending to remove seasonality effect as depicted in eq.4 were mapped as reported respectively in Figures 2 and 4. It is worth to note that in figures 2 and 4 only

unchanged significant pixels within the pastures of the cadastre are displayed.

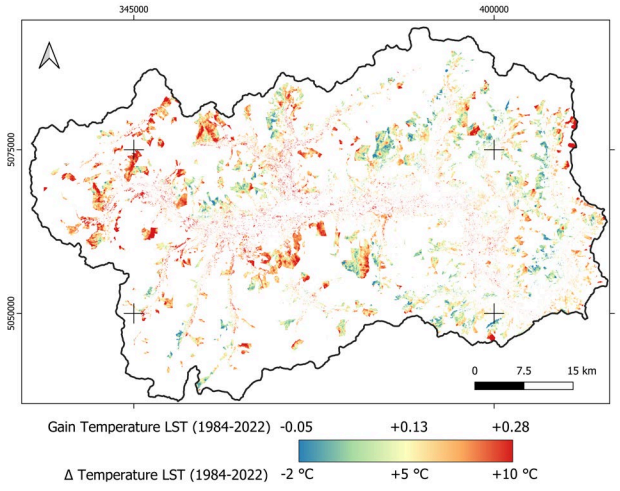

Figure 2. LST unchanged significant pixels gain map and relative increase of temperature assuming as reference 1984. (Reference system UTM/ED50 zone 32 N, EPSG: 23032).

Starting from the modelled LST maps the difference of LST between the years 1984 and 2022 was calculated at pixel level. Frequency distribution of LST gain areas was provided in figure 3. It is interesting to highlight that more than the 85% of the overall AV surface pastures have deeply increased their LST in the investigated period (positive gain values). About 44% of pastures from 1984 to 2022 have suffered LST increase of almost 6°C, while around 56% of pastures have suffered an LST increase in the last 39 years upper to 6°C.

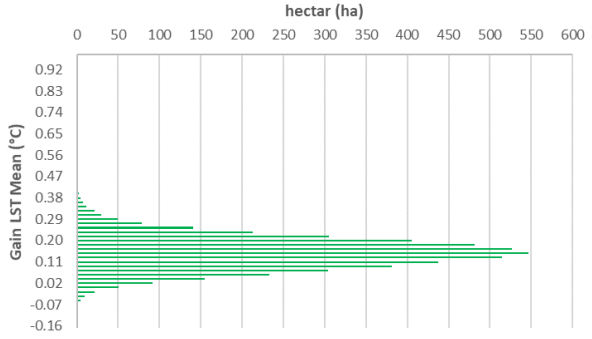

Figure 3. Pastures areas distribution (expressed in hectar) according most representative binned classes of Gain LST (°C).

Then, a general increase in NDVI occurs as mapped in figure 4.

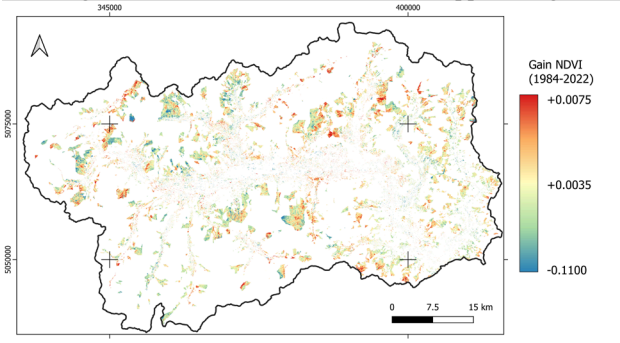

Figure 4. NDVI unchanged significant pixels gain map. (Reference system UTM/ED50 zone 32 N, EPSG: 23032).

Comparing LST and NDVI gain maps, it is interesting to note that following the increase in LST there was also an increase in biomass productivity and that it therefore also exerts a mitigating reaction compared to the real temperature. However, it should be underlined that this process is only possible in the presence of water availability. If it turns out to be a limiting factor, especially in periods of greater demand and full vegetative activity (for e.g. summer heatwaves), the effects on pasture productivity can be important. In fact, today in order to produce the same quantity of biomass (hay) compared to 1984 because of LST increase, it also requires more water because the effect on evapotranspiration is greater (see fig.2 and 4). In fact, the investigations on pastures reaction to climate changes looking for eventual relationship between local behaviour and topographic features have shown that: (a) LST Mean Gain is higher in AV Eastern pastures then in the Western. Eastern pastures have a steeper increasing LST then the Western; (b) LST Mean Gain is higher in AV Northern pastures then in the Southern. Northern pastures are suffering a steeper increase in LST then Southern, nevertheless the gain amplitude is not so wide then in E-W; (c) LST Gain mean is higher in AV in the bottom of the valley however between 2000-3000 m it rises up. Bottom pastures are more exposed to rising LST like those located at high altitude. in the latter case, this is probably due to the major presence of tare (like rocks and presence and lower biomass); (d) no relationship with the slope. In all cases there were significance p-value < 0.05. Finally, in pastures where the biomass has always expressed a high vigour value (lower NDVI gain), it seemed not to be able to mitigate the thermal increase (observe in fig.5 the yellow and green cluster gain and offset respectively), while in poorly vegetated pastures or in pixels subjected to a change of cover due to recolonization by herbaceous species and therefore with sparse and reduced vegetation (high gain of NDVI) there are lower marked thermal gain see red clusters in figure 5 below.

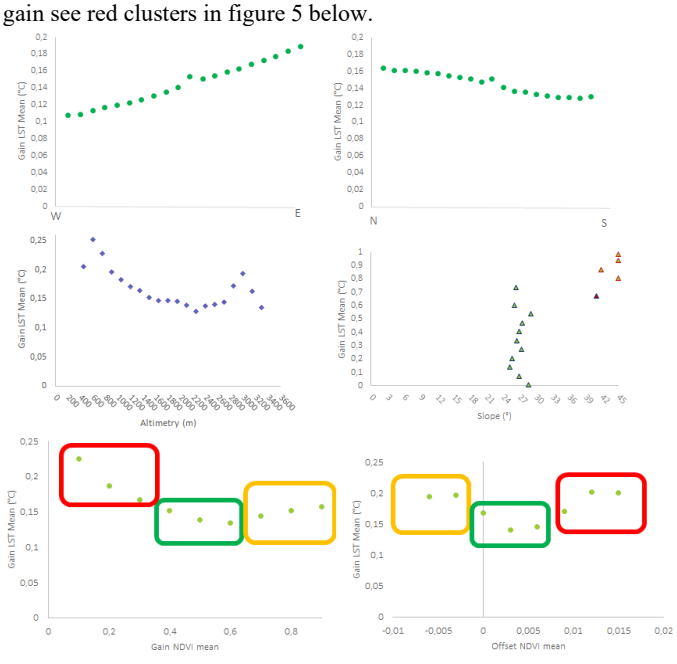

Figure 5. LST, NDVI and terrain relationship to characterize alpine pastures in the climate change framework.

4. CONCLUSIONS

EO data with particular regard to Landsat missions allow to understand and preliminary quantify how alpine pastures

respond to climate change and detect the main drivers of such changes as shown by other studies (Orusa et al. 2020; Orusa, Borgogno Mondino 2021; Orusa et al. 2024). In the last 39 years AV pastures LST increased up to 6°C in many pastures (56%). N-E pastures are affected by a steeper increase in temperature then those in S-W respecting to the past. Pastures at the bottom of the valley and near peaks are more affected by the LST rising up. A slightly mitigation in terms of temperature seems to be offered only by pastures with sparse vegetation that has colonized new areas (i.e. bare soils within pasture gaps patches) through the time investigated.

ACKNOWLEDGEMENTS

A remarkable thanks to Annalisa Viani for the external support in performing this study, as well as, Marta Galvagno to let us present preliminary results in the final conference of LIFE PastorAlp in March 2023 in Bard (AO), Italy.

REFERENCES

Bagliani, Marco Maria, Maria Cristina Caimotto, Gianni Latini, e Tommaso Orusa. 2019. «Lessico e Nuvole: le parole del cambiamento climatico».

Banskota, Asim, Nilam Kayastha, Michael J Falkowski, Michael A Wulder, Robert E Froese, e Joanne C White. 2014. «Forest monitoring using Landsat time series data: A review». *Canadian Journal of Remote Sensing* 40 (5): 362–84.

Bellini, Edoardo, Marco Moriondo, Camilla Dibari, Luisa Leolini, Nicolina Staglianò, Laura Stendardi, Gianluca Filippa, Marta Galvagno, e Giovanni Argenti. 2022. «Impacts of Climate Change on European Grassland Phenology: A 20-Year Analysis of MODIS Satellite Data». *Remote Sensing* 15 (1): 218.

Bolton, Douglas K, Josh M Gray, Eli K Melaas, Minkyu Moon, Lars Eklundh, e Mark A Friedl. 2020. «Continental-scale land surface phenology from harmonized Landsat 8 and Sentinel-2 imagery». *Remote Sensing of Environment* 240: 111685.

Caimotto, Maria Cristina, Daniela Fargione, Cristiano Gino Furiassi, Tommaso Orusa, Piovan Alex, e others. 2020. «Parlare è pensare». In *Lessico e nuvole: le parole del cambiamento climatico (seconda edizione)*, 281–84. Università degli Studi di Torino.

Carella, Emanuele, Tommaso Orusa, Annalisa Viani, Daniela Meloni, Enrico Borgogno-Mondino, e Riccardo Orusa. 2022. «An Integrated, Tentative Remote-Sensing Approach Based on NDVI Entropy to Model Canine Distemper Virus in Wildlife and to Prompt Science-Based Management Policies». *Animals* 12 (8): 1049.

Carlson, Bradley Z, Monica C Corona, Cédric Dentant, Richard Bonet, Wilfried Thuiller, e Philippe Choler. 2017. «Observed long-term greening of alpine vegetation—a case study in the French Alps». *Environmental Research Letters* 12 (11): 114006.

Carlson, Toby N, e David A Ripley. 1997. «On the relation between NDVI, fractional vegetation cover, and leaf area index». *Remote sensing of Environment* 62 (3): 241–52.

Conrad, Olaf, Benjamin Bechtel, Michael Bock, Helge Dietrich, Elke Fischer, Lars Gerlitz, Jan Wehberg, Volker Wichmann, e Jürgen Böhner. 2015. «System for automated geoscientific analyses (SAGA) v. 2.1. 4». *Geoscientific Model Development* 8 (7): 1991–2007.

De Marinis, Pietro, Samuele De Petris, Filippo Sarvia, Giacinto Manfron, Evelyn Joan Momo, Tommaso Orusa, Gianmarco Corvino, Guido Sali, e Enrico Mondino Borgogno. 2021. «Supporting Pro-Poor Reforms of Agricultural Systems in Eastern DRC (Africa) with Remotely Sensed Data: A Possible Contribution of Spatial Entropy to interpret Land Management Practices». *Land* 10 (12): 1368.

Ermida, Sofia L, Patrícia Soares, Vasco Mantas, Frank-M Göttsche, e Isabel F Trigo. 2020. «Google earth engine open-source code for land surface temperature estimation from the landsat series». *Remote Sensing* 12 (9): 1471.

Ermida, Sofia L, Isabel F Trigo, Carlos C DaCamara, e Jean-Louis Roujean. 2018. «Assessing the potential of parametric models to correct directional effects on local to global remotely sensed LST». *Remote Sensing of Environment* 209: 410–22.

Floris, Irene, Andrea Vannuccini, Carmela Ligotti, Noemi Musolino, Angelo Romano, Annalisa Viani, Daniela Manila Bianchi, Serena Robetto, e Lucia Decastelli. 2024. «Detection and Characterization of Zoonotic Pathogens in Game Meat Hunted in Northwestern Italy». *Animals* 14 (4): 562.

Fu, Bolin, Feiwu Lan, Shuyu Xie, Man Liu, Hongchang He, Ying Li, Lilong Liu, et al. 2022. «Spatio-temporal coupling coordination analysis between marsh vegetation and hydrology change from 1985 to 2019 using LandTrendr algorithm and Google Earth Engine». *Ecological Indicators* 137: 108763.

Godde, Cécile M, Randall B Boone, Andrew J Ash, Katharina Waha, Lindsey L Sloat, Philip K Thornton, e Mario Herrero. 2020. «Global rangeland production systems and livelihoods at threat under climate change and variability». *Environmental Research Letters* 15 (4): 044021.

Gorelick, Noel, Matt Hancher, Mike Dixon, Simon Ilyushchenko, David Thau, e Rebecca Moore. 2017. «Google Earth Engine: Planetary-scale geospatial analysis for everyone». *Remote sensing of Environment* 202: 18–27.

Herzog, Felix, e Irmi Seidl. 2018. «Swiss alpine summer farming: current status and future development under climate change». *The Rangeland Journal* 40 (5): 501–11.

Ippoliti, Carla, Luca Candeloro, Marius Gilbert, Maria Goffredo, Giuseppe Mancini, Gabriele Curci, Serena Falasca, et al. 2019. «Defining ecological regions in Italy based on a multivariate clustering approach: A first step towards a targeted vector borne disease surveillance». *PloS one* 14 (7): e0219072.

James, Barry, Kang Ling James, e David Siegmund. 1987. «Tests for a change-point». *Biometrika* 74 (1): 71–83.

Jiménez-Muñoz, Juan C, José A Sobrino, Antonio Plaza, Luis Guanter, José Moreno, e Pablo Martínez. 2009. «Comparison between fractional vegetation cover retrievals from vegetation indices and spectral mixture analysis: Case study of PROBA/CHRIS data over an agricultural area». *Sensors* 9 (2): 768–93.

Kennedy, Robert E., Zhiqiang Yang, Noel Gorelick, Justin Braaten, Lucas Cavalcante, Warren B. Cohen, e Sean Healey. 2018. «Implementation of the LandTrendr algorithm on google earth engine». *Remote Sensing* 10 (5): 691.

Latini, Gianni, Marco Bagliani, e Tommaso Orusa. 2021. *Lessico e nuvole: le parole del cambiamento climatico*. Youcanprint.

Orusa, Tommaso, e Enrico Borgogno Mondino. 2021. «Exploring Short-Term Climate Change Effects on Rangelands and Broad-Leaved Forests by Free Satellite Data in Aosta Valley (Northwest Italy)». *Climate* 9 (3): 47.

Orusa, Tommaso, Duke Cammareri, e Enrico Borgogno Mondino. 2022a. «A Possible Land Cover EAGLE Approach to Overcome Remote Sensing Limitations in the Alps Based on Sentinel-1 and Sentinel-2: The Case of Aosta Valley (NW Italy)». *Remote Sensing* 15 (1): 178.

———. 2022b. «A Scalable Earth Observation Service to Map Land Cover in Geomorphological Complex Areas beyond the Dynamic World: An Application in Aosta Valley (NW Italy)». *Applied Sciences* 13 (1): 390.

Orusa, Tommaso, e E Borgogno Mondino. 2019. «Landsat 8 thermal data to support urban management and planning in the climate change era: A case study in Torino area, NW Italy». In *Remote Sensing Technologies and Applications in Urban Environments IV*, 11157:111570O. International Society for Optics and Photonics.

Orusa, Tommaso, Riccardo Orusa, Annalisa Viani, Emanuele Carella, e Enrico Borgogno Mondino. 2020. «Geomatics and EO data to support wildlife diseases assessment at landscape level: a pilot experience to map infectious Keratoconjunctivitis in Chamois and phenological trends in Aosta Valley (NW Italy)». *Remote Sensing* 12 (21): 3542.

Orusa, Tommaso, Annalisa Viani, e Enrico Borgogno-Mondino. 2023. «IRIDE the Euro-Italian Earth Observation Program: Overview, Current Progress, Global Expectations and Recommendations». *perspective* 2: 10.

———. 2024. «Earth Observation Data and Geospatial Deep Learning AI to Assign Contributions to European Municipalities Sen4MUN: An Empirical Application in Aosta Valley (NW Italy)». *Land* 13 (1): 80.

Orusa, Tommaso, Annalisa Viani, Duke Cammareri, e Enrico Borgogno Mondino. 2023. «A Google Earth Engine Algorithm to Map Phenological Metrics in Mountain Areas Worldwide with Landsat Collection and Sentinel-2». *Geomatics* 3 (1): 221–38.

Orusa, Tommaso, Annalisa Viani, Boineelo Moyo, Duke Cammareri, e Enrico Borgogno-Mondino. 2023. «Risk Assessment of Rising Temperatures Using Landsat 4–9 LST Time Series and Meta® Population Dataset: An Application in Aosta Valley, NW Italy». *Remote Sensing* 15 (9): 2348.

Parracciani, Cecilia, Daniela Gigante, Onisimo Mutanga, Stefania Bonafoni, e Marco Vizzari. 2024. «Land cover changes in grassland landscapes: Combining enhanced Landsat data composition, LandTrendr, and machine learning classification in google earth engine with MLP-ANN scenario forecasting». *GIScience & Remote Sensing* 61 (1): 2302221.

Peringer, Alexander, Viktoria Frank, e Rebecca S Snell. 2022. «Climate change simulations in Alpine summer pastures suggest a disruption of current vegetation zonation». *Global Ecology and Conservation* 37: e02140.

Racine, Jeffrey S. 2012. *RStudio: a platform-independent IDE for R and Sweave*. JSTOR.

Rubio, E, V Caselles, e C Badenas. 1997. «Emissivity measurements of several soils and vegetation types in the 8–14, µm Wave band: Analysis of two field methods». *Remote Sensing of Environment* 59 (3): 490–521.

Samuele, De Petris, Sarvia Filippo, Tommaso Orusa, e Borgogno-Mondino Enrico. 2021. «Mapping SAR geometric distortions and their stability along time: a new tool in Google Earth Engine based on Sentinel-1 image time series». *International Journal of Remote Sensing* 42 (23): 9135–54.

Sarvia, Filippo, Samuele De Petris, Tommaso Orusa, e Enrico Borgogno-Mondino. 2021. «MAIA S2 Versus Sentinel 2: Spectral Issues and Their Effects in the Precision Farming Context». In *International Conference on Computational Science and Its Applications*, 63–77. Springer.

Tartaglino, Andrea, e Tommaso Orusa. 2020. «Bilancio energetico/Energy Balance in Lessico e nuvole: le parole del cambiamento climatico II ed. Università degli studi Torino». In *Bilancio Energetico*, 61–63. Università degli studi di Torino.

Viani, Annalisa, Tommaso Orusa, Enrico Borgogno-Mondino, e Riccardo Orusa. 2023. «Snow Metrics as Proxy to Assess Sarcoptic Mange in Wild Boar: Preliminary Results in Aosta Valley (Italy)». *Life* 13 (4): 987.

Viani, Annalisa, Tommaso Orusa, Sara Divari, Stella Lovisolo, Stefania Zanet, Enrico Borgogno-Mondino, Riccardo Orusa, e Enrico Bollo. 2023. «Bartonella spp. distribution assessment in red foxes (Vulpes vulpes) coupling geospatially-based techniques» 76° Convegno SISVET, Bari. https://hdl.handle.net/2318/1938950.

Viani, Annalisa, Tommaso Orusa, Maria Lucia Mandola, Serena Robetto, Manuela Belvedere, Giovanna Renna, Sonia Scala, Enrico Borgogno-Mondino, e Riccardo Orusa. 2023. «R07. 5 Tick's suitability habitat maps and tick-host relationships in wildlife. A One Health approach based on multitemporal remote sensed data, entropy and Meta® population dataset in Aosta Valley, NW Italy.» In *GeoVet 2023 International Conference*.

Vincenzi, Stefano, Angelo Porrello, Pietro Buzzega, Marco Cipriano, Pietro Fronte, Roberto Cuccu, Carla Ippoliti, Annamaria Conte, e Simone Calderara. 2021. «The color out of space: learning self-supervised representations for earth observation imagery». In *2020 25th International Conference on Pattern Recognition (ICPR)*, 3034–41. IEEE.

WHEAT TRAITS RETRIEVAL THROUGH MACHINE LEARNING AND HYPERSPECTRAL DATA: MODELLING PERFORMANCE AND INTERPRETATION

R. Heidarian Dehkordi[1], G. Candiani[1], M. Ranghetti[1,5], L. Parigi[1], F. Nutini[1], C. Cesaraccio[2], S. Mereu[2], P. Duce[2], F. Serralutzu[3], D. Cillis[4], A. Genangeli[2], F. Carotenuto[2], B. Gioli[2], M. Boschetti[1*]

[1] Institute for Electromagnetic Sensing of the Environment, Italian National Research Council, Italy - ramin.heidariandehkordi@gmail.com, (candiani.g, nutini.f, ranghetti.m, parigi.l, boschetti.m)@irea.cnr.it
[2] Institute of BioEconomy, Italian National Research Council, Italy - beniamino.gioli@cnr.it, (carla.cesaraccio, pierpaolo.duce, simone.mereu, federico.carotenuto, andrea.genangeli)@ibe.cnr.it
[3] Institute for the Animal Production System in the Mediterranean Environment (ISPAAM), Italian National Research Council, Italy francesca.serralutzu@gmail.com
[4] IBF Servizi S.p.A., Italy - d.cillis@ibfservizi.it
[5] Department of Earth and Environmental Sciences, University of Milano-Bicocca, Italy

KEY WORDS: Hyperspectral remote sensing, Machine learning, crop traits, model interpretation

ABSTRACT:

Crop traits monitoring is a fundamental step for controlling crop productivity in the context of precision agriculture and field phenotyping. Currently, the use of hyperspectral data in machine learning regression algorithms (MLRAs) has attracted increasing attention to alleviate the challenges associated with traditional crop trait measurements. In this framework, an experiment was set up to assess the performance of partial least squares regression (PLSR) and random forest (RF) models to estimate several wheat crop traits (leaf area index: LAI, canopy water content: CWC, canopy chlorophyll content: CCC, and canopy nitrogen content: CNC) at the canopy level, using full-range hyperspectral data (350 – 2500 nm) as inputs. The study compared the performance of the two MLRA focusing on the physical interpretation of the results for each particular crop trait. Overall, PLSR provided remarkably higher accuracy, tested with a cross-validation strategy, as compared to RF for all the crop traits. In particular, PLSR denoted R^2 (nRMSE%) values of 0.72 (11.97%), 0.77 (10.89%), 0.70 (14.61%), and 0.74 (14.38%) for LAI, CWC, CCC, and CNC, respectively. All PLSR models indicated robust prediction capability (RPD > 1.4). In general, analysis of band importance revealed physically-meaningful and consistent patterns for each specific crop trait.

1. INTRODUCTION

1.1 Crop traits estimation with Machine Learning

In the field of modern agriculture, the need for precision and efficiency has never been more critical. The increase of global population and food demand, as well as climate change impact, are making agricultural production unstable and unpredictable, placing notable pressure on agricultural systems. In this context is fundamental to increase productivity while mitigating the environmental impacts of farming. One of the most promising avenues of innovation lies in the development of crop trait estimation through remote sensing technology for field phenotyping activity and precision farming implementation. The goal of field phenotyping is to understand how plants respond to various environmental conditions, stressors and management practices in real-world non-controlled settings. On the other hand, Precision Farming, also known as Precision Agriculture or Smart Farming, is an innovative approach to agricultural management that leverages technology and data-driven techniques to optimise various aspects of crop production. These activities need reliable and efficient production of quantitative information on plant traits to assess crop status and identify strategies for a sustainable and less impacting management. Remote Sensing technology is indeed the most effective technological solution to estimate and map crop traits in space and time, especially considering hyperspectral data, which can provide the full range spectral information needed to perform a diagnostic assessment of different plant parameters (Hank et al., 2019). Hyperspectral measurements have been successfully utilised in several previous studies to describe structural (e.g. leaf area index: LAI - Liang et al., 2020) and biochemical parameters (e.g. nitrogen – Heidarian Dehkordi et al., 2022). Data driven Machine Learning Regression Algorithms (MLRA) can provide a powerful means of exploiting the rich spectral information contained in hyperspectral data, enabling precise and non-invasive estimation of critical crop traits. Further research is needed to investigate the performance of MLRA for crop traits estimation due to several compelling reasons: i) assess model accuracy for product exploitation, ii) understand MLRA results to gain trust and acceptance among users and iii) evaluate exportability of model in different contexts.

1.2 Objective

In this framework, the objective of this study was threefold: i) set-up a field phenotyping experiment that produce a variety of crop condition to create a bundle dataset of crop ground data and spectral measurements, ii) conduct MLRA analysis to assess model performance and iii) interpret model significance and robustness by analysing the importance of the different spectral regions selected by model in relation to the specific plant parameter considered. Indeed, the use of MLRA models as black boxes can be very risky: therefore, model interpretation is fundamental for the exploitation of the developed solution in other contexts.

2. MATERIAL AND METHODS

2.1 Study area and ground dataset

A controlled experiment was conducted in the framework of the E-CROPS project (https://www.e-crops.it/). The study site (corners NW: 39° 45' 23" N, 8° 35' 58" E; SE: 39° 45' 21" N, 8° 36' 7" E) was an agricultural field in Arborea (Oristano –

Sardinia, Italy), planted with durum wheat (Triticum aestivum L.). To generate a wide range of crop traits - hence a wide range of spectral information - different set of agricultural inputs were used over the field (Figure 1). The field was split divided in two parts with different soil preparation: "minimum tillage" (L1) and "traditional ploughing" (L2), in the upper and lower portions of the field, respectively. The experimental design consisted in constituted a block of three replicates as R1, R2, and R3, representing the western, middle, and eastern parts of the field. Each replicate included a fully randomised set of four different wheat cultivars as Beltorax (V1), F. Camillo (V2), Giulio (V3), M. Aurelio (V4) as well as four different N-treatments as "Aziendale-30%" (N1), "Aziendale (N2)", "Aziendale+30% (N3)", and "Variable rate" (N4), for a total of totalling 96 experimental plots of 6 m × 3 m within the field. Due to crop emergence failure in two plots, and excessive presence of weed in 6 plots, a total of 88 plots were monitored.

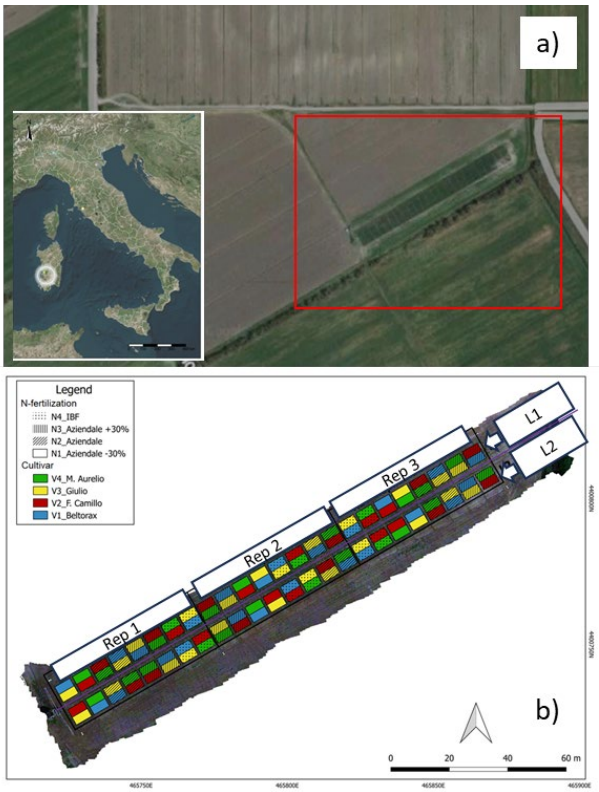

Figure 1 Study site in Arborea (OR) (a) and investigated experimental plots (b).

N- treatment Kg/ha	1° Stem elongation 20/04/2022	2° Flowering 23/05/2022
N1	52	0
N2	52	38
N3	52	65
N4	52	8 - 24

Table 1. N treatment of experiments.

The fertilisation was split in two periods (end of tillering and beginning of flowering), as reported in Table 1. In particular, N4 represented an expert base variable rate definition, based on ground measurements of LAI and chlorophyll content.

2.1.1 Crop traits: measurements were performed during three campaigns (28th April, 14th May, and 28th May, 2022) as follows:

- **LAI (Leaf area index)** was measured using an LI-COR LAI2200 plant analyser along transects according to A-10×B-A scheme in which A and B represent above and below canopy measurements for each experimental plot;
- **CCC (Canopy Chlorophyll content)** was derived from leaf chlorophyll content (LCC), measured in laboratory from 3 leaf disks sampled on the last fully-developed leaf, by multiplying LCC and the corresponding LAI values;
- **CWC (Canopy Water content)** was calculated by multiplying leaf water content (LWC) by LAI values; LWC was determined for five plants within each experimental plot, measuring fresh and dry weight (oven-dried at 50°C for about three days) of three leaf discs with 8 mm diameter, sampled on the last fully-developed leaf.
- **CNC (Canopy Nitrogen Content)** was retrieved multiplying Leaf Nitrogen Content (LNC) by LAI values; LNC was calculated by multiplying leaf mass per area for the leaf nitrogen concentration (N%), determined using a CN element analyser, for the aforementioned leaf discs.

LCC, LWC and LNC, due to the effort required for destructive sampling, samples were collected only for the soil treatment "L2" and variety "V4 and V3", corresponding to a total of 24 analysed plots (1 soil x 2 varieties x 3 replicates x 4 N-treatments). Samples cardinality for the LAI and CWC/ CCC/ CNC is respectively 264 (88 plots x 3 dates) and 72 (24 plots x 3 dates).

2.1.2 Spectral data: Proximal spectral measurements were acquired using a handheld spectrometer (Spectral Evolution - RS-5400) over the three field campaigns. The spectrometer has a full spectral range of 350-2500 nm with a spectral sampling interval (SSI) of 1 nm. Four spectral measurements were collected on each experimental plot at approximately 1 m above the canopy, with a nadir viewing angle and under clear sky conditions. Care was taken to avoid the presence of weeds and shadows within the measuring footprint. A reference panel was sensed before and after each measurement to derive reflectance. The plot reflectance was derived averaging the four reflectance spectra measured in each plot. Moreover, the atmospheric contaminated regions between 1350-1500 nm and 1750-2000 nm were excluded. It is worth noting that during the first campaign, the spectral measurements of 50 plots were not recorded due to instrumental issues. Considering the intersection from ground and spectral measurements, the final DB includes the following cardinality per traits: LAI (#232); CWC (# 61), CCC (#61) and CNC (#44).

2.2 Machine learning modelling

Partial Least Squares Regression (PLSR) and Random Forest (RF), recognized among the best performing algorithms, were selected for this study. PLSR, for instance, is well-suited for extracting meaningful relationships between spectral bands and crop traits, by reducing the dimensionality of hyperspectral data and identifying key spectral features. For example, Hansen and Schjoerring (2003) exploited this technique for canopy nitrogen content estimation. On the other hand, Random Forest is known for its robustness and ability to handle complex, nonlinear relationships in data, making it valuable for modelling intricate relationships between spectral signatures and crop traits (Zheng et al., 2022). RF has been successfully used for LAI estimation (Liang et al., 2020), biomass and yield (Marshall et al., 2022).
The model development, including training and cross-validation was performed using the "caret" package in R (Kuhn, 2008). We used a repeated k-fold cross-validation approach (with k = 10 folds and N = 5 repeats), for traits with high cardinality (n > 100;

i.e. LAI), whilst the leave-one-out (LOO) cross-validation approach was performed for those traits with low cardinality.

2.2.1 Assessment of results and model interpretation:

To assess the quality of the MLRA models generated for each crop trait, we computed the coefficient of determination (R^2), the Normalised Root Mean Square Error (nRMSE; normalized by range of samples) and the Ratio of the Performance to Deviation (RPD). Finally, variable influence on projection was calculated using the "VIP" package in R (Greenwell and Boehmke, 2020). This analysis was performed for each trait and model to assess the physical soundness of the identified solution. VIP graphs (wavelength vs importance) were investigated and commented to highlight the most important variables for crop traits' retrieval in this study.

3. RESULTS AND DISCUSSION

3.1 Model performance

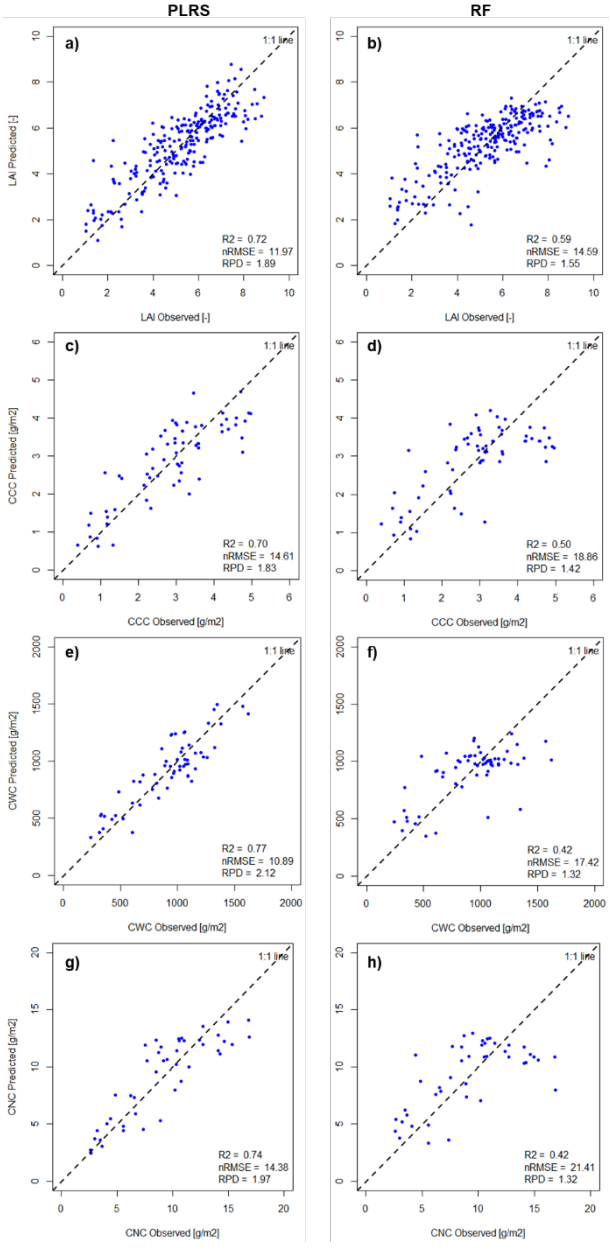

Figure 2. Scatter plots and cross validation performance metrics for the different traits (rows) and MLRA considered (columns). Left and Right column report results for PLSR and RF; traits: LAI (a & b), CCC (a & b), CWC (a & b), and CNC (g & h).

Figure 2 provides the scatter plot in cross validation of the eight analysed model (4 traits x 2 MLRA). Overall, the accuracy of the models were remarkably high (up to $R^2 > 0.7$) for the considered canopy-level traits (i.e. LAI, CWC, CCC, and CNC). In general, PLSR outperformed RF for the examined traits and all the models indicated either good or excellent prediction capability for the traits retrieval with RPD values greater than 1.4. This can be due to the capacity of the method to handle high dimensionality data by projecting them to latent structures that maximise the variance of predictors and observations. PLSR is considered a standard for crop traits retrieval from leaf level spectra (Burnett et al., 2021). Regarding the crop traits investigated CWC and CNC showed excellent results (RPD ~ 2). To tackle the multicollinearity of the hyperspectral data in RF, we performed principal component analysis (PCA) with 20 components as a dimensionality-reduction technique, and then repeated the RF models. As expected, such PCA-based RF models led to more accurate results for crop traits retrievals as compared to the RF models with full-range hyperspectral data. PCA-based RF models indicated R^2 (nRMSE%; RPD) values of 0.76 (11.39%; 1.98), 0.73 (14.25%; 1.87), 0.70 (14.51%; 1.59), and 0.62 (17.36%; 1.62) for LAI, CCC, CWC, and CNC retrievals, respectively (graphs not shown; detailed analysis in Heidarian et al 2024 - under review). It is worth mentioning that for the interpretation of the models (Section 3.2) the initial RF models (using the full-range hyperspectral data) were kept allowing to assess the importance of all the spectral bands for crop trait retrievals.

3.2 Model interpretation

The use of hyperspectral data in crop trait analysis within a data-driven approach presents several challenges. Multicollinearity of hyperspectral data determine the strong correlation between bands, which can complicate the identification of individual bands or wavelengths that are genuinely informative for predicting crop traits. Moreover, in high-dimensional data, there's a higher likelihood of finding spurious correlations between certain spectral bands and crop traits. These correlations might not be meaningful or predictive on other dataset but could appear significant in the data. Analysing VIP in PLSR models is indeed fundamental to assess the model's reliability. VIP analysis reported in Figure 3 demonstrates the reliability of identified models. Specific wavelengths at SWIR (1716-1745 nm) and NIR (1057-1120 nm), Green, and the Red-Edge bands respectively showed the highest importance for LAI retrieval. The best-performing bands for CCC retrieval were situated in Red-Edge and Green spectral bands, confirming the well-known importance of these regions in relation to chlorophyll presence. Visible regions followed by Red-Edge were of higher importance for the retrieval of CWC; though specific and diagnostic water absorption regions around 910 nm and 1200 nm were also identified. However, SWIR bands were not of particular importance for CWC retrieval It is worth mentioning that the maximum water absorption in leaf, as recorded by contact measurements, occurs around 1400, 2000 and 2400-2500 nm (Ferret et al. 2021). However, these regions were partially or completely removed by the analysis of remote sensing data due to atmospheric contamination. The influence of water absorption in vegetated canopy is still visible for wavelength close to 2000 nm and greater than 2400 nm.

Finally, VIP analysis of the CNC model showed how subtle the nitrogen contribution to spectral reflectance is, highlighting the absence of significantly important bands or regions. Nonetheless,

with respect to the other crop traits, the VIP analysis showed how SWIR spectral regions, in particular between 1700-1800 nm and 2100-2300 nm, appeared to be important, alongside both the Red-Edge and Visible regions part of the spectrum to retrieve CNC. The influence over all spectral range is a well-known feature characteristic of dry matter content in the leaves and the VIS/NIR part can be influenced by covariance with LAI.

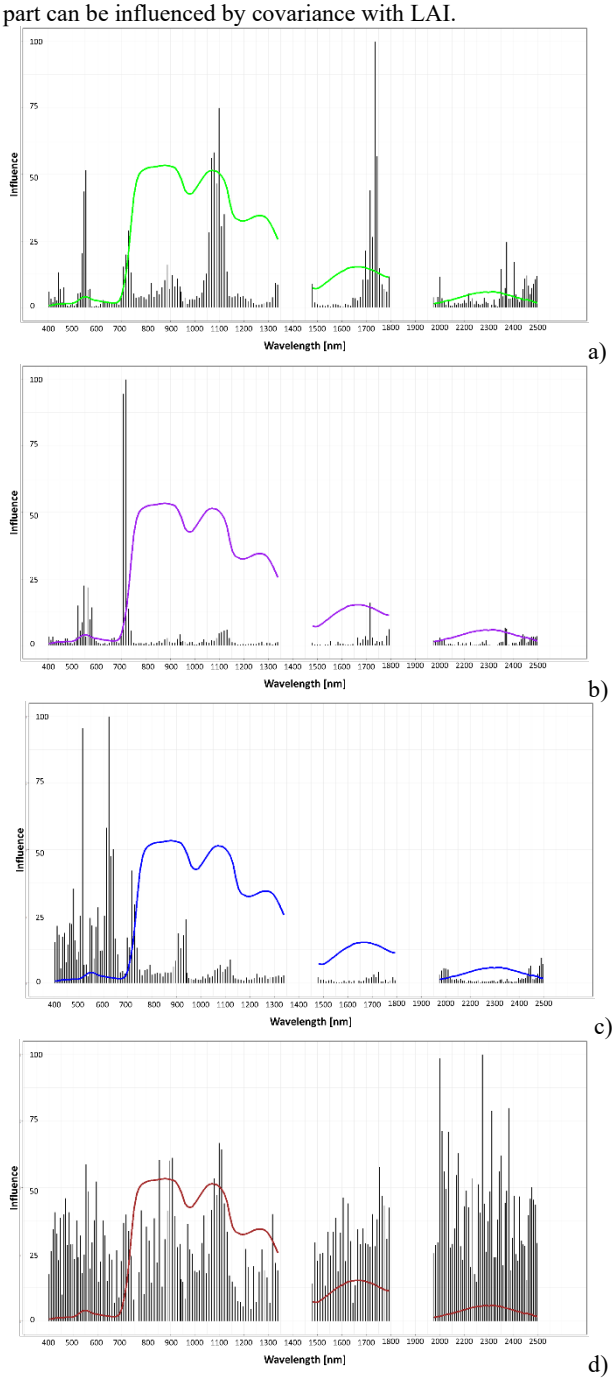

Figure 3. Importance of spectral bands importance for the different PLSR models for the traits: a) LAI, b) CCC, c) CWC and d) CNC.

4. CONCLUSION

We demonstrated that full-range hyperspectral data, in combination with MLRA algorithms, can provide accurate estimates of wheat crop traits at the canopy level. The successful use of hyperspectral data in MLRA algorithms was further highlighted by the physically meaningful modelling performances in accordance with the subtle structural and biochemical crop properties. Overall, PLSR provided remarkably higher accuracy, tested with a cross-validation strategy, as compared to RF for all the crop traits. More precisely, PLSR denoted R^2 (nRMSE%) values of 0.72 (11.97%), 0.77 (10.89%), 0.70 (14.61%), and 0.74 (14.38%) for LAI, CWC, CCC, and CNC, respectively. All PLSR models indicated robust prediction capability with RPD values greater than 1.4, and amongst them, CWC was found to have excellent prediction performance, with an RPD higher than 2. RF models for LAI and CCC showed good prediction capabilities ($R^2 > 0.5$), whilst RF models of neither CWC nor CNC were reliable ($R^2 \sim 0.4$). However, the significance and robustness of data driven models lie not only in their predictive power but also in their interpretability. Although machine learning models can excel in making accurate predictions, they often operate as 'black box' solutions, making it difficult to understand the underlying factors and relationships. In this context, the need for transparency and interpretability is critical to develop and propose automatic models to monitor crop status. In general, the analysis of VIP coefficients of the identified models revealed physically meaningful and consistent patterns for each specific crop trait investigated.

Different spectral features were identified for the different traits coherent with the expected canopy level characteristics. This confirms the importance of the availability of full-range sensors such as the operative (e.g. ASI-PRISMA and DLR-ENMAP) and planned (e.g. ESA-CHIME and NASA-SBG) missions for natural and agricultural vegetation monitoring.

Our results confirm that such hyperspectral-based MLRA approaches could be a powerful tool to accurately monitor the crop status throughout the phenological season, to improve high-throughput phenotyping activities and to further aid precision agricultural practices.

- ACKNOWLEDGEMENTS

This research was funded by the Project PON «R&I» 2014–2020—Azione II "E-crops—Technologies for Digital and Sustainable Agriculture" funded by the Italian Ministry of University and Research (MUR) under the PON Agrifood Program (Contract ARS01_01136).

- REFERENCES

Burnett, A.C., Anderson, J., Davidson, K.J., Ely, K.S., Lamour, J., Li, Q., Morrison, B.D., Yang, D., Rogers, A., Serbin, S.P., 2021. A best-practice guide to predicting plant traits from leaf-level hyperspectral data using partial least squares regression. J. Exp. Bot. 72, 6175–6189. https://doi.org/10.1093/jxb/erab295

Féret, J.B., Berger, K., de Boissieu, F., Malenovský, Z., 2021. PROSPECT-PRO for estimating content of nitrogen-containing leaf proteins and other carbon-based constituents. Remote Sens. Environ. 252, 112173. https://doi.org/10.1016/j.rse.2020.112173

Greenwell, B.M., Boehmke, B.C., 2020. Variable Importance Plots—An Introduction to the vip Package. R J. 12, 343–366. https://doi.org/10.32614/rj-2020-013

Hank, T.B., Berger, K., Bach, H., Clevers, J.G.P.W., Gitelson, A., Zarco-Tejada, P., Mauser, W., 2019. Spaceborne Imaging Spectroscopy for Sustainable Agriculture: Contributions and Challenges, Surveys in Geophysics. Springer Netherlands. https://doi.org/10.1007/s10712-018-9492-0

Hansen, P.M., Schjoerring, J.K., 2003. Reflectance measurement

of canopy biomass and nitrogen status in wheat crops using normalized difference vegetation indices and partial least squares regression. Remote Sens. Environ. 86, 542–553. https://doi.org/10.1016/S0034-4257(03)00131-7

Heidarian Dehkordi, R., Nutini, F., Mereu, S., Candiani, G., Peppo, M. De, Boschetti, M., 2022. Retrieving Biophysical And Biochemical Crop Traits Using Continuum-Removed Absorption Features From Hyperspectral Proximal Sensing, in: 2022 12th Workshop on Hyperspectral Imaging and Signal Processing: Evolution in Remote Sensing (WHISPERS). pp. 1–8. https://doi.org/10.1109/WHISPERS56178.2022.9955090

Heidarian Dehkordi, R., Candiani, G., Nutini, F., Carotenuto, F., Gioli, B., Cesaraccio, C., & Boschetti, M. (2024). Towards an Improved High-Throughput Phenotyping Approach: Utilizing MLRA and Dimensionality Reduction Techniques for Transferring Hyperspectral Proximal-Based Model to Airborne Images. Remote Sensing, 16(3), 492. Remote Sens. 2024, 16(3), 492; https://doi.org/10.3390/rs16030492

Kuhn, M., 2008. Building predictive models in R using the caret package. J. Stat. Softw. 28, 1–26. https://doi.org/10.18637/jss.v028.i05

Liang, L., Geng, D., Yan, J., Qiu, S., Di, L., Wang, S., Xu, L., Wang, L., Kang, J., Li, L., 2020. Estimating crop lai using spectral feature extraction and the hybrid inversion method. Remote Sens. 12, 1–27. https://doi.org/10.3390/rs12213534

Marshall, M., Belgiu, M., Boschetti, M., Pepe, M., Stein, A., Nelson, A., 2022. Field-level crop yield estimation with PRISMA and Sentinel-2. ISPRS J. Photogramm. Remote Sens. 187, 191–210. https://doi.org/https://doi.org/10.1016/j.isprsjprs.2022.03.008

Zheng, J., Song, X., Yang, G., Du, X., Mei, X., Yang, X., 2022. Remote Sensing Monitoring of Rice and Wheat Canopy Nitrogen: A Review. Remote Sens. 14, 5712. https://doi.org/10.3390/rs14225712

SPECTROSCOPIC DETERMINATION OF CROP RESIDUE COVER USING EXPONENTIAL-GAUSSIAN OPTIMIZATION OF ABSORPTION FEATURES AND RANDOM FOREST WITH PRISMA DATA

M. Pepe* [1], K. Fakherifard, R. Heidarian Dehkordi, F. Nutini, G. Candiani, M. Boschetti

Institute for Electromagnetic Sensing of the Environment, National Research Council, Italy
(pepe.m, fakherifard.k, nutini.f, candiani.g, boschetti.m)@irea.cnr.it

KEY WORDS: Hyperspectral remote sensing; Non-Photosynthetic Vegetation; Sustainable agriculture; Machine Learning; PRISMA

ABSTRACT:

In this study, hyperspectral data from the PRISMA satellite are analysed, using spectroscopic methods in combination with machine learning regression techniques, to map post-harvest crop residue coverage percentages, in agricultural land. Exponential Gaussian Optimization of known diagnostic absorption regions serves to extract higher-level spectroscopic parameters that are then utilized as input variables in machine learning regression algorithm (i.e., random forest). The use of a spectral library to train the regressive model overcomes the issue of finding a large training sample and increase the method transferability. The good model performance, in both training and test, allowed mapping demonstration on two seasons, yielding results that well align with ground observations, underscoring the robustness of the approach.

1. INTRODUCTION

Measuring and mapping non-photosynthetic vegetation (NPV) is considered a key topic in remote sensing of sustainable agriculture and carbon farming, likewise in the perspective of climate robustness of agricultural systems. NPV, in fact, represents an important factor in water, nutrient and carbon cycling. The mapping of NPV presence and the characterization of its quantities are relevant to monitoring soil conservation and regenerative field management practices, while some of them are strictly connected to the presence and quantity of aboveground biomass of crop residues and litter, at critical points in time.

Studies on NPV mapping by EO data benefit from the availability of hyperspectral data, as due to the high spectral resolution, and particularly at shortwave infrared wavelengths where, from 1.6 to 2.3µm, the main spectral diagnostic features of carbon-based constituents of plants are apparent (Daughtry, 2001). The launch of new generation hyperspectral satellites, as PRISMA (PRecursore IperSpettrale della Missione Applicativa) and, more recently, EnMAP (Environmental Mapping and Analysis Program) offers research opportunities in this field (Verrelst et al. 2023), which was previously investigated mainly by means of proximal and aerial sensing.

Early studies proved the potential of PRISMA to map crop residues (CR) presence at parcel level exploiting the well-known lignin-cellulose absorption feature centred around 2.1µm (Pepe et al. 2020). Berger et al. (2021) applied to PRISMA imagery hybrid approaches to retrieve NPV biomass in croplands by training machine leaning regression algorithm (MLRA) on the base of radiative transfer model (RTM) simulations. More recently, Pepe et al. (2022) exploited spectroscopic approaches with Exponential Gaussian Optimization (EGO) of specific absorption features together with Machine Learning classification algorithm, to map CR presence as related to field management practises. The latter paradigm is also proposed in this study, but, in this case, it is aimed at quantifying Crop Residue Cover (CRC) percentages on PRISMA hyperspectral data using spectroscopic feature analysis and MLRA techniques.

2. MATERIALS AND METHODS

Our primary aim was to identify distinct spectral characteristics that serve as reliable indicators of crop residues. To achieve the initial goal of this study, we conducted an exploratory analysis on absorption bands of the spectra of crop residues.

We use for the purpose an extensive and well documented spectral library (Hively et al. 2021), namely "Reflectance spectra of agricultural field conditions supporting remote sensing evaluation of non-photosynthetic vegetation cover", made available online by USGS (https://doi.org/10.5066/P9XK3867). It consists of 916 in situ surface reflectance spectra collected using a proximal full range spectroradiometer (350 to 2500 nm), and annotated with the corresponding fractions of CR, Bare Soil (BS) and (if any) Green Vegetation (GV), as estimated by point sampling the digital photograph corresponding to the radiometer field-of-view. This spectral library was analysed to infer the predictive relationship for the quantification of CRC on PRISMA data. To facilitate this process, the USGS spectral library was initially spectrally resampled to align with PRISMA bands.

The hypothesis is that some spectral intervals diagnostic for different surface characteristics – as related to plant pigments, canopy water, lignin-cellulose, and clay minerals – could represent sufficient information to quantify CRC in an accurate manner, considering their ability to spectrally characterize GV, CR and BS, which are the components of post-harvested crop fields. This has been confirmed by the exploratory analysis on the USGS database.

The methodological approach to CRC mapping of PRISMA involves two main steps. Firstly, it employs the Exponential Gaussian Optimization (Pompilio et al. 2009, 2014) technique to return the estimation of 4 descriptive parameters of an absorption bands[1]: depth (s), center (μ), width (σ), and asymmetry (k) and saturation (t), as a function of wavelengths (λ) according to equation 1.

$$EGO(\lambda) = -\frac{s}{1-e^{\frac{-1}{2}t}}\left[1 - e^{\frac{-1}{2}\left(te^{\frac{-1}{2}\left(\frac{\lambda-\mu}{\sigma+k(\lambda-\mu)}\right)^2}\right)}\right] \quad (1)$$

* Corresponding author

[1] the saturation parameter (t) is set to a negligible value and not allowed to vary, since saturation is unlikely to occur in this case.

EGO serves a dual purpose: modelling specific absorption features while reducing the spectral dimension of the dataset. This reduction in dimensionality is crucial for efficient analysis. The 4 knowledge-based absorption bands - plant pigments (Δλ1: 530 – 866 nm), canopy water (Δλ2: 1078 – 1262 nm), lignin-cellulose (Δλ3: 2036 – 2199 nm), clay minerals (Δλ4: 2183 – 2261 nm) - were optimized. The application of EGO, fitting each of the 4 spectral intervals with 4 parameters, results in a feature reduction from the original 230 spectral bands to 16 parameters. After the EGO fitting, the Random Forest (RF) MLRA is leveraged to conduct non-linear regression, facilitating the prediction and mapping of CRC based on the optimized spectral characteristics.

The PRISMA images used in this study are acquired over a large farm test site (around 3800ha) located in Jolanda di Savoia (North-Eastern Italy). Crop Residue Cover of cereals, mainly winter wheat, were considered for the study. A field survey was conducted to collect ground truth over two seasons (2021 and 2022): either crop conditions after harvest, and field spectra annotated with CRC percentages, were sampled in the test site and used for the validation of the mapping approach performances.

3. RESULTS AND DISCUSSION

Figure 1 illustrates an example of EGO fitting outcomes for training spectra of the resampled USGS database, for the classes of interest: GV (Δλ1 and Δλ2), CR (Δλ3), and BS (Δλ4). As depicted in Figure 1, the Δλ3 and Δλ4 intervals exhibit relatively minor features (note that y-axis values are different for each plot), which are nonetheless significant for detecting crop residues and bare soil. It's important to highlight that EGO Modelling excels in preserving and enhancing subtle information that might otherwise remain inconspicuous.

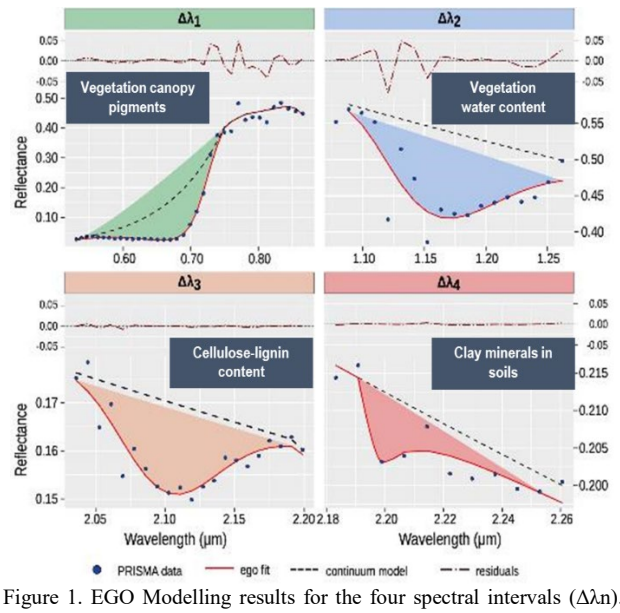

Figure 1. EGO Modelling results for the four spectral intervals (Δλn). Bottom side of each plot reports target log spectra (points), the continuum model (dashed lines), and the EGO fit (red lines). Top side: model residuals of EGO fit (dash-dot lines). (From Pepe et al. 2022).

The set of parameters resulting from EGO was used for training a Random Forest model. This model was validated against an independent spectral library, then applied to PRISMA imagery to obtain Crop Residue Cover maps.

. By deriving a regressive model based on RF algorithm from the USGS spectral library, through a knowledge-based fitting process (i.e. EGO modelling of four diagnostic spectral regions), the model captured and revealed the significance of various investigated features. Figure 2 illustrates this feature importance assessment in the form of a bar graph ranking from the most informative (top) to the least one (bottom). The feature importance graph was constructed based on the Mean Squared Error (MSE) associated with each feature space.

Notably, the most critical parameters were identified as the depth, asymmetry, centre, and width of the Cellulose\lignin (LCB) absorption band (Δλ3), which aligns with our knowledge-based expectations. Figure 3 illustrates the scatter plot between the observed and predicted NPV, as well as accuracy metrics obtained in cross validation (K-fold) by the regression model. The points are evenly distributed around the expected baseline, resulting in an R-squared value of 77%, and a low Mean Squared Error (MSE) of 0.022. Such results prove the method to be accurate enough to predict CRC.

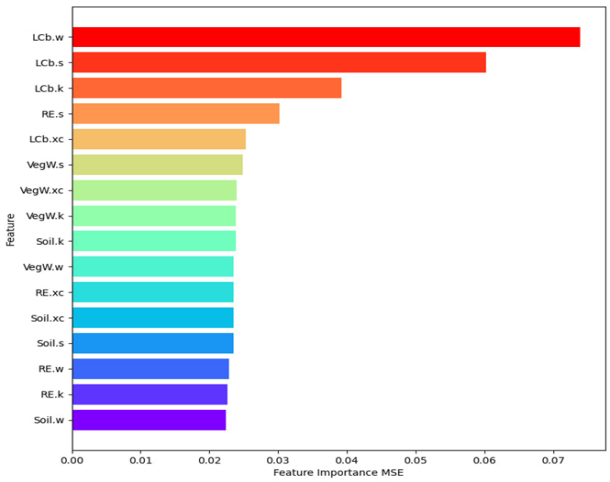

Figure 2. A bar plot of 16 spectroscopic features was generated using the MLRA, Random Forest, with a 10-fold cross-validation approach and 5 iterations.

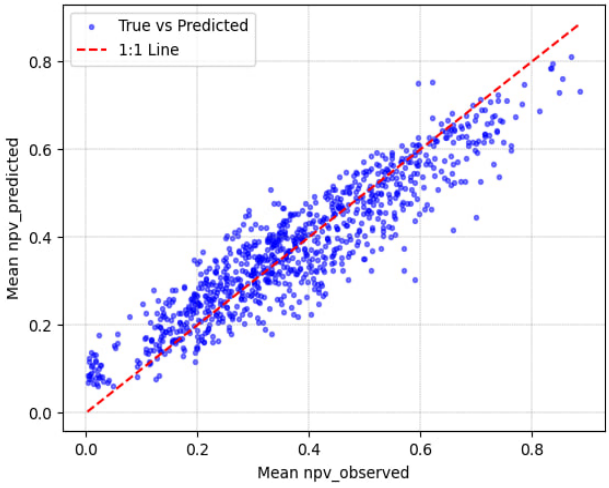

Figure 3. Observed vs Predicted NPV in cross validation

To further enhance the model, we proposed a further feature space reduction. Out of the 16 parameters extracted and ranked as reported in the feature importance graph (Figure2), we selected the top 8 parameters, setting a MSE threshold at 0.024. These 8 parameters were then used to train a new RF model. The objective was to determine if training with these selected

parameters would result in improved performance. The new model, assessed in cross validation with K-fold strategy (10-fold, 5 iterations), show a very high correlation between prediction and observation reaching an R-squared value of 81.8%, and outperforming the results obtained considering all features. Also, the MSE decreased to 0.017, indicating improved accuracy. Overall, the performance of the new model with reduced features was highly satisfactory. Figure 4 displays the updated scatter plot, showcasing the relationship between Observed and Predicted NPV obtained for the USGS spectral library.

The validation phase involved applying the final model to an independent spectral dataset acquired in 2021 in the study site. The independent data set is a spectral library of around 100 field spectra, annotated with CRC visually estimated at 10% steps (10%, 20%, 30% …). The model performance on this independent dataset (Figure 4, right panel) aligns well with cross validation results obtained in training., with R-squared value of 77.2%, an MSE of 0.028, all falling within our satisfactory range of outcomes.

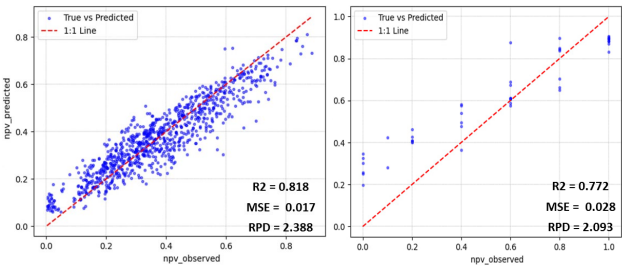

Figure 4. Scatter plot and error metrics of: new enhanced RF model from on USGS dataset, using 8 most valuable features (left). On the right scatter plot and error metrics on independent validation dataset from field data.

The predictive Random Forest model was then applied to the primary dataset, represented by two PRISMA images acquired over Jolanda di Savoia on June 21st, 2021 and July 3rd 2022, to estimate and map the quantity of crop residue coverage percentage in the region of interest. The results obtained for the June 21st, 2021 are depicted in Figure 5. This CRC map aligns well with the ground reference data shown in Figure 6 and obtained from the field survey observations. In the map, pixels marked in red correspond to high NPV coverage, which, according to the reference map, indicates a significant presence of standing dead vegetation (i.e., mature wheat not yet harvested). To assess model performance on a different season, the model was applied to the PRISMA image acquired on July 3rd 2022, after wheat harvest.

The mapping results for 2022 (Figure 7) demonstrated a remarkable level of consistency with the ground reference map (Figure 8), which has been inferred from the crop map with the help of farmer's intelligence. Overall, the model accurately identified areas characterized by CR presence. This achievement in CRC mapping underscores the model's ability to maintain its performance across temporal variations hence dealing with uncertainty and variability occurring in natural systems. Nevertheless, to achieve precise quantitative estimates, further extensive fieldwork is required to validate absolute crop residue presence and its fractional cover concerning soil background and vegetation.

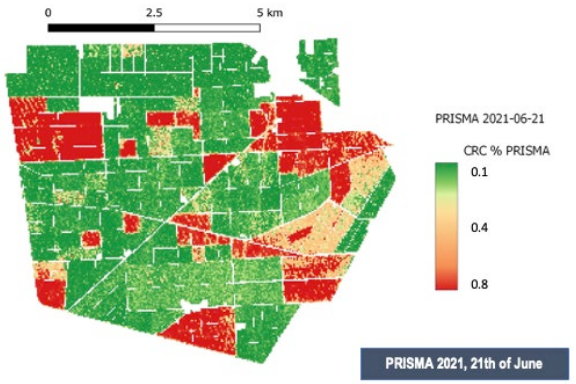

Figure 5. Pixel level Crop Residue Cover (CRC) map using PRISMA imagery acquired on June 21, 2021

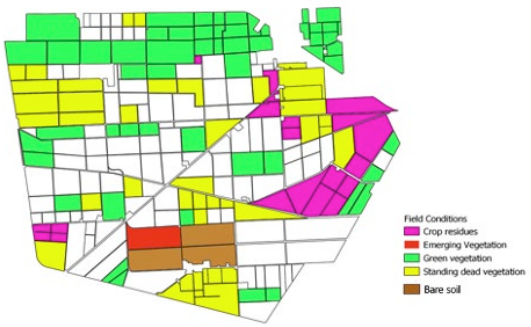

Figure 6. Ground reference map from field observations in 2021 (scale is the same of fig. 5).

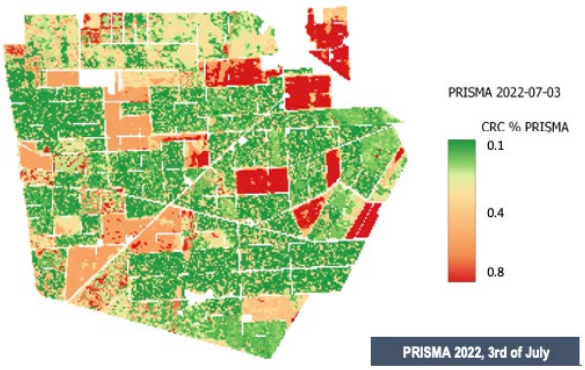

Figure 7. Pixel level Crop Residue Cover (CRC) map using PRISMA imagery acquired on July 3, 2022.

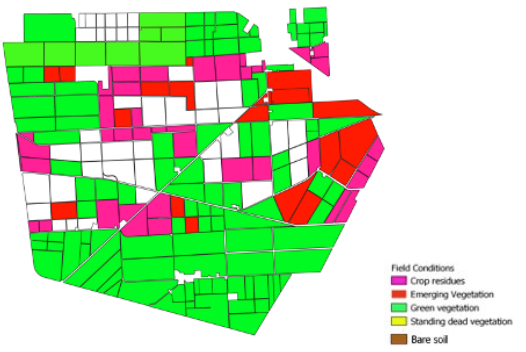

Figure 8. Ground reference map derived from crop map and information from the farm in 2022.

4. CONCLUSION

In this research, we have introduced a workflow, encompassing two steps, designed for mapping crop residue coverage (CRC), exploiting spaceborne imaging spectroscopy from PRISMA data. Our workflow has yielded very satisfactory findings. First, we have demonstrated the fitness for purpose of the Exponential Gaussian Optimization (EGO) model. This approach has significantly enhanced the information content of the spectral intervals of interest, as related to plant pigments, canopy water, lignin-cellulose and clay minerals, while reducing the feature space from 230 bands to 16 metrics layers. Besides, the use of machine learning played a pivotal role to find a non-linear regression between this reduced space and Crop Residue Cover information. The use of a spectral library to train the Random Forest (RF) regressive model overcomes the issue of finding a large training sample, without the use of simulated data, whereas reaching very good levels of predictive capabilities. This is proved by applying the RF to independent field datasets and satellite images. In this regard, our mapping demonstration has yielded results that align with ground observations, underscoring the robustness of our approach. Moreover, the application of the model on datasets from two different crop seasons, shows similar performance, proving the model robustness and its temporal transferability.

In summary, our discoveries proved the substantial potential of PRISMA data in monitoring and quantify NPV, spanning from individual fields to farm scales. Our overarching objective is to further advance and refine this comprehensive model, ensuring its continued effectiveness over time and expanding its adaptability to a wide range of spatial contexts. In our future works, we will focus on rigorously assessing the model performance. This assessment will involve the use of ground-level Crop Residue Cover (CRC) data at the PRISMA scale, encompassing data from 2022 and 2023. These ground-level observations will serve as a valuable benchmark to evaluate the model performance under real-world conditions. Additionally, we plan to leverage PRISMA time series data to continuously monitor CRC dynamics. This approach will provide insights into how CRC changes over time and how well our model adapts to these variations. Furthermore, we intend to enhance the model capabilities by incorporating Radiative Transfer Model (RTM) simulations. This will expand the training dataset and account for a broader range of factors that influence reflectance, including soil moisture, different mixture of target presence and sensors viewing geometry. This refinement process aims to bolster the model accuracy and broaden its applicability to various environmental conditions. In summary, our future work encompasses three key objectives: 1) Testing the robustness of the CR model against field-collected ground data from 2022 and 2023, at the PRISMA scale; 2) Leveraging RTM simulations to augment the training dataset and to consider different factors influencing reflectance, such as moisture; 3) Continuously monitoring CRC dynamics using PRISMA time series data to assess changes in time due to agro-management and target decomposition. These efforts collectively aim to advance our understanding and application of NPV mapping, contributing to more accurate and versatile environmental assessments.

ACKNOWLEDGEMENTS

This study was co-funded by the Italian Space Agency (ASI) in the framework of the PRIS4VEG – ASI SCIENZA project [2022-5-U.0]. The Authors would like to thank Patrizia Sacco (ASI) for her support for satellite data procurement.

REFERENCES

Berger, K., Hank, T., Halabuk, A., Rivera-Caicedo, J.P., Wocher, M., Mojses, M., Gerhátová, K., Tagliabue, G., Dolz, M.M., Venteo, A.B.P., & Verrelst, J. , 2021. Assessing Non-Photosynthetic Cropland Biomass from Spaceborne Hyperspectral Imagery. *Remote Sensing*, 13(22), 4711.

Daughtry C.S.T., 2001. Discriminating crop residues from soil by shortwave infrared reflectance. *Agronomy Journal*, 93, pp. 125-131.

Hively, W.D., Lamb, B.T., Daughtry, C.S., Serbin, G., Dennison, P., Kokaly, R.F., Wu, Z. & Masek, J.G., 2021. Evaluation of SWIR Crop Residue Bands for the Landsat Next Mission. *Remote Sensing*, 13(18), 3718.

Pepe, M., Pompilio, L., Gioli, B., Busetto, L. & Boschetti, M., 2020. Detection and classification of Non-Photosynthetic Vegetation from PRISMA hyperspectral data in croplands. *Remote Sensing*, 12(23), 3903.

Pepe, M., Pompilio, L., Ranghetti L., Nutini F. & Boschetti, M., 2022. Mapping spatial distribution of crop residues using PRISMA satellite imaging spectroscopy. *European Journal of Remote Sensing*, 1-16.

Verrelst, J., Halabuk, A., Atzberger, C., Hank, T., Steinhauser, S., & Berger, K., 2023. A comprehensive survey on quantifying non-photosynthetic vegetation cover and biomass from imaging spectroscopy. *Ecological Indicators*, 155, 110911.

LEAF AREA INDEX AND CANOPY CHLOROPHYLL CONTENT ESTIMATION OF ARABLE CROPS FROM SENTINEL-2 WITH GAUSSIAN PROCESS REGRESSION: A MULTI-SITE, YEAR AND CROP VALIDATION

A. Crema[1]*, M. De Peppo[1], F. Nutini[1], G. Candiani[1], G.A. Re[2], F. Sanna[2], C. Cesaraccio[3], B. Gioli[3], M. Boschetti[1]

[1] Institute for Electromagnetic Sensing of the Environment, Italian National Research Council, Italy - depeppo.margherita@gmail.com (crema,a, candiani.g, nutini.f, boschetti.m)@irea.cnr.it

[2] Institute for the Animal Production System in the Mediterranean Environment (ISPAAM), Italian National Research Council, Italy federico.sanna@cnr.it, gianni.re@ispaam.cnr.it

[3] Institute of BioEconomy, Italian National Research Council, Italy - beniamino.gioli@cnr.it, (carla.cesaraccio, pierpaolo.duce)@ibe.cnr.it

KEY WORDS: Machine Learning; Gaussian Processes Regression; BioPar; Sentinel-2

ABSTRACT:
Spatio-temporal estimation of crop bio-parameters (BioPar) is required for agroecosystem management and monitoring. BioPar such as Canopy Chlorophyll Content (CCC) and Leaf Area Index (LAI) contribute to assess plant physiological status and health at leaf and canopy level. Remote sensing techniques are instrumental in spatially explicit CCC and LAI retrieval of arable crops across different scales. Machine Learning (ML) techniques, especially Gaussian processes regression (GPR), has outperformed traditional approaches based on Vegetation Index in BioPar estimation. However, being ML model based on data driven approach it is necessary to thoroughly evaluate the performance of GPR across different sites, seasons, and crop types to assess the exportability of the models. This study aimed to develop a transferable GPR algorithm using a large dataset collected over several years (2018-2022), on different locations (5 sites) and with different canopy conditions by sampling 10 different arable crops. The study objectives included developing a robust GPR algorithm for LAI and CCC estimation from Sentinel-2 data, validating GPR against independent datasets, and comparing results with other methods and available products. The study utilized 301 (209 crop + 92 soil spectral) CCC and 301 LAI observations for GPR model training. Validation on independent datasets (698 LAI and 364 CCC) revealed the reliability of GPR estimation, compared to Sentinel-2 Level 2 Prototype Processor (SL2P) estimates. LAI and CCC estimation metrics varied across datasets achieving coherent and similar performance between the two method (GPR and SL2P). In general, SL2P model better fits the overall data with slightly higher R^2 values with respect to GPR especially for LAI parameter. GRP estimates provided better results when accuracy analysis is performed by crops showing lower RMSE (Root Mean Square Error) and MAE (Mean Absolute Error). GPR outperforms SL2P for mais and wheat in particular for CCC parameter. These results showed the potential of GPR in BioPar estimation, especially when a robust training set was used. BioPar estimation using Sentinel 2 data provided high-quality quasi-weekly information, essential for smart crop management and early warnings in decision support systems.

1. INTRODUCTION

Remote sensing, with its capacity to provide near real-time and comprehensive information, has emerged as an indispensable tool for monitoring crop health and growth (Defourny et al., 2019; Weiss et al., 2020). In the context of precision farming, the accurate estimation of vegetation biophysical parameters through remote sensing techniques (Verrelst et al., 2019) plays a key role in the effective management of agricultural crops.
Two of the most critical biophysical parameters in this context are Leaf Area Index (LAI) and Canopy Chlorophyll Content (CCC). LAI represents the extent of foliage cover, aiding in the assessment of crop density and growth, while CCC is an indicator of photosynthetic activity. These parameters are central in decision-making processes because offering insights into crop health and vigor. The incorporation of LAI and CCC estimates into operational workflows enables farmers to make informed decisions about fertilization, thereby optimizing crop management and reducing environmental impact. However, achieving accurate parameter estimations is no simple task and a variety of retrieval methods for BioPar extraction (Verrelst et al., 2019) have been applied to optical data (multi and hyperspectral). The theoretical framework of the multitude of retrieval methods was accurately given by Verrelst et al., 2015 with four main methodological categories: i) Parametric regression methods (Clevers et al., 2017; Crema et al., 2020); ii) Nonparametric regression methods (Campos-Taberner et al., 2016; De Peppo et al., 2021; Upreti et al., 2019); iii) Physically based model inversion methods (Berger et al., 2018; Sehgal et al., 2016) and iv) Hybrid regression methods (Candiani et al., 2022; Ranghetti et al., 2022; Rossi et al., 2022). All these categories are not rigid and definitive and we are witnessing new development together with improvements in the computational capacity and the progress in new imaging sensors.
In order to meet the increasing demand for tools to support the site-specific management of crops, we need to improve estimation accuracy but also systems operations. For this reason, the data provided by Sentinel-2 represent an optimal solution due to the spatial (10-20m) and temporal resolution of the sensor that allow to have BioPar maps at a suitable scale for operational practices (Bontemps et al., 2015; Defourny et al., 2019; Segarra et al., 2020) .
In this study, we evaluated the potential of non-parametric approaches and robustness of ML methods for multi-temporal BioPar retrieval by Sentinel-2 multispectral data. The specific objectives were: (i) develop a transferable GPR algorithm for LAI and CCC estimation by exploiting a robust multi-crop, multi-year and multi-site dataset; (ii) assess GPR BioPar retrieval performance against ground measurements acquired over independent dataset; (iii) compare result with the product freely available from Sentinel Application Platform (SNAP) using SL2P.

2. MATERIALS AND METHODS

2.1 Study area and Dataset

Data collection aimed to assess the robustness of non-parametric methods concerning diverse sources of variability of BioPar, including specific conditions related to crop species, agronomic

* Corresponding author

practices (density) growth stages, farms, and years. With the objectives of effectively capture the site-specific differences in BioPar variability, LAI and CCC ground-measurements were collected during several field campaigns. The measures, performed contemporary to S2 data acquisition, were collected on an Elementary Sampling Units (ESU) of 20x20 m according to the Validation of Land European Remote Sensing Instruments (VALERI) sampling strategy (Baret et al. 2005).

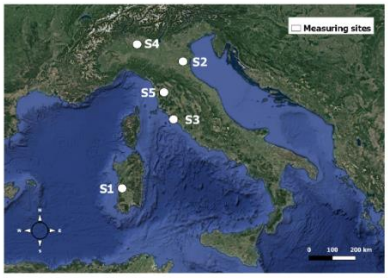

Figure 1:Study areas of ground measurements: S1 (Arborea); S2 (Ferrara); S3 (Grosseto); S4 (Milano); S5 (Pisa)

Different study areas located in central and northern part of Italy (Figure 1) were investigated collecting data of ten different crops: alfalfa, maize, wheat, emmer, pea, sugarbeet, barley, rice, sorghum and soybean. In particular, to achieve a robust multi-crop, multi-year and multi-site dataset, the ground BioPar measurements were conducted over different growing seasons from 2018 and 2022 (Table 1) characterized by different growing periods and canopy structures and considering different agronomic conditions. A total of 907 (573) LAI (CCC) observations were collected with standard instrumentation like LAI2200 (MC100) (Tagliabue et al., 2022), hemispherical photography (Dualex) (Crema et al., 2020) and SunScan (De Peppo et al., 2021) during the campaigns. Grubbs' test for data anomalies was performed to identify potential outliers.

Table 1: Multicrop, multiyear and multisite database with ground measurements cardinality. T indicates training dataset; V indicates validation dataset

Site	Location	Year	Crop	LAI	CCC	Use	Reference
S1_1	Arborea	2021	alfalfa barley	52	40	V	
S1_2	Arborea	2022	alfalfa	35	34	V	
S2_1	Ferrara	2018	maize	71	71	T	Crema et al. 2020
S2_2	Ferrara	2019	wheat	20	40	V	Crema et al. 2020
S2_3	Ferrara	2020	alfalfa maize pea soybean sugarbeet wheat	47	47	T	Tagliabue et al 2022
S2_4	Ferrara	2021	barley emmer maize soybean rice wheat sugarbeet	91	91	T	Tagliabue et al 2022
S2_5	Ferrara	2021	maize soybean	71	67	V	
S2_6	Ferrara	2022	barley wheat	71	68	V	
S2_7	Ferrara	2022	maize rice sorgum soybean	30	28	V	
S3	Grosseto	2018	maize	87	87	V	Candiani et al. 2022
S4	Milano	2022	maize	54	0	V	
S5_1	Pisa	2018	maize	173	0	V	De peppo et al 2021
S5_1	Pisa	2019	wheat	105	0	V	De peppo et al 2021

The S2 Level 2A (L2A) images over the growing seasons were acquired using sen2r R package (Ranghetti et al., 2020) providing seasonal time-series of Bottom of Atmosphere (BOA) reflectance. All cloud-free images, collected in correspondence with the in situ monitoring period (±5 days from ground data collection), were used to analyse the relationship between measured ground BioPar and S2 data. A zonal statistic was performed to extract S2 pixels values using the centroid of each ESU as reference. S2 bands at10 m (B02, B03, B04, and B08) and 20 m (B05, B06, B07, B08A, B11, and B12) were selected for the analysis, resampling all bands to 20 m spatial resolution.

2.2 Machine learning model

Among the different available MLR algorithms, GPR is considered promising for LAI and CCC mapping (Campos-Taberner et al., 2016; Verrelst et al., 2013, 2012) and in general this is also the algorithm more exploited in hybrid approaches (Candiani et al., 2022; Tagliabue et al., 2022). GPR is a non-linear non-parametric regression algorithm that learn the relationship between the input (e.g. reflectance) and output (e.g. LAI or CCC) fitting a flexible model directly from the data and providing both a predictive mean and a predictive variance (uncertainty). The theoretical aspects of GPR are deeply described in Rasmussen, 2004 and in Verrelst et al., 2019 and in studies that applied this approach with hyperspectral (Caicedo et al., 2014; Verrelst et al., 2012) and multispectral data (Estévez et al., 2020).. In addition, the model is trained and validated relatively fast Following De Peppo et al., 2021, GPR was selected as the best-performing algorithm for LAI prediction for arable crops. Few studies have examined the performance of GPR in predicting crop parameters when applied to different site, season and crop typology (i.e. validation using independent dataset).Moreover, the retrieved BioPar were also compared against LAI and CCC generated by the Neural Network (NN) model implemented into the S2LP of the Sentinel Application Platform (SNAP) (Weiss and Baret, 2016) for all the S2 images.

2.2.1 Training and cross validation performance

We first generated 301 (209 from vegetation + 92 soil) data pairs (reflectances-BioPar values) from valuable multiyear data set (S2_1, S2_3, S2_4) with the simultaneous presence of LAI and CCC data (Crema et al., 2020; Tagliabue et al., 2022) for model training, and then evaluated model performance with the remaining 698 (364) LAI (CCC) samples (Table 1). The accuracy of the model in cross validation was assessed using K-fold approach (Kohavi, 1995), where the dataset was randomly split into k = 10 subsets of equal size repeated 5 times. The coefficient of determination (R^2), the mean absolute error (MAE) and root mean square error (RMSE) were calculated to assess the prediction accuracy.

2.2.2 Independent validation to assess model exportability

A robust model validation was performed using nine independent datasets (Table 1). BioPars estimated using the GPR model were compared with LAI and CCC values collected in different sampling areas and years to test the transferability of the developed model.

3. RESULTS AND DISCUSSION

The GPR model assessment was performed considering the average of coefficient of determination estimated between ground-and predicted BioPar and the average value of RMSE and MAE from the cross-validation. Overall estimation metrics in cross validation ranges from R^2=0.89 (MAE=0.49; RMSE=0.74) for LAI variable to R^2=0.83 (MAE=0.28; RMSE=0.43) for CCC (Figure 2).

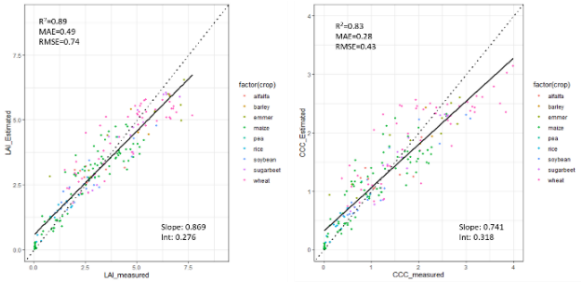

Figure 2: Cross-validation results of LAI (m^2 m^{-2}) and CCC (g m^{-2} estimation from GPR. (p-values < 0.05)

In order to evaluate and compare the accuracy of predictions at pixel level (i.e. for available ESU) both for data driven GPR and NN of S2LP, validation results on independent data were evaluated considering the single crops (Table 1).

Table 2: CCC GPR and CCC SL2P metrics derived from independent validation (p-values < 0.05)

Crop	Methods	R2	MAE	RMSE
alfalfa	CCC GPR	0.07	0.65	0.76
alfalfa	CCC SL2P	0.12	0.65	0.78
barley	CCC GPR	0.58	0.57	0.64
barley	CCC SL2P	0.62	0.73	0.86
maize	CCC GPR	0.59	0.43	0.56
maize	CCC SL2P	0.5	0.78	1.21
soybean	CCC GPR	0.85	0.28	0.41
soybean	CCC SL2P	0.87	0.36	0.63
wheat	CCC GPR	0.78	0.53	0.64
wheat	CCC SL2P	0.84	1.07	1.31

Table 3: LAI GPR and LAI SL2P metrics derived from independent validation (p-values < 0.05)

Crop	Methods	R2	MAE	RMSE
alfalfa	LAI GPR	0.08	1.03	1.3
alfalfa	LAI SL2P	0.08	1.44	1.77
barley	LAI GPR	0.53	1.3	1.59
barley	LAI SL2P	0.56	1.12	1.51
maize	LAI GPR	0.51	0.94	1.16
maize	LAI SL2P	0.46	0.96	1.39
rice	LAI GPR	0.47	1.1	1.3
rice	LAI SL2P	0.73	1.2	1.36
sorghum	LAI GPR	0.8	0.45	0.52
sorghum	LAI SL2P	0.9	0.39	0.45
soybean	LAI GPR	0.69	0.98	1.37
soybean	LAI SL2P	0.89	0.68	1
wheat	LAI GPR	0.49	0.93	1.18
wheat	LAI SL2P	0.4	1.05	1.38

LAI and CCC estimation metrics varies across datasets (Table 2;Table 3) . The results showed that for both LAI and CCC, GPR retrieval is reliable and comparable with SL2P estimates for all crops and in some cases better. The estimates of vegetation biophysical variables given by the toolbox S2LP embedded in SNAP represented the reference product. NNs are the most widely-used tools and SNAP Biopar have been evaluated in previous studies with diverse results (Estévez et al., 2020; Kganyago et al., 2020; Xie et al., 2019).

The estimates showed an agreement between the GPR and S2LP results on single crops/dataset. In general, the two models showed no partialities for individual crops and were consistent in performance except for lower errors in GPR_CCC retrieval. Regarding CCC, GPR showed a higher coefficient of determination only for maize (CCC_GPR R^2=0.59; CCC_S2LP R^2=0.50) but MAE and RSME (i.e., ~0.4 to ~0.75) were always better than S2LP (RMSE ~0.6 to ~1.3) for all the crops. S2LP estimates for wheat and maize resulted significantly overestimated (data not shown) when compared to ground data showing MAE and RMSE value almost double than GPR (see table 2).

With regard to LAI, GPR presented a better coefficient of determination for maize (LAI_GPR R^2=0.51; LAI_S2LP R^2=0.46) and wheat (LAI_GPR R^2=0.49; LAI_S2LP R^2=0.4) together with MAE and RSME while for the remaining crops S2LP performs better. Also on rice, the LAI estimated by GPR has lower R^2 but better MAE and RMSE than S2LP. These results confirmed the tendency of SNAP-derived products to have higher errors as found by Kganyago et al., 2020 with MAE and RMSE > 2 and Fernandes et al., 2014 with reasonably unbiased LAI estimates with acceptable error (<;1 unit) and validation sites with larger (>1 unit) error.

The satisfactory error metrics confirm the substantial robustness of the GPR prediction and its consistency with existing products as found in other validation studies (Brown et al., 2021; Campos-Taberner et al., 2018). The GPR model performed well for most crops despite the diversity of species and locations and alfalfa was the only crop to have unsatisfactory results for both retrieval approaches (R^2=0.08), probably due to the law quality of ground data (LAI) with LAI max data higher respect to the literature (Verger et al., 2009).

Applying the GPR model to an independent data we highlighted the prediction robustness over different areas both globally and by single crop. In general, we noted that the performance was less influenced by the training data set as usually observed (Mao et al., 2019; Verrelst et al., 2019). Estévez et al., 2020 demonstrated the feasibility of LAI retrieval from S2 in a hybrid machine learning framework using GPR with higher accuracies and lower uncertainties (R^2=0.78, RMSE= 0.60) compared to the SNAP toolbox. However, as mentioned by Upreti et al., 2019, the accuracies found by most of the studies using GPR with ML or hybrid were not validated against independent ground data, such as in the present work.

However, despite an overestimation of low-LAI values with GPR, the positive linear relationship between the measured and predicted values was confirmed by the slope values close to 1as found also by (De Peppo et al., 2021). This finding is in agreement with the outcomes of Verrelst et al., 2015 that indicated how GPR was the most effective algorithm for LAI retrieval.

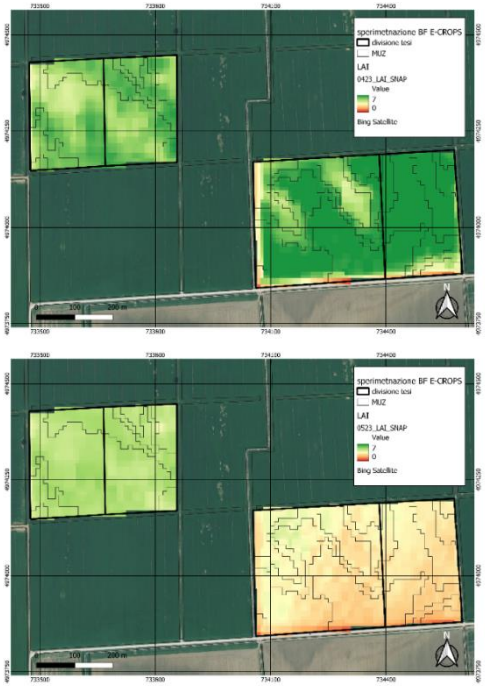

Figure 3: LAI maps of winter wheat of S2 farm in 2023. Black lines represent the boundaries of management zones derived from a soil map. above 23rd of april; below 23th of may.

The BioPar maps generated by the prediction allowed to highlight the spatial patterns present within the field during the season as shown for LAI in Figure 3. Spatial and temporal variability correctly pointed out crop (wheat) growth differences according to a soil map of the farm situated in S2 farm. This study allowed us to leverage all available information from a multi-year multisite and multicrop dataset, thus providing greater accuracy in BioPar prediction than ML model trained with local training datasets.

4. CONCLUSION

Overall the results demonstrated the potentiality of a data driven GPR machine learning approach in LAI and CCC estimations of arable crops when a robust training set is exploited, such condition guarantee a spatial-temporal transferability. The results of cross-validation confirm the theoretical GPR retrieval performance of this ML method. In addition, this work verified the model stability when applied to an independent data set and compared the performance with existing products as generated by the SNAP toolbox, which is framed in an hybrid approach using radiative transfer model simulation and neural network as retrieval algorithm. This analysis allowed for a full assessment of the robustness and exportability of the developed model and the results were in line with other studies with independent model simulations. It is important to remark that, despite medium high R_2, S2LP shows overestimation for CCC in particular for wheat and corn as highlighted by high MAE and RMSE values. Being LAI and CCC quantitative crops Biopar, the lower values of errors of the GPR model can lead to prefer this model even for R_2 slightly lower than the S2LP model. In addition, this ML technique is faster and more easily applied than NNs that are closed balck-box that require a relatively long time for training. Such maps (decametric quasi-weekly) are a fundamental input for decision support systems devoted to smart crop management and early warning indication. Many precision agriculture techniques could thus benefit from information generated with ideal quality and frequency for site-specific practices aimed at reducing inputs and improving the use-efficiency of fertilizers.

ACKNOWLEDGEMENTS

This research was funded by the Project PON «R&I» 2014–2020—Azione II—"E-crops—Technologies for Digital and Sustainable Agriculture" funded by the Italian Ministry of University and Research (MUR) under the PON Agrifood Program (Contract ARS01_01136).

REFERENCES

Berger, K., Atzberger, C., Danner, M., D'Urso, G., Mauser, W., Vuolo, F., Hank, T., 2018. Evaluation of the PROSAIL model capabilities for future hyperspectral model environments: A review study. Remote Sens. https://doi.org/10.3390/rs10010085

Bontemps, S., Arias, M., Cara, C., Dedieu, G., Guzzonato, E., Hagolle, O., Inglada, J., Matton, N., Morin, D., Popescu, R., Rabaute, T., Savinaud, M., Sepulcre, G., Valero, S., Ahmad, I., Bégué, A., Wu, B., de Abelleyra, D., Diarra, A., Dupuy, S., French, A., Akhtar, I. ul H., Kussul, N., Lebourgeois, V., Page, M. Le, Newby, T., Savin, I., Verón, S.R., Koetz, B., Defourny, P., 2015. Building a data set over 12 globally distributed sites to support the development of agriculture monitoring applications with Sentinel-2. Remote Sens. 7, 16062–16090. https://doi.org/10.3390/rs71215815

Brown, L.A., Fernandes, R., Djamai, N., Meier, C., Gobron, N., Morris, H., Canisius, F., Bai, G., Lerebourg, C., Lanconelli, C., Clerici, M., Dash, J., 2021. Validation of baseline and modified Sentinel-2 Level 2 Prototype Processor leaf area index retrievals over the United States. ISPRS J. Photogramm. Remote Sens. 175, 71–87. https://doi.org/10.1016/j.isprsjprs.2021.02.020

Caicedo, J.P.R., Verrelst, J., Munoz-Mari, J., Moreno, J., Camps-Valls, G., 2014. Toward a semiautomatic machine learning retrieval of biophysical parameters. IEEE J. Sel. Top. Appl. Earth Obs. Remote Sens. 7, 1249–1259. https://doi.org/10.1109/JSTARS.2014.2298752

Campos-Taberner, M., García-Haro, F.J., Busetto, L., Ranghetti, L., Martínez, B., Gilabert, M.A., Camps-Valls, G., Camacho, F., Boschetti, M., 2018. A Critical Comparison of Remote Sensing Leaf Area Index Estimates over Rice-Cultivated Areas: From Sentinel-2 and Landsat-7/8 to MODIS, GEOV1 and EUMETSAT Polar System. Remote Sens. 2018, Vol. 10, Page 763 10, 763. https://doi.org/10.3390/RS10050763

Campos-Taberner, M., García-Haro, F.J., Camps-Valls, G., Grau-Muedra, G., Nutini, F., Crema, A., Boschetti, M., 2016. Multitemporal and multiresolution leaf area index retrieval for operational local rice crop monitoring. Remote Sens. Environ. 187, 102–118. https://doi.org/10.1016/j.rse.2016.10.009

Candiani, G., Tagliabue, G., Panigada, C., Verrelst, J., Picchi, V., Caicedo, J.P.R., Boschetti, M., 2022. Evaluation of Hybrid Models to Estimate Chlorophyll and Nitrogen Content of Maize Crops in the Framework of the Future CHIME Mission. Remote Sens. 14. https://doi.org/10.3390/rs14081792

Clevers, J.G.P.W., Kooistra, L., van den Brande, M.M.M., 2017. Using Sentinel-2 data for retrieving LAI and leaf and canopy chlorophyll content of a potato crop. Remote Sens. 9, 405. https://doi.org/10.3390/rs9050405

Crema, A., Boschetti, M., Nutini, F., Cillis, D., Casa, R., 2020. Influence of Soil Properties on Maize and Wheat Nitrogen Status Assessment from Sentinel-2 Data. Remote Sens. 12, 2175. https://doi.org/10.3390/rs12142175

De Peppo, M., Taramelli, A., Boschetti, M., Mantino, A., Volpi, I., Filipponi, F., Tornato, A., Valentini, E., Ragaglini, G., 2021. Non-parametric statistical approaches for leaf area index estimation from sentinel-2 data: A multi-crop assessment. Remote Sens. 13, 2841. https://doi.org/10.3390/rs13142841

Defourny, P., Bontemps, S., Bellemans, N., Cara, C., Dedieu, G., Guzzonato, E., Hagolle, O., Inglada, J., Nicola, L., Rabaute, T., Savinaud, M., Udroiu, C., Valero, S., Bégué, A., Dejoux, J.F., El Harti, A., Ezzahar, J., Kussul, N., Labbassi, K., Lebourgeois, V., Miao, Z., Newby, T., Nyamugama, A., Salh, N., Shelestov, A., Simonneaux, V., Traore, P.S., Traore, S.S., Koetz, B., 2019. Near real-time agriculture monitoring at national scale at parcel resolution: Performance assessment of the Sen2-Agri automated system in various cropping systems around the world. Remote Sens. Environ. 221, 551–568. https://doi.org/10.1016/j.rse.2018.11.007

Estévez, J., Vicent, J., Rivera-Caicedo, J.P., Morcillo-Pallarés, P., Vuolo, F., Sabater, N., Camps-Valls, G., Moreno, J., Verrelst, J., 2020. Gaussian processes retrieval of LAI from Sentinel-2 top-of-atmosphere radiance data. ISPRS J. Photogramm. Remote Sens. 167, 289–304. https://doi.org/10.1016/j.isprsjprs.2020.07.004

Fernandes, R., Weiss, M., Camacho, F., Berthelot, B., Baret, F., Duca, R., 2014. Development and assessment of leaf area index algorithms for the Sentinel-2 multispectral imager, in: 2014

IEEE Geoscience and Remote Sensing Symposium. pp. 3922–3925. https://doi.org/10.1109/IGARSS.2014.6947342

Kganyago, M., Mhangara, P., Alexandridis, T., Laneve, G., Ovakoglou, G., Mashiyi, N., 2020. Validation of sentinel-2 leaf area index (LAI) product derived from SNAP toolbox and its comparison with global LAI products in an African semi-arid agricultural landscape. Remote Sens. Lett. 11, 883–892. https://doi.org/10.1080/2150704X.2020.1767823

Kohavi, R., 1995. A Study of Cross-Validation and Bootstrap for Accuracy Estimation and Model Selection, in: Proceedings of the 14th International Joint Conference on Artificial Intelligence - Volume 2, IJCAI'95. Morgan Kaufmann Publishers Inc., San Francisco, CA, USA, pp. 1137–1143.

Mao, H., Meng, J., Ji, F., Zhang, Q., Fang, H., 2019. Comparison of machine learning regression algorithms for cotton leaf area index retrieval using Sentinel-2 spectral bands. Appl. Sci. 9, 1459. https://doi.org/10.3390/app9071459

Ranghetti, L., Boschetti, M., Nutini, F., Busetto, L., 2020. "sen2r": An R toolbox for automatically downloading and preprocessing Sentinel-2 satellite data. Comput. Geosci. 139.https://doi.org/10.1016/j.cageo.2020.104473

Ranghetti, M., Boschetti, M., Ranghetti, L., Tagliabue, G., Panigada, C., Gianinetto, M., Verrelst, J., Candiani, G., 2022. Assessment of maize nitrogen uptake from PRISMA hyperspectral data through hybrid modelling. Eur. J. Remote Sens. 00, 1–17. https://doi.org/10.1080/22797254.2022.2117650

Rasmussen, C.E., 2004. Gaussian Processes in Machine Learning, in: Bousquet, O., von Luxburg, U., Rätsch, G. (Eds.), Advanced Lectures on Machine Learning: ML Summer Schools 2003, Canberra, Australia, February 2 - 14, 2003, Tübingen, Germany, August 4 - 16, 2003, Revised Lectures. Springer Berlin Heidelberg, Berlin, Heidelberg, pp. 63–71. https://doi.org/10.1007/978-3-540-28650-9_4

Rossi, M., Candiani, G., Nutini, F., Gianinetto, M., Boschetti, M., 2022. Sentinel-2 estimation of CNC and LAI in rice cropping system through hybrid approach modelling. Eur. J. Remote Sens. 00, 1–20. https://doi.org/10.1080/22797254.2022.2117651

Segarra, J., Buchaillot, M.L., Araus, J.L., Kefauver, S.C., 2020. Remote sensing for precision agriculture: Sentinel-2 improved features and applications. Agronomy. https://doi.org/10.3390/agronomy10050641

Sehgal, V.K., Chakraborty, D., Sahoo, R.N., 2016. Inversion of radiative transfer model for retrieval of wheat biophysical parameters from broadband reflectance measurements. Inf. Process. Agric. 3, 107–118. https://doi.org/10.1016/j.inpa.2016.04.001

Tagliabue, G., Boschetti, M., Bramati, G., Candiani, G., Colombo, R., Nutini, F., Pompilio, L., Rivera-Caicedo, J.P., Rossi, M., Rossini, M., Verrelst, J., Panigada, C.,2022. Hybrid retrieval of crop traits from multi-temporalPRISMA hyperspectral imagery. ISPRS J. Photogramm.Remote Sens. 187, 362–377.https://doi.org/10.1016/j.isprsjprs.2022.03.014

Upreti, D., Huang, W., Kong, W., Pascucci, S., Pignatti, S., Zhou, X., Ye, H., Casa, R., 2019. A comparison of hybrid machine learning algorithms for the retrieval of wheat biophysical variables from sentinel-2. Remote Sens. 11, 481.https://doi.org/10.3390/rs11050481

Verger, A., Martínez, B., Coca, F.C. De, García-Haro, F.J., 2009. Accuracy assessment of fraction of vegetation cover and leaf area index estimates from pragmatic methods in a cropland area. Int. J. Remote Sens. 30, 2685–2704. https://doi.org/10.1080/01431160802555804

Verrelst, J., Alonso, L., Camps-Valls, G., Delegido, J., Moreno, J., 2012. Retrieval of Vegetation Biophysical Parameters Using Gaussian Process Techniques. IEEE Trans. Geosci. Remote Sens. 50, 1832–1843. https://doi.org/10.1109/TGRS.2011.2168962

Verrelst, J., Alonso, L., Rivera Caicedo, J.P., Moreno, J., Camps-Valls, G., 2013. Gaussian Process Retrieval of Chlorophyll Content From Imaging Spectroscopy Data. IEEE J. Sel. Top. Appl. Earth Obs. Remote Sens. 6, 867–874.https://doi.org/10.1109/JSTARS.2012.2222356

Verrelst, J., Malenovský, Z., Van der Tol, C., Camps-Valls, G., Gastellu-Etchegorry, J.P., Lewis, P., North, P., Moreno, J., 2019. Quantifying Vegetation Biophysical Variables from Imaging Spectroscopy Data: A Review on Retrieval Methods. Surv. Geophys. https://doi.org/10.1007/s10712-018-9478-y

Verrelst, J., Rivera, J.P., Veroustraete, F., Muñoz-Marí, J., Clevers, J.G.P.W., Camps-Valls, G., Moreno, J., 2015. Experimental Sentinel-2 LAI estimation using parametric, non-parametric and physical retrieval methods - A comparison. ISPRS J. Photogramm. Remote Sens. 108, 260–272. https://doi.org/10.1016/j.isprsjprs.2015.04.013

Weiss, M., Baret, F., 2016. S2ToolBox Level 2 products: LAI, FAPAR, FCOVER 53.

Weiss, M., Jacob, F., Duveiller, G., 2020. Remote sensing for agricultural applications: A meta-review. Remote Sens. Environ. 236. https://doi.org/10.1016/j.rse.2019.111402

Xie, Q., Dash, J., Huete, A., Jiang, A., Yin, G., Ding, Y., Peng, D., Hall, C.C., Brown, L., Shi, Y., Ye, H., Dong, Y., Huang, W., 2019. Retrieval of crop biophysical parameters from Sentinel-2 remote sensing imagery. Int. J. Appl. Earth Obs. Geoinf. 80, 187–195. https://doi.org/10.1016/j.jag.2019.04.019

CONSISTENCY BETWEEN MOD16A2 POTENTIAL EVAPOTRANSPIRATION TIME SERIES AND AGRO-METEO BASED MODELS IN PIEMONTE (NW ITALY)

A. Farbo , F. Sarvia , S. De Petris , F. Ghilardi *, E. Borgogno-Mondino

DISAFA – Department of agriculture, forest and food sciences; University of Torino – Italy
(alessandro.farbo; filippo.sarvia; samuele.depetris; federica.ghilardi; enrico.borgogno)@unito.it

KEY WORDS: Potential Evapotranspiration, Remote Sensing, MODIS, ET0

ABSTRACT:

The summer of 2022 in Europe was characterized by severe droughts and heatwaves that affected agricultural sector, especially in Italy. The frequency of such events is expected to increase in the future due to climate change effects, making it crucial to manage water resources at regional scale. Potential and Actual Evapotranspiration can be used for agricultural water requirements analysis in order to plan available water resources management. Remote sensing products such as 8-days MOD16A2 offer estimates of potential evapotranspiration at a global scale. However, due to its coarse geometric resolution, some doubts arise about the consistency of MOD16A2 estimates which may locally show significant errors in respect to ground data. These errors analysis its crucial especially for agronomic purposes where local treatments, possibly driven by remotely sensed deductions, are expected to mitigate yields losses. This study explores the consistency between MOD16A2 potential evapotranspiration and the 8-days cumulated one derived from 135 meteorological stations in Piemonte region (NW-Italy) during 2022, using both temporal and spatial approaches. The temporal approach shows a significant high correlation between the potential evapotranspiration temporal profiles. However, a poor correlation was found concerning spatial consistency suggesting that MOD16A2 estimates have low accuracy, but their trend and seasonality are coherent. Biases between MOD16A2 and meteorological station have been addressed for, thus making MOD16A2 a reliable tool for managing water resources if previously ground calibrated.

1. INTRODUCTION

Over the last few years, the world was characterized by severe droughts and heatwaves that affected the agricultural sector, especially in Europe. The frequency of such events is expected to increase in the future due to climate change effects, making it crucial to manage water resources at regional scale. There are many factors influencing this phenomenon and analyzing them is crucial to try to limit its effects (Jacob and Winner, 2009). Phenomena such as the increase in CO_2 linked to various anthropological activities (Ukhurebor et al,2020; Baer and Singer, 2018), production of energy or material goods (Elshkaki, 2023), deforestation (Ellwanger et al., 2020) and food production (Mirón et al., 2023) play a fundamental role as key elements of climate change. The effects of this phenomenon on planet earth are innumerable, such as global warming, extreme weather events, warming of the oceans and their acidification, decreasing biodiversity and the availability of water resources.

Especially in 2022, the agricultural sector has been greatly affected by the effects of climate change, especially considering the water requirements of crops (Borgogno-Mondino et al., 2022; DePetris et al., 2022).

This type of deficit represents a certain risk to farmers' livelihoods and the entire agri-food sector.

For a better and more effective management of water resources at regional scale, intervening in the planning and protection of the agricultural sector is essential. Evapotranspiration obviously plays a major role in water resource management: in this context, potential and actual evapotranspiration (ET0 and ETc, respectively) can be used for the analysis of water requirements in agriculture.

The use of remote sensing and global data can be a method for analyzing these processes (Farbo et al., 2024; DePetris et al., 2024), taking advantage of the availability of such information (Farbo et al., 2022a, 2022b). The Moderate Resolution Imaging Spectroradiometer (MODIS) by NASA is an instrument supporting two satellites (Terra and Aqua) that plays a key role in the analysis of global dynamics related to the planet. The use of these data provides a useful tool for better understanding the processes involved in crop water requirements and water resource management (Orusa et al. 2023; Orusa and Mondino 2019). The global availability of this data is a great advantage in terms of applicability and replicability (Viani et al., 2023). Such information may contribute globally to the analysis and evaluation of the impacts of climate change. Analyzing these with the mentioned available resources means effective action in the effort to mitigate the impacts of climate change, not only in the agricultural sector.

Despite all the advantages of the use of MODIS for evapotranspiration analysis, one of the product's limits is

* Corresponding author

related to the geometric resolution of evapotranspiration estimates. This represents a potential problem at the local assessment level, potentially leading to significant errors compared to ground- based data observations. Other instruments, such as meteorological stations, provide ground-based evapotranspiration assessments, which are useful for different agricultural crop management.

Interpreting and analyzing the consistency between locally and remotely available data provides the tools for mitigation of water losses and optimisation of farm management in the context of crop treatments.

Considering the availability of local information from the meteorological service, the aim of this work is to analyze the consistency using both temporal and spatial approaches between MOD16A2 Potential Evapotranspiration and the 8-days cumulated one derived from meteorological stations in the Piedmont region (NW Italy) during 2022

2. MATERIALS AND METHODS

2.1 Study area

The research was carried out in the Piemonte Region, located in Northwestern Italy. This region is extensively farmed and features various crop types (Ghilardi et al., 2023; 2022), making the agricultural sector a vital component of its economy. The Piemonte Region features a network of meteorological stations distributed across its entire territory, provided by the Rete Agrometeorologica Piemonte (RAM) service. In alignment with the study's objectives, meteorological stations situated in flat, agricultural areas were selectively chosen from the available options (as depicted in Figure 1). As a result, the study area (AOI) was delimited to cover solely the geographical region corresponding to these 135 selected meteorological stations.

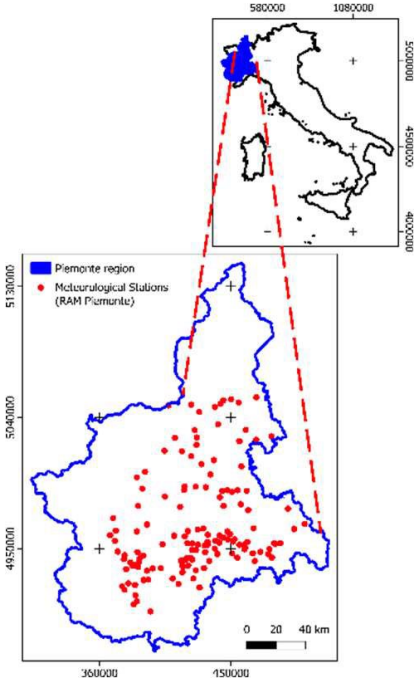

Figure 1. Spatial distribution of meteorological stations in the Piemonte region.

2.2 Available data

Ground data were obtained from the 135 RAM meteorological station, covering the period from 1st January 2022 to 30th September 2022. Daily ET0 values were calculated using the Penman-Monteith equation.
Within MODIS mission, the MOD16A2 product provides two main types of data: Potential Evapotranspiration (PET) and Actual Evapotranspiration (ET). This study focuses exclusively on Potential Evapotranspiration. MOD16A2 products are characterized by 8-day temporal resolution and 500 m of spatial resolution, making it a useful tool for supporting regional decisions.
Google Earth Engine platform was used to retrieve the 8-day time series (TS) for the reference period (1st January - 30th September). To ensure that only representative data were used, observations without clouds were specifically selected. PET TS were extracted using the 135 RAM meteorological stations location so that PET and ET0 TS are spatially consistent.
Since the PET and ET0 time series have different observation intervals (8-days and daily, respectively), the ET0 TS were accumulated every 8 days in order to facilitate the comparison with PET

2.3 Space-domain analysis

Evapotranspiration processes are subject to the influence of various factors, the impacts of which can change based on topographical variables (Famiglietti and Wood, 1995). To evaluate the consistency of PET measurements throughout the entire region, a linear model was employed. This model enabled a comparative analysis of the ET0 and PET metrics, which are represented as follows (eq. 1):

$$PET_i = \alpha \cdot ET0_i + \beta \quad (1)$$

where PET_i and $ET0_i$ respectively represent the MODIS data and all weather station observations in the study area on a specific date. This relationship was observed and maintained over time, providing a dynamic understanding of how PET varies with ET0 across different spatial points and throughout different periods within the year.

Given the well-established understanding that spatial patterns can vary over time (Bosch and Hewlett, 1982), R^2, the Mean Error (ME) and the Mean Absolute Error (MAE) were computed and analyzed throughout the entire year according to eq. 2 and 3. This analysis provided insights into the temporal evolution of the spatial relationship between PET and ET0, contributing to a better understanding of this dynamic process.

$$ME = \frac{1}{n}\sum_{i-1}^{n}(ETO_i - PET_i) \quad (2)$$

$$MAE = \frac{1}{n}\sum_{i-1}^{n}|ETO_i - PET_i| \quad (3)$$

2.4 Time-domain analysis

Prior research has identified variations in MODIS evapotranspiration products, with potential overestimations or underestimations of ground reference data observed depending on the specific study area (Mu et al., 2007). To examine whether any discernible patterns exist in potential

biases within the AOI, temporal analyses were conducted. The objective of these analyses was to determine if the PET TS exhibited comparable trends in comparison to the ground reference ET0 for each meteorological station within the AOI.

The assessment of bias and trends utilized linear models, which were represented as (eq. 4):

$$PET_i = \alpha \cdot ET0_i + \beta \qquad (4)$$

where PET_i and $ET0_i$ represented the TS pair corresponding to the i-th meteorological station. The model parameters α and β provided a means to quantify the slope and offset, allowing for the identification of biases between PET and ET0.

Similarly to section 2.3, MAE and R^2 were assessed for each meteorological station.

2.5 Modis Calibration

Biases identified in section 2.4 underscore the presence of spatial misalignment between PET and ET0, thereby indicating that the MODIS product may not be entirely reliable for water resource management. To rectify this issue, the PET data require calibration based on the ground reference data.

In pursuit of this calibration, a reverse model, relying on equation 2, was employed. In this model, $ET0_i$ served as the dependent variable, aiming to derive the necessary model parameters for calibrating PET_i observations, as expressed in equation 5:

$$\widehat{PET_l} = \alpha \cdot PET_i + \beta \qquad (5)$$

Where $\widehat{PET_l}$ represents the calibrated PET_i observations.

Subsequently, the calibrated data were employed instead of the uncalibrated data for the space-domain analysis (section 2.3). The resulting R^2 and MAE metrics were then compared to those obtained from the uncalibrated MODIS data.

3. RESULTS

3.1 Space-domain analysis

Spatial analyses were conducted for the 33 available dates. The evolution of R^2 is depicted in Figure 2, while Figure 3 presents the changes in ME and MAE over the specified period of interest.

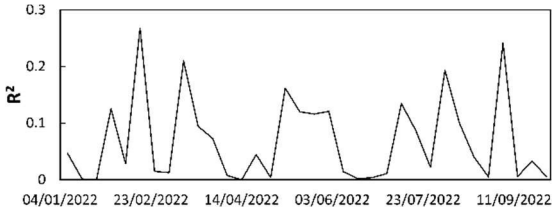

Figure 2. Evolution of R^2 derived from eq. 1 over the period of interest.

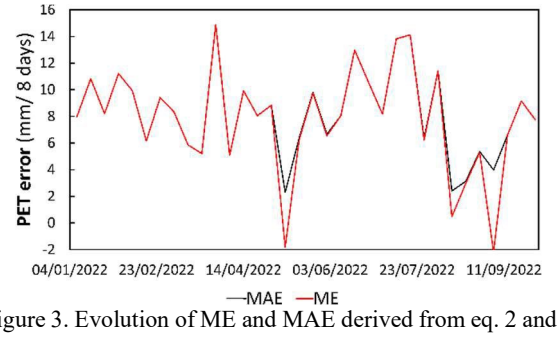

Figure 3. Evolution of ME and MAE derived from eq. 2 and 3 over the period of interest.

Figure 2 shows that PET and ET0 are poorly related over the entire period of interest, meaning that the MODIS data cannot be directly used to estimate ET0 over AOI.
Interestingly, Figure 3 indicates that ME and MAE are almost always aligned, highlighting an average MODIS underestimate equal to 8 mm in 8 days compared to reference data throughout the reference period. Possibly, the PET measurements are affected by the low spatial resolution of the MODIS sensor (500 m) (Sharma et al., 2016).

3.2 Time-domain analysis

Time-domain analyses were conducted across the 135 meteorological stations, and the findings indicate that PET and ET0 exhibit similar temporal trends (Figure 4).

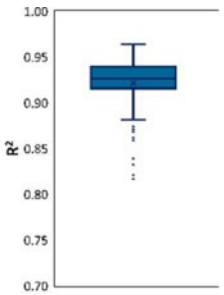

Figure 4. Boxplot representing the models' R^2 statistical distribution derived from equation 4

In particular, the model parameters α and β show a close alignment between the two measurements (with α approximately equal to 1). However, a noteworthy bias is evident, reaffirming the observation made in section 3.1, namely, that MODIS PET consistently underestimates ET0 by an average of 7-8 mm every 8 days (Figure 5).

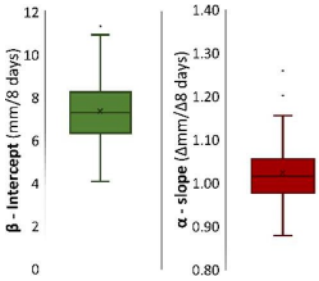

Figure 5. Boxplot representing the models' β (intercepts, in green) and α (slopes, in red) statistical distribution derived from eq. 4

3.3 Modis Calibration

Sections 3.1 and 3.2 have confirmed the presence of notable biases between PET and ET0 data, casting doubt on the reliability of the MOD16A2 PET product for regional water resource management.

To address these issues, temporally calibrated $\widehat{PET}$ measurements were then compared to ground data following a similar approach as in section 3.1.

The newly obtained R^2 were then compared with the R^2 values derived using native values and these comparisons are presented in Figure 6.

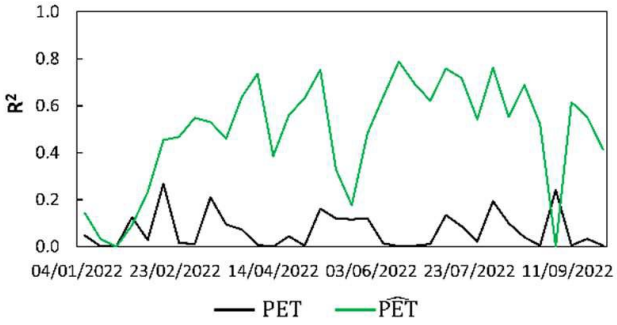

Figure 6. Evolution of R^2 from PET (black line) and $\widehat{PET}$ (green line) over the period of interest.

Notably, the introduction of temporally calibrated $\widehat{PET}$ data led to a significant increase in R^2 values during a substantial portion of the crop phenological season.

Similarly, the MAE associated with $\widehat{PET}$ data showed a noteworthy decrease, resulting in an average value of approximately 3 mm over an 8-day period across the entire reference period. This indicates a reduction in the daily error to 0.4 mm on average (Figure 7).

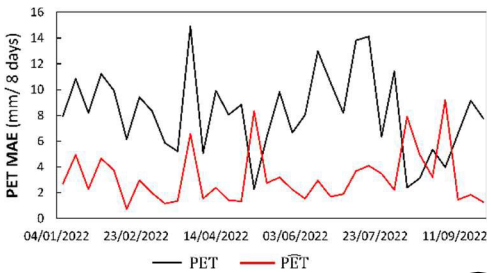

Figure 7. Evolution of PET (black line) and $\widehat{PET}$ (green line) MAE over the period of interest.

4. CONCLUSIONS

Remote sensing data, with specific reference to MODIS mission, allow to globally analyse the potential evapotranspiration. However, several previous studies highlighted the misalignment between MOD16A2 data to ground reference from meteorological stations. This work analysed both spatially and temporally. Spatial based analyses found poor relations between MODIS and meteorological stations, showing that raw MOD16A2 data have to be used with caution. Temporal based analyses, conversely, highlighted the capability of MOD16A2 to catch the same temporal trend of reference meteorological stations. However, some biases have been found, specifically MOD16A2 product consistently underestimate the daily potential evapotranspiration by 1 mm. Once MOD16A2 product has been calibrated, the spatial analyses have been performed once again and this time the results showed a consistent relationship with ground data and a daily potential evapotranspiration error lower than 0.4 mm. Thus, it is possible to conclude that raw MOD16A2 data should be previously ground calibrated in order to be fully employed at regional scale for water resources management.

5. REFERENCES

Baer, H.A.; Singer, M. The Anthropology of Climate Change: An Integrated Critical Perspective; Routledge, 2018; 5. Elshkaki, A. The Implications of Material and EnergyEfficiencies for the Climate Change Mitigation Potential of Global Energy Transition Scenarios. Energy 2023, 267, 126596.

Borgogno-Mondino, E.; Farbo, A.; Novello, V.; Palma, L. de A Fast Regression-Based Approach to Map Water Status of Pomegranate Orchards with Sentinel 2 Data. Horticulturae 2022, 8, 759.

Bosch, J.M.; Hewlett, J.D. A Review of Catchment Experiments to Determine the Effect of Vegetation Changes on Water Yield and Evapotranspiration. J. Hydrol. 1982, 55, 3–23, doi:10.1016/0022-1694(82)90117-2.

De Petris, S.; Sarvia, F.; Parizia, F.; Ghilardi, F.; Farbo, A.; Borgogno-Mondino, E. Assessing Mixed-Pixels Effects in Vineyard Mapping from Satellite: A Proposal for an Operational Solution. Comput. Electron. Agric. 2024, 222, 109092, doi:10.1016/j.compag.2024.109092.

Ellwanger, J.H.; Kulmann-Leal, B.; Kaminski, V.L.; Valverde-Villegas, J.; VEIGA, A.B.G.; Spilki, F.R.; Fearnside, P.M.; Caesar, L.; Giatti, L.L.; Wallau, G.L. Beyond Diversity Loss and Climate Change: Impacts of Amazon Deforestation on Infectious Diseases and Public Health. An. Acad. Bras. Ciênc. 2020, 92.

Famiglietti, J.S.; Wood, E.F. Effects of Spatial Variability and Scale on Areally Averaged Evapotranspiration. Water Resour. Res. 1995, 31, 699–712, doi:10.1029/94WR02820.

Farbo, A.; Meloni, R.; Blandino, M.; Sarvia, F.; Reyneri, A.; Borgogno-Mondino, E. Spectral Measures from Sentinel-2 Imagery vs Ground-Based Data from Rapidscan© Sensor: Performances on Winter Wheat. In Geomatics for Green and Digital Transition; Borgogno-Mondino, E., Zamperlin, P., Eds.; Communications in Computer and Information Science; Springer International Publishing: Cham, 2022; Vol. 1651, pp. 211–221 ISBN 978-3-031-17438-4.

Farbo, A.; Sarvia, F.; De Petris, S.; Basile, V.; Borgogno-Mondino, E. Forecasting Corn NDVI through AI-Based Approaches Using Sentinel 2 Image Time Series. ISPRS J. Photogramm. Remote Sens. 2024, 211, 244–261, doi:10.1016/j.isprsjprs.2024.04.011.

Farbo, A.; Sarvia, F.; De Petris, S.; Borgogno-Mondino, E. Preliminary Concerns about Agronomic Interpretation of NDVI Time Series From Sentinel-2 Data: Phenology and Thermal Efficiency of Winter Wheat in Piemonte (NW Italy). Int. Arch. Photogramm. Remote Sens. Spat. Inf. Sci. 2022, 43, 863–870.

Farbo, A.; Trombetta, N.G.; de Palma, L.; Borgogno-Mondino, E. Estimation of Intercepted Solar Radiation and Stem Water Potential in a Table Grape Vineyard Covered by Plastic Film

Using Sentinel-2 Data: A Comparison of OLS-, MLR-, and ML-Based Methods. Plants 2024, 13, 1203, doi:10.3390/plants13091203.

Fiske, S.J.; Crate, S.A.; Crumley, C.L.; Galvin, K.; Lazrus,

Ghilardi, F.; Petris, S.D.; Farbo, A.; Sarvia, F.; Borgogno-Mondino, E. Exploring Stability of Crops in Agricultural Landscape Through GIS Tools and Open Data. In Proceedings of the International Conference on Computational Science and Its Applications; Springer, 2022; pp. 327–339.

Ghilardi, F.; Virano, A.; Prandi, M.; Borgogno-Mondino, E. Zonation of a Viticultural Territorial Context in Piemonte (NW Italy) to Support Terroir Identification: The Role of Pedological, Topographical and Climatic Factors. Land 2023, 12, 647.

H.; Lucero, L.; Oliver-Smith, A.; Orlove, B.; Strauss, S.; Wilk, R. Changing the Atmosphere: Anthropology and Climate Change. Final Rep. AAA Glob. Clim. Change Task Force 2014, 137.

Jacob, D.J.; Winner, D.A. Effect of Climate Change on Air Quality. Atmos. Environ. 2009, 43, 51–63.

Mirón, I.J.; Linares, C.; Díaz, J. The Influence of Climate Change on Food Production and Food Safety. Environ. Res. 2023, 216, 114674.

Mu, Q.; Heinsch, F.A.; Zhao, M.; Running, S.W. Development of a Global Evapotranspiration Algorithm Based on MODIS and Global Meteorology Data. Remote Sens. Environ. 2007, 111, 519–536, doi:10.1016/j.rse.2007.04.015.

Orusa, T.; Mondino, E.B. Landsat 8 Thermal Data to Support Urban Management and Planning in the Climate Change Era: A Case Study in Torino Area, NW Italy. In Proceedings of the Remote Sensing Technologies and Applications in Urban Environments IV; International Society for Optics and Photonics, 2019; Vol. 11157, p. 111570O.

Orusa, T.; Viani, A.; Cammareri, D.; Borgogno Mondino, E. A Google Earth Engine Algorithm to Map Phenological Metrics in Mountain Areas Worldwide with Landsat Collection and Sentinel-2. Geomatics 2023, 3, 221–238, doi:10.3390/geomatics3010012.

Orusa, T.; Viani, A.; Moyo, B.; Cammareri, D.; Borgogno-Mondino, E. Risk Assessment of Rising Temperatures Using Landsat 4–9 LST Time Series and Meta® Population Dataset: An Application in Aosta Valley, NW Italy. Remote Sens. 2023, 15, 2348, doi:10.3390/rs15092348.

Samuele, D.P.; Federica, G.; Filippo, S.; Enrico, B.-M. A Simplified Method for Water Depth Mapping over Crops during Flood Based on Copernicus and DTM Open Data. Agric. Water Manag. 2022, 269, 107642, doi:10.1016/j.agwat.2022.107642.

Sarvia, F.; De Petris, S.; Ghilardi, F.; Xausa, E.; Cantamessa, G.; Borgogno-Mondino, E. The Importance of Agronomic Knowledge for Crop Detection by Sentinel-2 in the CAP Controls Framework: A Possible Rule-Based Classification Approach. Agronomy 2022, 12, 1228, doi:10.3390/agronomy12051228.

Sharma, V.; Kilic, A.; Irmak, S. Impact of Scale/Resolution on Evapotranspiration from Landsat and MODIS Images. Water Resour. Res. 2016, 52, 1800–1819, doi:10.1002/2015WR017772.

Ukhurebor, K.E.; Aigbe, U.O.; Olayinka, A.S.; Nwankwo, W.; Emegha, J.O. Climatic Change and Pesticides Usage: A Brief Review of Their Implicative Relationship. AU EJournal Interdiscip. Res. ISSN 2408-1906 2020, 5.

Viani, A.; Orusa, T.; Borgogno-Mondino, E.; Orusa, R. Snow Metrics as Proxy to Assess Sarcoptic Mange in Wild Boar: Preliminary Results in Aosta Valley (Italy). Life 2023, 13, 987, doi:10.3390/life13040987.

Viani, A.; Orusa, T.; Mandola, M.L.; Robetto, S.; Belvedere, M.; Renna, G.; Scala, S.; Borgogno-Mondino, E.; Orusa, R. R07.1 Tick's Suitability Habitat Maps and Tick-Host Relationships in Wildlife. A One Health Approach Based on Multitemporal Remote Sensed Data, Entropy and Meta® Population Dataset in Aosta Valley, NW Italy. GeoVet 2023 Int. Conf. 2023.

Algorithm & sensors

DEVELOPMENT OF A PHOTOVOLTAIC SYSTEM EXTRACTION INDEX FOR THE DETECTION OF LARGE PV PLANTS USING SENTINEL-2 IMAGES

C. Ladisa [1]*, M.A. Aguilar [2], A. Capolupo [1], Eufemia Tarantino[1], F.J. Aguilar[2]

[1] Department of Civil, Environmental, Land, Construction and Chemistry (DICATECh), Politecnico di Bari, via Orabona n.4, I- 70125 Bari, Italy (claudio.ladisa, alessandra.capolupo, eufemia.tarantino)@poliba.it

[2] Department of Engineering and Research Centre CIAIMBITAL, University of Almería, Almería, Spain (maguilar, faguilar)@ual.es

KEY WORDS: Object-Based Image Analysis, Sentinel 2, medium-resolution satellite images, photovoltaic panels

ABSTRACT:

The importance of solar power, known for its wide availability and low emissions, is underscored by the growing adoption of renewable energy, driven by environmental concerns and technological progress. Large photovoltaic (PV) plants require constant monitoring for efficiency and reliability. Remote sensing offers a cost-effective solution for accurately capturing plant size, shape, and location data. Satellite imagery, especially from open-source satellites such as Sentinel-2 (S2) and Landsat 9, has revolutionized remote sensing, enabling the development of machine-learning algorithms for PV system classification. While various spectral indices, such as the Normalized Difference Water Index (NDWI) and the Normalized Difference Vegetation Index (NDVI), enhance accuracy in water and vegetation areas, no specific index exclusively designed for PV extraction exists because of the diverse deployment settings of PV arrays. This study introduces a tailored Photovoltaic system extraction index (PVSEI) for S2 images in two regions known for large PV installations: Viterbo (Italy) and Seville (Spain). PVSEI combines different spectral bands to maximize the contrast between the solar panels and the surroundings. Employing Object-Based Image Analysis (OBIA) for accurate identification, multiresolution segmentation was used to create segments based on scale, shape, and compactness. The Decision Tree (DT) classifier consistently ranked PVSEI as the most effective. Accuracy assessment using the Overall Accuracy (OA), Kappa Index of Agreement (KIA), Producer Accuracy (PA), User Accuracy (UA), and F1 consistently yielded excellent results, with an OA exceeding 98%. KIA ranged from 0.74 to 0.82 for segmentated objects. Overall, PVSEI excelled in both study areas, with occasional challenges in distinguishing bare soil objects resembling PV systems.

1. INTRODUCTION

The global population surge and increased productivity driven by the Industrial Revolution have led to a higher demand for energy, predominantly met by fossil fuels, resulting in harmful greenhouse gas emissions (Asif and Muneer, 2007). This has adverse effects on both the environment and human well-being. In contrast, solar energy emerges as a promising, abundant, and cost-effective renewable option capable of meeting global energy needs (Trappey et al., 2016). Its consistently superior production efficiency positions it as a leading contender for a worldwide energy solution (Panwar et al., 2011). The adoption of solar PV systems has seen a substantial rise, driven by falling costs and robust policy support in regions like Europe, the United States, Japan, China, and India (Haegel et al., 2017). However, implementing PV panels on a large scale may require a significant portion of Earth's surface (Tsoutsos et al., 2005). While solar parks offer the advantage of generating renewable energy, they also pose disadvantages, including land degradation due to substantial landscape alterations, potential loss of biodiversity and habitat disruption, and landscape fragmentation (Hernandez et al., 2014). As the PV power production industry continues to rapidly grow, there is an urgent need for detailed monitoring and mapping of large solar parks (Yang and Xia, 2022). Traditional on-site surveys are time-consuming and can become outdated and less accurate over time. Therefore, there is a critical need for a straightforward, dependable, and non-intrusive data-gathering method (Jiang et al., 2021). Leveraging medium- and high-resolution satellite imagery can greatly benefit the detection and study of PV (Zhang et al., 2023). Over the past decade, satellite data properties have significantly improved, enabling remote sensing applications in various sectors, including land-use surveys, and urban and rural planning (Tarantino and Figorito, 2012). Additionally, the availability of open-source data from satellites like S2 and Landsat 9 has made widespread use of remote earth observations feasible, eliminating the need for expensive resources and restrictions on large-area applications. Many studies have successfully detected PV solar farms by combining remote sensing methods with machine learning classification algorithms, such as Random Forest (RF), even with moderate-quality imagery (Plakman et al., 2022; Ladisa et al., 2022a; Zhang et al., 2023). Spectral data from individual bands or spectral indices derived from band combinations, such as NDVI and NDWI, have served as primary training data for the RF models used in the literature (Plakman et al., 2022). The novelty of this study was the development of a new index specific to the extraction of PV panels since it has never been studied thoroughly due to the different specific layouts of PV panels and the different types of soil under the panels. The primary objective of this research is to assess the performance of a spectral index using an OBIA approach in Viterbo, Italy, and Seville, Spain, both known for their significant PV installations, at two different seasons (February and August) specifically designed for S2 satellite data.

2. STUDY AREA

The study focuses on two distinct areas: the southern region of Sevilla, spanning Dos Hermanas, Utrera, and Los Palacios y Villafranca municipalities; and the province of Viterbo, specifically Montalto di Castro in western Lazio. These locations stand out due to the presence of significant PV solar parks, including the renowned "Don Rodrigo" in Seville and "Montalto di Castro Photovoltaic Plant" in Viterbo. Notably, both are among the largest solar farms in Europe. The cropped area of the Seville study site, centered at 37.2118° N and 5.8580° W

* Corresponding author

(WGS84), covers 241771.23 km^2, whereas the cropped area of the Viterbo study site, located at 42.42714° N and 11.63392° E (WGS84), covers 25554.39 km^2.

3. DATASETS AND PRE-PROCESSING

Four cloud-free S2 images from 2022 were selected from the ESA Copernicus Scientific Data Hub (https://scihub.copernicus.eu). Two images were chosen for each study area, one in February and another one in August, to assess seasonal variations in PV panel spectral characteristics. The Sevilla area images used WGS84 datum with UTM 30N zone projection, while the Viterbo area images used WGS84 datum with UTM 32N zone projection. Due to low reflectance in the visible and infrared range of solar panels (Czirjak, 2017), 10 m and 20 m resolution bands were employed. At 10 m resolution, bands included Blue (458-523 nm), Green (543-578 nm), Red (650-680 nm), and Near Infrared (NIR8: 785-900 nm). At 20 m resolution, bands covered Red Edge 1 (694-713 nm), Red Edge 2 (731-749 nm), Red Edge 3 (769-797 nm), Narrow Near InfraRed (NIR8a: 848-881 nm), Shortwave Infrared-1 (SWIR1: 1565-1655 nm), and Shortwave Infrared-2 (SWIR2: 100-2280 nm). Bands with resolution over 10m were resampled to 10m using ESA's SNAP (Sentinel Application Platform) software. After resampling, images were cropped, and defective pixels were masked within the Quantum GIS (QGIS) environment (version 3.22).

4. METHODOLOGY

Figure 1 illustrates the workflow of this study.

4.1 Multi-Resolution Segmentation

Following previous research recommendations, we employed the multi-resolution segmentation (MRS) algorithm in the eCognition environment (Trimble, Sunnyvale, California, USA) for image segmentation (Ladisa et al., 2022b). This approach involves a hierarchical merging of regions. Its effectiveness hinges on three key factors: (a) the scale parameter, governing the level of permissible heterogeneity in resultant segments; (b) the Shape parameter, which assigns importance to both the shape and spectral color of objects; and (c) compactness and criterion smoothness weight (compactness), crucial for maximizing overall coherence (Czirjak, 2017). To ascertain the optimal segmentation parameters for processing S2 images, we utilized the command line software AssesSeg (Novelli et al., 2017), which identifies the most suitable parameter combination based on the modification Euclidean Supervised Distance (ED2The scale, shape, and compactness parameters used in both study areas are in Figure 1

4.2 Manual pre-classification and spectral signature analysis

Objects exhibiting the highest pixel density of PV panels were designated as "PV," while all other objects received the label "NO_PV". A subset of these objects, consisting of forty PV and forty NO_PV objects, was chosen from each image for spectral signature analysis. The NO_PV objects were further categorized into four classes, each comprising ten objects: Vegetation (VEG), agricultural land (AGRO), bare soil (BARE), and urbanized (URBAN). This methodology facilitated a comparative examination of spectral characteristics between PV panels and different land use categories (Ladisa et al., 2022a).

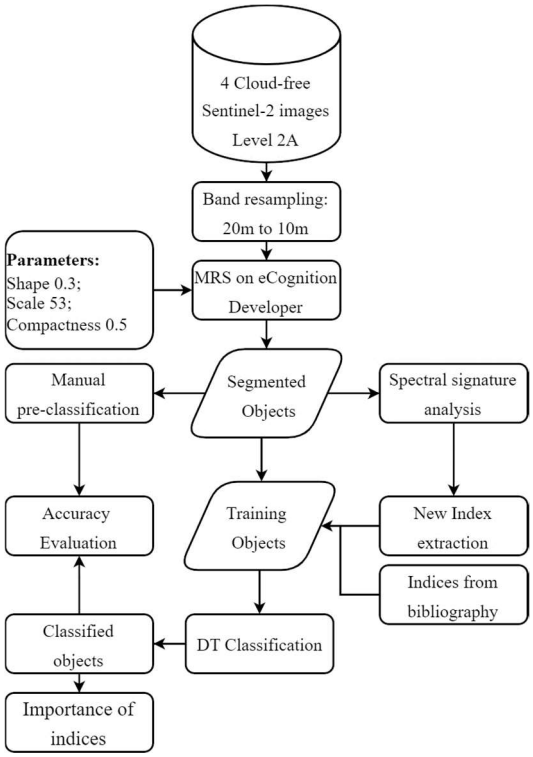

Figure 1. The operational pipeline of the utilized approach

As depicted in Figure 2, an example of the spectral signature obtained from the average values of the objects within the mentioned classes is provided for the Seville study area in February.

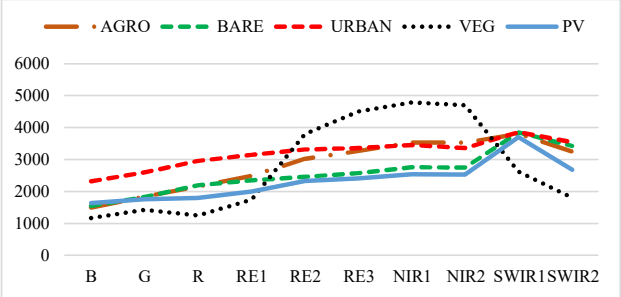

Figure 2. Spectral signature area of Sevilla in February

The classification of land use classes was conducted via a manual assessment of both S2 and Google Earth Professional images.

4.3 Photovoltaic Solar Extraction Index

A new spectral index was created because of the study of spectral signatures. It was intended to capture the distinctive trend of the spectral signature of PV objects. Except for a peak in the SWIR1 band, the spectral signature of PV panels was characterized by noticeably low values in both the visible and infrared regions, as shown in Figure 2. Consequently, the ratios between SWIR1 and SWIR2, as well as between SWIR1 and NIR1, were added to create the Photovoltaic Solar Extraction Index (PVSEI), which is represented in Equation 1.

$$PVSEI = \frac{SWIR1^{\,2}}{SWIR2 * NIR2} \quad (1)$$

Therefore, the sum of the two ratios will be larger when the peak is accented, and as a result, the value of the index will be higher.

4.4 Features extraction

In this study, in addition to PVSEI, various other indices used in previous research on solar farm mapping were tested. Among these, NDVI and NDWI were used (Zhang et al., 2023; Plakman et al., 2022), along with other indices such as the Normalized Difference Build-up Index (NDBI), Normalized Difference Soil Index (NDSI), and Modified Bare Soil Index (MBI), to assess the presence of uncovered soil (Chen et al., 2022). Indices related to plastic covers, such as the Plastic Greenhouse Index (PGHI), and metal covers, such as the color steel building index (CSBI), were also explored for the first time in this context (Aguilar et al., 2022). All these indices were derived from each S2 image and object obtained in the segmentation process described above. This approach was applied to each study site using the eCognition v. 9.5.

4.5 Decision tree modeling

To assess the efficacy of the newly derived index in pinpointing solar parks within the S2 imagery, a straightforward classifier was employed: decision tree (DT) (Breiman et al., 1984). This classifier, characterized by minimal subdivisions and singular threshold values, proved to be optimal for benchmarking the new index against existing literature (Aguilar et al., 2022). It has previously demonstrated utility in diverse applications, including delineating plastic coverings and mapping open-air crops (Peña-Barragán et al., 2011). For the generation of DT models, each image in the study utilized objects categorized as PV and those labeled as NO_PV, which served as training sets for the DT. Specifically, STATISTICA v. 10 (StatSoft Inc., Tulsa, OK, USA) was used both to calculate the DT models via a 10-fold stratified cross-validation procedure, with PV or NO_PV classes as the dependent variable and to evaluate the importance of each index for classification purposes.

4.6 Accuracy analysis

For each image, an estimated confusion matrix was created. As a result, Overall Accuracy (OA), Kappa Index of Agreement (KIA), Producer Accuracy (PA), User Accuracy (UA), and F1 were calculated.

5. RESULTS

5.1 Segmentation

Table 1 presents the outcomes of the MRS process. Alongside the total count of segmented objects per image, it also shows the number of objects manually labeled for subsequent DT training.

Study Area	Month	N° of segmented objects	Objects labeled as PV	Objects labeled as NO_PV
Sevilla	February	27226	662	26564
	August	25132	632	24500
Viterbo	February	20619	367	20252
	August	21217	373	20844

Table 1. Segmentation results

5.2 DT Results

Figure 3 shows the outcomes of the DT model in the four case studies. The PVSEI index, developed in this work, appears explicitly in the first subdivisions of the DT models in three out of four cases.

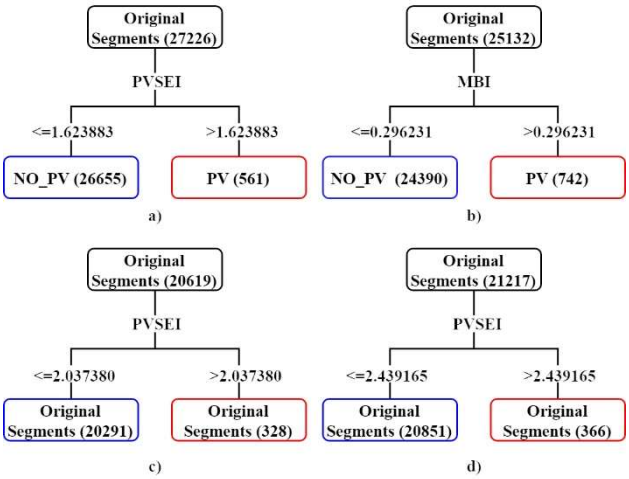

Figure 3. DT results: a) Sevilla February; b) Sevilla August; c) Viterbo February; d) Viterbo August

5.3 Importance ranking

Figure 4 vividly illustrates the performance of the PVSEI in comparison to other indices. Even in the case of Sevilla in August, where it doesn't claim the top position in the importance ranking, it still attains an importance value surpassing 90%.

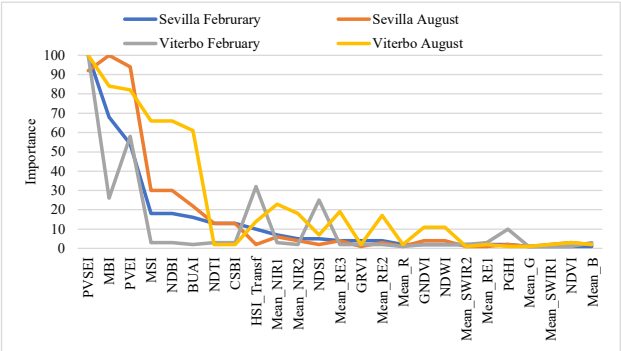

Figure 4. Importance

5.4 Accuracy

Table 2 shows the accuracy assessment results. Remarkably, both OA and KIA values demonstrate consistently high performance across all four images. However, it is important to note that PA, UA, and F1 scores reveal a notable presence of false positives. This can be attributed, at least in part, to the imbalanced distribution of the dataset between PV and non-PV objects.

Study Area	Month	OA	KIA	PA (PV/NO_PV)	UA (PV/NO_PV)	F1 (PV/NO_PV)
Sevilla	February	98.1	0.73	67.98/99.58	80.21/99.2	73.59/99.39
	August	98.61	0.738	81.01/99.06	69/99.51	74.53/99.28
Viterbo	February	99.13	0.738	70.3/99.06	78.66/99.46	74.24/99.56
	August	99.08	0.731	73.61/99.55	74.32/99.52	73.61/99.53

Table 2. Accuracy results

6. DISCUSSION AND CONCLUSION

The demand for efficient large-scale PV systems requires continuous monitoring, a task addressed by remote sensing technologies. Previous studies have made significant progress in this area, even with open-source data like S2 (Plakman et al.,

2022). However, a tailored spectral index for identifying PV solar parks was lacking. Using OBIA allowed for precise spectral analysis. PVSEI was formulated, capturing the distinct trend of the PV class compared to others. The DT model played a crucial role in benchmarking PVSEI against other indices and in image classification. DT analysis showed PVSEI leading in three out of four cases, highlighting its importance. Although MBI surpassed PVSEI in August Seville, PVSEI remained highly significant. Notably, in August Seville, the bare soil spectral signature closely resembled that of PV areas due to similar traits. However, the findings of the error matrix (Table 2) validate the robust accuracy of PVSEI classification, underscoring the novelty of this research in creating a pertinent index for mapping PV installations from S2 imagery. This index holds potential as a foundational element for upcoming machine learning or deep learning algorithms. The study lays a solid groundwork for the practical integration of PVSEI into satellite image classification, offering implications for the monitoring and management of PV solar parks.

REFERENCES

Aguilar, M. A., Jiménez-Lao, R., Ladisa, C., Aguilar, F. J., & Tarantino, E., 2022. Comparison of spectral indices extracted from Sentinel-2 images to map plastic-covered greenhouses through an object-based approach. *GIScience & Remote Sensing*, https://doi.org/10.1080/15481603.2022.2071057.

Asif, M., and T. Muneer. 2007.Energy supply, its demand, and security issues for developed and emerging economies. *Renew. Sustain*., https://doi.org/10.1016/j.rser.2005.12.004.

Breiman, L., J. H. Friedman, R. A. Olshen, and C. I. Stone., 1984. Classification and Regression Trees. *Boca Raton FL: Chapman & Hall/CRC Press*, https://doi.org/10.1201/9781315139470.

Chen, Z., Kang, Y., Sun, Z., Wu, F., & Zhang, Q., 2022. Extraction of Photovoltaic Plants Using Machine Learning Methods: A Case Study of the Pilot Energy City of Golmud, China. *Remote Sensing* https://doi.org/10.3390/rs14112697.

Czirjak, D., 2017. Detecting photovoltaic solar panels using hyperspectral imagery and estimating solar power production. *Journal of Applied Remote Sensing. Journal of Applied Remote Sensing*, https://doi.org/10.1117/1.JRS.11.026007.

Haegel, N., T. Buonassisi, F. Armin, R. Garabedian, M. Green, S. Glunz, D. Feldman., 2017. Terawatt-Scale Photovoltaics: Trajectories and Challenges. *Science*, https://doi.org/10.1126/science.aal1288.

Hernandez, R. R., S. B. Easter, M. L. Murphy-Mariscal, F. T. Maestre, M. Tavassoli, E. B. Allen, C. W. Barrows., 2014. Environmental Impacts of Utility-Scale Solar Energy. *Renewable and Sustainable Energy Reviews*, https://doi.org/10.1016/j.rser.2013.08.041.

Jiang H., Yao, L., Lu, N., Qin, J., Liu, T., Liu, Y. and Zhou, C., 2021. Multi-resolution dataset for photovoltaic panel. *Earth System Science Data*, https://doi.org/10.5281/zenodo.5171712.

Ladisa, C., Capolupo, A., Ripa, M. N. and Tarantino, E., 2022b. Evaluation of eCognition Developer and Orfeo ToolBox Performances for Segmenting Agrophotovoltaic Systems from Sentinel-2 Images. In International Conference on Computational Science and Its Applications, Springer. https://doi.org/10.1007/978-3-031-10545-6_32.

Ladisa, C., Capolupo, A., Ripa, M. N., & Tarantino, E., 2022a. Combining OBIA approach and machine learning algorithm to extract photovoltaic panels from Sentinel-2 images automatically. *Remote Sensing for Agriculture, Ecosystems, and Hydrology*, SPIE. https://doi.org/10.1117/12.2636451.

Panwar, N., S. Kaushik, S. Kothari. Role of renewable energy sources in environmental protection: a review. *Renew Sustain Energy Rev*, 2011: 1513-1524.

Novelli, A., Aguilar, M. A., Aguilar, F. J., Nemmaoui, A. and Tarantino, E., 2017 AssesSeg-A command line tool to quantify image segmentation quality: A test carried out in southern Spain from satellite imagery. *Remote Sensing*, MDPI AG, https://doi.org/10.3390/rs9010040.

Peña-Barragán, J. M., M. K. Ngugi, R. E. Plant, and J. Six., 2011 Object-based Crop Identification Using Multiple Vegetation Indices, Textural Features, and Crop Phenology. *Remote Sensing of Environment*, https://doi.org/10.1016/j.rse.2011.01.009.

Plakman, V., Rosier, J., & van Vliet, J., 2022 Solar park detection from publicly available satellite imagery. *GIScience & Remote Sensing*, https://doi.org/10.1080/15481603.2022.2036056.

Tarantino, E. and Figorito, B., 2012 Mapping Rural Areas with Widespread Plastic Covered Vineyards Using True. *Remote Sensing*, https://doi.org/10.3390/rs4071913.

Trappey, A. J. C., C. V. Trappey, H. Tan, P. H. Y. Liu, S. Je Li, and L. Cheng Lin., 2016 The Determinants of Photovoltaic System Costs: An Evaluation Using a Hierarchical Learning Curve Model. *Journal of Cleaner Production*, https://doi.org/10.1016/j.jclepro.2015.08.095.

Tsoutsos, T., N. Frantzeskaki, and V. Gekas., 2005 Environmental Impacts from the Solar Energy Technologies. *Energy Policy*, https://doi.org/10.1016/S0301-4215(03)00241-6.

Yang, Y., and S. Xia., 2022 China must balance renewable energy sites. *Science*, https://doi.org/10.1126/science.adf3720.

Zhang, H., Tian, P., Zhong, J., Liu, Y., & Li, J., 2023 Mapping Photovoltaic Panels in Coastal China Using Sentinel-1. *Remote Sensing*, https://doi.org/10.3390/rs15153712.

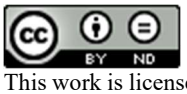

BRIGHT TARGET DETECTION ON SAR RAW DATA BASED ON DEEP CONVOLUTIONAL NEURAL NETWORKS

G. Cascelli [1], C. Guaragnella [2], D. Nitti [1], A. Morea [1], K. Tijani [1], N. Ricciardi [1], R. Nutricato [1]

[1] Geophysical Applications Processing, Bari, Italy

(giorgio.cascelli.ext, alberto.morea, khalid.tijani, nicolo.ricciardi, raffaele.nutricato, davide.nitti)@gap.srl.eu

[2] Department of Electrics and Information Engineering, Politecnico di Bari, Italy - cataldo.guaragnella@poliba.it

KEY WORDS: SAR raw data detection; Deep Convolutional Neural Networks

ABSTRACT:

The use of SAR imagery has been a vital part of several scientific domains, including environmental monitoring, early warning systems, and public safety. Raw data acquired by the radar sensor is typically processed to create a Single Look Complex (SLC) image, which is a high-resolution image of the scene being observed. Processing raw data requires a significant amount of computer power and it is almost never practical to do it on board of a satellite platform. As a direct consequence, the data is transmitted back to the ground segment to be processed. The objective of next-generation studies is to optimize Earth Observation (EO) data processing and image creation in order to deliver EO products to the end user with very low latency using a combination of advancements in the on-board parts of the data chain.

In this scenario, the present work focuses on the detection of high-backscattering objects (bright targets) and proposes to eliminate any pre-processing by training a Deep Convolutional Neural Network (DCNN) to directly perform the detection on raw data. Due to the limited availability of training SAR raw data available in scientific literature regarding the specific topic of high-backscattering objects detection, we propose and investigate a physically and statistically based approach to simulate realistic synthetic training SAR raw datasets that are then used to train and evaluate a state-of-the-art deep neural residual network.

We finally show that the trained DCNN can detect successfully high-backscattering objects on real raw data extracted from ERS imagery archive.

1. INTRODUCTION

Since the deployment of the first satellite equipped with a Synthetic Aperture Radar (SAR) into orbit in 1978 (Evans, 2005), the use of SAR imagery has been a vital part of several scientific domains, including environmental monitoring, early warning systems, and public safety. SAR could be described as "non-literal imaging" since the raw data does not resemble an optical image and is incomprehensible to humans. For this reason, raw data is typically processed to create a Single Look Complex (SLC) image, which is a high-resolution image of the scene being observed (Figure 1). The processing of raw data to create a SLC image is known as focusing step (Cruz, 2022) and involves several steps, including range compression, Doppler centroid estimation and azimuth compression.

Typically, for target detection, a despeckle filtering is also included in this processing stage (Banerjee, 2018). As a result, the processing of raw data requires a significant amount of computer power and is almost never practical to do it on board. As a direct consequence, the data is transmitted back to the ground segment to be processed.

The objective of next-generation studies is to optimize Earth Observation (EO) data processing and image creation in order to deliver EO products to the end user with very low latency using a combination of advancements in the on-board parts of the data chain.

In this work, we focus on the detection of high-backscattering objects (bright targets) and propose to eliminate any pre-processing by training a Deep Convolutional Neural Network (DCNN) to directly perform the detection on raw data.

The rationale for this approach is linked to the consideration that both focusing and despeckling are actually spatial filtering operations (space-variant or space-invariant depending on the chosen algorithm) and therefore can be ultimately described mathematically using the convolution operation. Considering that DCNN is a typical deep-learning model that uses convolution operations and nonlinear mapping to effectively extract target features (Zhang, 2022), there exists a need to further investigate approaches that integrate into a single DCNN algorithm both the pre-processing and the detection stage, therefore working directly on raw data.

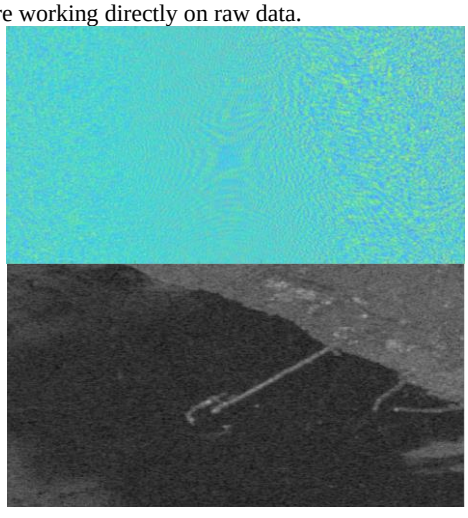

Figure 1. SAR data acquired by ERS-1 ESA mission over the port of Manfredonia (Italy). Top: real part of raw data. Bottom: amplitude of the SLC obtained by focusing the raw data.

More specifically, our study attempts to eliminate any pre-processing by training a DCNN to directly detect point-like

* Corresponding author

strong scatterers on raw data. This indeed might substantially shorten the delivery time thus improving the efficiency of the relevant satellite-based monitoring services.
In this regard, the availability of training data represents one of the critical issues for the development of machine learning algorithms. In fact, the efficacy of the final machine learning-powered solution for a specific application is ultimately determined by the quality and amount of the training data.
However, to date, there is a limited availability of training SAR raw data available in scientific literature regarding the specific topic of high-backscattering objects detection. Furthermore, their generation from real data is a time-consuming task.
In this work, we propose and investigate a physically and statistically based approach to simulate high-backscattering objects and generate realistic synthetic training SAR raw datasets.
We then trained and evaluated a state-of-the-art DCNN on the generated synthetic dataset and successively validated it on real raw data extracted from ERS imagery archive (ESA, 2023).
It is one of the first experiments proposed in the SAR literature and results are quite encouraging, as they reveal that a well-trained DCNN can correctly recognize strong scattering objects on SAR raw data.

2. DATA AND MATERIALS

This research study is aimed at the implementation of a DCNN-based approach capable to detect point-like high-backscattering targets directly on SAR raw data. This required two main steps: (1) the implementation of a SAR simulator of raw data; (2) the configuration and training of a DCNN by using the training datasets generated with the SAR simulator.

2.1 Dataset Simulator

The implementation of the simulator followed an approach based on a low level of complexity aimed at developing a fast and automatic simulator, thus discarding advanced physical models due to the large number of external parameters to consider and their complex interaction.
We also discarded approaches based on the extraction of the training dataset directly from real images since it is in general a time-consuming activity and requires expert SAR operators.
As a result, we implemented a hybrid physical-statistical raw data simulator based on the generation of the following two contributions that are then summed together to generate noisy raw data images:

1. Point scatterers physically simulated assuming:
   - Each target is simulated as a single point scatterer;
   - the acquisition geometry of ERS mission (Table 1);
   - a fixed backscattering coefficient;
   - a variable position of the target in the scene.
2. As outlined in [(Gao,2010), either in the high-resolution or low-resolution case, with the ideal hypothesis of a sea background having a constant radar cross section and the central limit theorem, both the real and imaginary parts are Gaussian-distributed. Although more complex modeling can be proposed, the analysis carried out on a number of different crops of ERS-1/2 raw complex data shows that it is acceptable to model both the real and the imaginary parts with a truncated Gaussian distribution characterized by:
   - truncation limits according to ERS data quantization of the real and imaginary parts performed by the 5-bit analog-to-digital converter of the ERS acquisition system. This allows the quantized data to take integer values in the range of -16 (-2^4) to +15 ($+2^4-1$).
   - a mean value equal to zero;
   - a standard deviation that was varied in order to generate different noise intensity levels thus obtaining different Signal-to-Clutter Ratio (SCR) values according to the following expression:

$$SCR = 10 \log_{10}\left(\frac{P_{Obj}}{P_n}\right) \qquad (1)$$

where P_{Obj} = Average intensity of the object
P_n = Average intensity of the noise

Parameter	Value
Carrier Frequency	5,3 GHz
Signal Bandwidth	15,55 MHz
Sampling Frequency	18,96 MHz
Pulse Width	37.1 μs
Pulse Repetition Frequency	~ 1,68 kHz
Antenna Aperture	10 m
Look Angle	23 degrees
Radar Velocity	~ 7,12 km/s
Radar Height	785 km
Full-Frame Raw Image Size	~30000 pixels (azimuth) ~5600 pixel in (range)
Raw Image Spacing	~4 m (azimuth) ~8 m (range)
Length of radar pulse	~700 pixels

Table 1. Main parameters of the ERS mission (ESA, 2023).

2.2 DCNN training

Following the proposed approach, we have simulated a stack of 12000 image crops with 6000 crops containing only clutter noise and 6000 crops containing point-like scatterers with different level of clutter noise (Figure 2), thus simulating an SCR varying from 42 dB to 56 dB.
The main objective of the DCNN is to classify the input crops into two categories: Bright Target (i.e. presence in the given crop of a dominant strong scatterer) and No Bright Target (absence in the given crop of a dominant strong scatterer).
For this study, we looked at the effects of different cropping dimensions on raw data. The use of small crops is recommendable in order to reduce uncertainty about the point-like scatterer position and to reduce training and classification times. Following several tests, we determined that the best trade off is a crop size of 100 × 100 samples. Although this size is significantly shorter than the impulse response (see Table 1), it was observed that when the crop is centred on the point-like scatterer peak response, it captures most of the energy of the bright target radar return.
The simulated dataset was used to train a deep neural residual network, known as "ResNet" that can be considered a state-of-the-art Deep Convolutional Neural Network (He, 2015).
More specifically, the 80% percent of the dataset was used for training, while the remaining images were equally divided between validation, which is performed periodically during training phases, and testing, which is performed at the conclusion of the training.
ResNets use so-called residual blocks that implement shortcut connections in the network architecture. The stack of convolution

layers within each residual block only needs to learn a residual term that refines the input of the residual block toward the desired output. This makes the ResNet easier to train because the shortcut connections enable the direct propagation of information and gradients across multiple layers of the network, leading to better gradient flow and the convergence properties of the network during calibration. This ensures high flexibility for this DCNN and increases the potential to understand more complex features. The ResNet used in this work was created and trained on Matlab. The command used to create its structure is resnetLayers(inputSize, numClasses), which creates a 2D residual network with an image input size specified by inputSize and a number of classes specified by numClasses.
In these conditions, the net managed to achieve high accuracy during the training phase with the simulated raw data. The training phase was stopped after several iterations exceeding 95% up to 100% of accuracy, as illustrated in Figure 3.

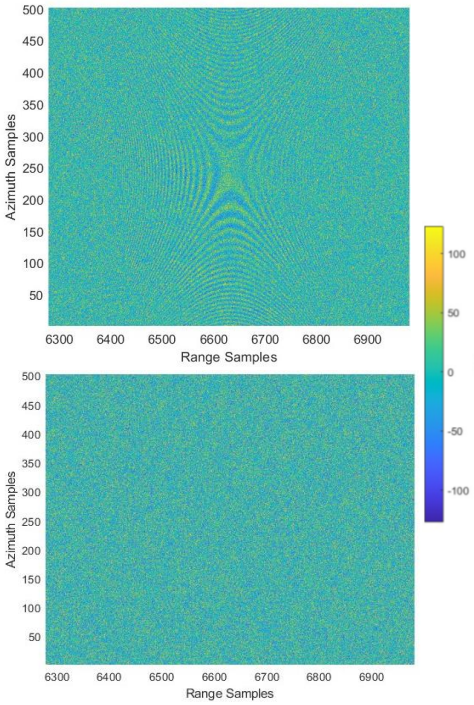

Figure 2. Example of real part of simulated raw data. Top: bright scatterer in a clutter noise (SCR = 35 dB). Bottom: clutter noise only.

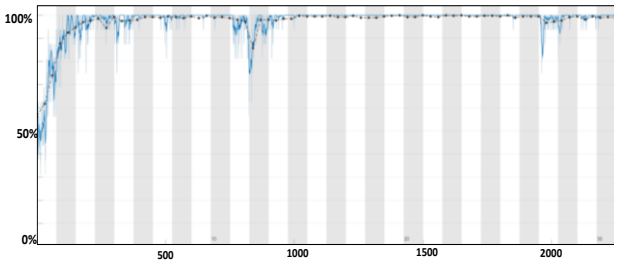

Figure 3. Training phase of the proposed ResNet. X axis: number of training iterations; y axis: accuracy achieved at each iteration. Blue curve: training accuracy; black curve: validation accuracy.

2.3 DCNN validation with real data

Finally, we conducted a thorough test of DCNN detection capability of high-backscattering targets using real ERS data.

A preliminary test was carried out on a sea scenario by extracting a first crop from an ERS image in a pure sea area with no presence of targets (Figure 4) and a second crop with the presence of a ship (Figure 5).
The DCNN was able to correctly detect both the ship and the sea-only area with a very high probability as illustrated in the first two lines of Table 2.
Sea scenarios are in general less complex than land scenarios. Further investigations were then carried out on land areas. To this aim, 9 land crops were extracted from ERS images corresponding to three different situations:

- 3 point-like bright scatterers (PS), Figure 6.
- 3 wide-area bright scatterers (WA), Figure 7.
- 3 areas with no bright scatterers (NO), Figure 8.

The experimental results are detailed in Table 2 where it is possible to observe that all the three types of targets have been correctly detected. In particular, it is important to note that although the DCNN was trained only with point-like bright scatterers, it was able to correctly identify wide-area bright scatterers.
It is also interesting to note that the raw data related to the ship case show an evident (although noisy) pattern, typical of an impulsive radar response. On the contrary, in the case studies selected in land areas, this pattern is not recognizable, confirming the greater difficulty of operating in a land context compared to a sea context.

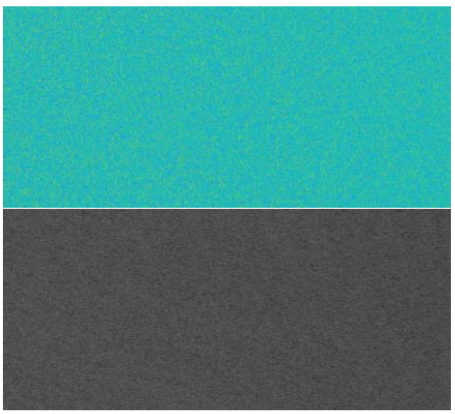

Figure 4. Example of sea-only radar response. Top: raw image. Bottom: Amplitude of the SLC.

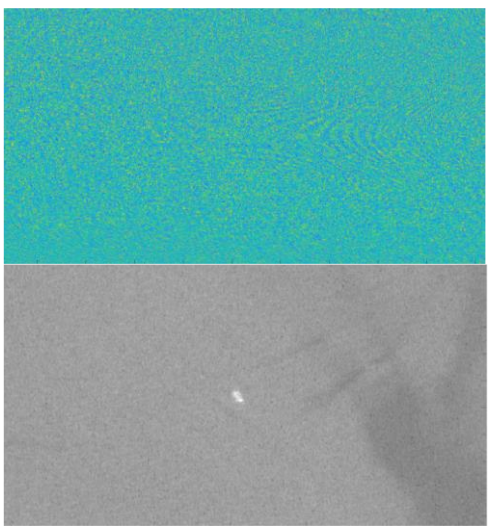

Figure 5. Example of ship radar response. Top: raw image (it can be noted the presence of a typical noisy pattern of the impulsive radar response). Bottom: Amplitude of the SLC.

Target ID	Type	Bright Scatterer Detection Probability [%]	SCR [dB]
1	SHIP	100%	-
2	SEA	0.00%	28
3	PS	97,33%	7
4	PS	99,82%	21
5	PS	99,72%	13.7
6	WA	100,00%	9
7	WA	71,75%	7.8
8	WA	100,00%	18
9	NO	0,02%	-
10	NO	0,00%	-
11	NO	0,02%	-

Table 2. Bright targets detection probability for 2 test case in sea areas and the 9 test cases in land areas, extracted from real ERS raw data. PS: point-like bright scatterers; WA: wide-area bright scatterers; NO: no bright scatterers. The third column shows the probability associated with the presence of a bright scatterers. Ideally it is expected 0% for SEA and NO targets and 100% for SHIP, PS, and WA targets.

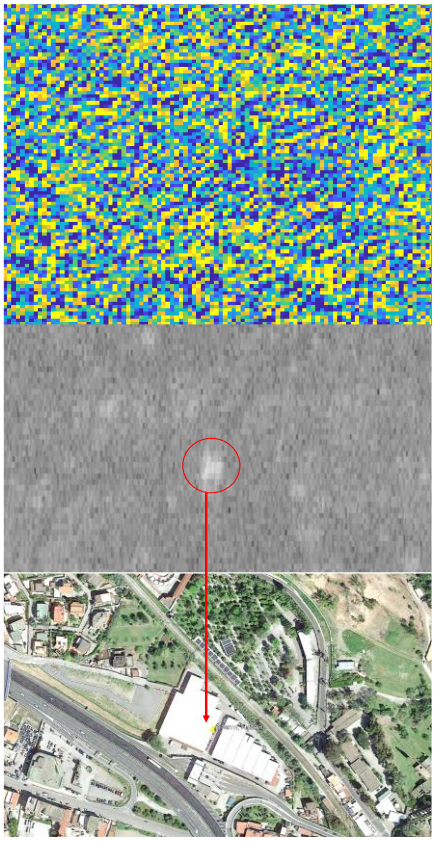

Figure 7. Example of wide-area strong scatterer. Top: raw image. Middle: Amplitude of the SLC. Bottom: Google Earth image.

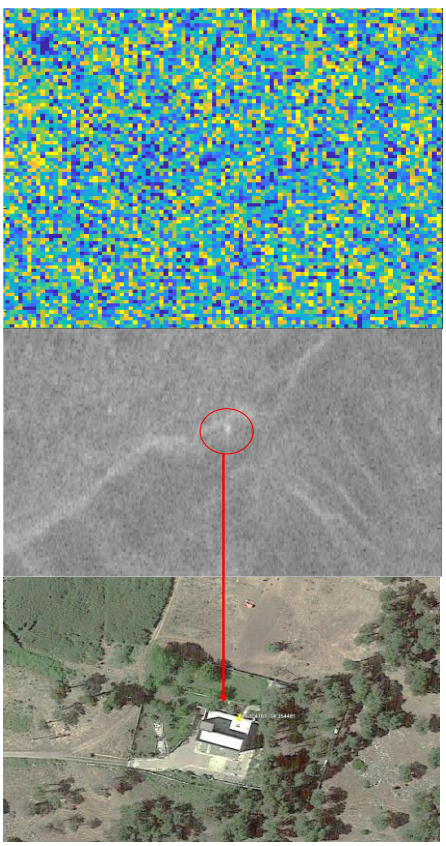

Figure 6. Example of point-like strong scatterer. Top: raw image. Middle: Amplitude of the SLC. Bottom: Google Earth image.

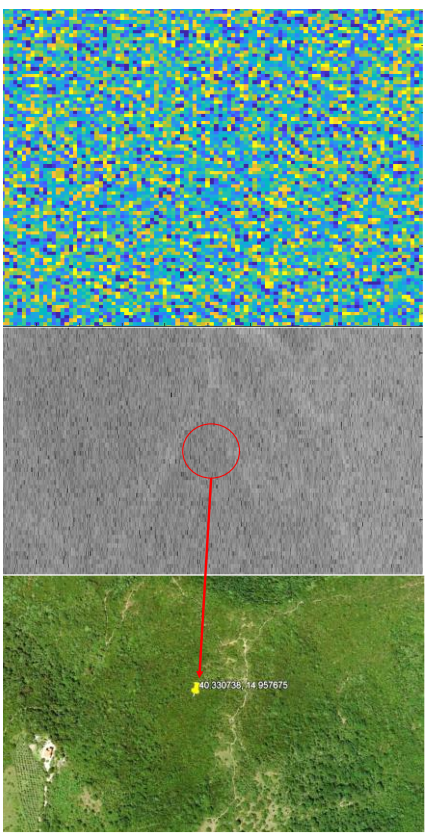

Figure 8. Example of area with no strong scatterers. Top: raw image. Middle: Amplitude of the SLC. Bottom: Google Earth image.

3. CONCLUSIONS

In this study, we have proposed a complete framework aimed at the detection of high-backscattering (bright) targets applied directly to SAR raw data by means of a DCNN.
We have proposed a simple and automatic simulation method for generating the training data set.
The simulator simulates radar echoes of point-like scatterers combined with clutter noise integrated into complex matrices that represent the simulated raw dataset.
Point-like scatterers are simulated by means of a single-point physical model, whereas the clutter noise is simulated by means of a statistical model based on a truncated gaussian distribution.
The simulation was carried out in realistic conditions by using acquisition parameters of the ERS mission.
State-of-the-art ResNet DCNN was configured with the aim to categorize SAR raw data crops into two classes (High-backscattering target and No target).
The DCNN was able to achieve 100% overall accuracy with simulated data with an SCR in the range of 42 ÷ 56 dB.
It is a range of very high SCR values. This choice derives from the need to train the network in conditions where it is very clear the pattern that it has to identify, that is the impulse response of the SAR system.
In particular, it was noted that the DCNN ability to recognize this pattern is learned better when it operates in conditions of high SCR and this ability is preserved on real data even for SCR with lower values.
In this regard, final analyses were carried out with 2 case studies in sea areas (1 ship in a sea area and 1 sea-only area) and 9 case studies in land areas (3 point-like strong scatterers, 3 wide-area strong scatterers and 3 areas with no strong scatterers) extracted from ERS real data and correctly detected by the trained DCNN.
The results confirm that although the DCNN was trained with very high SCR values, it performed very well in real cases with lower SCR values.
In particular, real cases exhibit an SCR from 7 dB to 28 dB.
This confirms that the proposed simulation methodology accurately represents the main characteristics of real high-backscattering targets and their interactions with clutter.
Furthermore, the results obtained in this work give evidence that target detection on SAR raw data is feasible thus opening interesting solutions related to the possibility to reduce the computational cost of the detection algorithms detection thanks to the possibility to skip the focusing and despeckling processing steps.
This also opens interesting topics that will be investigated in future works related to:

- performance assessment with a wider range of SCR values;
- performance assessment with other SAR missions operating with different polarization, acquisition geometries, bands and spatial resolution (e.g., COSMO-SkyMed);
- performance assessment in the case of different target sizes and analyses of interference caused by targets placed close to each other;
- opportunities analysis in terms of on-board implementations. The possibility to perform detection as soon as data are taken, would enable the transmission to ground of alert signals only, with notable reduction of both latency and downlink bandwidth, thus opening interesting real-time monitoring scenarios.

ACKNOWLEDGEMENTS

This work was carried out in the framework of the APP4AD project (“Advanced Payload data Processing for Autonomy & Decision”, Bando ASI “Tecnologie Abilitanti Trasversali”, Codice Unico di Progetto F95F21000020005), funded by the Italian Space Agency (ASI). ERS data are provided by the European Space Agency (ESA).

REFERENCES

Banerjee S., Sinha Chaudhuri, S., 2018. A Review on various Speckle Filters used for despeckling SAR images. Second International Conference on Computing Methodologies and Communication (ICCMC), Erode, India, 2018, pp. 68-73, doi: 10.1109/ICCMC.2018.8487958.

Cruz, H., Véstias, M., Monteiro, J., Neto, H., Duarte, R.P, 2022. A Review of Synthetic-Aperture Radar Image Formation Algorithms and Implementations: A Computational Perspective. Remote Sens. 2022, 14, 1258. https://doi.org/10.3390/rs14051258.

ESA, 2023. SAR (ERS). https://earth.esa.int/eogateway/instruments/sar-ers.

Evans, D. L., Alpers W., Cazenave A., Elachi C., Farr T., Glackin D., Holt B., Jones L., Liu W. T., McCandless W., Menard Y., Moore R., Njoku E., 2005. Seasat—A 25-year legacy of success, Remote Sensing of Environment, Volume 94, Issue 3, 2005, Pages 384-404, ISSN 0034-4257, https://doi.org/10.1016/j.rse.2004.09.011.

Gao, G. Statistical modeling of SAR images: A survey. Sensors 2010, 10, 775 https://www.mdpi.com/1424-8220/10/1/775

He, K., Zhang, X., Ren, S., Sun, J., 2015. Deep Residual Learning for Image Recognition. CoRR 2015, abs/1512.03385, [1512.03385].

Zhang, Y., Hao, Y, 2022. A Survey of SAR Image Target Detection Based on Convolutional Neural Networks. Remote Sensing 2022, 14. 538 https://doi.org/10.3390/rs14246240.

A DCNN-BASED APPROACH FOR REAL-TIME OIL SPILL DETECTION BY USING SAR DATA

K. Tijani , A. Morea , N. Ricciardi , D.O. Nitti , R. Nutricato

Geophysical Applications Processing s.r.l., c/o Dipartimento di Fisica Interateneo di Bari, Bari, Italy,
(khalid.tijani, alberto.morea, davide.nitti, nicolo.ricciardi, raffaele.nutricato)@gapsrl.eu

KEY WORDS: Marine disasters, Oil spill, Ship and Novelty detection, DCNN, Semantic segmentation, SAR.

ABSTRACT:

In recent years, the real-time on-board detection of environmental disasters through Synthetic Aperture Radar (SAR) technology on satellite platforms has emerged as a transformative advancement in disaster monitoring. This cutting-edge approach allows for the real-time identification and response to emergency events, thereby playing a crucial role in averting potential harm to both human populations and the environment.
This research focuses on harnessing the potential of SAR technology for the rapid and accurate detection of sea oil spill events, a well-known critical environmental concern.
In particular, the work is focused to the critical software optimizations necessary to facilitate implementation of on-board real-time processing and data downlink capabilities. To this aim a Deep Convolutional Neural Network (DCNN) approach is proposed for the segmentation and classification of SAR intensity images.
An experimentation phase is dedicated to the validation of the proposed approach with real SAR datasets containing oil spill, look-alike, ship, sea, land and novelty (mainly rain cells) classes.
The results exhibit an overall accuracy of 93% and demonstrate the validity of the proposed approach.

1. INTRODUCTION

Oil spills, resulting from the negligent or accidental release of liquid petroleum hydrocarbons into water bodies like oceans, rivers, or lakes, pose significant threats to marine ecosystems, human health, and local economies. Traditional methods of monitoring, such as visual and infrared sensors, are constrained by various factors, including poor visibility during adverse weather conditions or at night.
In contrast, SAR technology has emerged as a potent tool for oil spill detection due to its capacity to operate under various conditions, including low visibility and nighttime scenarios. Current research endeavors are largely dedicated to the prompt detection of oil spills using SAR technology, an essential step toward implementing timely mitigation measures.
To address this challenge comprehensively, we propose an approach that integrates a suite of innovative methods for real time oil spill detection. The workflow is based on four main points:

- Leveraging Deep Learning Techniques: our methodology harnesses the power of deep learning, specifically deep convolutional neural networks (DCNNs) based on DeepLab v3+ and ResNet-18 libraries. These advanced models excel in accurately segmenting and classifying identified oil spill cases.
- Creating a comprehensive database: we have meticulously constructed a comprehensive database for training our models. This database harmonizes data from publicly available repositories such as CleanSeaNet and TenGeoP-SARwv with a third dataset specifically built by the authors by processing known and documented case studies identified in the sea area in front of the port of Brindisi (Southern Italy).
- On-Board Satellite Processing: we achieved real-time detection capabilities by means of an on-board processing optimized for an efficient use of the limited computing resources available on the satellite platform. The proposed processing implements all fundamental SAR data processing steps involving focusing, despeckling, land/sea mask generation, contrast enhancement. The output of this processing represents the input of the DCNN-based segmentation and classification of the following classes: oil spill, look-alike, ship, sea, land, novelty.
- Efficient Data Downlink: finally, we have incorporated an efficient data downlink process that enables the transmission to the ground segment of only the radar chips centered to the events of interest thus avoiding the transmission of the full frame of SAR data.

Details of the proposed methodology are given in the following section.

2. METHODOLOGY

The proposed approach integrates two software tools.
The first software tool generates (and augments) the training database by extracting and identifying several marine phenomena from SAR data images. It assigns specific classes to the detected phenomena.
More specifically, the resultant training database integrates 4035 cases. As illustrated in Figure 1, each case in the database includes two images: the input SAR intensity image and the relevant labels image, which categorizes each pixel of the SAR image into the sea, look-alike, oil spill, ship, novelty (mainly rain cells), and land classes.
The images in the database have a size of 512 x 512 pixels, this is a tradeoff between the need to work with large patches to enable a better context analysis and the need to reduce computational cost for the DCNN training.
The second software tool implements a modular on-board processing for near-real-time oil spill monitoring. The software modules implement the sequential tasks illustrated in Figure 2 and detailed in the following.

* Corresponding author

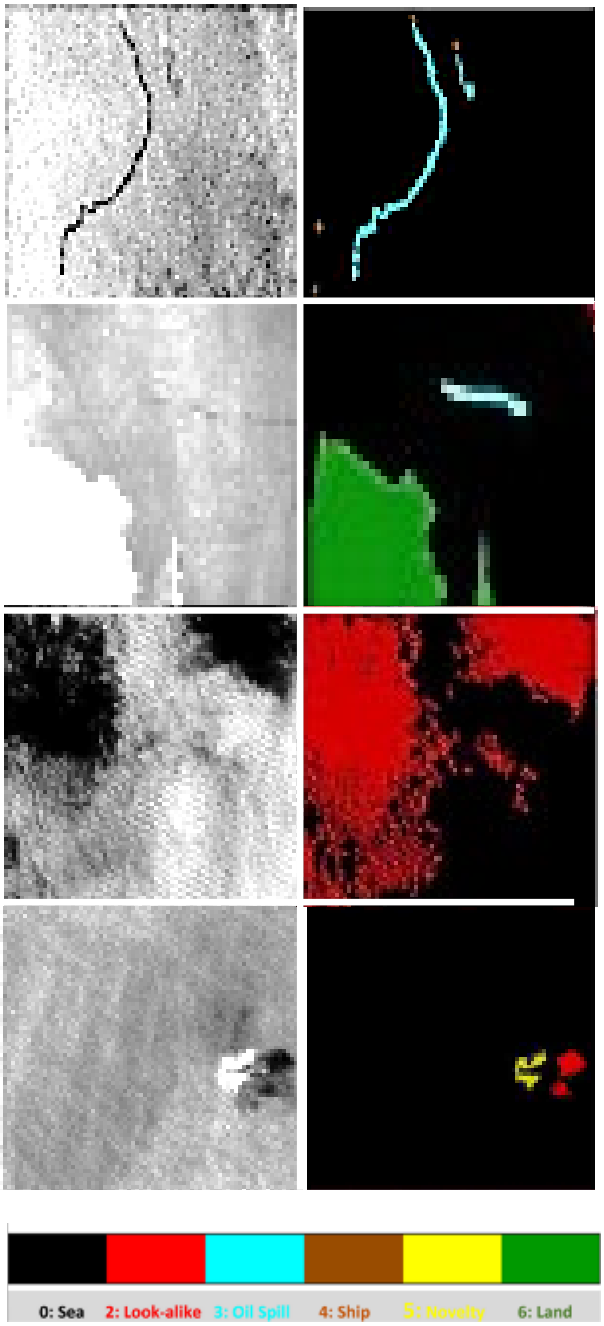

Figure 1. Examples of data available in the training database. Each known case in the database includes two images: the input SAR image (left column) and the classified labels image (right column). The available classes include sea, look-alike, oil spill, ship, novelty, and land as indicated in the colorbar in the bottom of the figure.

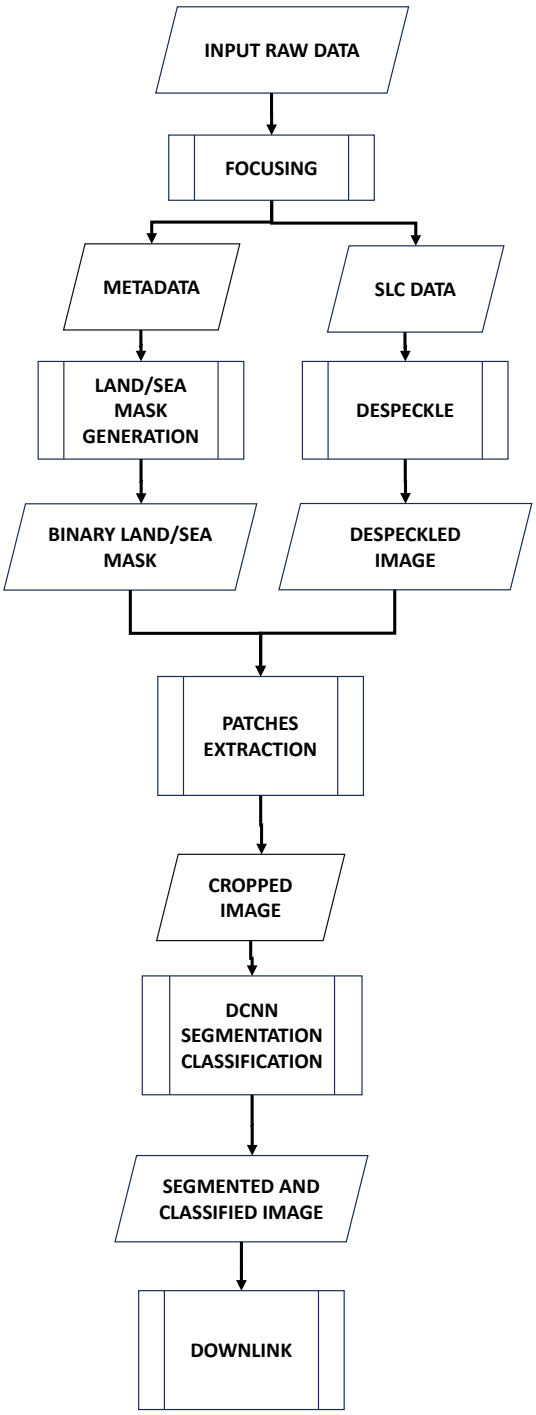

Figure 2. Flow chart of the oil spill detection prototype.

Focusing: As illustrated in Figure 3, this module implements the Range-Doppler algorithm (Bamler, 2004). To reduce the computational cost this module implements decimation of the data and neglects the range migration. This approach speeds up the processing at the expense of reduced spatial and radiometric resolution of the resulting focused image. Considering that oil spill events of interest have a large extension, the resulting resolution penalization can be neglected.

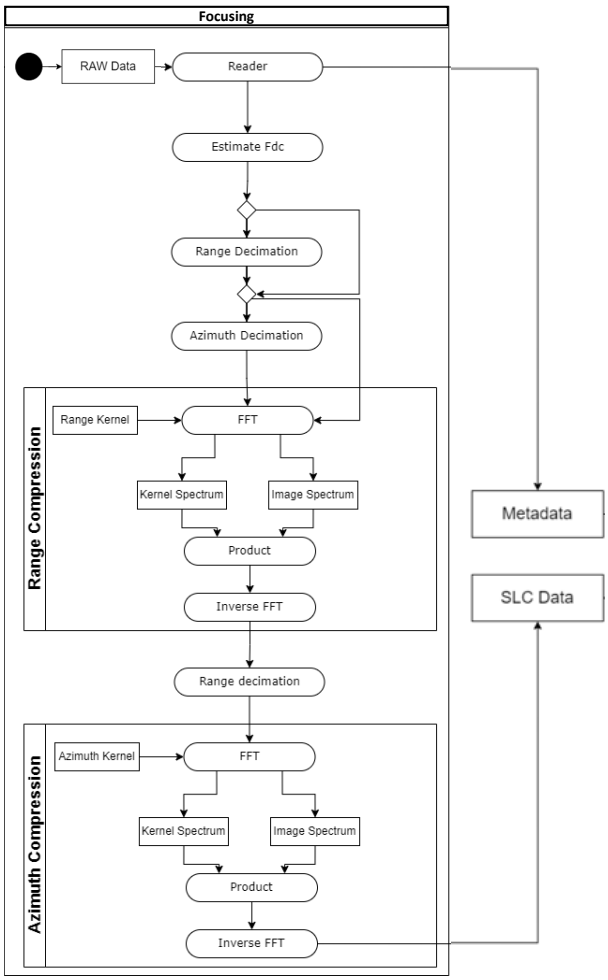

Figure 3. Flow chart of the Focusing Module.

Despeckle: Due to the need to decrease the impact of speckle noise (Singh et al., 2016) on the amplitude of the focused SAR intensity image, a filtering module has been included in the software architecture.

We adopted a simple average filter; it has shown appropriate noise reduction and at the same time can be efficiently implemented in the frequency domain, as illustrated in Figure 4.

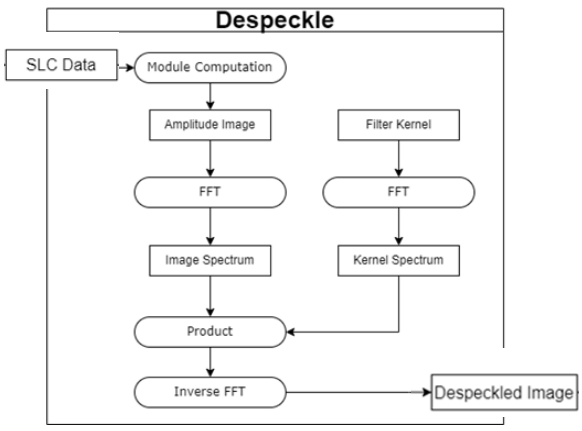

Figure 4. Flow chart for the Filtering Module

Land-Sea Mask Generation: as illustrated in Figure 5, this module masks out the land in the acquired radar scene to facilitate the subsequent detection phase. This module therefore has the objective of generating a binary land-sea mask that can subsequently be applied to the SAR intensity image. Its implementation (as detailed in Figure 6) requires an input world coastline polygon that is then intersected with the radar scene. Optionally, the binary mask is also dilated to take into account inaccuracies of input coastline polygon.

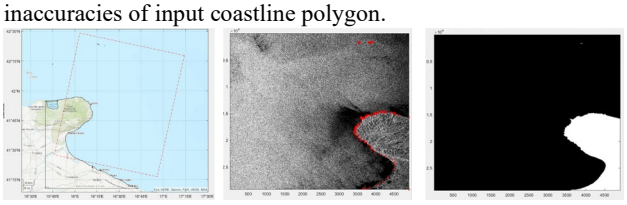

Figure 5. Example of output generated by the Land-Sea mask generation step. Left: coastline (black polygon) and footprint of the satellite image (red rectangle). Middle: coastline (red polygon) in radar coordinates overlapped onto the SAR intensity image. Right: Land-Sea Mask in radar coordinates.

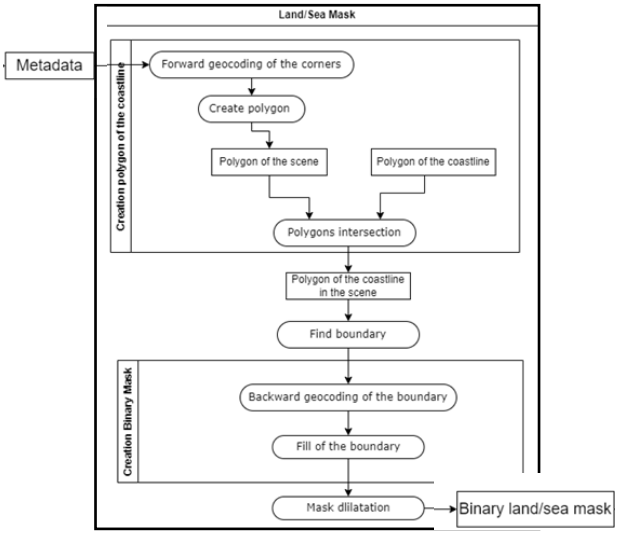

Figure 6. Flow chart of the Land-Sea Mask Generation Module.

Patches Extraction: before proceeding with the detection of the events of interest, some post processing operations of the SAR intensity image are needed, which make semantic segmentation easier. More specifically, as illustrated in Figure 7, after applying the land-sea mask to the whole despecked intensity image, this module splits the whole SAR image into patches of appropriate size as required by the DCNN. As already stated, the best trade-off was found with patches of 512 × 512 pixels. A contrast enhancement procedure is then applied by clipping the tails of the histogram of the intensity values of the patch pixels.

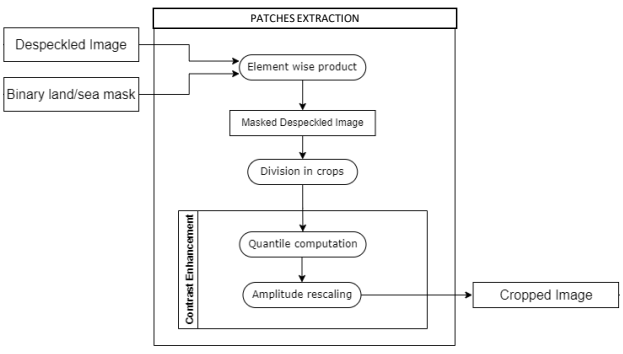

Figure 7. Flow chart of the Patches Extraction Module.

DCNN Segmentation and Classification: the segmentation module uses a semantic DCNN based on DeepLab v3+ with

ResNet-18 network (Krestenitis et al., 2019) as illustrated in Figure 8. This model enables accurate segmentation and classification of input patches into 6 classes: ships, oil spill, look-alike, land, sea, and novelty (mainly rain cells). As illustrated in Figure 9, a patch mosaicking is subsequently applied to obtain a segmented and classified image of the same size as the full frame input focused and filtered image.

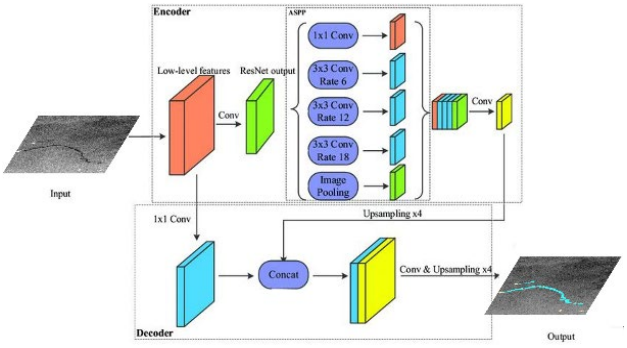

Figure 8 DeepLab v3+ convolutional neural network for semantic image segmentation Based on ResNet-18.

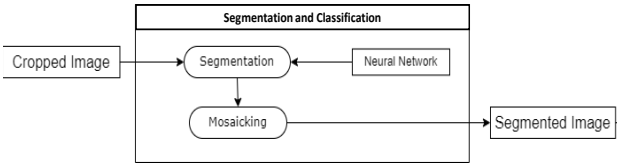

Figure 9. Flow chart of the DCNN Segmentation and Classification Module.

Downlink: as detailed in Figure 10, this module sends the data of interest to the ground segment. Data is packaged on the basis of the settings indicated by the operator. In particular, it is possible to send raw or intensity radar chips that include any combination of the following classes: ships, oil spills, look-alikes and novelties. The size of the available chip is configurable through dilation morphological operators and in the case that more than one event of interest fall into the same chip, they are integrated into a larger chip in order to avoid duplication of data transmitted to the ground segment.

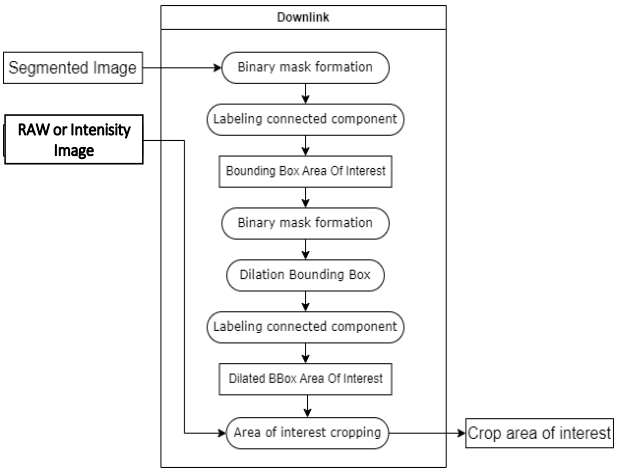

Figure 10. Flow chart of the Downlink Module.

3. RESULTS AND DISCUSSION

All the modules described in the previous section were implemented and tested with real SAR data. The results show that the proposed system achieves good performance.

More specifically, as illustrated in Figure 11, the confusion matrix demonstrates the system's robustness, in detecting oil spills (93%), ships (92%), and novelty objects (99%), with an high overall accuracy equal to 93%.

Examples of successful application of the proposed approach to real case studies extracted from ERS SAR data are given in Figure 12.

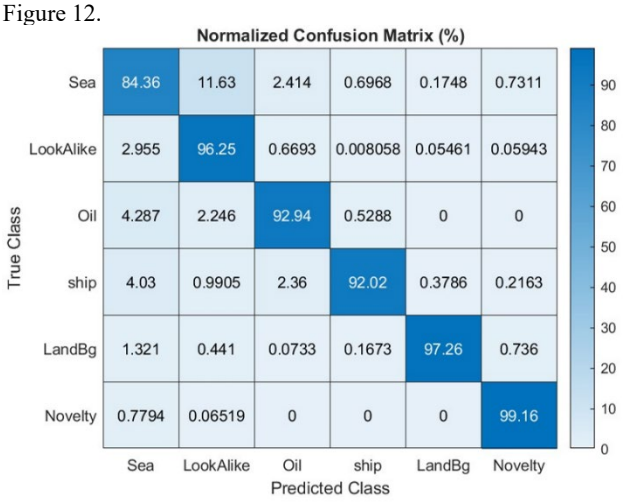

Figure 11. Confusion matrix obtained during the test of the proposed system with real cases.

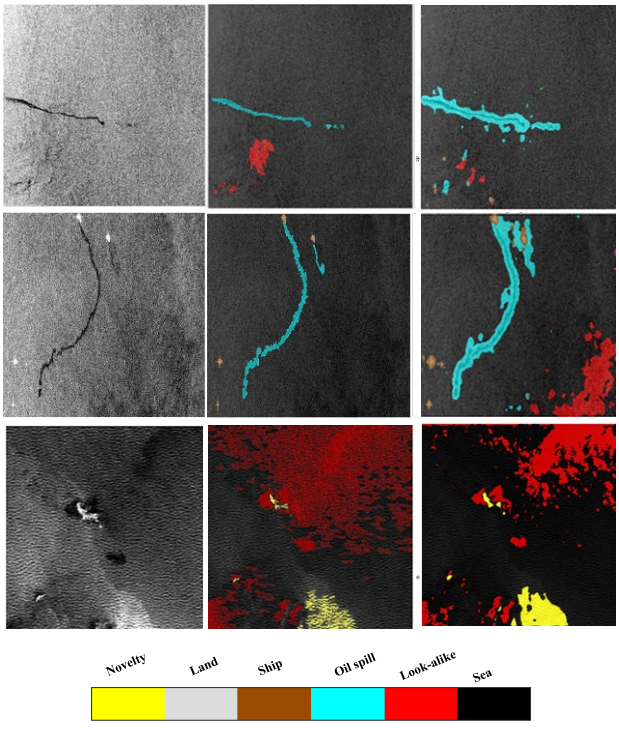

Figure 12. Left: examples of three SAR patches including oil spill events (first two rows) and novelty events (third row) provided in input to the DCNN segmentation and classification step. Middle: ground truth data. Right: results generated by the DCNN.

Preliminary computational performance tests have been carried out with an ERS raw image of 30233 lines and 5616 pixels. Execution time and memory occupation for each module have been measured on a common laptop with a CPU Intel i7 and 16 GB RAM and are reported in Table 1.

Module	Execution Time [s]	Memory Occupation [GB]
Focusing	15	2.5
Despeckle	10	1.2
Land/Sea Mask Generation	3	0.1
Patches Extraction	2	0.4
DCNN Segmentation and Classification	10	0.6
Patch Mosaicking and Downlink	12	1.3

Table 1. Computation performance of each module of the software prototype.

In synthesis, a total execution time of 52 seconds with a peak RAM memory of 2.5 GB was requested for the processing of a full frame ERS image covering approximately an extension of 100 km × 100 km. Assuming an average ERS satellite platform velocity of 7.7 km/s, it results that a 100-km stripe is acquired in 13 s. Assuming also a 12% duty cycle for ERS mission, it results that the available processing time to process a 100-km stripe is 81.7 s according with the following expression:

$$\text{Max Proc Time} = \frac{100-12}{12} \cdot 13\ [s] = 81.7\ s \qquad (1)$$

The available processing time (81.7 s) compared with the measured processing time (52 s) gives enough margin for implementation of this prototype on a dedicated hardware platform for onboard computing.

4. CONCLUSION

The proposed approach implements a promising solution for real-time oil spill and ship monitoring through the fusion of SAR technology and deep learning. It significantly enhances processing speed while reducing downlink bandwidth by transmitting only relevant data. More specifically, it involves:

- An optimized pre-processing of the SAR raw data (focusing, despleckling, land-sea masking, block partitioning and contrast enhancement).
- A DCNN-based segmentation and classification module able to assign to each pixel of the input image a specific class selected among ships, oil spill, look-alike, sea, land and novelty (mainly rain cells).
- A downlink that optimizes data sent to the ground segment by selecting only raw or intensity radar chips that include the events (or classes) of interest.

It must be emphasized that the software discussed is a prototype experimental system, designed to operate on a satellite in orbit. It has been specifically calibrated to detect medium to large-sized oil spills in real-time, a key objective that addresses critical operational needs for monitoring and rapid response to marine pollution events. Given the intrinsic limitations regarding the computational resources available on a satellite platform, the reduction in spatial resolution and the employment of frequency filtering have been implemented as necessary actions to mitigate speckle in SAR imagery. These measures allow us to preserve the system's computational efficiency to the fullest. Such constraints are common in satellite applications, and our choices have been guided by an aim to optimize the balance between image quality and operational feasibility within the context of limited onboard computing power. Additionally, we wish to clarify that at the time of the study, we exclusively employed VV polarization, as it represents the sole polarization available from the ERS mission, which was chosen for this preliminary evaluation. Undoubtedly, the access to quad-polarization SAR data, would add significant value to the analysis, enabling us to explore more sophisticated algorithmic approaches and potentially more accurate classifications.

Based on these observations, future research directions involve:

- expanding the dataset involving a complete selection of L, C and X-Band SAR missions and comparing performance with several machine learning approaches.
- Analyze the impact of spatial resolution degradation introduced by despeckle filtering with respect to small size oil spills events.
- Use of polarimetric data to improve detection capabilities as discussed in (Migliaccio, 2015).
- Exploitation of external key information such as Automatic Identification System data.
- Enhancement of detection accuracy by recognizing that oil spill detection transcends a mere dark area search algorithm, encompassing a more intricate process rooted in underlying physical principles. In view of all this matter the use of DCNN can be even more useful once properly framed in a firm physical approach.
- Implementing the software on a hardware platform specific for on-board processing.

ACKNOWLEDGEMENTS

This work was carried out in the framework of the APP4AD project ("Advanced Payload data Processing for Autonomy & Decision", Bando ASI "Tecnologie Abilitanti Trasversali", Codice Unico di Progetto F95F21000020005), funded by the Italian Space Agency (ASI). ERS, ENVISAT and Sentinel-1 data are provided by the European Space Agency (ESA).

REFERENCES

Bamler, R., 1992. A comparison of range-Doppler and wavenumber domain SAR focusing algorithms, in IEEE Transactions on Geoscience and Remote Sensing, vol. 30, no. 4, pp. 706-713, July 1992, doi: 10.1109/36.158864.

M. Migliaccio, F. Nunziata & A. Buono, 2015. SAR polarimetry for sea oil slick observation, International Journal of Remote Sensing, 36:12, 3243-3273, DOI: 10.1080/01431161.2015.1057301

Singh, P., and Shree, R., 2016. Analysis and effects of speckle noise in SAR images, 2016 2nd International Conference on Advances in Computing, Communication, & Automation (ICACCA) (Fall), Bareilly, India, 2016, pp. 1-5, doi: 10.1109/ICACCAF.2016.7748978.

Krestenitis, M., Orfanidis, G., Ioannidis, K., Avgerinakis, K., Vrochidis, S., Kompatsiaris, 2019. I. Oil Spill Identification from Satellite Images Using Deep Neural Networks. Remote Sens. 2019, 11, 1762. https://doi.org/10.3390/rs11151762

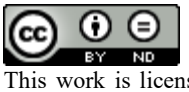

FROM SPACE ASSETS TOWARDS SCIENTIFIC DOWNSTREAM AND APPLICATIONS: TRENDS IN THE HYPERSPECTRAL DOMAIN

R. Guarini [1]*, M.L. Battagliere [2]

[1] Agenzia Spaziale Italiana (ASI), Matera, Italy
rocchina.guarini@asi.it
[2] Agenzia Spaziale Italiana (ASI), Roma, Italy
maria.battagliere@asi.it

KEY WORDS: PRISMA, hyperspectral, Earth Observation applications, PRISMA SCIENZA Programme

ABSTRACT:

Satellites with high spatial and spectral resolution have changed the way of considering the environment and environmental phenomena. PRISMA (PRecursore IperSpettrale della Missione Applicativa), launched in March 2019, has become the first hyperspectral satellite mission in Europe representing an innovative technology in the field of satellite remote sensing. With the aim to support and promote the scientific use of PRISMA mission, the Italian Space Agency (ASI) published a call addressed to the Italian EO Community, named "PRISMA SCIENZA" programme. In this framework, ASI co-financed 15 proposals focused on different topics of interest: agriculture and forestry, inland and coastal waters, air quality, ecosystems structure and composition, ice and snow, raw materials, cultural heritage and natural hazards. This paper provides an overview of the trends observed during the implementation of this programme, with a focus on the projects related to vegetation thematic area, highlighting the relevance of hyperspectral data for 1) forest cover analysis to support National Forest Inventory (AFORISMA project), 2) Controlling of Landfill and Environment Assessment Research (CLEAR-UP project), 3) Ecosystem functions, habitats, and diversity characterization analysis (HYPERECOS project), 4) developing algorithms for the retrieval of plant functional traits in agricultural and forest ecosystems (PRIS4VEG project), 5) Improved estimation of forest carbon sequestration from PRISMA retrieval of canopy nitrogen and photosynthetic potential (PRISMA-FOREST-NC project), 6) Topsoil properties Estimation for Agriculture (TEHRA project). These projects, as well as the PRISMA SCIENZA initiative overall, intend to support the full data exploitation of the mission and strategically promote the development of Italian know-how in the sector of hyperspectral remote sensing.

1. INTRODUCTION

The PRISMA (PRecursore IperSpettrale della Missione Applicativa) high-resolution space and spectral satellite is on orbit from the end of March 2019. PRISMA is a demonstrative spaceborne mission fully deployed by the Italian Space Agency (ASI). PRISMA completed the offer in the Earth Observation space segment of ASI, until now essentially based on the Synthetic Aperture Radars (SAR) of the COSMO-SkyMed constellation. PRISMA is the first hyperspectral satellite mission in Europe of the new generation with full range VNIR-SWIR coverage and represents the technological vanguard in the field of satellite remote sensing. PRISMA integrates the 30m hyperspectral imagery operating in the VNIR-SWIR range with 237 spectral bands and a 5m panchromatic camera (PAN), sensitive to all colours (Caporusso G et al. 2020). Indeed PRISMA is a new generation sensor that provide for the first time European full range VNIR-SWRI data.

Other initiatives were already available. DLR DESIS mission is hyperspectral but limited to 400 - 1050 nm in VNIR (https://www.dlr.de/eoc/desktopdefault.aspx/tabid-13622/23667_read-54280/) as well as CHRIS from UK Space Agency can be considered hyperspectral again but limited to VISNIR (https://earth.esa.int/eogateway/instruments/chris).

With this innovative sensor, ASI has provided the scientific community with a tool capable of acquiring images of the Earth's surface containing information on the chemical-physical composition of the objects present in the observed scene, providing a unique information contribution for various applications. Further development of new hyperspectral sensors with higher performance is also underway by ASI (ASI website, 2022).

In order to raise awareness of the PRISMA mission, ASI has set up a research funding program, called "PRISMA SCIENZA" (Licciardi et al. 2022) to prepare data exploitation and applications development for the mission. The programme supports R&D projects proposed by experts in hyperspectral remote sensing sector from national public research institutions to industries, also in the framework of international partnerships. The main goal is to support the science community to explore new application potentials, to develop software tools for hyperspectral data processing and to maximize the use of PRISMA data also in combination with other Earth Observation missions.

The "PRISMA SCIENZA" program is of strategical interest for ASI as it intends to:

- know the skills and scientific interests of the entire national community of users of the PRISMA mission;
- stimulate and strategically involve the national community in the scientific use of data from the PRISMA mission and in the exploration of its potential;
- broaden the spectrum of possible applications of mission data;
- strategically promote the development of Italian know-how and strengthen existing skills in the hyperspectral remote sensing sector.

As the vegetation topic covers the 33% of projects, it is the most representative thematic area for the PRISMA SCIENZA call. Thus, in this paper the projects related to this topic are mainly presented, trying also to underline the impact of the scientific downstream applications based on PRISMA data exploitation on

* Corresponding author

the Sustainable Development Goals (SDGs) of the United Nations Agenda 2030.

2. THE PRISMA SCIENZA PROGRAMME

The ASI's PRISMA SCIENZA ASI programme supports R&D projects that have been selected following a competitive procedure through research call. Forty-one proposals were received and, among these, twenty-three have been considered eligible. Most of these projects have been proposed by teams consisting of both Academic and Industrial partners (41% universities, 35% research centers; 24% SMEs), and this simplifies the technology transfer process. ASI financed the first 15 proposals that are focused on different topics of interest, such as agriculture and forestry, inland and coastal waters, air quality, ecosystems structure and composition, ice and snow, raw materials, cultural heritage and natural hazards.
In the context of a more sustainable management of natural resources, the quantitative and spatialized estimation of functional traits of terrestrial vegetation in agro-forestry plays a fundamental role (Figure 1).

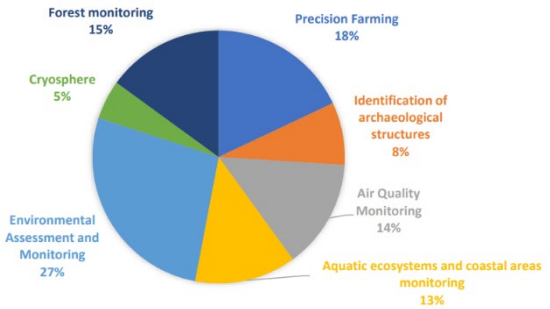

Figure 1 Observed trends in topics of interest in the PRISMA SCIENZA programme

In this context, six of the fifteen projects (33%) are related to the "agriculture and forestry" thematic area over three topics; the 67% of topics of interest are splitted over three topics: Forest monitoring, Precision Farming and Environmental Assessment and monitoring.

2.1 PRISMA SCIENZA projects

The six projects of PRISMA SCIENZA programme, related to vegetation thematic area are dedicated to the relevance of hyperspectral data for 1) forest cover analysis to support National Forest Inventory (AFORISMA), 2) Controlling of Landfill and Environment Assessment Research (CLEAR-UP), 3) Ecosystem functions, habitats, and diversity characterization analysis (HYPERECOS), 4) developing algorithms for the retrieval of plant functional traits in agricultural and forest ecosystems (PRIS4VEG), 5) Improved estimation of forest carbon sequestration from PRISMA retrieval of canopy nitrogen and photosynthetic potential (PRISMA-FOREST-NC), 6) Topsoil properties Estimation for Agriculture (TEHRA).

2.1.1 AFORISMA (Apprendimento automatico per l'analisi di coperture FORestali con dati IperSpettrali della missione prisMA a supporto dell'inventario forestale nazionale).
This project, spanning two years, starting from July 2022, is focused on the classification of forest cover for updating the National Forest Inventory and monitoring forest response to the occurrence of extreme weather events (Figure 2).

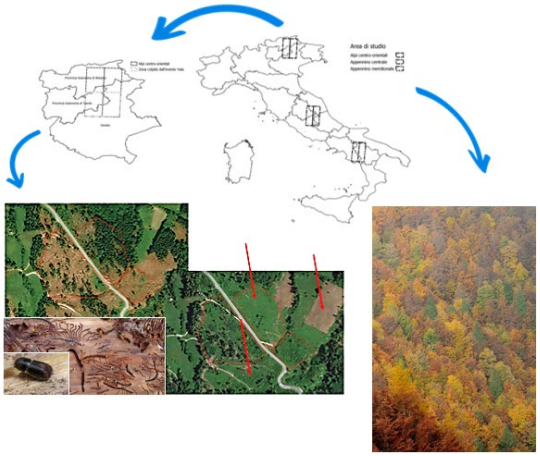

Figure 2 Study area of the AFORISMA project.

The AFORISMA project partners include the Centro di ricerca Foreste e Legno del Consiglio per la ricerca in agricoltura e l'analisi dell'economia agraria (CREA-FL), Università degli Studi di Trento / Dipartimento di Ingegneria e Scienza dell'informazione (UNITN), Arma dei Carabinieri – Comando Unità Forestali, Ambientali e Agroalimentari (CUFAA) and the University of Extremadura, Escuela Politécnica de Cáceres - Department of Technology of Computers and Communications, Hyperspectral Computing Laboratory (UNEX).
AFORISMA project is organized in two main lines of activities:

1. Characterization of the specific composition of forest stands, with: automatic classification of forest categories and tree species; production of related wall-to-wall maps, extended continuously over large areas large (potentially the entire national territory); periodic update of classification and maps with high frequency Early observation of changes accelerated by climate change; decision support in terms of management and silvicultural practices
2. Monitoring the response of forest stands to the occurrence of extreme weather events: identification of the reaction of tree vegetation in areas damaged by extreme events; as entity damage suffered and recovery capacity of the vegetation survived the event; as the ability to reconstitute new vegetation layers (by natural regeneration) in totally destroyed areas; the hyperspectral data can be used to identify changes spectrally selective and of very small magnitude (not possible with multispectral data).

Considering that AFORISMA is a useful project addressed in the development of methods of processing and analysis of PRISMA data aimed at recognizing the different forest categories and the tree species that characterize them, as well as monitoring the stresses induced by extreme meteorological events and quantifying the recolonization by the tree and shrub vegetation in the phases following the event, it provides a contribution to the SDGs (Sustainable Development Goals) 15 (Life on land).

2.1.2 CLEAR-UP (Control of Landfill and Environment Assessment Research Using Prisma) project aims to use PRISMA data for the identification of soil and air pollutants produced by landfills (Figure 3), to map heavy metals, harmful emissions (CH4, CO2, Nox) and vegetative stress.
The implementation of in situ and EO data management system is foreseen.

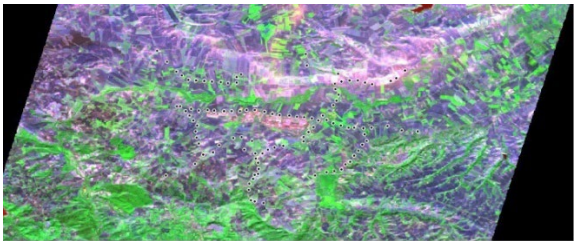

Figure 3 PRISMA image acquired on the Melfi (PZ, Basilicata Region, Italy) site with the relevant sampling points.

The CLEAR-UP project partners include the Università Sapienza di Roma Scuola di Ingegneria Aerospaziale (UniSapienza-SIA), Consiglio Nazionale delle Ricerche-Istituto di Metodologie per Analisi Ambientale (CNR-IMAA), SERCO Italia S.p.A., Euro.Soft s.r.l. and the Aerospace Engineering Faculty-University of Brasilia (AEF-UNB).
CLEAR-UP is a useful project for monitoring legal and illegal landfills, contributing to the SDGs 11 (Susteinable cities and communities).
CLEAR-UP will span two years, starting from October 2022.

2.1.3 HYPERECOS (HYPERspectral prisma data for ECOSystem functions, habitats, and diversity characterization) project proposes to develop new algorithms for mapping and monitoring ecosystem functions, habitats and their biodiversity, through the use of PRISMA hyperspectral data. This project is focused on the use of PRISMA data (Figure 4) - alone or in conjunction with other systems - for analyzing ecosystems and get a classification of habitats at fine scale, a retrieval of ecosystem functional properties and a correlation with biological by estimating biophysical parameters diversity in various ecosystems types: forests, alpine pastures and wetlands.

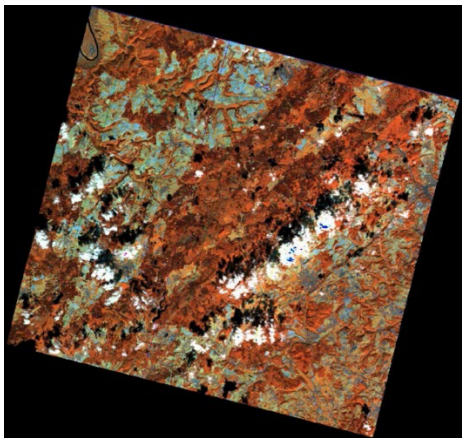

Figure 4 PRISMA SWIR data, in RGB Bands 50-125-200, of National Park Hunsrück-Hochwald (Germany), 2020-09-11

The HYPERECOS project partners include Università della Tuscia – Dipartimento Scienze Agrarie e Forestali (UniTUS DIBAF), EURAC RESEARCH, TERRASYSTEM s.r.l., Consiglio per la ricerca in agricoltura e l'analisi dell'economia agraria (CREA-FL) and the Trier University, Environmental Remote Sensing and Geoinformatics, Germany (UniTrier).
HYPERECOS is a useful project for developing methods to process and analyse different EO data in order to define experimental protocols able to highlight functional traits and habitat diversity. HYPERECOS contributes to the SDGs 15.
HYPERECOS will span two years, starting from May 2022.

2.1.4 PRIS4VEG (Sviluppo di algoritmi per la stima di parametri funzionali della vegetazione terrestre da dati PRISMA in ambito agro-forestale) project is aimed at creating the methodological basis for the development of a PRISMA data processing chain for i. the generation of level 3 products related to vegetation, i.e. biophysical/biochemical parameters derived from PRISMA reflectance data (At-surface Reflectance, L2D product) ii. the evaluation of the contribution of these L3 level products in the generation of higher level products (L4), i.e. products that are the result of further processing levels (e.g. statistical analysis or multi-level integration) or assimilation into agronomic/environmental modelling. In the Figure 5, the Ticino Regional Park that is one of the PRIS4VEG study site, is represented.

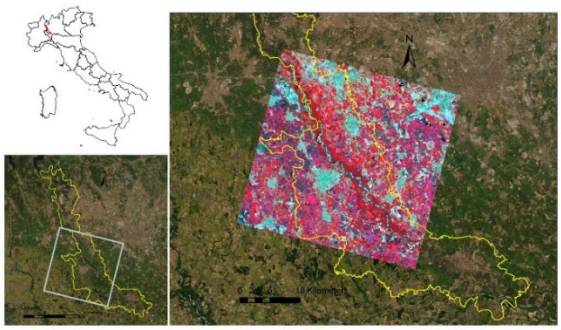

Figure 5 PRIS4VEG study area, Ticino Regional Park (Lombardy Region, Italy).

The achievement of these objectives will be guaranteed development of algorithms for the estimation of functional parameters of terrestrial vegetation from PRISMA data in the agro-forestry sector.
The PRIS4VEG project partners include the Università degli Studi di Milano–Bicocca (UNIMIB), CNR-Istituto per il Rilevamento Elettromagnetico dell'Ambiente (IREA), CNR-Istituto di Metodologie per Analisi Ambientale (CNR-IMAA), Università degli Studi della Tuscia - Dipartimento di Scienze Agrarie e Forestali (DAFNE), Natural resources department, Faculty of Geoinformation Science and Earth Observation, University of Twente.
PRIS4VEG is a useful project for demonstrating the value of such products for environmental monitoring applications and in support of sustainable agro-practices, contributing to the SDGs 12 (responsible production and consumption) and 15, indirectly to the SDGs 2.
PRIS4VEG will span two years, starting from April 2022.

2.1.5 PRISMA-FOREST-NC (Improved estimation of forest C sequestration from PRISMA retrieval of canopy N and photosynthetic potential) project. The main goal of PRISMA-FOREST-NC is to estimate leaf nitrogen concentration, canopy nitrogen content, canopy maximum carboxylation rate (potential CO_2 gain) and Leaf Area Index (LAI).
This research is aimed at:

- develop innovative methods for estimating the concentration and content of nitrogen (N) and photosynthetic potential (Vcmax, maximum carboxylation rate) of the canopies of forest covers, through the integration of PRISMA hyperspectral images with data from two monitoring networks (International Co-operative Programme on Assessment and Monitoring of Air Pollution Effects on Forests, ICP Forests);
- evaluate the errors associated with the decoupling between the ICP Forests spatial resolution (5 plants), the PRISMA images (30 m) and the footprint of the FLUXNeT

measurements (200-500 m), through two dedicated campaigns;
- demonstrate the impact of the information thus obtained on the forecast of the financial statements carbon (C) of forest covers, through the assimilation of PRISMA images in a biogeochemical model of the ecosystem, and the analysis of the greater predictive capacity compared to a baseline;
- demonstrate the relevance of using PRISMA images compared to Copernicus images Sentinel 2 at lower spectral resolution, analyzed with the same work chain.

The PRISMA-FOREST-NC project partners include Alma Mater Studiorum-Università di Bologna,-Dipartimento Scienze e Tecnologie AgroAlimentari (UNIBO-DISTAL), CNR-Istituto per la BioEconomia (IBE) and the Istituto di Fisica Applicata "Nello Carrara" (CNR-IFAC).
PRISMA-FOREST-NC is a useful project for demonstrating the relevance of the use of PRISMA images in comparison to other EO data, analysed with the same work chain. PRISMA-FOREST-NC contributes to the SDGs 12, 13 (climate action) and 15.
PRISMA-FOREST-NC will span two years, starting from May 2022.

2.1.6 TEHRA (Topsoil properties Estimation from Hyperspectral Remote sensing for Agriculture) project aims at develop methods and algorithms for PRISMA product generation to monitor and map soil properties of agronomic and environmental interest, in support of more sustainable and climate-smart precision agriculture strategies and environmental policies. The main objective of TEHRA project is to study methods and algorithms to estimate topsoil parameters (Casa et al. 2023) of agronomic interest: soil texture (clay, sand, silt), SOC (Soil Organic Carbon), soil moisture, Available Water Content (AWC), soil nutrients such as Potassium, Phosphorous.

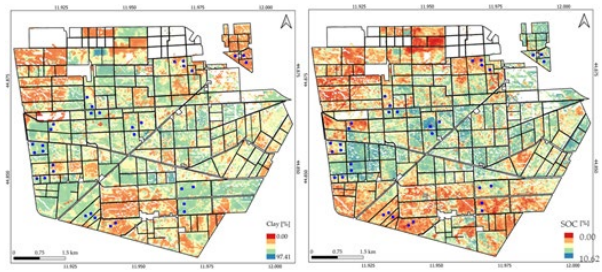

Figure 6 Mapping of clay (left) and soil organic carbon (right) on the Jolanda di Savoia farm from PRISMA using a multi-date approach

The Figure 6 shows the results of the mapping of topsoil properties obtained for the area of Jolanda of Savoia Bonifiche Ferraresi farm, using a multi-date approach.

The TEHRA project partners include Università degli Studi della Tuscia, Dipartimento di Scienze Agrarie e Forestali (UNITUS-DAFNE), e-GEOS, CNR-Istituto di Metodologie per Analisi Ambientale (IMAA) and the Tel Aviv University (TAU).
TEHRA is a useful project for developing methods and algorithms for the estimation of soil properties of agronomic and environmental interest from PRISMA satellite hyperspectral data, that could support: 1) the adoption of more sustainable and climate-smart farming practises, e.g. through the implementation of precision agriculture applications; 2) monitoring in support of agricultural and environmental policies, e.g. related to climate change and for the encouragement of the adoption of practices preserving soil health. TEHRA project contributes directly to the SDGs 12 and 13, indirectly to the SDGs 1 and 2.
TEHRA will span two years, starting from May 2022.

3. CONCLUSIONS

The main scope of the PRISMA SCIENZA programme, funded by ASI, is the use of PRISMA data for a wide range of research and applications, to foster the integrated use of PRISMA data in conjunction with data from other missions and sources,
This paper summarized the primary goals and activities of PRISMA SCIENZA programme mainly in the field of vegetation with agro-forest-sector analysis. As hyperspectral data contains rich features in the spectral domain, the vegetation monitoring is an important research field to explore the full capabilities of the PRISMA hyperspectral sensor, for example, testing new algorithms for feature selection, model and map specific vegetation characteristics, such as biophysical and biochemical quantities, monitor stress factors such as nitrogen deficiency, moisture deficiency, or drought conditions.
Numerous PRISMA SCIENZA projects, although they are in a preliminary stage, are demonstrating the added value provided by PRISMA data acquired ad hoc during the project activities lighting also the contribution that the exploitation of this data can provide to achieve some of the goals of the Agenda 2030. More in general, it is worth of mention, that all the projects included in this initiative provide also a contribution to SDG 4 (quality education) allowing to support training of specialist profiles.

REFERENCES

ASI website, 2022, PRISMA2G: siglato il contratto tra ASI e Thales Alenia Space, https://www.asi.it/2022/02/prisma2g-siglato-il-contratto-tra-agenzia-spaziale-italiana-e-thales-alenia-space-per-lavvio-della-fase-di-studio-destinata-allo-sviluppo-del-satellite-di-seconda-generazione/

Casa R., Bruno R., Falcioni V., Marrone L., Pascucci S., Pignatti S., Priori S., Rossi F., Tricomi A., and Guarini R., 2023. Topsoil properties estimation for agriculture from PRISMA: the TEHRA project. International Geoscience and Remote Sensing Symposium (IGARSS), Pasadena, California, 16 - 21 July.

Caporusso G., Lopinto E., Lorusso R., Loizzo R., Guarini R., Daraio M.G., Sacco P. (2020) The hyperspectral PRISMA mission in operations. Proc. IGARSS Conference, Waikoloa, HI, USA, 26 Sept.-2 Oct. 2020. DOI: 10.1109/IGARSS39084.2020.9323301.

Licciardi G.A., Guarini R., Battagliere M.L., Tapete D., Candela L., Coletta A., 2022. The Italian Space Agency satellite data exploitation programmes in support of the downstream sector, 73rd International Astronautical Congress (IAC), Paris, France, 18-22 September, IAC-22- B5.3.1 Page 1 of 6.

COMPARING LINE-OF-SIGHTS OF CURRENT SSO/MIO X-BAND SAR MISSIONS AT MID-LATITUDE AND RADAR CROSS SECTIONS OF QUAD-CORNER REFLECTORS

A. Parisi[1,2]*, D.O. Nitti[2], R. Nutricato[2], G. Preziosa[3], A. M. Loconsole[1], F. Prudenzano[1], C. Guaragnella[1]

[1] Department of of Electrical and Information Engineering, Polytechnic University of Bari, Italy
(alessandro.parisi, antonellamaria.loconsole, francesco.prudenzano, cataldo.guaragnella)@poliba.it
[2] Geophysical Applications Processing - GAP s.r.l., Bari, Italy
(alessandro.parisi, davide.nitti, raffaele.nutricato)@gapsrl.eu
[3] Department of Physics "Michelangelo Merlin", Polytechnic University of Bari, Italy - giovanni.preziosa@poliba.it

KEY WORDS: SAR, monostatic RCS, Quad-CR, X-Band, MIO, SSO

ABSTRACT: Artificial passive reflectors are often employed as stable radar targets in many Interferometric Synthetic Aperture Radar (InSAR) applications. Depending on the shape of radar targets, as well as on SAR satellite characteristics, the pointing satellite-to-target direction able to guarantee the best radar detectability can vary. As the matter of fact, Line-Of-Sight (LOS) projections of SAR missions depends on the latitude, as well as on the characteristics of SAR missions (e.g., satellite orbits, passes, antenna orientation, incidence angle). The present study aims at investigating the ability of the quad-corner reflector (quad-CR), which is a passive reflector able to backscatter the incident radar waves over a wide range of radar viewing angles in both elevation and azimuth, to operate as coherent radar target in InSAR application at mid-latitude considering LOS projections of currently operating X-Band SAR satellite missions. To do this, two steps have been carried out: 1) simulations of X-Band SAR missions to retrieve LOS projections for an area of interest located in Central Italy; 2) simulations in elevation and azimuth of radar backscattering of quad-CRs. As a results of such comparison, it emerges the capability of this radar target to ensure a good radar backscattering covering many LOS directions in accordance with currently operating X-Band SAR missions.

1. INTRODUCTION

In the field of Interferometric Synthetic Aperture Radar (InSAR), the absence of stable and coherent natural targets can pose a threat to the effectiveness of its application (Ferretti et al., 2001). Radar reflectors, which can be either active or passive, are designed to enhance the radar backscattering from the target to radar platforms. Their ability to backscatter radar signals is defined monostatic Radar Cross Section (RCS) expressed in dBsm, which represent one of the main parameter that characterizes a radar reflector (Knott, 1993). Considering X-Band applications, relatively compact passive radar reflectors can provide a significant monostatic RCS. As a result, passive radar reflectors are more employed in X-Band SAR applications than active ones due to their and low-cost and effectiveness in terms of construction and maintenance.

Depending on the installation latitude of radar target, as well as on the characteristics of SAR missions, such as satellite orbits and incidence angles, many satellite-to-target Line-Of-Sight (LOS) projections exist. Concerning on X-band SAR missions and regarding satellite orbits, they can be either Sun-Synchronous Orbit (SSO) or Mid-Inclination Orbit (MIO) depending on the inclination angle of the orbital plane. SSO orbits have inclinations slightly higher than 90 degrees, while MIO orbits are around 45 degrees. To whom regards to incidence angles, which represents the angle between the vertical line and the Satellite-to-Target LOS direction, it can vary according to many factors (e.g., SAR imaging mode, topographic variations). Moreover, LOS projections can differ by the satellite passes, which can be either ascending (asc) or descending (desc), and the orientation of SAR antenna, which can be only right-looking, only left-looking or both right- and left-looking.

In the light of the above and concerning currently operating X-Band SAR missions, this study aims at investigating LOS projections at mid-latitude in comparison with a radar reflector able to guarantee wide range of radar viewing angles in both elevation and azimuth, which is the quad-Corner Reflector (quad-CR) (Doerry, 2014). As known, depending on the shape of radar targets, the pointing target-to-satellite direction able to guarantee the best radar detectability can vary both in elevation and in azimuth. Among the more diffuse shape of artificial radar reflectors in InSAR application, there is the trihedral CR (Sarabandi & Tsen-Chieh Chiu, 1996). As the matter of fact, it has the ability to guarantee a good RCS targeting the backscattering in the desired direction with a good radar detectability, that is about 40° of both azimuth and elevation angles at -3 dBsm (Doerry, 2014). However, due to its shape, it is not able to cover more radar viewing angles. Thus, in the light of currently operating X-Band SAR missions and derived multiple LOS projections at the same installation latitude of radar target, it raises the need to install artificial reflectors, such as the quad-CR, able to guarantee a good radar detectability in more LOS directions with the same radar reflector. Moreover, as at mid-latitudes X-band SAR satellites with MIO orbits has LOS projections with a strong vertical (Up-Down) and horizontal (North-South) components, and ones with SSO orbits has LOS projections with a strong vertical (Up-Down) and horizontal (East-West) components, a 3D displacement vector can be obtained by the InSAR processing of LOS projections derived by SAR missions with both SSO and MIO orbits.

This study has been conducted with reference to an Area Of Interest (AOI) located in Central Italy (Rome, 41°54' latitude N) by simulating satellite orbits of currently operating X-band SAR missions with both SSO and MIO orbits. As a consequence, horizontal LOS projections have been derived at the selected latitude. Next, monostatic RCSs of quad-CRs with triangular plates have been simulated both in elevation and azimuth, while considering various geometric measures of base and height. The results of this comparison between LOS projections and monostatic RCSs of quad-CRs have been discussed highlighting their relevance in current InSAR applications.

* Corresponding author

2. MATERIALS AND METHODS

As already highlighted, this study provides a comparison between horizontal LOS projections derived by simulations of SSO/MIO orbit and RCS simulations of quad-CRs with triangular plates with different L/h ratios (Figure 1).

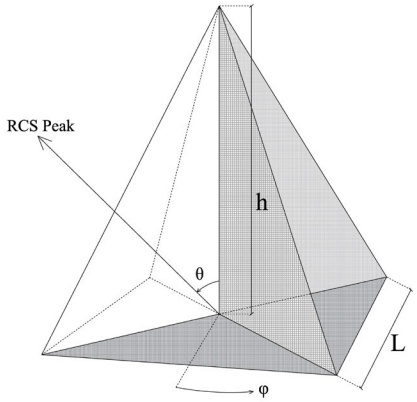

Figure 1: Simulated passive radar reflector: Quad-CR (h = height; L = base; φ = azimuth angle; θ = elevation/incidence angle).

Orbit simulations have been carried out through the software *Analytical Graphics, Inc. Satellite Tool Kit* (AGI-STK) considering orbit inclinations of currently operating X-Band SAR satellite missions (see Table 1). Reference values of orbit inclinations have been chosen among ones of currently operating SAR satellite missions:

- 97.4° for SSO orbits;
- 44° and 53°, respectively, for MIO orbits.

Table 1: Main currently operating and concluded(*) X-Band SAR satellite missions (source: www.eoportal.org).

Satellite mission	Orbit Inclination	Frequency (GHz)	Source
Capella-6	53.0° (MIO)	9.4 - 9.9	Capella Space (US)
Capella-7 and Capella-8	97.4° (SSO)		
Capella-9 and Capella-10	44.0° (MIO)		
Cosmo-SkyMed	97.86° (SSO)	9.60	Italian Space Agency
KOMPSAT-5	98.1° (SSO)	9.66	Korea Aerospace Research Institute
SAR-Lupe Constellation	98.2° (SSO)	9.65	German Ministry of Defence
SIR-C/X-SAR*	57° (MIO)	9.6	DLR, ASI, NASA-JPL
TerraSAR-X TanDEM-X	97.44° (SSO)	9.65	German Space Agency
UMBRA constellation	97.4° (SSO)	9.80	Umbra Space (US)
RISAT-2*	41° (MIO)	9.59	Indian Space Research Organisation
SEOSAR/Paz	97.44° (SSO)	9.65	Hisdesat (Spain)

Consequently, horizontal LOS projections of simulated SSO/MIO orbits have been derived with reference to the latitude of the AOI located in Central Italy (Rome, 41°54' latitude N). Regarding each horizontal LOS projection, figure 2 and table 2 show track angles, which represent the angles between the East direction and the projection on the ground of the Satellite-to-Target LOS direction, measured clockwise (Capes & Passera, 2022).

Table 2: Simulated track angles (measured clockwise with reference to the East) for X-Band SAR satellite missions with SSO and MIO orbits at the AOI latitude (A=asc; D=desc; R=right; L=left).

Orbit inclination	*Inclination*	*Passes*	*Look*	*LAT 41°54' Track angles (degrees)*
MIO	44°	A	R	-106
			L	74
		D	R	-74
			L	106
MIO	53°	A	R	-128
			L	52
		D	R	-52
			L	128
SSO	97.4°	A	R	167
			L	-13
		D	R	13
			L	-167

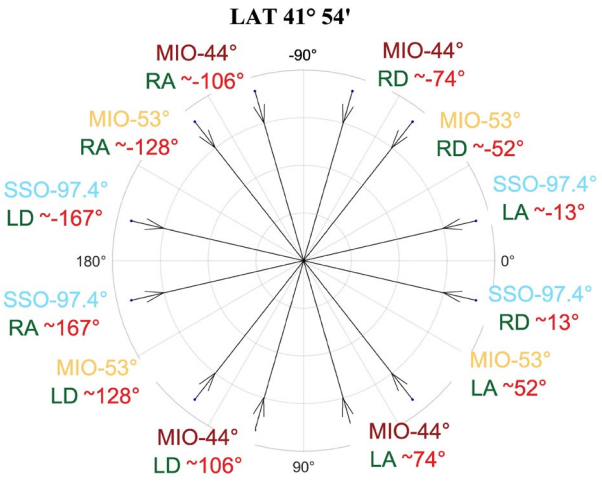

Figure 2: Horizontal LOS projections related to simulated SAR satellite missions operating with different orbit inclinations (SSO-97.4°, MIO-53° and MIO-44°) with reference to the AOI latitude (Rome, 41°54' latitude N). Track angles (measured clockwise with reference to the East) are in red (A=asc; D=desc; R=right; L=left).

The RCS simulations for quad-CRs with triangular plates have been carried out using a 3D electromagnetic software, specifically *CST Studio Suite*® (Dassault Systèmes, 2020). These simulations covered various viewing angles in both elevation (θ) and azimuth (φ). The selected reference frequency for these simulations is 9.66 GHz, in line with currently operating X-Band SAR missions (see Table 1).
A reference value of 38° has been chosen as reference incidence angle. It represents the average incidence angle of X-Band SAR

missions listed in Table 1. It is worth noting that incidence angles in these missions may vary between 10° and 70°.
Monostatic RCS simulations have been performed for quad-CRs varying the L/h ratios, which permits the precise vertical targeting of the RCS peak. Monostatic RCS simulations of quad-CR with various L/h ratios have been carried out in both elevation (at 1° intervals for θ ranging from 0° to 90°) and azimuth (at 1° intervals for φ ranging from 0° to 360°).

3. RESULTS AND DISCUSSION

Figure 3 depicts the results of RCS simulations for quad-CRs with various L/h ratios. It illustrates the incidence angles, measured with reference to the Zenith, associated with peak RCS as the L/h ratio varies. Moreover, it shows the vertical variation of radar detectability, considered as -3 dBsm (Corenman et al., 1995), when the L/h ratio of quad-CRs changes.

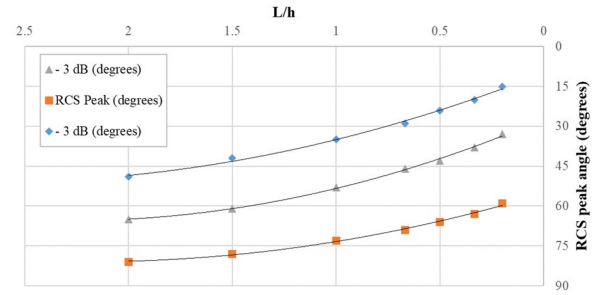

Figure 3: Incidence angles (see figure 1) and radar detectability (-3 dBsm) related to peak RCS of simulated quad-CRs with various L/h ratios.

It emerges that as the ratio between the base (L) and the height (h) (L/h) decreases, which means increasing the height of the quad-CR relative to the base L, the incidence angle related to the peak RCS shifts vertically towards sharper angles. When the L/h ratio is 1, the angle associated with the peak RCS is approximately 54°, whereas the angle is ~38°, which corresponds to the reference incidence angle considered in this case study, when the L/h ratio is 1/3. Moreover, it arises that by decreasing the L/h ratio of the quad-CR, there is a slight increase in vertical radar detectability, which changes from approximately 32° for an L/h ratio of 0.5 to values of about 44° with a ratio of 0.2. In particular, for L/h = 1, vertical radar detectability is approximately 38°, while for L/h = 1/3, it is about 43°.
Considering a quad-CR with a L/h ratio equal to 1/3 (#quad-CR1), which target the RCS peak in the desired vertical direction (~38°), figure 4 shows the horizontal RCS values in comparison with the horizontal LOS projections derived by simulations of SSO/MIO orbits at the selected AOI latitude in Central Italy (Rome, 41°54' latitude N). Figure 4 even shows the width of the main lobe (-3 dBsm) that represents the reference value of the radar detectability (Corenman et al., 1995). Radar detectability of #quad-CR1 with reference to ~38° as incidence angle is approximately 176° represented by four main lobes of ~44° symmetrically and mirror-like oriented, which means roughly 49% of the overall φ.
When comparing LOS projections of SSO/MIO orbits with reference to the AOI latitude and the RCS simulation of the #quad-CR1, the best orientation of this radar reflector results 0° North in the horizontal plane. The selected orientation effectively guarantees a good RCS to LOS projections with strong E-W and N-S components targeting SSO-97.4° (losing approximately 0.6 dBsm with reference to the peak RCS) and MIO-44° orbits (losing about 1.2 dBsm with reference to the peak RCS).
As shown in figure 4, LOS projections related to MIO-53° are not targeted. As it is sufficient to cover only one LOS projection with a strong N-S component (in this case LOS projections related to MIO-44°) for any 3D displacement-related InSAR analysis, this does not result as a limiting factor.
Thus, the #quad-CR1 demonstrates its ability to be employed as coherent radar target in InSAR processing related to both SSO and MIO orbits, attempting to the assessment of the 3D vector related to land displacement.
To improve horizontal radar detectability by expanding the azimuth angle coverage and consequently increasing the likelihood of targeting more LOS projections, it is necessary to raise the L/h ratio.

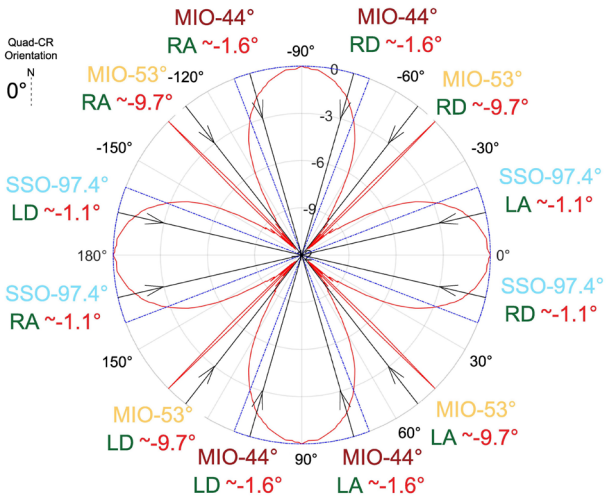

Figure 4: Comparison between the horizontal monostatic RCS of quad-CR with L/h =1/3 - #quad-CR1 (in red RCS with reference to peak RCS), radar detectability (in blue), and LOS projections of simulated SSO/MIO orbits (in black).

Figure 5 displays the horizontal monostatic RCS considering a quad-CR with a L/h ratio equal to 1 (#quad-CR2) with reference to an incidence angle of ~38°. It is worth noting that RCS values are reported with reference to the relative peak RCS at ~38°, as the absolute peak RCS occurs at ~54° and is higher (+2 dBsm) than the relative RCS peak. As shown, radar detectability of #quad-CR2 with reference to ~38° as incidence angle increases with respect to the #quad-CR1. As the matter of fact, radar detectability is approximately 204° with four main lobes of ~51°, which means around 57% of the overall φ. However, it has a slight reduction in radar detectability in elevation, approximately by 5° (Figure 3).
Although there is an increase of about 7° per main lobe for a total gain of about 28°, which increases the overall azimuth coverage of the quad-CR, as in the previous case (Figure 4) the coverage of the overall LOS projections related to the considered SSO and MIO orbits is unchanged at the AOI latitude. Moreover, in this case it is important to keep in mind that the #quad-CR2 should be sized considering the loss of 2 dBsm due to the difference between the absolute and relative RCS peaks.
However, in the field of InSAR processing, these radar targets are built to be installed in contexts such as slopes and buildings. Thus, radar reflectors with a lower L/h ratio (#quad-CR2) can be preferred because it results less bulky, as well as it can have

a good stability and a lower sail effect with regard to wind action.

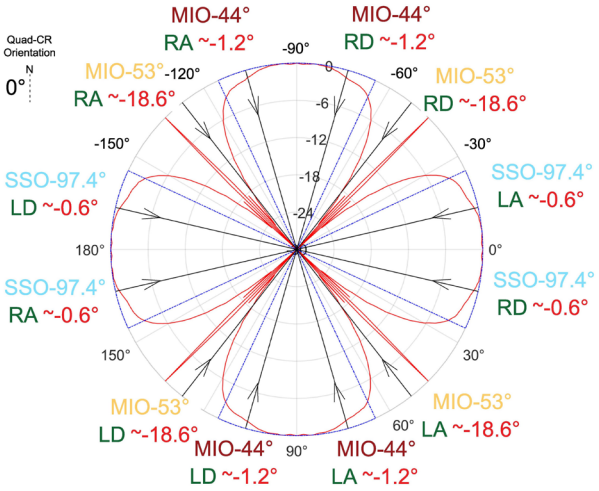

Figure 5: Comparison between horizontal monostatic RCS of quad-CR with L/h =1 (in red relative RCS), radar detectability (in blue), and LOS projections of simulated SSO/MIO orbits (in black).

4. CONCLUDING REMARKS

This work aims at investigating the ability of the quad-CR to operate as coherent radar target in InSAR application considering LOS projections of currently operating X-Band SAR missions with reference to an AOI located in central Italy. As a result, the main aspects related to the installation of quad-CRs in comparison with simulated LOS projections of currently operating X-Band SAR missions with SSO/MIO orbits at the reference latitude (Rome, 41°54' latitude N) have been shown.

First of all, quad-CR results as an easy-to-install radar target, requiring only a horizontal plane and a horizontal installation angle. It is also capable to cover more horizontal directions if compared with a classic trihedral CR. As the matter of fact, quad-CR has four main lobes of more than 40° symmetrically and mirror-like oriented, which means approximately 50% of the overall azimuth (φ) angles, whereas the trihedral CR has only one lobe of about 40° in both elevation and azimuth. Thus, quad-CR demonstrates its ability to cover more LOS projections at the same location derived by many SSO and MIO orbits attempting to the assessment of the 3D vector of land displacement. Moreover, due to its shape, quad-CR has the same phase centre that is independent from LOS directions.

Then, the present work shows the results of RCS simulations with regards to a reference incidence angle (38°) derived by currently operating X-Band SAR missions. RCS simulations have been carried out considering quad-CRs with many L/h ratios, in particular showing advantages and disadvantages while considering a quad-CR with a L/h ratio equal to 1/3 (#quad-CR1), as well as one with a symmetrical structure (L/h = 1 - #quad-CR2).

As a result of such comparison, it emerges that #quad-CR1 is able to target the peak RCS in the desired incidence/elevation angle with a good horizontal radar detectability (~176°) and a vertical radar detectability (~43°) greater than one of #quad-CR2 (~38°). However, with reference to the horizontal radar detectability, #quad-CR2 has a greater radar detectability (~204°). Moreover, it is less bulky than #quad-CR1, as well as it can have a good stability and a lower sail effect with regard to wind action. In the light of the above, #quad-CR2 seems to be more effective than #quad-CR1. It is worth noting that #quad-CR2 has to be sized correctly considering the loss of RCS due to the difference between the relative and the absolute RCS peak, which is about 2 dBsm.

ACKNOWLEDGEMENTS

This work has been carried out in the in the framework of the Project “Monitoraggio di spostamenti con transponder RADAR” granted by the Regional Government of Puglia Region, RIPARTI project number 2a171b1e, POC PUGLIA FESRT-FSE 2014/2020.

REFERENCES

Capes, R., & Passera, E. (2022). *End-to-end implementation and operation of the European Ground Motion Service (EGMS). Product Description and Format Specification*. https://land.copernicus.eu/user-corner/technical-library/egms-product-description-document

Corenman, J., Hawley, C., Honey, D., & Honey, S. (1995). *Radar Reflector Tests*. www.ussailing.org/wp-content/uploads/2018/03/radar-reflector-tests.pdf

Dassault Systèmes. (2020). *CST Studio Suite High Frequency Simulation (Version 2020.0 - 8/16/2019)*.

Doerry, A. W. (2014). Reflectors for SAR Performance Testing. In *Sandia Report SAND2008-0396*. http://www.ggki.hu/~banyai/Reflectorok/reflector080396.pdf

Ferretti, A., Prati, C., & Rocca, F. (2001). Permanent scatterers in SAR interferometry. *IEEE Transactions on Geoscience and Remote Sensing*, *39*(1), 8–20. https://doi.org/10.1109/36.898661

Knott, E. F. (1993). *Radar Cross Section Measurements* (Vol. 1990, Issue 2). Springer US. https://doi.org/10.1007/978-1-4684-9904-9

Sarabandi, K., & Tsen-Chieh Chiu. (1996). Optimum corner reflectors for calibration of imaging radars. *IEEE Transactions on Antennas and Propagation*, *44*(10), 1348–1361. https://doi.org/10.1109/8.537329

ASSESSMENT OF LINEAR INFRASTRUCTURE DEFORMATION USING EGMS-INSAR DATA AND GEOENVIRONMENTAL FACTORS THROUGH MACHINE LEARNING: RAILWAYS AND HIGHWAYS OF LOMBARDY REGION, ITALY

R. Eskandari *, M. Scaioni , Z. Wang

Dept. of Architecture, Built Environment and Construction Engineering, Politecnico di Milano, via Ponzio 31, 20133 Milano, Italy
(rasoul.eskandari; marco.scaioni; ziyang.wang)@mail.polimi.it

KEY WORDS: Ground Deformation, Geo-Environmental Factors, Synthetic Aperture Radar Interferometry (InSAR), European Ground Motion Service (EGMS), Machine Learning, Linear Infrastructure

ABSTRACT:

Assessment and monitoring of deformations imposed on principal linear infrastructures by natural and man-made factors and addressing the phenomenon play an important role in the management of these assets and support decision-making policies in the context of risk management and mitigation. This study utilizes a Machine Learning (ML) approach for deformation analysis of highways and railways of the Lombardy region, Italy, by combining the deformations derived from InSAR analysis and geo-environmental characteristics. The vertical displacement velocities (mm/year) extracted from European Ground Motion Service (EGMS) datasets covering these infrastructures are utilized as the target input deformation data. The conditioning features considered in this work include elevation, slope angle, slope aspect, precipitation, curvature, solar radiation, and Normalized Difference Vegetation Index (NDVI). Several ML models with different characteristics have been exploited, including Decision Tree (DT), Linear regression (LR), Light GBM (LG), XGBoost (XG), Random Forest (RF) and Extra Trees (ET). After evaluating the accuracy of the trained models (using Receiver Operating Characteristic (ROC) and Spearman criteria), the cause-effect relationship has been established and the major triggering factors have been detected (using SHapley Additive exPlanations (SHAP) and Permutation Feature Importance (PFI)). The results showed that XG, RF and ET are respectively the most accurate models for this type of analysis. Also, it has been seen that rainfall is the most influencing cause of the detected deformation, together with the high importance of Elevation for highways and Solar radiation for railways.

1. INTRODUCTION

Linear Infrastructures, characterized by a high level of systemic vulnerability (Hellström, 2007; Penny et al., 2018), are subject to several environmental and geological hazards. In the context of risk assessment and management, monitoring these important assets plays an important role in establishing maintenance planning and preventive measures against disruptive phenomena, such as ground deformation due to natural and anthropogenic causes. In-situ and traditional infrastructure monitoring approaches, such as high-precision levelling measurements (Sevil et al., 2021), are known to be costly and time-consuming. On the other hand, satellite Remote Sensing (RS) techniques, such as Synthetic Aperture Radar (SAR) Interferometry (InSAR), are recognized to be promising tools for monitoring and condition assessment of infrastructures (Macchiarulo et al., 2022).

As an essential branch of the Copernicus Land Monitoring Service (CLMS), the European Ground Motion Service (EGMS) provides freely accessible ground deformation data spatially covering almost all European countries. The deformation time time-series contained in the datapoints are acquired based on InSAR processing of Sentinel-1 images from Jan 2016 to Dec 2021 and from Jan 2018 to Dec 2022 in first and second updates, respectively (up to the publication date of this work) (Crosetto et al., 2020; Costantini et al., 2022). The dataset has been successfully used in several cases such as deformation analysis of critical linear infrastructures (Eskandari and Scaioni, 2023) and other applications (Crosetto and Solari, 2023).

The Lombardy region is well-known to be prone to serious hydrogeological hazards, such as landslides, particularly during heavy rains and snow melts, which can cause damage to the infrastructure (Antonielli et al., 2019). Being located in a seismically active area, and the highways passing through several zones that are at risk of earthquakes(Garbin and Priolo, 2013), can pose a risk to the stability of the infrastructure such as bridges and tunnels. High groundwater level and soil instability is an ordinary condition in the region, causing ground settlements (Gattinoni and Scesi, 2017; Ikuemonisan et al., 2021). These conditions would result in displacement on the infrastructures, particularly in areas where the soil is composed of soft or poorly compacted material.

In this study, InSAR-derived deformation dataset detected on and nearby of the principal linear infrastructures, geo-environmental parameters, and Machine Learning (ML) techniques have been integrated to address the major causes of this complex phenomenon, specifically emphasizing railway and highway in Lombardy region, Italy. The study provides a well-stablished insight on the appropriate ML models to be used for this type of analysis (by careful evaluation of the accuracy of the models) and ground deformation-triggering factors for the principal linear infrastructures in the region (by utilizing reliable feature importance detection algorithms).

2. MATERIAL AND METHOD

This work targets the highways (as the principal roads) and railways of Lombardy region, North of Italy, to search for the major causes of deformation imposed to these linear infrastructures. In this section, the inputs used for the general analysis, the Machine Learning (ML) techniques, and the performed analyses to evaluate the ML techniques and address the major factors are described. Figure 1 show the overall workflow of this work.

* Corresponding author

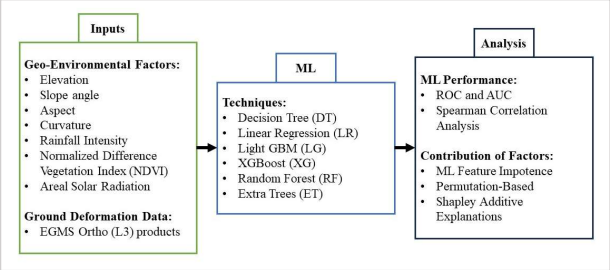

Figure 1. The general workflow adopted in this work.

2.1 Inputs

The geo-environmental input of this analysis is composed of Elevation (derived from $20m \times 20m$ Digital Elevation Model (DTM) of Lombardy region), slope angle, slope aspect, curvature (these last three are obtained through spatial analysis of DTM), rainfall, Normalized Difference Vegetation Index (NDVI) (spatial resolution of $300m$ from Copernicus Global Land Service) and solar radiation, to be correlated with vertical ground deformation rate [mm/year] from Ortho (L3) products of EGMS dataset, detected on these linear assets by Sentinel-1 InSAR analysis. EGMS L3 products provide valuable information on the vertical (up-down) and horizontal (east-west) deformations by using the Line of Sight (LOS) measurements (considering both ascending and descending satellite orbit tracks) of GNSS-calibrated InSAR measurements from European Space Agency (ESA) Sentinel-1 mission. The calibrated and processed Sentinel-1 datapoints (L2B products) have been downsampled on a uniform grid $100m$ spatial resolution to form L3 products. Therefore, the L3 datapoints used in this study, covering the highways and railways, may contain deformation information from a small neighbourhood surrounding the assets.

2.2 Machine Learning Approach

In order to establish the relationship between the geo-environmental factors (features) and vertical ground deformation (target) of railways and highways, multiple machine learning techniques with different characteristics are exploited in this study, including Decision Tree (DT), Linear Regression (LR), Light GBM (LG), XGBoost (XG), Random Forest (RF) and Extra Trees (ET) (interested readers may refer to these work for more information and application of the models (Mahesh, 2020; Shehadeh et al., 2021; Shebl et al., 2023)). It should be noted that the Train-Validation ratio is 7:3 for all the training operations, and the reason for this selection is the higher performance of this ratio (Nguyen et al., 2021) for this type of analysis.
Concerning DT and ET methods, it is suggested not to be used when a strong relationship exists among the conditioning factors. One effective way to check this condition is to use multi-collinearity analysis, which serves as a crucial operation in data preprocessing, particularly in ground deformation analyses. In this study, to perform multi-collinearity analysis and evaluation of inter-factor relationships, tolerance (TOL) and variance inflation factor (VIF) parameters are used as the reciprocals.

2.3 Performance and Importance Analyses

In machine learning, the Receiver Operating Characteristic (ROC) curve is a graph showing the performance of a classification model at all classification thresholds. To compute the points in an ROC curve, it is possible to evaluate a logistic regression model many times with different classification thresholds, but this would be inefficient. Fortunately, there's an efficient, sorting-based algorithm that can provide this information, called Area under the ROC Curve (AUC). Theoretically, the ROC curve and AUC based on the validation dataset are known as the predictive rate curve (Hong et al., 2015; Tacconi Stefanelli et al., 2020).
Besides AUC, the Spearman rank correlation coefficient is used to evaluate the inter-correlation between the ML Models in terms of the obtained results. The coefficient, ranging between 0 and 1, is a statistical measure used to evaluate the strength and direction of the monotonic relationship between two variables (Xiao et al., 2016). It is often used to compare the performance of machine learning models by calculating the correlation between the predicted values and the actual values. A higher correlation indicates a better fit between the predicted and actual values and thus a more accurate model (Ali et al., 2017).
After evaluating the performance and reliability of ML models, it is crucial to assess the contribution of each conditioning factor (features) in the established model for each model. The operation involves identifying the relative importance (global impact) of each feature used in a predictive model, in terms of its contribution to the overall accuracy of the model. It allows for determining which features are the most relevant for predicting the target variable and gaining insights into the underlying relationships and patterns in the data, with a high potential to be particularly useful for understanding complex models. Among the variety of simple to complex methods for feature importance analysis, two well-known techniques are used which are described in the following (Scavuzzo et al., 2022; Kaneko, 2022):

- SHapley Additive exPlanations (SHAP): the algorithm utilizes a game theory-based method that measures the contribution of each feature to the model's prediction for a particular data point. It computes the average impact of each feature across all possible combinations of features and assigns a score to each feature based on its contribution to the model's output.
- Permutation Feature Importance (PFI): the method involves shuffling the values of each feature in the dataset and measuring the effect on the model's performance. The higher the drop in performance after shuffling a feature, the more important that feature is considered to be.

3. RESULTS

As the first data analysis to check the suitability of the factors for DT and ET methods, the multi-collinearity analysis results are reported in Table 1. A TOL value greater than 0.1 typically indicates independence of the factor under examination from the other factors (Shang et al., 2023), and as indicated in the results, it can be understood that the data are appropriate to be fed to algorithms.

Table 1. Multi-collinearity results

Factors	highway		railway	
	TOL	VIF	TOL	VIF
Elevation	0.281	3.556	0.272	3.678
Slope	0.645	1.551	0.311	3.219
Aspect	0.994	1.006	0.993	1.008
Curvature	0.983	1.017	0.997	1.003
Solar radiation	0.651	1.537	0.744	1.344
Rainfall	0.293	3.417	0.570	1.754
NDVI	0.978	1.023	0.899	1.113

3.1 ML Performance

Table 2 lists the Area Under ROC Curve (AUC) values for different ML models (considering both highway and railway cases). In general, it has been shown that an AUC of 0.5 suggests no discrimination, 0.7 to 0.8 is considered acceptable, 0.8 to 0.9 is considered excellent, and more than 0.9 is considered outstanding. As it can be understood from Table 1, after the XgBoost model that has the best performance (acceptable for highways and excellent for railways), RF and ET show better accuracy, respectively, than other models. It should be noted that, in general, the performance for the railway network is always better than the case of the highway, which announces the better correlation between geo-environmental factors and ground deformation phenomena related to railways. It may be related to the better backscattering properties of railway networks (than highways,
mostly built from asphalt), and consequently, more accurate InSAR-derived deformations on these assets.
Figure 2 shows the matrix of Spearman rank correlation coefficient values of models for both cases of highway and railway networks. Here, again, the best intercorrelation can be seen among XG, RF and ET for both cases, and the overall higher performance for the railway networks is obvious. LR model shows a reasonable correlation with the above-mentioned three models in terms of the final output of the model, which enhances the consistency between the outcomes of Table 2 and Figure 2. The ensembles model is also considered here which is a weighted combo of XG and RF models (weights of 5 and 1, and weights of 2 and 1 for highway and railway cases, respectively).

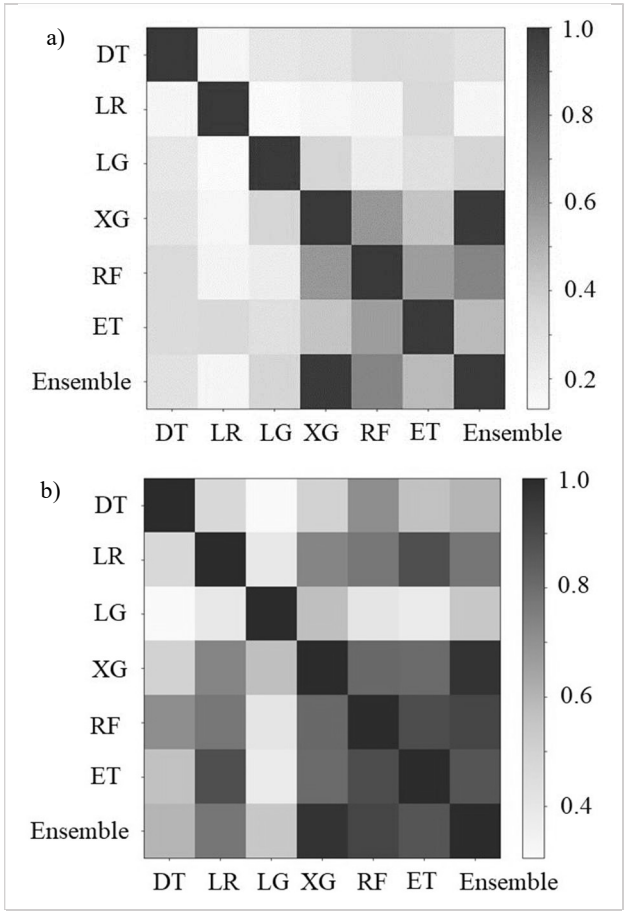

Figure 2. Spearman rank correlation coefficient values for a) highways and b) railways

Table 2. AUC value for the ML models

Models	highway	railway
Decision Tree	0.50	0.73
Linear Regression	0.60	0.76
LightGBM	0.70	0.72
XgBoost	0.78	0.80
Random Forest	0.77	0.78
ExtraTrees	0.73	0.78

3.2 Factor Importance Analysis

This section presents the results of the crucial step of feature (factor) importance. This enables to identify the condition factors having more correlation with the ground deformation occurrence to the linear infrastructure, according to the decision made by each model after the training. Figure 3 illustrate the global relative feature importance detected by Auto ML toolbox of ArcGIS Pro software for each ML model for both railway and highways. For highways, rainfall and elevation are selected to be the most affecting factors by the set of, in the order of importance, [XG, ET, LF, RF] and [LG, DTLR, XG], respectively. NDVI and slope angle are identified to be the next affecting factors, detected by both XG and LG models. On the other hand, almost all the models agree with the high importance of rainfall intensity in

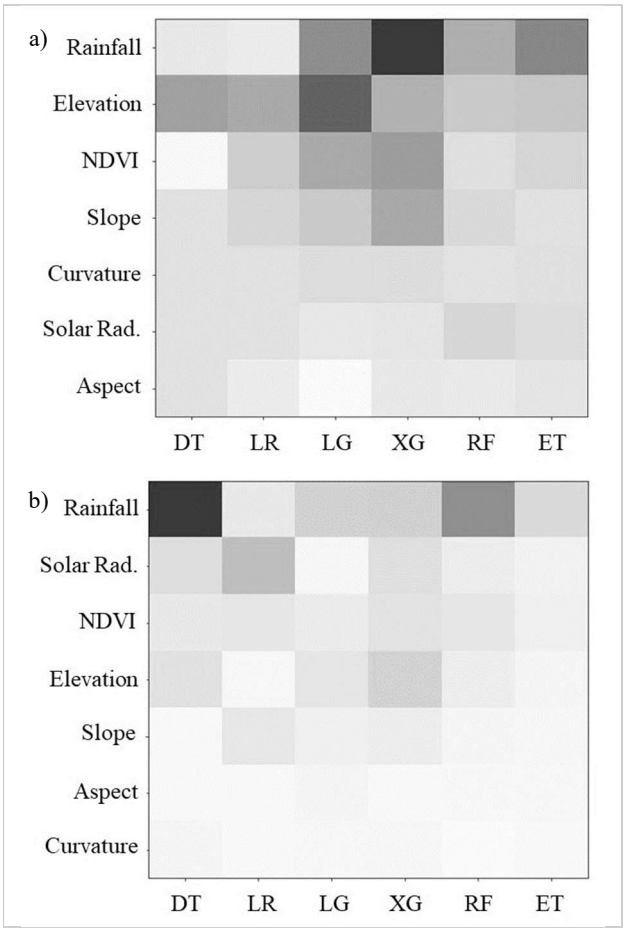

Figure 3. Global relative feature importance according to each ML model by Auto ML toolbox of ArcGIS Pro for a) highways and b) railways

terms of the correlation with ground deformations imposed on railways, with solar radiation and elevation ranked as the subsequent influencing factors identified by LR and XG, respectively. The rank rising of Solar radiation (from highway to railway) and the almost neutral effect of aspect and curvature can be of interest in this analysis.

Regarding SHAP and PFI criteria, Table 3 summarizes the results in terms of the detection of the most affecting factors. PFI agrees with the findings from Figure 3 concerning the very high importance of combined rainfall-elevation for highways and rainfall for railways. SHAP detects the single rainfall intensity factor (for all the ML models) as the most affecting feature in the case of highways, which neglects the effect of elevation, NDVI and slope (compared to Figure 3 and PFI outcomes). However, for the railway case, the effect of solar radiation and NDVI is detected besides the high importance of rainfall. It is worth noting that the overall identification of rainfall intensity by this study, as the main triggering factor for ground deformations imposed on critical linear infrastructures in the Lombardy region, coincides with the results of the other studies regarding the major cause of land surface displacements in the region.

Table 3. Most affecting factors detected by SHAP and PFI

	PFI		SHAP	
Model	highway	railway	highway	railway
DT	elevation	rainfall	rainfall	rainfall
LR	elevation	solar rad.	rainfall	solar rad.
LG	elevation	rainfall	rainfall	NDVI
XG	rainfall	rainfall	rainfall	solar rad.
RF	rainfall	rainfall	rainfall	rainfall
ET	rainfall	rainfall	rainfall	rainfall

4. CONCLUSION

The study takes advantage of the machine learning approach to correlate the geo-environmental factors with the displacements imposed on the critical linear infrastructures of the Lombardy region, Italy. The principal outcomes of this work can be summarized below:

- For Highway and Railway assessment and addressing the major causes of deformations, the ML models of XgBoost, Random Forest, and Extra Trees show the best performance and prediction accuracy.
- Rainfall intensity is the major cause of the deformation occurring to Railways and Highways in the Lombardy region. Elevation, Normalized Difference Vegetation Index, and Areal Solar Radiation are the other factors most affecting linear infrastructures in terms of deformation.

Taking advantage of freely available and downsampled EGMS L3 products and simple machine learning approaches, this study significantly contributes to the understanding of ground deformations imposed on linear infrastructures in the Lombardy region and the leading factors causing this phenomenon. However, it is expected that using advanced networks (such as Deep learning approaches) together with other InSAR products with higher spatial resolution (such as EGMS L2B datasets) may provide a more detailed and deeper comprehension of the field, particularly for localized phenomena, which will be aimed at the future studies.

5. REFERENCES

Ali, R., Lee, S.,Chung, T. C., 2017. Accurate multi-criteria decision making methodology for recommending machine learning algorithm. Expert Systems with Applications, 71, 257-278.

Antonielli, B., Mazzanti, P., Rocca, A., Bozzano, F.,Dei Cas, L.: A-DInSAR Performance for Updating Landslide Inventory in Mountain Areas: An Example from Lombardy Region (Italy), 10.3390/geosciences9090364, 2019.

Costantini, M., Minati, F., Trillo, F., Ferretti, A., Passera, E., Rucci, A., Dehls, J., Larsen, Y., Marinkovic, P., Eineder, M., Brcic, R., Siegmund, R., Kotzerke, P., Kenyeres, A., Costantini, V., Proietti, S., Solari, L.,Andersen, H. S., 2022. EGMS: Europe-Wide Ground Motion Monitoring based on Full Resolution Insar Processing of All Sentinel-1 Acquisitions. Proceedings IGARSS 2022 - 2022 IEEE International Geoscience and Remote Sensing Symposium, 5093-5096.

Crosetto, M.,Solari, L., 2023: Satellite Interferometry Data Interpretation and Exploitation: Case Studies from the European Ground Motion Service (EGMS). Elsevier.

Crosetto, M., Solari, L., Balasis-Levinsen, J., Casagli, N., Frei, M., Oyen, A.,Moldestad, D. A., 2020. Ground deformation monitoring at continental scale: the European ground motion service. The International Archives of Photogrammetry, Remote Sensing and Spatial Information Sciences, 43, 293-298.

Eskandari, R.,Scaioni, M., 2023. EUROPEAN GROUND MOTION SERVICE FOR BRIDGE MONITORING: TEMPORAL AND THERMAL DEFORMATION CROSS-CHECK USING COSMO-SKYMED INSAR. Int. Arch. Photogramm. Remote Sens. Spatial Inf. Sci., XLVIII-1/W2-2023, 1235-1241.

Garbin, M.,Priolo, E., 2013. Seismic Event Recognition in the Trentino Area (Italy): Performance Analysis of a New Semiautomatic System. Seismological Research Letters, 84, 65-74.

Gattinoni, P.,Scesi, L., 2017. The groundwater rise in the urban area of Milan (Italy) and its interactions with underground structures and infrastructures. Tunnelling and Underground Space Technology, 62, 103-114.

Hellström, T., 2007. Critical infrastructure and systemic vulnerability: Towards a planning framework. Safety Science, 45, 415-430.

Hong, H., Pradhan, B., Jebur, M. N., Bui, D. T., Xu, C.,Akgun, A., 2015. Spatial prediction of landslide hazard at the Luxi area (China) using support vector machines. Environmental Earth Sciences, 75, 40.

Ikuemonisan, F. E., Ozebo, V. C.,Olatinsu, O. B., 2021. Investigating and modelling ground settlement response to groundwater dynamic variation in parts of Lagos using space-based retrievals. Solid Earth Sciences, 6, 95-110.

Kaneko, H., 2022. Cross-validated permutation feature importance considering correlation between features. Analytical Science Advances, 3, 278-287.

Macchiarulo, V., Milillo, P., Blenkinsopp, C., Reale, C.,Giardina, G., 2022. Multi-temporal InSAR for transport infrastructure monitoring: recent trends and challenges. Proceedings of the Institution of Civil Engineers – Bridge Engineering, 1-26.

Mahesh, B., 2020. Machine learning algorithms-a review. International Journal of Science and Research (IJSR).[Internet], 9, 381-386.

Nguyen, Q. H., Ly, H.-B., Ho, L. S., Al-Ansari, N., Le, H. V., Tran, V. Q., Prakash, I.,Pham, B. T., 2021. Influence of Data Splitting on Performance of Machine Learning Models in Prediction of Shear Strength of Soil. Mathematical Problems in Engineering, 2021, 4832864.

Penny, D., Zachreson, C., Fletcher, R., Lau, D., Lizier, J. T., Fischer, N., Evans, D., Pottier, C.,Prokopenko, M., 2018. The demise of Angkor: Systemic vulnerability of urban infrastructure to climatic variations. 4, eaau4029.

Scavuzzo, C. M., Scavuzzo, J. M., Campero, M. N., Anegagrie, M., Aramendia, A. A., Benito, A.,Periago, V., 2022. Feature importance: Opening a soil-transmitted helminth machine learning model via SHAP. Infectious Disease Modelling, 7, 262-276.

Sevil, J., Benito-Calvo, A.,Gutiérrez, F., 2021. Sinkhole subsidence monitoring combining terrestrial laser scanner and high-precision levelling. 46, 1431-1444.

Shang, H., Su, L., Chen, W., Tsangaratos, P., Ilia, I., Liu, S., Cui, S.,Duan, Z.: Spatial Prediction of Landslide Susceptibility Using Logistic Regression (LR), Functional Trees (FTs), and Random Subspace Functional Trees (RSFTs) for Pengyang County, China, 10.3390/rs15204952, 2023.

Shebl, A., Abriha, D., Fahil, A. S., El-Dokouny, H. A., Elrasheed, A. A.,Csámer, Á., 2023. PRISMA hyperspectral data for lithological mapping in the Egyptian Eastern Desert: Evaluating the support vector machine, random forest, and XG boost machine learning algorithms. Ore Geology Reviews, 161, 105652.

Shehadeh, A., Alshboul, O., Al Mamlook, R. E.,Hamedat, O., 2021. Machine learning models for predicting the residual value of heavy construction equipment: An evaluation of modified decision tree, LightGBM, and XGBoost regression. Automation in Construction, 129, 103827.

Tacconi Stefanelli, C., Casagli, N.,Catani, F., 2020. Landslide damming hazard susceptibility maps: a new GIS-based procedure for risk management. Landslides, 17, 1635-1648.

Xiao, C., Ye, J., Esteves, R. M.,Rong, C., 2016. Using Spearman's correlation coefficients for exploratory data analysis on big dataset. Concurrency and Computation: Practice and Experience, 28, 3866-3878.

IMPROVE SENTINEL-2 TIME SERIES CONSISTENCY WITH S2SDB DATABASE FOR OPERATIONAL IMAGE CO-REGISTRATION

F. Filipponi *

CNR - Italian National Research Council, Institute of Environmental Geology and Geoengineering (IGAG), Italy
(formerly: ISPRA – Istituto Superiore per la Protezione e la Ricerca Ambientale, Italy) (federico.filipponi@cnr.it)

KEY WORDS: Sentinel-2 MSI, co-registration, AROSICS, S2SDB

ABSTRACT:

Copernicus Sentinel-2 MSI satellite data exhibit variable geolocation spatial accuracy, resulting in a weak spatial coherence that significantly affect time series consistency at pixel level. Although the evolution of Sentinel-2 MSI processing baselines aims, among other objectives, to improve image co-registration with respect to a Global Reference Image (GRI), geospatial accuracy is still not adequate for detailed time series analysis.
To undertake operational image co-registration, Sentinel-2 Shift DataBase (S2SDB) has been established. The S2SDB contains information about horizontal linear local shifts, generated using AROSICS software, which can be easily applied to any Sentinel-2 MSI spectral band or spatially explicit derived products, using various image processing software solutions. The DataBase, by releasing simple but relevant information with an open access data policy, can contribute to reduce time and computational effort required to significantly improve spatial coherence and time series consistency of Sentinel-2 MSI imagery.

1. INTRODUCTION

Copernicus Sentinel-2 satellite constellation allows to sense Earth surface at high spatial and spectral resolution and its high revisit frequency foster new advances for land monitoring capacity. Sentinel-2 MSI data exhibit variable geolocation spatial accuracy, resulting in a weak spatial coherence that significantly affect time series consistency at pixel level. Despite evolving Sentinel-2 MSI processing baselines aims, among other objectives, to improve image co-registration with respect to a Global Reference Image (GRI), geospatial accuracy is still not adequate for detailed time series analysis. The release of the GRI has been repeatedly delayed, re-processing of past Sentinel-2 MSI data is currently not planned, and the expected global geo-registration accuracy needs to be confirmed in an operational setting (Rufin et al., 2020).
Here comes the need to provide users with an effective tool to perform fast and effective co-registration of Sentinel-2 MSI acquisitions over time, improving spatial coherence and time series consistency.
Global co-registration algorithms, which identify horizontal linear shift to be applied to all image pixels, include area-based methods, feature-based approaches, integration of feature-based and area-based least squares matching on hierarchical layers (LSReg) (Yan et al., 2016). Characteristic Sentinel-2 MSI co-registration error patterns, in the form of block-like error clusters, follow the flight line direction and are likely also related to the individual detector arrays and with the sensor orbit track and movements in space" (Scheffler et al., 2017). Since Sentinel-2 MSI temporal co-registration is not consistent throughout the entire image, identification of multiple horizontal linear shifts for a single image is required. Local co-registration algorithms, that allow to identify horizontal linear shifts for a set of tie-points, include two-dimensional sub-pixel disparity measurement algorithm based on block matching (QPEC / Medicis) (Cournet et al., 2016), and phase correlation for sub-pixel shift estimation in the frequency domain utilizing the Fourier shift theorem (Scheffler et al., 2017).
Methodologies to quantify image shifts, developed in recent years, require considerable computational effort to effectively co-register satellite acquisition time series.
To undertake operational image co-registration, a DataBase containing simple but relevant information about horizontal linear local shifts, that can be easily applied to any Sentinel-2 MSI spectral band or spatially explicit derived product using various image processing software solutions, can represent a valuable tool.
Objectives of the presented initiative are: i) generate Sentinel-2 MSI local Shifts DataBase (S2SDB) for operational image co-registration, over Italian national territory; ii) report and discuss horizontal linear shift statistics.

2. MATERIALS AND METHODS

Satellite optical multispectral imagery acquired by MSI sensor aboard Copernicus Sentinel-2 satellite constellation have been used for the analysis of horizontal linear local shifts. The high spatial resolution (10 m, 20 m and 60 m), the high revisit time (5 days with two satellites), and the 13 spectral bands (from the visible to shortwave infrared) are the characteristics of the Sentinel-2 Multi-Spectral Instrument (MSI) sensor. All Sentinel-2 MSI acquisitions (bottom of atmosphere reflectance – L2A) acquired in the period November 2015 – January 2023, with cloud cover lower than 90%, were collected for the geographic extent corresponding to Italian national territory (65 granules). Copernicus Sentinel-2 MSI data, processed at level 2A by CNES using MAJA atmospheric correction algorithm, were collected from THEIA Land data center catalogue (61 available granules). Sentinel-2 MSI data processed at level 2A using Sen2Cor atmospheric algorithm, for the remaining 4 granules not available from the above-mentioned catalogue, were collected from the Copernicus Open Access Hub.
Collected satellite acquisitions, representing bottom of the atmosphere reflectance, orthorectified, terrain-flattened and atmospherically corrected, were masked for invalid pixels (cloud, cloud cirrus, cloud shadow, topographic shadow, snow, edge, and high sun zenith angle) and for water areas. Spectral band named B4, corresponding to red radiometric interval (665

* Corresponding author

nm), was used for subsequent image matching in co-registration analysis, as it is used as reference for operational band-to-band Sentinel-2 MSI co-registration (Gascon et al., 2017).
Automated and Robust Open-Source Image Co-Registration Software (AROSICS), designed to perform automatic subpixel co-registration of two satellite image datasets based on an image matching approach working in the frequency domain (Scheffler et al., 2017), was used to identify horizontal linear local shifts. It was selected considering its ability to use a local co-registration approach, and its demonstrated application with Sentinel-2 MSI acquisitions (Stumpf et al., 2018). In addition, the use of Fourier shift theorem should reduce time variability issues (i.e. related to vegetation phenology). AROSICS procedure combines a multistage workflow for effective detection of false positives, including three levels of filtering: i) removal of tie-points with low reliability according to internal tests; ii) SSIM filtering; iii) RANSAC outlier detection. Structural Similarity Index Measure (SSIM) is a weighted measurement of the difference between two images structure, contrast, and luminance discrepancies (Wang et al. 2004). It is used to filter tie-points where shift correction does not increase image similarity. The widely used state-of-the art algorithm RANSAC (Fischler et al., 1981) is capable of interpreting data containing a significant percentage of gross errors and is therefore ideal for applications in automated image analysis in which interpretation is based on the data provided by error-prone feature detectors.

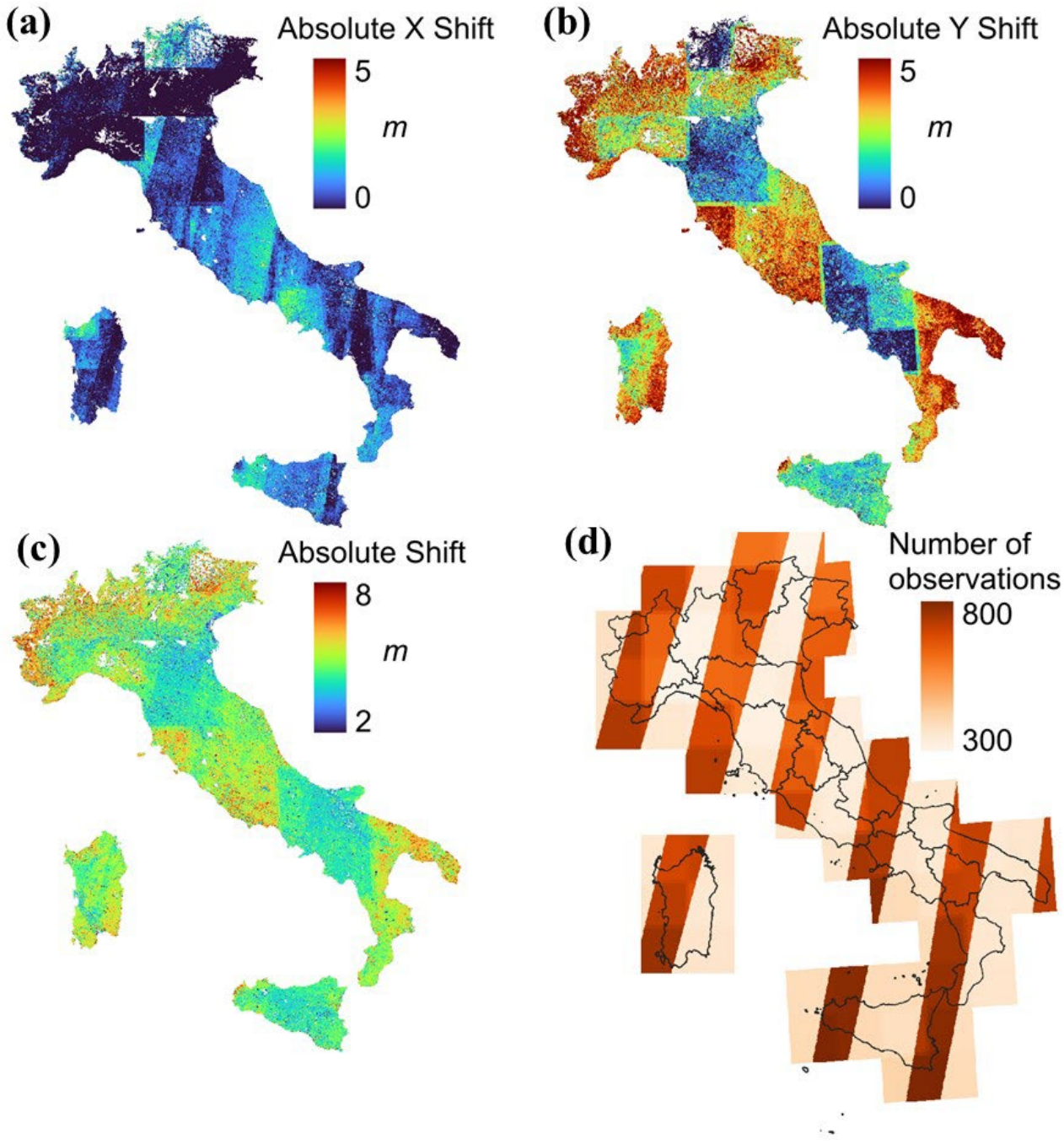

Figure 1. (a) Absolute X shift. (b) Absolute Y shift. (c) Absolute shift. (d) Number of satellite observations (analysed period: November 2015 – January 2023).

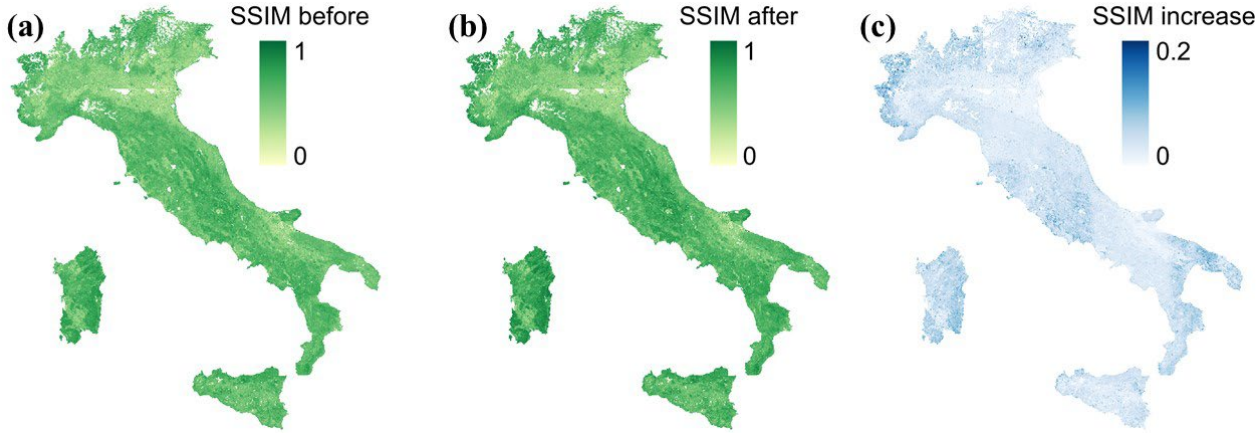

Figure 2. Structural Similarity Index Measure (SSIM) variation.

AROSICS was configured using the following settings: grid size: 1220 m; window size: 64 pixels, max points: 7000; max shift: 5 pixels; minimum reliability: 40%. Co-registration algorithms require that a single satellite acquisition, named master, be selected for image matching with all other satellite acquisitions, names slaves. The master acquisition for each Sentinel-2 granule was selected based on the following criteria: i) be acquired during summer 2021, in order to have a single reference year and avoid snow and ice cover as much as possible; ii) containing as few masked pixels as possible.

Identified horizontal linear local shifts were used to perform statistical analysis on the shift in X and Y directions for several Sentinel-2 MSI processing baselines, valid tie-points, reliability and SSIM variation.

Finally, the identified horizontal linear local shifts were used to generate sets of Ground Control Points (GCPs), that were entered into the Sentinel-2 MSI local Shifts DataBase (S2SDB).

All the analysis was done using software SNAP, AROSICS, Python, QGIS and R-cran.

3. RESULTS AND DISCUSSION

To perform operational image co-registration, Sentinel-2 Shift DataBase (S2SDB) has been established. The S2SDB contains information about horizontal linear local shifts, that can be easily applied to any Sentinel-2 MSI spectral band or spatially explicit derived product, using various image processing software solutions.

Currently, S2SDB provides information about horizontal linear local shifts, for each single Sentinel-2 MSI acquisition over the Italian national territory. It consists in a set of txt file containing Ground Control Points (GCPs), available for both 10 m and 20 m spatial resolution. The text file can be used in several software tools to perform local image warping, in order to improve the spatial co-registration of images acquired at different times. Its purpose is to improve spatial coherence and significantly reduce data processing requirements, as it allows the local horizontal linear shift processing step not to be repeated each time an image temporal stack is generated.

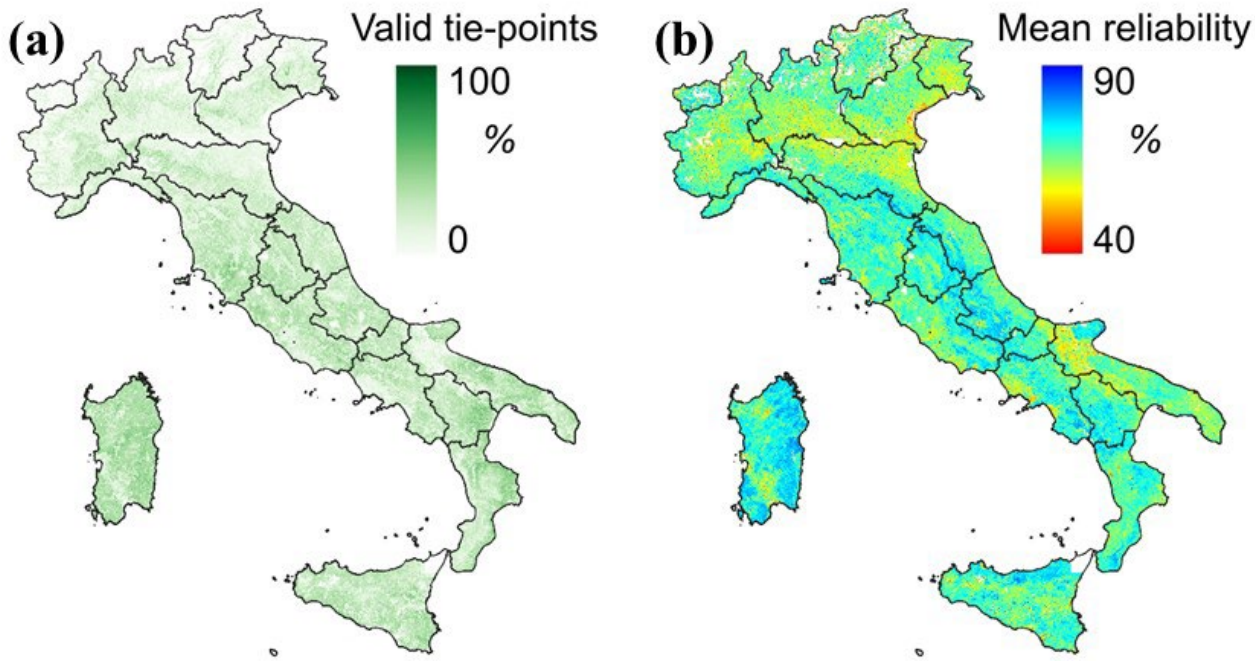

Figure 3. (a) Percentage of valid tie-points. (b) Percentage of mean reliability.

S2SDB features makes it reproducible and suitable for the use in operational services by improving time series consistency at pixel level. S2SDB (version v1) contains GCPs of about 36000 individual Sentinel-2 MSI images, acquired within the period November 2015 - January 2023 and related to 65 Sentinel-2 granules, corresponding to the coverage of Italian national territory. The total S2SDB volume is about 2.11 GB. GCPs file corresponding to satellite acquisitions with 5 or less tie-points remaining after the false positives filtering procedure, was not been generated. S2SDB can be freely accessed at: https://github.com/ffilipponi/S2SDB.

The resulting absolute shifts in X, Y and both directions are shown in Figure 1 maps, along with the number of satellite observations, that clearly represents the overlapping areas of satellites relative orbits.

Maps in Figure 2 shows the SSIM variation, that increases of about 0.1. Figure 3 shows the percentage of valid tie points, that on average reaches 25%, along with the mean reliability, that is lower in cropland areas, probably due to small inter-annual changes in parcels boundaries.

Figure 4 shows the variation in absolute shifts between Sentinel-2 MSI data processing baselines. Baseline 03 and baseline 04 have improved absolute shifts compared to baseline 02. However, there is still field to improve the operational standard products.

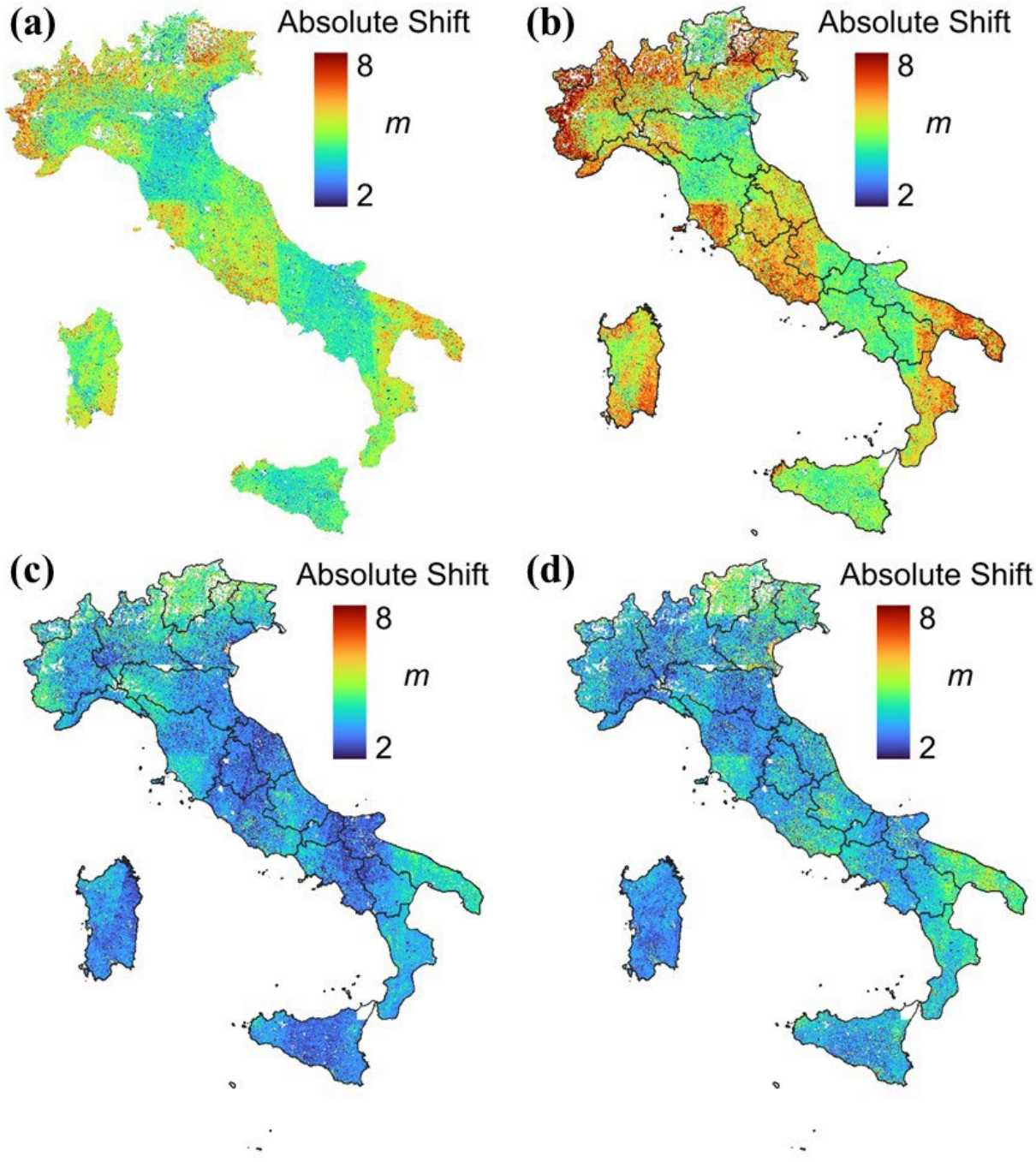

Figure 4. (a) Absolute shift for the full analysed period: November 2015 – January 2023. (b) Absolute shift for baseline 02. (c) Absolute shift for baseline 03. (d) Absolute shift for baseline 04.

Maps in Figure 4, particularly Figure 4b, exhibit greater shifts in correspondence of topographically complex areas. The reasons could be related to a multitude of factors, including the different orbit and the Digital Elevation Models inadequate resolution, in combination with co-registration error patterns in the form of block-like error clusters. Variations in absolute shifts between different baselines, decreasing from baseline 03 onward, suggest the use of different Digital Elevation Models in the process of image orthorectification, that was changed in different baselines for geometric refinement purpose.
Geospatial accuracy of master reference images is still weak and does not correspond to real world. To overcome this limitation, future improvements of the S2SDB should consider using a different master image. Alternatives could be the use of temporal composite to reduce number of masked pixels, the use of satellite optical multispectral VHR data, although there are economic costs issues, or the use of aerial imagery, with issues related to timeliness of release and acquisition date information. Another S2SDB improvement, to be considered for future developments, is the extension of the window size, in order to better deal with partial coverage of the granule extent in some Sentinel-2 MSI acquisitions.
The S2SDB, by releasing simple but relevant information with an open access data policy, can contribute to reduce time and computational effort required to significantly improve Sentinel-2 MSI imagery spatial coherence and time series consistency. Improved co-registration may also contribute to strengthen satellite sensor interoperability by producing denser time series to improve Earth observation land monitoring for a wide range of applications (e.g. forest logging). The information stored in the S2SDB have been successfully used to improve Earth Observation derived products, like phenological metrics estimates (Filipponi et al., 2022).

ACKNOWLEDGEMENTS

This work contains modified Copernicus Sentinel data (2023). Sentinel-2 MSI data used were available at no cost from Copernicus Open Access Hub.

REFERENCES

Cournet, M., Giros, A., Dumas, L., Delvit, J.M., Greslou, D., Languille, F., Blanchet, G. (2016). 2D Sub-Pixel Disparity Measurement Using QPEC / Medicis, *ISPRS - International Archives of the Photogrammetry, Remote Sensing and Spatial Information Sciences*, vol. 41B1, pp. 291–298. https://doi.org/10.5194/isprs-archives-XLI-B1-291-2016

Filipponi, F., Smiraglia, D., & Agrillo, E. (2022). Earth Observation for Phenological Metrics (EO4PM): Temporal discriminant to characterize forest ecosystems. *Remote Sensing*, 14(3), 721. https://doi.org/10.3390/rs14030721

Fischler, M.A.; & Bolles, R.C. (1981). Random Sample Consensus: A Paradigm for Model Fitting with Applications to Image Analysis and Automated Cartography. *Commun. ACM*, 24, 381–395. https://doi.org/10.1145/358669.358692

Gascon, F., Bouzinac, C., Thépaut, O., Jung, M., Francesconi, B., Louis, J., Lonjou, V., Lafrance, B., Massera, S., Gaudel-Vacaresse, A., …, & Fernandez V. (2017). Copernicus Sentinel-2A Calibration and Products Validation Status. *Remote Sensing*, 9, 584. https://doi.org/10.3390/rs9060584

Rufin, P., Frantz, D., Yan, L., & Hostert, P. (2020). Operational coregistration of the sentinel-2A/B image archive using multitemporal landsat spectral averages. *IEEE Geoscience and Remote Sensing Letters*, 18(4), 712-716. https://doi.org/10.1109/LGRS.2020.2982245

Scheffler, D., Hollstein, A., Diedrich, H., Segl, K., & Hostert, P. (2017). AROSICS: An automated and robust open-source image co-registration software for multi-sensor satellite data. *Remote sensing*, 9(7), 676. https://doi.org/10.3390/rs9070676

Stumpf, A., Michéa, D., & Malet, J. P. (2018). Improved co-registration of Sentinel-2 and Landsat-8 imagery for Earth surface motion measurements. *Remote Sensing*, 10(2), 160. https://doi.org/10.3390/rs10020160

Wang, Z.; Bovik, A.C.; Sheikh, H.R.; & Simoncelli, E.P. (2004). Image quality assessment: From error visibility to structural similarity. *IEEE Trans. Image Process.*, 13, 600–612. https://doi.org/10.1109/TIP.2003.819861

Yan, L., Roy, D. P., Zhang, H., Li, J., & Huang, H. (2016). An automated approach for sub-pixel registration of Landsat-8 Operational Land Imager (OLI) and Sentinel-2 Multi Spectral Instrument (MSI) imagery. *Remote Sensing*, 8(6), 520. https://doi.org/10.3390/rs8060520

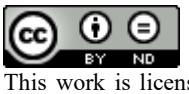

Earth Observation: current challenges and opportunities for environmental monitoring

Edited by
Associazione Italiana di Telerilevamento (AIT)

Trends in Earth Observation is Directly Edited and published by AIT and it is aimed at hosting peer-review contributions that result as an extension of selected contributions to the biannual AIT Congresses. The Volume will therefore be published every two years.

This volume, organized in 4 thematic chapters, includes 34 contributions

Trends in Earth Observation is indexed by scopus and Web of Science

ISSN 2612-7911

ISBN 978-88-944687-2-4